AGARD

ADVISORY GROUP FOR AEROSPACE RESEARCH & DEVELOPMENT

7 RUE ANCELLE, 92200 NEUILLY-SUR-SEINE, FRANCE

AGARD ADVISORY REPORT 305

Cooperative Programme on Dynamic Wind Tunnel Experiments for Manoeuvring Aircraft

(Programme en coopération sur l'expérimentation dynamique en soufflerie pour la manœuvrabilité de l'avion)

Report of the Fluid Dynamics Panel Working Group 16.

North Atlantic Treaty Organization
Organisation du Traité de l'Atlantique Nord

The Mission of AGARD

According to its Charter, the mission of AGARD is to bring together the leading personalities of the NATO nations in the fields of science and technology relating to aerospace for the following purposes:

- Recommending effective ways for the member nations to use their research and development capabilities for the common benefit of the NATO community;
- Providing scientific and technical advice and assistance to the Military Committee in the field of aerospace research and development (with particular regard to its military application);
- Continuously stimulating advances in the aerospace sciences relevant to strengthening the common defence posture;
- Improving the co-operation among member nations in aerospace research and development;
- Exchange of scientific and technical information;
- Providing assistance to member nations for the purpose of increasing their scientific and technical potential;
- Rendering scientific and technical assistance, as requested, to other NATO bodies and to member nations in connection with research and development problems in the aerospace field.

The highest authority within AGARD is the National Delegates Board consisting of officially appointed senior representatives from each member nation. The mission of AGARD is carried out through the Panels which are composed of experts appointed by the National Delegates, the Consultant and Exchange Programme and the Aerospace Applications Studies Programme. The results of AGARD work are reported to the member nations and the NATO Authorities through the AGARD series of publications of which this is one.

Participation in AGARD activities is by invitation only and is normally limited to citizens of the NATO nations.

Published October 1996

ISBN 92-836-1043-1

Printed by Canada Communication Group
45 Sacré-Cœur Blvd., Hull (Québec), Canada K1A 0S7

DISCLAIMER NOTICE

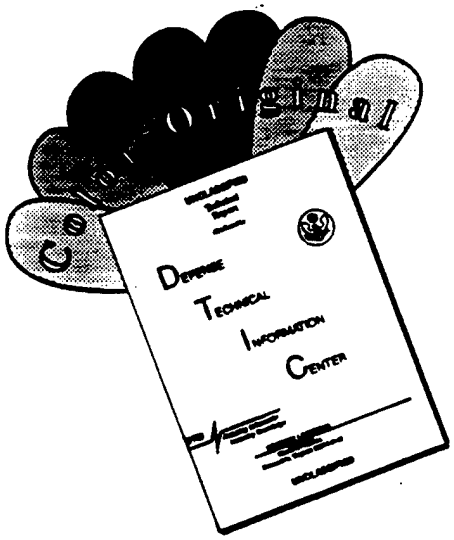

THIS DOCUMENT IS BEST QUALITY AVAILABLE. THE COPY FURNISHED TO DTIC CONTAINED A SIGNIFICANT NUMBER OF COLOR PAGES WHICH DO NOT REPRODUCE LEGIBLY ON BLACK AND WHITE MICROFICHE.

Cooperative Programme on Dynamic Wind Tunnel Experiments for Manoeuvring Aircraft

(AGARD AR-305)

Executive Summary

This report describes a multinational cooperative programme set up by the AGARD Fluid Dynamics Panel in response to the continuing interest among the NATO countries in dynamic wind tunnel testing. Such testing is essential for obtaining the aerodynamic information required to predict the behaviour of an aircraft performing angular motions. At *low angles of attack* this occurs primarily when the aircraft performs a small-amplitude oscillatory motion resulting from a disturbance or a control deflection. The dynamic stability can then be predicted by solving linear equations of motion in which the aerodynamic reactions are represented by the so called stability derivatives, obtainable from oscillatory experiments. At *high angles of attack* this occurs when the aircraft is involved in a spin, in which case rotary-balance data are required, or performs a rapid manoeuvre, in which case both rotary-balance and large-amplitude oscillatory data are needed. Such data are often non-linear and time dependent, compounding the complexity of the prediction and analysis.

The programme consisted of a series of dynamic experiments on models of a schematic combat aircraft configuration and of two generic aircraft forebodies. Ten wind tunnel facilities in seven countries were involved. The primary objectives were (1) to examine the reliability of test techniques and (2) to obtain a data base for dynamic data at high angles of attack. Whenever possible, flow visualization experiments were included to gain a better understanding of the complex flow fields involved.

It was found that for situations where the flow over the model was stable, the dynamic results from different test facilities, for all practical purposes, were consistent. In other cases, the results often displayed a bi-stable character. Thus, despite the unpredictability of the flow in such cases, the tests could still provide a control system designer with the absolute magnitude of the required design loads and the angle of attack at which the flow could become unstable.

The Working Group report, and the technical reports from the participating organizations on which it is based, provide for the first time a unique, comprehensive data base for rotary and oscillatory characteristics of a schematic combat aircraft configuration over a large range of angles of attack. The report also includes comprehensive dynamic results on surface pressures, forces and moments on two forebody configurations, obtained in a pressurized wind tunnel. Such results can be used for validation of future numerical codes in this field.

It is expected that the data and conclusions in this report will prove valuable for the design of highly manoeuvrable combat aircraft, missiles and — perhaps — also high-performance submarines. The data should also provide important inputs for the modelling of aerodynamic reactions in high-fidelity flight and manoeuvre simulators. If included at the design stage, such data may be instrumental in establishing realistic manoeuvre envelopes without compromising safety and at reduced cost.

Programme en coopération sur l'expérimentation dynamique en soufflerie pour la manœuvrabilité de l'avion

(AGARD AR-305)

Synthèse

Ce rapport décrit un programme multinational de coopération instauré par la Commission de la Dynamique des Fluides, en réponse à l'intérêt permanent au sein des pays membres de l'OTAN pour le domaine des tests en soufflerie dynamique. Ce type de test est essentiel pour obtenir les informations aérodynamiques nécessaires afin de prévoir le comportement d'un avion effectuant des évolutions aux incidences critiques. A faible incidence, les premières constatations sont que lorsque l'aéronef s'engage dans un mouvement oscillatoire de petite amplitude, c'est la conséquence d'une perturbation ou d'une diminution de contrôle. La stabilité dynamique peut alors être prévisible en résolvant les équations linéaires du mouvement dans lesquelles les réactions dynamiques sont représentées par les dérivées des équations d'équilibre en vol, obtenues des expérimentations sur les mouvements oscillatoires. A grande incidence, les résultats montrent que lorsque l'aéronefs s'engage en vrille, il faut faire appel aux équations d'équilibre en rotation, ou bien, que lorsque l'aéronef effectue une manœuvre rapide, il faut faire appel simultanément aux données d'équilibre en rotation et à celles des mouvements oscillatoires de grande amplitude. De telles données sont pour la plupart non-linéaires et fonction du temps, augmentant la complexité des prédictions et des analyses.

Le programme a consisté en une série d'expériences dynamiques, sur des modèles de configuration d'avions de combat types, et de deux avions de même genre en stade de développement. Dix souffleries de sept Nations ont été utilisées. Les premiers objectifs étaient d'examiner la fiabilité des techniques de tests, et d'obtenir une base de données pour des résultats dynamiques à grande incidence. A chaque fois que cela était possible, des expériences de visualisation du flux ont été introduites afin de gagner en meilleure compréhension des champs de flux complexes induits.

Il a été mis en évidence que dans les situations pour lesquelles le flux au-dessus de la maquette était stable, les résultats dynamiques en provenance de différents endroits de test étaient réalistes quelque soient les objectifs recherchés. En revanche, en d'autres situations, les résultats étaient mitigés. Cependant, en dépit de la précarité du flux dans les derniers cas cités, les tests pouvaient tout de même apporter une idée des systèmes de contrôle avec un ordre de grandeur des charges du concept testé et de l'incidence pour laquelle le flux pouvait devenir instable.

Le rapport du Groupe de travail, et les rapports techniques des organisations impliquées, fournissent pour la première fois, une base de données unique et accessible pour les charactéristiques en oscillation et en rotation de la configuration d'un avion de combat type, en couvrant un large éventail d'incidences. Le rapport inclut également les résultats dynamiques sur les pressions de surface, les forces et les couples qui s'exerceront sur deux configurations de prototypes, obtenus dans une soufflerie pressurisée. De tels résultats pourront être utilisés pour la validation des futures codes numériques dans ce domaine.

Il est attendu pour l'avenir que les données et le conclusions de ce rapport seront applicables au concept de l'avion de combat de grande manœuvrabilité, aux missiles et, peut-être, également aux sous marins de grande performance. Les données devront aussi contribuer à la modèlisation des réactions aérodynamiques des simulateurs de vol de grande fiabilité. Il peut être envisagé à ce stade de la conception que de telles données pourront être instrumentales dans la réalisation des enveloppes de manœuvre réalistes sans compromettre la sécurité et à coût réduit.

Contents

* Chapter Editors and Reviewers are indicated in Parentheses

* Chapter Editors and Reviewers are indicated in Parentheses

Recent Publications of the Fluid Dynamics Panel

AGARDOGRAPHS (AG)

Turbulent Boundary Layers in Subsonic and Supersonic Flow
AGARD AG-335, July 1996

Computational Aerodynamics Based on the Euler Equations
AGARD AG-325, September 1994

Scale Effects on Aircraft and Weapon Aerodynamics
AGARD AG-323, July 1994

Design and Testing of High-Performance Parachutes
AGARD AG-319, November 1991

Experimental Techniques in the Field of Low Density Aerodynamics
AGARD AG-318 (E), April 1991

Techniques Expérimentales Liées à l'Aérodynamique à Basse Densité
AGARD AG-318 (FR), April 1990

A Survey of Measurements and Measuring Techniques in Rapidly Distorted Compressible Turbulent Boundary Layers
AGARD AG-315, May 1989

Reynolds Number Effects in Transonic Flows
AGARD AG-303, December 1988

REPORTS (R)

Hypersonic Experimental and Computational Capability, Improvement and Validation
AGARD AR-319, Vol. I, Report of WG 18, May 1996

Parallel Computing in CFD
AGARD R-807, Special Course Notes, October 1995

Optimum Design Methods for Aerodynamics
AGARD R-803, Special Course Notes, November 1994

Missile Aerodynamics
AGARD R-804, Special Course Notes, May 1994

Progress in Transition Modelling
AGARD R-793, Special Course Notes, April 1994

Shock-Wave/Boundary-Layer Interactions in Supersonic and Hypersonic Flows
AGARD R-792, Special Course Notes, August 1993

Unstructured Grid Methods for Advection Dominated Flows
AGARD R-787, Special Course Notes, May 1992

Skin Friction Drag Reduction
AGARD R-786, Special Course Notes, March 1992

Engineering Methods in Aerodynamic Analysis and Design of Aircraft
AGARD R-783, Special Course Notes, January 1992

Aircraft Dynamics at High Angles of Attack: Experiments and Modelling
AGARD R-776, Special Course Notes, March 1991

ADVISORY REPORTS (AR)

Aerodynamics of 3-D Aircraft Afterbodies
AGARD AR-318, Report of WG 17, September 1995

A Selection of Experimental Test Cases for the Validation of CFD Codes
AGARD AR-303, Vols. I and II, Report of WG 14, August 1994

Quality Assessment for Wind Tunnel Testing
AGARD AR-304, Report of WG 15, July 1994

Air Intakes of High Speed Vehicles
AGARD AR-270, Report of WG 13, September 1991

Appraisal of the Suitability of Turbulence Models in Flow Calculations
AGARD AR-291, Technical Status Review, July 1991

Rotary-Balance Testing for Aircraft Dynamics
AGARD AR-265, Report of WG11, December 1990

Calculation of 3D Separated Turbulent Flows in Boundary Layer Limit
AGARD AR-255, Report of WG10, May 1990

Adaptive Wind Tunnel Walls: Technology and Applications
AGARD AR-269, Report of WG12, April 1990

CONFERENCE PROCEEDINGS (CP)

Progress and Challenges in CFD Methods and Algorithms
AGARD CP-578, April 1996

Aerodynamics of Store Integration and Separation
AGARD CP-570, February 1996

Aerodynamics and Aeroacoustics of Rotorcraft
AGARD CP-552, August 1995

Application of Direct and Large Eddy Simulation to Transition and Turbulence
AGARD CP-551, December 1994

Wall Interference, Support Interference, and Flow Field Measurements
AGARD CP-535, July 1994

Computational and Experimental Assessment of Jets in Cross Flow
AGARD CP-534, November 1993

High-Lift System Aerodynamics
AGARD CP-515, September 1993

Theoretical and Experimental Methods in Hypersonic Flows
AGARD CP-514, April 1993

Aerodynamic Engine/Airframe Integration for High Performance Aircraft and Missiles
AGARD CP-498, September 1992

Effects of Adverse Weather on Aerodynamics
AGARD CP-496, December 1991

Manoeuvring Aerodynamics
AGARD CP-497, November 1991

Vortex Flow Aerodynamics
AGARD CP-494, July 1991

Missile Aerodynamics
AGARD CP-493, October 1990

Aerodynamics of Combat Aircraft Controls and of Ground Effects
AGARD CP-465, April 1990

Computational Methods for Aerodynamic Design (Inverse) and Optimization
AGARD CP-463, March 1990

Applications of Mesh Generation to Complex 3-D Configurations
AGARD CP-464, March 1990

Fluid Dynamics of Three-Dimensional Turbulent Shear Flows and Transition
AGARD CP-438, April 1989

Validation of Computational Fluid Dynamics
AGARD CP-437, December 1988

Aerodynamic Data Accuracy and Quality: Requirements and Capabilities in Wind Tunnel Testing
AGARD CP-429, July 1988

Aerodynamics of Hypersonic Lifting Vehicles
AGARD CP-428, November 1987

Aerodynamic and Related Hydrodynamic Studies Using Water Facilities
AGARD CP-413, June 1987

Applications of Computational Fluid Dynamics in Aeronautics
AGARD CP-412, November 1986

CHAPTER 1

INTRODUCTION

1.0 GENESIS

There is now considerable interest in highly agile fighter aircraft, capable of flying at high angles of attack and of performing rapid, large-amplitude manoeuvres under such conditions. Such manoeuvres result in highly non-linear aerodynamic characteristics involving, asymmetric and unsteady flows, which also usually contain several systems of vortices. To correctly and efficiently predict such high angle-of-attack rapid manoeuvres, the structure of these very complex flows must be properly understood and the resulting aerodynamic loads must be accurately determined. At the present time, the best way to achieve this is by conducting appropriate wind-tunnel experiments, with aircraft models performing rotary or oscillatory motions, or even - if feasible - a representative combination of these motions. In all cases such dynamic experiments should be conducted at high angles of attack, representative rates, and (for oscillatory motions) also large amplitudes. The oscillatory experiments should preferably include not only angular but also translational motions. The results should include not only aerodynamic coefficients and static and dynamic stability derivatives, but also the effect of time histories and detailed information on the flow fields involved, such as can be obtained by means of pressure measurements and flow visualization studies.

One type of dynamic experiment mentioned above, namely when the aircraft model performs a rotary motion in the wind tunnel, has been reviewed recently by AGARD FDP Working Group 11. The results were published in 1991 as AGARD Advisory Report No. 265 and included, inter alia, a review of the experimental test rigs ("rotary balances") used in the various NATO countries as well as representative rotary test results. It was pointed out that in the 60 years or so of their existence the rotary balances were mostly used for obtaining data required for prediction of the spin characteristics of aircraft (usually general aviation and fighter aircraft). In most cases the data were found to be reliable and sufficient for the purpose for which they were intended.

The present requirement for predictions of rapid high angle-of-attack manoeuvres has opened up a new area for application of rotary-balance data. It was found that some of these applications may require improved data accuracy and a better definition and resolution of results; this may be achieved through a refinement or further development of the present data acquisition and data reduction methods. Also required is a better understanding of the various scale effects and aerodynamic interference effects, inherent in this type of experiment. Furthermore, the new area of application may require studies of rather complex and unorthodox configurations, extension of the speed range to high subsonic speeds and introduction of various perturbations of the basic rotary motion. As mentioned earlier, the data may have to include, in addition to aerodynamic coefficients, also the effect of time histories and information on the flow field around the aircraft.

1.1 OBJECTIVES

The experimental data available to Working Group 11 were insufficient to draw definite conclusions regarding many of the above points. A new AGARD activity, the FDP Working Group 16, was therefore started in 1991 with the primary objective to conduct a rather ambitious, multinational, multifacility collaborative programme of dynamic tests, using a suitably designed schematic fighter configuration. Although the main emphasis of the programme was on reliability of rotary experiments, it was realized at an early stage, that oscillatory experiments (both angular and translational) and combinations of rotary and oscillatory experiments were important integral parts of our experimental arsenal and had to be considered at the same time. Some flow visualization studies and pressure measurements on rotating models were included to enhance our understanding of the flow phenomena under dynamic conditions.

In addition to the experimental activities, the collaborative programme comprised an important analytical part, in which the aerodynamic modelling, aerodynamic analysis, interpretation of dynamic data, as well as flight mechanics applications, were examined. This analytical part was based, to a large extent, on the data obtained in the experimental part of the collaboration.

It is expected that the unique, comprehensive data base obtained and especially the information on the effect of systematic variation of many parameters during the experimental programme will be of direct interest to aircraft project aerodynamicists and that the conclusions and recommendations arising out of the analysis part may offer assistance and guidance to aircraft designers.

1.2 PARTICIPATING ORGANIZATIONS

Six NATO countries, viz. Canada, France, Germany, Italy, the United Kingdom and the United States, participated in the collaborative programme. In addition, a data exchange was established with Sweden. The following organizations in the above countries took part in the activities of the Working Group:

Canada:
- Institute for Aerospace Research (IAR), NRC

France:
- ONERA-Institut de Mécanique des Fluides de Lille (IMFL)
Germany:
- Dornier Luftfahrt GmbH
Italy:
- AerMacchi S.p.A.
- Politecnico di Torino (TPI)
Sweden:
- Flygtekniska Forsoksanstalten (FFA)
United Kingdom:
- Defense Research Agency, Bedford (DRA)
United States:
- Eidetics Corporation
- NASA Langley Research Center

Experiments were performed in wind tunnels of all the above organizations, except for Dornier, Eidetics and NASA Langley. In addition, wind-tunnel experiments were conducted at NASA Ames Research Center. Water-tunnel studies were performed at IAR, AerMacchi and Eidetics.

1.3 INFRASTRUCTURE OF THE WORKING GROUP

The activities of the Working Group were divided into two phases:
Phase 1: Experimental Programme
Phase 2: Analysis and Final Report

Phase 1, the Experimental Programme, was divided into three subprogrammes:

-Subprogramme 1: Rotary Balance Methodology and Rotary Data on a Schematic Fighter Configuration:
- assessment of the accuracy of rotary experiments
  - support interference
  - wind-tunnel wall interference
  - interfacility comparison
- setting up a comprehensive data base for rotary data for a schematic fighter configuration, including effects of:
  - model component build-up (including strakes)
  - angle of attack
  - rotation rate
  - Reynolds Number

All experiments under Subprogramme 1 were conducted with a specially designed AGARD WG 16 configuration, described in detail in Chapter 2. Models were made in two different sizes and were fabricated through joint efforts of several of the participating organizations. The experiments were performed in the following wind tunnels:

- ONERA-IMFL 4m Vertical Wind Tunnel (SV4)
- DLR 3m Low Speed Tunnel
- AerMacchi 2m Low Speed Tunnel
- FFA 3.6m Low Speed Tunnel (Ltl)
- DRA Bedford 13ft x 9ft Low Speed Tunnel
- NASA Ames 7ft x 10ft Subsonic Wind Tunnel

-Subprogramme 2: Prediction of Rotary Aerodynamics and Rotary Data on Forebodies:
- obtaining rotary data (including pressure data under rotary conditions) on a series of generic forebodies
- providing these data for validation of CFD codes for rotary flows (codes being developed outside of the Working Group)

Forebody models (described in Chapter 2) were all manufactured at NASA Langley and all experiments were conducted at DRA Bedford and DRA Farnborough.

-Subprogramme 3: Aerodynamic Analysis of Rotary and Oscillatory Data on a Schematic Fighter Configuration:
- creation of a comprehensive data base for oscillatory data for a schematic fighter configuration, including effects of
  - angles of attack and sideslip
  - frequency and amplitude
  - wind speed
  - time history
  - presence of simultaneous rotation
- provision of data (including flow visualization data) for the analysis and interpretation phase of the WG programme

The same configuration was used as in Subprogramme 1. Oscillations included both angular (pitch, yaw or roll) and/or translational (heave and sway) degrees of freedom. Cross and cross-coupling effects were usually included. The experiments were performed in the following wind tunnels:
- IAR 2m x 3m Low Speed Wind Tunnel
- ONERA-IMFL 4m Spin Tunnel
- ONERA-IMFL 2.4m Horizontal Low Speed Tunnel
- DRA Bedford 13ft x 9ft Low Speed Wind Tunnel

The oscillatory experiments in the ONERA-IMFL Vertical Wind Tunnel were conducted using the unique "oscillatory-coning" capability in that tunnel.

The three Subprogramme Coordinators are named in Section 1.6.

In Phase 2, Analysis and Final Report, the work was organized by chapters. Each chapter had an appointed Editor, whose function was to put together the pertinent information from the other participants in the chapter, select the appropriate material, write the text and organize the figures. Each chapter was then examined by two or three appointed Chapter Reviewers, who sent their comments directly to the chapter Editor, and then by the Working Group as a whole. Chapter Editors and Chapter Reviewers for each chapter are listed in the List of Contents.

The progress of work was chronicled in a series of letters from the chairman to the members of the Working Group. There were 40 such letters.

The present volume constitutes the final report of the Working Group. Its organization is apparent from the List of Contents. After a brief description of the models, facilities

and programmes, the rotary data for the schematic fighter configuration are presented (Chapter 3) and analyzed (Chapter 4). The same is then done with the oscillatory data (Chapter 5,6 and 8). The results for the forebody models are presented in Chapter 7. This is followed by a brief chapter with the summary and conclusions. Included in the appendices are (1) a list of original experimental reports from the participating organizations, with individual test matrices for the experiments on the WG16 configuration, (2) an updated review of rotary balances (first presented in AGARD AR265), (3) a discussion of Reynolds number simulation in high-alpha tests, and (4) a tentative analysis and interpretation of data obtained on the WG16 configuration.

1.4 WORKING GROUP MEETINGS

In the period from 1991 to 1996 the Working Group held six regular meetings:

1. IAR, NRC, Ottawa
   April 4-5, 1991

2. AGARD, Paris and ONERA-IMFL. Lille
   May 11-13, 1992

3. DRA, Bedford
   April 14-16, 1993

4. Politecnico di Torino and AerMacchi, Varese
   April 12-15, 1994

5. DRA, Bedford
   February 13-17, 1995

6. Seville
   September 25-29, 1995

There was also a small editorial meeting at DRA Bedford on March 25-29, 1996.

Considerable assistance as well as most congenial hospitality were extended to the Working Group by the various host organizations, for which the Group expresses it sincere appreciation.

In addition to the above meetings of the full Working Group, the three Subprogrammes were initially discussed and set up at smaller meetings of members participating in these subprogrammes. These meetings were organized in conjunction with some other AGARD or similar activity and were held at:

- Subprogramme 1: Brussels, April 26, 1991
- Subprogramme 2: Bedford, May 1991
- Subprogramme 3: Toulouse, May 1, 1991

1.5 WORKING GROUP MEMBERS

CANADA
- Dr. Martin Beyers
  (Subprogramme 3 Coordinator)
  IAR, Ottawa

- Dr. Kazimierz Orlik-Rückemann
  (Chairman and FDP member)
  IAR, Ottawa

FRANCE
- Mr. Dominique Tristrant
  ONERA-IMFL, Lille

- Mr. Robert Verbrugge (Meeting 1,2,3,6)
  ONERA-IMFL, Lille

GERMANY
- Dr. Bernhard Wagner (Meeting 1,2)
  (FDP member)
  Dornier Luftfahrt GmbH, Friedrichshafen

- Dr. Horst Otto (Meetings 1,2,3,4)
  DLR, Braunschweig

ITALY
- Mr. Livio Visintini
  AerMacchi S.p.A. Venegono

- Prof. Fulvia Quagliotti (Meetings 3,4,5,6)
  (FMP member)
  Politecnico di Torino

UNITED KINGDOM
- Mr. Charles O. O'Leary
  (Subprogramme 1 Coordinator)
  DRA, Bedford

UNITED STATES
- Mr. Joseph R. Chambers (Meeting 1)
  (Deputy Chairman)
  NASA Langley Research Center
  Hampton, Virginia

- Mr. Gerald N. Malcolm
  Eidetics Corporation
  Torrance, California

- Ms. Dana Dunham (Meetings 2,3,4,5,6)
  (Subprogramme 2 Coordinator)
  (alternate to Mr. Chambers)
  NASA Langley Research Center
  Hampton, Virginia

OBSERVERS
- Ms. Dana Dunham (Meeting 1)
  NASA Langley Research Center, USA

- Mr. Lars Fernkrans (Meeting 4)
  FFA, Sweden

CONSULTANTS
- Dr. Lars Ericsson (Meetings 4,5,6)
  USA

- Prof. Fulvia Quagliotti (Meeting 2)
  Politecnico di Torino, Italy

- Dr. Jean Ross (Meeting 2)
  United Kingdom

1.6 ACKNOWLEDGEMENTS

The Working Group expresses its appreciation to the many individuals in various countries who assisted the Working Group members in carrying out their task. This includes, in particular:

CANADA (IAR)
- Ms. Roxanne Préseault (report production and graphics)
- Ms. H.J. Cai (aerodynamic testing and flow field analysis)

FRANCE (ONERA-IMFL)
- M. Marc Vanmansart (graphics and analysis)
- M. Laurent Plackaert (data processing)
- M. Frederic Gauthier (data processing)
- M. Jean-Pierre Evrard (aerodynamic testing, TB)
- M. Christophe Verbeke (aerodynamic testing, PQR)

ITALY (AerMacchi)
- Mr. Roberto Pertile (aerodynamic tests, analysis and reporting; water tunnel test supervision)
- Mr. Francesco Pacori (model manufacture and test supervision)
- Mr. Fausto Giuliani (wind-tunnel tests)
- Mr. Marco Boscolo (water-tunnel model and tests)
- Mr. Paolo Cardi (water-tunnel model and tests)

ITALY (TPI)
- Mr. Giorgio Guglieri (aerodynamic testing)
- Mr. Attilio Parodi (graphics)

SWEDEN (FFA)
- Mr. Farshad Rafatnia (wind-tunnel tests and reporting)

UNITED KINGDOM (DRA)
- Mr. Brian Weir (wind-tunnel tests and data processing)
- Mr. Jon Walker (wind-tunnel tests and data processing)

UNITED STATES (Eidetics)
- Mr. Brian Kramer (aerodynamic testing, analysis, graphics)
- Mr. Carlos Suarez (aerodynamic testing, analysis, graphics)

UNITED STATES (BAR)
- Mr. J. Ralston (wind-tunnel tests, reporting)
- Mr. H. Pauley (wind-tunnel tests)
- Mr. E. Dickes (wind-tunnel tests)

CHAPTER 2
ROTARY AND OSCILLATORY EXPERIMENTS

2.0 INTRODUCTION

The cooperative programme of rotary and oscillatory experiments was carried out over a period of approximately two years in several countries. This chapter presents a description of the different rigs, models, test techniques and facilities. Only fairly general descriptions will be given: references to other reports giving full details of the rigs and facilities are given in the text. The rationale for the various tests made is also stated but details of the model configurations, model attitudes, wind-tunnel conditions, etc. are given in the chapters describing the results.

Organisations participating in the programme of testing and type of test made are shown in the table below. In addition, to help in the interpretation of wind-tunnel test results, water-tunnel tests were carried out by AEM, EI and IAR. The objective of these tests was to visualise the flow under steady and rotary conditions for the main configurations of interest. A brief description of the facilities, models and test programmes is given in the relevant sections. Nomenclature used in the report is predominantly that used by NASA. Exceptions will be noted in the text.

Organisation	Type of test	Section
AerMacchi (AEM), Italy	Rotary	2.2
Defence Research Agency (DRA), United Kingdom	Rotary & Oscillatory	2.3
Deutsche Forschungsanstalt für Luft und Raumfahrt (DLR), Germany	Rotary	2.4
Eidetics Corporation/NASA Ames (EI), USA	Rotary	2.5
Institute for Aerospace Research, (IAR), Canada	Oscillatory	2.6
Institut de Mécanique des Fluides de Lille (ONERA-IMFL), France	Rotary & Oscillatory	2.7
Politecnico di Torino (TPI), Italy	Oscillatory	2.8
Flygtekniska Försöksanstalten (FFA), Sweden	Rotary	2.9
NASA Langley/Bihrle Applied Research/DRA	Rotary (pressure measurements)	2.10

Table 2.1 Participating organisations and tests made

2.1 DESCRIPTION OF MODELS TESTED

2.1.1 Model Configuration

The configuration selected for the cooperative programme is shown in Fig 2.1. It is based on the Langley/Eidetics generic combat aircraft model (Ref 1). The body is cylindrical with a tangent-ogive nose of relatively high fineness ratio, i.e. l/d = 4. The wings, tail surfaces and leading edge root extensions (LEX) are of flat-plate section with chamfered leading and trailing edges and tips. Wing leading edges are swept at 45°. Models were manufactured to allow configuration build-up tests with body alone (B), body-wing (BW), body-wing-LEX (BWL) and body-wing-LEX-horizontal/vertical tails (BWLHV). During initial tests (Ref 2) the models were fitted with forebody strakes (S) and cross-flow transition fixing (T) as described below in 2.1.4 and shown in Fig 2.2

Three models were manufactured for testing in Europe and North America and designated WG16A, WG16CA and WG16B. The WG16A and WG16CA models are nominally identical but WG16B is smaller, at 0.73 the scale of the other two models.

2.1.2 Model WG16A

This model (Fig 2.3) was designed by ONERA-IMFL. The fuselage was manufactured by Aermacchi, the tail setting discs by DRA and the wings, LEX and tail surfaces by DLR. The model was assembled and inspected at the Politecnico di Torino.

The body was turned from aluminium alloy in six sections, 1.5 mm thick, with integral formers for local stiffness and strength, especially where wings and tail surfaces were attached. One section forms the balance adaptor which was manufactured, to their own requirements, by each organisation testing the model. For most of the tests the model was rear sting mounted but an aperture with closure plate was provided in the central part of the body for bottom or top-entry sting mounting.

The wings and tail surfaces are made of aluminium alloy/honeycomb sandwich material: 1 mm thick plates bonded on to a honeycomb core. The edges of the surfaces, which are all 40° included angle, are made of glass-epoxy composite. Wing and vertical tail root fittings are aluminium alloy but the adjustable horizontal tail fitting is steel. The LEX is made of plastic.

The model weighs approximately 6.5 kg; with some variation due to the particular balance adaptor fitted.

2.1.3 Model WG16CA

This model is identical to WG16A in its external dimensions. It was manufactured by IAR based on IMFL's original design, which had been locally modified. Three noses were manufactured, one of which has a rotatable tip. The nose strakes were attached by means of a precision jig. For the complete configuration (BWLHVST), 0.3 mm grit (60#) was applied in strips. An adapter with an internal steel sleeve and bulkhead construction was designed to fit onto the oscillatory balance. The model was statically balanced, so that its CG is located at the reference centre. The model mass is 7.5 kg.

2.1.4 Model WG16B

This model (Fig 2.4) was designed and manufactured at DRA Bedford, primarily for testing on rotary balances. It is constructed mainly from aluminium alloy and weighs about 10 kg including balance adaptor. Two aft-bodies are available, with wings and without. The other surfaces are removable, allowing model build-up tests. Horizontal tails can only be set at zero deflection. The model can be mounted on either a rear-entry or top-entry sting (for high-α tests). The only geometrical difference, apart from scale, between this model and WG16A is that the wing tips are chamfered at 60° instead of 40° included angle.

2.1.5 Nose Strakes and Transition Tripping

It is well known that the flow on high-finess ratio forebodies, such as the one on the WG16 model, are characterized by asymmetric vortex flow regimes at angles-of-attack above a certain onset value. For values of angles-of-attack above onset of asymmetry the flow is highly dependent on model micro-asymmetries and random disturbances and also on boundary layer transition positions and test Reynolds number. Although the high sensitivity of the test configuration may be desirable for highlighting any spurious interference effect, the random character of asymmetric vortex flow may also make the interpretation of test results an impossible task. For this reason it was decided that the test should not only consider the basic clean forebody, but also an alternate configuration where the flow was manipulated in a way to make it more predictable and repeatable. This could be obtained by avoiding random effects due to uncertain boundary layer transition and by fixing the separation points on the apex of the forebody by using nose strakes. Position and size of such devices were selected during initial tests of model B at DRA[3] and based on previous experience.

Grit strips were applied at radial positions ±40° along the forebody from the nose apex to the start of the LEX. Forebody strakes (Fig 2.2) were fitted at radial positions of ±105°, one fuselage diameter in length and 0.1 diameters in height above the forebody surface at the trailing edge. The strakes were attached perpendicular to the forebody surface. Transition tripping was fixed at radial locations ±40° from bottom centreline running from the tip of the nose to the LEX apex. During the course of tests at the different organizations two different types of transition devices were used;

- "grit" bands of 0.2 to 0.3mm height , used by DRA, EI and FFA.
- strips of resin disks consisting of one row of micro-cylinders of the same 0.2 to 0.3mm height as above, 1.0mm diameter and equispaced 2.5mm, used by AEM, TPI, IMFL and FFA.

Although the purpose of both transition tripping devices was the same, their effectiveness could not be investigated and spurious effects due to their relatively large size cannot be ruled out, given the difficulty in actually forcing boundary layer transition at the low local Reynolds numbers typical of all WG16 model tests.

2.2 AERMACCHI (AEM), ITALY

2.2.1 Description of the Static and Rotary Balance

Tests were made on both static and rotary balances. The static balance (Fig 2.5) is a rear sting support mounted on a vertical strut and allows angle of attack variation in the range 0° to 45°. Tests on rotary balance were made on the standard Aermacchi rotary balance which is unchanged from the description included in Ref. 3. A rear cranked sting was used for $\alpha \leq 40°$ and a top sting for $\alpha > 40°$ (Fig 2.6).

For model WG16 A a comparison of top and rear sting results was made for $\alpha = 30°$ and 40°. Figure 2.7 shows model WG16A in the open wind tunnel on the top-entry sting of the rotary balance.

The test procedure is as follows:

1 Set up model configuration, attitude and approximate balance of the rotating assembly.
2 Obtain wind-off data at a set of positive and negative rotation rates (normally 5 values each).
3 Obtain wind-on data for the required set of test

points. Test points are normally taken from maximum negative rotation speed to maximum positive rotation speed.

The data reduction procedure is sketched in Fig 2.8 and includes some up-dates on that given in Ref 3 as follows:

* The balance calibration matrix includes second order interactions.

* Inertia tares and balance offset are measured by taking a total of ten wind-off measurement, five speeds in both clockwise and counterclockwise directions. A linear interpolation is then made between adiacent points after subtraction of the small amount of damping which is assumed to be proportional to rotation speed.

* Gross aerodynamic forces and moments acting on the model wind-off and wind-on are obtained immediately after data acquisition.

2.2.2 Description of Wind Tunnel

The AEM wind tunnel used for tests of WG16 A and B models is a low speed, open jet, 2m diameter circular test section tunnel with a closed, single return circuit. Tests can also be made with a closed test section by fitting removable transparent walls. A fixed pitch five bladed fan, driven by a 820 HP direct current motor, gives a wind tunnel speed up to 85 m/s (280 ft/sec) but usual test speeds are 50 and 60 m/s (164 ft/sec , 197 ft/sec). The dimensions of the usable jet are: length = 1.7 m (5.6 ft), diameter = 1.4 m. (4.6 ft). The contraction ratio is 5.18 and turbulence level is below 1% RMS.

2.2.3 Summary of Test Programme

Static balance tests were made on model WG16B in different configurations and have been used for comparison with rotary balance results at zero rotation and with similar static results from other wind tunnels.

Rotary balance tests were made in open and closed wind tunnel test sections with both models WG16A and WG16B. Different model supports were used, allowing evaluation of wind tunnel wall and model support interference effects.

Effects of nose strakes, boundary layer transition tripping, Reynolds number and angle-of-sideslip were also investigated.

2.2.4 AEM Water Tunnel and Rotary Rig Description

Water tunnel flow visualization in rotary flow conditions were conducted at AEM using a water tunnel designed and built by Eidetics International which has been in operation since 1989 (Fig 2.9). It is a continuous flow water tunnel with a horizontal test section 36" high by 24" wide by 72" long. (0.91x0.61x1.83 m). The test section has glass sides and bottom. The model can also be observed through a downstream window. Water velocity can be varied continuously up to 1.3 ft/sec (0.4 m/s). The water tunnel normally uses a remotely operated rear sting support.

During 1992 a rotary rig support was designed and built by AEM in order to allow the visualization of flows in rotary conditions.

Figure 2.10 shows, in schematic form, the main elements of the rotary rig. An electric motor with a reduction box is mounted above the water tunnel hinged cover and rotation is transmitted to the immersed shaft by a cogged pulley placed inside a shrouded stem. The vertical model support is fairly long to avoid upstream interference. Deflection of the support is insignificant because forces generated during water tunnel tests are very small.

The immersed shaft, on the centerline of the water tunnel, rotates on two ball bearings. The shaft is coupled to a dye distributor downstream and supports the rotary arm via a clamp upstream. The dye distributor provides a continuous supply to the model during rotation. A screw on the clamp allows rotary arm radius to be changed. A sting is mounted on the rotary arm with a facility for setting incidence and roll angle. The entire rotary rig is fixed to the water tunnel hinged cover for ease of access to the model.

2.2.5 Model and Water Tunnel Test Program

The water tunnel model, manufactured in aluminium alloy by AEM, is 1:3.5 scale relative to model A. The fuselage is made in two sections and is hollow to allow passage for the dye tubes. The forebody has four longitudinal rows of 6 holes each for dye injection. Another four dye injections are made at the LEX apex and at the LEX-wing leading-edge junction. The model is painted white for clear flow visualization and photography.

The aim of this water tunnel investigation was the study of the characteristic flow patterns on the WG-16 model in the range of angles of attack from 24° to 60° as investigated in wind tunnel tests at zero and non-zero rotation rates. Tests were made on WG16 complete configuration (BWLVHTS) and with strake off (BWLVHT). Also the model support components of other research organisations conducting rotary balance tests were represented, as show in Fig 2.11 Possible qualitative interference effects of these components with the vortical flow system of the forebody, difficult to detect in wind tunnel experiments, could be shown. By changing the size of the supports, the effect of model scale could also be studied.

The program for flow visualization tests is summarised in Fig 2.12

2.3 DEFENCE RESEARCH AGENCY (DRA), UNITED KINGDOM

2.3.1 Oscillatory Rig

2.3.1.1 Description

The main component of the rig, shown in Fig 2.13, is a model support sting which can be oscillated in five degrees

of freedom, i.e. pitch, heave (plunge), yaw, sideslip and roll. Forces acting on the model are measured by a strain gauge balance which is integral to the sting. For all modes except the roll mode the flared downstream end of the sting is mounted on a swinging arm assembly which converts a rotational shaft drive on the wind-tunnel axis to oscillatory harmonic motion using a 'scotch yoke' slider-in-slot mechanism. Amplitude of the motion is varied by adjusting the throw of the slider within a limit of ±50 mm. The slot is aligned horizontally for pitch and plunge motion and vertically for yaw and sideslip motion. Change of alignment is accomplished by rotating the whole assembly through 90°. The sleeve mounting for the swinging arms fits over the shaft housing and the base plate is bolted to the support structure in either of the two positions. For translational motion, i.e. heave and sideslip, the swinging arms are parallel. For pitch and yaw motion the rear stationary pivots of the swinging arms are moved further apart as shown in Fig. 2.13 b.The centre of oscillation coincides with the balance axis. Frequency of oscillation is dependent on shaft speed which is controlled by a servo valve. For the roll mode the shaft is rigidly connected to the sting and an oscillatory signal to the servo valve gives the required oscillatory motion about the sting axis.

A hydraulic power pack, situated outside the wind-tunnel working section supplies the motor with fluid at 1500 psi pressure via a rigid pipe and swivel joint linkage. The whole assembly is mounted on a carriage which is traversed along the twin support quadrants to vary angle-of-attack up to a limit of 42°. Model motion is measured with an accelerometer in the model, linear for plunge and sideslip tests and angular for pitch and yaw tests. For the roll mode, an LVDT measures model displacement. The accelerometer signals are also used to cancel inertial loadings on the strain gauge balance. The sensitive axes of the accelerometers are re-aligned in the appropriate direction for each type of test.

2.3.1.2 Method of test

Before wind-tunnel testing the accelerometers and the strain gauge balance are calibrated and first order balance interactions are removed by means of a signal mixing unit. With the model mounted on the balance, signals due to inertial loading are cancelled, wind-off, at the required test frequencies using the accelerometer tare controls on the mixing unit. For wind-on tests, at the desired frequencies and amplitudes, the measurements are further corrected by subtracting residual wind-off signals at the same frequency and amplitude. For the pitch, heave, yaw and sideslip modes the amplitude is set by adjusting the throw on the slider and frequency is set by adjusting the speed of the hydraulic motor. For roll tests frequency and amplitude are set on the electronic control system. The angle-of-attack range is normally 0° to 42°.

Tests were made in the 13ft x 9ft (4m x 2.7m) Low Speed Wind Tunnel at DRA Bedford. This is a closed circuit, atmospheric pressure, continuous operation facility with a very low turbulence level of 0.025% longitudinal at maximum speed of 90 m/s. The present tests were made at 25 m/s for longitudinal tests and 30 m/s for lateral tests.

2.3.1.3 Summary of test programme

Model WG16A was tested to investigate the following effects:

a. Nose strakes and forebody grit strips
b. Leading edge root extension (LEX)
c. Oscillation frequency

Tests were made in five degrees of freedom to obtain a complete set of small amplitude longitudinal and lateral stability derivatives.

2.3.2 Rotary Balance

2.3.2.1 Description

A diagram of the apparatus in the 13ft x 9ft Low Speed Wind Tunnel is shown in Fig 2.14. A five component balance (axial force excluded) is machined on to the end of the sting which can be axially rotated by means of a worm and wheel mechanism in the sting carrier (crank). The root end of the sting fits into a socket in the carrier and is clamped with pinch bolts. The sting can be traversed along the rotor to vary angle of attack in 1° increments. Three sting cranks are available to cover angle-of-attack ranges: a. -12° to 40°, b. 8° to 60°, and c. 50° to 100° (top-entry sting). Weights can be fixed to the ends of the rotor to maintain static balance. The rotor is is mounted on the drive shaft by means of a tapered joint. The shaft runs in bearings in a cast steel housing and is driven, through a 3:1 reduction gearbox, by a hydraulic rolling vane motor. A pump unit situated outside the working section of the wind tunnel supplies the motor with fluid at 1500 psi pressure. Rotational speed is controlled by a servo valve with feedback from a tacho-generator geared to the drive shaft. Strain gauge balance signals are brought out by a cable through a bore hole in the drive shaft and a slip-ring unit at the motor end of the shaft. Vibration level on the rig is continuously monitored with an accelerometer on the forward shaft bearing housing.

2.3.2.2 Test procedure

Prior to installation of the apparatus in the wind tunnel it is necessary to statically balance the rotating assembly, i.e. the rotor, sting carrier, sting and model. With the sting carrier set at each of the test angles of attack weights are added to the weight carriers to balance the assembly about the axis of rotation. Balance weights applicable to each angle of attack are noted for use during the wind-tunnel tests.

When the apparatus has been assembled in the working section of the wind tunnel the sting is set at zero angle-of-attack and the strain-gauge balance is calibrated in the usual way by static loading. The amplified balance signals are passed through an 'interaction matrix' with variable potentiometers to cancel outputs on channels other than the loaded one.

After calibration the model is assembled on the balance and the test procedes as follows:

1. Model configuration and angle of attack are set as required and the appropriate balance weights fitted.
2. With wind off, the model is rotated and readings are taken over a range of clockwise (positive) and counterclockwise (negative) speeds.
3. Then, at identical rotation speeds to those set

wind-off, balance data are recorded for each wind speed required. For each direction of rotation, data are recorded starting at zero rpm, increasing incrementally to the maximum rpm.

2.3.2.3 Summary of test programme

The aims of the tests were:

a. To establish a forebody configuration for which the characteristics were relatively insensitive to minute variations in the surface finish of the model and to wind-tunnel test conditions (temperature, humidity, and turbulence level) such that:
   (i) sideforces at zero rotation were small for all angles-of-attack,
   (ii) force variations with positive and negative rotations were continuous and of similar magnitude

b. Test the basic model at angles-of-attack from 0° to 90° using rear and top-entry model supports.

c. Obtain some test data on the effects of model components, eg leading edge root extension (LEX), at selected angles of attack.

2.4 DEUTSCHE FORSCHUNGSANSTALT FÜR LUFT UND RAUMFAHRT (DLR), GERMANY

2.4.1 Description of Apparatus

The rotary balance and working section of the 3.25m x 2.8m low speed wind tunnel are shown in Fig 2.15. The required capabilities and the range of simulation which have been established for the development of the rotary balance are also shown in Fig 2.15. The present test arrangement allows rotary coefficients to be determined in the horizontal wind tunnel by means of a measuring system similar to that used for steady force and moment measurements.

Tests with the rotary balance can be conducted up to a unit Reynolds number of 5.5 x 10^6 per meter in the closed, variable slotted and open test sections of the wind tunnel. The rate of rotation may be varied up to 300 rpm in either clockwise or counterclockwise direction.

The specified total range of angle of pitch between 10° and 90° is covered by using three different interchangeable stings. The angle of sideslip is manually adjusted by rotating the front part of the sting about its axis, which is the longitudinal or vertical body axis of the model, depending on the sting being used.

The rotary rig has the capability of changing the angle of pitch remotely within a range of 30°, even during rotation and wind-on conditions. This capability allows the engineer to set the angle of pitch continuously, to increase the test efficiency and to better investigate hysteresis effects in the stall and post-stall regimes of rolling or spinning aircraft.

2.4.2 Measurment and Control System

In general, the measuring technique applied to the rotary balance corresponds to the conventional technique that is used to measure steady forces and moments acting on a model in the wind tunnel. The rate of rotation of the balance is kept constant by an electro-hydraulic control system. The angle of pitch can be set remotely. The measuring system is organized as follows:

- measurement of the mean values of tunnel parameters by integrating digital voltmeters
- measurement of the mean values of the angle of pitch by an integrating digital voltmeter via a slip-ring unit
- measurement of forces and moments using a six-component strain-gauge balance
- measurement of the rate of rotation using trigger impulses by a fast ADC via a slip-ring unit
- storing of the signal history and integration of the signals numerically in the computer
- data output (listing, diagrams)

While the signals of relevant data representing the test conditions are fed over integrating digital voltmeters into the computer, all analog signals from the rotating system are converted by a fast ADC and transferred to an HP 1000 computer. In rolling tests the model is subject to periodic gravity loads superimposed on the steady aerodynamic and inertial loads. The fast digitizing of the balance signals allows the investigator to study the time history of each individual signal of the balance and to check for distortions.

2.4.3 Test Procedures

It is possible to prepare a test sequence by first acquiring the rotary data for wind-off conditions in the parking/calibration room of the rig for all configurations to be tested. However, in order to prevent any error in the final results, wind-off data normally are measured in the tunnel. A test sequence, consisting of test runs with and without airflow, is usually carried out so that all parameters such as the angle of attack and sideslip and the dynamic pressure are kept constant while the rate of rotation is altered in steps.

Damping derivatives due to rolling at sideslip conditions are obtained by manually setting the angle of roll at the sting and remotely setting the angle of pitch.

For all these test sequences, a complete set of data, consisting of:
- rate of rotation
- angle of pitch/attack
- angle of roll
- angle of yaw
- dynamic head
- six aerodynamic coefficients
- static pressure
- static temperature

- reduced frequency
is obtained for every individual rate of rotation.

The zero point of the balance is read at the beginning and end of a test run for a slowly rotating model (4 rpm). The inertial forces resulting from the slow rate of rotation are negligibly small. However, the resistance of the slip rings can be better accounted for when the model is in motion. The second reading of the zero point at the end of a test run is used to correct for the zero point drift of the balance signals during the course of the test sequence.

2.4.4 Summary of tests made

This information is not available.

2.5 EIDETICS INTERNATIONAL/NASA AMES (EI), USA

2.5.1 Description of Rig

The Eidetics/Ames rotary-balance apparatus is a modified rig developed originally at NASA-Ames and last used in 1983. It is driven by a hydraulic pump and motor system with a tachometer used as feedback to a servo-valve for speed control. New hardware to support the model was recently designed by Eidetics International and constructed for tests with an F/A-18 model to investigate forebody vortex control techniques under rotating conditions. The same hardware was used for this test. The maximum rotation speed for the new hardware is 350 rpm. Figures 2.16 and 2.17 show the new apparatus as installed in the 7ft x 10 ft wind tunnel, including a C-strut, strut arm and sting. The angle of attack is adjusted with discrete positions of the sting/clevis on the C-strut (0 to 60° in 3° increments) and sideslip angle is set by rolling the sting in the strut arm. The balance signals are brought across the rotating interface by cables running through a hollow motor drive shaft and a 50-channel slip ring unit mounted near the rear of the motor. For each discrete angle of attack setting the rig is statically balanced by adding or subtracting weights on the end of the C-strut.

2.5.2 Summary of Test Conditions

Most of the model configurations were tested at three different free stream velocities, 200 ft/sec (60 m/s), 150 ft/sec (45 m/s), and 100 ft/sec (30 m/s) in order to assess Reynolds number effects. The corresponding Reynolds numbers were 0.955, 0.720, and 0.478 x 10^6 based on wing mean aerodynamic chord of 0.758 ft, or 0.302, 0.226, and 0.151 x 10^6, based on the fuselage diameter of 0.2394 ft. All of the various configurations from body alone to full configuration were tested at angles of attack of 24°, 39°, and 51° and only the full configuration at 60°. Some of the configurations, primarily those without strakes, were tested only at the high and low Reynolds numbers.

2.5.3 Description of Eidetics Water Tunnel Rotary Balance Rig

Eidetics has developed a rotary balance test capability for their Model 2436 Flow Visualization Water Tunnel. The tunnel has the same basic configuration as the AerMacchi tunnel (also built by Eidetics) shown in Fig. 2.9. The basic model support is also similar. However, the rotary balance apparatus and the method for driving it are different from the Aermacchi rotary balance rig shown earlier in Fig 2.10. The Eidetics rig is shown in Fig 2.18. The model support roll-drive mechanism is used to rotate the C-strut mechanism about the wind (water) axis. The angle-of-attack is adjusted by manually positioning the arm and sting at any angle between 0° and 60°. Roll angles (or, in effect, sideslip angles) can be set by rolling and clamping the sting in the arm. Simultaneous flow visualization and force/moment measurements can be obtained by using a new waterproof high sensitivity 5-component balance (axial force excluded). The method of testing provides for 2 or 3 revolutions of the model in each direction while acquiring data. Limiting the number of rotation cycles eliminates the need for either slip rings or a "fluid" slip ring to pass the coloured dye across the rotating interface to the model. Both the balance wires and the dye tubes are allowed to wrap up behind the rotary rig by leaving a generous service loop. Results from the water tunnel tests will be discussed in Chapter 4.

2.6 INSTITUTE FOR AEROSPACE RESEARCH (IAR), CANADA

2.6.1 Wind Tunnel, Model and Support System

The tests were conducted in the IAR 2m x 3m Low Speed Wind Tunnel, a continuous flow facility operating at ambient test section pressures and temperatures in the speed range up to 120 m/s. The maximum attainable Reynolds number is 8.1 x 10^6 per meter. The turbulence intensity, σ_v, determined from the standard deviation of the streamwise velocity component near the test section centreline, averaged over Nt periods of 0.25 s, was measured as shown in Table 2.2. With the WG16CA model at $\alpha = 39.5°$, there was an increment in σ_v at 75 m/s such that $\sigma_v = 0.19\%$.

The model was sting-mounted in the wind tunnel. The sting protruded from a strut cantilevered through the wind tunnel floor. A moving section of the floor travels with the strut and connects with roll-up mechanisms on either side of the test section. When the strut moves in an arc with a centre on the model rotation axis the pitch angle of the model could be changed in the range $-40° \leq \sigma \leq 40°$. Higher pitch angles, up to a maximum of $\sigma = 54°$, could be attained by offsetting the sting. The layout of the asymmetric support system is shown in Fig 2.19.

In order to eliminate or alleviate the effect of support asymmetry, a non-structural image strut providing the mirror image of the real strut was installed in some of the high-α tests. A view of the test installation with the image strut in the wind tunnel is shown in Fig 2.20.

V_∞	σ_v	sampling rate	N_t	filtered frequency
30 m/s	0.12%	5,000	52	<2,500 Hz
75 m/s	0.15%	20,000	13	<10,000 Hz

Table 2.2 Turbulence intensity in IAR wind tunnel

2.6.2 Oscillatory Balance

The 15,000 N pitch / yaw forced-oscillation apparatus was developed to investigate the dynamic characteristics of aircraft models at high angles of attack. The apparatus comprises a driving / positioning system (aft end), and an oscillating mechanism and dynamic balance (front end).

The driving system provides precise harmonic motion. The operating frequencies are in the range 0-15 Hz. A clutch-operated mechanism with a precise angular encoder is used for remote adjustment of roll angle in the range -150° to 180°. Combining roll angles with pitch angles permits testing at arbitrary angles of sideslip.

The dynamic balance consists of a 5-component measuring element and a cross-flexure pivot. Both of them were gauged to measure the aerodynamic loads acting on the model and indicate the instantaneous attitude of the model and information on the primary motion of the system. Several oscillation amplitudes in the range 0.4° to 1.5° are available by adjusting the cam eccentricity. A novel balance design provides not only high enough sensitivity, but also a large load capacity:

Normal Force	15,000 N
Side Force	10,000 N
Pitch Moment	1,000 Nm
Yawing Moment	1,000 Nm
Rolling Moment	150 Nm

The operation in various oscillatory modes was controlled by a computer. The data were recorded on-line and processed in real time.

2.6.3 Data acquisition and reduction system

The data acquisition and reduction system is used to obtain the in-phase and quadrature components of the balance outputs synchronous with primary deflection, to reduce the dynamic data and finally to calculate the aerodynamic derivatives.

As is well known, during the tunnel tests the balance signals are contaminated with noise due to flow unsteadiness and electronic pickup, etc. The following methods, based on analogue or digital techniques, have been implemented in the present system to extract the desired signals in the significant noise environment.

(a) The products of the balance outputs with reference signals were low-pass filtered to eliminate the alternating components, yielding DC values proportional to the desired signal components.

(b) The information is obtained either in the time domain, by cross-correlating an in-phase reference signal with the pertinent balance outputs, or in the frequency domain, using Fast Fourier Transform (FFT) techniques to obtain the amplitude and phase of the reactions with respect to the primary deflection.

The various analog signals originating from the balance and other transducers are amplified and filtered prior to being digitized by a 16-channel A/D converter. The data reduction flow diagram is shown in Fig 2.21

2.6.4 Summary of Test Programme

The BWLHV, BWLHVST and BWHV configurations were tested in the IAR 2m x 3m Low Speed Wind Tunnel at the following test conditions:
velocity: 20, 25, 30, 70 m/s
angle of attack:from: 0° to 53°
angle of sideslip: 0°, ±5°, ±10°
tail deflection: 0°, ±30°
mode of motion: static, pitching/yawing oscillation
amplitude: 1.2°, 0.5°
frequency: 5 Hz
In addition, some surface oil flow and laser sheet flow visualization was conducted in static tests.

Various factors were investigated that influenced the static aerodynamic coefficients and the static and dynamic force and moment derivatives. They were tip geometry, Reynolds number, configuration, sideslip, amplitude, horizontal tail deflection and support asymmetry.

2.7 ONERA-IMFL, FRANCE

2.7.1 Oscillatory Rig ('PQR')

2.7.1.1 Description of the Apparatus

The test setup allows kinematic representation of the Euler degrees of freedom commonly used in flight mechanics. The heading angle, ψ and roll angle, ϕ can be adjusted, but remain constant through a given test. The third degree of freedom, pitch (θ) is motorised. The system is installed in the IMFL's horizontal wind tunnel which is 2.4 m in diameter and has an open test section. The model is mounted on a rear sting and the rig is designed so that the bulky elements remain outside the airstream during tests (Figs 2.22 and 2.23). For their lightness and strength, composite materials were used for the moving parts (support arms and sting) resulting in the following test capability:

$-20° < \psi < +15°$
$-180° \leq \phi < +180°$
$-90° \leq \theta < 100°$
$\therefore |\dot{\theta}| < 500°/sec, \ |\ddot{\theta}| < 5000°/sec^2$
$V < 50$ m/s

Frequency of the first structural mode is 13.5 Hz with a typical model weight of 3.5 kg
The θ axis is driven by a hydraulic motor, capable of high acceleration and velocity.

2.7.1.2 Test Capabilities
The kinematics of the apparatus are specified in terms of the Euler angles ψ, θ, ϕ and the angles α and β. These relations show that:
- any variation in θ induces a variation in the angle of attack α and/or in sideslip, β for any ψ and ϕ;
- at zero ϕ, the domain ($-90° < \alpha < 100°$; $-20° < \beta < 15°$) can be explored with varying angle of attack and constant sideslip, in which case we have the relation $q = \dot{\theta}$;
- at $\phi = 90°$, the angles of attack and sideslip are interchanged, as are the yaw and pitching rates;
- r and $\dot{\beta}$ are related by the relation $r \cos \alpha = -\dot{\beta}$ and the effects of these parameters can be investigated up to $\alpha = 20°$.

In the static mode, measurements can be made through a very wide range of incidence ($-100° < \alpha < 100°$) for sideslip angles of less than 20°. For $\alpha > 40°$, the carbon fiber support arm is clear of the test section airstream.
Slow α or β sweeps can be performed for static data with no significant rig interference. Dynamic terms like $(C_{mq} + C_{m\dot{\alpha}})$, $(C_{nr} - C_{n\dot{\beta}} \cos \alpha)$ can be calculated for different angles of attack by applying harmonic type motions of moderate amplitude in $q + \dot{\alpha}$ or in $r - \dot{\beta}$.

It should be noted that the center of gravity of the model remains fixed in the test section, so that by setting a zero acceleration at this point $T(g) = 0$ leads to intrinsic relations between the aerodynamic variables, and in particular between β, α, p and r:

$$\dot{\beta} + r \cos \alpha - p \sin \alpha = 0$$

Compared to rotary rigs, the PQR rig is driven differently within this relation, and in a way quite complementary. The motion control device was designed so that it is possible to apply an arbitrary $\theta(t)$ law within the limits of the passband of the actuator + moving part + model system, including the following (illustrated in Fig. 2.24):

(1) sinusoidal motion schedule, $\theta(t) = \theta_m + \theta_M \sin 2\pi ft$.
The value of θ_M and of f, i.e. the input amplitude and frequency, are subject only to the constraints:

$$|\dot{\theta}_{max}| = 2\pi f \theta_M < 500°/s$$

$$|\ddot{\theta}_{max}| = 4\pi^2 \theta_M < 5000°/s^2,$$

and within the available deflection, i.e. $-100° < \theta < 100°$.

A typical device input in forced oscillations is a low amplitude oscillation (1° to 2°) at a frequency of the order of 5 Hz. By limiting the frequency to 1 Hz, very large-amplitude pitching oscillations (100°) can be obtained.

(2) ramp type schedule,
$\theta = \theta_0 + \Theta t$, Θ = constant.
These tests are more severe than the previous ones in the sense that, in order to achieve a constant pitch rate Θ over as large an interval $[\theta_1, \theta_2]$ as possible, the maximum acceleration $\ddot{\theta}$ has to be used to get up to speed, and to slow down again before the shutdown.

(3) arbitrary schedule, $\theta(t)$. These laws can be chosen to reproduce the angle of attack history of an aircraft pointing type manoeuvre at high angles of attack, and return to normal flight. In flight tests on combat aircraft models at the IMFL laboratories, large pitching dynamic excursions were produced by pitch-up deflection, then pitch-down with ailerons and canards. The typical variation of such a sequence is entirely reproducible on the "PQR" apparatus.

2.7.1.3 Test Data Analysis
The analysis of the test data generated by dynamic simulation devices requires special attention. On the PQR apparatus, the motion is controlled by a hydraulic servo system, and the pressure, velocity and angular position are monitored. The control for a given motion is obtained by applying the desired $\theta_c(t)$ law to the input of this system. The real motion depends on the system in closed loop.

The process applied to ramp-type tests, or more generally those tests for which an arbitrary schedule is programmed, are processed in much the same way as flight tests. A low-pass filter is the desirable approach, at a frequency that should be determined on the basis of the spectrum lines of the test rig and of the responses to previous harmonic tests.

In wind tunnel tests on dynamic test rigs, the classical procedure is to take the difference between a wind-on test, and a kinematically similar wind-off test. This is not strictly accurate, since small aerodynamic forces may arise even when the model is moved about in motionless air .

The aerodynamic effect can be obtained by calculating the forces due to gravity and inertia and subtracting them from the forces measured in a wind-on test. This is strictly accurate, but it means that the quantities measured by the balance - the center of gravity and the moments of inertia - have to be identified precisely beforehand. This can be done using the test facility itself, by appropriate wind-off tests. This approach is necessary for tests using the PQR apparatus operated in closed loop.

2.7.1.4 Summary of Test Programme
The emphasis of the tests was on demonstrating different types of test data obtainable for a complete combat configuration rather than on testing a variety of model configurations. Hence the model WG16A was tested with and without forebody strakes/grit strips. The test programme included :

- slow α-sweeps at sideslip for static data,
- small amplitude pitch and yaw tests to measure derivatives,

- large amplitude pitch oscillations,
- α-ramps at various pitch rates.

2.7.2 ROTARY BALANCE ("TOURNE-BROCHE")

2.7.2.1 Description and Specification

The installation of the rotary balance in the vertical wind tunnel offers the specific conditions for direct simulation of developed steady spins. An important advantage of this approach is the elimination of the mechanical load variations produced by the gravitational forces which would occur in a horizontal-type tunnel.

The wind tunnel has an open working section, 4 m in diameter and the maximum speed is 45 m/s.

The apparatus is shown in Figure 2.25. The different motion and adjustment degrees of freedom provided by the rig are the following:

Φ: Rotation about the axis of the sting ($\pm$ 180°).

Θ_2 : Rotation perpendicular to the Tourne-Broche axis of rotation. This rotation around the moment center of the balance is obtained by the displacement of the curved arm introducing an angle between the axis of the sting (longitudinal reference axis) and the direction parallel to Ω in the symmetry plane of the curved arm $\Theta_2 = \Theta$ when the Tourne-Broche axis of rotation is vertical.

Ω: rotation rate ($\pm$700 °/sec)

Ψ: heading angle

λ : tilt angle of the whole apparatus with respect to the velocity vector.

Slow λ-sweeps are used to acquire static data ($0° < \lambda < 30°$) and oscillatory coning tests are made for fixed λ between 0° and
20°. Static data can be obtained by using Θ_2 at $\lambda = 0°$ or with λ-sweeps at different Θ_2 values.

For the present test series the model was mounted on a rear sting and a 10° crank was needed to reach 75° angle-of-attack during oscillatory coning tests. Full details of the mechanical features and kinematic analysis of the apparatus are given in reference 1.

A newly installed flow visualization technique using smoke and a laser light sheet was also used in the tests.

2.7.2.2 Data Acquisition/Signal Processing

In 1993, the rotary balance facility was equipped with a new data acquisition system. Data acquisition can be triggered manually by an operator or monitored by a logical unit which can start or stop the acquisition process as analogue or logical signal values exceed specified thresholds.

The new acquisition system can process up to 32 analogue and 16 logical channels. The sampling frequency can vary up to 30 KHz and the analogical-digital conversion is made by a 12 bit encoder.

For the present tests, data were sampled at 300 Hz with low pass filtering at 100 Hz to respect Shannon criteria. Numerical data are stored on disc and processed off-line. Average values of coefficients are calculated for 180 intervals of the parameter Ψ. FFT filtering is then used to eliminate noise and structural frequencies. More details of the data reduction procedure are given in reference 1.

2.7.2.3 Flow Visualization

To help in understanding the flow field structure around a rotating model a flow visualization technique has been developed for use on the IMFL rotary balance.

As model angle of attack is increased beyond the attached flow regime, vortices created by the body, wing and other components will eventually burst. The strength of the vortices, their position relative to the model and location of vortex breakdown will change as functions of angle of attack and sideslip. In dynamic tests, like oscillatory coning, these angles will be time dependent. Owing to convective time lags there will be time delays in the adjustment of the flowfield and consequent dynamic effects on measured forces. In large amplitude motion there can also be large hysteresis effects on measured coefficients, especially for slender wing/body configurations.

To provide some insight into these complex unsteady flow phenomena an experimental technique has been developed where a laser light sheet, rotating with the model, is used to illuminate the vortical flow. For understanding the flow characteristics in dynamic tests this technique is complimentary to surface pressure measurements which can also be made on rotating models. The feasibility and usefulness has been demonstrated recently and results are reported in Ref. 4. A general overview of the experimental technique is presented here.

The experimental set-up is shown in Fig 2.26. A 4W laser generator situated outside the wind tunnel test section provides the light source which is transmitted to the static part of the rotary balance by an optical fibre and thence to the rotating arm by means of an optical rotary transmitter. A set of cylindrical lenses creates a light sheet which is parallal to the y-axis of the model. The angle between this sheet and the z-axis can be changed remotely to visualize the flow at different longitudinal locations, allowing the study of vortex development and breakdown over the wing. The flow is seeded using smoke produced by oildroplets on a hot plate The smoke is passed through a pipe to several outlets situated approximately 3 metres up-stream of the model. The flow is observed using a video camera mounted above the sting mount at the rear of the model. Signals from the camera are transmitted to a recorder by means of a gold slip

ring assembly.

As an example of the results from the technique, the effect of rotary motion on the flowfield over a model forebody is shown in Fig 2.27. A comparison of flow visualization from static and coning motion tests (ω = 600°/sec) shows the change in the nature and position of the forebody vortices.

2.7.2.4 Summary of Test Programme

As for the tests with the PQR apparatus, the aim was to investigate the effects on data of test technique rather than configuration. The test programme included:

- slow α-sweeps for static data,
- coning tests at low and high α and with sideslip,
- oscillatory coning tests for measurement of derivatives,
- large-amplitude oscillatory coning tests.

2.8 POLITECNICO DI TORINO (TPI), ITALY

2.8.1 Description of Oscillatory Rig

The apparatus (Fig 2.28) was designed for static and small-amplitude pitch and roll oscillatory tests on aircraft models in the Politecnico di Torino D3M low speed wind tunnel. It is of the direct forced oscillation type with servo-mechanical operation. A vertical strut supports the model and strain gauge balance which is connected by links and levers to an oscillating vertical rod. The linkage can be changed to drive the model in either pitch or roll. The aerodynamic loads acting on the model are measured with a 5 component internal strain gauge balance (axial force excepted). The average measurement uncertainty of the force transducer is $\sigma = \pm 0.75\%$ as a percentage of the total aerodynamic load acting on the model at V = 40 m/s.

Oscillatory motion of the model is excited by means of a driving unit placed under the floor of the wind tunnel test section. The unit is powered by a DC motor and is linked to the main rod, which drives the model, by a gearbox connected to an adjustable flywheel. The oscillation amplitude of the model is set by adjusting the flywheel radius in the range ±50 mm which corresponds to a pitch or yaw amplitude of ±3.5°. The oscillation frequency (maximum 5 Hz for lighter models) is set by the rotation speed of the DC motor. Angle-of-attack and sideslip are varied using stepper-motors to drive the lever at the rear of the model for angle-of-attack and to rotate the vertical strut for sideslip.

The range of adjustment is -7° to 45° for α and -13° to 13° for β. The mechanical system is controlled by a Servo Data Electronic Control Unit which is interfaced to a control PC allowing synchronisation with the Data Aquisition Computer. Model attitude and oscillation is controlled with an open loop system and harmonic distortion due to changes in geometry of the various linkages is corrected by appropriate software.

Experiments were conducted in the D3M low speed wind tunnel which has a closed circuit with a contraction ratio of 5.44. The test section is circular, of diameter 3 m. The turbulence level is 0.3%, at V_∞ = 50 m/s.

2.8.2 Data Acquisition

For static measurements the balance outputs were multiplexed and measured by a high precision integrating voltmeter, taking an average over 50 samples with an integration period of 20 ms.

For dynamic tests, the signals from the strain gauge balance were measured with a high speed 12 bit analog-to-digital converter. Using a parallel sample and hold unit the balance outputs were sampled at 512 samples/s/channel for a period of 10 s. The coefficients were averaged over a number of six periods (i.e. 60 s) and the repeatability of these six measurements was evaluated as a percentage of data range for the pitch mode only (V = 30 m/s, $\beta = 0°$, k = 0.083, $\theta = \pm 1°$).

The signal analysis software is based on Fourier analysis, as in-phase and out-of-phase load components are evaluated for wind-on/off conditions. Derivatives measured and repeatibility are shown in Tables 2.3 and 2.4 respectively.

2.8.3 Summary of Tests Made

Static and pitch and roll tests were made to investigate the following effects:

- longitudinal transition fixing on forebody
- forebody strakes
- leading edge root extension (LEX)

The primary dynamic derivatives measured and measurement accuracy are given in Tables 1 and 2 below. Cross-coupling derivatives can also be measured.

Test condition	Static derivatives	Dynamic derivatives
Pitch mode	$C_{Z\alpha}$	$C_{Zq} + C_{Z\dot{\alpha}}$
	$C_{m\alpha}$	$C_{mq} + C_{m\dot{\alpha}}$
Roll mode	$C_{Y\beta} \sin\alpha$	$C_{Yp} + C_{Y\dot{\beta}} \sin\alpha$
	$C_{l\beta} \sin\alpha$	$C_{lp} + C_{l\dot{\beta}} \sin\alpha$
	$C_{n\beta} \sin\alpha$	$C_{np} + C_{n\dot{\beta}} \sin\alpha$

Table 2.3 Derivatives measured

Coefficient	$\alpha < 20°$ (%)	$\alpha > 20°$ (%)
$C_{Z\alpha}$	±1	±2.7
$C_{m\alpha}$	±1.2	±4.9
$C_{Zq} + C_{Z\dot{\alpha}}$	±1	±2
$C_{mq} + C_{m\dot{\alpha}}$	±1	±3.6

Table 2.4 Repeatability of dynamic measurements

2.9 AERONAUTICAL RESEARCH INSTITUTE OF SWEDEN (FFA)

2.9.1 Description of Rig and Wind Tunnel

The low speed wind tunnel LTl is an atmospheric, continuous, closed circuit tunnel with a test section diameter of 3.6 m and a length of 8 m. Maximum wind speed is 85 m/s. There are two interchangeable test sections.

The rotary balance rig was constructed and built in the mid 1980's (Fig 2.29). It is driven by a hydraulic pump and motor. An electrical motor is used to set the angle of attack (α) remotely. Angles of attack up to ±150° can be set by using different sting mountings (Fig 2.30), a rear entry sting for 0°-40°, two top entry stings for 1) 30°-70° and 2) 60°-100° (Fig.2.33). By using the same stings and yawing and rotating the model 180°, angle of attack outside the range 0°-100° can be achieved. At α = 40° the distance between the model reference centre and the sector beam can be increased by 0.5 m (Fig. 2.31) in order to investigate the interference effects of the apparatus.

The rotation speed range is ±15 to ±360 rpm at a wind speed of 60 m/s and a model weight of 8 kg. The rig is designed to accommodate models of fighters in the scale range: 1/10 to 1/15.

2.9.2 Test Procedure

(a) Model configuration and angle of attack are set as required.

(b) Wind-on data was acquired as follows: the sector beam is fixed in a vertical position by using a rod, the wind speed is increased from zero to the required speed and a static reading is made. Then the wind speed is reduced to zero and the rod is removed. The wind speed is set to required speed again and the model is rotated around the wind axis at a range of different positive and negative rotation speeds. The positive rotation direction is the clockwise direction looking upstream. Measurements were made at approximately the following rotation speeds in the given order:

n = 30, 50, 80, 110, 150, 200, 250, 300, 325, -30, -50, -80, -110, -150, -200, -250, -300, -325 rpm.

Data are acquired during 22 cycles with a sampling rate of 150 data points during every complete cycle regardless of the rotation speed.

(c) Wind-off data are usually acquired after every wind-on test at approximately the same rotation speeds as for the wind-on tests. After the last rotation with wind-on, the wind speed is reduced to zero without changing the rotation speed, and wind-off data are acquired at:

n = -325, -300, -250, -200, -150, -110, -80, -50, -30, 30, 50, 80, 110, 150, 200, 250, 300, 325 rpm.

In some tests wind-off data are acquired before wind-on runs, in the following order:

n = 30, 50, 80, 110, 150, 200, 250, 300, 325, -30, -50, -80, -110, -150, -200, -250, -300, -325 rpm.

The procedure for one complete test, including setting the model at the required attitude, wind-on and wind-off data samplings, data reduction and printing of the results takes about 50 minutes.

2.9.3 Data Acquisition and Reduction

Signals from the six component balance and position indicator go through slip rings, and then together with tachometer signals go through an amplifier, a 10 Hz filter and an analogue-digital converter to the buffer memory of the data acquisition computer of the tunnel. Data sampling is interrupted when data over 22 complete cycles at a constant rotation speed have been collected. After this, data reduction is done and the result is stored.

The gravity component of the forces and moments is eliminated by averaging the signal over a complete cycle.

In order to take into account the damping effect of the air displaced by the model in the wind-off runs, the balance signals from clockwise and counter clockwise rotations are averaged. This averaged value is taken as the inertia component of the wind-off loads.

The damping component is found by subtracting the inertia component from the wind-off loads.

2.9.4 Corrections

The free stream flow was surveyed at the tunnel centre line with a Prandtl tube. Cross flow angles in the horizontal and vertical direction were measured to less than 0.5°. The construction of the rotary balance apparatus does not allow any compensation for the cross flow by changing the attitude of the rotation axis.

Rotation speed with wind-on and wind-off data sampling are not identical, they can vary up to four rpm. A sixth degree polynomial fit is used to minimise the effect of different rotation speeds at wind-on and wind-off readings.

The model attitude is slightly changed during the wind-on runs compared with wind-off runs due to aerodynamic forces and moments, but this is assumed to have only minor effects on the results and therefore no effort has been made to compensate for this effect.

The model attitude changes also because of centrifugal forces. Both the structure and the internal balance are deflected, but in different directions. The internal balance deflection increases α while the deflection of the structure decreases α. At the highest rotation rate, at $\alpha = 40°$, there was a 0.3° reduction in α due to deflection of the structure and an increase of 1.3° due to deflection of the internal balance, resulting in a total increase in α of 1°. The change in α due to inertial forces was not compensated for since it was not possible to change α during rotation.

2.9.5 Summary of Test Program

Static and rotary tests were made on model WG16B. The following effects were investigated over an angle-of-attack range of 0°-69°:

- angle of attack,
- configuration build up,
- Reynolds number,
- forebody longitudinal transition fixing,
- type of model support,
- rotary rig interference,
- forebody nose strakes,
- nose strake asymmetries,
- repeatability.

2.10 NASA LANGLEY/BIHRLE APPLIED RESEARCH/DRA (Pressure measurements on rotating models)

2.10.1 Scope of Tests

As part of a NASA/DRA Joint Aeronautical Programme an experimental study was made of the effects of Reynolds number on forces generated by wind-axis rotation of simple fuselage bodies. Rotary balance experiments, including force and moment and surface pressure measurements, were conducted on circular and rectangular section aftbodies with hemispherical and ogive noses at the DRA Bedford 13ft x 9ft atmospheric wind tunnel and the 8ft x 6ft pressurised wind tunnel at DRA Farnborough in the United Kingdom. The bodies were tested at 60° and 90° angle of attack for a wide range of Reynolds numbers in order to observe the effects of laminar, transitional, and turbulent flow separation on the forebody characteristics when rolling about the velocity vector.

A photograph of the rectangular ogive model installed on the rotary balance apparatus in the 13ft x 9ft low-speed tunnel is shown in Figure 2.32. The models were pressure-tapped with six circumferential rows of taps on the forebody and two on the aftbody, as shown in Figure 2.33. All models were 36 inches long, with a diameter of 6 inches. Station zero represented the tip of the forebody, station 12 the forebody break-point, and station 36 the overall length. Taps were located at stations 1, 2, 4, 6, 8, 11, 29, and 32.5. The total number of surface pressure ports was 254 for each configuration. There were 32 pressure taps at each body station except station 1, which only accommodated 30 taps. Trip strips and strakes were tested on the circular ogive configuration at 60 degrees angle of attack. The trip strips were narrow thin pieces of metal with small, raised holes punched in them. One strip was attached on each side of the nose of the circular ogive model, 80 degrees from the bottom centerline, and extended down the sides until about 3 inches from the aft end. The strakes were thin pieces of metal mounted perpendicular to the model surface on either side of the nose, approximately 0.5 inches wide by 4 inches long and placed 135° from the bottom centerline.

2.10.2 Test Conditions

The tests were conducted over a range of Reynolds numbers (based on diameter) from about 0.08 to 2.25 million, a Mach number range of 0.024 to 0.21, and at angles of attack of 60 and 90 degrees. The rotation rate varied from $\Omega b/2V = 0.0$ to 0.4 in both positive (clockwise) and negative (counter-clockwise) directions. Pressure data were taken concurrently with force and moment data during each run.

2.10.3 Data Acquisition and Processing

To measure the pressures, a 780B Pressure Measurement System from Pressure Systems Inc. (PSI) was used, along with eight electronic scanning pressure modules (ESP-32) containing 32 ports each for a total of 256 ports. The modules used for the low-Reynolds number tests at Bedford were rated at a maximum range of ±2.5 psi while those for the high Reynolds number tests at Farnborough were ±5.0 psi. The plastic tubes from each port on the model surface were connected to one side of the differential pressure transducers mounted inside the model. The transducers converted the pressures to voltages. The voltage level for each of the ports was transmitted through the rig sliprings to the Data Acquisition and Control Unit in the tunnel control room. Voltages for all ports were then converted to pressures and coefficients and stored in a PC. The number of pressure readings averaged at each rotation rate to arrive at a final value for each port was determined by the available system memory and from experience gained in previous rotary balance pressure and force tests. Forty readings were taken at each port over a 4 second time interval. These readings were then averaged to determine the final pressure value. The error specification of the PSI 780B System was ±0.10% of full scale in a worst case. Drift in the system was the largest single cause of error in these tests, primarily due to temperature variations in the tunnel that affected the transducers. Re-zeroing the system at the start of each rotational sweep kept drift errors to a minimum. System zero checks indicated a worst case drift error of ±0.08%. Repeat runs showed additional accuracy errors within ±0.04%. The combination of these errors produced an overall system accuracy for these tests of within ±0.12% of the full-scale value of the transducers.

2.10.4 Presentation of Data

The force and moment data is typically presented as a function of non-dimensionalized rotation rate, $\Omega b/2V$, for Reynolds numbers based on body diameter ranging from approximately 80,000 to 2,200,000. Software tools to visualize experimental data in an expeditious fashion were used in the analysis of the pressure data obtained at the Bedford and Farnborough facilities.The surface pressures were assigned color values and mapped onto a three-dimensional surface model of the configuration. Since the model could be positioned at any attitude, the flow effects could be examined over the entire configuration. The software also has the capability to display pressure increments between two flow conditions and to highlight a desired range of pressure coefficients. In this manner, flow effects due to rotation rate, angle of attack, or Reynolds number were easily observed.

2.11 REFERENCES

1 Special Course on Aircraft Dynamics at High Angle of Attack: Experiments and Modelling. AGARD-R-776 (1991)

2 C O O'Leary, B Weir, J M Walker. Continuous Rotation Tests of a Combat Aircraft Model in a Low Speed Wind Tunnel.
DRA Tech Memo Aero/Prop 42 (1993)

3 Report of the Fluid Dynamics Panel Working Group 11 - Rotary-Balance Testing for Aircraft Dynamics.
AGARD-AR-265 (1990)

4 D. Farcy, B. Leporcq (ONERA-IMFL). High Angle-of-Attack Flow Visualization During Rotary Motion.
Euromech Colloquium 335 on: "Image Techniques and Analysis in Fluid Dynamics", Roma, 5-7 June, 1995

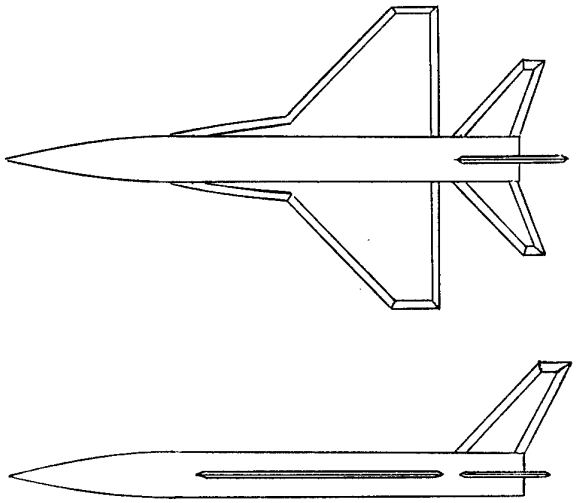

Fig 2.1 General arrangement of generic combat aircraft model

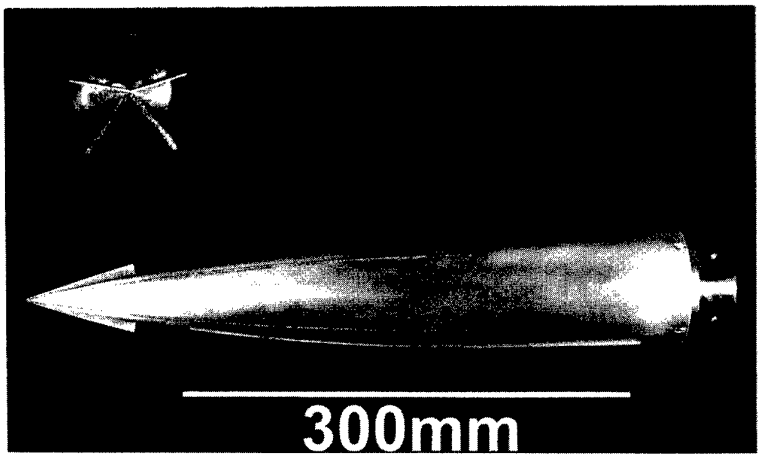

Fig 2.2 Forebody strakes and transition fixing on model WG16B

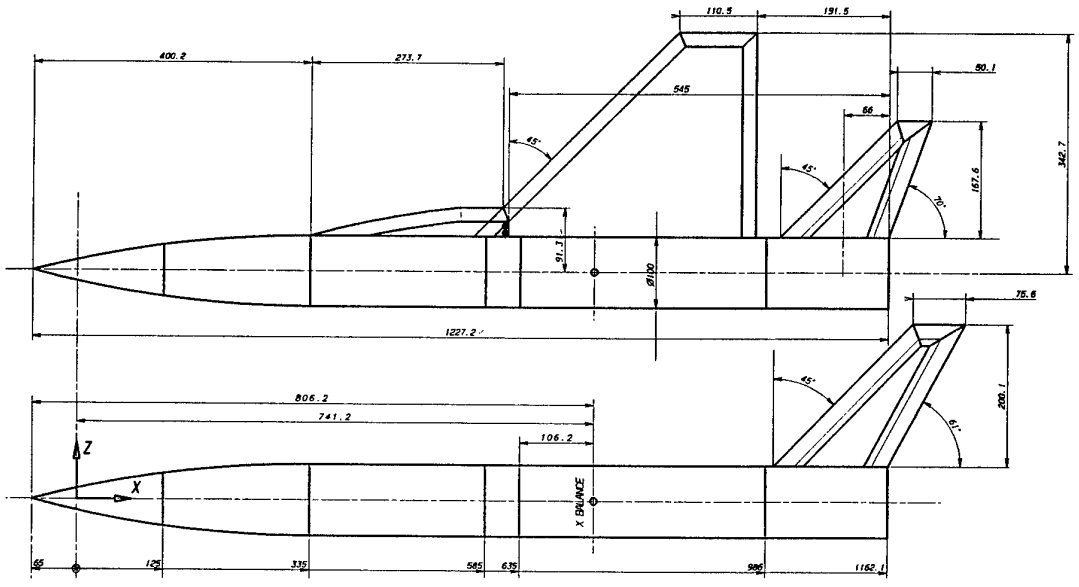

Fig 2.3 Model WG16A

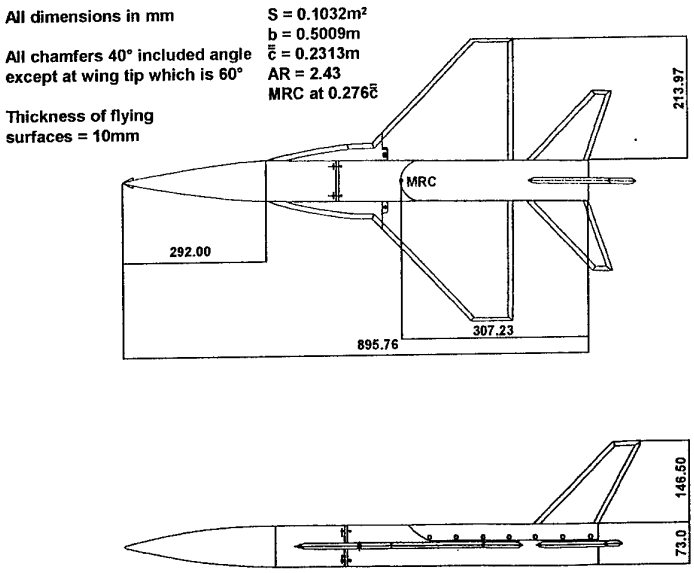

Fig 2.4 Model WG16B

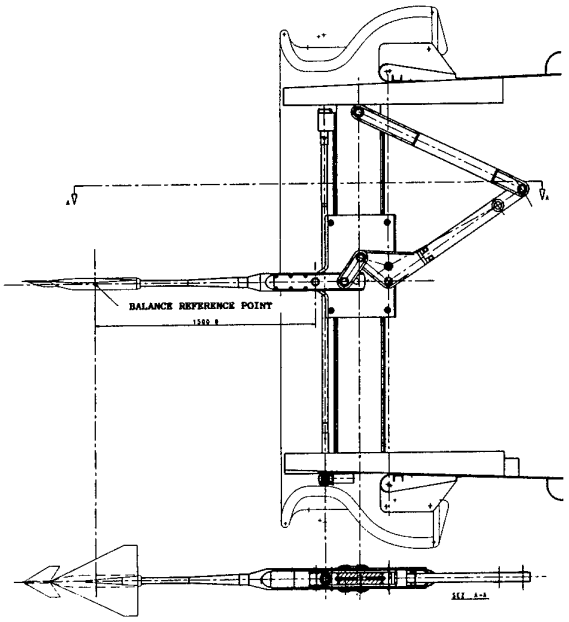

Fig 2.5 AEM static balance

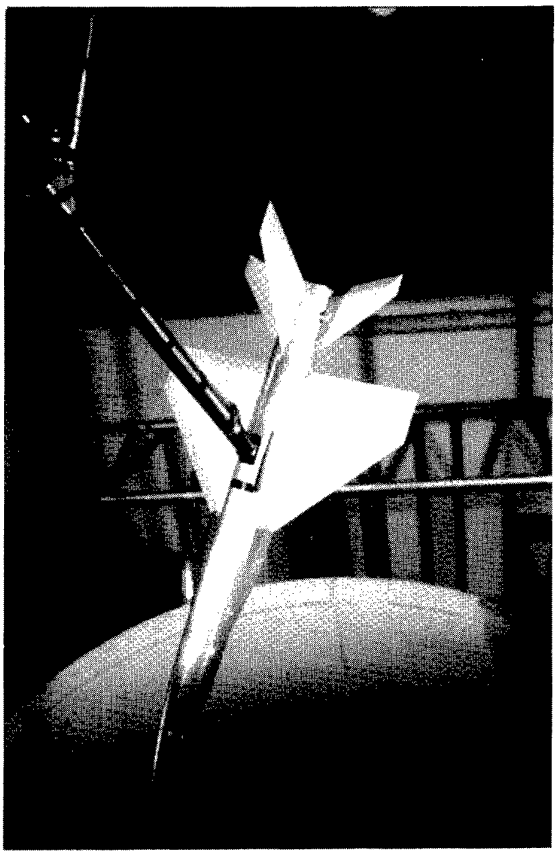

Fig 2.7 WG16A model on rotary balance in AEM wind tunnel

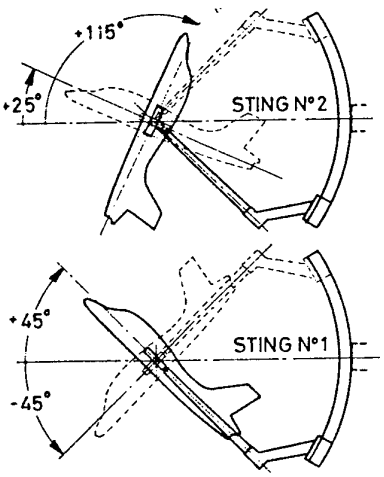

Fig 2.6 AEM rotary balance stings

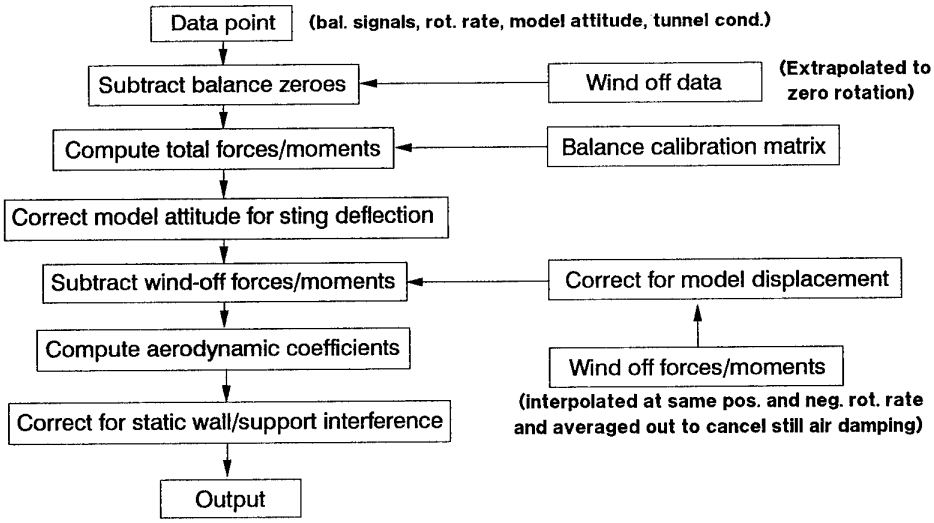

Fig 2.8 AEM data reduction scheme for rotary balance tests

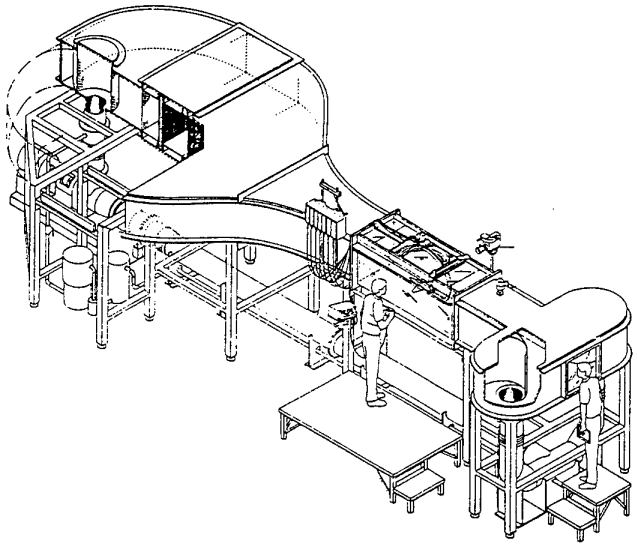

Fig 2.9 Eidetics EI2436 water tunnel at AEM

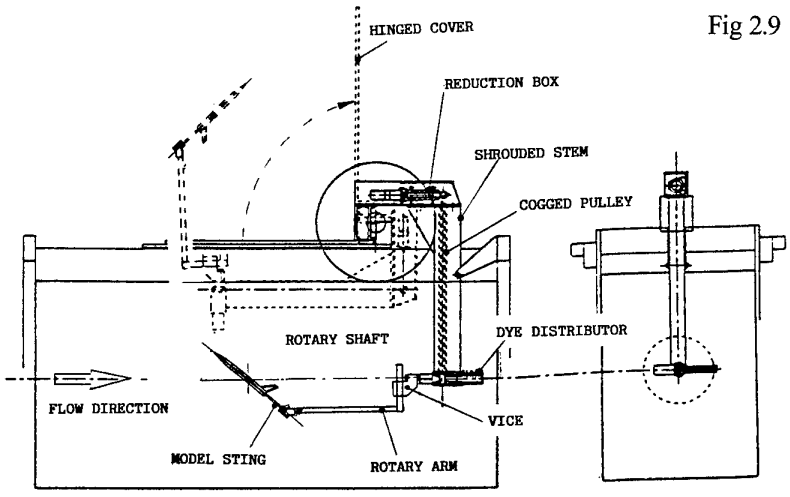

Fig 2.10 Schematic view of AEM rotary rig in water tunnel

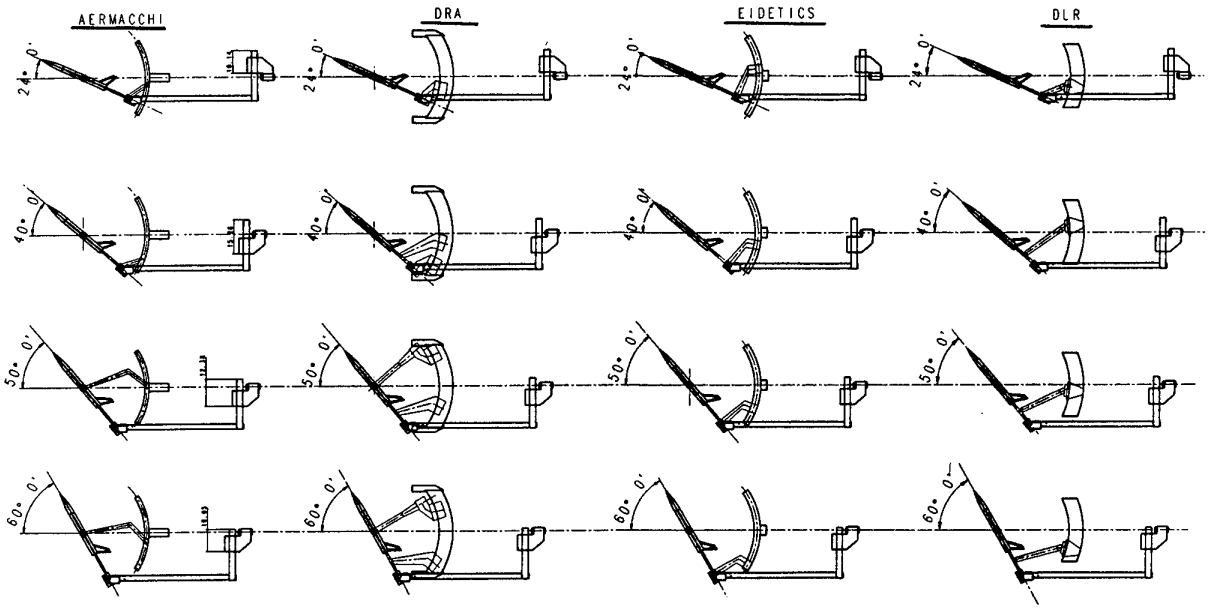

Fig 2.11 Water tunnel flow visualization at AEM - model and rear arc configurations

REFERENCE RUNS : ARC-STING OFF				
CONFIG.	ALPHA (deg.)	OMB2V (rad)	STING	ARC
a) BWLVHTS b) BWLVHT	24. 40. 50. 60.	0 " " "	OFF " " "	OFF " " "

CONFIG. BWLVHTS : COMPLETE CONFIG. WITH TRANSITION AND NOSE STRAKES
" BWLVHT : AS ABOVE WITHOUT NOSE STRAKES
(*1) UNFRA : UNFAIRED ROTARY ARC

CONFIG.	ALPHA (deg.)	OMB2V (rad)	AEM STING	AEM ARC
A/BWLVHTS	24. 40. 50. 60.	0. " " "	REAR " TOP "	UNFRA (*1) " " "
"	24. 40. 50. 60.	0. " " "	REAR " TOP "	ON " " "
"	40.	0.	TOP	ON
B/BWLVHTS	24. 40. 50. 60.	0. " " "	REAR " TOP "	ON " " "
"	40. 50.	" "		

DRA STING	DRA ARC	EI STING	EI ARC	DLR STING	DLR ARC
CRNK40 " CRNK60 "	ON " " "	REAR " "	ON " "	STING1 STING2 " "	ON " " "
CRNK60 TOP	ON "				

A/BWLVHT	24. 40. 50. 60.	0. " " "	REAR " TOP "	ON " " "	
B/BWLVHT	24. 40. 50.	0. " "	REAR " TOP	ON " /	CRNK40 " CRNK60 ON " REAR ON " " STING1 ON STING2 " "
B/BWLVHT	40.	0.			CRNK60 ON

Fig 2.12 Flow analysis with rotary rig in AEM water tunnel

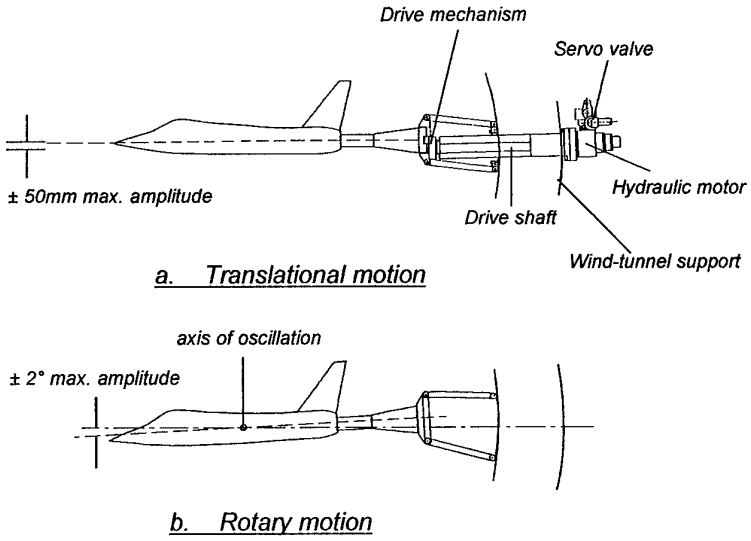

Fig 2.13 General arrangement of DRA Inexorable Drive Rig

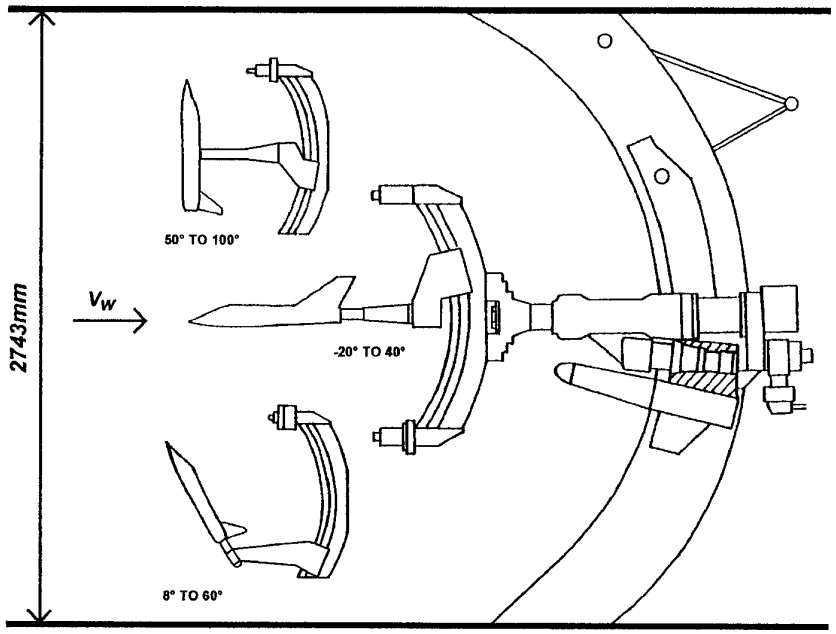

Fig 2.14 General arrangement of DRA rotary balance

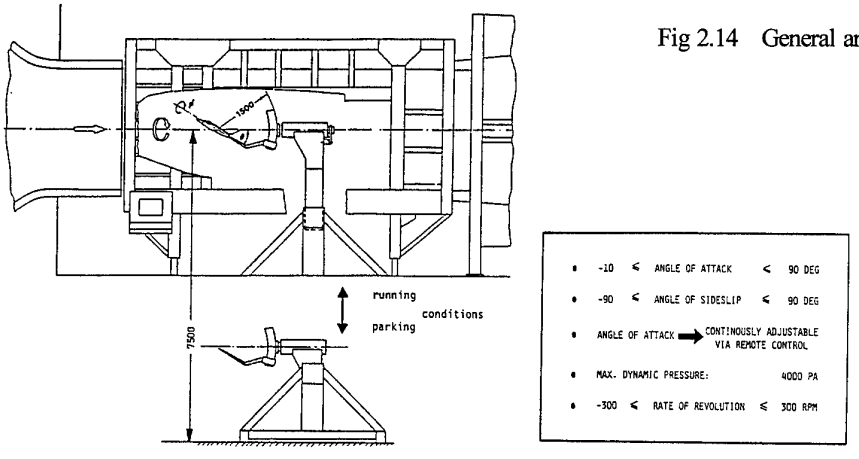

Fig 2.15 DLR rotary balance in Braunschweig 3.25m x 2.8m low speed, closed section wind tunnel

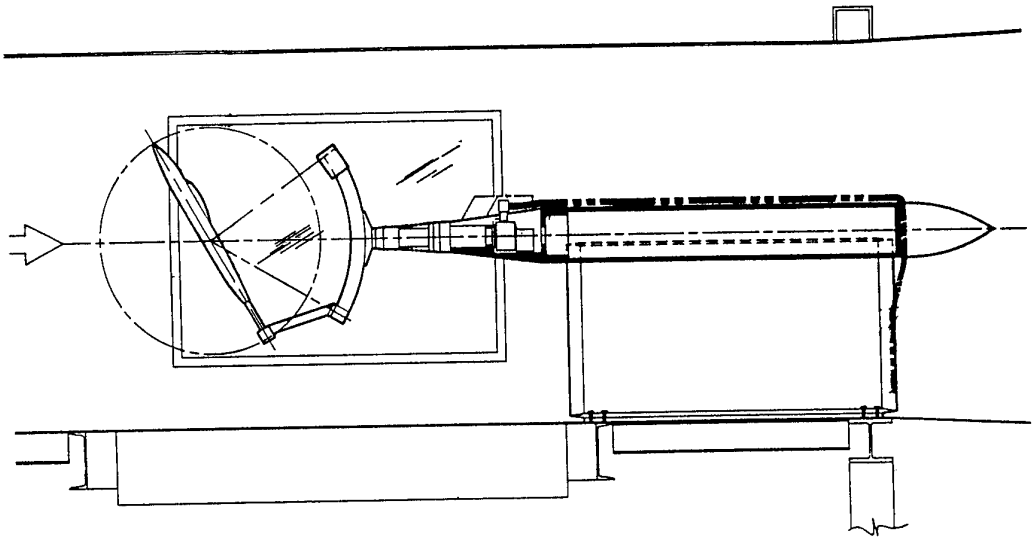

Fig 2.16 General arrangement of NASA Ames/Eidetics rotary balance and support system in 7ft x 10ft wind tunnel

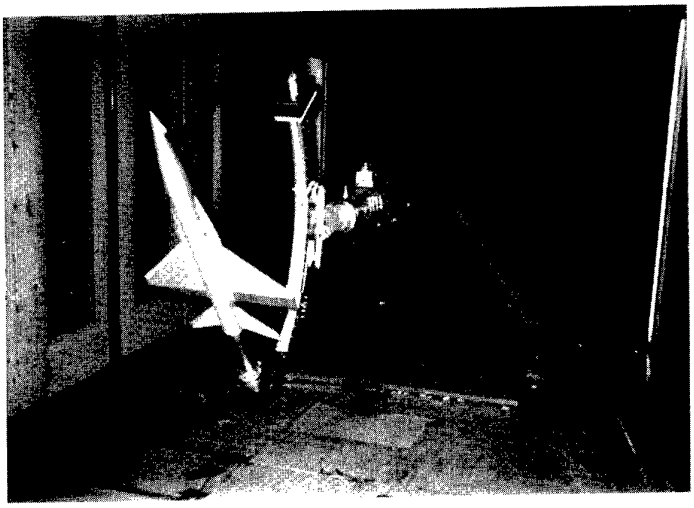

Fig 2.17 WG16B model on NASA Ames/Eidetics rotary balance

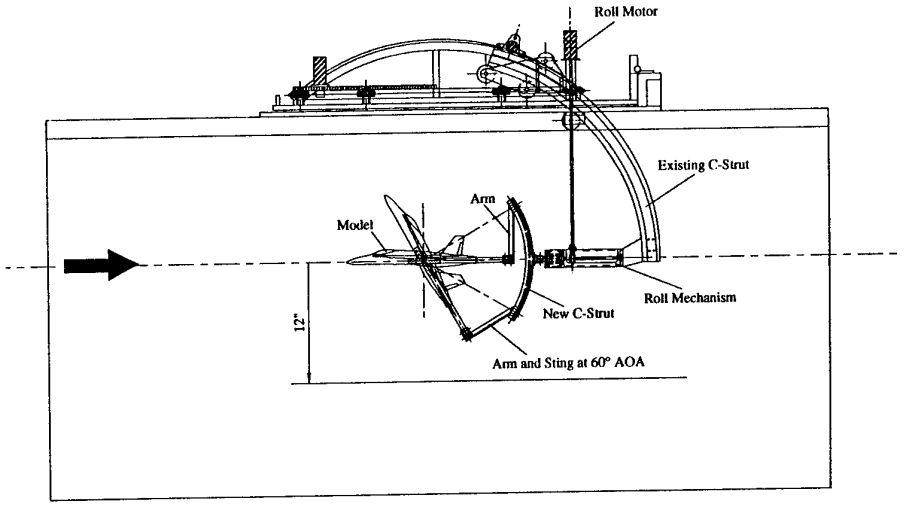

Fig 2.18 Eidetics rotary rig in EI2436 water tunnel

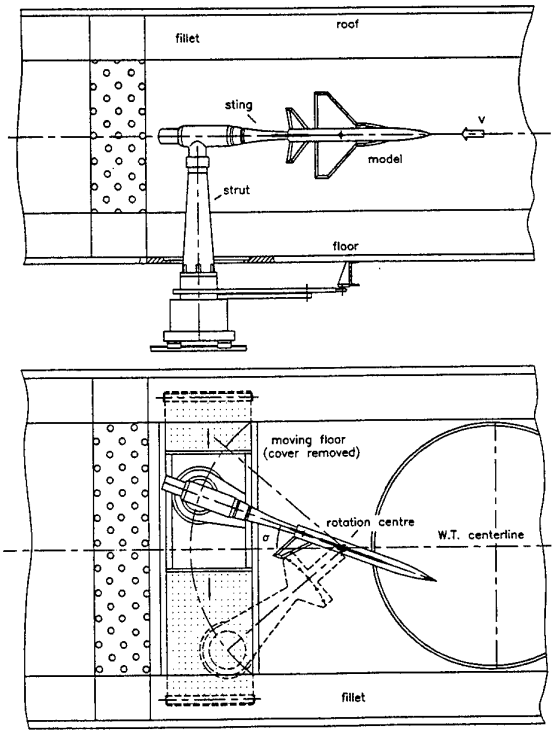

Fig 2.19 IAR asymmetric support system for oscillatory tests

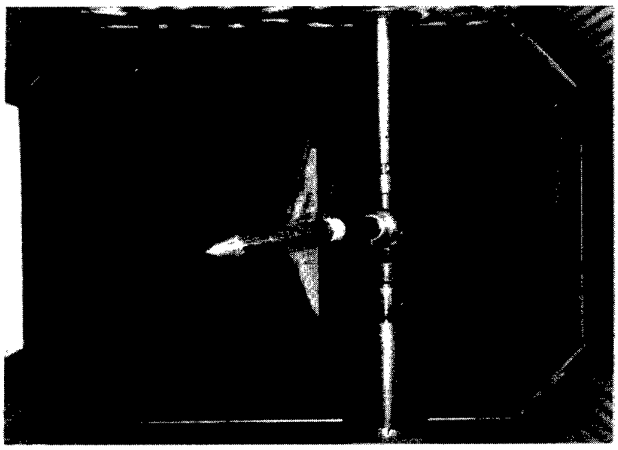

Fig 2.20 IAR oscillatory rig with image strut fitted in wind tunnel

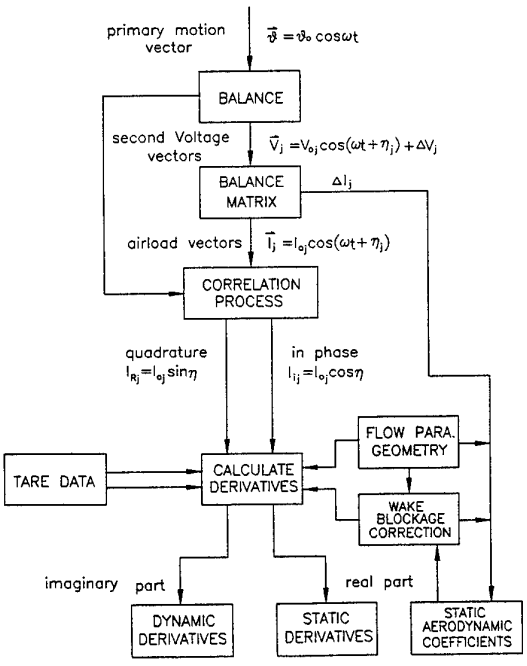

Fig 2.21 IAR data reduction for oscillatory tests

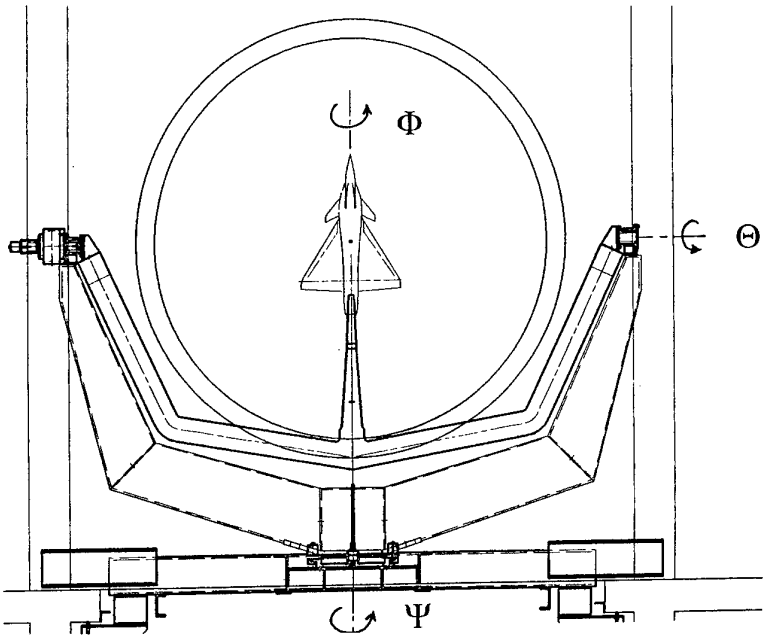

Fig 2.22 ONERA-IMFL 'PQR' rig in open-section wind tunnel

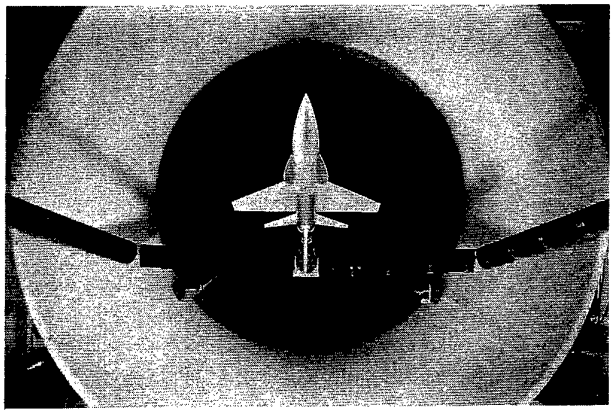

Fig 2.23 WG16A model on PQR rig

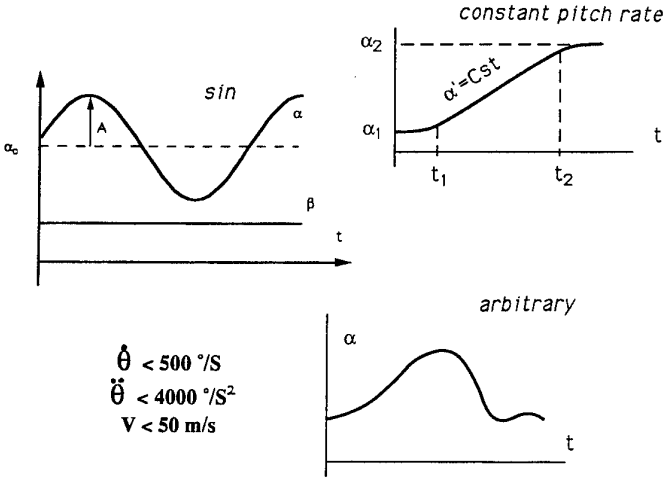

Fig 2.24 Typical motion time-histories for PQR rig

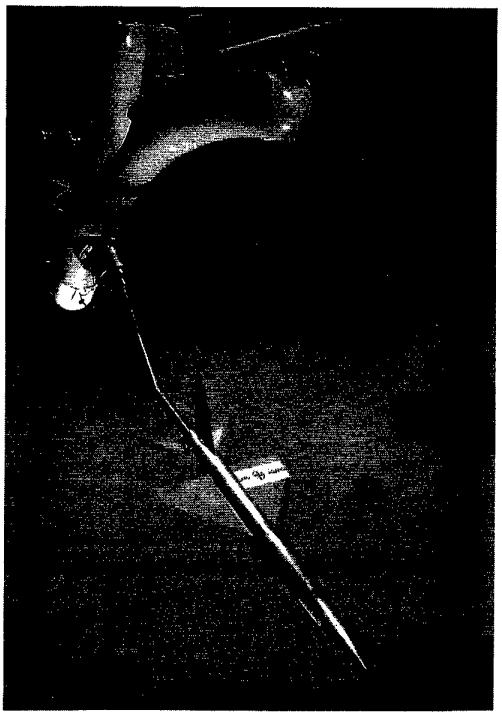

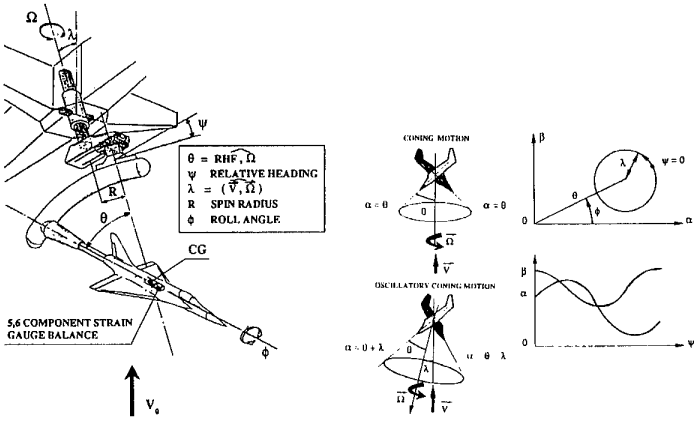

Fig 2.25 ONERA-IMFL 'Tourne-Broche' oscillatory coning rig installed in 4m vertical wind tunnel 'SV4'

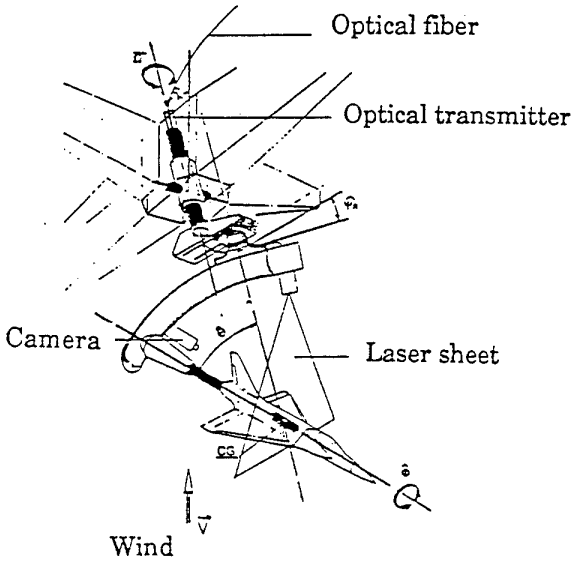

Fig 2.26 Flow visualization on Tourne-Broche

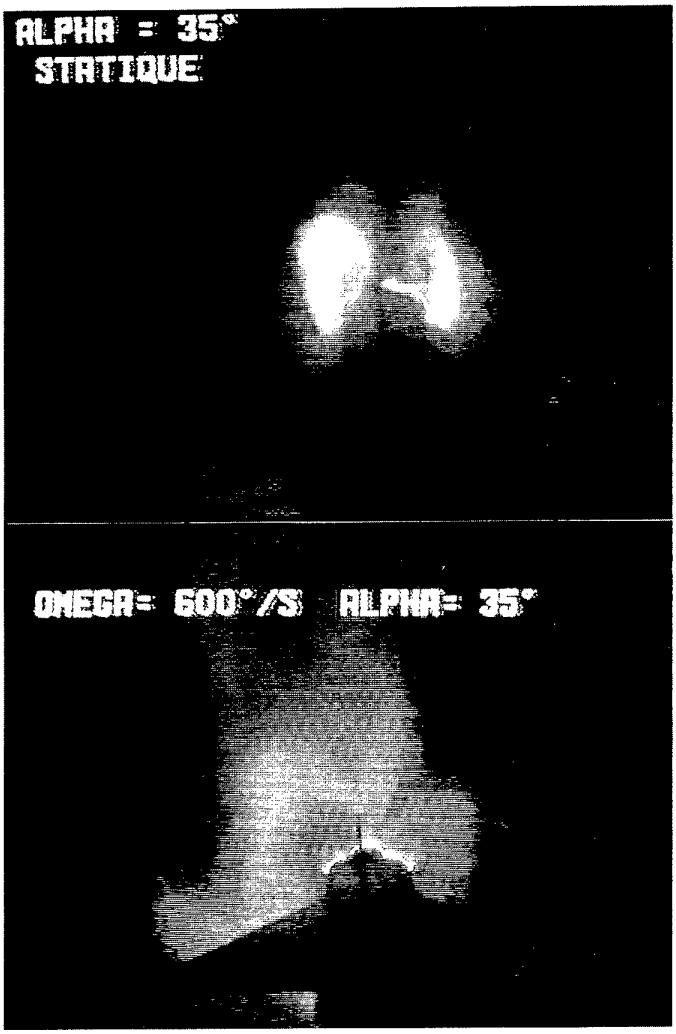

Fig 2.27 Example of flow visualization on Tourne-Broche

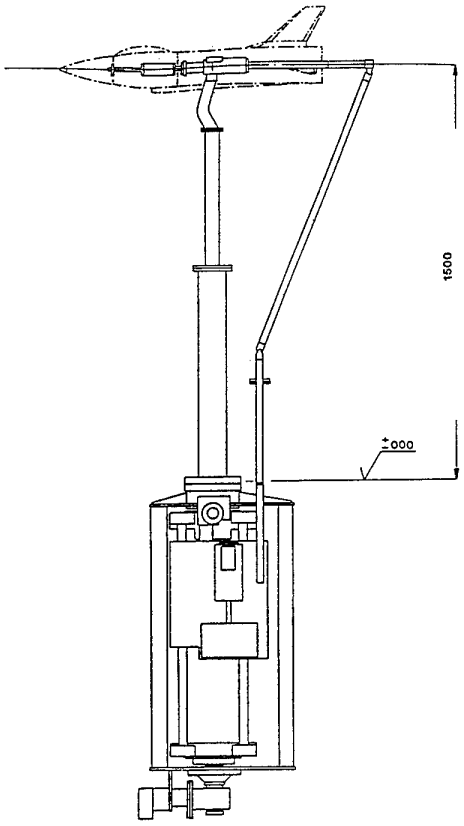

Fig 2.28 The TPI oscillatory balance

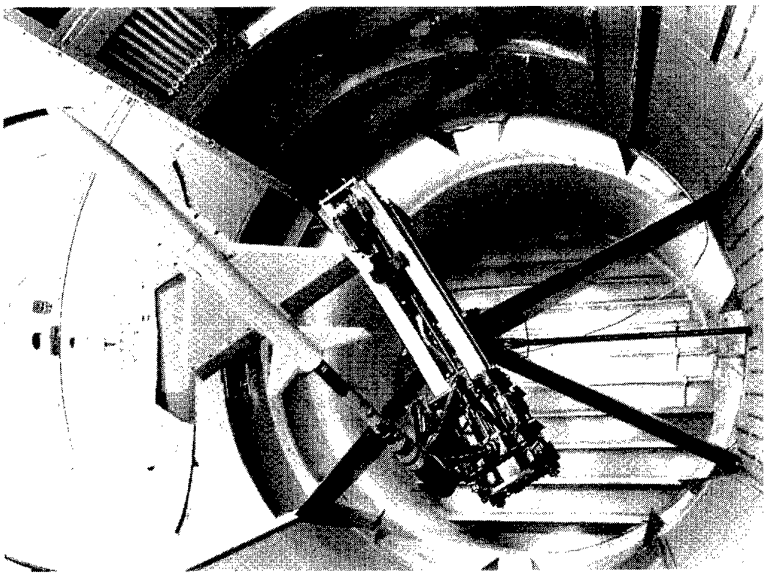

Fig 2.29 FFA rotary balance in LT1 wind tunnel

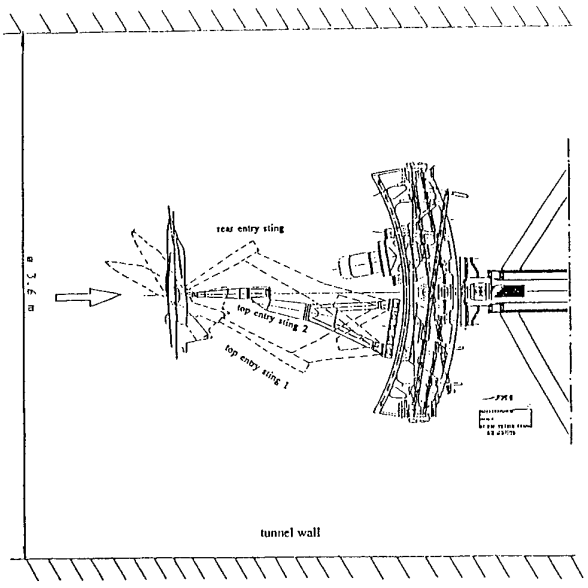

Fig 2.30 FFA rotary balance sting options

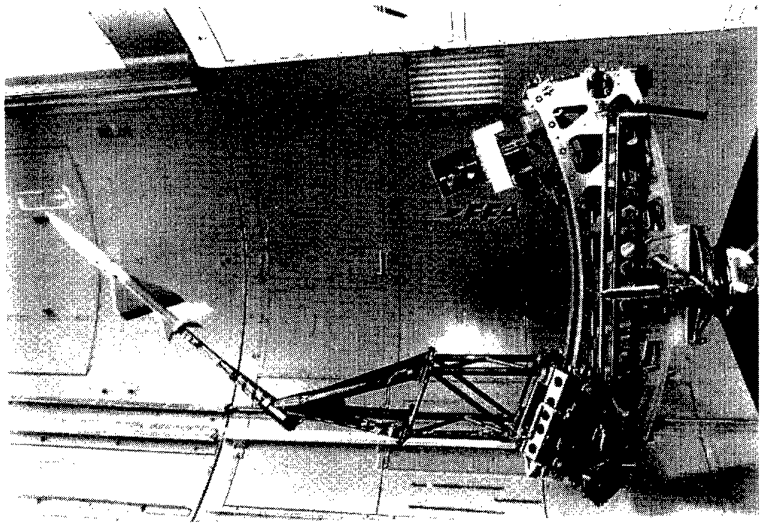

Fig 2.31 FFA rotary balance with o.5m sting extension in LT1 wind tunnel

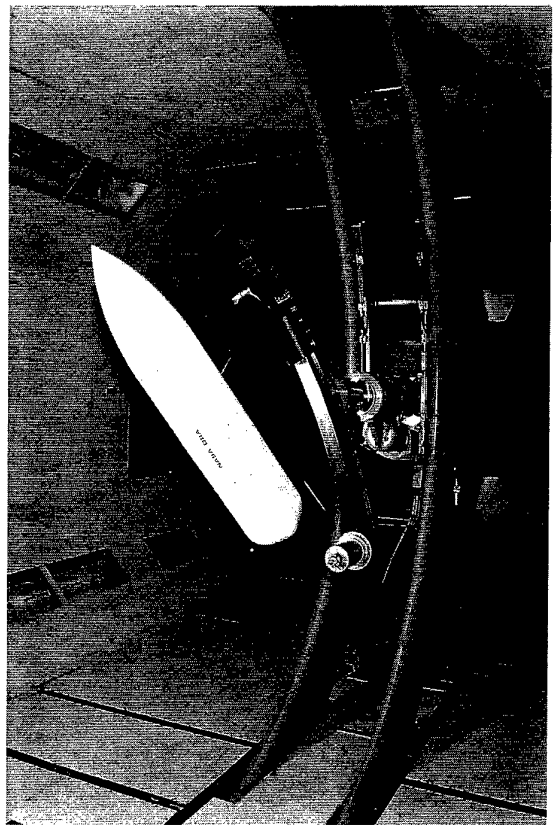

Fig 2.32 NASA/DRA generic forebody model on DRA rotary balance in 13ft x 9ft low speed wind tunnel

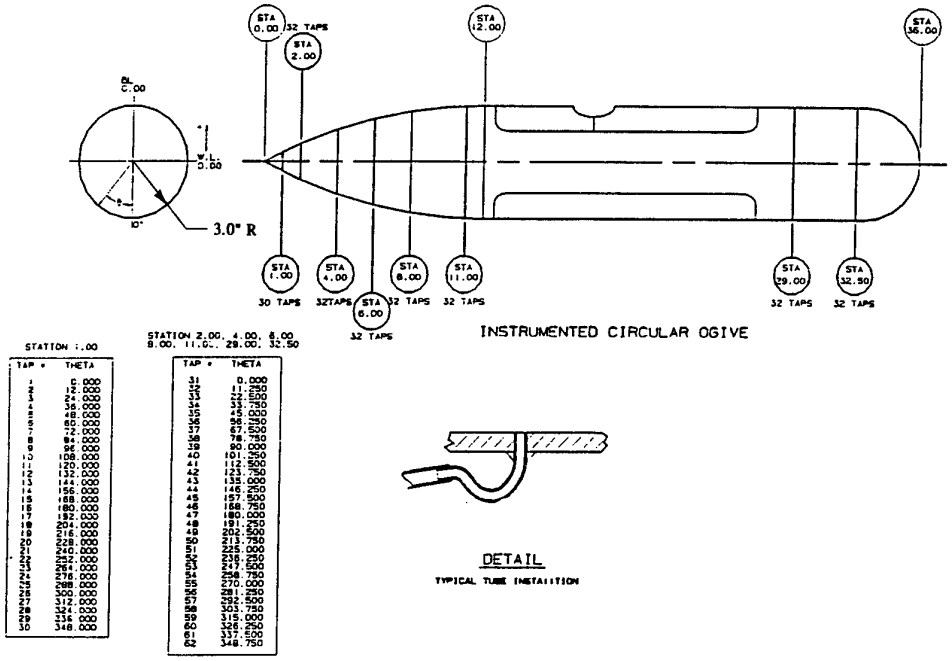

Fig 2.33 Sketch of circular-ogive forebody showing locations of pressure tappings

CHAPTER 3

ROTARY RESULTS ON AIRCRAFT MODELS

3.0 INTRODUCTION

This chapter presents coning test results obtained as part of the Cooperative Program. Six organizations (AerMacchi, DLR, DRA, Eidetics, FFA and ONERA/IMFL) performed rotary balance experiments on a common generic fighter configuration. Tests were conducted on several rotary balance rigs in several facilities with two models of different scales.

These data bases provide information on different parametric effects which are of great significance for the experimental technique of rotary testing, in particular at high angles of attack.

Each organization has carried out numerous investigations (see Appendix 1) involving different parameters. Consequently, in order to avoid repetition, a selection of illustrative results for each specific parameter has been made, and each of them is based on data from only one organization. Thus, a comprehensive set of selected rotary data which illustrates significant trends and effects of model configuration, aerodynamic variables and test conditions, is presented.

Interfacility comparisons will be discussed in Chapter 4.

3.1 FOREBODY CONFIGURATION EFFECTS (DRA , Model B)

The effects of transition fixing for forebody crossflow were investigated by application of 0.2 mm grit in strips 3 mm wide, symmetrically disposed from the X-Z plane and stretching from the tip of the nose to the X-station coincident with the LEX apex. Two radial positions, ϕ_t, measured from the bottom centre of the nose were tested : $\phi_t = \pm 70°$ and $\phi_t = \pm 40°$. Grit was also applied to the lower nose area between the strips and 10 mm aft of the nose apex. Tests were carried out at 60m/s corresponding to a Reynolds number based on body diameter of 3×10^5.

The variation of C_n with reduced rotation rate, $\omega b/2V$, for the body alone at $\alpha = 40°$, 50° and 60° is shown in Fig 3.1. Results are compared for three cases : transition free, $\phi_t = \pm 40°$ and $\phi_t = \pm 70°$. With transition free the coefficients are non-zero at zero rotation rate for all values of α and there are discontinuities at $\alpha = 50°$ and $\alpha = 60°$. With transition fixed at $\phi_t = \pm 40°$ these zero offsets are reduced but there are discontinuities at $\alpha = 50°$. Variations of C_n for positive and negative rotation are dissimilar. When transition is fixed at $\phi_t = \pm 70°$ there are marked discontinuities and zero offsets at $\alpha = 40°$ and $\alpha = 50°$.

Numerous tests on static models have shown that as angle of attack is increased beyond approximately 25° forebody vortices become asymmetric and yawing moments result. In static tests it has been established that the presence of longitudinal transition trips on the forebody reduced random effects of free transition. The results of these rotary tests indicate that, at high angles of attack, large changes in yawing moment are likely as rotation rate is varied, even with transition fixing. The angular position of the transition strip ϕ_t does affect the nature of the variation of yawing moment with $\omega b/2V$ but for both cases there is apparent "flipping" of the asymmetry at particular rotation rates.

Based on the work of Malcolm (Ref 1), Bihrle (Ref 2) and recent rotary tests on combat configurations at DRA, strakes of length 1.0 D and height 0.1 D, where D = maximum diameter of the body, were fixed to the nose at radial position $\phi_s = \pm 105°$. The effect of the strakes on C_n, for the body alone, is shown in Fig 3.2 for α = 40° and 50°. Results are compared for strakes off, transition fixed (at $\phi_t = \pm 40°$) and strakes on, transition fixed. Additionally, for $\alpha = 40°$, results are compared for strakes on, transition free. It is apparent that only when strakes and transition fixing are both in place are zero offsets and discontinuities virtually eliminated and there is similar but opposite variation in C_n for positive and negative rotation rates, i.e. variation is anti-symmetric about zero rotation rate. Strakes have the effect of forcing symmetric vortex separation at the nose apex, which has a dominating effect on the forebody flow but the transition bands are required to maintain symmetry along the entire length of the tapered forebody.

The effect of forebody strakes on the complete configuration (BWLHVT) is shown in Figs 3.3 , 3.4 & 3.5 for $\alpha = 40°$, 50° & 60° respectively. With strakes on, the magnitudes of sideforce and yawing moment variations are again reduced and zero offsets and discontinuities virtually eliminated. Rolling moment varies anti-symmetrically about the origin with strakes on, but with strakes off variations are irregular and there are large zero offsets. Results with transition free are also shown for $\alpha = 40°$ in Fig 3.3. There is a large increase in sideforce and pitching moment variation with rotation rate and a change in the sign of rolling moment. Repeat runs (not in the figures) showed erratic variations in the strakes-off data, but good repeatability with strakes-on.

The results showed that for the body alone and for the complete configuration, forebody strakes with longitudinal transition fixing consistently reduced zero offsets, discontinuities and dissimilar changes in magnitude for positive and negative rotation rates.

It was therefore decided to adopt forebody strakes at $\phi_s = \pm 105°$ and transition fixing at $\phi_t = \pm 40°$ as the baseline forebody configuration. Front and underside views of the forebody are shown in Fig 3.6.

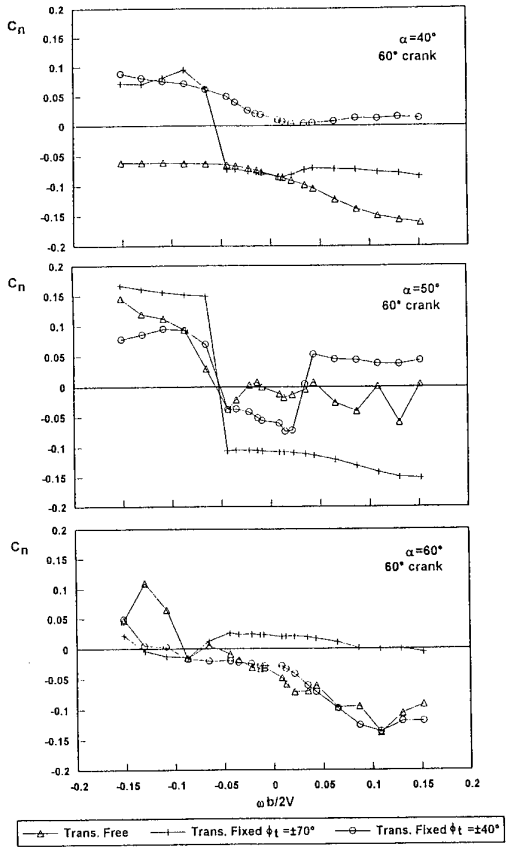

Fig 3.1 - Config : B, Effect of transition fixing on forebody at $\alpha = 40°, 50°$ and $60°$

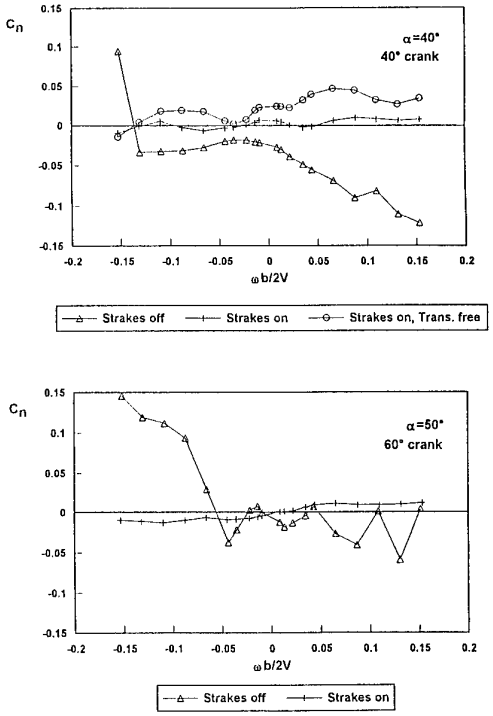

Fig 3.2 - Config : BT, Effect of nose strakes on forebody at $\alpha = 40°$ and $50°$

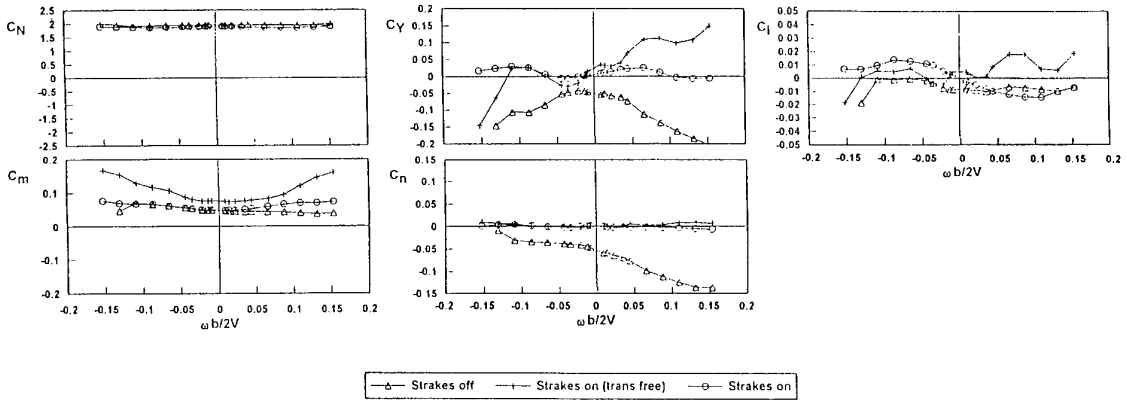

Fig 3.3 - Config : BWLHV(S)T, Effect of nose strakes at $\alpha = 40°$, 40° crank

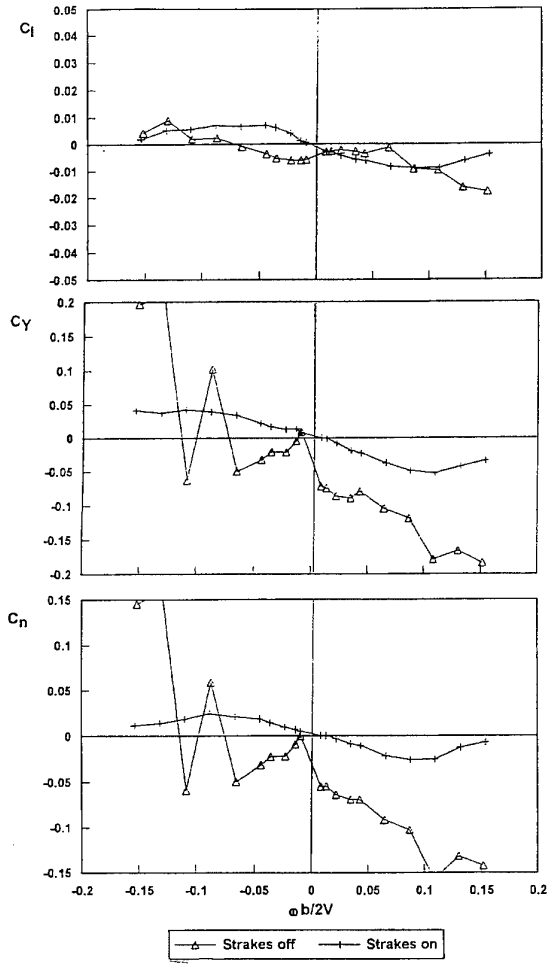

Fig 3.4 - Config : BWLHV(S)T,
Effect of nose strakes at $\alpha = 50°, 60°$ crank

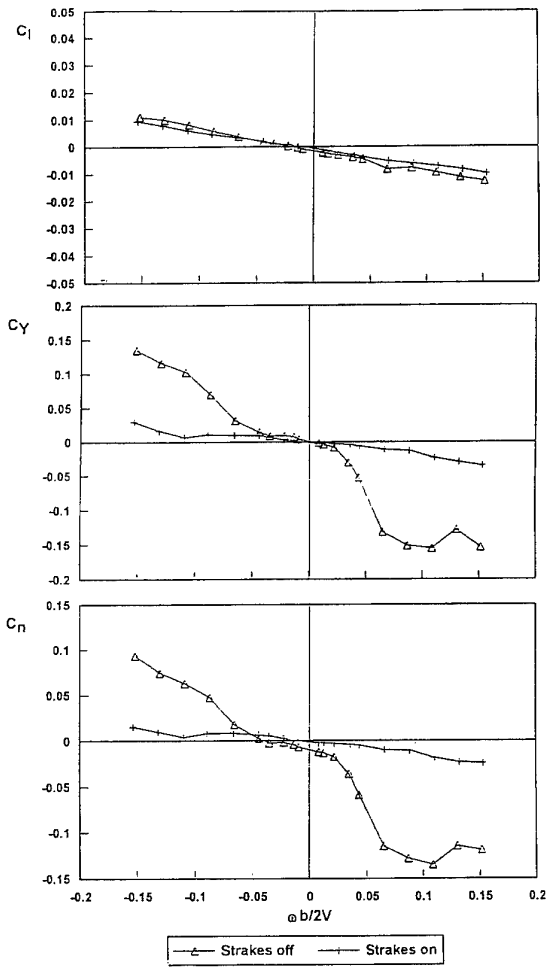

Fig 3.5 - Config : BWLHV(S)T,
Effect of nose strakes at $\alpha = 60°, 60°$ crank

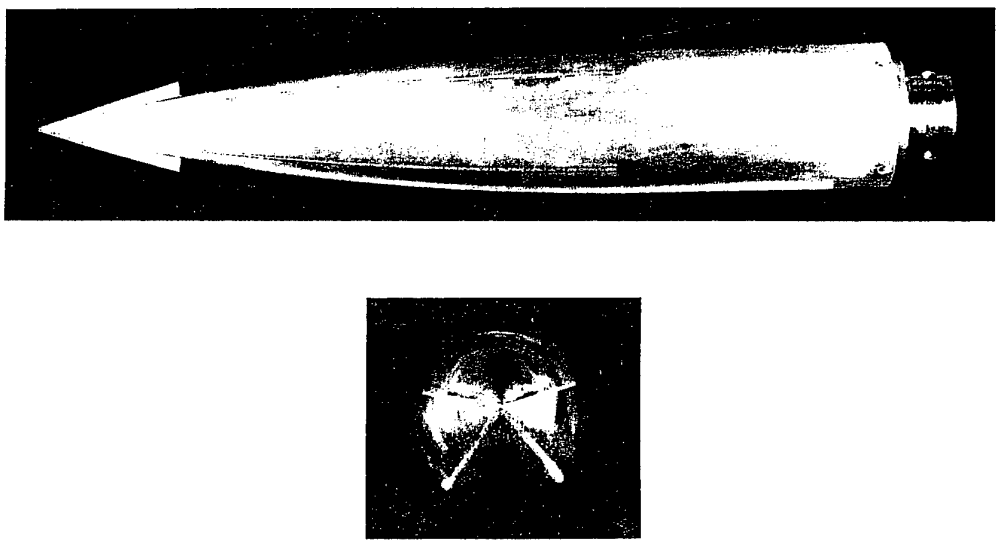

Fig 3.6 - Transition Fixing (T) and Strakes (S) on model forebody

3.2 EFFECTS OF TRANSITION FIXING TYPE (FFA , Model B)

The first parts of the tests were made with the transition strips applied by DRA. Two 0.2 mm high grit strips, 3 mm wide were symmetrically disposed on the windward side of the forebody at radial locations ± 40° from the x-z plane. The strips ran between the tip of the nose and the LEX apex.

The second series of tests were made with the transition strips applied by AerMacchi at the same position on the forebody. The AerMacchi grit strips were a string of resin disks with a thickness of 0.3 - 0.5 mm, a diameter of approximately 1.5 mm and a spacing of 2.5 mm.

Figure 3.7 presents effects of transition fixing at $\alpha = 40°$, 60 m/s, on body-alone with strakes. There is a larger zero offset with British trips (DRA) compared with Italian trips (AeM) for both yawing moment and side force.

The rolling and yawing moment characteristics are similar for both transition strips. The side force for the BS configuration appears to be more sensitive than other components to the type of transition fixing.

Figure 3.8 presents the effect of transition fixing at $\alpha = 32°$, 60 m/s, on the complete configuration with strakes.

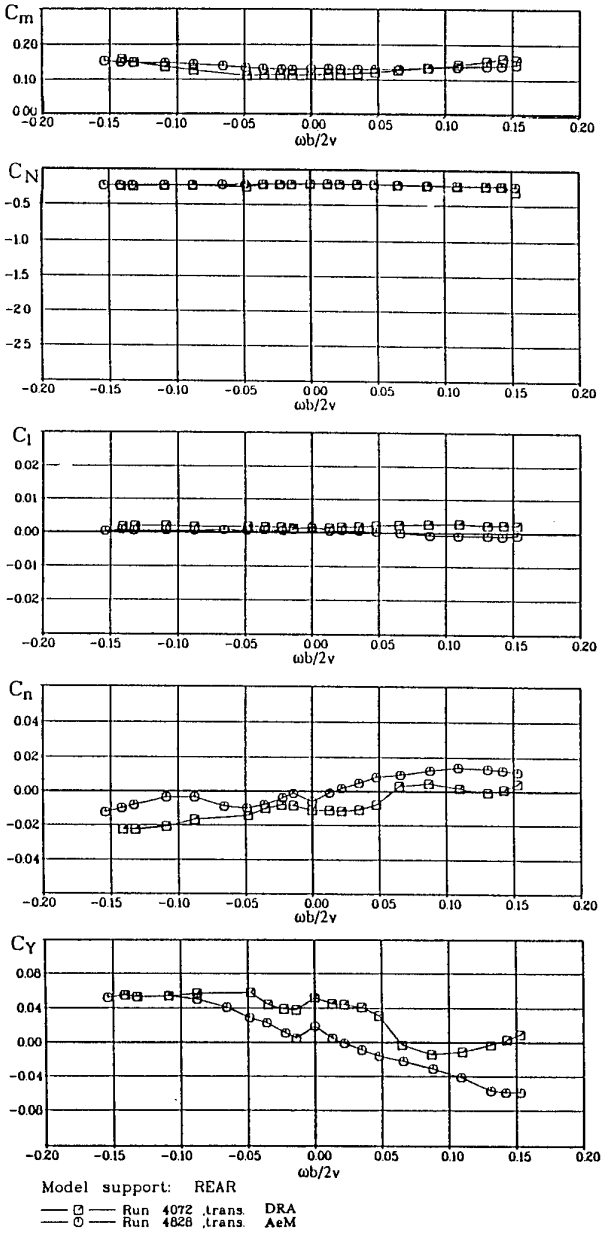

Fig 3.7 - BST Configuration
Effect of transition fixing type at $\alpha = 40°$, V = 60 m/s

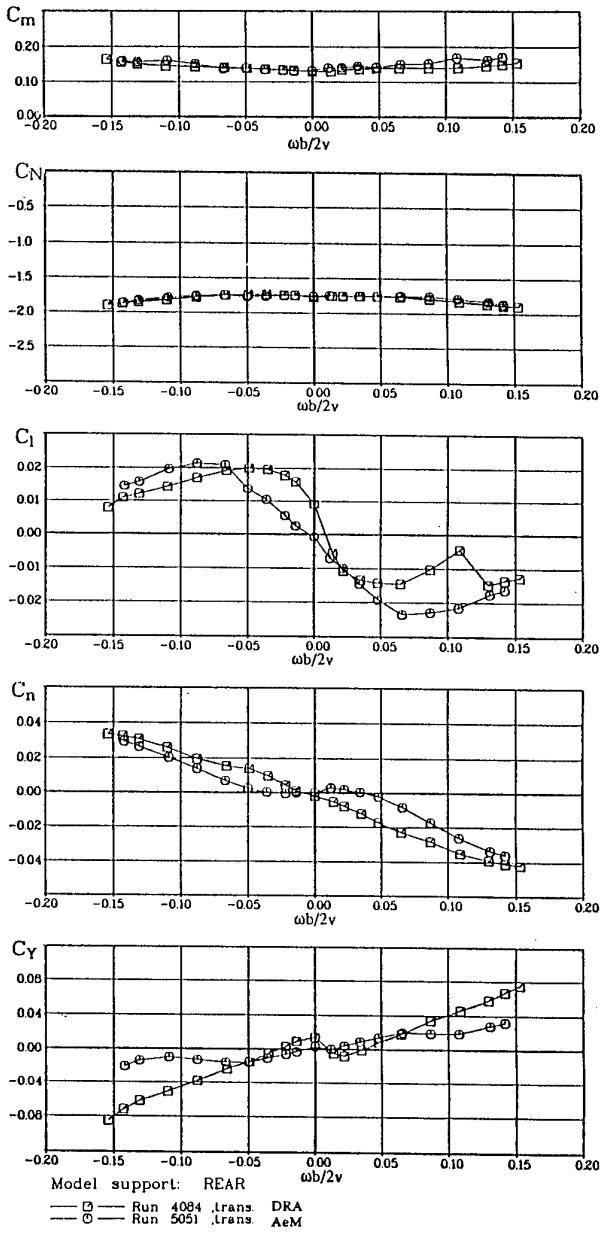

Fig 3.8 - BWLHVST Configuration
Effect of transition fixing type at $\alpha = 32°$, V = 60 m/s

C_l is more linear and has a much smaller zero offset with AeM than with DRA. C_n is neutrally stable at low Ω with AeM , but it is always stable with DRA. The stability in C_Y changes at low positive Ω with DRA, otherwise it is more stable than with AeM.

At α = 40° (Fig 3.9.a), there are some differences in C_l , C_n and C_Y, but they do not affect the general behaviour of the coefficients. There are no differences in normal force and pitching moment.

At lower velocity, V = 30 m/s (Fig 3.9.b), C_l , C_n and C_Y are asymmetric with AeM, and the changes with rotation rate are more regular than with DRA.

Generally, the DRA and AerMacchi transition strips have similar effects on the measured forces and moments. However, comparisons of Figs 3.9.a and 3.9.b suggest that by applying the DRA or AeM transition strips, a complete turbulent boundary layer is not achieved, because otherwise the yawing moments and side forces at 30 m/s and 60 m/s should be alike.

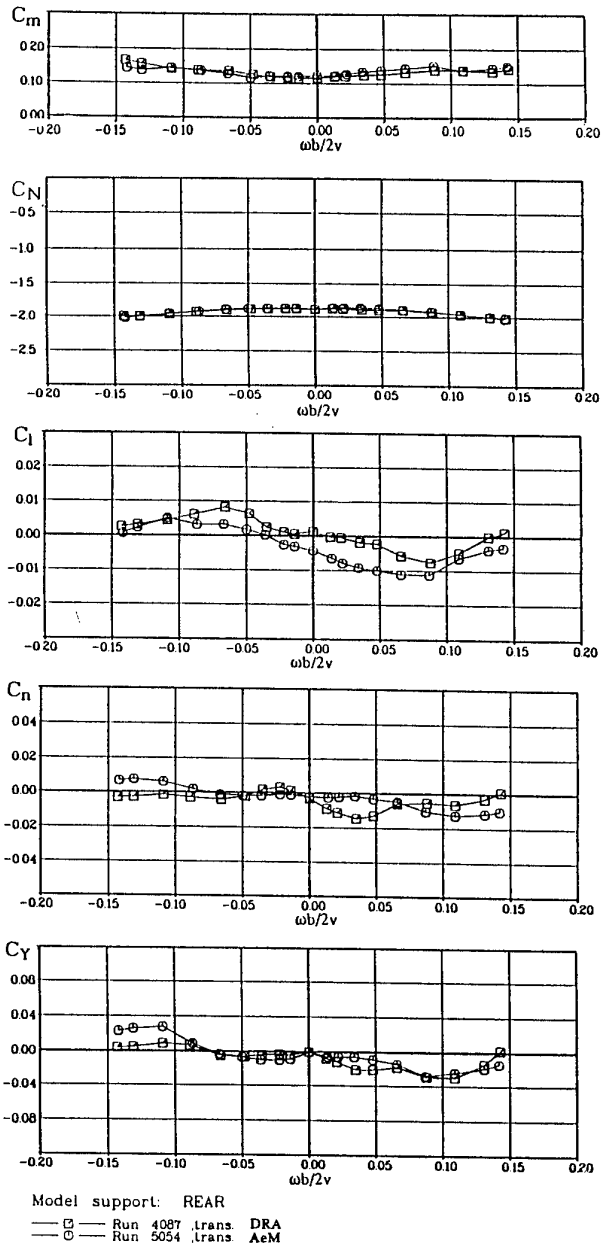

Fig 3.9.a - BWLHVST Configuration
Effect of transition fixing type at α = 40°, V = 60 m/s

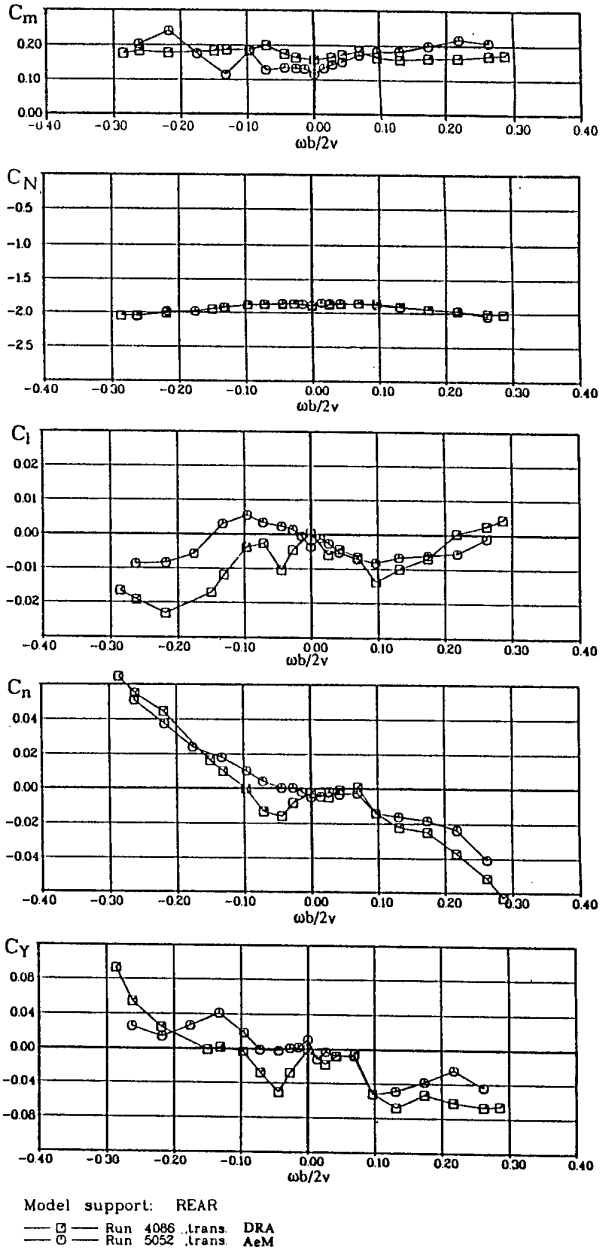

Fig 3.9.b - BWLHVST Configuration
Effect of transition fixing type at α = 40°, V = 30 m/s

3.3 REYNOLDS NUMBER EFFECTS (ONERA / IMFL , EIDETICS)

3.3.1 Static Tests (ONERA / IMFL, Model A, AeM transition trips)

On the "PQR" apparatus slow sweeps from 0 to 80 degrees of angle of attack were performed at different airspeed values in order to investigate Reynolds number effects in the test range.

Figure 3.10 shows results obtained on the complete clean configuration (BWLHV) for the varying Reynolds numbers based on the mean aerodynamic chord : 0.545 x 10^6 for V=25m/s, 0.655 x 10^6 for V=30m/s and 0.875 x 10^6 for V=40m/s. Data obtained at R=0.545 x 10^6 and 0.655 x 10^6 are quite similar. Only a slight Reynolds number effect can be noted for the highest Reynolds number tested. Indeed, at R= 0.875 x 10^6, normal force is larger for $22° < \alpha < 32°$ and a bit smaller at high angles of attack, for alpha greater than 40 degrees. In this α-range the pitching moment coefficient is smaller than for the lowest two Reynolds number tests. Explanation of this phenomenon was thought to be mainly due to sensitivity of the forebody flow to Reynolds number. Side force and yawing moment are not significantly influenced. The same asymmetry is encountered for different airspeed values in this Reynolds number range.

Figure 3.11 shows results obtained for the BWLHVST configuration for the same Reynolds numbers as previously. On this configuration fitted with transition tripping and strakes, Reynolds number effects are more significant. Moreover side force and yawing moment are smaller than on the clean configuration but they are not exactly nul for every Reynolds number and angle of attack. In fact forebody strakes force symmetric separations at the nose apex. However, these strakes are relatively short in comparison with the forebody and they effect a limited length of the forebody. With regards to Reynolds number effects obtained on the BWLHVST configuration two main tendencies can be noted:

-asymmetry decreases as Reynolds number increases : the higher the Reynolds number, the lower the side force C_Y and the yawing moment C_n. At the highest Reynolds number the flow is symmetric in the whole α-range.

-at high angles of attack, the pitch down tendency increases with Reynolds number.

These results are consistent with those obtained by Lamont (Ref 3) and Champigny (Ref 4) on ogive cylinder bodies or missiles. Experiments conducted at high angles of attack on such bodies have shown two main features:

1) Maximum overall side force is very dependent on the flow regime at separation: laminar, transitional or turbulent. Figure 3.12a presents maximum side force as a function of Reynolds number R_{eD} based on cylinder diameter. In laminar or turbulent separation regimes, flow is asymmetric and sideforce is not very sensitive to Reynolds number. However in transitional separation regime sensitivity to Reynolds number is large and side force tends to be significantly smaller.

On model A tests were performed for R_{eD} = 0.172 x 10^6 (V=25m/s), 0.207 x 10^6 (V=30m/s) and 0.276 x 10^6 (V=40m/s). These conditions correspond to a laminar separation for the forebody flow. This point has been confirmed by flow visualizations performed at IMFL on model A. Data obtained on the PQR apparatus with the clean configuration are in good agreement with Lamont results (Fig 3.10). Indeed, a large asymmetry of the flow and a low dependency on Reynolds number were obtained on the clean configuration. For the model fitted with nose strakes and forebody transition strips, results show that asymmetry is dependent on Reynolds number. This phenomenon is probably due to transition tripping which acts on the boundary layer and forces it closer to a transitional regime. In this case, adding transition tripping can be seen as an increase of effective Reynolds number for the forebody flow. Thus it corresponds to a displacement to the right on the curve in Fig 3.12a. Consequently results for the BWLHVST configuration are more sensitive to Reynolds number and asymmetry decreases as R increases (Fig 3.11) as obtained on forebodies in transitional regime.

2) The second feature is the Reynolds number effect on forebody normal force. On Fig 3.12b normal force coefficients obtained on an ogive cylinder configuration are plotted against alpha at different Reynolds numbers corresponding to laminar, transitional and turbulent regimes. It can be seen that normal force is much smaller in the transitional regime than in turbulent or laminar regimes. Consequently this result will cause lower values of pitching moment on a complete configuration at transitional Reynolds number.

Pitching moment results in Fig 3.10 and 3.11 are also in good agreement with the results of Lamont and Champigny. Indeed, for the configuration fitted with transition strips C_m is more sensitive to Reynolds number and pitching moment decreases with R (transitional regime). This phenomenon is less apparent on the clean configuration because forebody separation is then laminar.

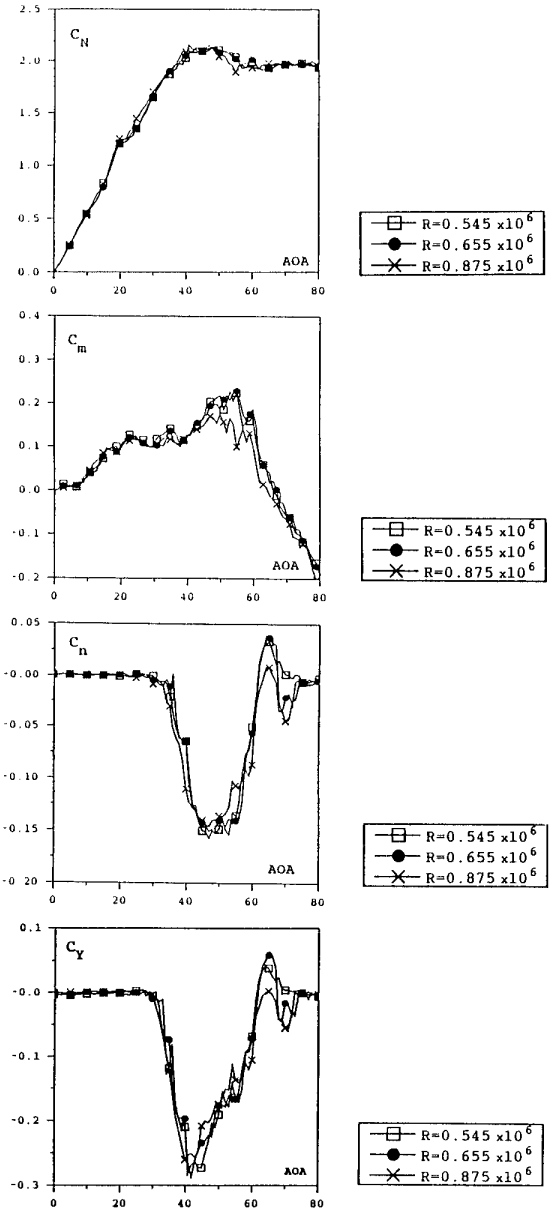

Fig 3.10 - BWLHV Configuration - Effect of Reynolds Number, Slow Sweeps in angle of attack

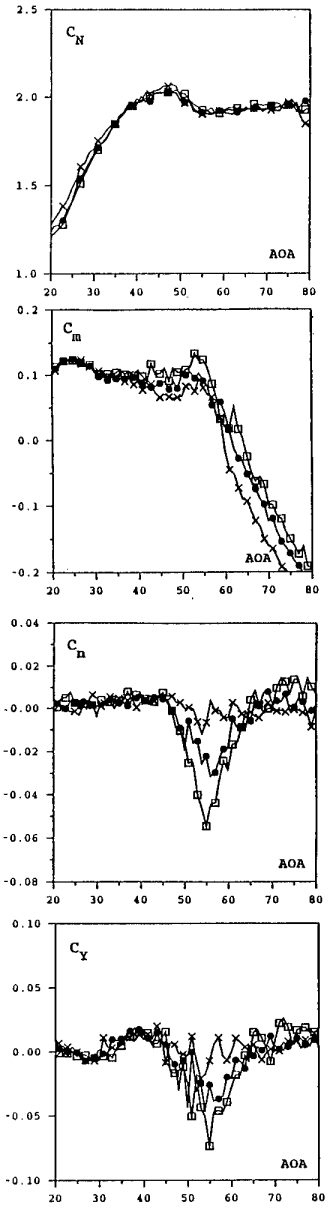

Fig 3.11 - BWLHVST Configuration - Effect of Reynolds Number, Slow Sweeps in angle of attack

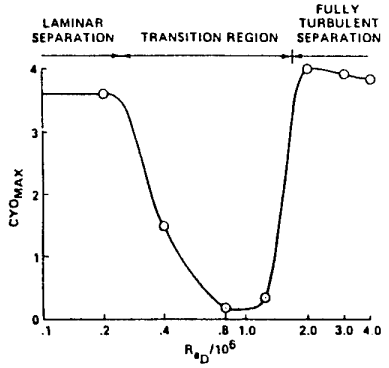

3.12.a -Variation of maximum overall side force with Reynolds Number Re_D

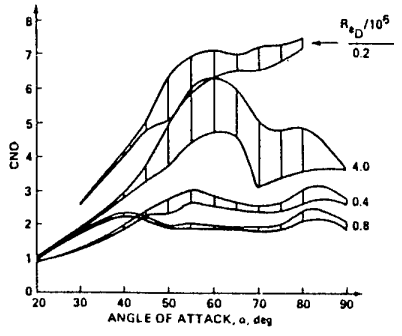

3.12.b -Variation of normal force with angle of attack at different Re_D

Fig 3.12 - Reynolds Number effect on an ogive cylinder (Ref 3.3)

3.3.2 Rotary Balance Tests (EIDETICS, Model B, DRA transition trips)

The following discussion focuses on the Reynolds number effects observed in rotary-balance tests conducted by Eidetics in the NASA Ames 7 x 10.Ft Wind Tunnel on Model B.

Figures 3.13 to 3.20 show the effects of Reynolds number on a series of build-up configurations (with transition strips and without forebody strakes) from body-alone (BT) to the complete configuration (BWLVHT) at angles of attack of 39° and 51°. For comparison, Figs 3.21 and 3.22 show the complete configuration with forebody strakes (BWLVHST). The Reynolds numbers were varied by changing the tunnel free stream velocity. The Reynolds numbers based on the wing mean aerodynamic chord for the varying velocities are 0.478×10^6 for V=100 ft/sec, 0.720×10^6 for V=150 ft/sec (Figs 3.18 and 3.19 only) and 0.955×10^6 for V=200 ft/sec. Probably more important for the body alone are the Reynolds numbers based on diameter of 0.151, 0.226 and 0.302 $\times 10^6$, respectively. This Reynolds number range for the body results in flow that is likely mostly laminar at the low velocity and transitional in the higher ranges. Where it varies from laminar to transitional will also depend on the angle of attack. The resulting boundary layer separation in cross flow will be very sensitive to variations in velocity and angle of attack in this range.

Figures 3.13 and 3.14 are for the body alone. The side force and yawing moments are substantially different for the two Reynolds numbers, and the differences are magnified with increasing angle of attack. The most significant effect is the change in overall slope with rotation rate. For the low Reynolds number at 39° AOA (Fig 3.13), the yawing moment would contribute to damping in roll about the velocity vector. At the higher Reynolds number, the slope is nearly zero and would play a neutral role. For 51° AOA (Fig 3.14) the low Reynolds number data show a damping contribution (anti-spin), and high Reynolds number results show a slight undamped (pro-spin) contribution. The rolling moment, as expected, is zero. These results show clearly that even with grit on the forebody to promote transition, it is still not possible to make the low Reynolds number results similar to the high Reynolds number results. This is not too surprising, considering that the flow field on the remaining part of the body behind the region where the transition strips are located is not necessarily going to be affected by the flow characteristics in the region of the transition strips, especially at high angles of attack. There are some small differences in the normal force and pitching moment with the lower Reynolds number resulting in slightly larger values for both coefficients, particularly at 51° AOA.

Figures 3.15 and 3.16 show the effect of adding the wing. Side force and yawing moments are still distinctly different for the two Reynolds numbers and very similar to the body-only data, suggesting that the wing doesn't have much effect on yawing moment and side force. As expected, there is now a measurable rolling moment produced by the wing. There are some differences with Reynolds number at 39° AOA (Fig 3.15), but results are nearly the same for both Reynolds numbers at 51° AOA (Fig 3.16). There remains a difference in the normal force, although small, and in the pitching moment at the two different Reynolds numbers.

Figures 3.17 and 3.18 show the additional effect of adding the LEX. There are no significant changes from the results of the body-wing configuration. The only real changes are in the rolling moment, particularly at the lower Reynolds number and mostly at the positive rotation rates. The lack of asymmetry in the data with positive and negative rotation directions is also strong evidence of the sensitivity of the flow field to the sharp forebody at high angles of attack, as discussed at length previously in Sections 3.1 and 3.2 and further in Section 3.7. The pitching moment differs as shown in the previous figures, but the normal force is nearly the same for both Reynolds numbers.

Figures 3.19 and 3.20 show the effect of adding the horizontal and vertical tails. For the most part the results are very similar to the body-wing-LEX configuration, indicating that the results are primarily dependent on the forebody configurations and the tails play a very minor role. There are still some significant differences between the data at the two different Reynolds numbers, particularly the yawing moment and side force. The rolling moment data are similar, but at the high positive rotation rates the rolling moment is still contributing a strong pro-spin contribution to the moment about the velocity vector. As in Figs 3.19 and 3.20 the normal force is nearly identical, and the pitching moments vary somewhat with different Reynolds numbers.

For comparison, Figs 3.21 and 3.22 show the complete configuration, as in Figs 3.19 and 3.20, but with strakes added to the forebody. There are also data for an intermediate Reynolds number. The first noticeable difference, which will be discussed at length later in Section 3.5, is that the strakes nearly eliminate the asymmetry of the forebody flow, resulting in yawing moment and side forces at zero rotation rate that are nearly zero. Also apparent is the elimination of Reynolds number effects for side force and yawing moment. Yawing moment is damped to neutral. Rolling moments still exhibit some sensitivity to Reynolds number, especially between the lowest and intermediate Reynolds numbers. The data at the two higher Reynolds numbers (for V=150 and 200 ft/sec) are nearly the same. The unstable rolling moment observed at high rotation rates on the configuration without forebody strakes (at 51° AOA, for example shown in Fig 3.20) is still apparent in Fig 3.19 for the strakes-on configuration. But now the behavior of the rolling moment with rotation rate has near mirror symmetry about zero rotation rate, which was not observed for the configuration with strakes off in Fig 3.20. The normal force values are nearly identical for all Reynolds numbers and the pitching moment at the lowest Reynolds number is higher, in general, than for the two higher Reynolds numbers.

The effect of the forebody strakes is to force a symmetric separation of the flow on the forebody which has a strong stabilizing effect on the forebody flow. The forebody flow separation locations and resulting vortex strengths and positions from left and right vortices are not allowed to vary with strakes as they are with a clean forebody. The sensitivity of the flow field to minor perturbations at the tip of the forebody has been nearly eliminated, resulting in a much better behaved and predictable flow field. This is the primary reason for choosing the configuration with strakes as the baseline configuration for comparison of experiments in different facilities discussed in Chapter 4.

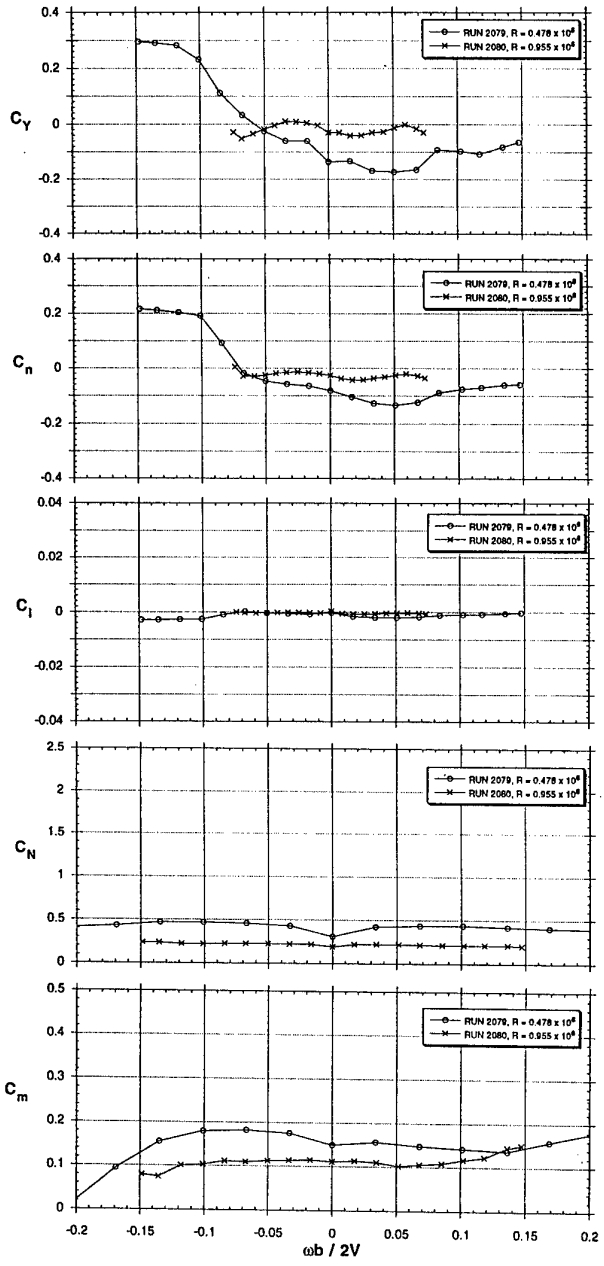

Fig 3.13 - Effects of Reynolds No.
body-alone (BT), $\alpha = 39°$
(R=0.478, 0.955 x 10^6 for V=100, 200 ft/s)

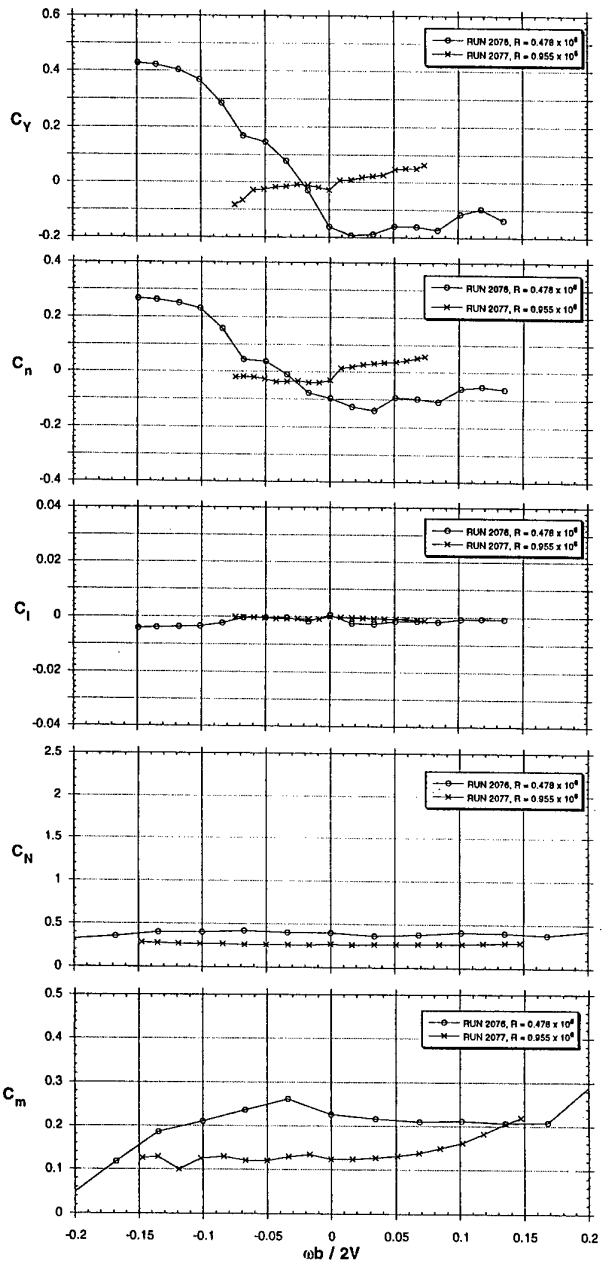

Fig 3.14 - Effects of Reynolds No.
body-alone (BT), $\alpha = 51°$
(R=0.478, 0.955 x 10^6 for V=100, 200 ft/s)

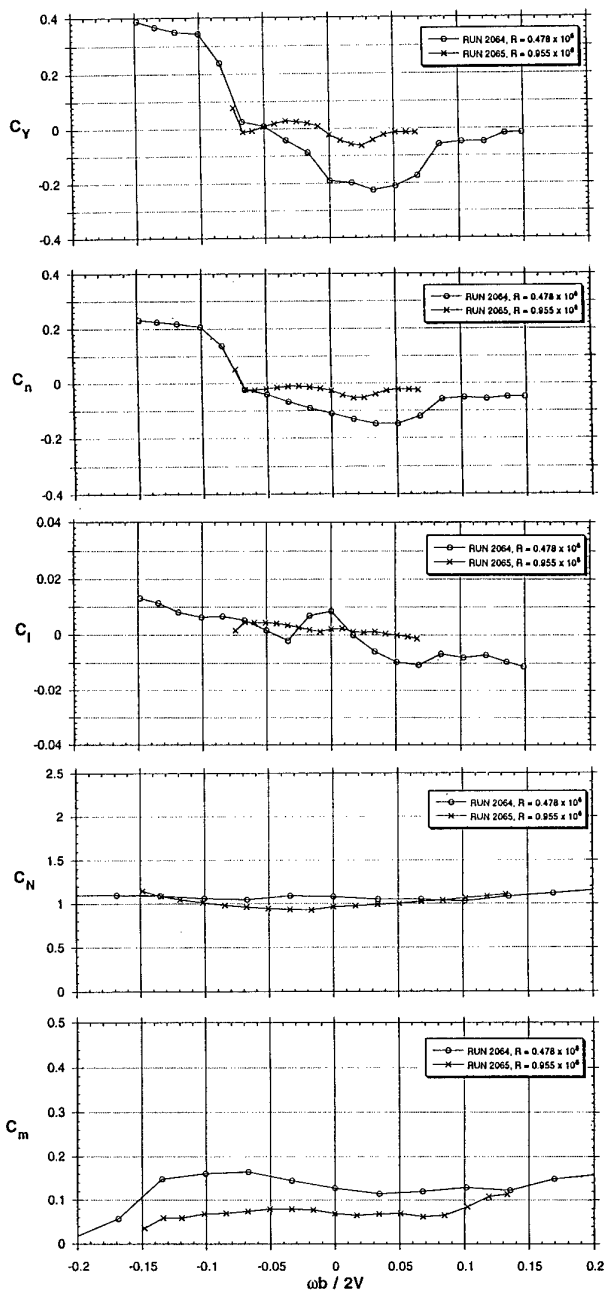

Fig 3.15 - Effects of Reynolds No.
body-wing (BWT), $\alpha = 39°$
(R=0.478, 0.955 x 10^6 for V=100, 200 ft/s)

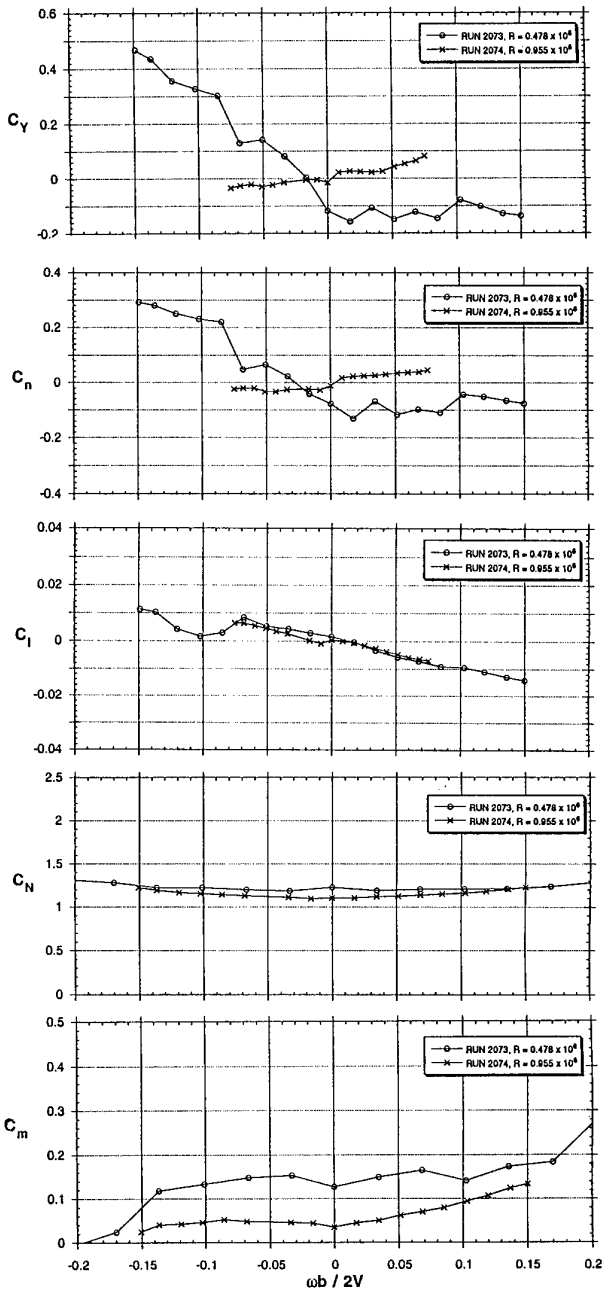

Fig 3.16 - Effects of Reynolds No.
body-wing (BWT), $\alpha = 51°$
(R=0.478, 0.955 x 10^6 for V=100, 200 ft/s)

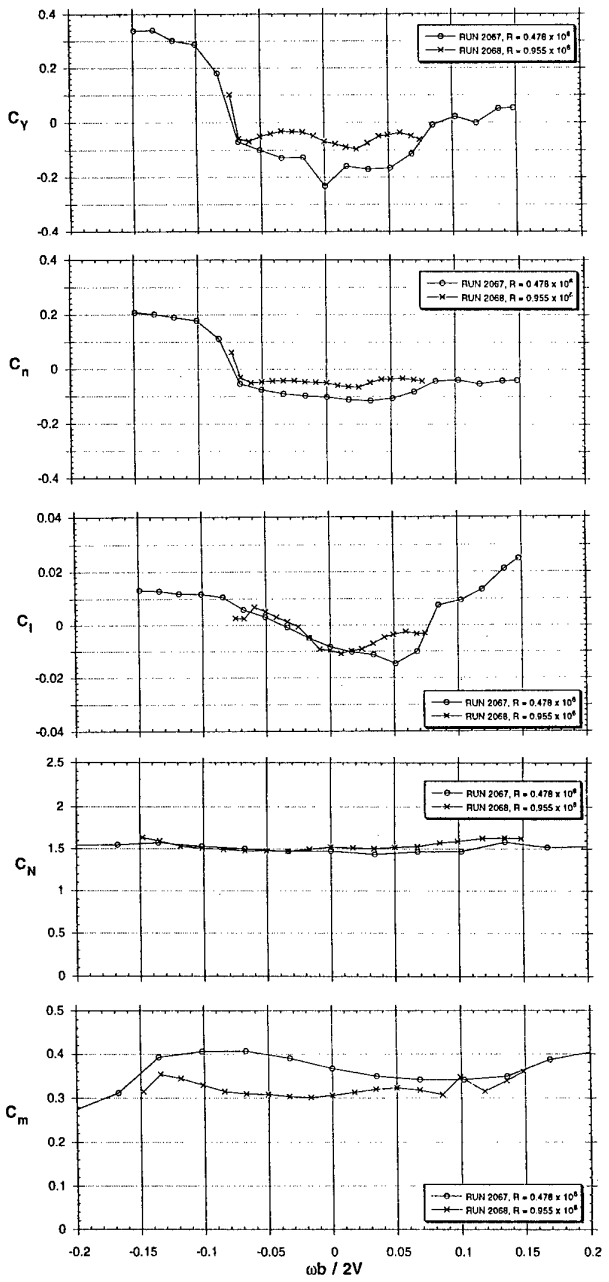

Fig 3.17 - Effects of Reynolds No.
body-wing-LEX (BWLT), $\alpha = 39°$
(R=0.478, 0.955 x 10^6 for V=100, 200ft/s)

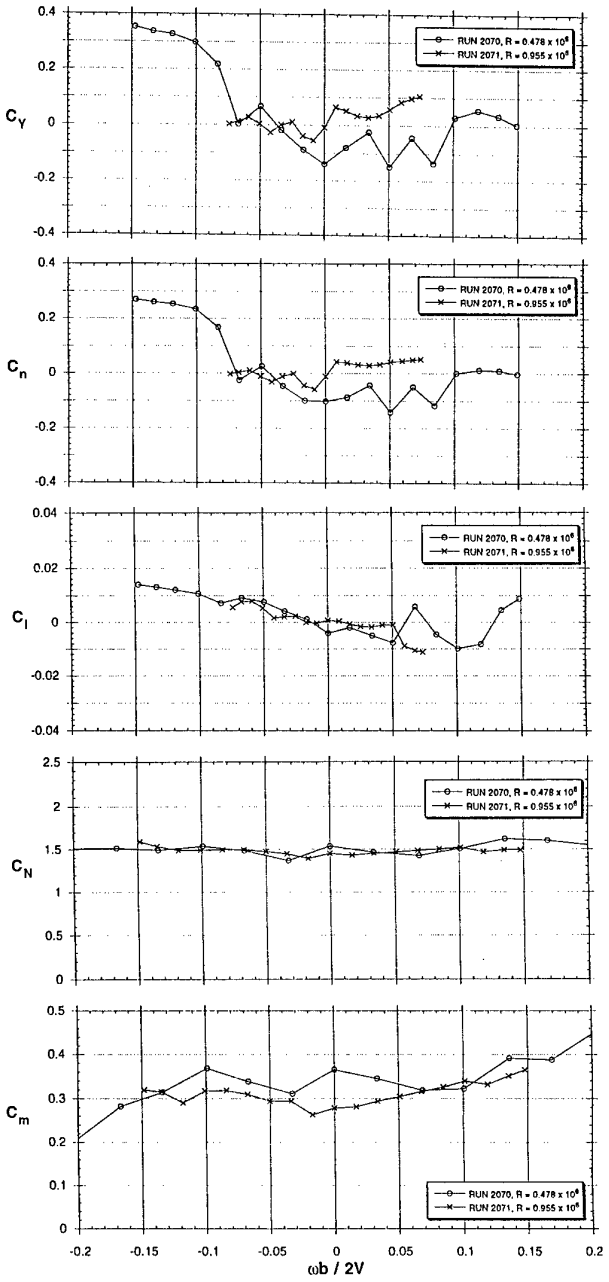

Fig 3.18 - Effects of Reynolds No.
body-wing-LEX (BWLT), $\alpha = 51°$
(R=0.478, 0.955 x 10^6 for V=100, 200ft/s)

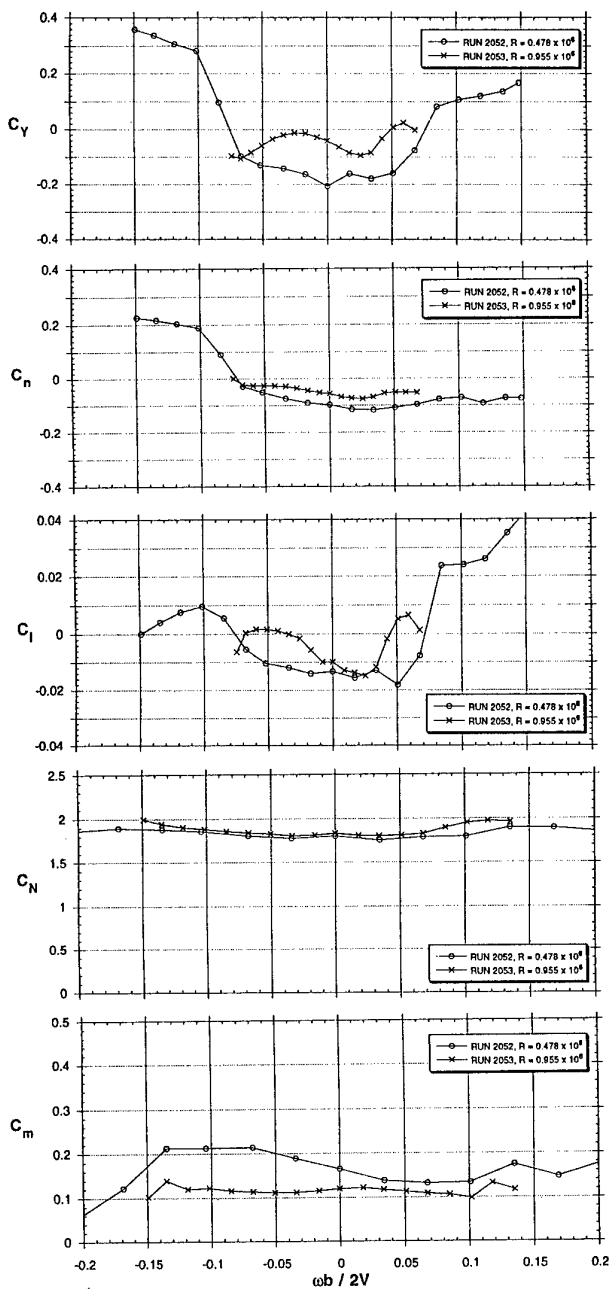

Fig 3.19 - Effects of Reynolds No.
body-wing-LEX-tails (BWLVHT), $\alpha = 39°$
(R=0.478, 0.955 x 10^6 for V=100, 200 ft/s)

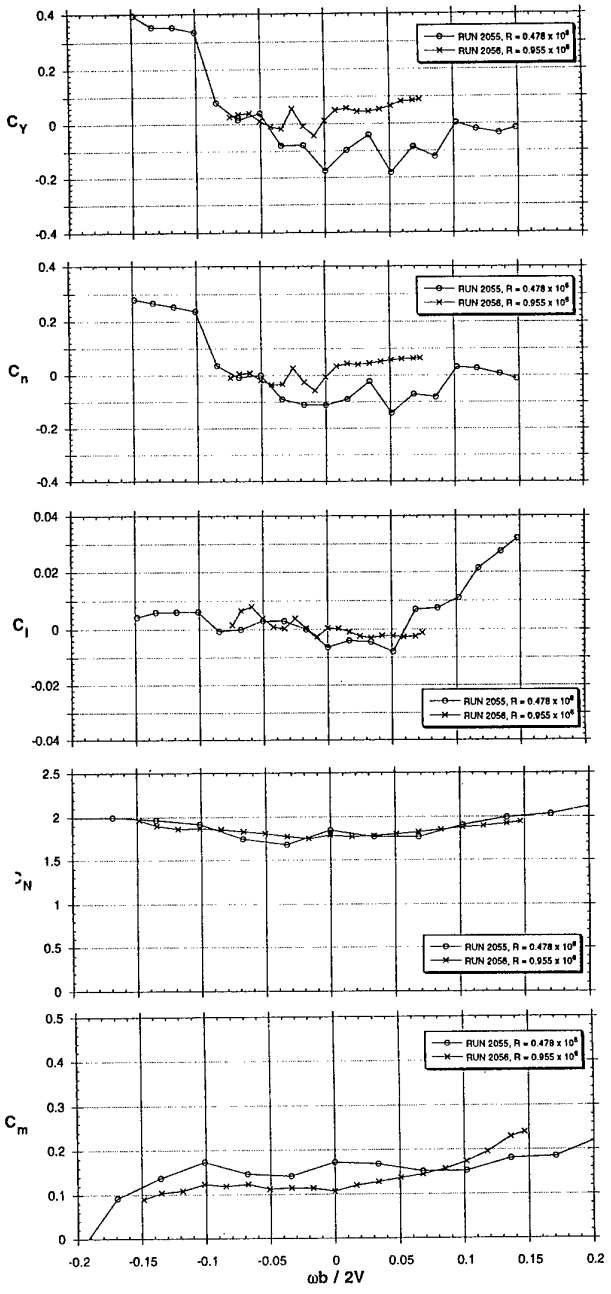

Fig 3.20 - Effects of Reynolds No.
body-wing-LEX-tails (BWLVHT), $\alpha = 51°$
(R=0.478, 0.955 x 10^6 for V=100, 200 ft/s)

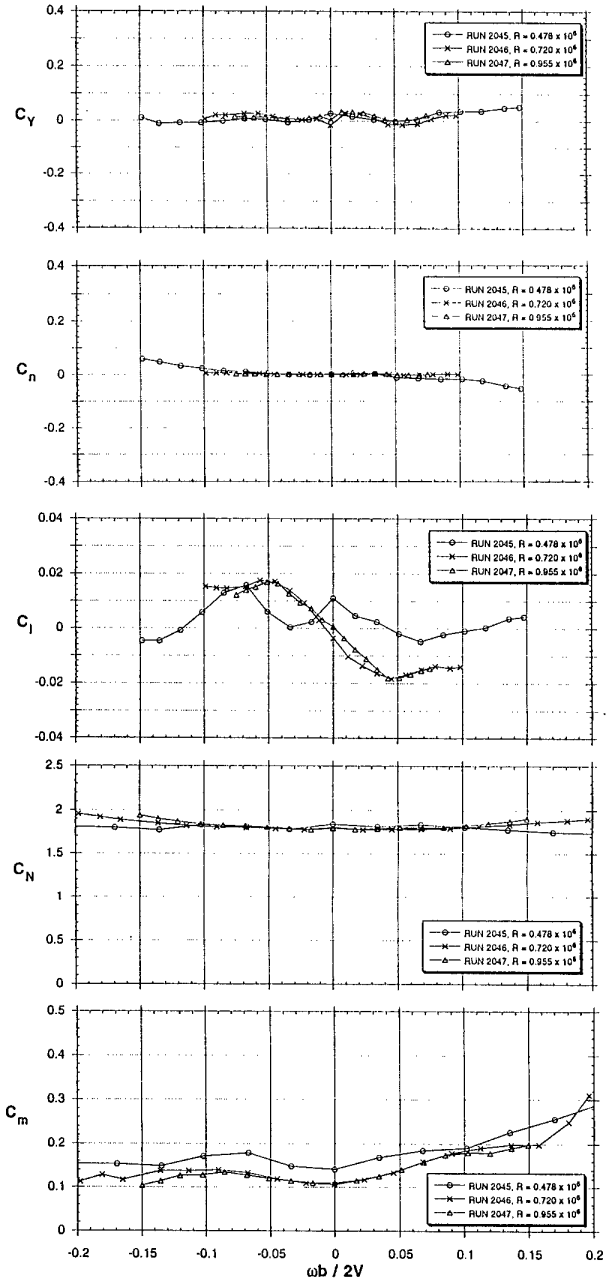

Fig 3.21 - Effects of Reynolds No.
body-wing-LEX-tails-strakes (BWLVHST) $\alpha = 39°$
(R=0.478, 0.955 x 10^6 for V=100, 200 ft/s)

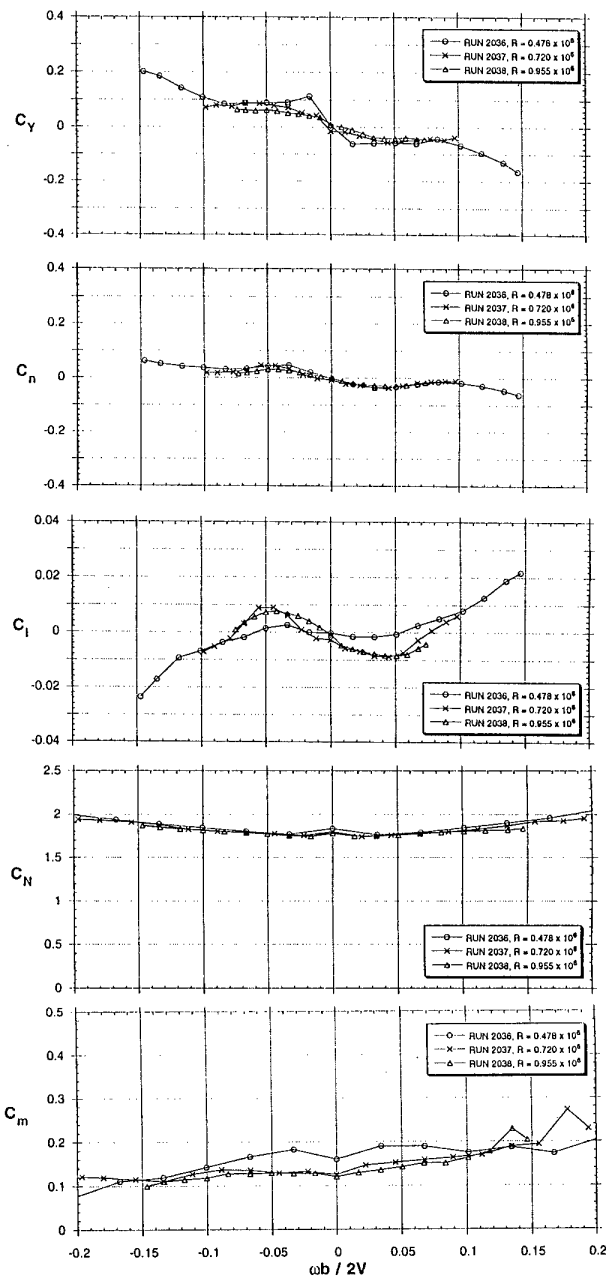

Fig 3.22 - Effects of Reynolds No.
body-wing-LEX-tails-strakes (BWLVHST), $\alpha = 51°$
(R=0.478, 0.955 x 10^6 for V=100, 200 ft/s)

3.4 MODEL SIZE EFFECTS - MODEL A VERSUS MODEL B (AerMacchi, AeM trans. trips)

The availability of two models of different sizes gave a unique opportunity for tests showing effect of model size within the same wind tunnel test section and on the same balance and rear sting support. This is a classical way to highlight effects of the finite size of the test section and thus of presence and amount of wall interference. The AerMacchi wind tunnel was properly sized for such an exercise. In fact model A represents a relatively "large" model for the tunnel : its wing area is 6.2% of tunnel cross section but, most important, overall length is 63% of tunnel diameter. Model B is definitely a small model since its wing area is 3.3% of tunnel cross section and its length is 46% of diameter. In this specific case, two further spurious effects exist and have to be taken into account, since they may, in principle, be as large as wall interference. Such effects include:

-varying support interference. In fact the relative size and distance of the balance rotating arm are different on models of different size, the arm being nearer and smaller (in relative terms) for the large model compared to the small one; this might in principle lead to different support interferences in the two cases ;

-the overall variability of results typical of the strake-off configuration at high angle of attack : in the angle-of-attack range $40° < \alpha < 50°$, results of the strake-off configuration depend on random factors even on the same model. This makes any comparison very uncertain for this configuration and angle-of-attack range and, therefore, no results of the strake-off configuration are shown ;

-any geometrical difference between the models. In this case, apart from normal manufacturing tolerances, which are not expected to give effect on results, a small difference exists between models A and B in the chamfer angle of the wing tips.

Tests were made in both open and closed wall test sections with very similar results. The comparison for the open test section case is shown in Figs 3.23 to 3.26. The four cases cover two low angle-of-attack conditions, when no forebody vortex flow is present, one intermediate angle of attack (24°) and one high angle of 40°.

The comparison at 0° and 8° AOA (Figs 3.23 and 24) shows perfect coincidence of normal and side forces as well as pitching moment. A small but significant difference is present on rolling and yawing moments : such a difference is consistently present in various conditions.

The comparison at 24° (Fig 3.25) shows in general a good agreement. The only significant feature is the absence of the temporary change of sign of rolling moment which is present on model A at about $\Omega = \pm 0.08$. The reason for the difference is unknown but this effect is not present when the model is tested in a closed test section (see Fig 3.54).

At 40° (Fig 3.26), the comparison shows an asymmetric flow condition on model B which is not present on model A. Some differences also appear in normal force and pitching moment. In fact, water tunnel flow visualizations simulating the relative size of rotating supports for models A and B did show some interference effects on the forebody vortex flow of model B at angles of attack of 40° and greater. But in general, although quantitatively different in some respects, the two results show comparable trends and effects.

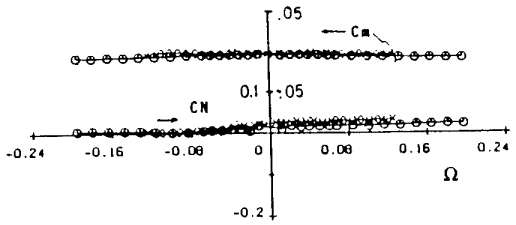

Fig 3.23 - Model A vs. Model B results - BWLVHST conf. AeM tests - $\alpha = 0°$

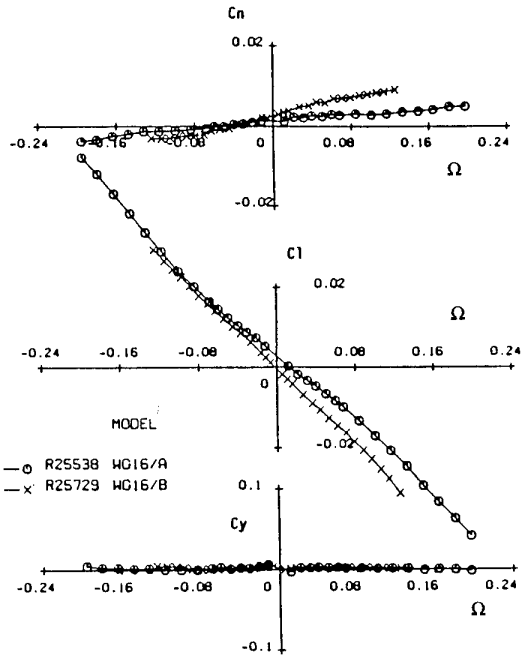

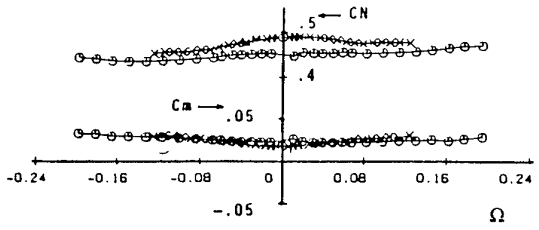

Fig 3.24 - Model A vs. Model B results - BWLVHST conf. AeM tests - $\alpha = 8°$

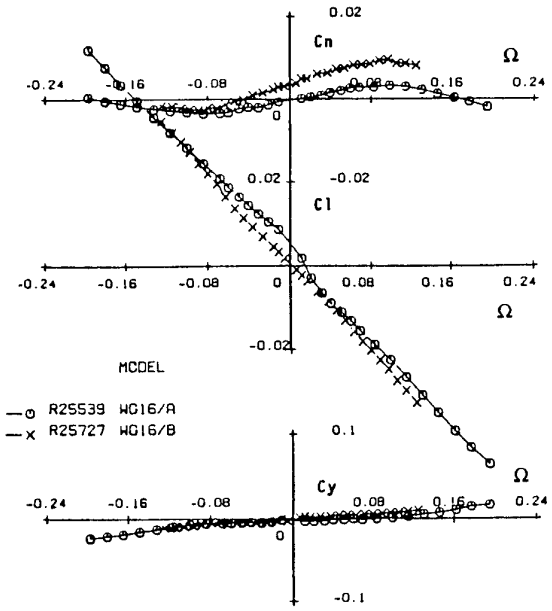

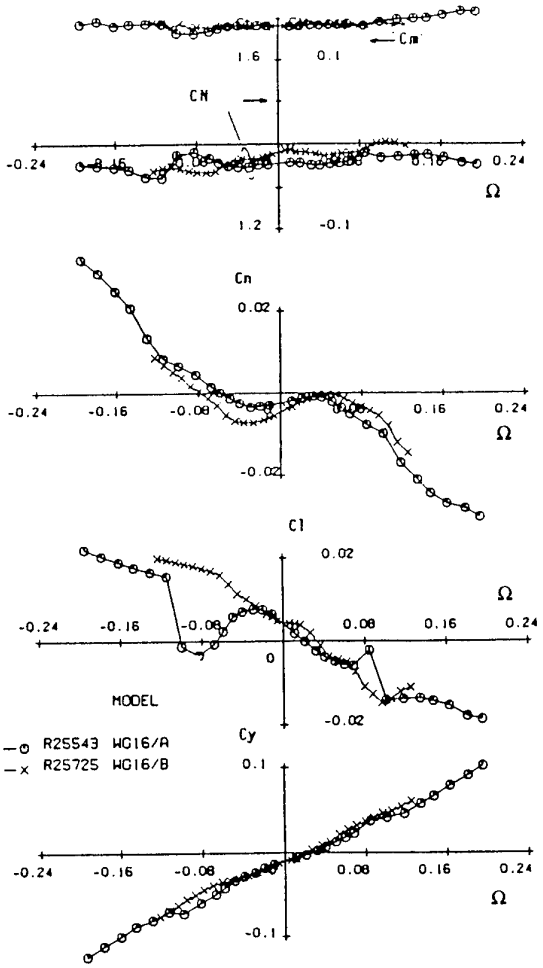

Fig 3.25 - Model A vs. Model B results - BWLVHST conf. AeM tests - $\alpha = 24°$

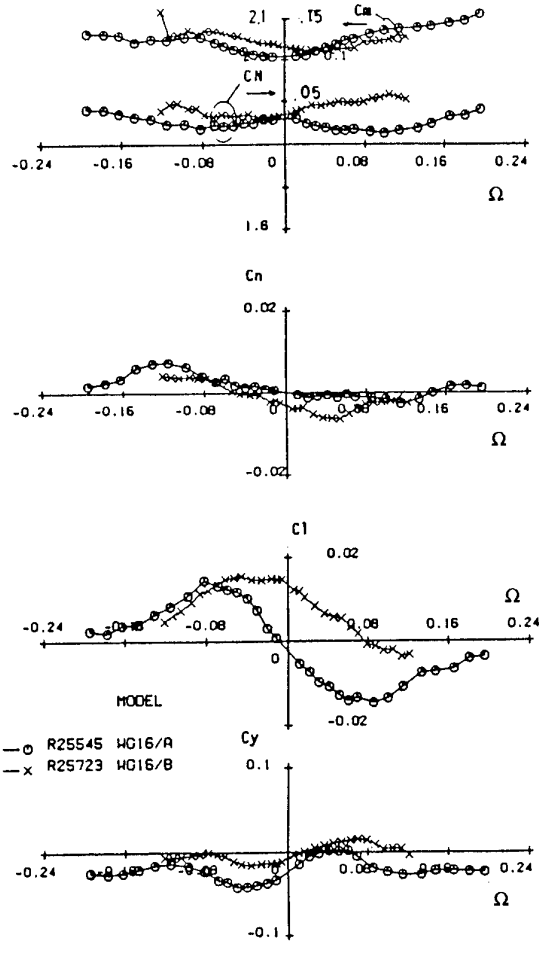

Fig 3.26 - Model A vs. Model B results - BWLVHST conf. AeM tests - $\alpha = 40°$

3.5 CONFIGURATION BUILD-UP EFFECTS, STRAKES-OFF & STRAKES-ON ,WITH TRANSITION (EIDETICS , Model B , DRA transition trips)

Figures 3.27 to 3.29 show a configuration buildup without forebody strakes for angles of attack of 24°, 39° and 51° at a Reynolds number of 0.955 x 10^6. Tests were carried out with transition fixing on the forebody as described in Section 3.1.

At 24° AOA, even though there does not appear to be much of an offset at zero rotation rate for yawing moment, there is a sizable rolling moment offset for all configurations except for body alone. Even though the vortices may be only slightly asymmetric at this angle of attack, the interaction of the forebody vortices with the LEX and wing flow fields can be significant. At this angle of attack, we know from prior water tunnel flow visualizations tests that the burst point of the LEX vortex is near the mid-chord of the wing and is very sensitive to the influence of the forebody vortices. Any asymmetry that exists in the forebody vortices in the proximity of the LEX vortex burst point can create large induced asymmetries in the LEX flow and, consequently on the wing flow, resulting in differential lift contributions. This appears to be the case, since the rolling moments are quite large at zero rotation rate. The zero-rotation offset in roll is also not influenced greatly by rotation, except in the case for body-wing, where it agrees with the body-wing-LEX configuration only at negative rotation rates. At positive rates, it tends to agree with the body-alone. Adding the LEX (and tail) tends to stabilize the asymmetric pattern, and the variation with rotation rate is less dramatic. However, the effect of rotation does not produce equal and opposite effects with positive and negative roll rates.

At 39° and 51° AOA in Figs 3.28 and 3.29, there is a much smaller effect on rolling moment offset and larger effects on the yawing moment. The effects of adding the wing to the body are very small at all rotation rates. Adding the LEX, however, provides a significant contribution to both the rolling and yawing moment variations. The asymmetry of the pitching moment with positive and negative rotation rates is somewhat unexpected, as discussed later. However, in examining the yawing moment and side force variations at 51° AOA, there is a consistency in their behavior with rotation rate (larger changes in positive direction with positive rotation than negative changes with negative rotation). The consistency with yawing moment and pitching moment would indicate a forward shift in the center of pressure that is reflected in both yawing and pitching moments with positive rotation rate and little or no shift with negative rotation rate. This is entirely possible with a high angle-of-attack induced flow asymmetry that is more sensitive to the perturbations contributed from rotating in one direction compared to the other, but it is not predictable.

For both angles of attack, there is a noticeable asymmetry in the pitching moment coefficient with positive and negative rotation rates. A systematic review of the rotary tare data and examining the wing-on raw data files have not revealed any apparent data reduction errors. The source of this asymmetry appears to be aerodynamic, but no explanation for the anomaly has yet been found. Since the normal force data are very symmetric about zero rotations, it would appear that, for some reason, there is a forward shift of the pitch center of pressure in only the positive rotation direction. As will be shown later, this trend is consistent with or without forebody strakes in place.

Figures 3.30 to 3.32 show a configuration buildup with forebody strakes at 24°, 39° and 51° AOA, respectively. The most interesting result at 24° is the significant difference in the effects on rolling moment of adding just the wing or adding the wing and the LEX. Adding the wing creates a negative damping contribution to rolling moment with rotation rate and, except for low rotation rates, adding the LEX reverses this effect to contribute a positive damping effect. Addition of the tails adds slightly to the positive damping in roll. The same reversal in behavior can be seen in the side force. Yawing moment does not seem to be affected much by the addition of components to the body. The difference in the LEX on and off results is likely related to the significant LEX vortices and their breakdown position left and right with rotation rate. From extensive water tunnel tests on this configuration performed by Eidetics in the early research on forebody vortex control, it is known that at 24° AOA and zero sideslip, the LEX vortices are bursting over the wing and any asymmetry in the flow due to either sideslip or rotation rate will produce large asymmetries, left and right, in the burst location. The increments in normal force and pitching moment with addition of the various components are as expected.

At 39° and 51° AOA in Figs 3.31 and 3.32, the contributions of the wing and other surfaces are generally to promote damping in roll (with the exception of the body-wing at low rotation rates at 39°). The effect on yawing moment is minimal at both angles of attack, indicating nearly symmetric forebody flow, due to the forebody boundary layer transition strips and strakes. There are measurable side forces, however, for 39° and 51°.

The asymmetry in pitching moment with rotation rate observed for the strakes-off configurations is also observed for the strakes-on configurations. The reason is unknown.

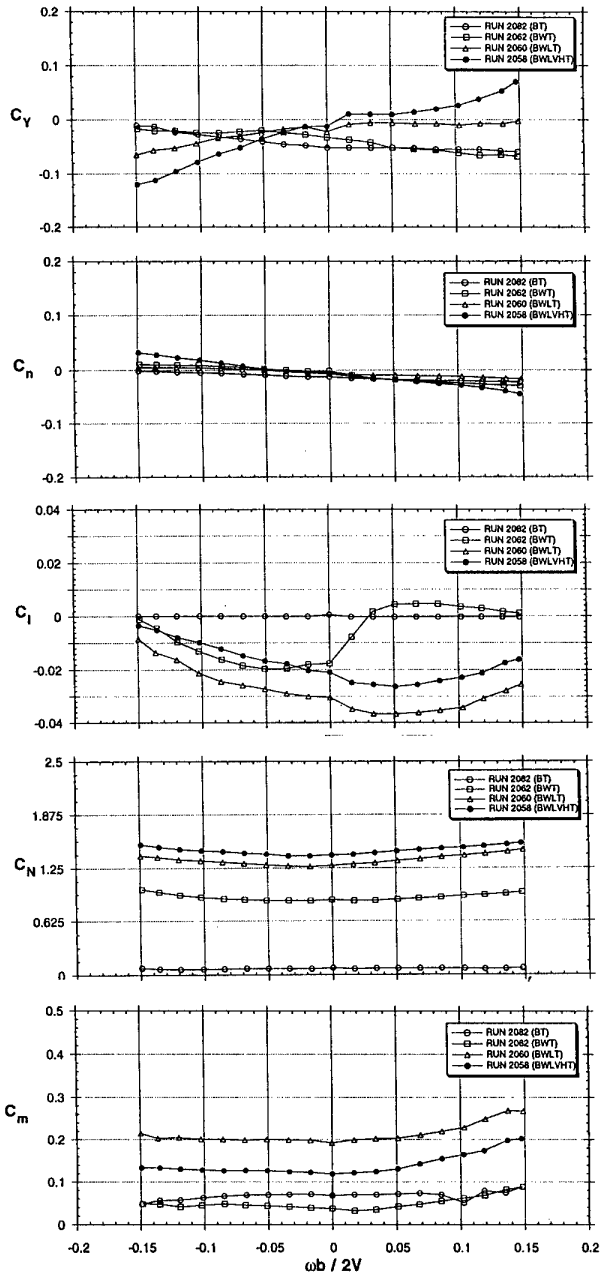

Fig 3.27 - Configuration buildup effects at $\alpha = 24°$, $R=0.955 \times 10^6$, strakes off

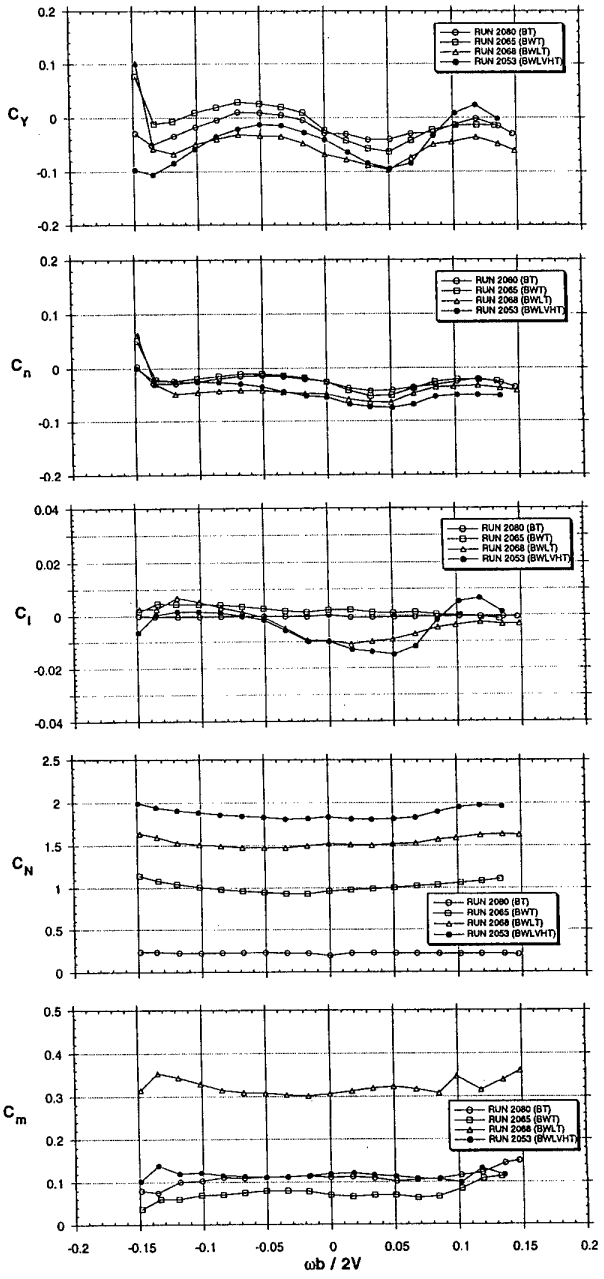

Fig 3.28 - Configuration buildup effects at $\alpha = 39°$, $R=0.955 \times 10^6$, strakes off

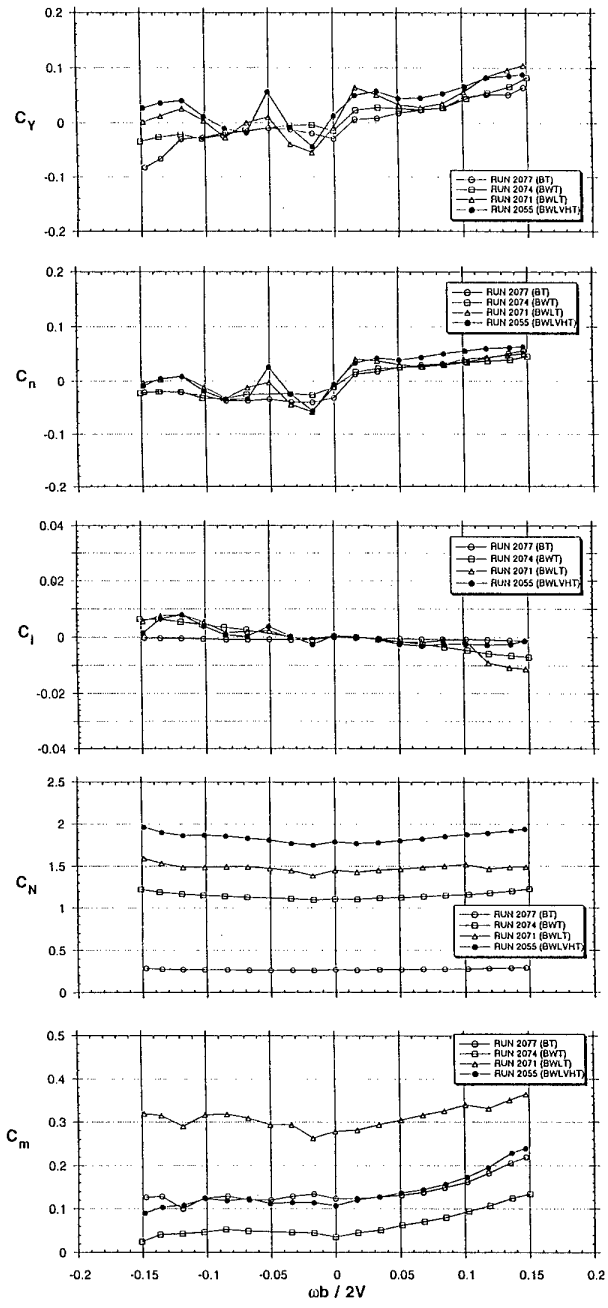

Fig 3.29 - Configuration buildup effects at $\alpha = 51°$, $R=0.955 \times 10^6$, strakes on

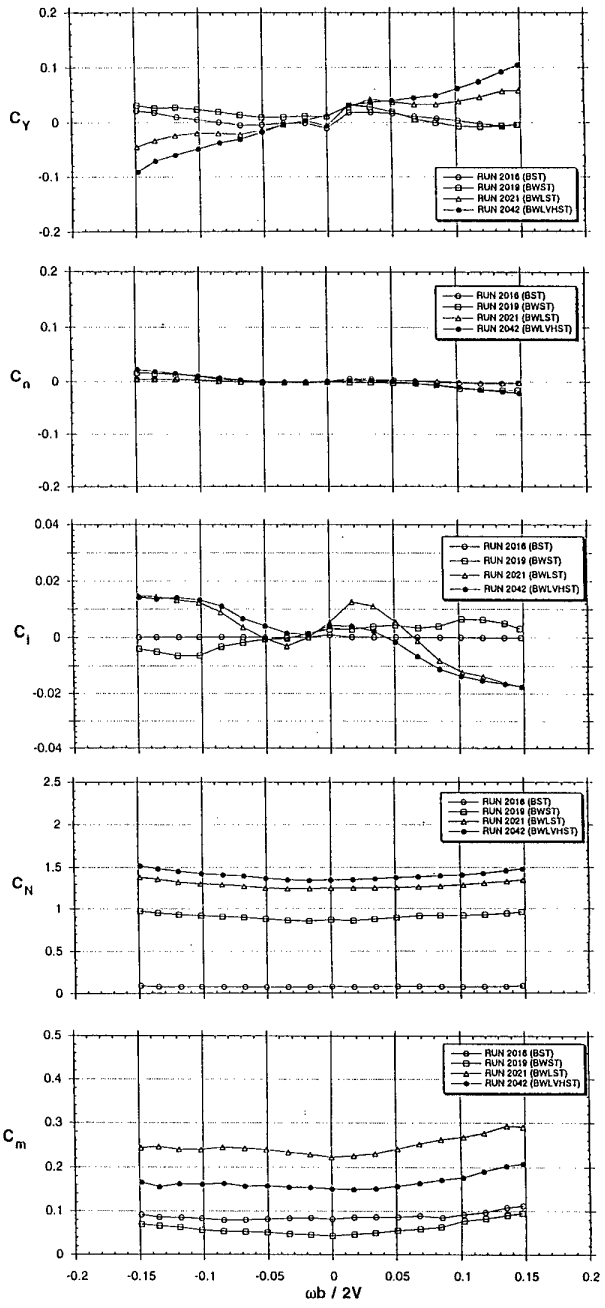

Fig 3.30 - Configuration buildup effects at $\alpha = 24°$, $R=0.955 \times 10^6$, strakes off

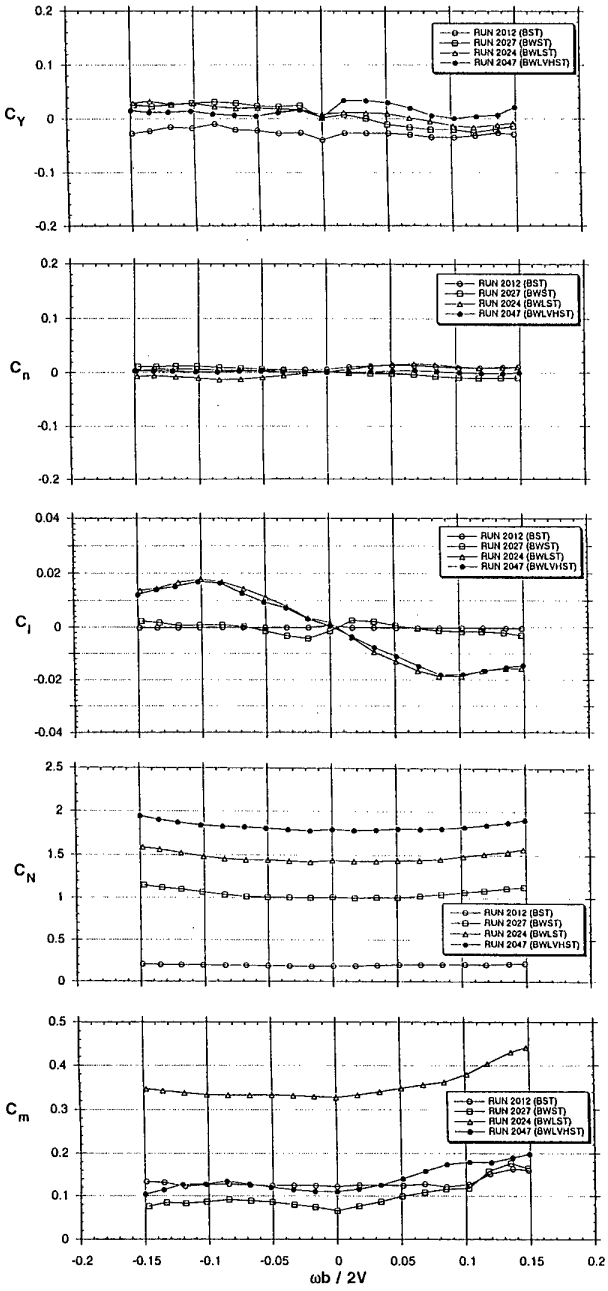

Fig 3.31 - Configuration buildup effects at $\alpha = 39°$, R=0.955x10^6, strakes on

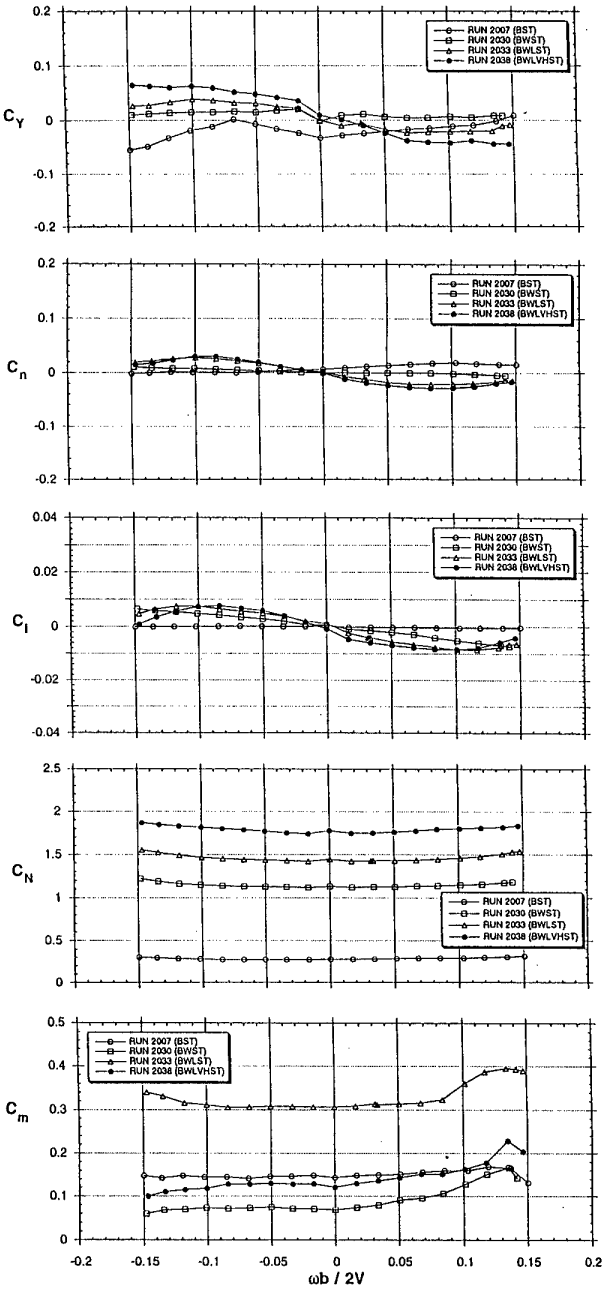

Fig 3.32 - Configuration buildup effects at $\alpha = 51°$, R=0.955x10^6, strakes on

3.6 SENSITIVITY TO NOSE STRAKES POSITION (FFA , Model B , AeM transition trips)

The forebody strakes have a large influence on test results. Sensitivity of results with respect to the strake position have been studied by means of rotary testing with small asymmetries in nose strake position.

Figure 3.33 shows the sensitivity of the angular position of nose strakes with respect to the normal of the surface, for the BWLHVST configuration (with the AeM Transition trips), at $\alpha = 40°$. In run 4866 the strakes were placed symmetrically and normal to the surface. In run 4861 the strakes were at 95° angle against the surface (this angle is counted ccw/cw looking down-stream for the port/starboard nose strake). In run 4863 the strakes made an 85° angle with the surface. These changes in the strakes angle did not have noticeable effects on the forebody flow, as can be seen in this figure.

Figure 3.34 shows results obtained with the same configuration at $\alpha = 40°$, with asymmetries in nose strakes position in X and Y. In run 5063, the strakes are symmetric. In run 5065 the port strake is moved backwards 2 mm. We see that this has little effect. In run 5068 the port strake is slightly asymmetric at the nose tip, i.e., the strake apex is moved up less than 1 mm (the rear end of the strake has not been moved). This asymmetry in the strake position introduces a large zero offset in C_l and affects the behaviour of C_l, C_n and C_Y. Even the pitching moment is affected. In run 5066 the port strake is moved 2 mm backwards and 2 mm upwards. We see that this change in the strake position completely changes the forebody flow.

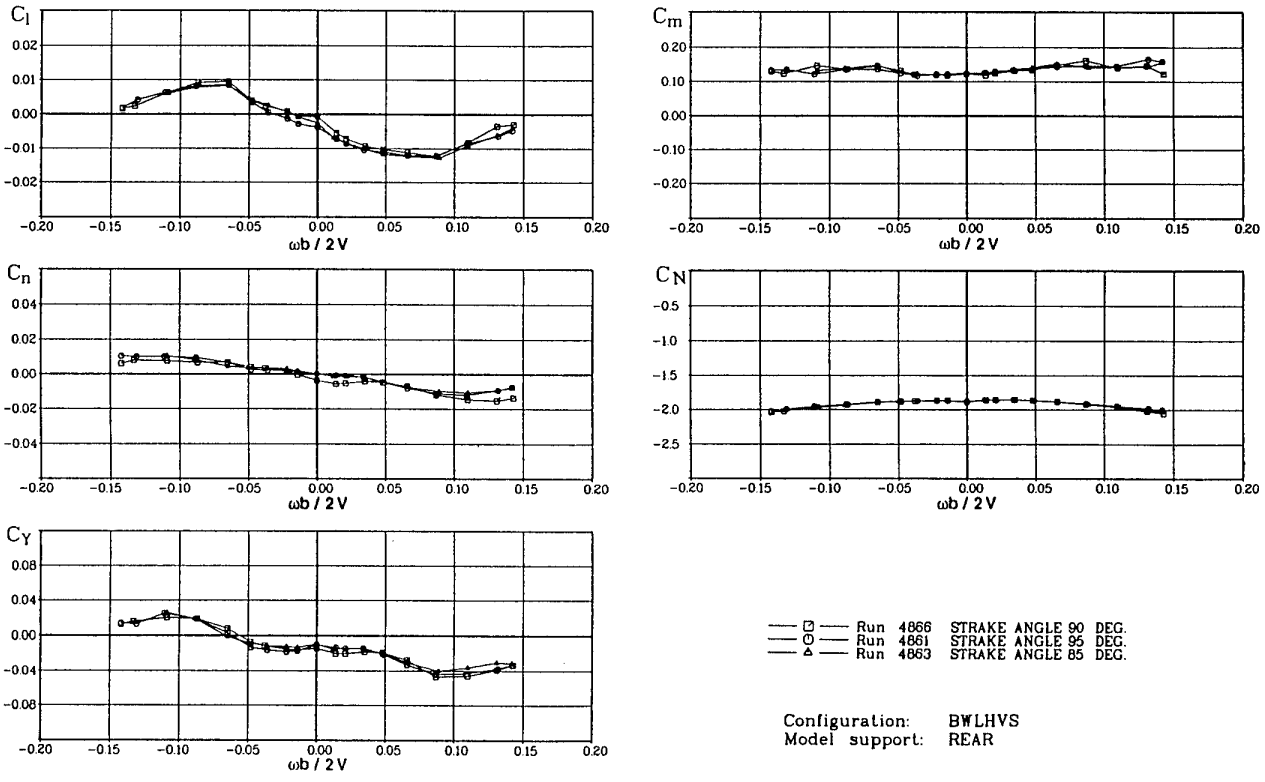

Fig 3.33 - Sensitivity to the nose strake position

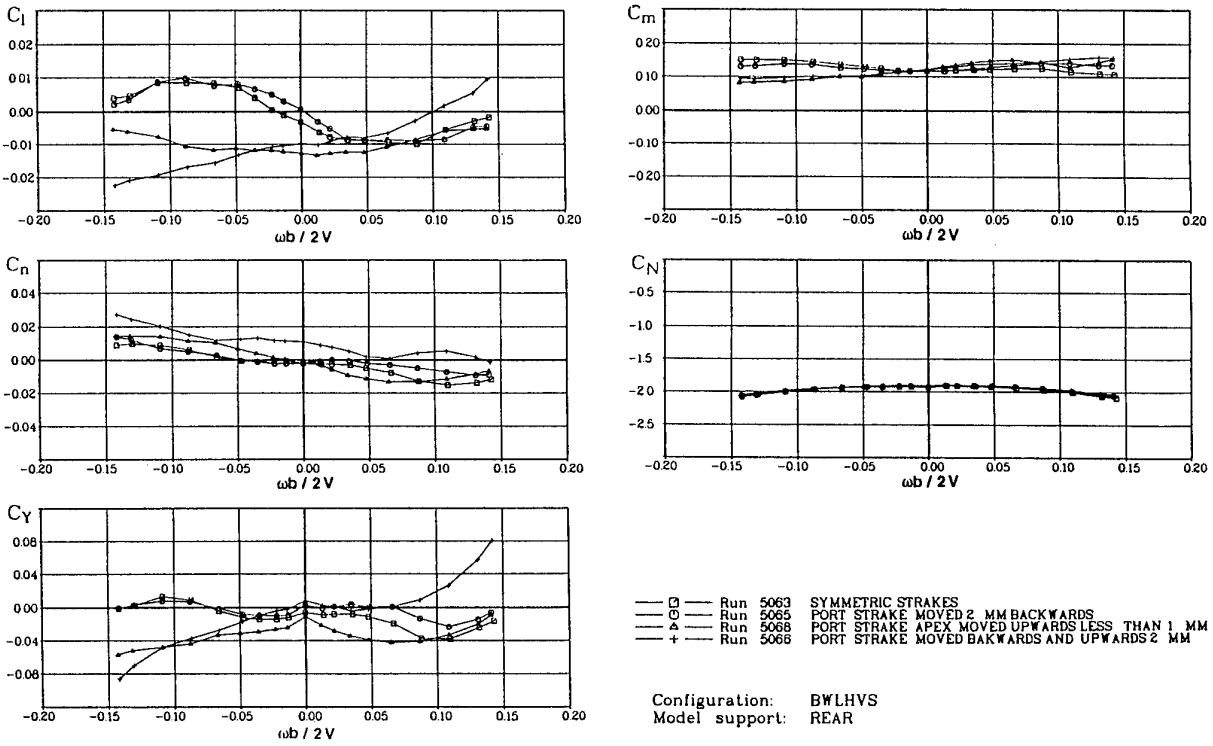

Fig 3.34 - Sensitivity to the nose strake position

3.7 EFFECT OF ANGLE OF ATTACK (DRA , Model B , DRA transition trips)

Results for the complete model with nose strakes and transition fixing as described in section 3.1 are shown in Figs 3.35 to 3.38 for angles of attack between 0° and 90°. In addition to the coefficient variations with $\omega b/2V$, the lateral derivatives $C_{l\omega}$, $C_{Y\omega}$ and $C_{n\omega}$ are plotted against α. These derivatives were obtained from the gradient of coefficients over the range : $\omega b/2V = \pm 0.04$. The tests were made using the rear-entry sting with 40° crank for $\alpha = 0°$ to 40° and the top-entry sting for $\alpha = 50°$ to 90°.

As shown in Fig 3.35, the variation of rolling moment coefficient C_l with rotation rate for $\alpha = 0°$ and 16° is fairly linear and stable (negative gradient) at all test rotation rates. Zero offsets are very small. For higher α's of 24°, 32° and 40° there are marked non-linearities in C_l vs $\omega b/2V$ with neutral or negative stability at higher rotation rates. Greater zero offsets are also apparent. Since all lifting surfaces are sharp edged, most of the rolling moment will be generated by differential vortex lift.

At the higher values of α and higher rotation rates, vortex breakdown is likely to occur first on the down-going outer wing which is at a higher effective angle of attack and therefore results in a loss of rolling moment opposing the motion. Rolling moment variation at higher angles of attack of 50°, 60°, 75° and 90° were made with a top-entry sting. As might be expected there are only small variations of rolling moment with rotation rate but two features are of interest. At low rotation rates the model is damped at all angles of attack except at $\alpha = 90°$ where the gradient is constant and positive. Zero offsets are smaller than at $\alpha = 32°$ and 40° and of opposite sign.

The reduction in roll damping with increasing angle of attack is clearly shown in the variation of $C_{l\omega}$. Variations of sideforce and yawing moment coefficients, C_Y and C_n, are shown in Figs 3.36 and 3.37 respectively. At low α, sideforce is generated mainly from sidewash effects on the fin due to differential lift on the wings and from fin incidence due to rolling. For positive rotation rate the sidewash is from port to starboard, since there is lower pressure on the down-going wing, giving a positive contribution, but the contribution from fin incidence is negative. At higher angles of attack forebody flows may also contribute to the sideforce. As shown in Fig 3.36 the gradient of net sideforce is zero for $\alpha = 0°$ but positive for angles of attack up to 32°. At $\alpha = 40°$ sideforce gradient diminishes at higher rotation rates. For $\alpha > 40°$ the sideforce gradient is mostly negative. The gradients of the yawing moment characteristics, C_n shown in Fig 3.37 are small and positive except at higher rotation rates for $\alpha = 24°$ and 32° when the gradients are mainly negative. For $\alpha > 40°$ the gradients are again near zero at low rotation rates and negative at higher rates. Thus sideforce gradient changes from positive to negative above $\alpha = 40°$ but the gradient of yawing moment is mainly stabilising at the higher rotation rates, suggesting that at the higher angles of attack there is a forward shift in centre of pressure of sideforce due to rotation rate.

As shown in Fig 3.38, variations of C_N and C_m are mainly linear and invariant with rotation rate. There is some variation of pitching moment: a symmetrical increase or decrease at high $\omega b/2V$ but the sign of the increment does not appear to be a consistent function of angle of attack.

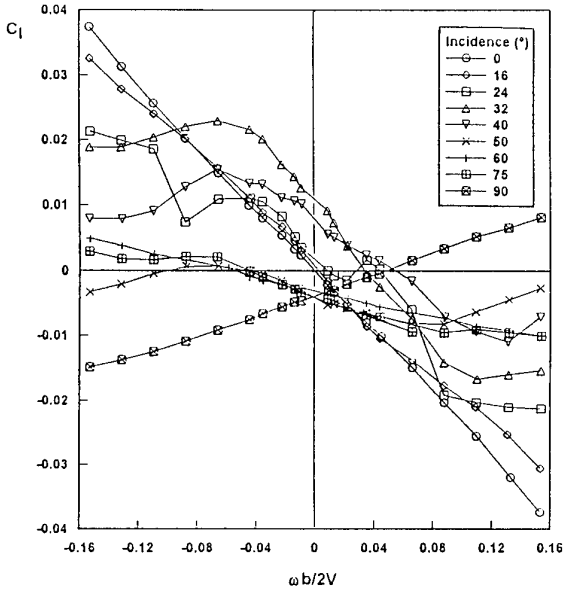

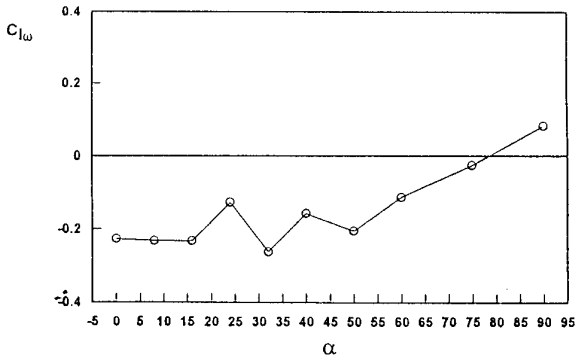

Fig 3.35 - BWLHVST Configuration, Effect of Angle of Attack on C_l and C_{lw}

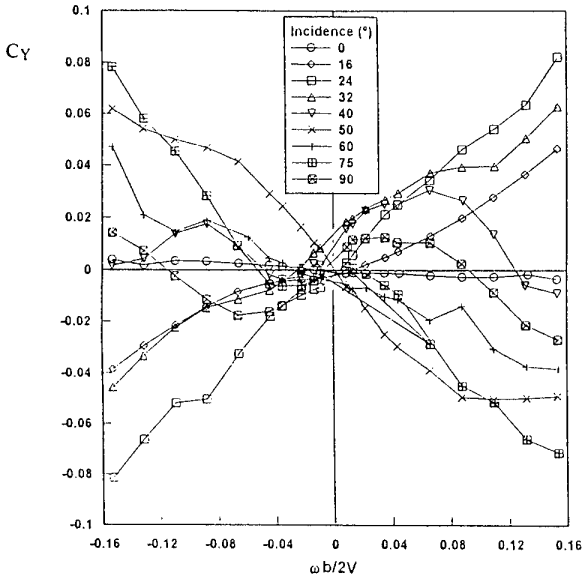

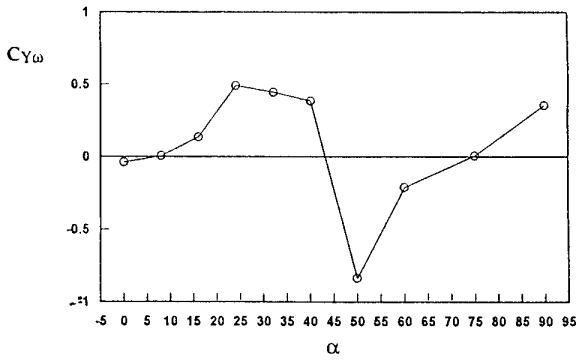

Fig 3.36 - BWLHVST Configuration,
Effect of Angle of Attack on C_Y and C_{Yw}

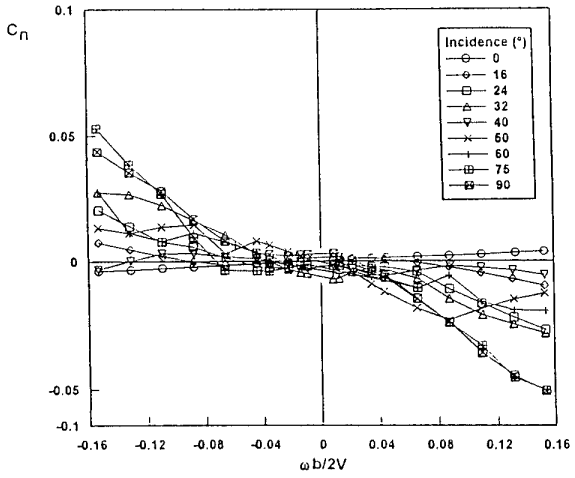

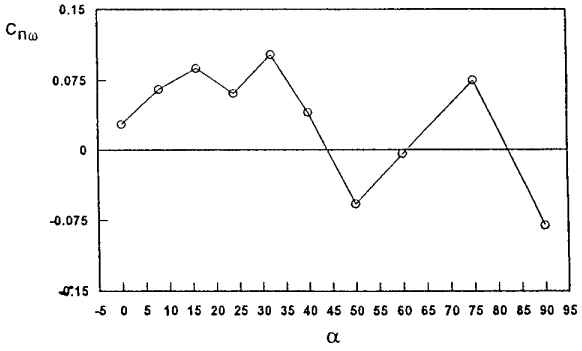

Fig 3.37 - BWLHVST Configuration,
Effect of Angle of Attack on C_n and C_{nw}

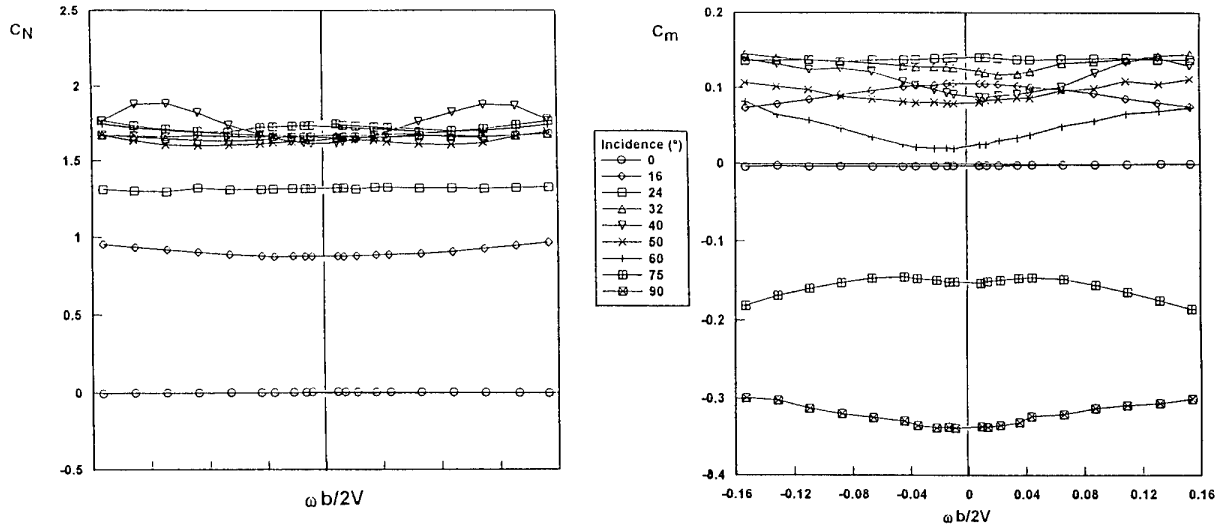

Fig 3.38 - BWLHVST Configuration, Effect of Angle of Attack on Longitudinal coefficients

3.8 EFFECT OF SIDESLIP (ONERA / IMFL , Model A , AeM transition trips)

Results for the complete configuration with nose strakes and transition fixing are shown in Figs 3.39 to 3.44 for angles of attack between 10° and 50° and for 4 values of sideslip : -5°, 0°, 5° and 10°. Coefficients are plotted against $\Omega = \omega b/2V$. Rotary tests were carried out on the TourneBroche, using a rear entry sting with 10° crank.

As shown in the figures, the effect of sideslip on normal and axial forces is very small, except at $\alpha = 30°$ where there is a loss of normal force due to sideslip. For α greater than 30°, the effect of rotation rate is more sensitive : C_N is close to a parabolic function of Ω.

On the pitching moment C_m, considerable effects of sideslip can be noted, particularly at $\alpha = 20°$, 25° and 50° (see Figs 3.40, 3.41 and 3.44). These effects are mainly due to the pitch rate q which is induced by sideslip as the model rotates ($q = \omega \times \sin ß$).

In fact, as shown on Figs 3.39 to 3.42, for tests at $ß = 5°$ and -5°, variations of pitching moment are symmetric with respect to Ω and ß. Thus, for positive (resp. negative) values of pitch rate q, i.e. when Ω and ß have the same sign (resp. contrary),a pitch-down effect (resp. pitch-up) is noted. Damping in pitch is effective up to $\alpha = 30°$. For $\alpha = 50°$ (Fig 3.44), zero offsets ($\Omega = 0$) show clearly that sideslip induces a noticeable pitch-up effect. Moreover, the effect of pitch rate is inverted as compared to low α ; a propelling effect of q on the pitching moment is noted. Symmetry of results with respect to sideslip and also with respect to rotation rate is very good, therefore symmetry with respect to pitch rate is quite satisfactory. Results obtained at ß = -5° and 5° show that the value of the dynamic derivative C_{mq} is positive at $\alpha = 50°$.

On the rolling moment coefficient C_l, Figs 3.40, 3.41b and 3.42 show that damping in roll is larger at zero sideslip than in other cases. This influence of sideslip on the slopes of C_l curves is particularly large at $ß = 10°$, for $\alpha = 25°$ and 30°, where an inversion of rolling moment is encountered as Ω increases. Correlation can be made with quasi-static data obtained during slow α-sweeps at $ß = 10°$ and -10°, on the "PQR" apparatus (see chapter 5). Figure 3.41a shows the coefficients C_l and C_n obtained for such increasing (↗) and decreasing (↘) slow α-sweeps. It should be noted there are changes in lateral stability as α increases. These changes do not happen as α decreases.

Hysteresis of large amplitude in C_l occurs as α evolves between 24° and 32°. In this α-range a smaller hysteresis effect is also found on the yawing moment. This phenomenon is probably due to instability of vortices on the wing.

During rotary tests at $ß = 10°$, as Ω increases slowly, effective angle of attack increases on the windward wing and decreases on the leeward wing. These slow evolutions of effective incidence on the wings produce large and steep variations of rolling moment (see Figs 3.41b and 3.42) similar to those encountered during slow sweeps in the same α-range: 24° to 32°.

These results are consistent with quasi-static test results. At $\alpha = 40°$, results for C_l are also largely influenced by sideslip and are complex at this value of incidence in the stall region.

At $\alpha = 50°$, where the flow is completely separated from the wing, the effect of ß on gradients is relatively small, resulting mainly in zero offsets of the curves due to static contribution of sideslip which can be noted in the rolling moment.

As for C_l, the effect of sideslip on the yawing moment coefficient C_n is on the gradients with respect to Ω. For α between 10° and 30° (Figs. 3.39 to 3.42), damping in yaw is smaller for tests at $ß = 0°$ than for tests where sideslip is not equal to zero. The opposite effect of sideslip on the rolling moment gradients was shown previously in this α-range.

Non linear behaviour of the yawing moment and side-force is also encountered on rotary tests with sideslip. In particular, for $\alpha = 25°$ and $ß = 10°$, yawing moment is similar to results at ß = 5° for positive rotation rates, but for negative Ω, the slope of C_n is larger for $ß = 10°$ than for $ß = 5°$. At $\alpha = 40°$ and 50° (Figs 3.43 and 3.44), symmetry of these nonlinear data with respect to sideslip (for ß = - 5° and 5°) is quite good .

Therefore, from a general point of view, it is concluded that sideslip has a large influence on rotary data : on zero offsets as well as on gradients. Moreover, some very non-linear effects on lateral stability, noted during rotary tests, can be correlated with hysteresis effects demonstrated during slow α-sweeps.

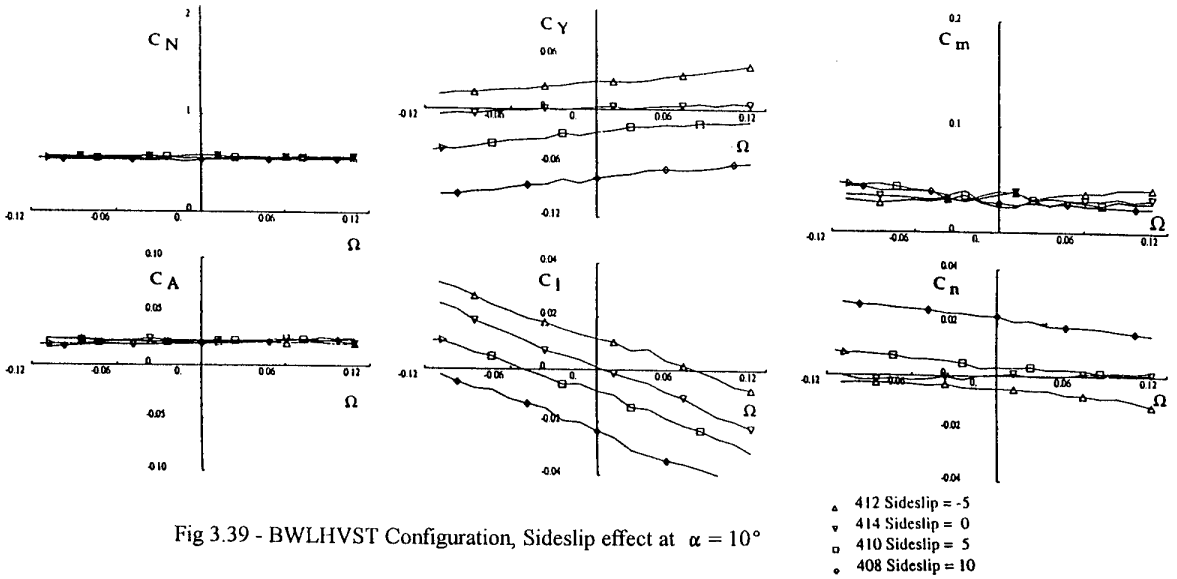

Fig 3.39 - BWLHVST Configuration, Sideslip effect at $\alpha = 10°$

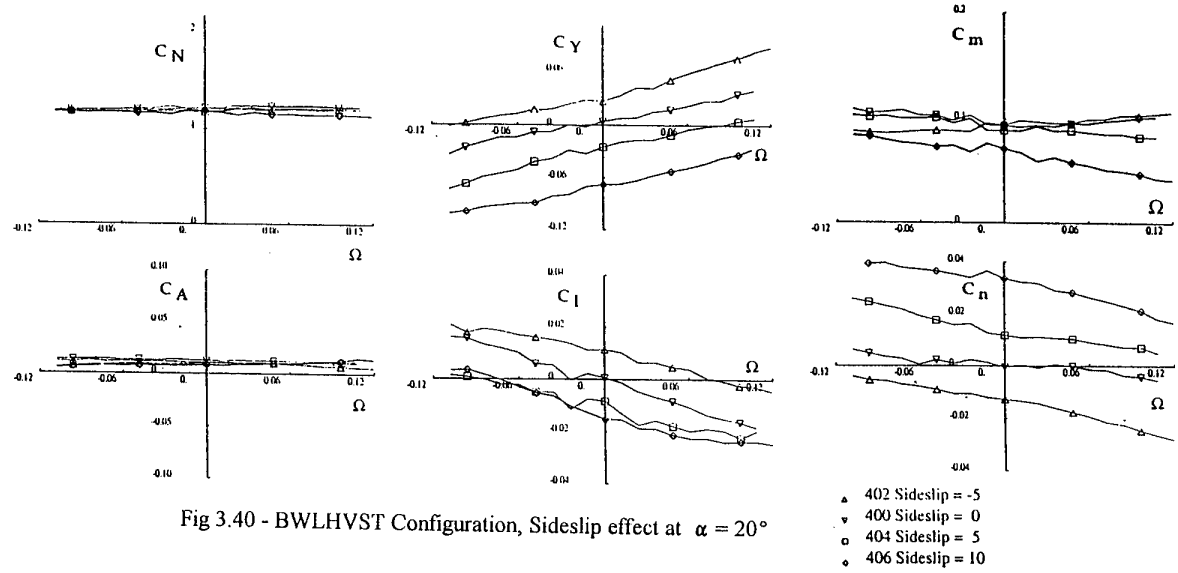

Fig 3.40 - BWLHVST Configuration, Sideslip effect at $\alpha = 20°$

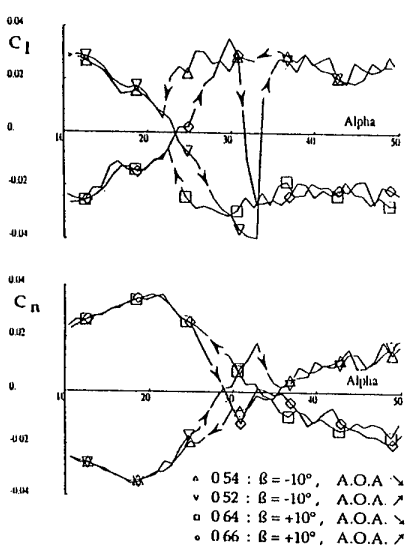

Fig 3.41.a - Slow α-sweeps

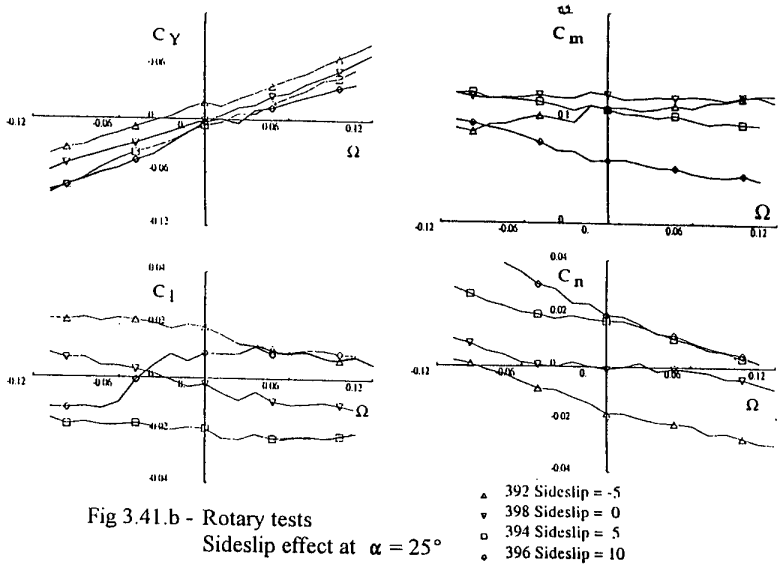

Fig 3.41.b - Rotary tests
Sideslip effect at $\alpha = 25°$

Fig 3.41 - BWLHVST Configuration

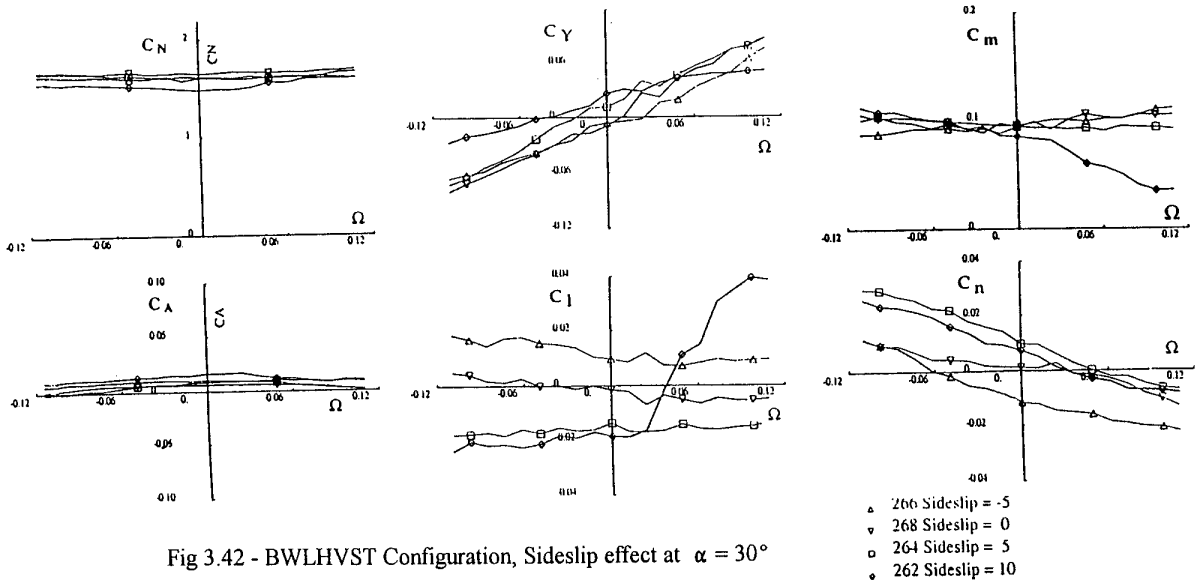

Fig 3.42 - BWLHVST Configuration, Sideslip effect at $\alpha = 30°$

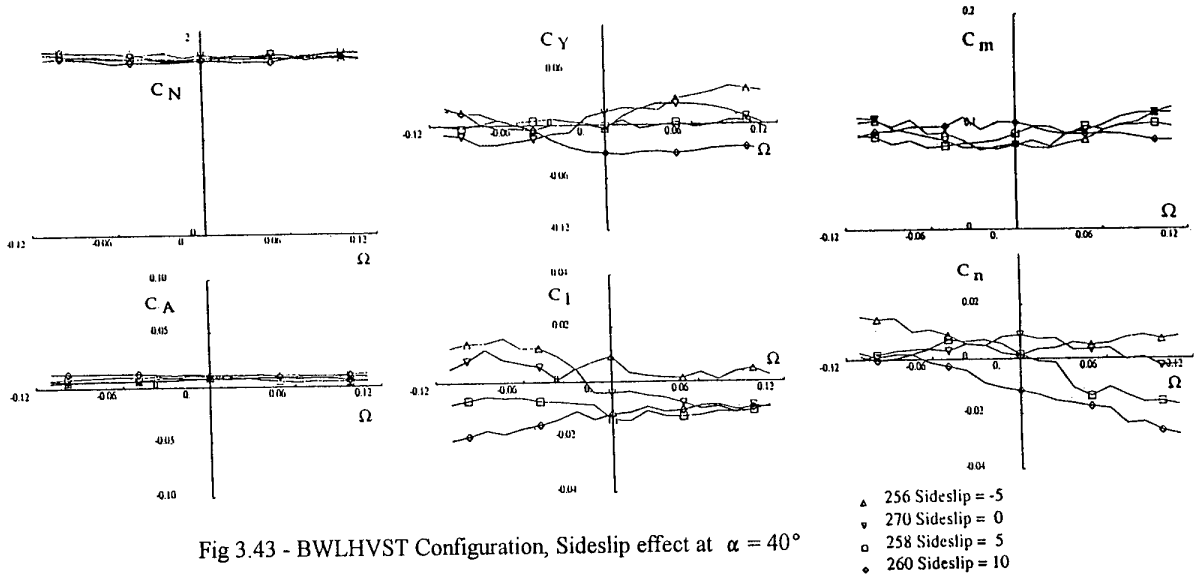

Fig 3.43 - BWLHVST Configuration, Sideslip effect at $\alpha = 40°$

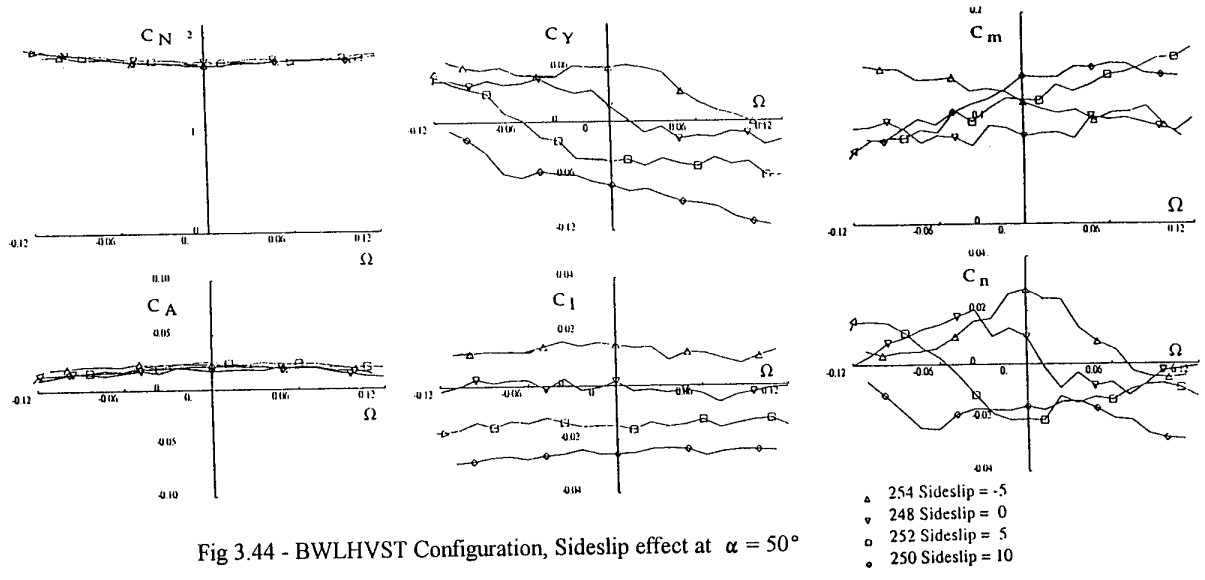

Fig 3.44 - BWLHVST Configuration, Sideslip effect at $\alpha = 50°$

3.9 INTERFERENCE EFFECTS ON THE ROTARY RIG (FFA , Model B , AeM trans. trips)

In order to investigate the interference effects of the large sector beam on the flow around the model, a 0.5 m extension framework was built (Fig 3.45). This extension made it possible to carry out wind tunnel tests at 40° AOA only. Tests were made on the complete configuration with AerMacchi transition trips; a rear entry sting was used. Figure 3.46 shows results without forebody strakes at V = 60m/s.

Figures 3.47 and 3.48 show results with forebody strakes at V= 60 m/s and 30 m/s respectively. The tests show that the model distance to the sector beam has only minor effects on the flow around the model and does not affect the overall behaviour of the force and moment coefficients. The largest effects are seen in Fig 3.48 at low rotation rates, where the slope of the C_l curve is larger for the run with the extension.

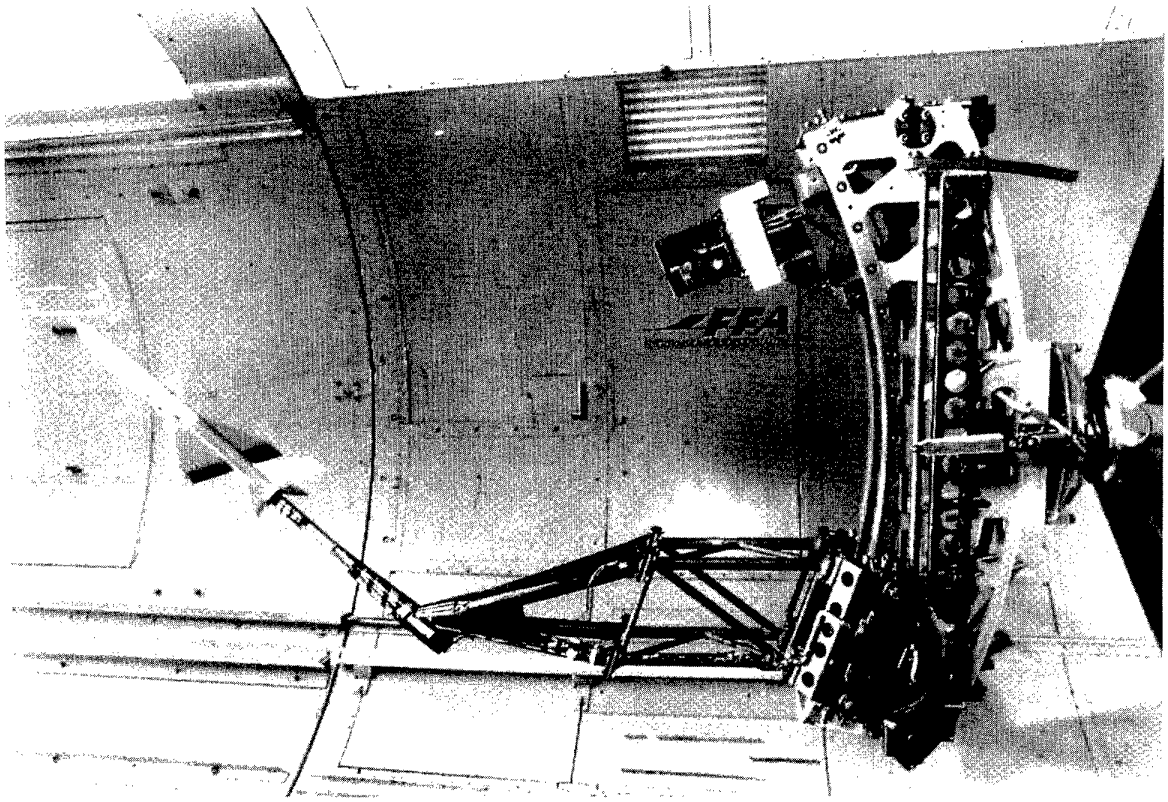

Fig 3.45 - Rotary rig at FFA with 0.5m extension

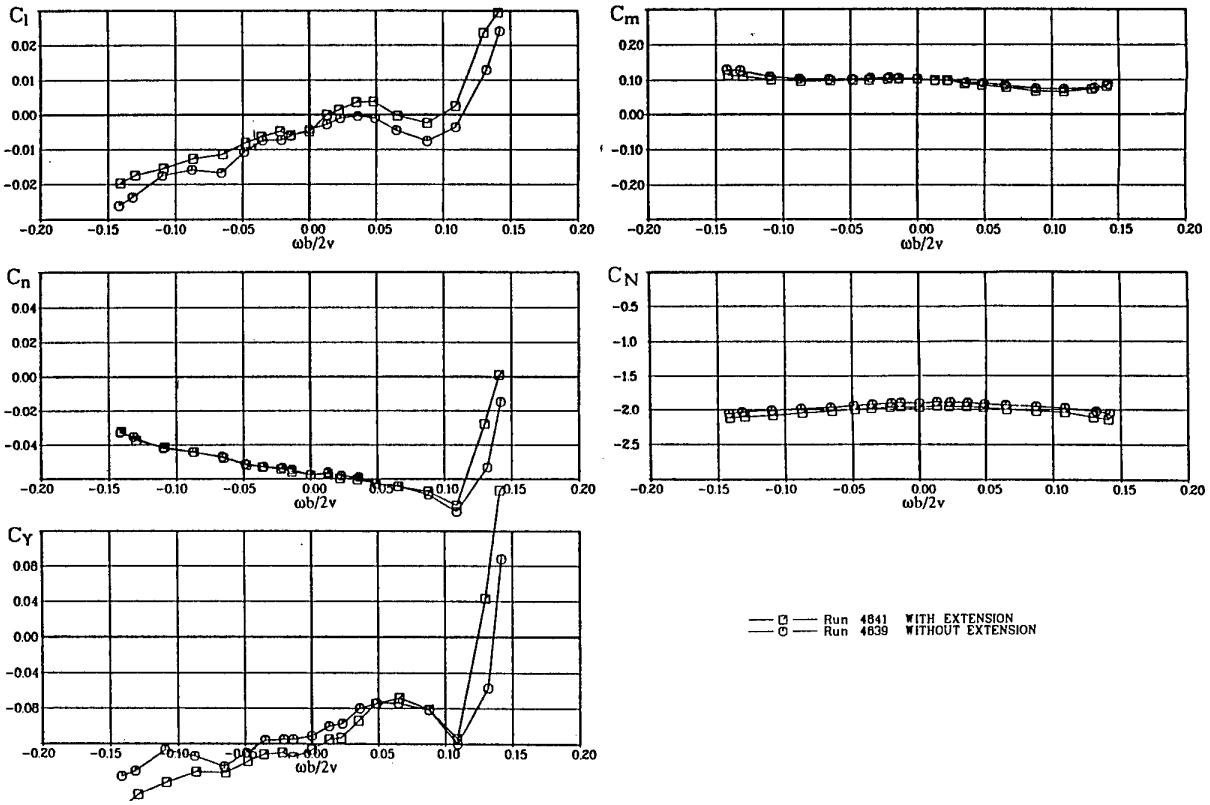

Fig 3.46 - BWLHVT Config., Interference effects on the rotary rig - $\alpha = 40°$, V= 60 m/s

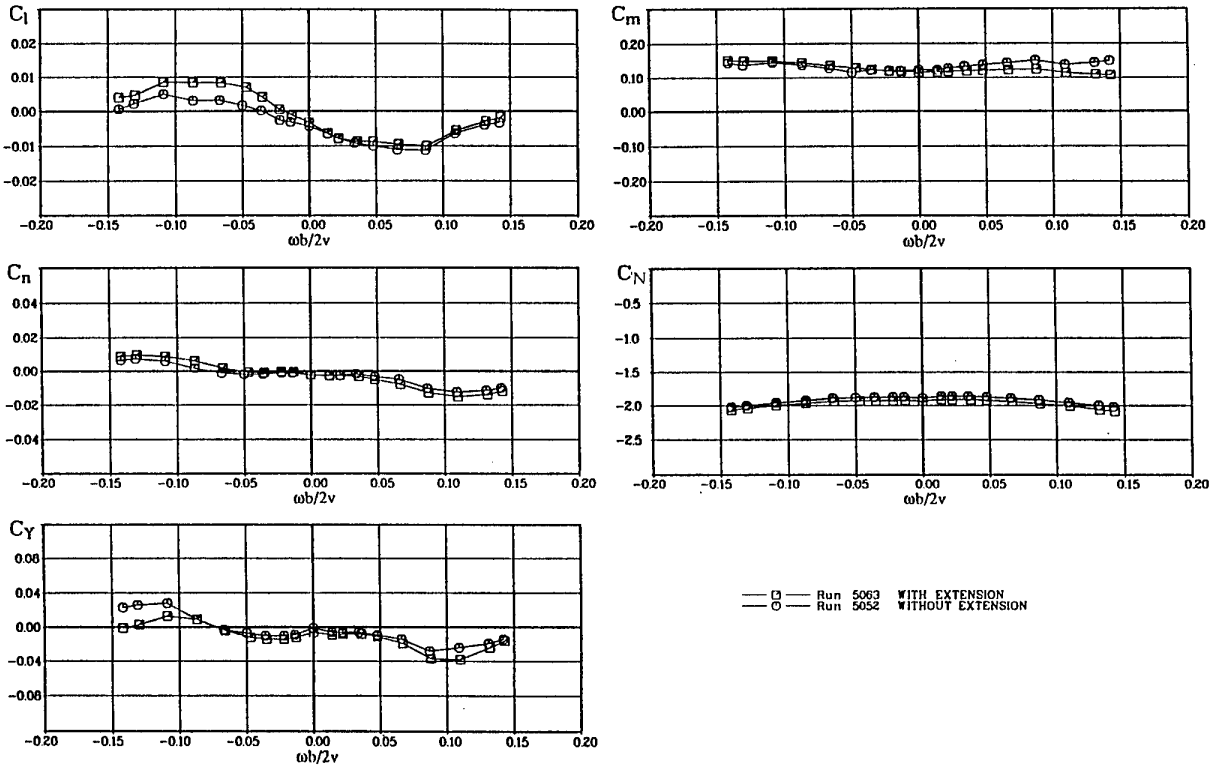

Fig 3.47 - BWLHVST Config., Interference effects on the rotary rig - $\alpha = 40°$, V= 60 m/s

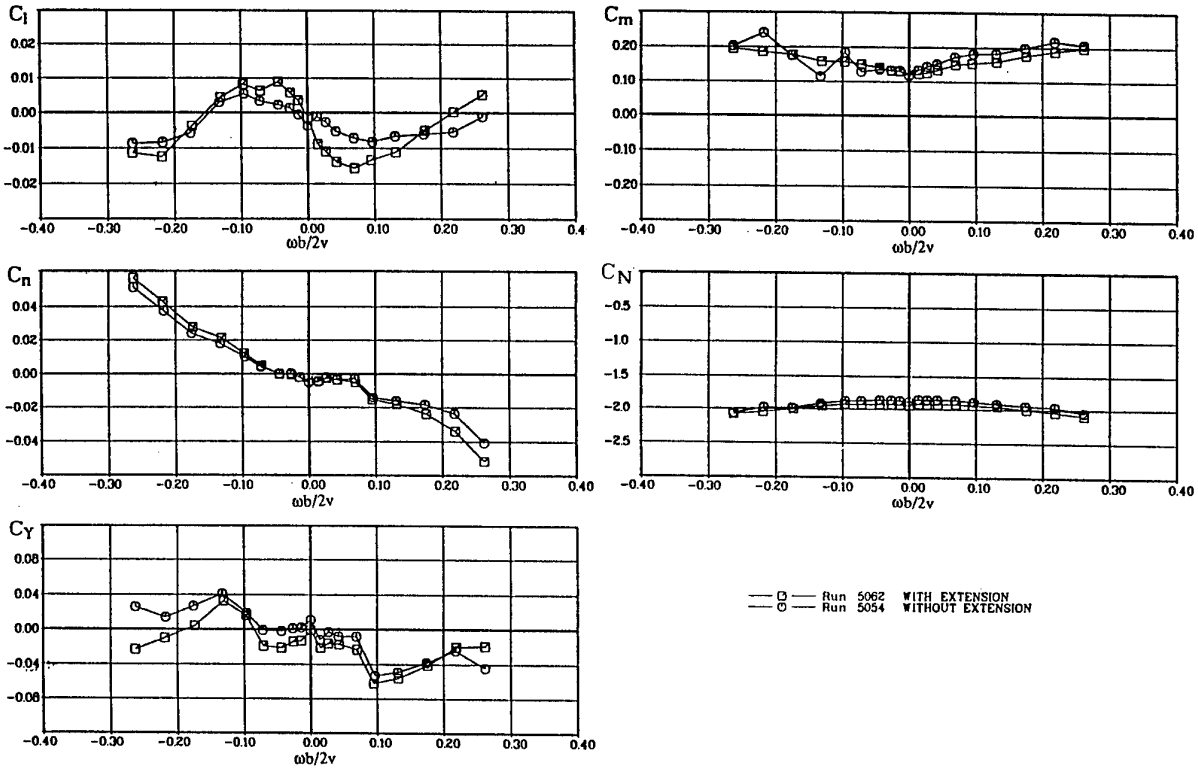

Fig 3.48 - BWLHVST Config., Interference effects on the rotary rig - $\alpha = 40°$, V= 30 m/s

3.10 EFFECT OF MODEL SUPPORT (DRA , Model B , DRA transition trips)

Two rear-entry sting supports and a top-entry sting used at DRA are shown in Fig 3.49. Lateral coefficients for the complete model supported on the rear-entry stings at $\alpha = 40°$ with 40° and 60° cranks are compared in Fig 3.50a, without nose strakes and Fig 3.50b, with strakes. With strakes off, variations with rotation rate are very non-linear, with large zero offsets. There are large differences in C_Y , C_n and C_l. In contrast, similar measurements for the model with strakes on show only small variations of C_Y and C_n, insignificant zero offsets and little difference in data from tests with the two cranks. There is some difference in the variation of C_l but the general trend is similar (Fig 3.50b).

For $\alpha = 50°$, results from tests with the rear-entry sting with 60° crank are compared with top-entry sting results in Fig 3.51. The results shown are for the complete model with strakes on. There is little difference in C_Y and C_n: the characteristics are anti-symmetric about the origin and zero shifts are negligible. Trends in the variation of C_l are similar for the two stings but there is some difference for negative rotation rates, mainly due to a small zero shift in the data from tests with the top-entry crank. Model support effects on the longitudinal coefficients C_N and C_m are also shown in Fig 3.51. The top-entry sting has the effect of reducing the normal force C_N and the nose-up pitching moment C_m.

When angle of attack is increased to 60° (Fig 3.52) there is again little difference in the variation of C_Y and C_n for tests with either of the model supports. Side forces are slightly reduced and rolling moment (C_l) variation becomes linear. The latter is due to the onset of wake-type low energy flow over both wings so that rolling moment is generated primarily by differential lower surface pressures.

Thus, for the model with nose strakes on, in the angle-of-attack range 40° to 60°, the model support has little effect on the measured sideforce and yawing moment and only a small effect on rolling moment. With nose strakes off, however, a change in rear sting crank produces wide variations in the measured coefficients at $\alpha = 40°$. As for the body alone, the nose strakes fix the forebody vortices so that the flow symmetry is relatively undisturbed by the change in pressure field due to downstream blockage. With strakes off the difference in support geometry apparently changes the zero offset and pattern of variation with rotation rate, resulting in large differences in the measured coefficients. Flow disturbance due to the top-entry sting also does not affect the lateral coefficients (strakes on) but as might be expected there is some loss of normal force through increased flow separation on the model upper surface. Suction is decreased forward of the reference axis and nose-up pitching moment is reduced.

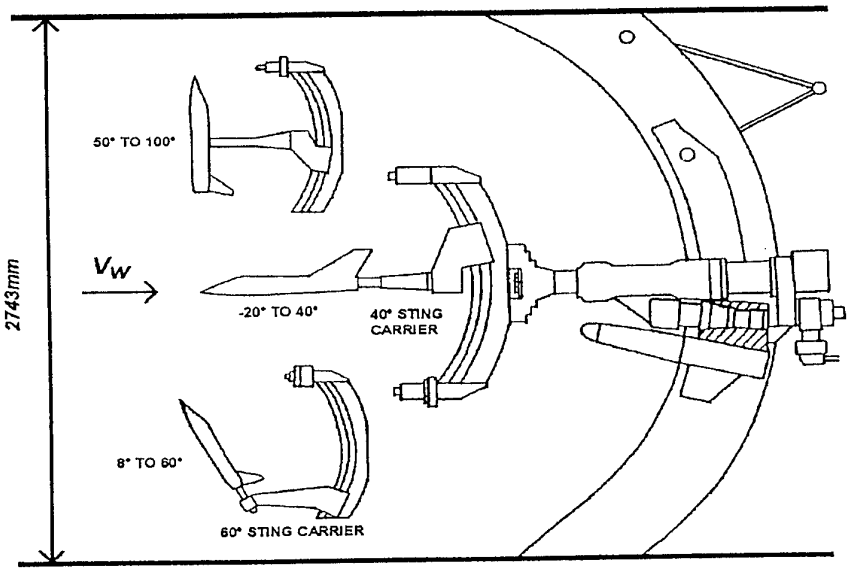

Fig 3.49 - DRA rotary balance in 13 ft x 9 ft Wind Tunnel

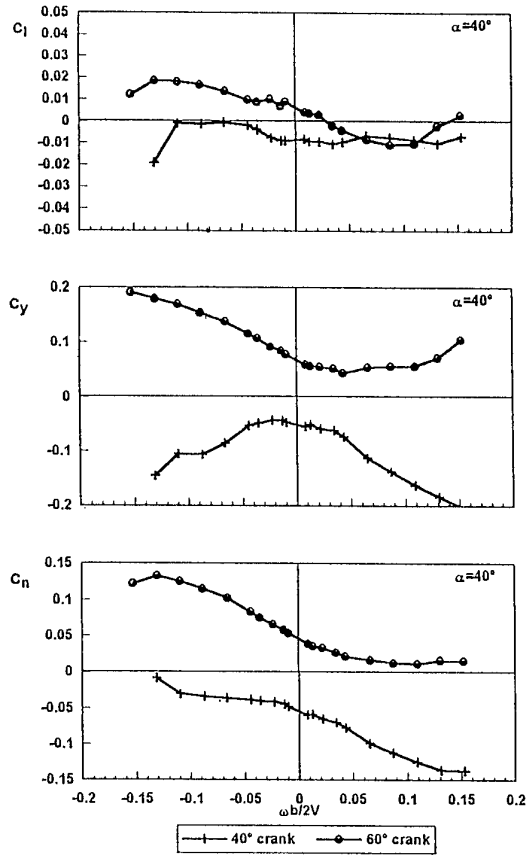

Fig 3.50.a - BWLHVT Configuration

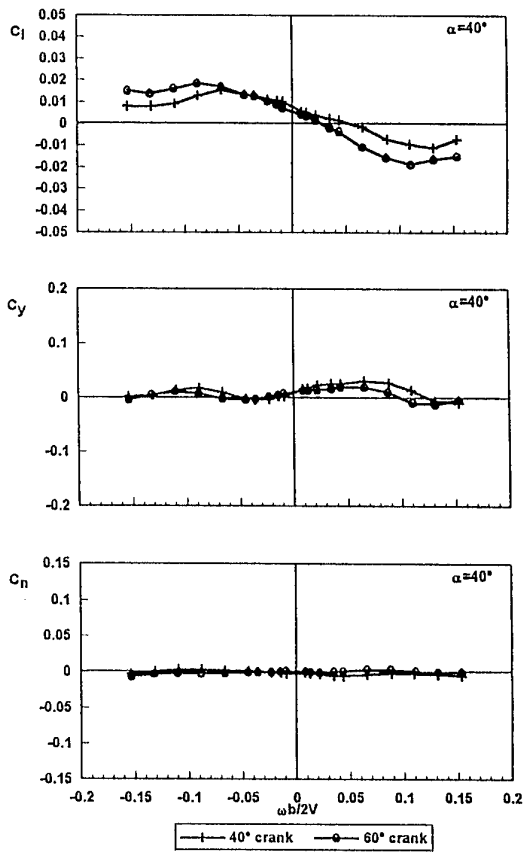

Fig 3.50.b - BWLHVST Configuration

Fig 3.50 - Effect of sting crank - $\alpha = 40°$

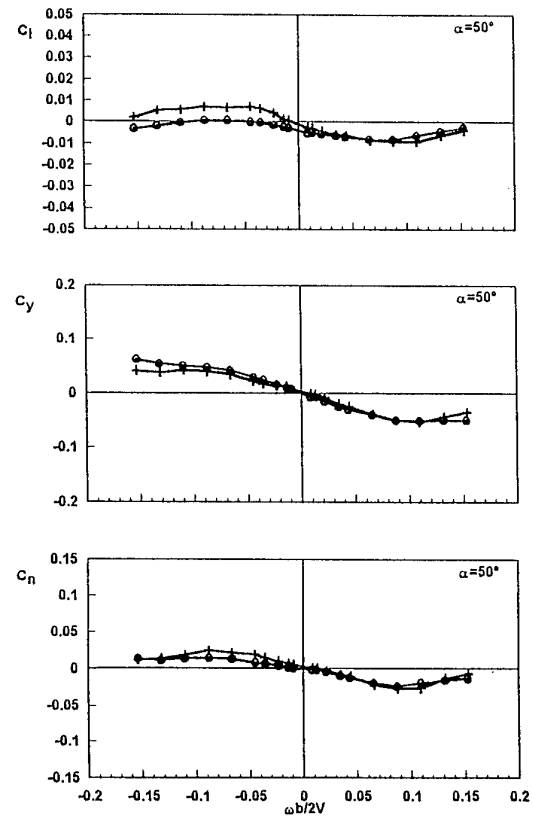

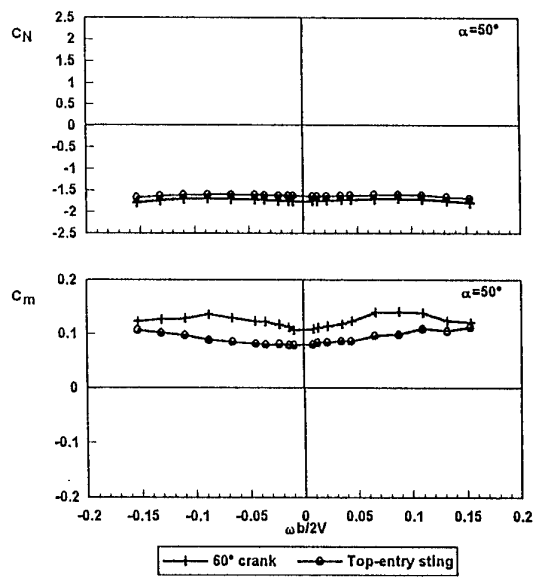

Fig 3.51 - BWLHVST Configuration
Effect of top-entry sting - $\alpha = 50°$

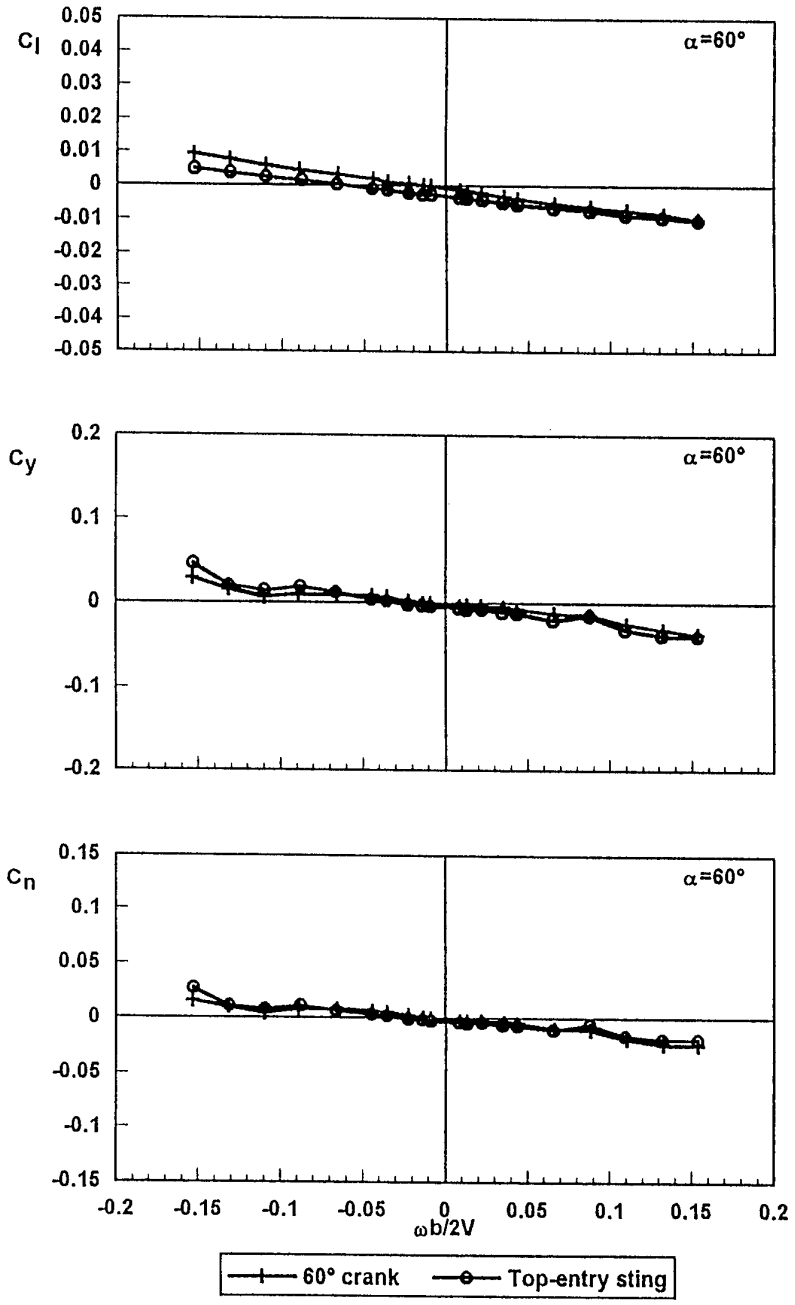

Fig 3.52 - BWLHVST Configuration. Effect of top-entry sting - $\alpha = 60°$

3.11 EFFECT OF WIND TUNNEL WALL TYPE : OPEN VERSUS CLOSED TEST SECTION
(AerMacchi , Model A, AeM transition trips)

In the AerMacchi wind tunnel, it is possible to test models in both open and closed test sections. The closed test section is a simplified set-up with the specific purpose of testing possible effects of the test section type. For the case of model WG-16 this gave a good opportunity to test for the effect of type of wind tunnel wall in a way that excludes any other spurious effects. Only differences in test section calibration could have an effect on such a comparison, but the two test sections had been carefully calibrated for the purpose. Other small differences, such as differences in effective angle of attack due to different wall induced upwash have been analyzed and found to be negligible.

Figures 3.53 to 3.56 show results of the comparison for the strakes-on configuration. The comparison shows almost perfect coincidence of results for the low angle-of-attack cases at 0°. The comparison is also very good at 24°, 40° and 50°, although small quantitative effects appear.

In general it was concluded that changes in coefficients due to tunnel wall type are small and no systematic effects could be identified.

For the strakes-off case, Figs 3.57 to 3.60 the situation is less clear cut. At low angle of attack, the comparison is again perfect. At 24°, significant differences are present, but they seem attributable to the presence of some flow asymmetry in the test in the open section. Differences become very large at 40°, clearly indicating the presence of a different asymmetric flow condition. Due to the random nature of such effects, they cannot be attributed to the change in tunnel walls, but more appropriately to the handling of the model during tunnel configuration change.

In conclusion, no significant effects of tunnel wall type (open versus closed) are visible on model configurations that have stable flow pattern.

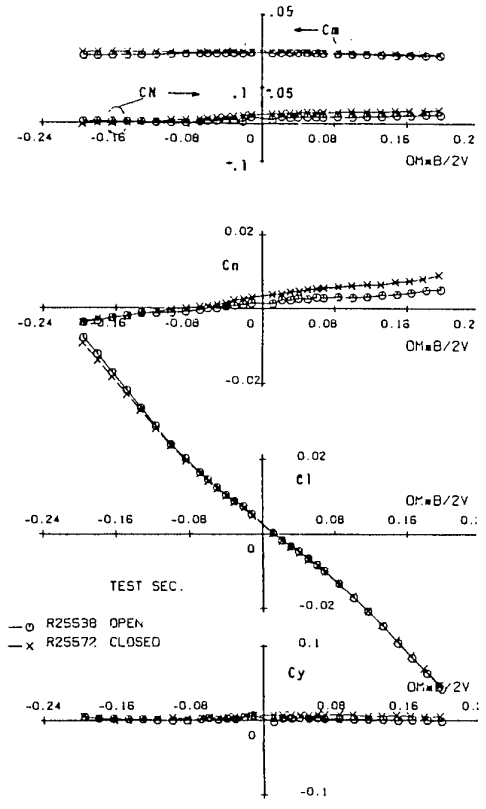

Fig 3.53 - Open versus closed test section walls
BWLHVST Configuration -
AeM tests - $\alpha = 0°$

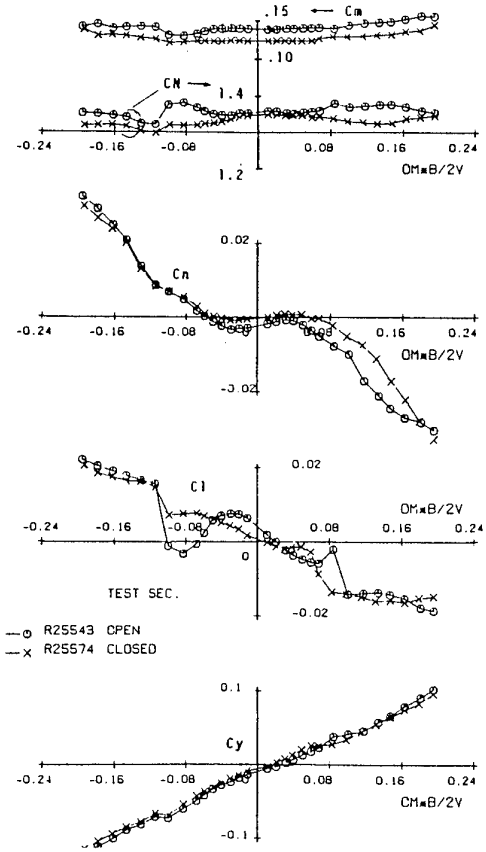

Fig 3.54 - Open versus closed test section walls
BWLHVST Configuration -
AeM tests - $\alpha = 24°$

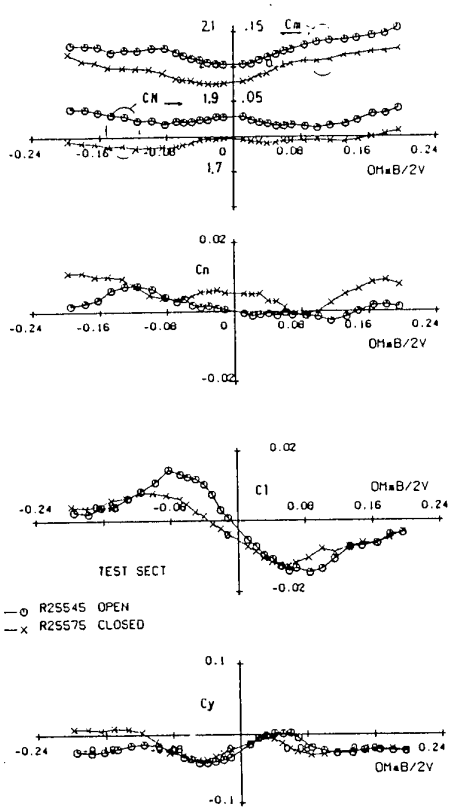

Fig 3.55 - Open versus closed test section walls
BWLHVST Configuration - AeM tests - $\alpha = 40°$

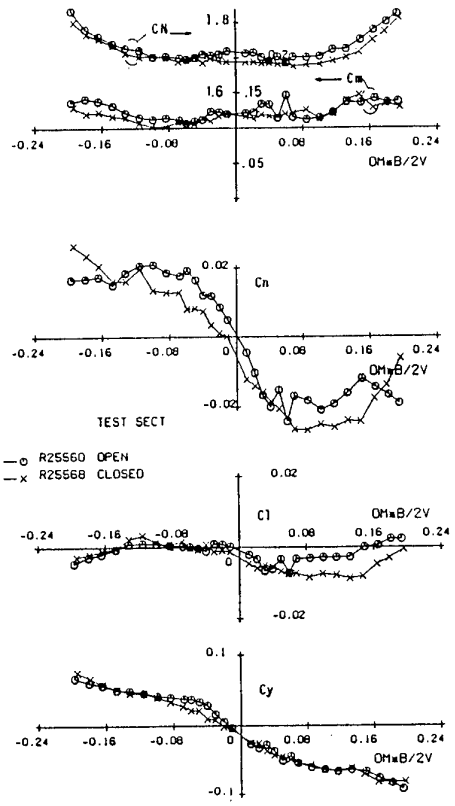

Fig 3.56 - Open versus closed test section walls
BWLHVST Configuration - AeM tests - $\alpha = 50°$

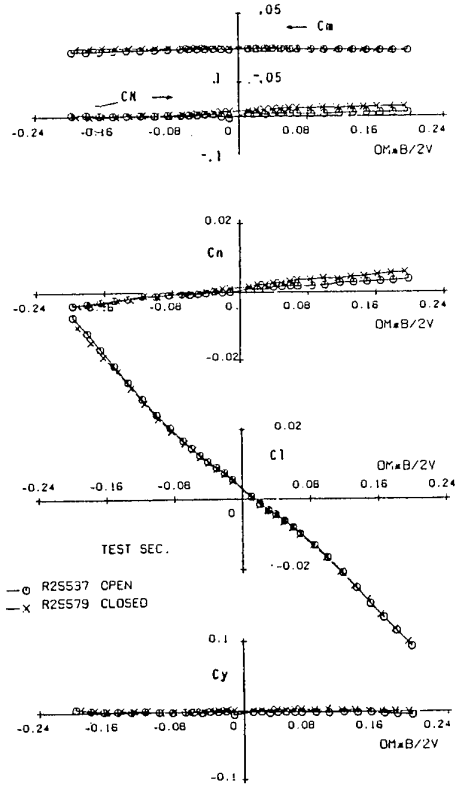

Fig 3.57 - Open versus closed test section walls
BWLHVT Configuration - AeM tests - $\alpha = 0°$

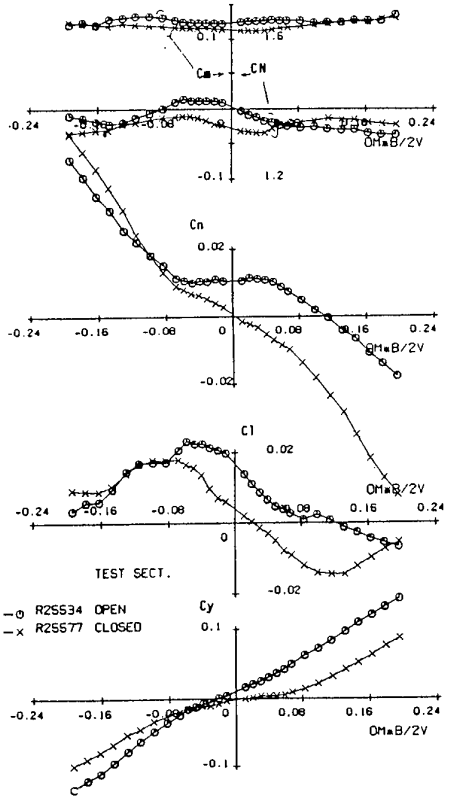

Fig 3.58 - Open versus closed test section walls
BWLHVT Configuration - AeM tests - $\alpha = 24°$

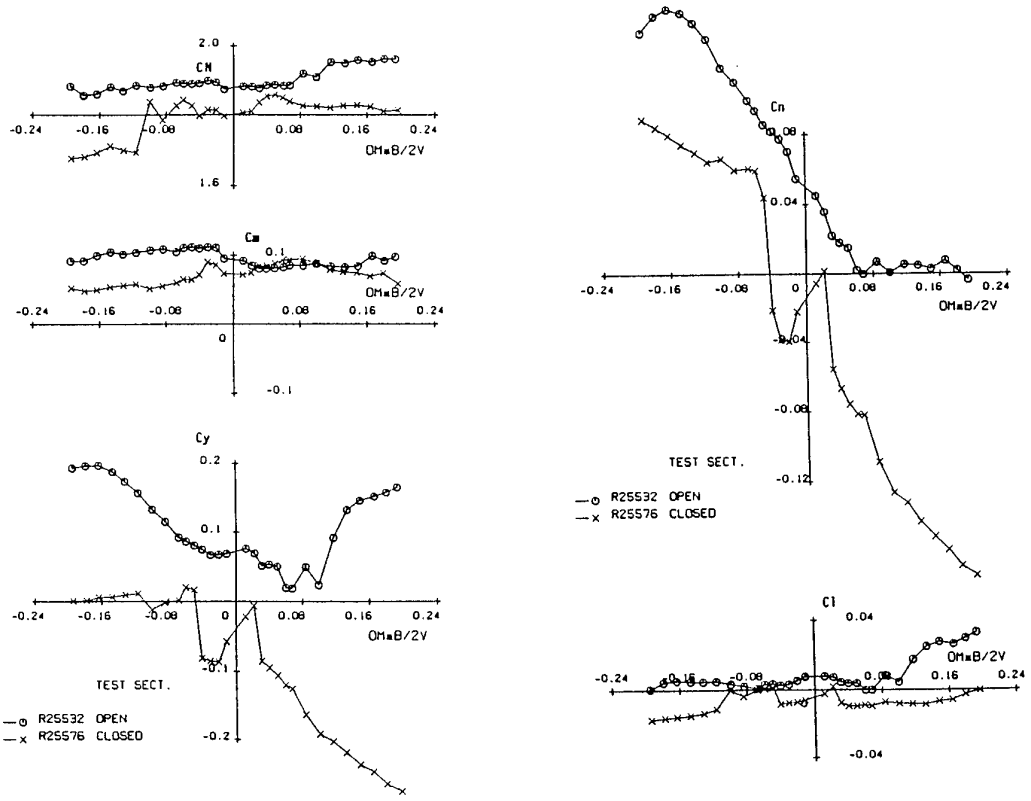

Fig 3.59 - Open versus closed test section walls, BWLHVT Config. - AeM tests - $\alpha = 40°$

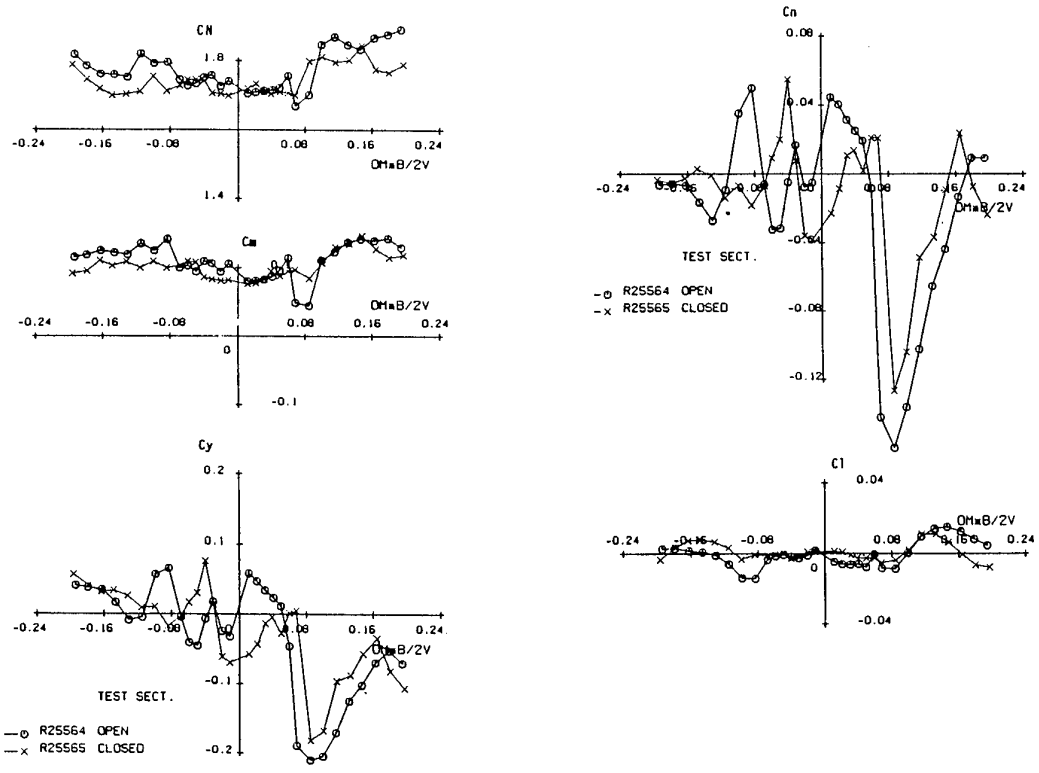

Fig 3.60 - Open versus closed test section walls, BWLHVT Config. - AeM tests - $\alpha = 50°$

3.12 REPEATABILITY TESTS (ONERA / IMFL , Model A , AeM transition trips)

Through this chapter, many results have been presented to show effects of model configuration (including transition fixing and strakes) and test conditions (Reynolds number, support interference, etc...). Some of these data show sensitivity to test variables, especially at high angles of attack where the flow around the model is not stable.

Consequently, before performing tests at high angles of attack, it was of interest to carry out some repeatability tests in order to assess accuracy and consistency of test results.

First, these repeatability test results are presented for quasi-static tests of the model on the TourneBroche where α-sweeps are carried out by tilting the whole apparatus with respect to the velocity vector (see 2.7.2). Figures 3.61 and 3.62 show such repeatability results for BWLHV and BWLHVST configurations. It can be immediately apparent that the repeatability is better on coefficients for the model with strakes and transition fixing on the nose. Opposite values of lateral coefficients can be found at high α for the basic configuration BWLHV (Fig 3.61) due to asymmetric forebody vortices. The sign of this asymmetry is not predictable .

The α-range [10° - 65°] is tested on the TourneBroche by means of two different α-sweeps with an overlapping of 5° in incidence. However, for these two different test cases, at the same incidence, the position of the model with respect to the support is different.

Consequently, in the stall region where the flow is unstable, small discrepancies are encountered, on the normal force particularly, as shown on Fig 3.62 for the BWLHVST configuration. These discrepancies on C_N are due to interference effects of the support which are encountered at $\theta_2 = 25°$, and not at $\theta_2 = 0°$ (see Fig 3.62). In the first test case, at high angle of attack, the model is in front of the support and its wake washes the support. Consequently, the positive pressure gradient induced by the support promotes separation of the flow on the model. Therefore, stall is obtained at a smaller value of α than in the other case where the wake does not interfere directly with the support because the model is shifted from the center of the test section ($\theta_2 = 0$) . It will be noted that these discrepancies, due to support interference effects, are also repeatable.

As the BWLHVST configuration provided excellent repeatability results for static tests, repeatability in rotary motion was tested. Figure 3.63 shows repeatability results for coning tests at $\beta = 0°$ and for different incidences 25°, 40° and 50°. Figure 3.64 presents the same type of results, but at $\alpha = 50°$ and for different values of sideslip : -5°, 0°, 5° and 10°. In these different cases, the repeatability of results is very good on all aerodynamic coefficients. Even the large non linear effects encountered on the yawing moment C_n are quite repeatable.

Therefore, as a conclusion, it seems that repeatability of rotary tests is good when repeatability of static tests is also good. The problem of repeatability is mainly due to stability of flow at high angle of attack which is not specific to rotary tests and can be assessed with static tests .

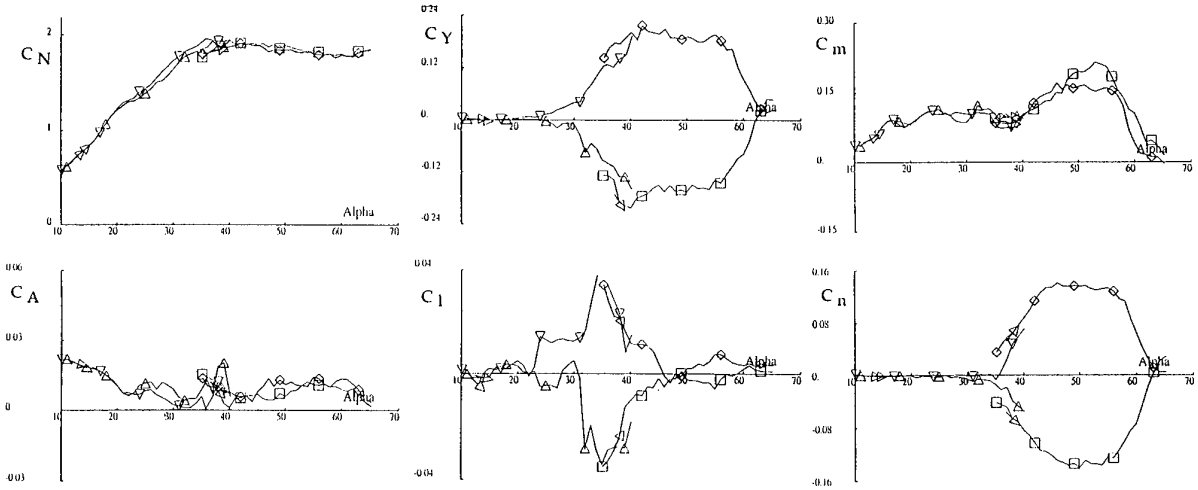

Fig 3.61 - BWLHV Configuration - slow AOA sweeps - Repeatability tests

△ 659 : $\Theta_2 = 0°$
▽ 818 : $\Theta_2 = 0°$
□ 663 : $\Theta_2 = 25°$
○ 820 : $\Theta_2 = 25°$

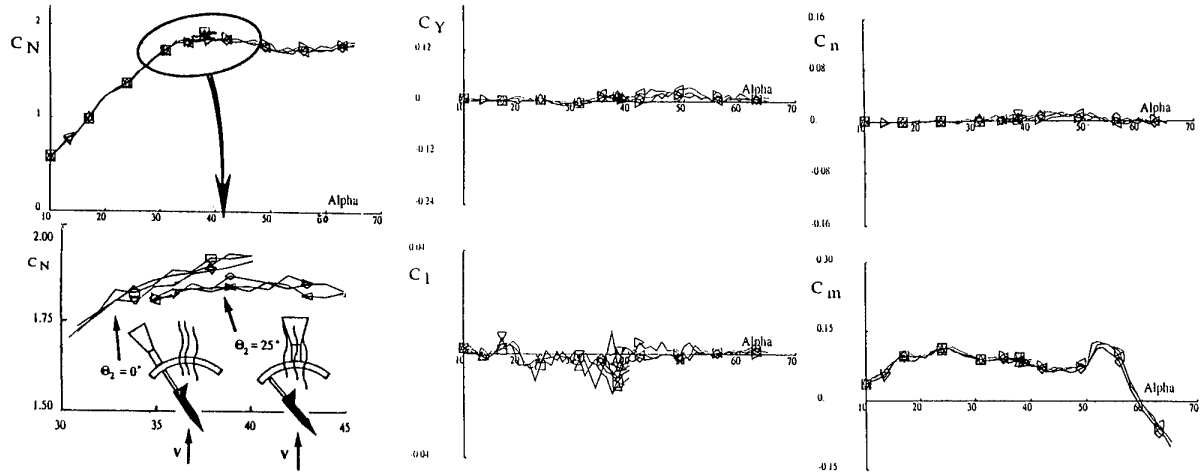

Fig 3.62 - BWLHVST Configuration - slow AOA sweeps - Repeatability tests

△ 209 : $\Theta_2 = 0°$ ◇ 203 : $\Theta_2 = 25°$
▽ 500 : $\Theta_2 = 0°$ ◁ 211 : $\Theta_2 = 25°$
□ 709 : $\Theta_2 = 0°$ ▷ 711 : $\Theta_2 = 25°$

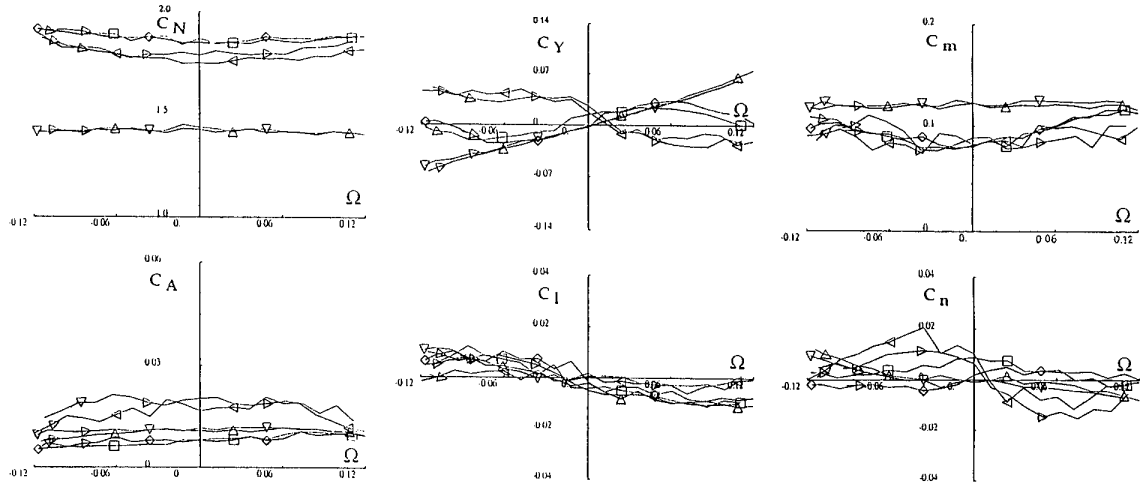

Fig 3.63 - BWLHVST Configuration - Repeatability tests at $\alpha = 25°, 40°$ and $50°, \beta = 0°$

△ 398 : AOA = 25° ◇ 719 : AOA = 40°
▽ 721 : AOA = 25° ◁ 248 : AOA = 50°
□ 270 : AOA = 40° ▷ 756 : AOA = 50°

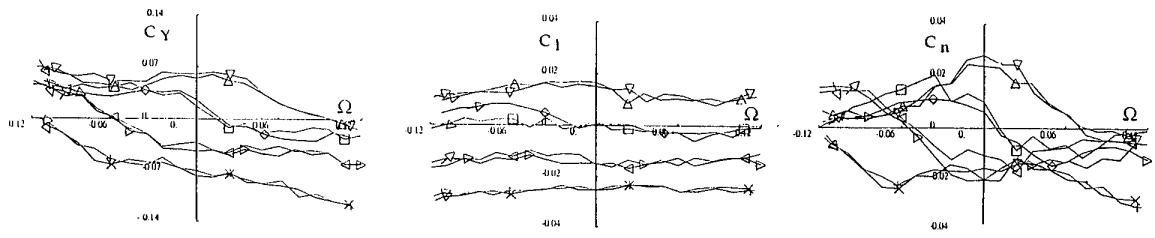

Fig 3.64 - BWLHVST Configuration - Repeatability tests at $\alpha = 50°, \beta = -5°, 0°, 5°$ and $10°$

△ 240 : ß = -5° ◁ 242 : ß = 5°
▽ 254 : ß = -5° ▷ 252 : ß = 5°
□ 248 : ß = 0° + 244 : ß = 10°
◇ 756 : ß = 0° × 250 : ß = 10°

3.13 REFERENCES

1. G. N. Malcolm
"Forebody Vortex Control" from Special Course on Aircraft Dynamics at High Angles of Attack : Experiments And Modelling.
AGARD-R-776, 1991

2. W. Bihrle, Jr., B. Barnhardt and E. Dickes
"Influence of Forebody Geometry on Aerodynamic Characteristics and a Design Guide for Defining Departure/Spin Resistant Forebody Configurations"
WRDC-TR-89-3079, 1989

3. P.J. Lamont
"Pressures Around an Inclined Ogive Cylinder with Laminar, Transitional or Turbulent Separation."
AIAA paper 80-1556 R

4. P.G. Champigny
"Stability of Side Forces on Bodies at High Angles of Attack."
AIAA paper 86-1776

CHAPTER 4

CORRELATION AND ANALYSIS OF ROTARY-BALANCE RESULTS

4.0 INTRODUCTION

Chapter 3 concentrated on comparisons of various effects investigated in each facility, such as forebody geometry, transition strips, Reynolds number, model size, etc. It was seen that some of these parameters had large effects on the results and some had very minor effects. The largest effect was the variation of the forebody geometry, in particular, the absence or presence of the forebody strakes. In this chapter, the focus of the discussion, with appropriate figures presented, is to compare results from different facilities. The primary purpose for the comparisons is to evaluate the differences in the results between the various facilities with different rigs and support systems, different test section geometries, and different data acquisition and reduction systems. The goal of these cooperative experiments on the same configuration and, in many cases, with identically the same model, is to determine the repeatability and reliability of rotary balance experiments given that every facility has a different geometry with varying relationships between the rig and the tunnel walls and their proximity to the model . The objective is to discover those parameters that have the most significant effects on the aerodynamic results and to ascertain which parameters are relatively unimportant.

In order to minimize the influence on the results of the differences already observed, such as those presented in Chapter 3, particularly the large variations due to the influence of the forebody strakes, the comparisons in this chapter will deal almost exclusively with configurations which have both strakes and transition strips. The data will be presented for several configurations beginning with body alone and progressing with a buildup of components to the complete configuration with LEX, wing, and tails. At the end of the chapter, a few comparisons are made for the complete configuration without strakes.

The comparison of data at different Reynolds numbers in Chapter 3 showed that the effects of Reynolds number for the model with strakes was measurable, particularly between the lowest and highest Reynolds numbers tested. The differences were minimal, however, within the higher Reynolds number range, say between 875,000 and 950,000. The approach for the comparisons in Chapter 4 is to use only data obtained at the highest Reynolds number possible from each facility with the intent that Reynolds number differences will not dominate the differences observed between facilities, enabling an assessment of other factors such as sting interference, wall effects, rig geometry, etc. For most tests this means that the chord Reynolds number is between 875,000 and 950,000. Most experimenters set their velocity conditions for the particular size model they were testing (A or B model) in order to match the Reynolds numbers of other facilities. For example, for the B model, the maximum velocity was typically 60 m/sec (200 ft/sec) and the A model was tested at 45 m/sec (150 ft/sec) resulting in a chord Reynolds number of 900,000-950,000.

For the A model tested on the rotary-balance rig in the ONERA-IMFL tunnel the maximum available velocity was 30 m/sec and the resulting Reynolds number was 655,000. However, they also acquired static data on the rotary-balance rig (non-rotating) at Reynolds number of 875,000 as well as 655,000. A collection of static data from many facilities, discussed in Section 4.1, will show that the aerodynamic differences were slight in the Reynolds number range between 875,000 and 950,000.

The rotary-balance data acquired by ONERA-IMFL, even though obtained at the lower Reynolds number of 655,000 where static data indicate some differences above 45° angle of attack, are included in the comparisons in this chapter. The premise, then, in comparing rotary-balance data between facilities in this chapter, is that Reynolds number effects between 875,000 and 950,000 should not be a major factor in evaluating the differences between facilities, particularly for the configuration with nose strakes. The data for Reynolds number of 655,000 may be affected by the lower Reynolds number, particularly above 45° angle of attack , but it is also included for comparison.

Data for the rotary-balance tests will be identified by facility or organization and run number as well as model size (A or B), type of sting mount (R-rear, T-top), type of transition strip (Br-DRA/British strips, It-AeM/Italian trips) and configuration designation (B-body, W-wing, L-LEX, H-horizontal tail, V-vertical tail, S-strake, T-transition strips). The test section configuration will be assumed to be closed unless otherwise marked as open (some of AerMacchi's and all of ONERA-IMFL tests). The principal experiments for comparison are the rotary balance tests, but there will also be some comparisons made initially from static test data, some of which were generated deliberately as part of the test matrix with angle of attack sweeps, and some which are derived from the zero-rotation data as part of the rotary balance test matrices. The rotary-balance data comparisons are made primarily at angles of attack of 24°, 40°, 50° and 60°. The aerodynamic coefficients compared are side and normal forces and yawing, rolling and pitching moments.

4.1 STATIC RESULTS

Static test results were acquired by several participants (ONERA-IMFL, FFA, AerMacchi and DRA) with specific tests devoted to acquiring angle of attack sweeps with the same rigs used for either rotary balance or forced-oscillation experiments. ONERA-IMFL static data were obtained on the same model (the A Model) on two different rigs. Some data were obtained on the rotary or Tourne-Broche rig in a vertical (spin) tunnel and some were obtained on the oscillatory or PQR rig in a horizontal tunnel, both of which have "open" test sections. FFA acquired static data on the same rig used for rotary-balance

tests. The model angle of attack is adjusted remotely with an electric drive system on the C-strut with the rig stationary. AerMacchi obtained a set of static data with their normal static test apparatus, a rear sting support mounted in a vertical strut allowing angles of attack from 0 to 45°. It should be noted that all of the specific static AerMacchi data were obtained in an open test section on Model B. AerMacchi (AM) also obtained zero rotation rate data in a closed test section. DRA acquired static data as part of the forced-oscillation experiments conducted on the A model in a closed test section. Other static data were acquired by all organizations as part of the rotary-balance experiments where the rotation rate was zero. Some of these results will be included for comparison.

Figure 4.1 shows some of the static data obtained for longitudinal and lateral-directional coefficients for angles of attack up to 70°. All of the data shown were obtained at zero sideslip and, in all cases, the models had transition strips and strakes on the forebody (BWLVHST). The primary emphasis in the discussion of the static results, is, therefore, on the longitudinal results, since the lateral-directional data would not be expected to vary significantly. Where the lateral-directional data differ from expectations, some comments are made. The quantity of data dictates that the presentation of static results be accomplished with two sets of plots. Figure 4.1a presents only data from tests that were conducted deliberately to establish the static aerodynamic characteristics with angle of attack sweeps. The presented curves represent several Reynolds numbers varying from 475,000 to 875,000. The purpose is to show whatever Reynolds number effects exist with data from many facilities. The curves in Fig 4.1b concentrate only on data acquired at the higher Reynolds numbers (greater than 875,000). The data include continuous curves and discrete data from non-rotating rotary-balance tests. The common set of data for both sets of curves is a static run from ONERA-IMFL (IMFL 20) which provides a reference for comparison between both figures.

4.1.1 Longitudinal Data

In Fig 4.1a the ONERA-IMFL data were taken on two different rigs. The data for Runs 18, 19 and 20 were acquired on the "PQR" apparatus during the forced oscillation test series. This rig is described in Chapter 2. The models are mounted at the base and the test Reynolds numbers are 0.545×10^6, 0.655×10^6 and 0.875×10^6, respectively. There are no significant Reynolds number effects on normal force for the runs on the PQR rig. However, there is some evidence to support the dependency of the pitching moment on Reynolds number at higher angles of attack (>45°). The trend at higher angles of attack is towards larger nose-down pitching moments with increasing Reynolds numbers.

For comparison, the data for IMFL Runs 709/711, which were acquired on the ONERA-IMFL rotary-balance rig or "Tourne-Broche" rig for the same model (Model A), are also shown. The model is rear-mounted on a 10° bent sting with the angle of attack continuously varied by the rig tilt mechanism (λ) from 0° to 30° and with the sting/arm assembly (Θ) at 0° or 25°, as shown earlier in Fig 2.28. Therefore, angle of attack varies from 10° to 40° for Run 709 and from 35° to 65° for Run 711, resulting in a 5° overlap. Thus, these two runs provide a comparison for the same model and sting arrangement with slightly different relationship to the main support strut. The agreement in the overlap region is quite good (best observed in the plot for pitching moment) with just a slight difference in the normal force at $\alpha = 40°$. The comparison of the "PQR" results to the "Tourne-Broche" results is also very good, with little or no differences up to about $\alpha = 35°$.

Above 35°, however, there are some significant differences in normal force and, to a lesser extent, in pitching moment. The data from the "PQR" rig (Runs 19 and 20) show a higher normal force and generally lower pitching moment. This difference is likely caused by the global influence of the "Tourne-Broche" rotary-balance support system and the divergence of the vertical wind tunnel test section where the rotary-balance rig is used, which is designed primarily for spin tests with free-spinning models. If the data from the PQR apparatus are considered to be the "standard" because the model is relatively free of model support effects, high angle of attack "stall" effects are triggered earlier on the Tourne-Broche (TB) rig. This is because of the influence of the strut system being closer to the model, which creates a positive pressure gradient and earlier separation of the flow on the model and bursting of vortices. The fact that the TB data from ONERA-IMFL agree pretty well with other rotary-balance data indicates that the effects of the strut system for the ONERA-IMFL TB rig are not unusual. All of the other rotary-balance data undoubtedly suffer to some degree from similar rig proximity effects, such as the presence of the support in the flow field wake of the model.

Static data obtained from the FFA tests are also shown for comparison. Runs 4859/4882 are from angle of attack sweeps with a rear-mounted B model from 0 to 40° and a top-mounted B model from 30° to 70°, respectively. The Reynolds number is 0.9×10^6. For the rear-mounted configuration, the normal force and pitching moments are comparable to the ONERA-IMFL data up to approximately $\alpha = 30°$. At angles of attack above 30° the FFA pitching moment is significantly larger (nose up) than the other data. Results for the top-mounted model are substantially different than for the rear-mounted model in the 30° to 40° range, illustrating a significant difference in the effects of the model/sting support relationship. Also, the top-mounted model data show significant differences in the normal force and pitching moment from the IMFL data for a rear-mounted model for all angles of attack above 30°. The combination of a lower normal force and larger nose-up pitching moment are consistent with the expected interference effects of a top-mounted sting inducing a positive pressure gradient or loss of velocity near the rear of the model, resulting in less "lift" at the rear.

Another set of data was obtained in the AerMacchi facility on their standard sting/support apparatus (up to 40° angle of attack). These data were obtained on the rear-mounted B model in an open test section at a Reynolds number of 0.95×10^6. The normal force and pitching moment data agree quite well with the majority of the other data with only slightly higher pitching moment than most of the other data

(except FFA). The DRA data at R=0.475 x 10^6 on a rear-mounted A model (up to 50° angle of attack) show good agreement with the majority of the other data. The effect of Reynolds number seems insignificant, at least up to 45° angle of attack.

Figure 4.1b shows data plots only from the higher Reynolds number runs available, i. e., Rn>875,000, including static angle of attack sweeps by ONERA-IMFL, FFA and AerMacchi and some individual data points from rotary-balance experiments (zero rotation rate) from various facilities. As an example, points from the AerMacchi (AM) rotary-balance tests with the A model (rear-mounted from 8° to 40° and top-mounted from 40° to 70°) and a rear-mounted B model are plotted. In addition, points from Eidetics, FFA and DRA are also plotted for comparison. In general, the rear-mounted data agree with the other rear-mounted data already discussed. The Eidetics (EI) data show good agreement with the IMFL data. Overall, the pitching moment coefficients show fairly good agreement but with a visible spread in the actual values. The largest differences seem to be for top-mounted versus rear-mounted models, for both normal force and pitching moment.

The general conclusion from all of the comparisons at the higher Reynolds numbers is that the data differences experienced by testing with different rigs in different tunnels occur primarily above angles of attack of 40°. The disagreements appear to be due mainly to the influence of the sting support on the model flow field, caused mainly by different proximities of the tunnel support system hardware to the model or, more significantly, by the presence of the sting mounted through the top of the model. The general effects observed are lower normal force and higher nose-up pitching moment values for top-mounted models than with rear-mounted models. The most desirable sting support system is one which mounts the model on the sting through the rear and as far from the support system as practical.

4.1.2 Lateral-Directional Data

A general observation on the lateral-directional data shows that the side force, yawing and rolling moment coefficients are near zero for angles of attack below 30° as one would expect for a symmetric model at zero sideslip. However, if the flow field is asymmetric because of forebody-induced vortex asymmetries, for example, these coefficients would not be expected to be zero throughout the entire angle of attack range. In Chapter 3, it was observed that for the forebody with strakes, the induced flow asymmetries are greatly reduced. However, as can be seen in Figs 4.1a/b, the magnitude of the asymmetry can vary depending on the test apparatus and wind tunnel combination. In general, the yawing moment and side force data are near zero for angles of attack up to 40° with the exception of the FFA data and AM Run C25714 data. There is a significant difference in the levels of the FFA data in the 30° to 40° range when the model mounting is changed from rear to top. The side force data remain offset from zero to above 30°. For angles of attack above 40°, much of the data show near zero side force and yawing moments with the exception of IMFL 19 and, to a lesser extent, IMFL 20, and FFA A4882 with the top mounted model.

In the course of ONERA-IMFL's experiments, the level of asymmetry seemed to correlate with Reynolds number, where the magnitude of asymmetry decreased with increasing Reynolds number when Reynolds number varied from 540,000 (V=25 m/sec) to 875,000 (V=40 m/sec). For the present test, these chord Reynolds numbers correspond to Reynolds numbers based on the forebody diameter of 172,000 and 277,000, respectively. This is consistent with the well-known behavior of forebody side forces and yawing moments with increasing Reynolds numbers as measured by Lamont (Ref. 3.3) and others (Champigny, for example, Ref. 3.4). In this range one expects to see the side force and yawing moment asymmetries largest at the lowest Reynolds numbers, as observed. Data from Lamont's experiments showed that the maximum side force on a slender forebody at high angles of attack (40° to 60°) decreases with increasing Reynolds number when the Reynolds number, based on the diameter of the forebody, increases continuously from approximately 200,000 to 1,000,000.

Experiments were conducted by Malcolm, etc. several years ago in the NASA Langley 12-foot low-speed tunnel (Refs. 1-3) with a generic fighter configuration nearly identical to the AGARD model (in fact, this generic configuration was the configuration that inspired the final choice of the AGARD models). These tests were run at a chord Reynolds number of 750,000 (187,000 based on forebody diameter) and showed side forces and yawing moments to be nearly zero for angles of attack up to 70°, as was observed on many of the runs in Fig 4.1. This model had the same forebody strakes (also mounted at 105°) but did not have transition strips. It should also be mentioned that the turbulence level of the 12-ft tunnel where these data were acquired is quite high, contributing, perhaps, to an earlier transition than would be expected in a tunnel with less turbulence, thereby simulating a Reynolds number somewhat higher than 187,000.

The point to be made is that the degree to which the forebody flow remains symmetric through the angle-of-attack range up to 45° is somewhat dependent on Reynolds number, despite the presence of strakes, but probably more important is the relationship between the model, support apparatus and tunnel walls. Represented in Fig 4.1b are many different combinations of model size, tunnel size, and support/rig geometries. It is not surprising to observe some differences, even though all of the data compared were acquired at similar Reynolds numbers, and the forebody flow separation was predetermined to a large extent by the forebody strakes.

Even though the forebody flow is forced to have nearly symmetric separation near the tip by the presence of strakes and transition strips, the flow field aft of the forebody strakes and ahead of the LEX can still be affected by the influence of induced pressure gradients in the leeward side flow field. It should also be noted that the installation of the forebody strakes by each experimenter was undoubtedly slightly different. There was no device to guarantee that the strakes were attached to the clean forebody in identically the same location with the same angle, etc. Each experimenter did his best to place them accurately.

Some experiments by AerMacchi and FFA showed that the degree of asymmetry at high angles of attack was fairly sensitive to the placement of the strakes (see Section 3.6) and the placement of transition strips (see Section 3.2).

4.2 ROTARY-BALANCE TESTS

4.2.1 Body-Alone with Strakes and Transition (BST)

The data shown in Fig 4.2 at $\alpha = 40°$ show some differences in side force and yawing moment from three different facilities with the same B model. The normal force and pitching moment are in good agreement for all examples shown. All of the data curves show that the side force and yawing moments vary non linearity with rotation rate. There is no general pattern for the curves from the various facilities except the "mean" slope, negative for side force and positive for yawing moment. All runs have models with DRA transition strips, with the exception of Run 4828 with the AEM strips. The two runs from DRA have different mounting angles associated with the rear mounted model (See Chapters 2 or 3 for the different geometries). The differences in side force and yawing moment due to different transition strips (same tunnel and rig) are about equivalent to the difference in mounting arrangements (DRA results). The Eidetics data show differences from the other results of about the same magnitude as the differences within the same facilities. The rolling moment is near-zero (as it should be) for all experiments, and the longitudinal results are in good agreement.

Figure 4.3 shows results for $\alpha = 50°$ from Eidetics and two runs from DRA with different mounting arrangements. The largest discrepancy is for rear vs top mounted models in the DRA facility. A similar comparison was shown earlier for the complete model in Fig 3.43 and the discrepancies were very similar. The sensitivity of the aerodynamics of the model without wings to the placement of the sting in the top of the model is very likely to be higher than if the wing were present. With the wing in place, as in Fig 3.43, the sting is in the wake of the wing and less likely to influence the flow on the model. Mounting in the rear of the model usually has less influence on the leeward flow field than mounting through the top. The characteristics of the data from the rear mounted models (Runs 2007 and 113) are similar, whereas the data for the top-mounted model (Run 134) is significantly different, indicating perhaps a reversal in the asymmetry of the flow with a reversal in the rotation rate. The yawing moments for the rear mounted models show a pro-rotation tendency (positive slope) while the top-mounted model shows an anti-rotation (negative slope) character.

4.2.2 Body-Wing with Strakes and Transition (BWST)

Figure 4.4 shows the effect of adding the wing to the basic body at $\alpha = 40°$. The comparisons include data from rear-mounted models and one top-mounted model. The three runs from FFA show differences in mounting arrangements and with different transition strips. The differences between the three runs are minimal, with the exception of Run 4096 with DRA(Br) transition strips which shows a change in slope of the side force and yawing moment curves above a rotation rate of 0.08. Overall, the differences between the five different sets of data are minimal, with a small difference in the rolling moment at zero rotation rate for the top mounted model. The pitching moment data show a slightly larger nose-up pitching moment for the Eidetics data at positive rotation rates. The reason for the higher values is unknown.

Figure 4.5 shows the same configuration at $\alpha = 50°$ with runs from three different facilities. The Eidetics data are obtained with a rear-mounted model and the DRA and FFA runs are with a top-mounted model. The results show very close agreement, with side force, yawing and rolling moments showing nearly the same mean slopes from each facility. The Eidetics pitching moment data show a slightly lower nose-up pitching moment at negative rotation rates and higher nose-up pitching moment at positive rotation rates than the other data. The Eidetics normal force data are slightly higher at all rotation rates than the other data. The reason for the differences is unknown but may well be linked to the fact that the Eidetics data come from a rear-mounted model and the other data from top-mounted models.

4.2.3 Body-Wing-LEX with Strakes and Transition (BWLST)

Figure 4.6 shows a comparison at $\alpha = 40°$ with the LEX added to the configuration. The data are from three facilities with two different mounting arrangements and two types of transition strips from the FFA facility. There are some small variations between the plotted data, but the character reflected in the slopes and overall shapes of the curves is very similar. The only discrepancy is in the Eidetics pitching moment at positive rotation rates. There are also small but measurable differences in the levels of normal force and pitching moment, with the top-mounted model showing the lowest normal force of all tests but comparable pitching moment. There are also some discrepancies relative to the slope of normal force. Increases in normal force values with increasing absolute values of rotation rate can be noted for Eidetics and, to a lesser extent, for FFA rear-sting data.

4.2.4 Body-Wing-LEX-Tails with Strakes and Transition (BWLVHST)

Figure 4.7 shows data for the complete configuration at $\alpha = 24°$. Included are data from tests performed in four different facilities and in the AerMacchi tunnel with A and B models. The agreement for the lateral-directional coefficients is very good. The slopes of all of the curves are comparable, and the variations with rotation rate are well-behaved. The only discrepancies are in the pitching moments with Eidetics data higher and IMFL data somewhat lower in mean value, as noted for static tests (see Fig 4.1). Moreover, Eidetics data tend to larger nose-up pitching moments at positive rotation rates as noted previously in Figs 4.4 to 4.6.

In Fig 4.8, a similar comparison is made for the complete configuration tested at $\alpha = 40°$ in many different facilities. The trends or shapes of the curves for the lateral-directional coefficients are similar but there are some noticeable shifts in the absolute values of the various plots. Even the normal force data are not in complete agreement at zero rotation rate. It is interesting to note that there is a difference between the A and B model data from the AerMacchi tests (AM 25575 and 25582), particularly in the lateral-directional coefficients. In general, the variation of yawing moment coefficients with rotation rate for the different facilities is quite dissimilar. The zero rotation rate asymmetries in yawing moment and side force are apparent, with the largest being the AerMacchi A model data and the IMFL "open" test section data. The rolling moment data have the same trends but differ in the absolute values. The higher non linearity of the DRA normal force data with rotation rate compared to the other data is also obvious. The reason is unknown, but is likely due to interference effects of the "R40 crank" sting mount configuration.

Similar to Fig 4.8, Fig 4.9 shows results for the complete configuration at $\alpha = 50°$ with different size models (A and B), different mounting schemes and different transition strips (Br or It). For the most part, the results are very similar. There are some differences in the data but no particular pattern that would point to any specific parameter such as model size, transition configuration, rear versus top mount, etc. as a cause. In particular, the shapes of the curves with rotation rate are in very good agreement even though the absolute levels of the various curves vary slightly. The ONERA-IMFL data, acquired with a rear-mounted model in an "open" test section at R=655,000, appear to differ somewhat from the rest of the data, particularly yawing moment and side force. This difference may be due to the effects of the open test section and the relatively lower Reynolds number. Reynolds number effects were shown in Section 4.1 to be important in the angle of attack range above 45° to 60°.

The final plot for the model with strakes is shown in Fig 4.10 These data are for 60° angle of attack. As shown in the previous figure, the data for different models, mounting schemes and transition strips are very similar, with the exception of the FFA 4873 rolling moment coefficient. Why the difference only appears prominently in the rolling moment is unknown. There are some differences in the pitching moment data, primarily in the level of the values instead of the shape of the curves. There are also significant differences in the values of normal force, even at zero rotation rate. There is good symmetry in the values for positive and negative rotation rates, except for the EI pitching moment data.

4.2.5 Body-Wing-LEX-Tails with Transition and without Strakes (BWLVHT)

The following four figures show some examples of comparisons between facilities for the complete configuration with forebody transition strips but without the forebody strakes. It should be pointed out that the scales for the aerodynamic coefficients are not the same as for the plots for the model with strakes, because, in many cases, the magnitude of the coefficients at higher angles of attack, particularly the side force and yawing moment, are much larger for the model without strakes. From the data presented and discussed in Chapter 3, it is clear that the model flow field is very sensitive to even minor changes to the test environment when the forebody strakes are removed. As discussed previously, the orientation of the forebody vortices, and their effect on the rest of the flow field, is very significantly influenced by the presence of any interference in the vicinity of the model. With strakes attached, the forebody flow separation characteristics are dictated primarily by the strake edges at angles of attack below approximately 45°. The comparisons which follow for the model without strakes are to illustrate the other end of the sensitivity spectrum from the examples shown earlier.

Figure 4.11 provides a comparison between two sets of data at 24° angle of attack. The EI data are for the B model mounted in the rear and the AM data are for the larger A model mounted in the rear. The side force is nearly identical and the yawing moment data are very similar. The rolling moment coefficients are substantially different for these two sets of data. The combinations of different models and different facilities, resulting in different proximities to the tunnel walls, etc. appear to have an influence on the wing flow fields, perhaps through the interaction of the forebody vortices and the wing LEX and the resulting effect on the wing flow. The pitching moments are similar except for the higher positive rotation rates.

Figure 4.12, for $\alpha = 40°$, clearly shows the wide variation that can result from tests in different facilities if the model has a high sensitivity to variations in the relationship between the model, sting, tunnel walls, etc. In fact, wide variations in the data can occur when tests are run in the same tunnel for models with sharp forebodies tested at high angles of attack. There have been many examples of experiments where there were significant differences in the level (and direction) of forebody vortex flow asymmetries simply by repeating the test at the same conditions. Often, the results are only truly repeatable if they are run back to back without any disturbance to the model. Test results have shown that even a finger print on the model near the tip can induce an asymmetric flow field to switch directions. When this occurs at static conditions (non-rotating), it is not unusual to see the forebody vortex flow field asymmetry reverse under rotary conditions. There is clear evidence of this phenomenon of reversal in direction in Fig 4.12, particularly in the side force and yawing moment.

To some degree, the data sets in Fig 4.12 tend to be grouped into two sets, each one being the opposite sign of the other. The exceptions are the AM runs 25721 and 25722. Run 25721 begins with maximum negative rotation rate and ends with maximum positive rotation rate. Run 25722 begins with maximum positive rotation rate and ends with maximum negative rotation rate. The result of this systematic change in the rotation rate reveals a hysteresis effect, where the value of the lateral-directional coefficients are dependent on the direction of the variation in rates. The grouping of the data into two sets of curves with opposite

signs illustrate a "bi-stable" flow field where the flow phenomena are easily triggered from one state to the other. The "bi-stable" character is driven by the bi-stable nature of the forebody vortices at high angles of attack where they can be asymmetric with either the left or right side vortices positioned higher above the forebody surface than its counterpart. The asymmetric separation associated with the asymmetric vortices causes the yawing moments to the right or left, respectively. The orientation can be changed very easily with a disturbance at the tip of the forebody or by pressure gradients in the leeward flow of the model produced by proximity to the sting or model support system components. With the high sensitivity of the model flow field with a sharp forebody, it is not surprising that there is a wide variation in the yawing moment and side force between the various facilities.

Although there is some scatter in the data, it is appears that the pitching moment and normal force data from the FFA experiments with a top-mounted model (FFA 4902) are low compared to the other data taken with the sting mounted in the rear of the model. This combination would indicate less force on the nose as a result of the top-mounted sting.

There is also a very wide variation of the rolling moment values. Positive and negative variations of the rotation rate induce local positive or negative variations of sideslip angle at the nose tip. In Fig 4.12, when the hysteresis happens, the rotation rate is approximately equal to 0.05. Such a rotation rate induces, at $\alpha = 40°$, a local sideslip angle of 4.3° at the nose tip, a significant level that could influence the pattern and stability of forebody vortices. Thus, the relative positions between left and right vortices can greatly change and, consequently, these vortices can burst at different locations above the wings, changing the rolling moment. Such a phenomenon was analyzed by IMFL in Section 3.8 for the BWLVHST configuration at sideslip (phenomenon existing in spite of the presence of strakes). As shown in this section, during static tests at sideslip, a hysteresis phenomenon was encountered for yawing and rolling moment coefficients as angle of attack was slowly increasing or decreasing. Presence of sideslip leads to multistable flow fields, encountered during slow angle-of-attack sweeps as well as rotary tests (see Chapters 3 and 5).

Comparing the data curves for the longitudinal coefficients, there are obvious similarities in the shape of curves, all of which show little variation with rotation rate. There are some noticeable differences in levels, however. Figure 4.13 shows data for the same configuration without strakes at $\alpha = 50°$. As in the previous figure for $\alpha = 40°$, there is wide disagreement between the various facilities.

In Fig. 4.14 the angle of attack has been increased to 60°. There are three cases to compare. The largest variations, as expected, are in the side force and yawing moment. It is important to note that even though there is a wide variation in the side force and yawing moment coefficients over the rotation range, there is almost no effect on the rolling moment. Clearly, the angle of attack is sufficiently high that the forebody vortices can no longer influence the flow from the LEX and the wing, but act primarily on the forebody itself. There is also a measurable difference in the pitching moments, although the normal forces are nearly identical, reflecting a significant shift in the center of pressure from one data set to the other.

4.2.6 Conclusions from Rotary-Balance Wind Tunnel Tests

The agreement of results from various facilities depends strongly on the type of configuration tested, as seen by comparing the results for the configuration with forebody strakes and transition strips and the results for the forebody without strakes. The model with strakes could be considered to be representative of more advanced fighter configurations because the sharp-edged strakes behave much like the chine cross section associated with these newer aircraft, creating a well-defined separation location for the forebody vortices. The other extreme is a configuration with a circular or near-circular forebody cross section with smooth sides which allows cross-flow separation to take place asymmetrically at certain Reynolds numbers and angles of attack. The result of the asymmetric separation is the generation of asymmetric loads on the forebody and, through the shed asymmetric vortices, an influence on the flow field aft of the forebody, as well. The level of asymmetry is subject to change from relatively minor disturbances in the flow field created either near the tip of the forebody or from resulting asymmetric pressure gradients in the leeward side flow field. The differences in sensitivities of the model flow fields to various effects, including support interference, wall effects, open and closed test sections, etc. for different models as characterized by the model with and without nose strakes show that the reliability of test results can be influenced significantly by the model geometry being tested.

When repeating comparisons presented above for the models with strakes and transition strips, there is an overall consistency of the data regardless of which facility and what size model is used. There were some minor differences in the results observed due to the proximity of the sting and/or the support system to the model, particularly from top-mounted stings. For the model without strakes, there was a wide variation in results, not only between facilities but in the same facility with changes to the overall test setup. This extreme sensitivity to variations in the test setup is typical of pointed slender configurations where the forebody flow field is determined by small variations in the flow near the tip or from induced pressure gradients in the leeward side flow field due to the proximity of test support hardware. Despite the wide variation in the geometry of the rotary-balance rigs used for these comparative tests, all of the rigs appear to be capable of acquiring reliable data for configurations where the model flow field is not unusually sensitive to small variations in the local flow conditions, such as those resulting from the use of forebody strakes. In general, for any test setup, the farther the model can be located from the support system, the better. It is good practice to test any particular model with more than one sting/support arrangement where practical, particularly with top-mounted versus rear-mounted models.

4.3 WATER TUNNEL TESTS AND FLOW VISUALIZATION

Both Eidetics and AerMacchi conducted water tunnel tests with models of the AGARD generic fighter complete configuration. Eidetics investigated a very limited number of conditions with emphasis on acquiring force and moment data from a newly developed water tunnel balance with simultaneous flow visualization. AerMacchi concentrated on investigating, through flow visualization comparisons, the vortex structures on the strake-on and strake-off configurations, the effect of rotation rate on them as well as the interference effects due to the presence of a rotary rig. For this purpose, the geometry of the AerMacchi rig was more extensively studied as representative of a generic shape, but effects of the specific DRA and Eidetics rigs were also investigated.

4.3.1 Eidetics Water Tunnel Tests

The Eidetics water tunnel is a continuous flow tunnel with a 2-ft wide, 3-ft high and 6-ft long glass test section. The model and 5-component balance were mounted on a recently constructed rotary-balance apparatus for the water tunnel and run at angles of attack of 40° and 50°. The complete configuration was run with and without the same forebody strakes as the wind tunnel model. The model did not have transition strips. The Reynolds number is approximately 9,000 based on mean wing chord, resulting in laminar flow on the model forebody that cannot be tripped by transition strips. Even though the Reynolds number is very low and the separation mechanism is somewhat different at low Reynolds numbers from what it is at high Reynolds numbers, the resulting leeside vortex flow field pattern is very similar. For the forebody with strakes, the flow separates at the edge of the strake, regardless of the Reynolds number, thus producing a flow field that is not very sensitive to Reynolds number. The results from this test were compared to rotary-balance data from Eidetics tests in the NASA Ames 7 x 10-ft wind tunnel with the rear-mounted B model and from DRA wind tunnel tests with the B model mounted at the rear with 40° and 60° crank stings. These wind tunnel test configurations can be seen in Chapter 2.

The water tunnel rotary-balance rig is shown in Fig 4.15 with a geometry very similar to the Eidetics rig used in the wind tunnel, with the capability for angles of attack from 0 to 60°. The model is approximately 1 ft in length. Figure 4.16 shows a flow visualization example for the model at α = 40° without strakes, and Figs. 4.17a and 4.17b show the model at α = 50° without and with strakes, respectively. The model at α = 40° in the water tunnel showed a symmetric forebody flow at zero rotation rate (static). With positive rotation (clockwise viewed from the rear) the right side (upwind) vortex assumes the higher position above the forebody and its breakdown position definitely moves aft. With negative rotation, the pattern reverses. At the maximum non-dimensional rotation rate of 0.15 the high vortex has a core trajectory that is above the vertical tail and a burst location that is near or just beyond the vertical tail, very near the C-strut of the rotary rig. In correlation with these changes to the forebody vortices, the burst point of the upwind LEX vortex is also displaced downstream, and the vortex on the opposite side is displaced upstream.

Such displacement can be interpreted as an effect of the increased downwash generated by the upwind forebody vortex which reduces the effective angle of attack of the LEX on the same side (therefore reducing the strength of the separation induced vortex and simultaneously the burst point moves further aft). Such variation in LEX vortex burst positions can be correlated with the well pronounced negative (damping) rolling moment generated by positive rotation at this angle of attack and have been confirmed in AerMacchi water tunnel tests.

In comparison, Fig 4.17 shows the model at α = 50° without and with strakes. At α = 50°, in static conditions, the forebody produces asymmetric vortices instead of symmetric vortices as in Fig. 4.16 at 40° angle of attack. However, the effect of rotation is very similar in producing the vortex pattern in response to the rotating motion. With strakes, the forebody vortices at zero rotation rate are very diffuse and difficult to define.

In the presence of a rotating model, there is a displacement of the vortices generated by the strakes that is similar to that observed on the forebody without strakes but much less well defined and with very limited displacement of burst points. The small variation in burst point location is primarily because the strengths of both upwind and downwind vortices are very similar due to the fact that flow separation is fixed by the strakes, with little influence from the rotational motion. There is little evidence of vortices in the region near the aft part of the model. This difference clearly correlates with the results of the wind tunnel tests discussed earlier, where the data obtained on the model with strakes in place is well behaved and shows no abrupt changes in value with rotation rate. Ground facility wall interference effects on the forebody flow field and the flow interactions with aft surfaces like the vertical tail are much more likely to be of concern for the model without strakes.

Examples of the forces and moments determined from the Eidetics water tunnel tests for the two cases shown in Figs 4.16 and 4.17b are shown in Figs 4.18 and 4.19. Figure 4.18 shows lateral-directional data without strakes at α = 40°. The water tunnel data are clearly within the range of the wind tunnel data. The yawing moment data show not only the same slope but actually agree in value with the DRA 60° crank results. The two "pairs" of curves for the yawing moment indicate clearly that the data represent two opposite orientations of the forebody vortices that remain in their positions throughout the rotation rate range. The rolling moment has the same characteristics as the wind tunnel data but with a value at zero rotation rate that is significantly different than the lowest rotation rates in each direction. It should be noted that the orientation of the forebody vortices observed in the flow visualization are consistent with the measured values of the yawing and rolling moments. That is, the vortices provide moments that are opposite to the rotation direction (stable) just as one would expect from the flow visualization where the vortex in the high position is on the windward side and the low vortex (higher suction) is on the leeward side or opposite to

the direction of rotation (providing a moment opposing the motion).

The results in Fig 4.19 are for the model with strakes at α = 50°. The results are compared to Eidetics and DRA wind tunnel data. The slopes of the curves for side force and yawing moment are greater for the water tunnel tests. The reasons are not clear. The Reynolds number of the water tunnel tests are two orders of magnitude less, which may have an effect on the fuselage flow aft of the strakes. The wing and tail surfaces are all fully separated so Reynolds number shouldn't be a major factor for these components. The flow visualization would suggest that the vortices from the forebody are too diffuse in the aft part of the model and not likely to interact to any great degree with the rotary rig components, therefore minimizing effects on the forces and moments. As seen earlier, the agreement between the two wind tunnel results is very good. An important point should be kept in mind for water tunnel tests. They are not intended to replace wind tunnel tests but to provide insight to the experimenter to understand the complexities of the flow field and to correlate flow visualization results to simultaneous force and moment measurements.

4.3.2 AerMacchi Water Tunnel Tests

AerMacchi conducted more extensive water tunnel tests in their water tunnel (built by Eidetics with identical dimensions) with the purpose of providing some insight into the effects of the various test apparatuses on the flow field of the common model. AerMacchi conducted flow visualization experiments on a 1:3.5 scaled model of WG-16A with a simple support rig, shown schematically in Fig 4.20a. Most tests were conducted by using an "arc" and "sting" (both rear and top-entry) representing scaled down versions of the AerMacchi rotary balance. Two different scales were used in order to represent geometrical layouts corresponding to both model A and model B wind tunnel tests.

They also examined the effect of an arc that is "faired" or rounded on the leading edge and shrouded on the trailing edge compared to an arc with squared cross section. Results were also obtained with the rotary rig hardware geometry representing AerMacchi, DRA and Eidetics rigs simulated as closely as practical. These configurations are shown in Fig 4.20b. Tests were run at angles of attack of 24°, 40°, 50° and 60° as shown. The basic rotary rig for the AerMacchi water tunnel is the rear support without the components labeled "sting "and "arc". The arc and sting are provided only to simulate a typical wind tunnel rotary rig configuration. The objective was to run tests at fixed conditions (angle of attack and rotation rate) with the different rig geometries and determine, if possible, whether the influence of the different rigs on the flow field could be observed and interpreted relative to what was measured in the wind tunnel tests.

Of course, due to the nature of water tunnel flow visualization, it is immediately evident that only a qualitative assessment of interference effects related to displacement or bursting of forebody and LEX vortices is possible. Other more quantitative effects, such as changes in local flow speed or direction cannot be detected and ruled out, although they are felt to be of lesser importance for this class of flows.

4.3.2.1 *Results for models with strakes*

The results of the tests with the forebody strakes in place are the easiest to summarize. Because, as seen from the Eidetics flow visualization photos and as observed in the AerMacchi tests, the forebody vortices are more localized to the front portion of the model and there is virtually no effect of either the arm or the sting on the flow patterns. In the AerMacchi tests the vortices emanating from the forebody and from the LEX are essentially unchanged due to the presence of the rotary-rig hardware. Neither the vortex core position nor the burst location are altered by adding the sting and arc components. This fact supports the conclusions from the wind tunnel tests for the complete model with strakes that only small variations in the results from facility to facility were observed.

4.3.2.2 *Results for models without strakes*

For the model without strakes, there was some evidence of interference at certain conditions at $\alpha = 40°$ and 50°. At α = 40° on the A model only those conditions where there was any evidence of interference will be discussed. At all other conditions there were no significant effects of the rotary rig hardware, as seen with the configuration with forebody strakes. The effects to be compared are due to the following support system geometry variations illustrated:

Fig 4.21 - straight base (rear) mounted sting support, no arc
Fig 4.22 - base mounted sting with faired arc
Fig 4.23 - top mounted sting with faired arc
Fig 4.24 - base mounted sting with DRA type arc and 40° crank

Base-mounted straight-sting support

The "baseline" data are shown with a straight sting only in Fig 4.21 . Fig 4.21a shows side and planform views at zero rotation rate. Without rotation, the two forebody vortices remain adjacent to the model surface with the vortices bursting symmetrically approximately at a mean position near the half-length of the fuselage. In real time, the location of the burst points fluctuate for and aft as much as 10-15% of the fuselage length. During rotation at $\omega b/2V$ = +/-0.1 (Fig 4.21b), there is a considerable difference in the left and right vortices. The downwind vortex (away from the direction of rotation) maintains the same basic characteristics as the non-rotating case but burst further forward. The upstream vortex lifts above the forebody/fuselage and breaks down beyond the vertical tail. The actual burst location varies for and aft with time during a rotation cycle. At $\omega b/2V$ = +/-0.15 (Fig 4.21c) the upwind vortex lifts even further above the fuselage and the burst location is well downstream of the vertical tail.

Base-mounted sting with faired arc

With the mounting arrangement changed to an arc and rear-sting combination, the resulting effects on the vortex flow field can be seen in Fig 4.22. At zero rotation rate (Fig 4.22a) the effect on the forebody vortices, by comparing to

Fig 4.21a, is negligible. At ωb/2V = +/-0.1 (Fig 4.22b), despite the fact that the upwind vortex burst location is near (in front of) the arc, by comparing with Fig 4.21b, there is no effect on the burst location compared to the straight sting without the arc. It is also worth noting that the upwind vortex (left side) passes to the left of the arc, but only slightly. One could predict that at higher rotation rates the arc might intersect the trajectory of the upwind vortex and have a significant influence on its burst point. Indeed, at rotation rates of +/-0.15 (Fig 4.22c), there are some apparent effects. For negative rotation (-0.15), comparing Fig 4.22c with Fig 4.21c, there appears to be little effect of the arc, despite the proximity of the vortex to the arc. However, at positive rotation rate (+0.15), compared to the straight sting configuration, the vortex core position appears to be influenced (perhaps leading to earlier bursting) by the arc. This effect was even more pronounced in tests with the B model.

Top-mounted sting with faired arc

The next comparisons are to evaluate the effects of a top-mounted sting, in the presence of the faired arc. Comparing Fig 4.22a to Fig 4.23a (non-rotating cases), there appears to be little, if any, effect of the top-mounted sting compared to the base-mounted sting. The forebody vortices burst in the about the same longitudinal location, which happens to be in the location of the top-mounted sting. At ωb/2V = +/-0.10 the upwind vortex appears to burst further forward due to the presence of the top-mounted sting. It should be noted, as mentioned before, that these pictures are one instant in time during the rotation and the location of the vortex positions and burst points fluctuate. On the whole, there is a significant influence of the top-mounted sting compared to the base-mounted sting. The top-mounted sting is well ahead of where the vortex would normally burst without the presence of the sting. This, undoubtedly, has an influence on the aerodynamic forces imparted to the model.

DRA 40° crank arc and base-mounted sting

The following comparison will evaluate the effects of a different arc (an approximation to DRA's 40° crank configuration vs AerMacchi's) using the same base-mounted sting. By comparing Fig 4.24a to Fig 4.22a (zero rotation rate) there is virtually no difference in the effects of these two arc geometries on the vortex flow field. At ωb/2V = +/-0.10 (Fig 4.24b and Fig 4.22b) there is a difference in the trajectory of the upwind forebody vortex. For the DRA arc (Fig 4.24b) the vortex stays well above the vertical tail, while, with the AerMacchi arc, the trajectory bends towards the vertical tail. As seen earlier, the effect of the AerMacchi arc was minimal compared to the straight base-mounted sting, which should have the least influence. It appears, therefore, that the DRA arc has more of a detrimental effect than the AerMacchi arc. The DRA arc is thicker, but slightly further behind the model. At higher a rotation rate (+/-0.15) a comparison of Figs 4.24c and Fig 4.22c shows that the differences are minimal, although observing the respective flow fields over the whole rotation cycle reveals that the vortex core location fluctuates in both cases and occasionally is in close proximity to the both arcs, usually causing an earlier breakdown in the vortex structure. Overall, it is difficult to state categorically that one arc configuration has more of an influence than the other. Any geometry that provides an obstruction to the vortex core at certain angles of attack and rotation rates will have an influence on the vortex structure, and, consequently, on the model forces.

4.3.3 Conclusions from Water Tunnel Tests

As a result of these flow visualization experiments, the differences in the wind tunnel data observed for the model without strakes from different rotary rigs are now better understood. It is certainly clear that the presence of the sting and arc can have an effect on the forebody vortices, particularly on burst location, which in turn affects the forces and moments. The degree of interference is very dependent upon the particular test condition, particularly the rotation rate and angle of attack. The critical factor appears to be whether the combination of angle of attack and rotation rate produces a vortex from the windward side of the forebody that is coherent for a sufficient distance downstream to allow it to come into proximity of the support system, especially the typical arc used to provide angle of attack changes. It is still not a certainty that, if the forebody vortex is well above the vertical tail but bursts prematurely (compared to the case with no interference), there is a significant effect on the body forces. Obviously, the closer the vortex is to the model, the more influence an alteration will have.

It is also revealing that the effect of adding the forebody strakes was not only to stabilize the forebody vortex pattern but also to strengthen the vortices, causing them to burst well upstream of the sting and arc components and minimizing the effect of the hardware on the vortex structure. The most troublesome component appears to be the top-mounted sting. If there is a means of reaching the desired angles of attack without resorting to a top-mounted sting, at least in the $\alpha = 40°$ to 50° range, one should strive for a rear-mounted sting configuration. It is also rather important, particularly for configurations with forebody vortices which remain coherent for some distance beyond the model, to maximize the distance between the model and the support hardware. For the most part, the rigs that have been tested provide reliable rotary-balance data. When changing mounting configurations on any rig it is desirable to have an overlap in angle of attack of at least 10°.

4.4 REFERENCES

1. Malcolm, G. , Lewis, L. and Ng, T., "Development of Non-Conventional Control Methods for High-Angle-of-Attack Flight Using Vortex Manipulation", USAF WL-TR-91-3041, June 1991.

2. Malcolm, G., "Aerodynamic Control of Fighter Aircraft by Manipulation of Forebody Vortices", AGARD CP-497, Paper No. 15, November 1991.

3. Malcolm, G., "Forebody Vortex Control", Progress in Aerospace Sciences, Pergamon Press, Vol. 28, pp. 171-234, 1991.

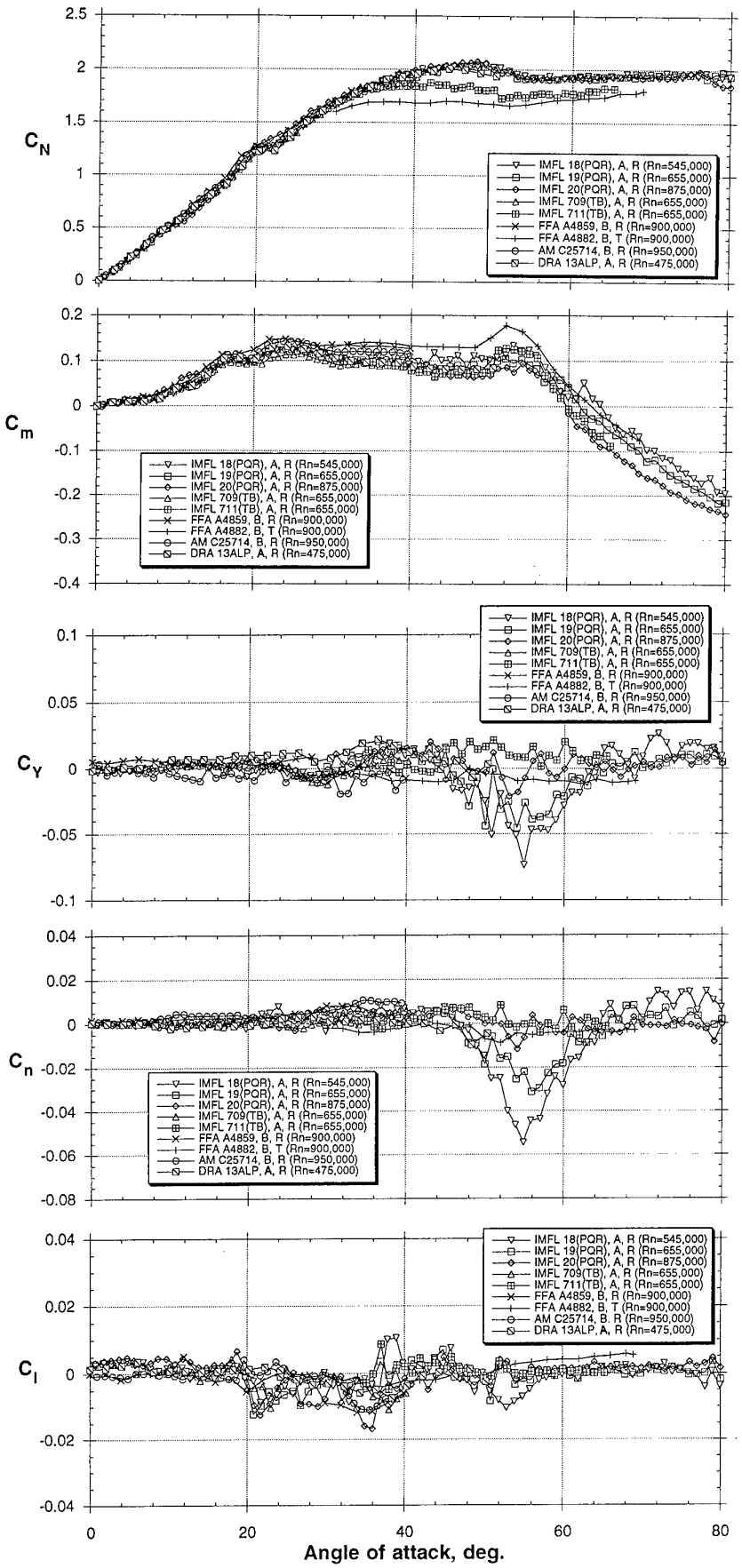

Figure 4.1 - Static data for complete configuration, BWLVHST

(a) Part 1 - Reynolds numbers from 0.475 to 0.900 x 10^6

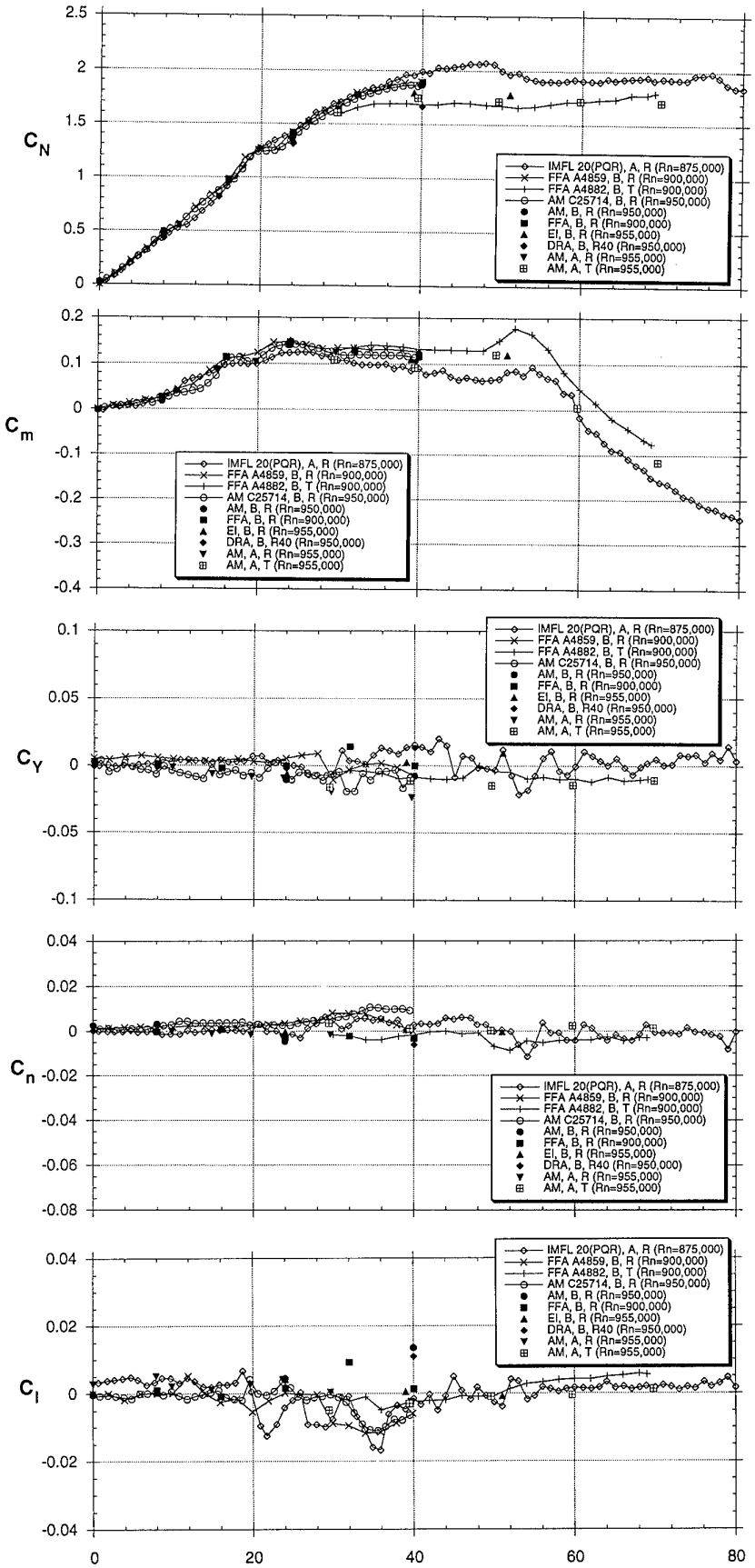

Figure 4.1 - Concluded

(b) Part 2 - Reynolds numbers from 0.875 to 0.955 x 10^6

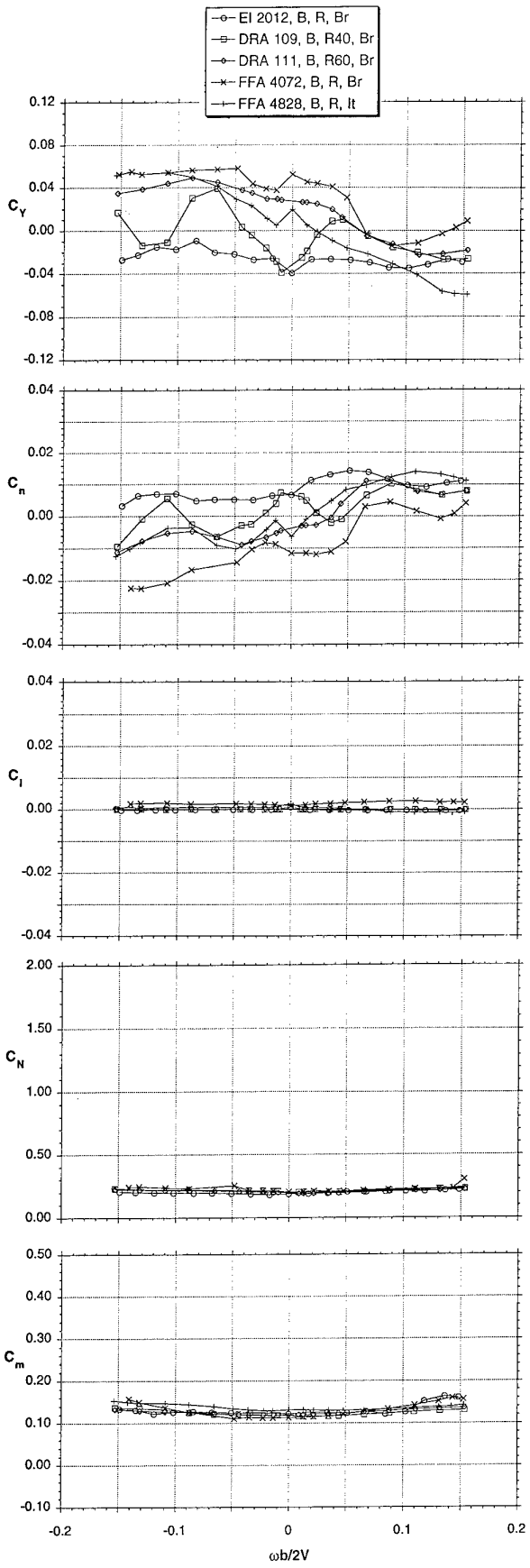

Figure 4.2 - Rotary-balance tests, BST, 40° AOA

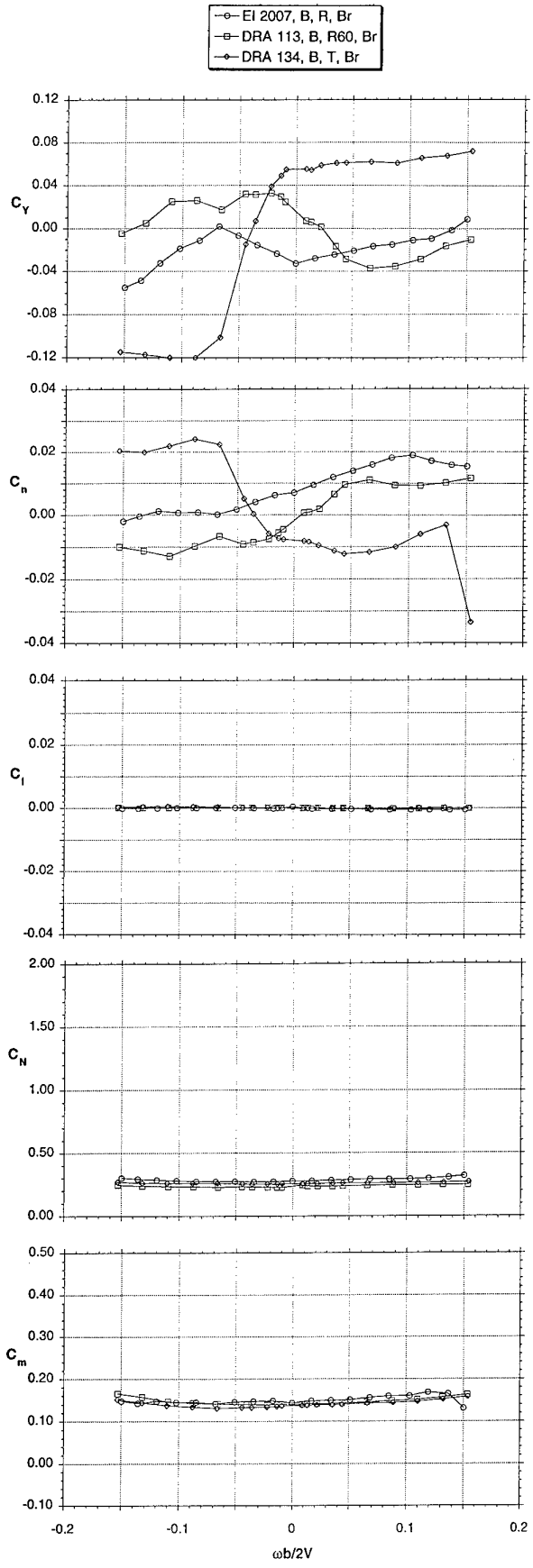

Figure 4.3 - Rotary-balance tests, BST, 50° AOA

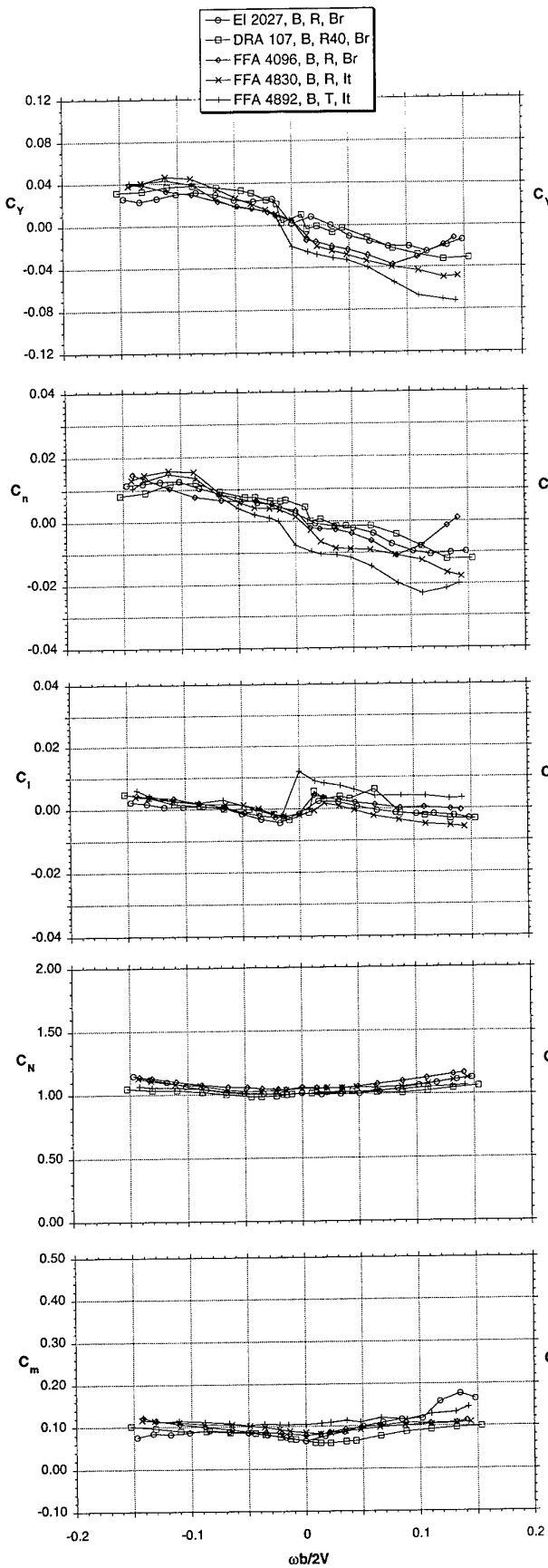

Figure 4.4 - Rotary-balance tests, BWST, 40° AOA

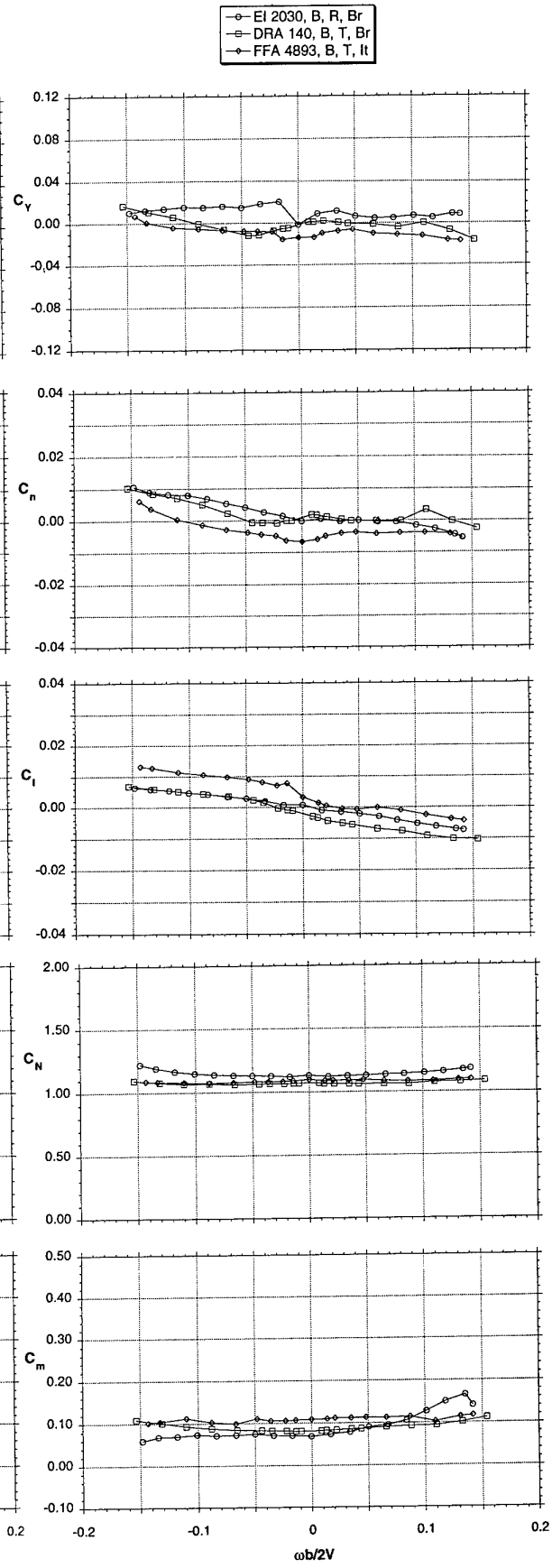

Figure 4.5 - Rotary-balance tests, BWST, 50° AOA

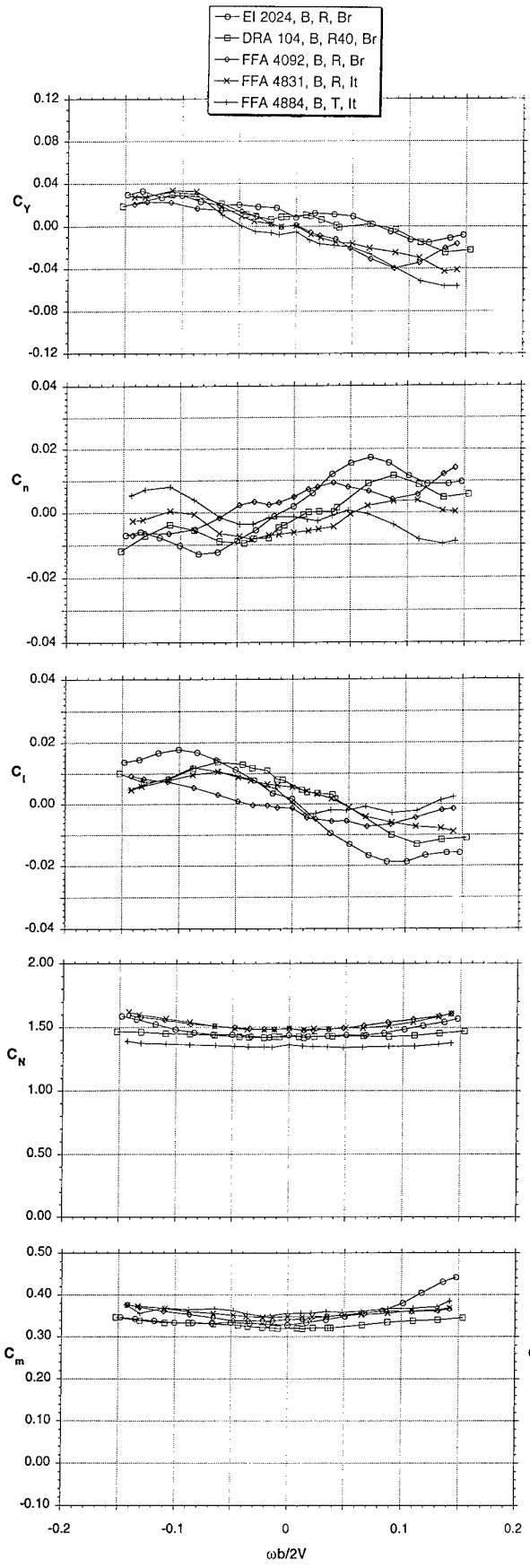

Figure 4.6 - Rotary-balance tests, BWLST, 40° AOA

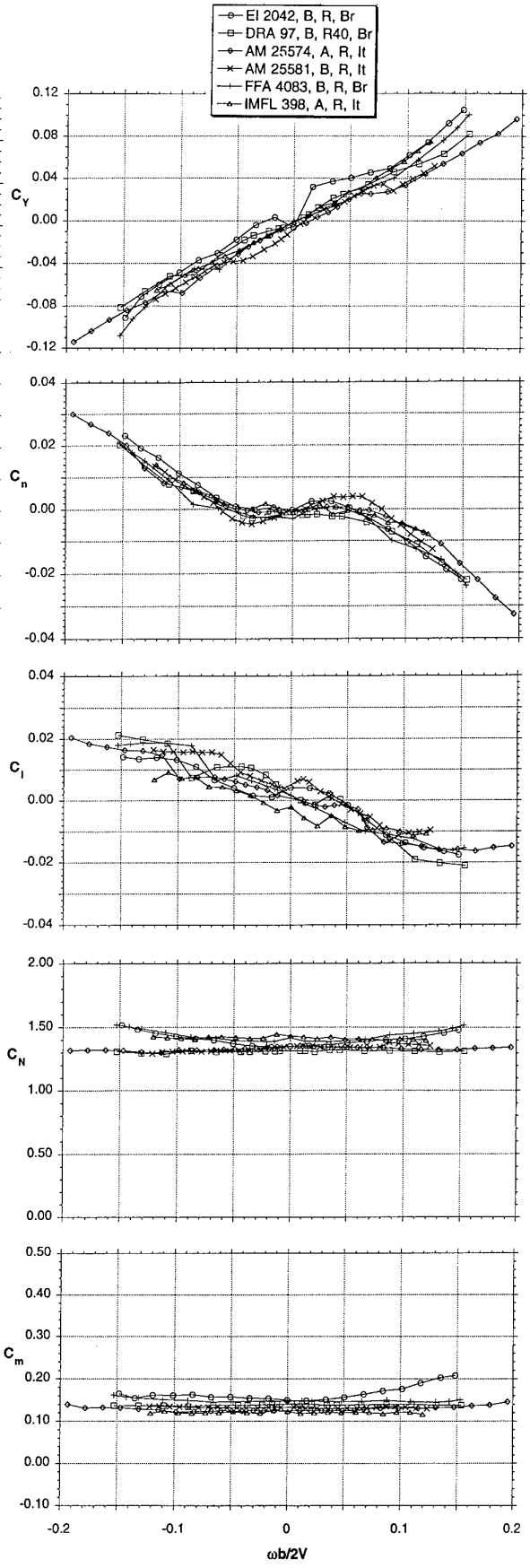

Figure 4.7 - Rotary-balance tests, BWLVHST, 24° AOA

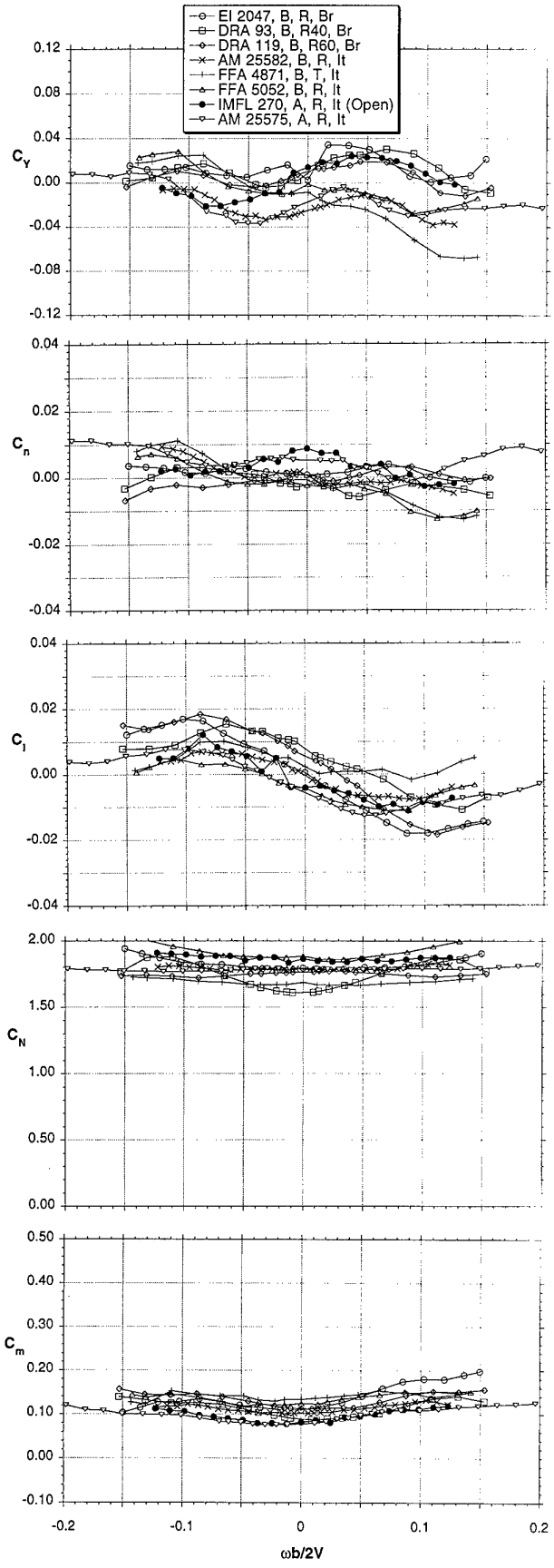

Figure 4.8 - Rotary-balance tests, BWLVHST, 40° AOA

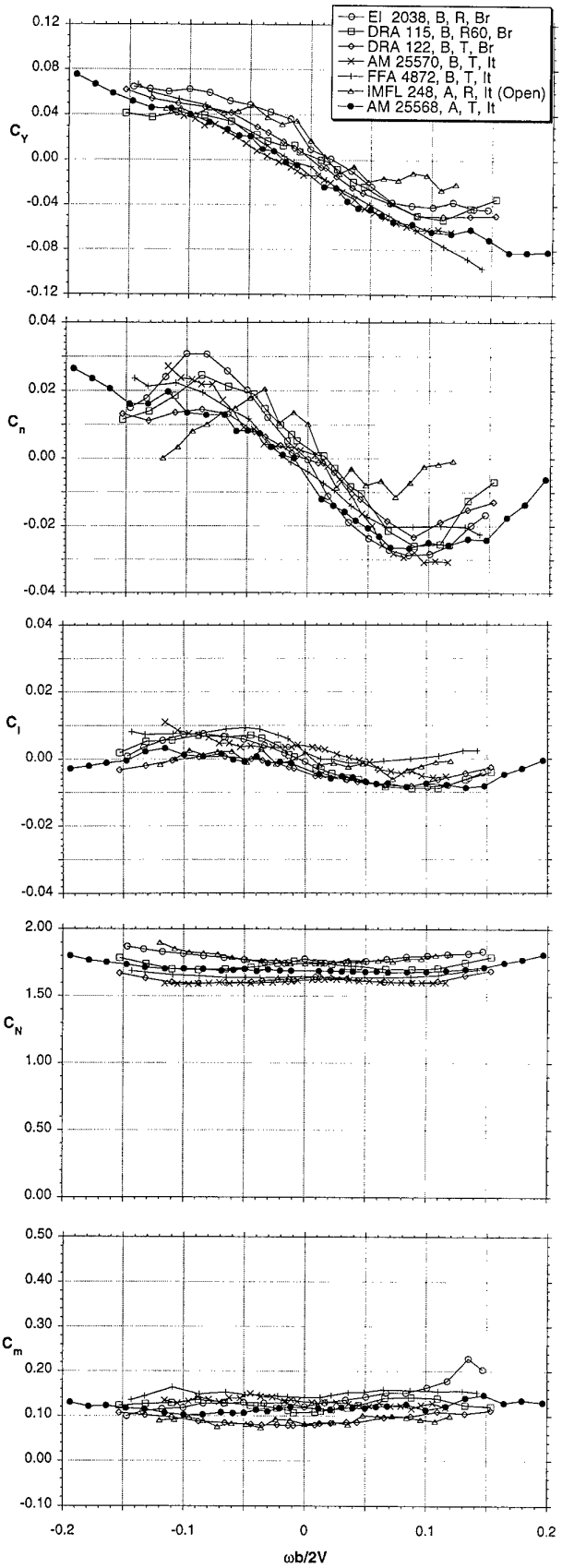

Figure 4.9 - Rotary-balance tests, BWLVHST, 50° AOA

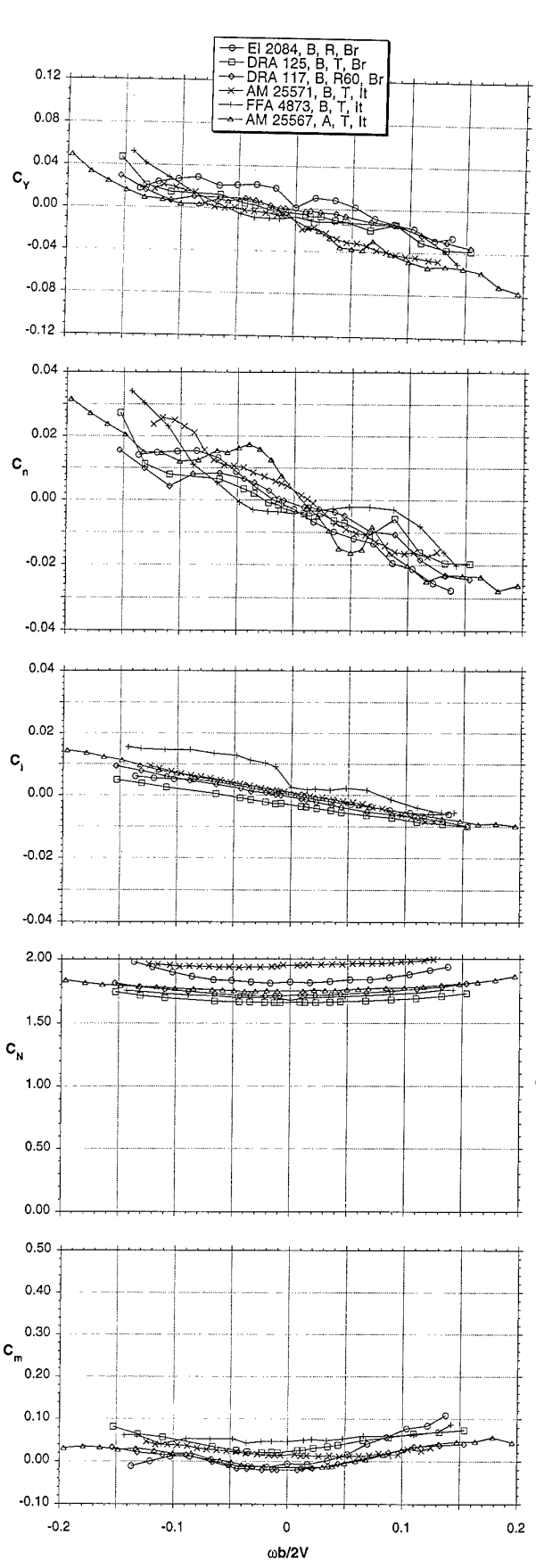

Figure 4.10 - Rotary-balance tests, BWLVHST, 60° AOA

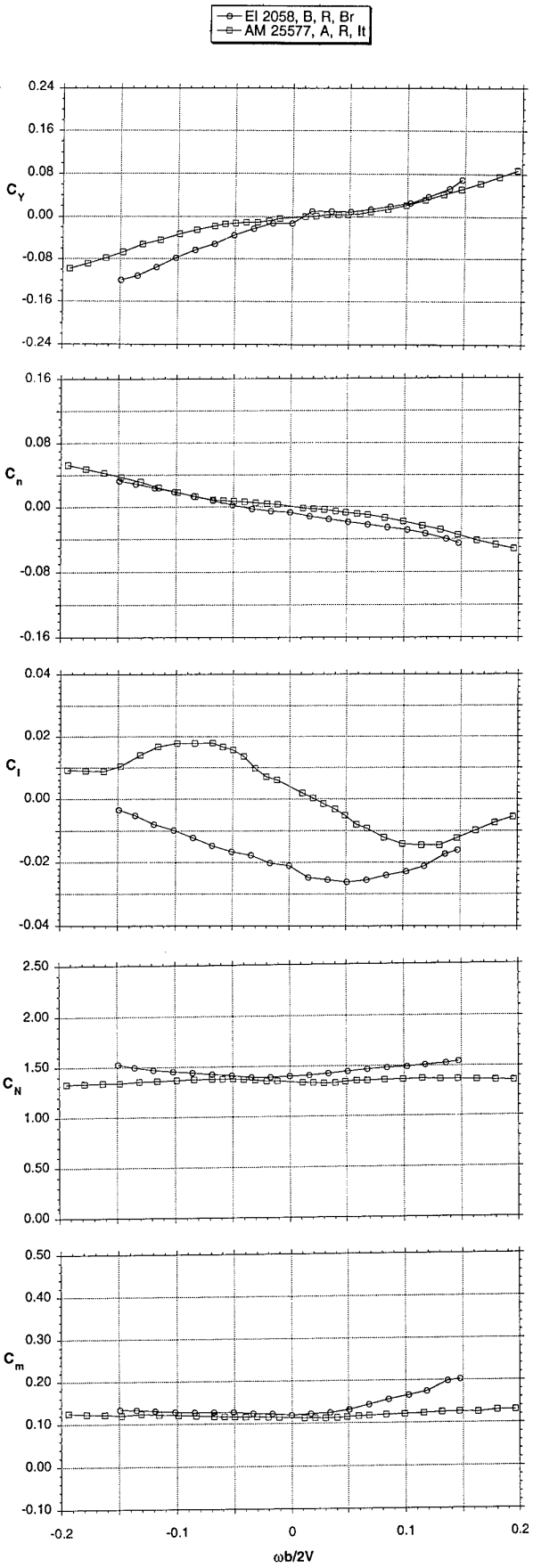

Figure 4.11 - Rotary-balance tests, BWLVHT, 24° AOA

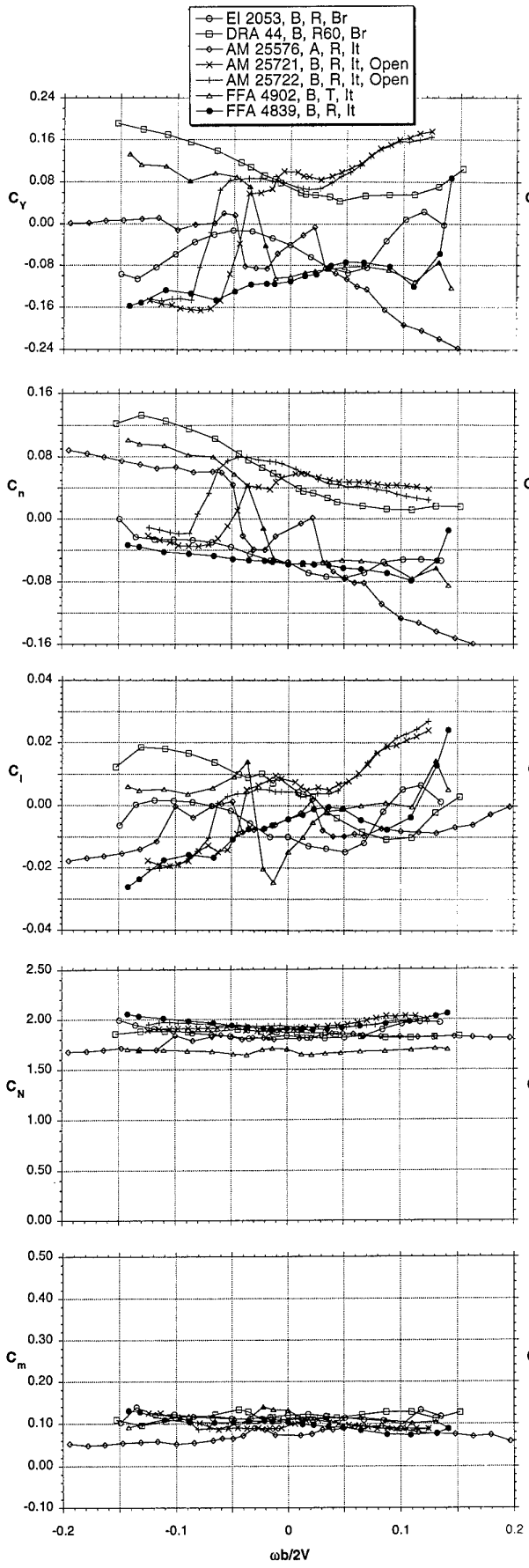

Figure 4.12 - Rotary-balance tests, BWLVHT, 40° AOA

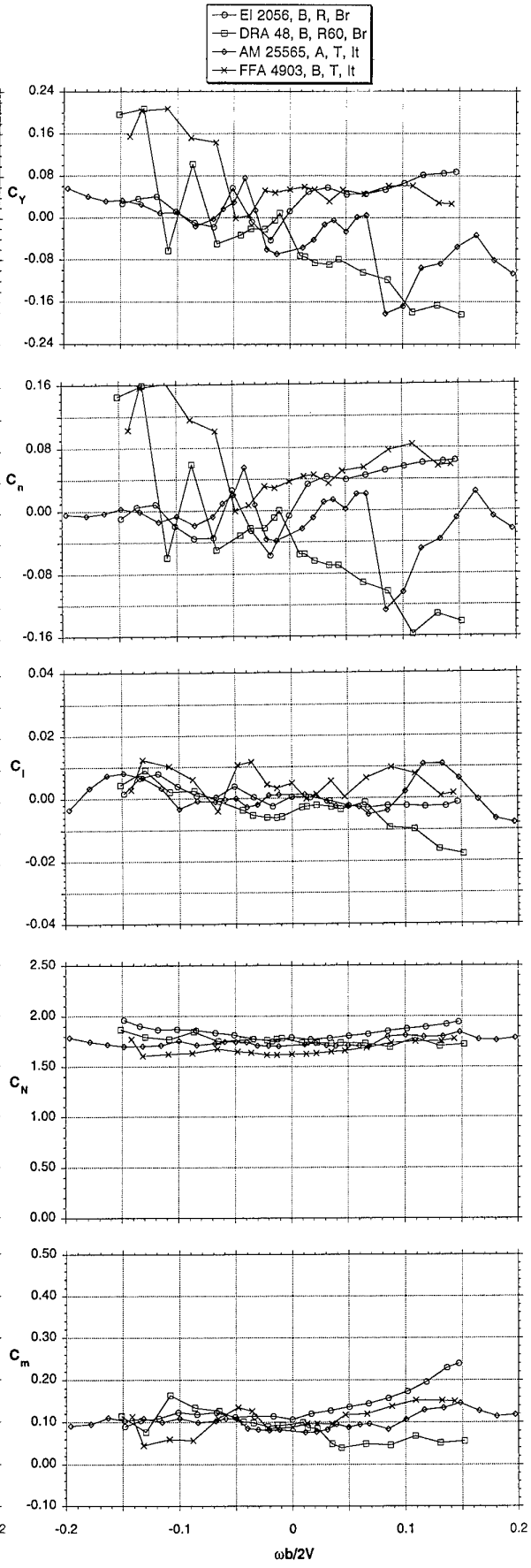

Figure 4.13 - Rotary-balance tests, BWLVHT, 50° AOA

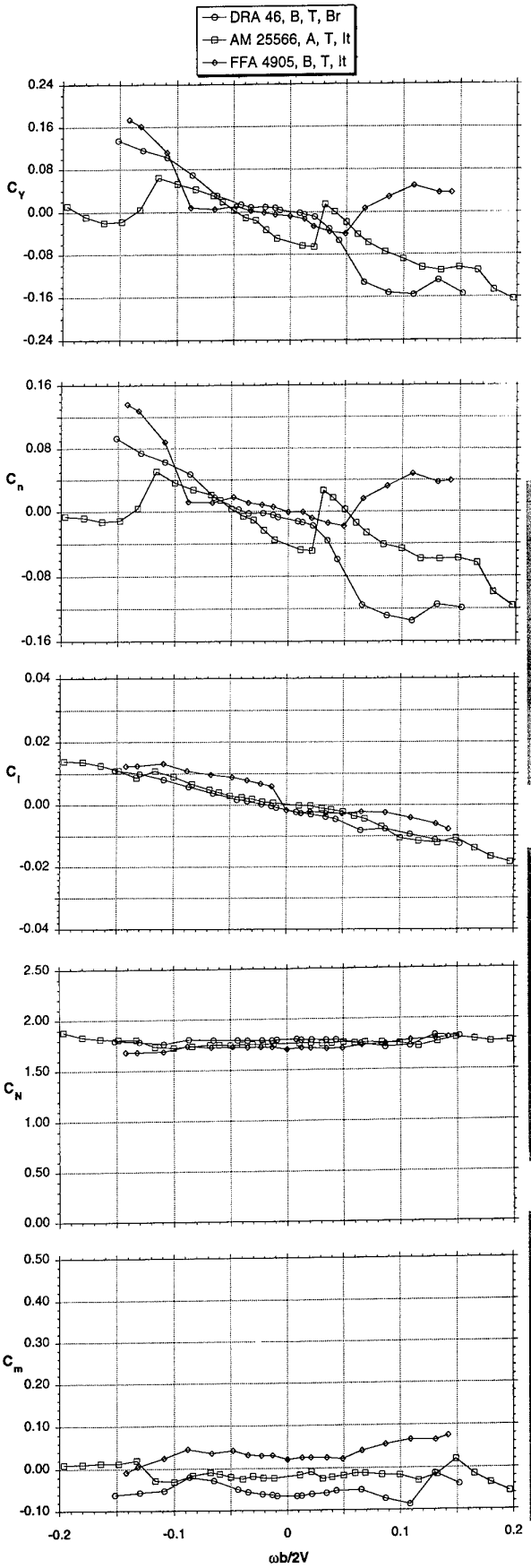

Figure 4.14 - Rotary-balance tests, BWLVHT, 60° AOA

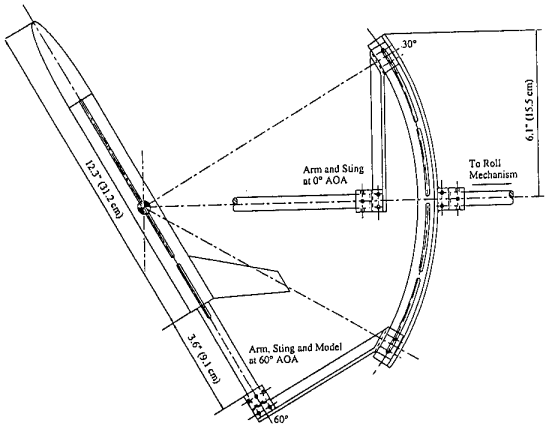

Figure 4.15 - Eidetics Water Tunnel Rotary-Balance Rig

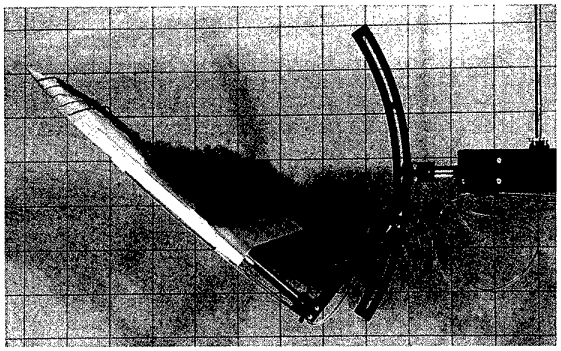

Static

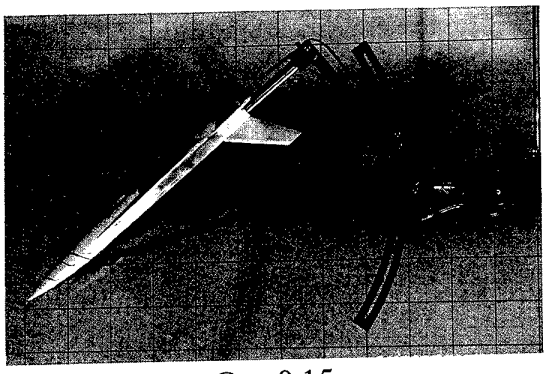

$\Omega = 0.15$

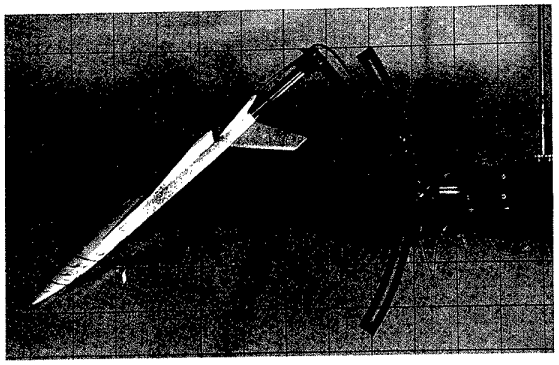

$\Omega = -0.15$

Figure 4.16 - Flow visualization photos, rotary-balance tests, Eidetics water tunnel, 40° AOA, strakes-off (BWLVH)

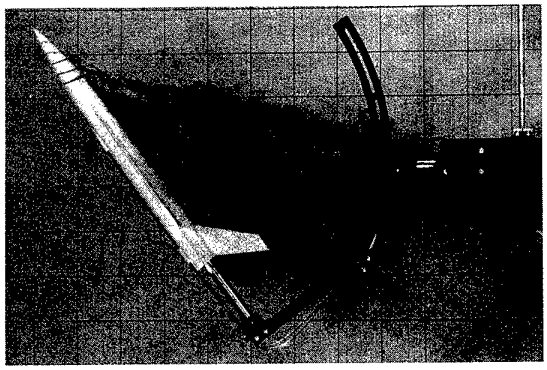

Static

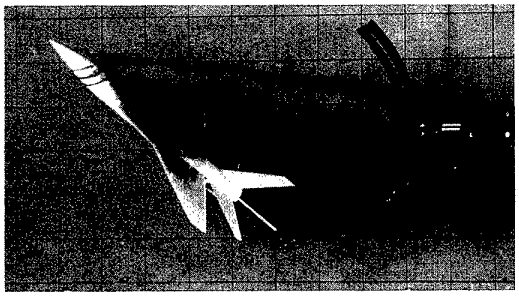

$\Omega = 0.15$

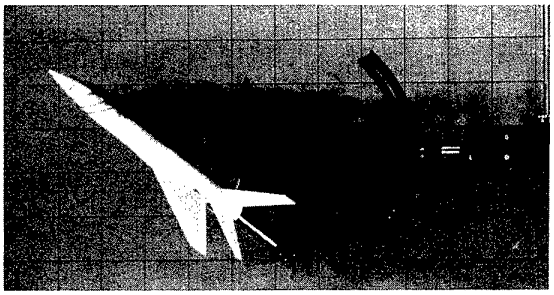

$\Omega = -0.15$

(a) Strakes-off, BWLVH

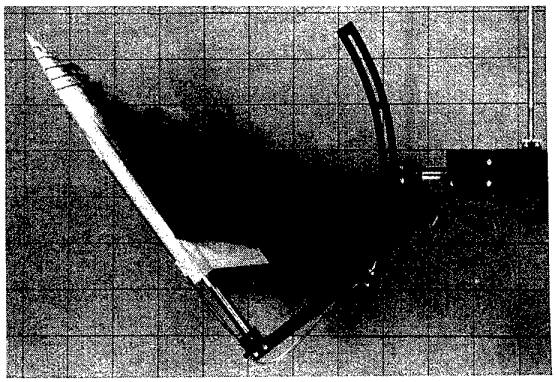

Static

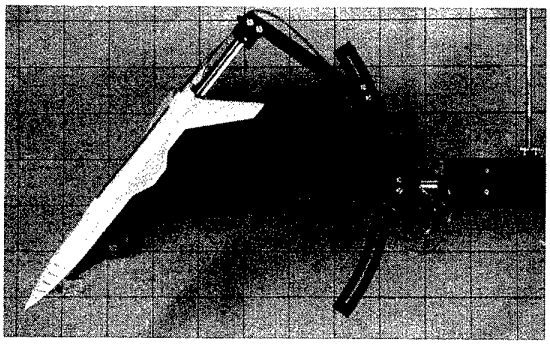

$\Omega = 0.15$

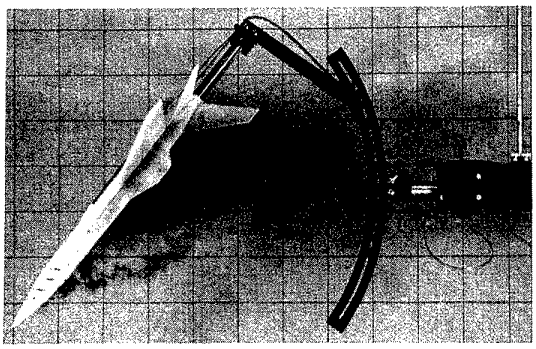

$\Omega = -0.15$

(b) Strakes-on, BWLVHS

Figure 4.17 - Flow visualization photos, rotary-balance tests, Eidetics water tunnel, 50° AOA,

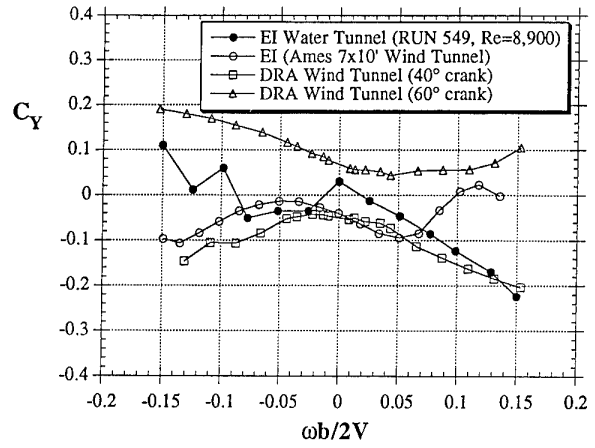

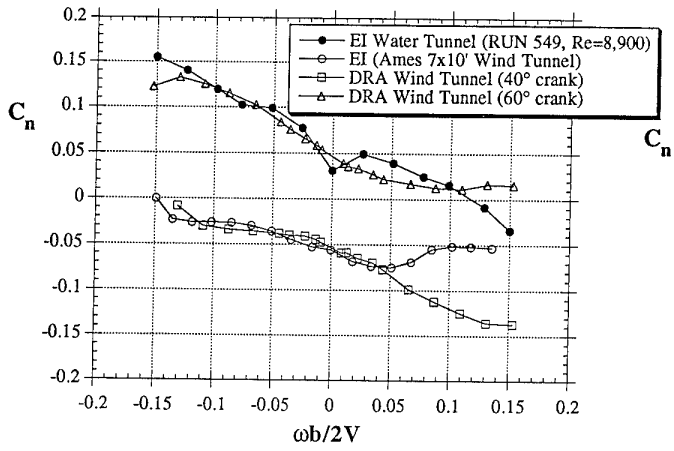

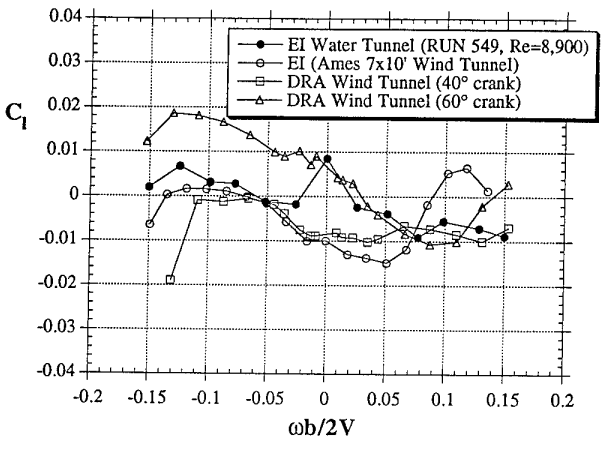

Figure 4.18 - Water/wind tunnel test comparisons, BWLVH, (strakes off), 40° AOA

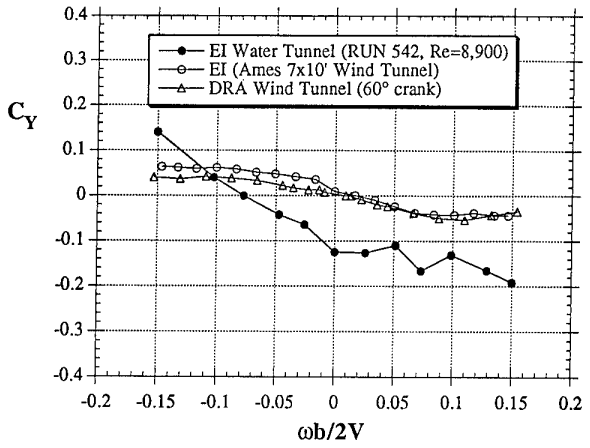

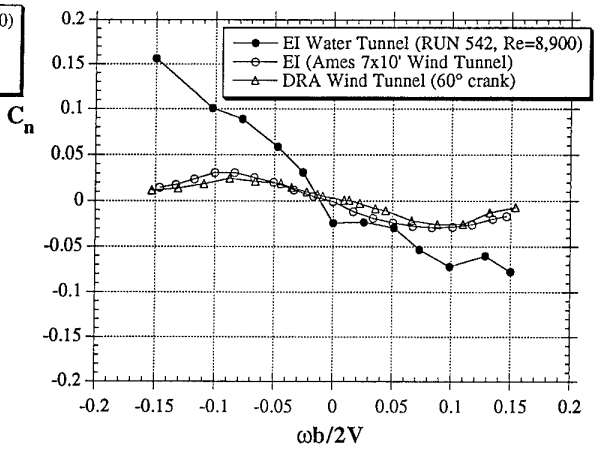

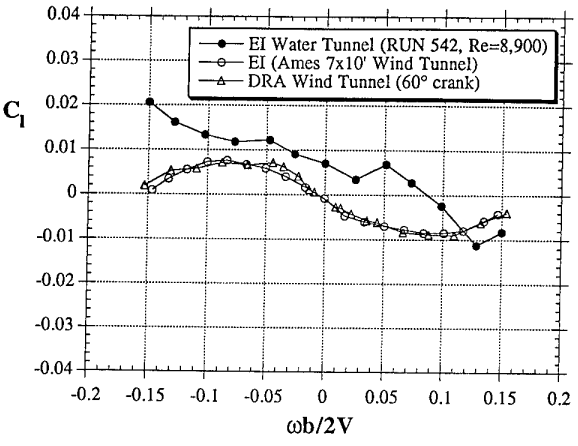

Figure 4.19 - Water/wind tunnel test comparisons, BWLVHS (strakes on), 50° AOA

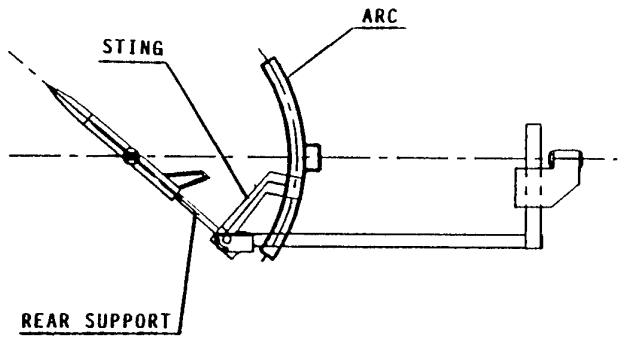

Figure 4.20(a) - AerMacchi water tunnel rotary-rig

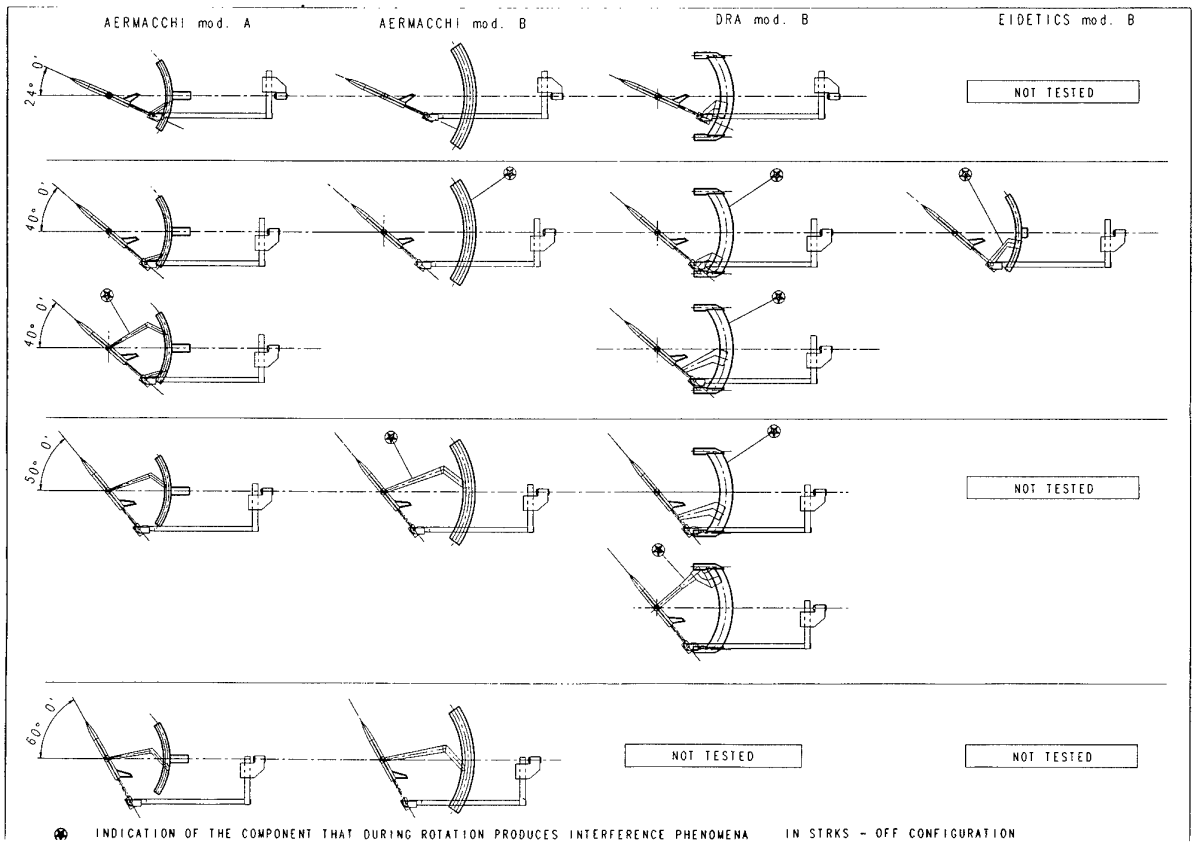

Figure 4.20(b) - Rotary-rig configurations tested in AerMacchi water tunnel

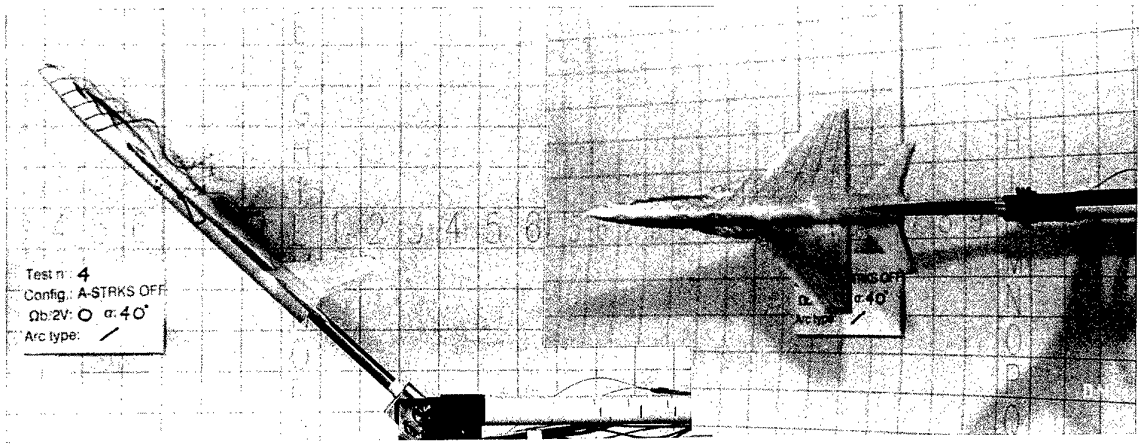

(a) ωb/2V = 0

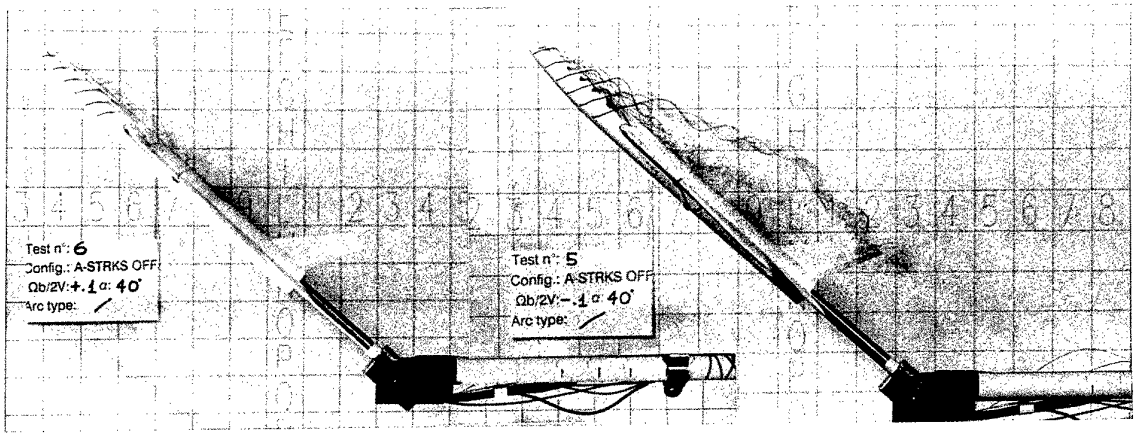

(b) ωb/2V = +/- 0.10

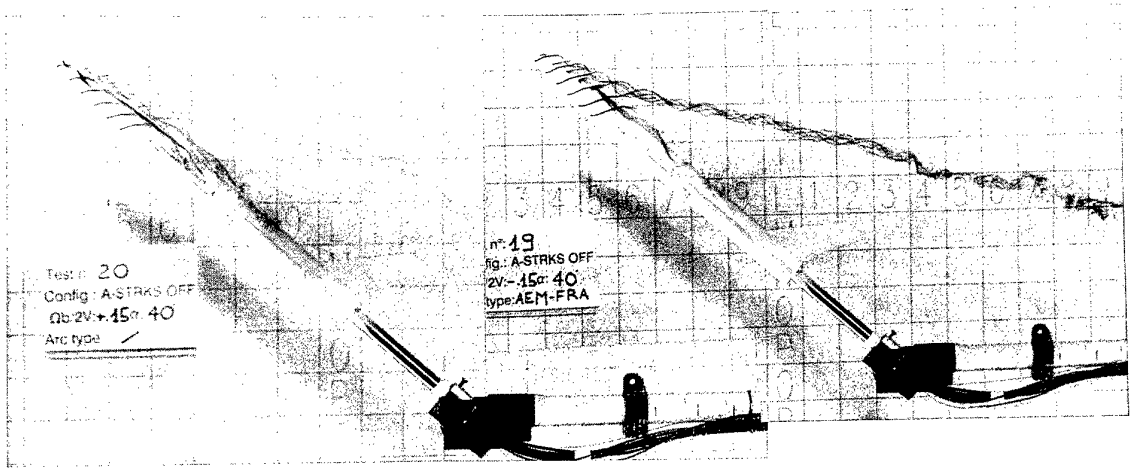

(c) ωb/2V = +/- 0.15

Figure 4.21 - AerMacchi water tunnel tests, straight sting, BWLHVT (no strakes), 40° AOA

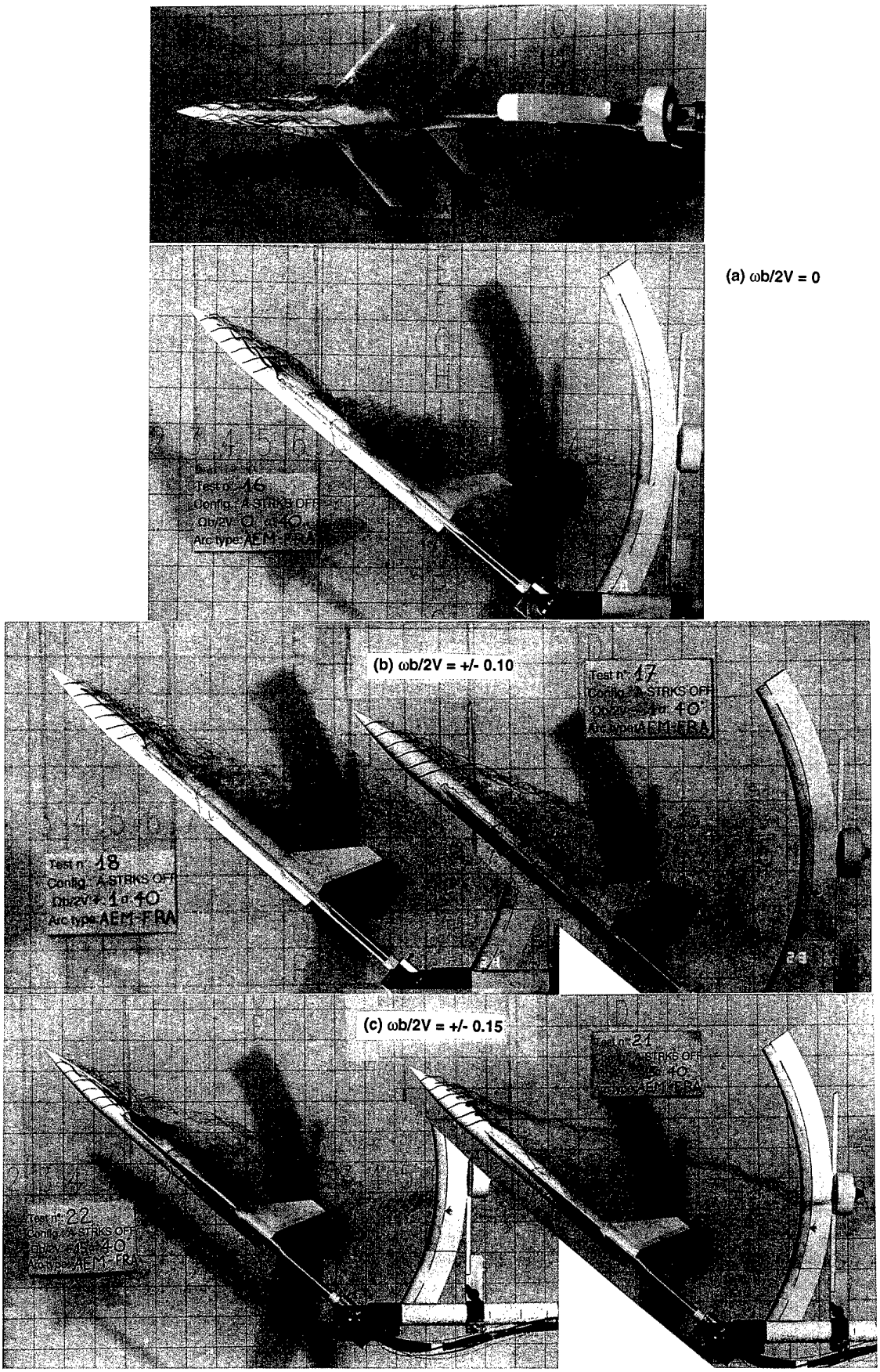

Figure 4.22 - AerMacchi water tunnel tests, base-mounted sting with faired arc, BWLHVT (no strakes), 40° AOA

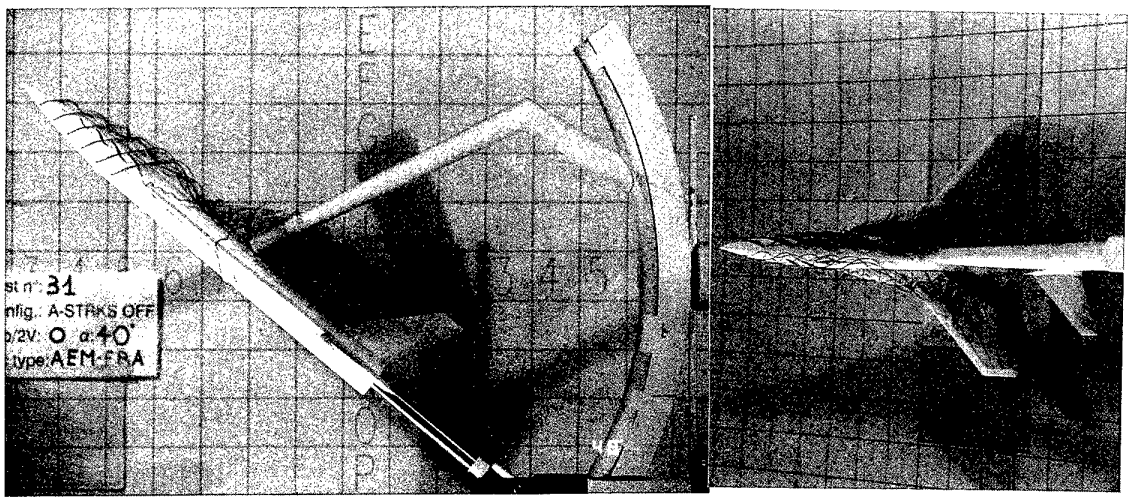

(a) ωb/2V = 0

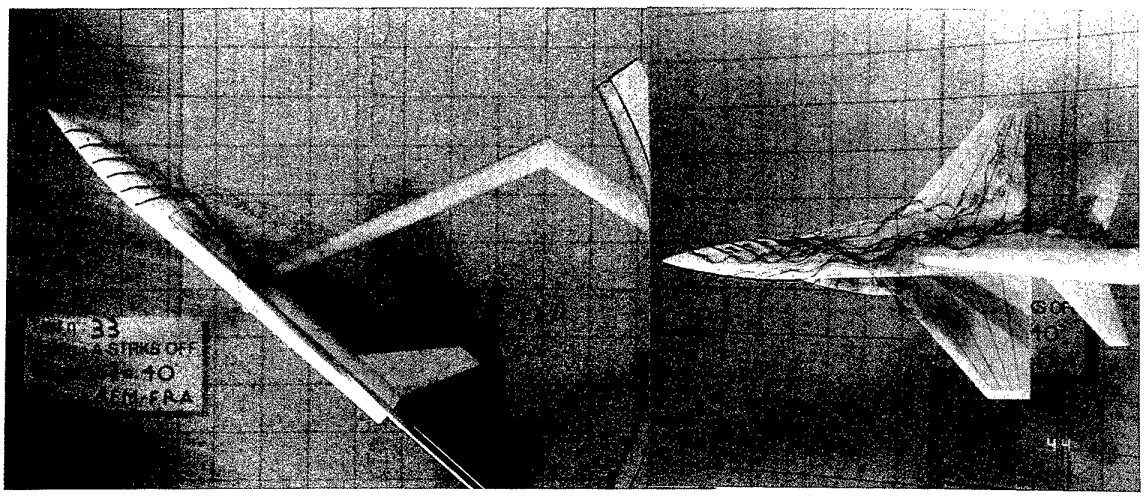

(b) ωb/2V = +0.10

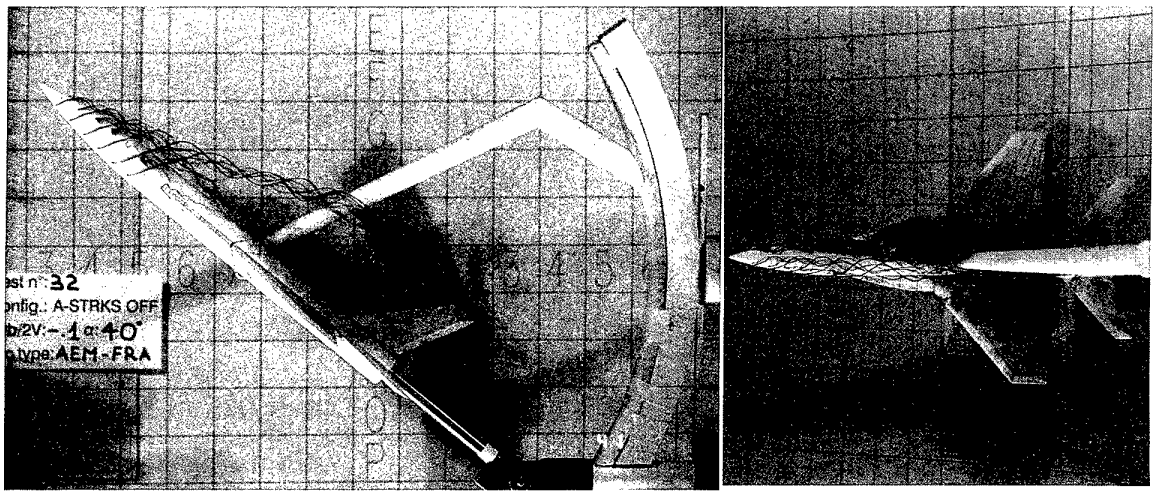

(c) ωb/2V = -0.10

Figure 4.23 - AerMacchi water tunnel tests, top-mounted sting with faired arc, BWLHVT (no strakes), 40° AOA

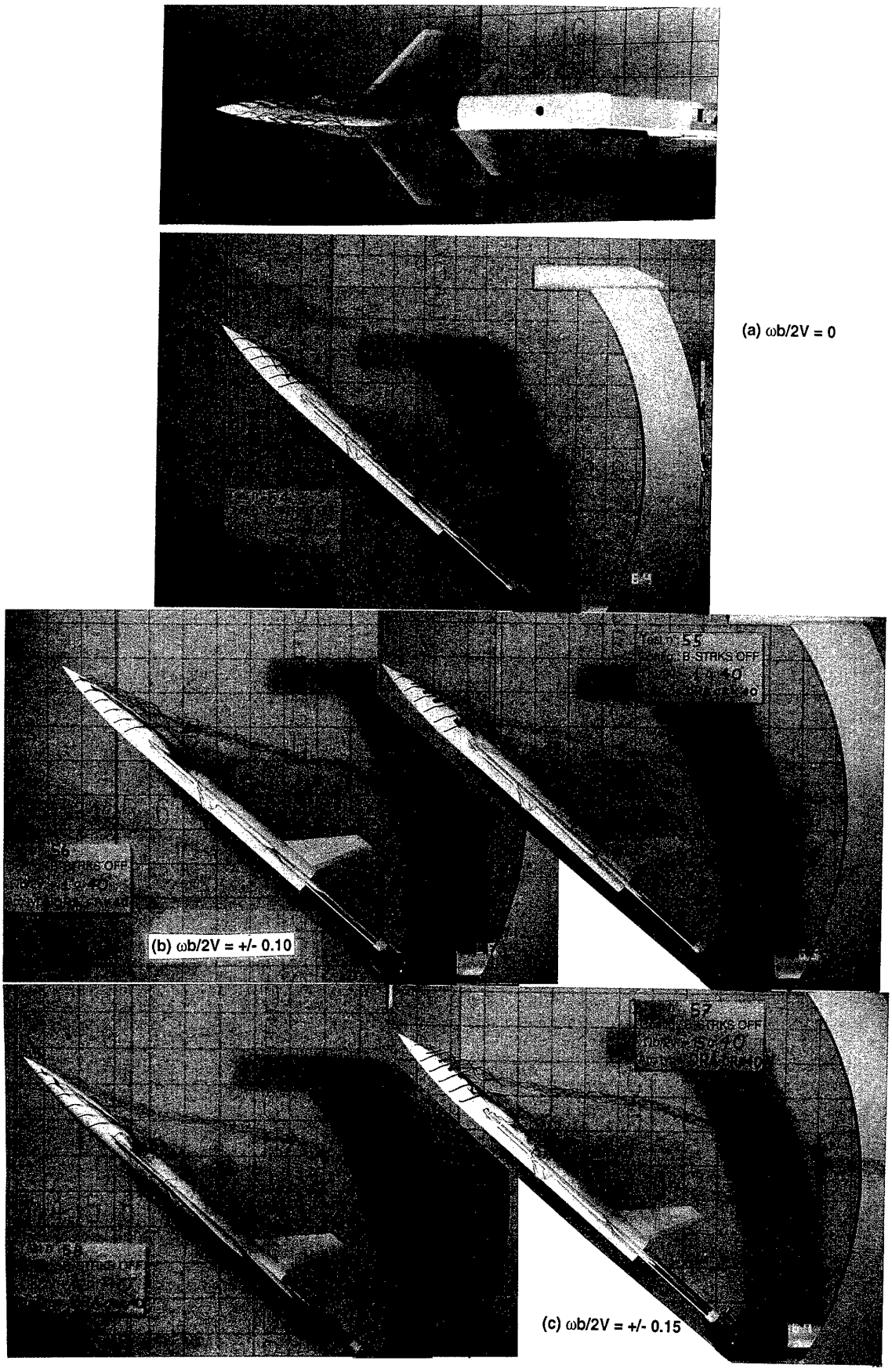

Figure 4.24 - AerMacchi water tunnel tests, base-mounted sting, DRA 40° crank and arc, BWLHVT (no strakes), 40° AOA

CHAPTER 5

OSCILLATORY TEST RESULTS

5.0 INTRODUCTION

The contribution of four organizations to the oscillatory test program allowed a fairly comprehensive coverage.
The test had several objectives:

- measure the derivatives using small-amplitude oscillatory rigs;
- investigate often neglected parameters such as angle of sideslip, test frequency and amplitude;
- measure cross derivatives and separate $\dot{\alpha}$ and $\dot{\beta}$ derivatives;
- compare measurements obtained from different rigs and wind tunnels and with different techniques;
- obtain force and moment data from large amplitude motion tests such as large amplitude longitudinal oscillations and ramp motions from IMFL "PQR" rig and large amplitude mixed longitudinal and lateral oscillations from oscillatory coning tests on IMFL "TourneBroche".

The whole set of results can be used in linearized mathematical models for the prediction of motion and allows a comparison with predictions using advanced non-linear models and data from large-amplitude tests.

Conventional oscillatory tests were performed at DRA, IAR and TPI, while ONERA-IMFL contributed both oscillatory and large amplitude tests. The general characteristics of the rigs, a description of measurement techniques and a presentation of test programs can be found in Chapter 2. In the present chapter an overview of test results will be made, highlighting specific effects investigated by each organization. A more detailed presentation will be given of results obtained for large amplitude and oscillatory coning tests owing to their unusual character.

All aerodynamic coefficients presented in the figures are referred to body axes according to the definition shown in Fig 5.1. A complete list of test runs as well as references to original test reports are reported in Appendix 1.

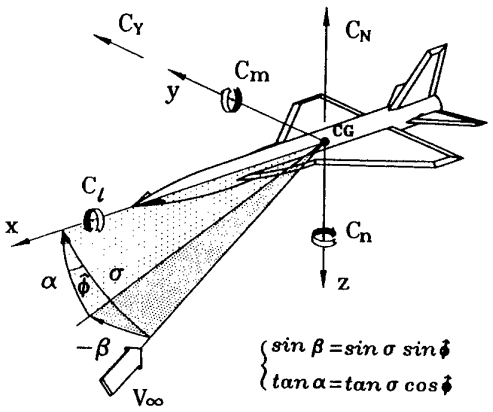

Fig. 5.1 The body axes reference system

5.1 DRA OSCILLATORY TESTS

5.1.1 Effect of Nose Strakes and Longitudinal Grit Strips on Body Alone

The effect of nose strakes and grit strips on static coefficients C_N, C_m, C_Y and C_n is shown in Fig 5.2. For $\alpha < 20°$, differences between the three configurations are negligible. For $\alpha > 20°$, there is a greater increase in C_N and nose-up C_m with increasing α for the clean forebody (without nose strakes and grit strips). For $\alpha > 30°$ there are also appreciably greater sideforces and yawing moments without grit or strakes. The presence of grit strips alone suppresses these asymmetric forces to some degree but adding the nose strakes reduces them to insignificant levels.

These data conform to classical behaviour of high fineness ratio forebodies when angle of attack is increased. For the body without grit and strakes asymmetric nose vortices start to develop in the 20° to 30° AOA range, increasing differential pressure on the sides of the forebody and the overall normal force and nose-up pitching moment. Sideforce due to asymmetric vortices reaches a peak at $\alpha \approx 40°$ but C_n continues to increase until $\alpha \approx 47°$, indicating a forward shift in the sideforce centre of pressure as angle of attack is increased beyond 40°. The purpose of the grit strips is to discourage asymmetric transition in the crossflow; however this has not totally eliminated the sideforce. Nose strakes are effective in fixing a symmetric forebody vortex formation at the apex and the grit strips maintain a symmetric flow for the length of the forebody. It is also apparent that forcing symmetric separation decreases the overall normal force and pitching moment.

5.1.2 Effect of Nose Strakes and Longitudinal Grit Strips on Complete Configuration

The combined effect of nose strakes and grit strips on C_N, C_m, C_Y and C_n for the complete configuration (BWLHV) in static

conditions is shown in Fig 5.3. Normal force and nose-up pitching moment are again reduced at high angles of attack when the model is tested with nose strakes and grit strips. For $\alpha > 35°$, the nose strakes and grit strips reduce the large sideforces and yawing moments to virtually zero, indicating that, as for the body alone, these devices are effective in suppressing the formation of asymmetric forebody vortices at high angle of attack. It is likely that it is the presence of the LEX which delays their formation to a higher angle of attack compared with the body alone.

Results from pitch and plunge tests are shown in Fig 5.4. The combined derivatives $(C_{mq} + C_{m\dot{\alpha}})$ and $(C_{Nq} + C_{N\dot{\alpha}})$ are obtained from the pitching mode and the components due to $\dot{\alpha}$, $C_{m\dot{\alpha}}$ and $C_{N\dot{\alpha}}$ are measured in the plunging mode. The model is damped in pitch at all angles of attack but the damping is close to zero for $\alpha < 5°$. Differences in the variation of both $(C_{mq} + C_{m\dot{\alpha}})$ and $C_{m\dot{\alpha}}$ due to nose strakes and grit strips are small. Examination of the plots suggests that most of the reversals in the variation with α are due to $C_{m\dot{\alpha}}$, including the large reversals at $\alpha \simeq 40°$. The variation of $(C_{Nq} + C_{N\dot{\alpha}})$ and $C_{N\dot{\alpha}}$ is similar with and without strakes and grit strips except that the large changes in magnitude in the region of $\alpha = 20°$ occur at a slightly lower angle of attack with strakes and grit strips. It is apparent that the large changes are due to the variation in the $\dot{\alpha}$ component.

Combined lateral derivatives measured in the yawing and rolling modes are shown in Fig 5.5. For $\alpha < 15°$ there is little difference in the damping-in-yaw derivative $(C_{nr} - C_{n\dot{\beta}} \cos \alpha)$. In the range $20° < \alpha < 33°$ the derivative is positive for tests with strakes and grit strips, whereas without these devices there is damping throughout the test AOA range. From the measurement of $C_{n\dot{\beta}}$ in the swaying mode, shown later in Fig 5.7, this positive trend is mostly due to the contribution from the $C_{n\dot{\beta}}$ component. It is therefore likely that the differences are due to the effect of the nose strakes and grit strips on the behaviour of the forebody vortices for varying β. There are also differences in the other combined derivatives due to nose strakes and grit strips but these are less significant.

5.1.3. Effect of LEX

Results from pitch and plunge tests with and without the LEX are shown in Fig 5.6 for the complete configuration with forebody strakes and grit strips.

Although there are some differences in the variation of $(C_{mq} + C_{m\dot{\alpha}})$ and $C_{m\dot{\alpha}}$ with and without the LEX the general trend in the variation with angle of attack is similar. For $\alpha > 30°$ the pitch damping with the LEX fitted is reduced.

Effects of the LEX on the normal force derivatives $(C_{Nq} + C_{N\dot{\alpha}})$ and $C_{N\dot{\alpha}}$ are more pronounced. In the AOA range $6° < \alpha < 34°$ both derivatives are more positive with the LEX off except where there is a 'spike' in the LEX-on characteristic at $\alpha \simeq 20°$. It is apparent that for $\alpha > 5°$ it is the $\dot{\alpha}$ component of $(C_{Nq} + C_{N\dot{\alpha}})$ which predominates and contributes most of the variation in the combined derivative. These results suggest that the LEX has a marked effect on the chordwise lag in normal force on the model. A discontinuity in the LEX-on characteristics at $\alpha \simeq 20°$ may be due to LEX vortex breakdown or a LEX/wing vortex interaction effect.

Results from yaw, sway and roll modes are shown in Fig 5.7. Differences in the yawing moment derivatives due to the LEX are most noticeable in the AOA range $20° < \alpha < 35°$ where the β component measured in the sway mode is the main contributor. The main contribution to $C_{n\dot{\beta}}$ is probably the lag of sidewash at the fin and the results suggest that the wake from the LEX modifies this sidewash lag. Differences in the rolling moment due to the LEX are also evident and here too the main contribution at high angle of attack is from the $\dot{\beta}$ component, $C_{l\dot{\beta}}$. In this case the likely cause is the lag in spanwise development of normal force which is affected by the presence of the LEX.

5.1.4 Effect of Oscillation Frequency

Results from pitch and plunge tests at two frequencies, $\Omega_c = 0.08$ and 0.16, are shown in Fig 5.8. Most of the effect of frequency on $(C_{mq} + C_{m\dot{\alpha}})$ and $C_{m\dot{\alpha}}$ is likely to originate from a downwash lag effect at the tail but, taking account of the scatter shown in repeat measurements of $C_{m\dot{\alpha}}$ at high α, it appears that the effect on pitching moment is small. However, differences in $(C_{Nq} + C_{N\dot{\alpha}})$ for $\alpha > 25°$ are appreciable and mostly due to the effect of frequency on the $C_{N\dot{\alpha}}$ component as indicated by the plunging mode measurement of this derivative. It is likely that with varying α, frequency has an effect on the chordwise lag in normal force on the forebody, LEX and wings, which is the main contributor to $C_{N\dot{\alpha}}$.

5.1.5 Repeatability of Data

In order to check repeatability of test data some test runs were repeated and an example of the results from two pitching mode tests is shown in Fig 5.9. In general, agreement between the two sets of data was good, including the spike in the variation of $(C_{Nq} + C_{N\dot{\alpha}})$ at $\alpha \simeq 20°$.

5.2 TPI OSCILLATORY TESTS

The TPI oscillatory rig was previously calibrated using the Standard Dynamics Model (SDM). Pitch, yaw and roll experiments were carried out and several comparisons with other reference results were performed[1-2]. The present experimental activity[3] was performed with the primary aim of obtaining an extended experimental set of data of WG16A model as representative of a highly maneuverable configuration using static and oscillatory wind tunnel measurement techniques. Furthermore, the analysis was concentrated on some aspects related with non-linear aerodynamics typically observed in the high AOA range, such as the effects of vortical asymmetries and vortex flow interactions. The accuracy of measurements and data repeatability were also evaluated.

5.2.1 Effect of Model Configuration

Model configuration has a significant effect on dynamic derivatives due to pitching. Longitudinal stability (Fig 5.10) is influenced by LEX removal and by the presence of forebody strakes. The first effect is due to the significant

interactions between lifting vortices, as confirmed by the static measurements. The second change is due to modification of aerodynamic asymmetries at high AOA, as a consequence of passive control of forebody flow separation due to the strakes. The effect of configuration on longitudinal pitch damping coefficients (Fig 5.11) is greater at higher angles of attack and is typically non-linear, possibly due to vortical flow lag effects on downwash at the tail.

The effect of forebody strakes and fixed transition on rolling moment derivatives due to roll is shown in Fig 5.12 and 5.13. With strakes and transition fixed, the roll damping is greatly reduced for $\alpha > 20°$, but this effect is not as apparent on the coefficient $C_{l_\beta} \sin \alpha$. Also, the positive unstable peak of the static lateral stability parameter at $35° < \alpha < 40°$ is smoothed.

5.2.2 Aerodynamic Cross-Coupling

Dynamic cross-coupling at high angle of attack is evident, both for the longitudinal and the lateral-directional derivatives (Fig 5.14 to 5.17). Yawing moment, rolling moment and side force coefficients due to pitch oscillation are negligible for lower angles of attack.

The non-linear coupling shown by the basic configuration is reduced to a negligible magnitude by adding forebody strakes. Similarly, limiting forebody vortex asymmetries minimizes the coupling of longitudinal components with roll motion, although both pitching moment and normal force damping derivatives are not negligible even for the straked configuration for $20° < \alpha < 30°$.

5.2.3 Effect of Sideslip

The symmetry of pitch damping derivatives with β in pitch is not verified at high α, due to support interference of the asymmetric strut. Data comparisons demonstrate that this effect is comparable with the measurement accuracy available in this AOA range. Roll derivatives are very dependent on angle of sideslip even for moderate incidence (Fig 5.18). This could be due to a sidewash effect on the vertical stabilizer and non-linear aerodynamic interactions due to forebody vortices.

5.2.4 Aerodynamic Stiffness Derivatives

The cross-coupling lateral and directional stiffness derivatives measured with both static and oscillatory techniques are presented in Figs 5.19 to 5.21. The comparisons prove that discrepancies exist between oscillatory results and static derivatives in the AOA range where the effects of asymmetries and separated flows are dominant.

5.2.5 Effect of Control Deflections

The longitudinal control derivatives C_{Z_δ} and C_{m_δ} were evaluated by numerical differentiation of static data obtained on the basic configuration for $\delta_e = 0°$ and $\delta_e = \pm 30°$ (Figs 5.22 and 5.23). The trend against α of the control effectiveness derivatives shows that important non-linearities are present, although lateral and directional static coefficients are not influenced by the tailplane deflections, even at high incidence.

5.3 IAR OSCILLATORY TESTS

The experimental programme performed by IAR for oscillatory tests of the WG16CA model was described in Chapter 2.5. Results obtained include a complete set of derivatives due to oscillation in pitch for the basic configuration, BWLVH and a complete set of derivatives due to oscillation in yaw for the BWLVHST configuration. In addition, some results were obtained for BWLVHST and BWVH in pitch oscillation and some investigation about effects of nose tip geometry was made by testing three different nose tip configurations. The effects of support asymmetry were also investigated[5] with the use of a mirror image strut system as described in sect. 2.5.1. Results obtained with the image strut are denoted by solid symbols. The effects of Reynolds number were investigated as well.

Notation specific to IAR tests includes $\tilde{C}_i$ (where i = l, m, n, N, Y), in order to indicate time-averaged aerodynamic loads under oscillatory conditions, C_{ik} (where k = α, β) for static aerodynamic derivatives and C_{ij} (where j = q, $\dot{\alpha}$, r, $\dot{\beta}$) for dynamic aerodynamic derivatives. All of them are referred to the body axes as shown in Fig 5.1. The composite fixed-axis derivatives are defined as follows:

$$C_{iq}^* = C_{iq} + C_{i\dot{\alpha}}$$
$$C_{ir}^* = C_{ir} - C_{i\dot{\beta}} \cos\alpha - C_{i\dot{\alpha}} \sin\alpha\tan\beta$$
$$C_{i\dot{\beta}}^* = C_{i\dot{\beta}} \cos\alpha$$

5.3.1 Pitch Oscillation Results

5.3.1.1 Nose Tip Geometry Effects

Model WG16CA has an interchangeable nose tip. Three different noses where in fact tested: a solid one, a rotatable one, and one nominally identical to the first one except for a slight nose asymmetry of 0.002d tip deflection as illustrated schematically in Fig 5.24. The latter is indicated as BWLVH-A.

The zero sideslip results obtained by rotating the model nose angle φ_n are shown in Figs 5.25 to 5.27. The results demonstrate that significant levels of the cross-coupling lateral-directional aerodynamic characteristics and aerodynamic derivatives C_{nq}^*, $C_{n\dot{\alpha}}$, C_{lq}^*, $C_{l\dot{\alpha}}$, C_{Yq}^*, $C_{Y\dot{\alpha}}$ occur at angles of attack beyond an onset angle of attack $\alpha_{on} \approx 29°$ which represents the onset of forebody vortex asymmetry. Their direction depend significantly on φ_n. This reveals that the onset and development of the unsteady, as well as steady, asymmetric aerodynamic loads under symmetric flow conditions are highly sensitive to forebody tip geometry. The micro-asymmetry dominates the magnitude and direction of the asymmetric loads, but the onset and development of asymmetry is influenced by support asymmetry and oscillatory motion. The levels of C_{nq}^*, C_{lq}^* and C_{Yq}^* are of the same order of magnitude as the corresponding direct damping in pitch, C_{mq}^* and C_{Nq}^*.

5.3.1.2 Configuration Effects

Figures 5.28 to 5.31 show the comparison of the pitch oscillation results for the BWLVH, BWLVHST and BWVH configurations. For the BWVH configuration at $\alpha \geq 10°$ the

normal force is lower than for the configurations with LEXs. The interaction with LEX vortices effectively delays breakdown of the wing leading edge vortices. The lateral-directional loads are approaching zero for the BWLVHST configuration at high α. This shows that the strakes with fixed transition are effective in reducing the zero sideslip asymmetry and in improving directional stability. Configuration BWLVH shows instead a well defined onset of asymmetry α_{on}. The onset angle for the BWVH, $\alpha_{on} = 25°$, is lower than for the BWLVH, $\alpha_{on} = 29° \div 32°$. All configurations are damped, with marginal static stability over most of the AOA range, but negative damping occurs in the vicinity of $\alpha = 5°$. The large effect of the support in the case of BWVH (Fig 5.28 and 5.30) is highly sensitive to Reynolds number.

Figure 5.31 shows the cross-coupling derivatives C_{nq}* and $C_{n\dot{\alpha}}$ for various configurations. Consistently with the mean lateral-directional loads described above, for BWLVHST, C_{nq}* and $C_{n\dot{\alpha}}$ approach zero in the full α range tested; however, for BWLVH and BWVH these derivatives show a steep rise or sharp decline as $\alpha > \alpha_{on}$, depending on the configurations tested, and the dynamic and static cross-coupling derivatives are in direct opposition.

5.3.1.3 Effects of Sideslip

The pitch oscillation data for the BWLVHST configuration at finite sideslip angles indicate that the changes of the lateral-directional aerodynamic coefficients or derivatives with angle of attack at positive and negative sideslip are almost symmetrical with respect to the zero-sideslip results and that the longitudinal results are generally close for positive and negative sideslip. Figure 5.32 shows the $\tilde{C}_Y$, $\tilde{C}_n$ and $\tilde{C}_l$ results at $\beta = \pm 5°$. For brevity, the corresponding derivatives[4] at $\beta = \pm 5°$ are not shown here.

It can be seen that yawing moments for $\beta = \pm 5°$ are approaching zero in the range of α between 32° and 42°, and their directions are reversed at $\alpha > 42°$. This may be caused by asymmetric cross-flow due to sideslip for the BWLHVST configuration. As mentioned above, and seen by comparing Figs 5.32 and 33, the strakes and strips effectively suppress zero-sideslip asymmetric loads at high incidence; on the other hand, the variation of flow separation asymmetry around the forebody with sideslip causes some sideslip dependent lateral-directional loads. Therefore, the asymmetric forebody vortices are not completely restrained, but displaced by the sideslip-induced asymmetry. As α was increased above 42° the asymmetry-induced yawing moment is de-stabilizing and increasing with α (Fig 5.32). For the basic configuration BWLVH the combined effects of forebody and sideslip-induced yawing moment and side force are also apparent but the former dominate at $\alpha \geq 29°$. In comparing Fig 5.32 with 5.33 it can be seen that some effect of the strakes is also visible at the lower incidences.

5.3.2 Yaw Oscillation Results

5.3.2.1 Nose Tip Geometry Effects

As mentioned above, the forebody flow separation asymmetry is highly sensitive to tip geometry and lateral motion. If large enough, the micro-asymmetry will dominate the magnitude and direction of the asymmetric loads even in the presence of motion. This phenomenon was verified in yaw oscillation tests for the basic configuration with a nose asymmetry of 0.002d tip deflection. The results demonstrate that this micro-asymmetry was large enough to completely determine the magnitude and direction of C_n, as shown in Fig 5.34. On the other hand, for the symmetrical nose the yaw oscillation effects dominated over the much smaller micro-asymmetry, thereby delaying the onset of steady asymmetrical vortex shedding. This result has clear implications both for high-α testing and for the control of the lateral loads in flight at high α[5].

In general, the results indicate that the conditions of incipient forebody vortex asymmetry are affected by various factors, including tip geometry, configurational features and support asymmetry. Under zero sideslip conditions, the onset angle varies between 25° to 32° (the semi-vertex angle of the nose is $\delta_n = 14.25°$ for WG16). The implications of these findings for flight prediction have been discussed in Reference 4.

5.3.2.2 Effects of Sideslip

The effect of sideslip angle on the longitudinal static aerodynamic coefficients is not significant. The normal force coefficients for $\beta = \pm 5°$ are basically in agreement with the zero sideslip case. The presence of sideslip slightly decreases the pitching moment coefficients in the range $\alpha < 32°$; however, this tendency is reversed for $\alpha > 32°$ (Fig 5.35).

The effects of sideslip on the lateral-directional aerodynamic coefficients $\tilde{C}_Y$, $\tilde{C}_n$ and $\tilde{C}_l$ are shown in Fig 5.36. At finite sideslip angles $\tilde{C}_Y$ is not symmetric with respect to the $\beta = 0°$ results. This is probably the result of support interference and model micro-asymmetry. In contrast, the rolling moment coefficient $\tilde{C}_l$ is not sensitive to this influence and its variation with angle of attack is quite symmetric for $\beta = +5°$ and -5°.

Unlike the results in pitch oscillation, $\tilde{C}_n$ is not symmetric in the range $30° \leq \alpha \leq 38°$. This is due to the lateral-directional loads from asymmetric forebody vortices, which are not completely restrained by the strakes.

The effects of sideslip on the direct dynamic derivatives C_{nr}*, C_{Yr}* are similar for positive and negative sideslip at α up to 42° as shown by Fig 5.37 and 5.40, respectively. At $\alpha = 20°$ β has a large effect on the cross derivative C_{lr}* (Fig 5.39). This is due to the time lag in the movement of the vortex burst on and off the trailing edges of the wing. Figure 5.38 shows that the cross-coupling derivative C_{mr}* changes significantly at $\alpha > 25°$ for $\beta = +5°$ and -5°. This is caused by the high sensitivity to sideslip of the cross-flow around the BWLVHST forebody at $|\beta| = 5°$, and forebody vortex asymmetry is not completely controlled by sideslip. Since the vortex asymmetry is likely to be locked to one side, the unsteady response in yaw oscillation will result in an increase in asymmetry at positive sideslip but a decrease at negative sideslip.
Associated with these asymmetric flow effects, the effect of sideslip on the static stability derivative $C_{n\beta}$* is significant at low α ($\alpha \leq 20°$) and at $\alpha \geq 35°$. Figure 5.40 shows that the presence of sideslip changes the sign of the lateral stability derivative $C_{Y\beta}$* in the range $25° < \alpha < 42°$.

The cross-coupling derivatives C_{mr}*, $C_{m\beta}$*, C_{Nr}* and $C_{N\beta}$* for BWLVHST due to yaw oscillation appear in Figs 5.38 and 5.41. Unlike the pitch-oscillation case, appreciable levels of C_{mr}* and C_{Nr}* exist at $\beta = 0$ and low α ($\alpha \approx 20°$), of the

same order of magnitude as the yaw damping derivatives. The static derivatives $C_{m\beta}$* and $C_{N\beta}$* change their sign twice, at α = 29° and α = 40°, respectively.

5.4 ONERA-IMFL TESTS ON "PQR" RIG

ONERA-IMFL test program was defined with the aim of demonstrating the different types of experiments and data relevant to the aerodynamics of manoeuvring combat aircraft which can be obtained by the rig. The following tests were performed:

- slow α or β-sweeps for quasi-static data ($\approx$3°/s);
- pitch and yaw oscillatory tests for evaluation of damping derivatives;
- large amplitude oscillations in pitch;
- α-ramps at various pitch rates.

All tests were performed at V=30m/s, except for some specific tests carried out to estimate Reynolds number effects. Results are presented for the complete configuration BWLHVST.

5.4.1 Static Tests

5.4.1.1 Effects of Sideslip (Fig 5.42)

On Fig 5.42 a slight sideslip effect is noted on C_N and C_m at β=5°. At β=±10° a measurable loss of normal force is encountered as angle of attack reaches approximately 31° to 33°. There is a large pitch-down increment with sideslip for 10° < α < 33°, but for higher angles of attack up to 80° the effect is opposite.

At high angles of attack forebody strakes suppress the asymmetry noticed on the BWLHV configuration. At β = ±10°, the rolling moment inverts at α = 24°, lateral stability is lost, then C_l changes sign again very suddenly as α approaches approximately 32°. This lateral instability is not encountered at β=±5°.

The pitching moment increase noted at β=±10° is simultaneous with the sudden decrease of normal force and variation of lateral stability. This phenomenon is probably due to unsteadiness of vortices at sideslip.

5.4.1.2 Hysteresis (Fig 5.43)

With the PQR apparatus it is possibile to perform slow sweeps with increasing or decreasing α at constant β. Consequently, it is ideally suited to investigate hysteresis effects and check on test repeatability. Data obtained with increasing or decreasing α are noted as α+ and α- respectively.

No significant hysteresis effect is found at zero sideslip. Repeatability of tests can also be judged as very good. In Fig 5.43 comparisons between increasing and decreasing α-sweeps at ±10 degrees of sideslip show that a hysteresis phenomenon occurs on C_N and C_m for 22° < α < 35°. In the same α-range, there is also a large hysteresis effect on the rolling moment coefficient C_l. The sudden change of sign of C_l, observed during α+ sweeps at sideslip +10° or -10°, is not encountered during α- sweeps. Lateral stability is maintained in the whole α-range as alpha decreases slowly. In the same α-range, a hysteresis effect of the same type is also observed on the yawing moment coefficient C_n, but it is not as large as for C_l. Symmetry of this hysteresis phenomenon for tests at β=10° and tests at β=-10° is quite good. The phenomenon is probably due to the forebody strakes. Indeed no hysteresis was found when performing similar tests on the BWLHV configuration.

5.4.2 Dynamic Tests

One of the main features of the PQR apparatus is that various types of motions can be performed: sinusoidal motion (at various amplitudes or frequencies), ramp motion or other types of programmed motions. For the present tests, oscillations of small amplitude were performed to identify dynamic derivatives to be compared with those obtained on other rigs. Some large amplitude motions were also performed on the model to obtain time histories of the aerodynamic coefficients during dynamic motions.

5.4.2.1 Small-Amplitude Pitch Oscillations (Fig 5.44)

The main goal of these tests is to identify the dynamic derivatives due to a pitch motion of the model. These tests are pure rotations in pitch of the model about the center of gravity and the following derivatives can be identified: $C_{iq}+C_{i\dot{\alpha}}$ for i= N or m. Table 5.1 gives the values of the dynamic derivatives obtained for three values of sideslip: 0°, +5° and -5°.

In Fig 5.44 some examples of coefficient time histories which were obtained for small amplitude pitch oscillations at several mean incidences and at constant value of sideslip β=5° are plotted against α. Oscillatory test results are plotted together with slow α-sweep data, so unsteady coefficients can be compared with these quasi-static data. Dynamic test results describe closed curves since they are periodic as the motion is. These plots can be interpreted as follows. On the closed curves, arrows have been added to indicate the time evolution of the aerodynamic coefficient. In the figure, the sign of the derivative can be directly interpreted: if the arrows on the closed curves are oriented in clockwise direction, the dynamic derivative is positive and vice versa. In particular the plots show that the derivative is always negative on C_m, i.e. the motion is damped. Indeed, for the same α-value, C_m corresponding to negative $\dot{\alpha}$ is greater than C_m corresponding to positive $\dot{\alpha}$.

Derivatives can also be estimated: on the curve, at the mean value of incidence, the difference between the two ordinates is a measure of the derivative with respect to $\dot{\alpha}$ and q. In particular, the plots indicate that dynamic derivative on C_N is larger at high α than at low α.

There are also some dynamic effects on lateral coefficients, particularly on C_Y, C_n and, to a less extent, on C_l. Dynamic effects are negligible at α=10°, but they are more significant at high α.

ANGLE OF SIDESLIP = 0°

ALPHA	10°	20°	25°	30°	40°
$C_{Nq}+C_{N\dot{\alpha}}$	1.25	4.94	5.62	14.30	19.94
$C_{mq}+C_{m\dot{\alpha}}$	-3.35	-5.31	-5.65	-5.70	-6.88

ANGLE OF SIDESLIP = -5°

ALPHA	10°	20°	25°	30°	40°
$C_{Nq}+C_{N\dot{\alpha}}$	3.76	4.38	12.90	12.98	17.49
$C_{mq}+C_{m\dot{\alpha}}$	-3.66	-4.27	-5.51	-6.59	-7.42

ANGLE OF SIDESLIP = +5°

ALPHA	10°	20°	25°	30°	40°
$C_{Nq}+C_{N\dot{\alpha}}$	3.91	6.93	9.79	10.26	18.58
$C_{mq}+C_{m\dot{\alpha}}$	-3.72	-5.05	-4.81	-7.51	-7.65

Table 5.1: Longitudinal dynamic derivatives of BWLHVST configuration. Pitch oscillation tests: f=2.5 Hz Ampl.=2.9° (see also Fig. 8.3)

5.4.2.2 Small-Amplitude Yaw Oscillations (Fig 5.45)

These oscillatory tests correspond to a pure rotation in yaw of the model about the center of gravity and consequently, the kinematic relationship between r and $\dot{\beta}$ is: $\dot{\beta}$ = -r cos α. Hence, the dynamic derivatives which are identified are:

$$C_{ir} - C_{i\dot{\beta}} \cos\alpha \quad , \quad \text{for i= Y, l or n}$$

Figure 5.45 presents some examples of time histories of aerodynamic coefficients, plotted against sideslip for α values of 0°, 10° and 20°. On these plots it can be seen that dynamic effects are negligible on longitudinal coefficients and increase with α on the rolling moment C_l. Results for the yawing moment C_n are complex and difficult to analyse directly on plots due to the existence of different harmonics in the signal. The amplitudes of these harmonics appear larger than the amplitude of the first harmonic (motion frequency) which seems low; consequently the dynamic derivative in yaw is small.

Table 5.2 gives the values of dynamic derivatives obtained with yaw oscillation tests and identified with the classic method known as "first harmonic method".

5.4.2.3 Large-Amplitude Pitch Oscillations (Fig 5.46-49)

The large amplitude dynamic tests were carried out in order to obtain aerodynamic data which are considered of great interest for aircraft manoeuvering at high angles of attack. Interpretation and analysis of these data can be conducted via correlation with other data from different dynamic motions and via mathematical modelling. In this section time histories of the aerodynamic coefficients for some large amplitude tests are presented. The frequency of oscillations is 1 Hz.

ALPHA	0°	0°	10°	20°	20°
BETA	0.24°	-4.76°	0.24°	0.24°	-4.45°
$C_{Yr}-C_{Y\dot{\beta}} \cos\alpha$	0.51	0.63	0.59	0.70	0.74
$C_{lr}-C_{l\dot{\beta}} \cos\alpha$	0.03	0.03	0.14	0.25	0.22
$C_{nr}-C_{n\dot{\beta}} \cos\alpha$	-0.11	-0.42	0.17	0.13	0.21

Table 5.2: Lateral dynamic derivatives of BWLHVST configuration - Yaw oscillation tests: f=2.5 Hz Ampl. 2.9°

Figure 5.46 shows some results obtained with pitch oscillations of 10° amplitude. In this condition, it can be noted that repeatability is very good and results are not influenced by forebody nose flow unsteadiness. Figures 5.47 to 49 give results for amplitudes of 10°, 18° and 29° at different values of mean incidence. Effects of both parameters can be analysed. It is immediately apparent that dynamic effects increase with mean angle of attack and amplitude. Large dynamic effects can be observed on the longitudinal coefficients C_N and C_m. Particularly, the value of C_{Nmax} and the value of angle of attack for C_{Nmax} are larger at both the largest amplitude and mean α.

A dynamic stall phenomenon is encountered during the motion: an overshoot of the linear regime occurs, then normal force is suddenly reduced, stall is steeper, the normal force decreases substantially and is smaller than in the steady case. During dynamic motion a hysteresis phenomenon occurs and a strongly time dependent behaviour of the aerodynamic coefficients is noted. Dynamic effects on pitching moment are also large as compared to static values. Unsteady effects can also be analysed in the frequency domain, where it can be noted that some harmonics of high amplitude are present in the dynamic loads, particularly on the pitching moment.
Dynamic effects on lateral coefficients are not very large. However, the moderate asymmetry encountered during slow α-sweeps is not present during dynamic tests (see Fig 5.49).

5.4.2.4 Alpha-Ramps (Fig 5.50)

Alpha-ramp motions are very similar to realistic pitch manoeuvers of combat aircraft at low speed and high angles of attack. Alpha-ramps were carried out at four different constant pitch rates ($qc/2V = 2.8\ 10^{-3}$, $5.5\ 10^{-3}$, $9.2\ 10^{-3}$ and $18.4\ 10^{-3}$) from 10° to 70° AOA.

Figure 5.50 shows results obtained for the different values of pitch rate at β = 0° and compares them with the slow sweep data. The following remarks can be made about these plots:

- a dynamic stall phenomenon occurs at high rates with a significant increase of the stall incidence and C_N max value;
- dynamic effects are much smaller at low angles of attack;
- increasing the pitch rate increases normal force but reduces pitching moment, in α-range of the test;
- at high angles of attack the configuration is very sensitive to dynamic motion: effects are noted even at qc/2V=.0028.

5.5 ONERA-IMFL OSCILLATORY CONING TESTS

Compared with other rotary rigs, the rotary balance at ONERA-IMFL (the "TourneBroche") is unique in that the axis of rotation can be tilted by an angle λ relative to the free-stream. Therefore, when rotary tests are performed with the TourneBroche, the rotation axis can be offset from the velocity vector thus creating sinusoidal variation of angle of attack and sideslip. This motion is known as "oscillatory coning". During a steady turn the rotation velocity ω is constant, but incidence and sideslip vary $\pm\lambda$ about their respective mean values.

Pure coning ($\lambda=0$), when associated with oscillatory coning ($\lambda\neq0$) allows the following derivatives to be determined[9]:

$$C_{iq}$$
$$C_{i\dot{\alpha}}$$
$$C_{ip} + C_{i\dot{\beta}} \sin\alpha$$
$$C_{ir} - C_{i\dot{\beta}} \cos\alpha$$

The oscillatory coning test program carried out on model WG16A included:

(i) identification of dynamic derivatives by performing small amplitude tests (λ = 2.5°) on BWLHV and BWLHVST configurations;
(ii) large amplitude oscillatory coning tests (λ = 5°, 10° and 20°) where unsteady aerodynamic phenomena were highlighted. The effects of the rotation rate ω and the amplitude λ on aerodynamic coefficients were examined (on BWLHVST configuration only).

In Fig 5.51 the variation of α and β are presented. It is represented nearly by a circle whose radius is equal to λ. The center of the circle is chosen by mean of parameters Θ_2 and ϕ (see Chapt. 2 or ref. 6 for definitions). If α_c and β_c are the coordinates of this center in the (α,β) plane, the rates are expressed as follows:

$$p = \omega \cos\alpha_c \cos\beta_c$$
$$q = \omega \sin\beta_c$$
$$r = \omega \sin\alpha_c \cos\beta_c$$

These tests are rotary and oscillatory, the rotation velocity ω also determining the angular frequency of the oscillation in α and β. As $\Omega = \omega b/2V$ is constant during the tests, the rates are also constant, whereas α and β vary sinusoidally.

5.5.1 Small-Amplitude Oscillatory Coning Tests (Fig 5.52)

Dynamic derivatives at five values of angle of attack (10°, 20°, 25°, 30°, 40°) were identified using the method described in Reference 7. Figure 5.52 gives an example of coefficient time histories plotted against angle of attack and obtained for the BWLHVST configuration at mean β equal to 0° and at $\Omega = \pm0.12$. The small amplitude tests are compared to static data obtained on the TourneBroche by performing slow α-sweep tests at $\beta=0$.

It can be seen that, for every longitudinal and lateral coefficient, the closed curves are shifted with respect to the static values. This global shift of each curve is due to the effect of the rotation rate Ω which would be measured in pure coning tests. The mean value of oscillatory coning test results corresponds to conventional rotary test results. As results are plotted for opposite values of Ω, it can be noted that the rotation rate effects are similar for clockwise and counterclockwise rotations on longitudinal coefficients and opposite on lateral coefficients. The breadth of the closed curves along the ordinate measures the magnitude of the dynamic contribution (due to $\dot{\alpha}$ and $\dot{\beta}$) for each coefficient. Symmetry of unsteady lateral data for positive and negative rotation rates is very good.

Dynamic derivatives identified for BWLHV and BWLHVST configurations are shown in Fig 5.53 (longitudinal q and $\dot{\alpha}$ derivatives), Fig 5.54 (lateral-directional rolling derivatives) and in Fig 5.55 (yawing derivatives).
By combining data from coning and oscillatory coning tests, effects of q and $\dot{\alpha}$ can be separated and the derivatives C_{iq} and $C_{i\dot{\alpha}}$ identified separately. Comparisons between derivatives of both configurations show that the effect of nose strakes on dynamic derivatives is important, even at low α. The BWLHV configuration is damped in yaw at all test angles of attack; for the BWLHVST configuration damping is reduced at low α and becomes unstable at high α.

For longitudinal coefficients, derivatives due to $\dot{\alpha}$ are significantly greater at high angles of attack for both configurations. Values of some derivatives seem to diverge at high α, in particular for the BWLHV configuration. Derivatives are based on the assumptions of linearity and of independency between longitudinal and lateral effects. Moreover, derivatives express only instantaneous values of aerodynamic coefficients as function of instantaneous parameters: α, β, q, $\dot{\alpha}$, etc. If the flow is unsteady, then aerodynamic coefficients are not only functions of the instantaneous values of these parameters, therefore derivatives do not correctly represent dynamic effects. At high α unsteady effects occur, hysteresis phenomena appear and consequently use of derivatives may be inappropriate, as shown at $\alpha=40°$.

5.5.2 Large-Amplitude Oscillatory Coning Tests

In order to provide non-linear and unsteady data representative of manoeuvers at high angle of attack, some large amplitude oscillatory coning tests were carried out on the BWLHVST configuration. These data can be compared with small-amplitude test data by calculating coefficient time histories of the same motion using the derivatives identified from small amplitude tests. Such comparisons are of interest to estimate non-linear and unsteady contributions on aerodynamic coefficients as obtained during large-amplitude motions. Comparisons of data from the TourneBroche rotary-balance with flight-test data have already been made for the Alphajet aircraft. It was shown[7] that large-amplitude oscillatory coning motions can provide significant and useful data for satisfactorily modelling aerodynamic coefficients of a manoeuvering aircraft at high angle of attack. Effects on aerodynamic coefficients of the two parameters amplitude (λ) and rotation rate (Ω) are presented next.

5.5.2.1 Amplitude Effect (Fig 5.56)

Oscillatory coning tests were carried out with high λ values of 10° and 20°, at mean β = 0°. This type of test has a similarity to large amplitude oscillatory tests on the PQR apparatus, with equivalent large variation of incidence, but it

includes also roll and yaw rates and sideslip effects. For each {mean α, mean β} couple, the corresponding trajectory in α-β plane was presented in Fig 5.51.

For clarity of presentation results of tests for different amplitudes at the mean α=40° and for one rotation rate (Ω=.12) are plotted in Fig 5.56. The pitch, roll and yaw rates are constant and identical for the different tests shown. However, the data presented include the effects of: α, β, $\dot{\alpha}$, $\dot{\beta}$ which vary during each test.

Several remarks can be made:

- dynamic effects are large in comparison with static variations;
- dynamic effects increase with amplitude λ;
- as the flow is separated, aerodynamic coefficients are much more sensitive to dynamic motion than at low α when the flow is attached;
- for large amplitude tests (high λ), nonlinear effects are found in coefficient time histories, mainly in the yawing moment;
- when a dynamic stall phenomenon is encountered, the value of C_{Nmax} and incidence at stall is substantially increased.

5.5.2.2 Rate Effect (Fig 5.57-58)

At λ=20°, mean β=0°, and at three values of mean angle of attack, tests for various values of Ω were carried out. Results are presented for mean α=40° and for different values of the rotation rate. For each test, the value of Ω was stabilized during several turns and data were acquired. Figure 5.57 shows results obtained for opposite values of Ω (±.04 and ±.12). Figure 5.58 shows results obtained for different positive values of Ω (.006, .06 and .10).

The direction of rotation has no significant influence on C_N and C_m: longitudinal results are quite similar for clockwise and counterclockwise rotations (Fig 5.57). This means that sideslip variation has no influence on longitudinal coefficients and also that repeatability of tests can be deemed as good.

The plots in Fig 5.58 show that the breadth of the loops along the ordinate increases with Ω, indicating an increase in dynamic effect. For high values of Ω, at maximum and minimum values of angle of attack, although $\dot{\alpha}$ is zero, the normal force is quite different from quasi-static data obtained at the same incidence. Therefore, C_N is time-dependent and is not only a function of the instantaneous values of α and $\dot{\alpha}$. Time lag of the flow with respect to the motion is evident at minimum α.

Regarding lateral coefficients, some comments can be made on static features of C_l and C_n. In Fig 5.58, for best understanding of results, the evolution of sideslip values as function of angle of attack is indicated on C_n plots. Test results of C_n at slow rotation rate (quasi-static test), show that directional stability changes sign at approximately α=33°. At this point β is close to 18° or -18°, and it is noted that behaviour of C_n is quite symmetric for positive and negative values of β. Similarly, on plots of the rolling moment at slow rotation rate, it can be seen that the lateral stability $C_{l\beta}$ changes sign twice: plots for opposite values of β intersect at α close to 24° and 32° respectively. These aerodynamic features in the yawing and rolling moment coefficients are quite consistent with static data as measured on the "PQR" apparatus.

Dynamic contributions due to rotation rate and $\dot{\beta}$ change the shape of curves of C_l and C_n, mainly for α < 45° (Fig 5.58). The loss of directional stability is still present, since plots of C_n for opposite values of β still intersect. However, in dynamic motion, the plots of rolling moment corresponding to opposite values of sideslip do not intersect and lateral instability disappears.

This result tends to confirm the sensitivity of the lateral instability noted for 24° < α <32°, as shown on the "PQR" apparatus by increasing- and decreasing-AOA sweeps at β=±10°. In these conditions a hysteresis phenomenon was encountered on the lateral stability of the BWLHVST configuration (see section 5.4.1.2 above). However, during oscillatory coning tests at slow rate, the rolling moment does not exhibit different behaviour as α is increasing and decreasing, and symmetry of C_l behaviour is preserved. C_Y, C_l and C_n data are nearly symmetric with respect to the α-axis for clockwise and counterclockwise rotations (Fig 5.57). The absolute value of Ω has only a small effect on side force (Fig 5.58).

5.6 REFERENCES

1. Guglieri, G., Quagliotti, F.B., "Dynamic Stability Derivatives Evaluation in a Low Speed Wind Tunnel", Journal of Aircraft, vol. 30, n. 3, 1993.

2. Guglieri, G., Fusco, F., "Experimental Investigation on Aircraft Dynamic Stability Parameters", Meccanica, vol. 28, n. 1, 1993.

3. Guglieri, G., Quagliotti, F.B., "Static and Oscillatory Tests on a Generic Combat Aircraft Model in a Low Speed Wind Tunnel", 19th ICAS Congress, Anaheim, USA, 1994.

4. Beyers, M.E., Cai, H.J. and Penna, P.J., " Flow-Field Interference Produced by an Asymmetrical Support Strut", IAR-AN-75, NRC, Canada, Jan. 1993

5. Beyers, M.E., "Interpretation of Experimental High-Alpha Aerodynamics Implication for Flight Prediction" (AIAA 94-0166, Jan. 1994), also Journal of Aircraft, March 1995.

6. Tristrant, D. and Beyers, M.E., "Oscillatory Coning", Chapter 4, AGARD-AR-265, Dec 1990, pp. 69-76.

7. Tristrant, D., "Correlation with Flight Tests", Chapter 11.3, AGARD-AR-265, Dec 1990, pp.217-218.

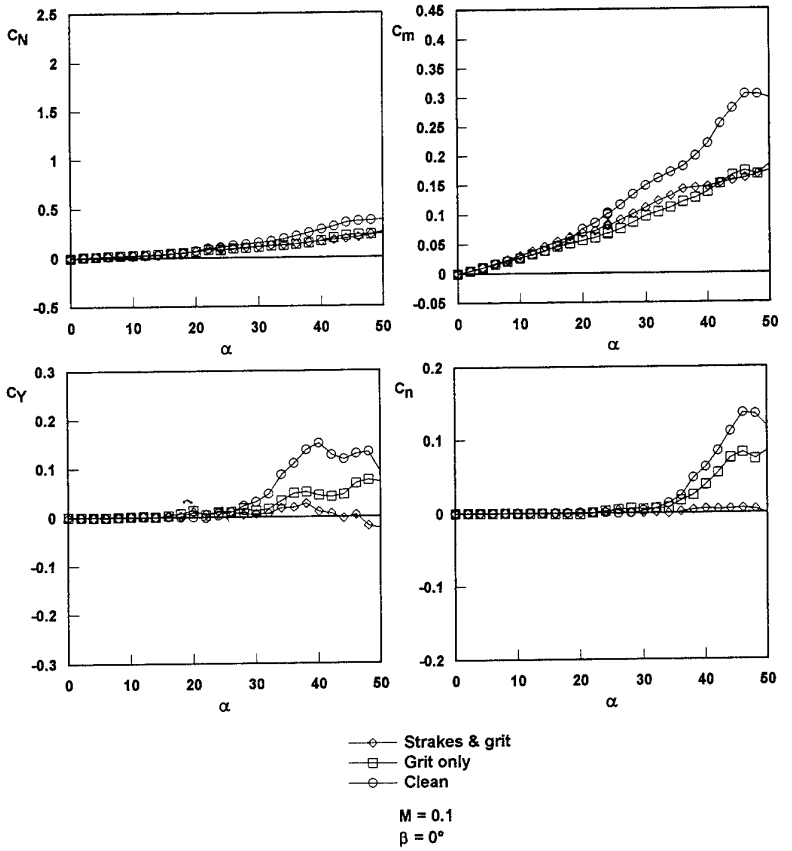

Fig. 5.2 Effect of forebody strakes and grit strips on static coefficients of body alone.

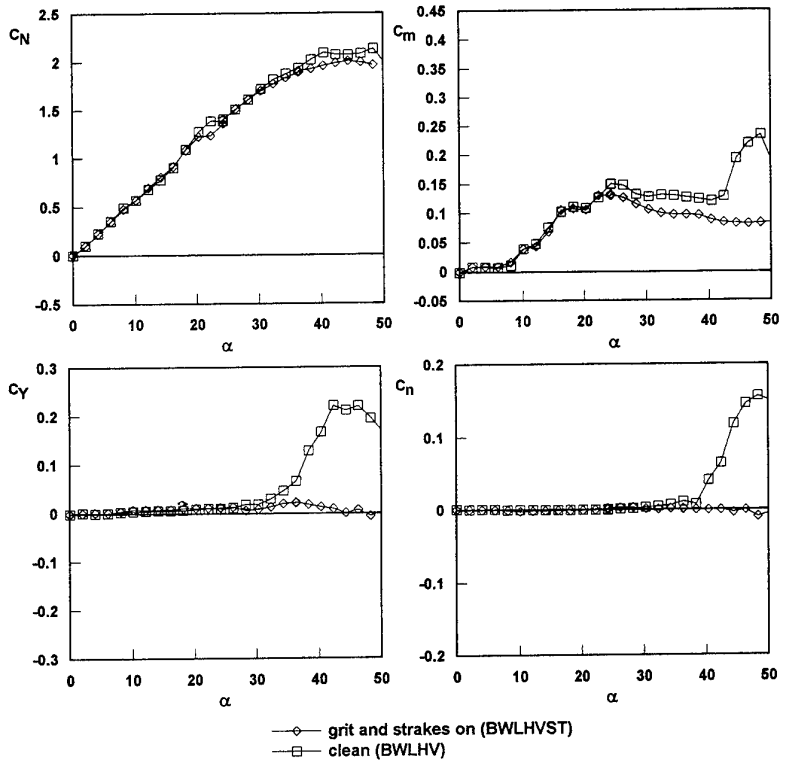

Fig. 5.3 Effect of forebody strakes and grit strips on static coefficients of complete model.

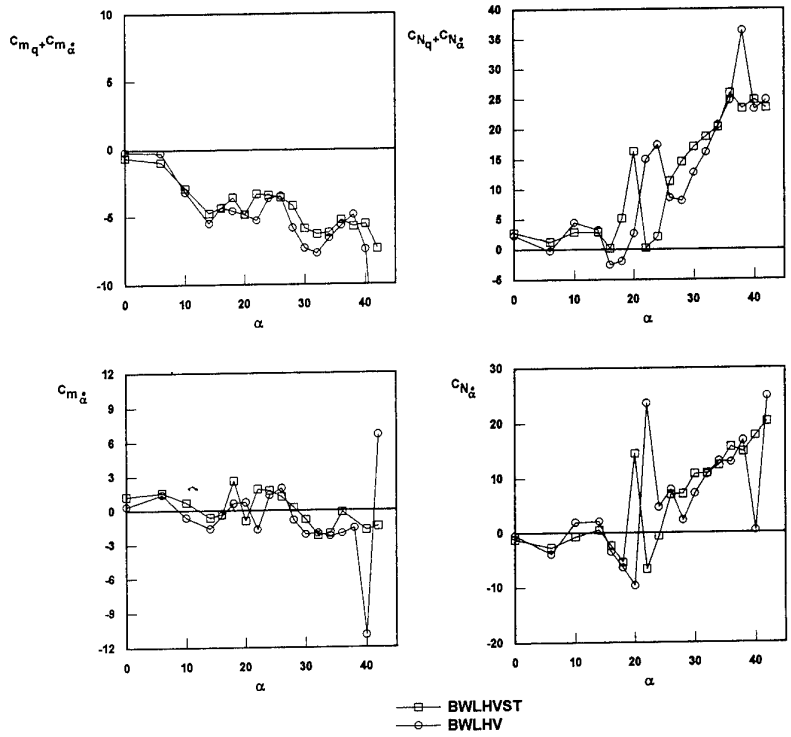

Fig. 5.4 Effect of forebody strakes and grit strips on derivatives from pitching and plunging modes.

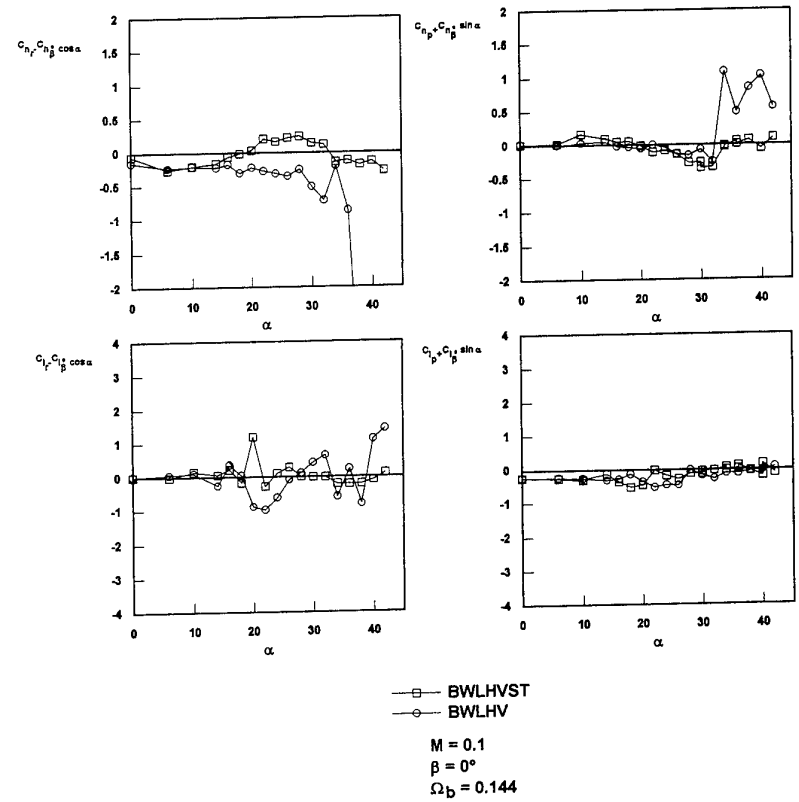

Fig. 5.5 Effect of forebody strakes and grit strips on derivatives from yawing and rolling modes.

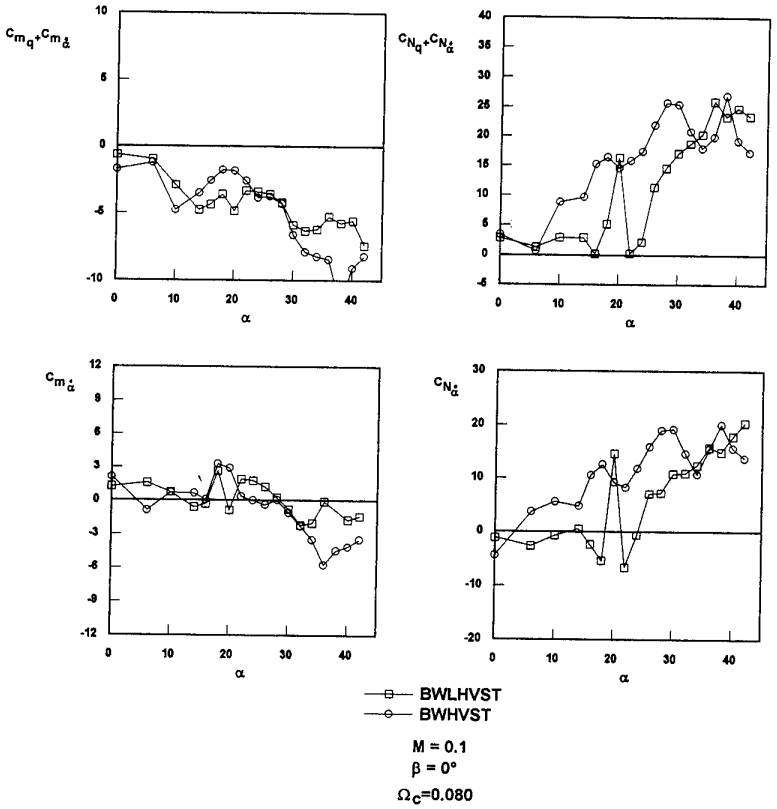

Fig. 5.6 Effect of LEX on derivatives from pitching and plunging modes.

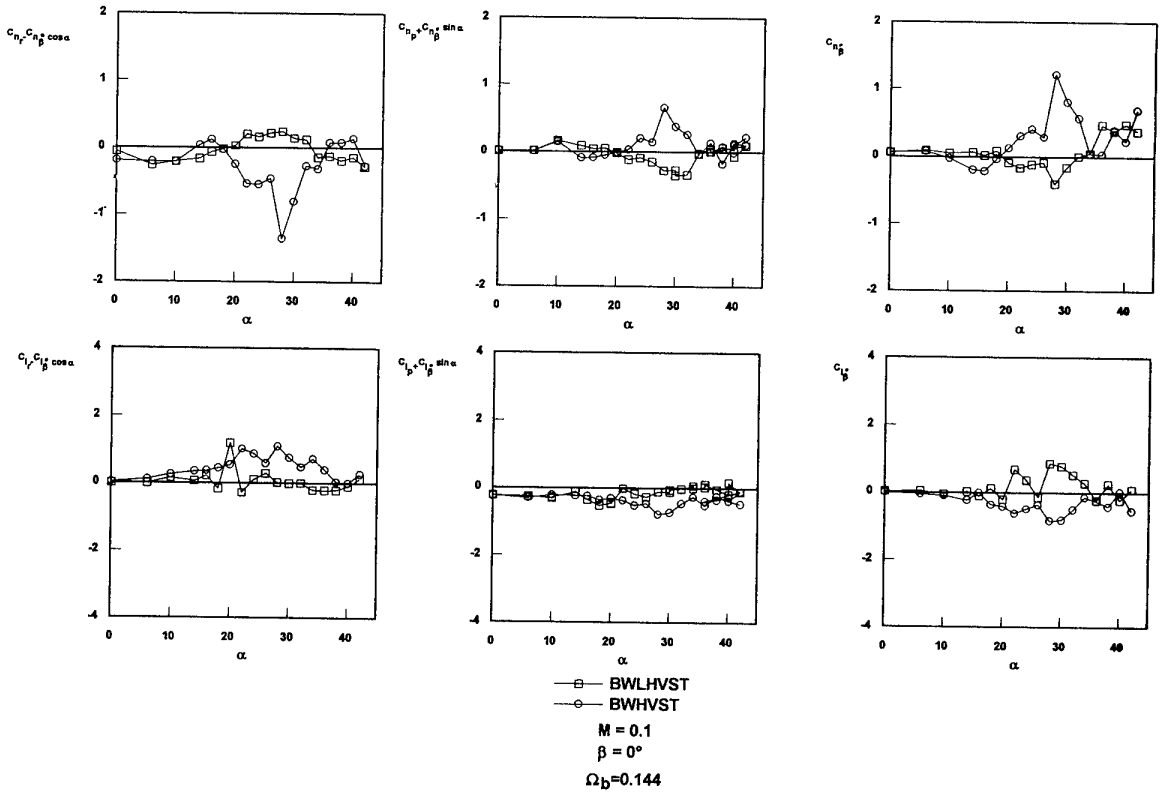

Fig. 5.7 Effect of LEX on derivatives from yawing, swaying and rolling modes.

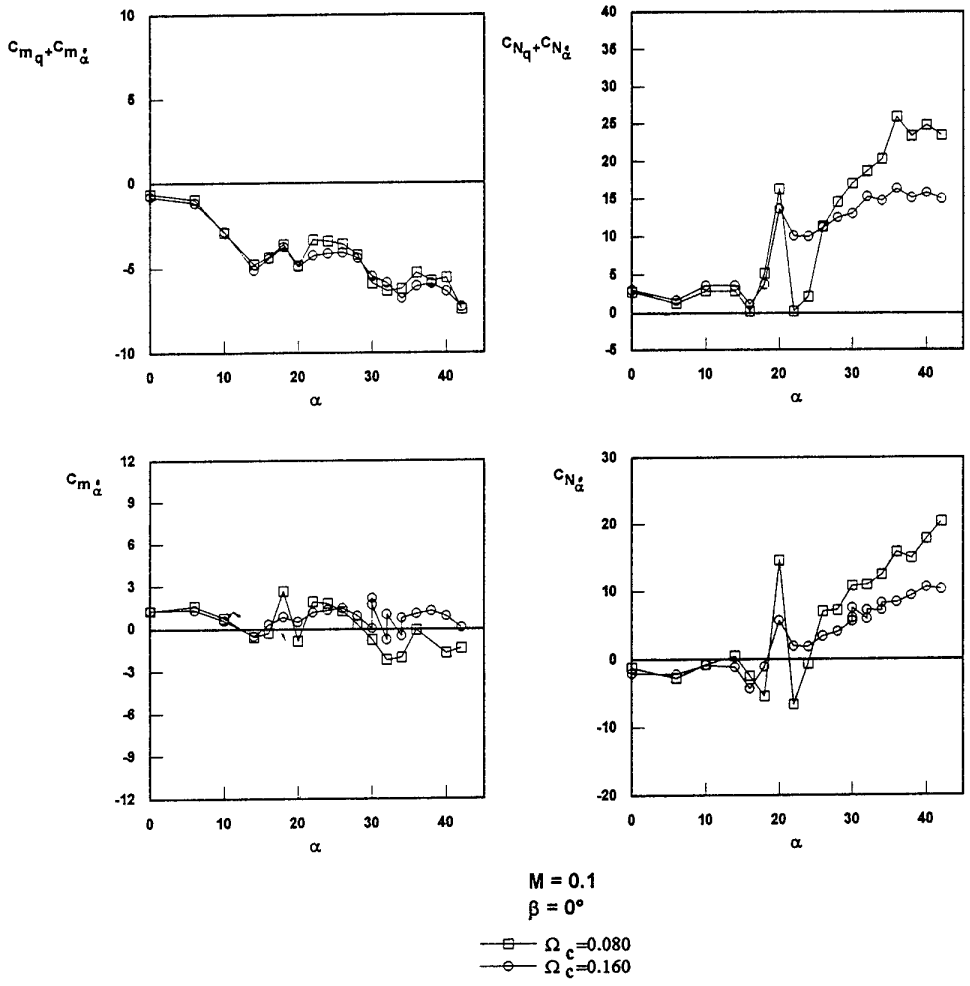

Fig. 5.8 Effect of frequency on derivatives from pitching and plunging modes.

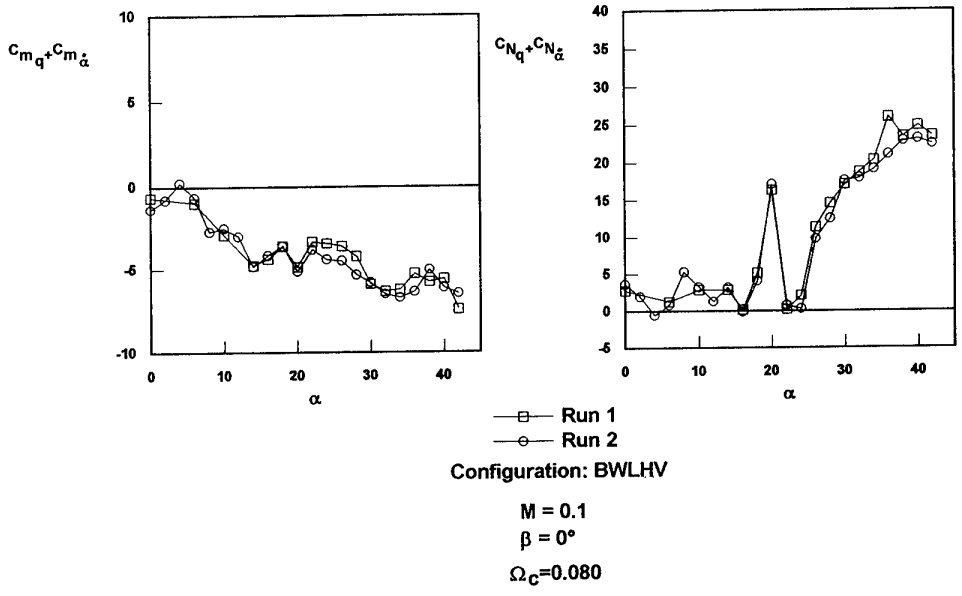

Fig. 5.9 Results from two pitching mode tests on the same configuration (data repeatability).

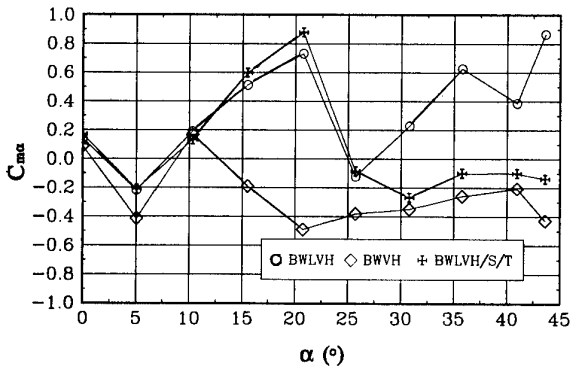

Fig. 5.10 The effect of configuration on Cmα
(V=30 m/s, β= 0°, k= 0.083, θ= ±1°).

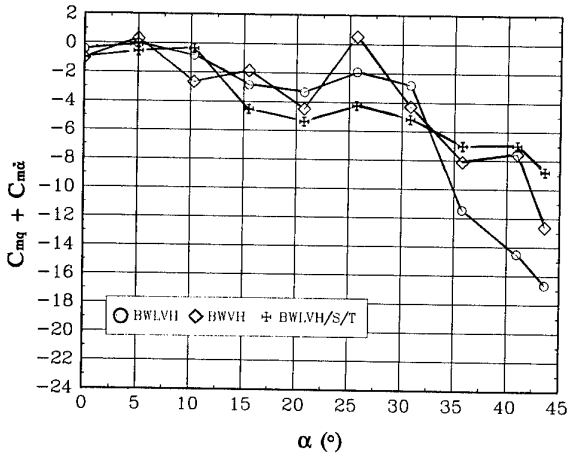

Fig. 5.11 The effect of configuration on $C_{mq}+C_{m\dot{\alpha}}$
(V=30 m/s, β= 0°, k= 0.083, θ= ±1°).

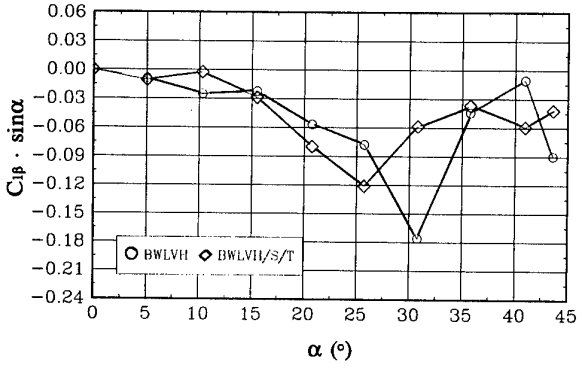

Fig. 5.12 The effect of configuration on $C_{y\beta}$ sinα
(V=30 m/s, β= 0°, k= 0.180, φ= ±1°).

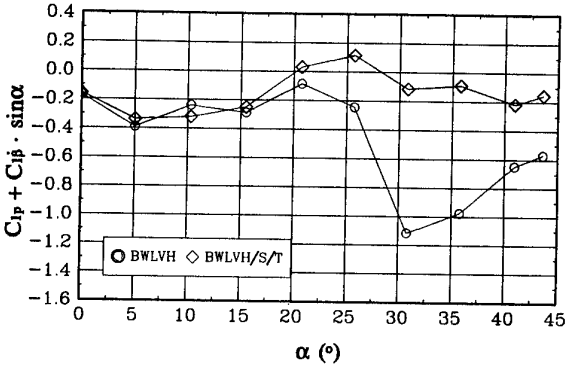

Fig. 5.13 The effect of configuration on $C_{lp}+C_{l\dot{\beta}}$ sinα
(V=30 m/s, β= 0°, k= 0.180, φ= ±1°).

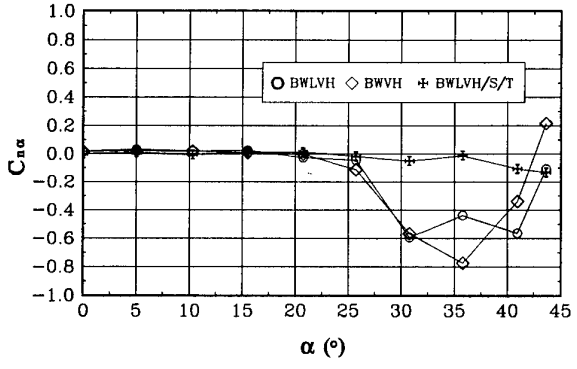

Fig. 5.14 The effect of configuration on $C_{n\alpha}$
(V=30 m/s, β= 0°, k= 0.083, θ= ±1°).

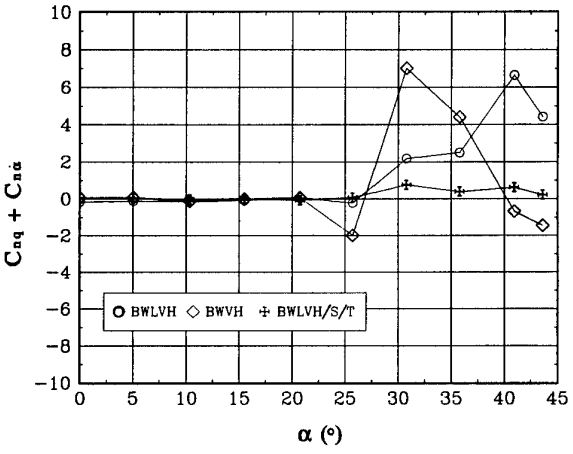

Fig. 5.15 The effect of configuration on $C_{nq}+C_{n\dot{\alpha}}$
(V=30 m/s, β= 0°, k= 0.083, θ= ±1°).

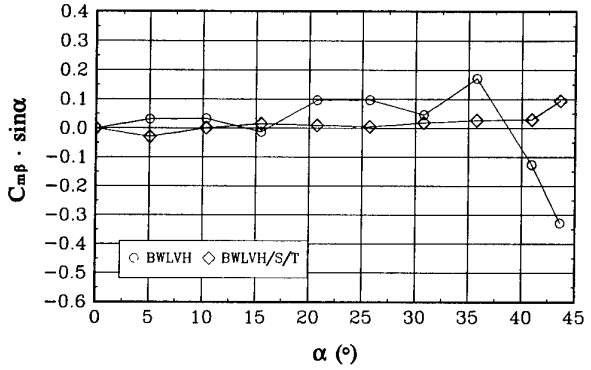

Fig. 5.16 The effect of configuration on $C_{m\beta}\sin\alpha$ (V=30 m/s, β= 0°, k= 0.180, φ= ±1°).

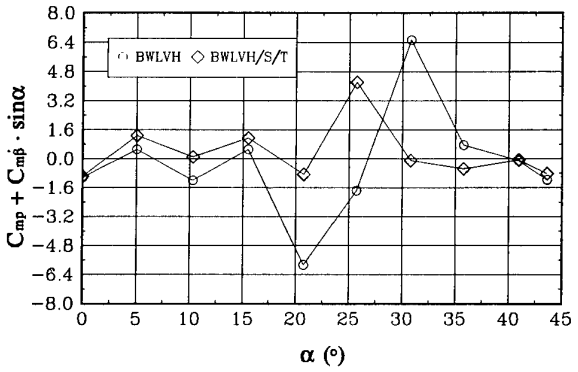

Fig. 5.17 The effect of configuration on $C_{mp} + C_{m\dot{\beta}}\sin\alpha$ (V=30 m/s, β= 0°, k= 0.180, φ= ±1°).

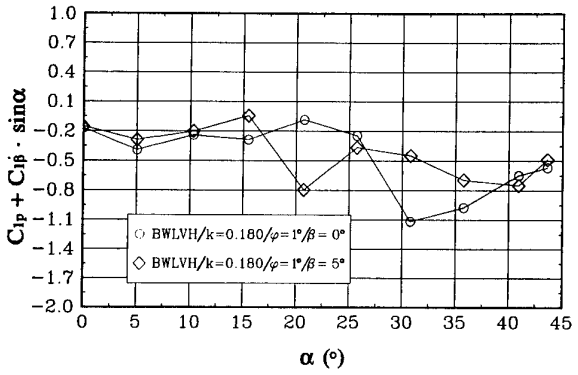

Fig. 5.18 The effect of sideslip on $C_{lp} + C_{l\dot{\beta}}\sin\alpha$ (V=30 m/s, k= 0.180, φ= ±1°).

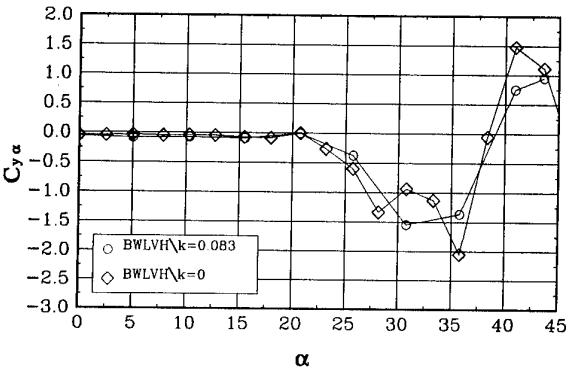

Fig. 5.19 The effect of oscillation frequency on $C_{Y\alpha}$: comparison with static data.

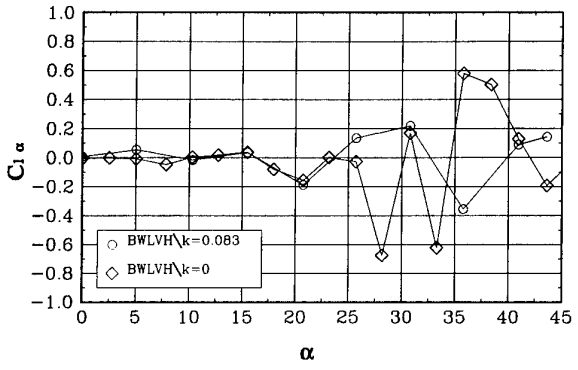

Fig. 5.20 The effect of oscillation frequency on $C_{l\alpha}$: comparison with static data.

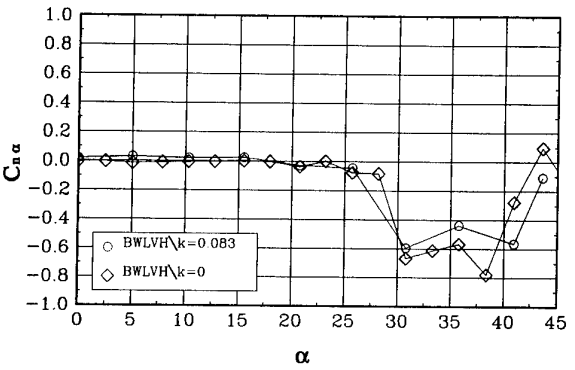

Fig. 5.21 The effect of oscillation frequency on $C_{n\alpha}$: comparison with static data.

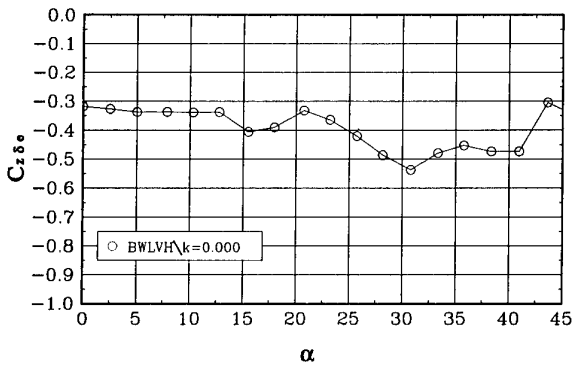

Fig. 5.22 The effect of horizontal stabilizer deflection on C_Z (V=30 m/s).

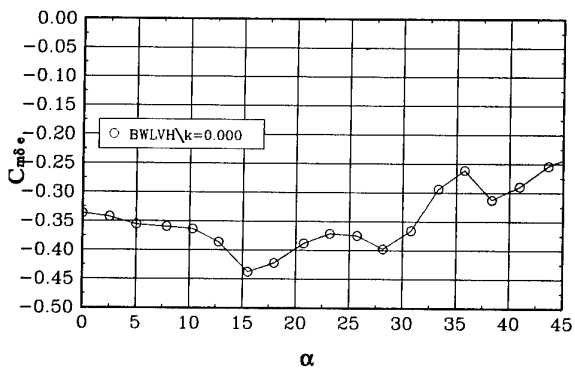

Fig. 5.23 The effect of horizontal stabilizer deflection on C_m (V=30 m/s).

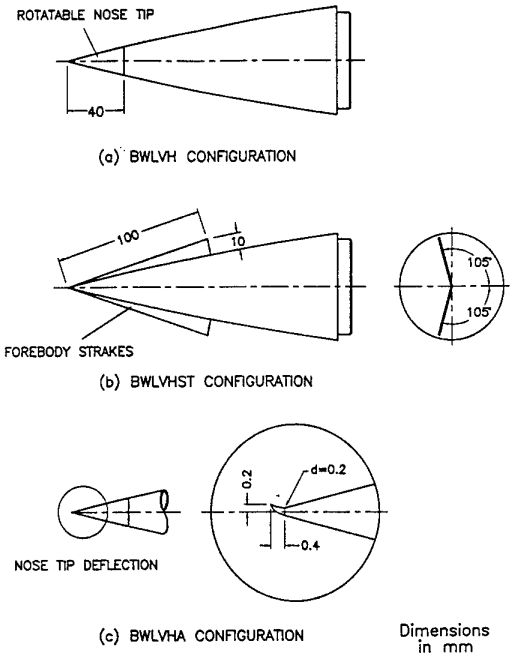

Fig. 5.24 WG16CA forebody configurations.

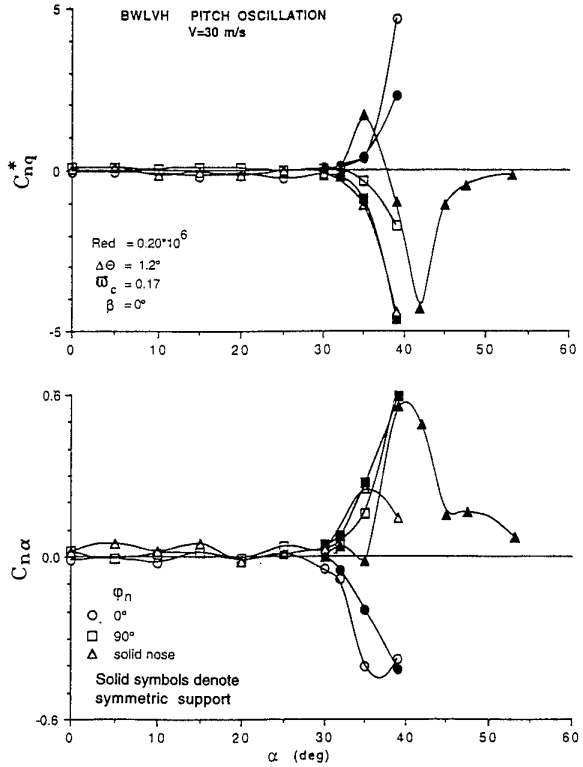

Fig. 5.25 Effect of rotating nose tip on the derivatives C_{nq}* and $C_{n\alpha}$

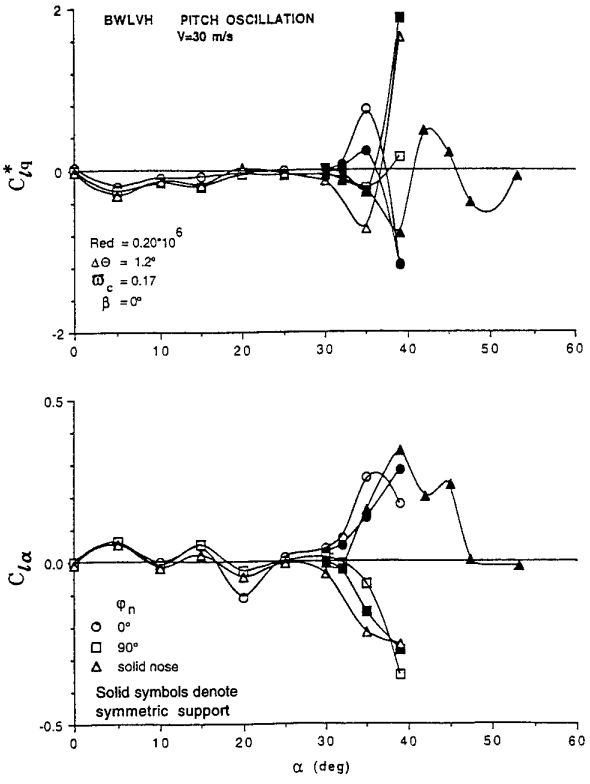

Fig. 5.26 Effect of rotating nose tip on the derivatives C_{lq}* and $C_{l\alpha}$.

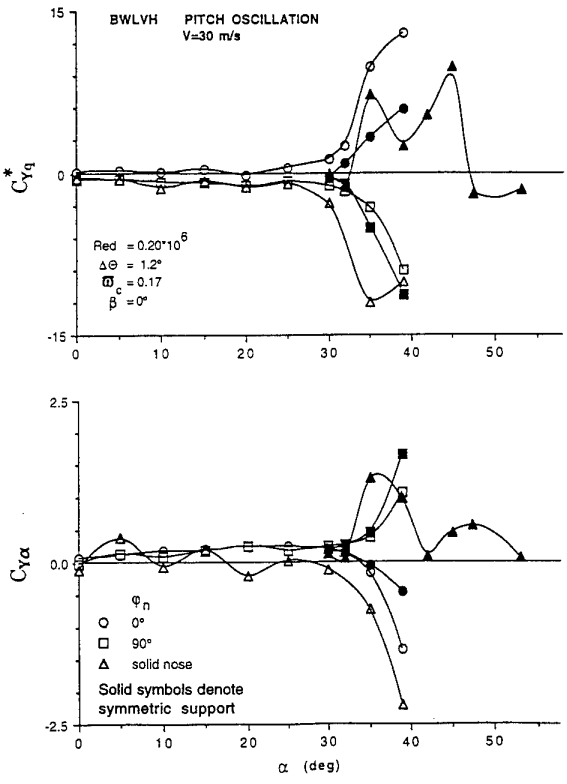

Fig. 5.27 Effect of rotating nose tip on derivatives C_{Yq}* and $C_{Y\alpha}$.

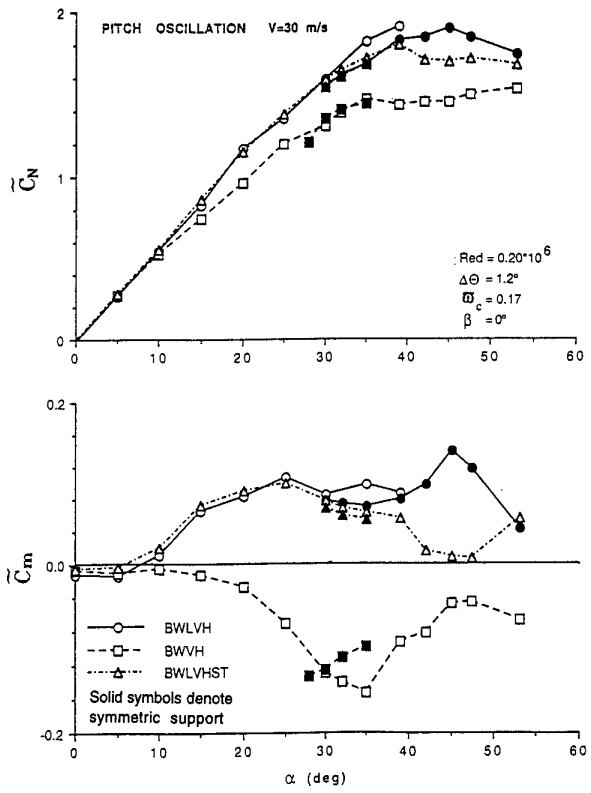

Fig. 5.28 Configurational effects on the longitudinal aerodynamic coefficients.

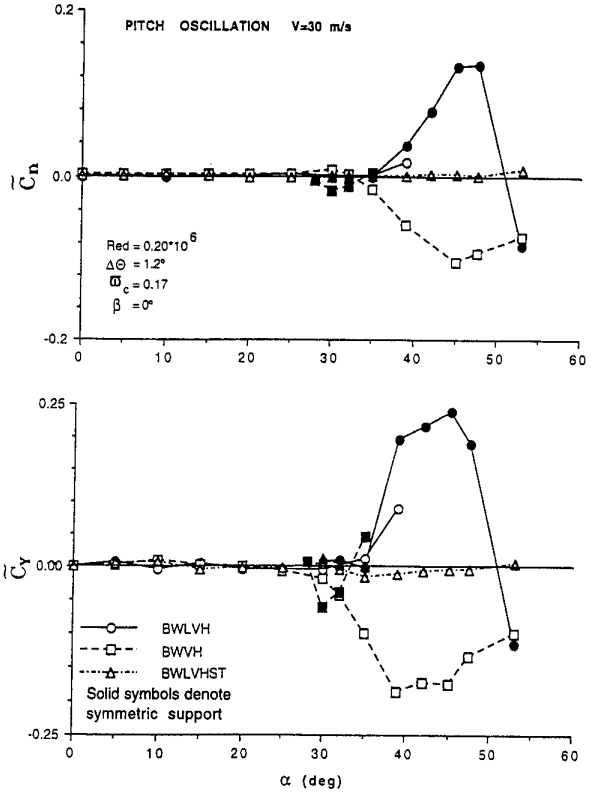

Fig. 5.29 Configurational effects on the lateral-directional aerodynamic coefficients.

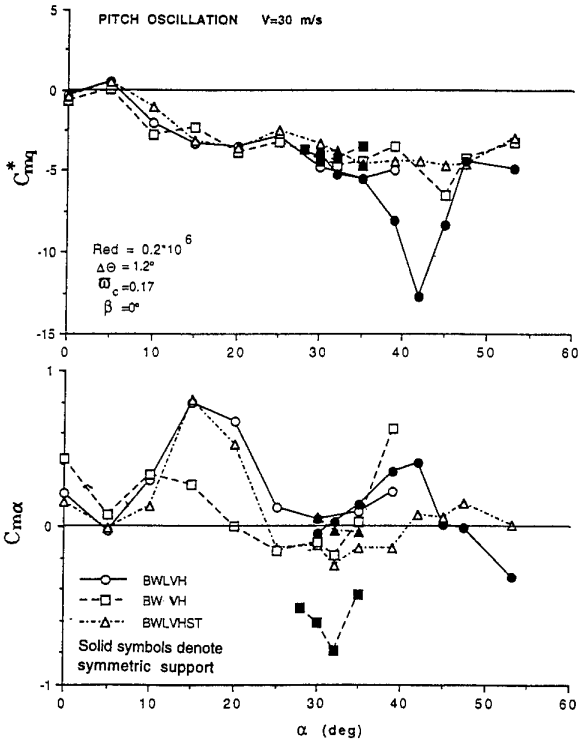

Fig. 5.30 Configurational effects on the derivatives C_{mq}* and $C_{m\alpha}$.

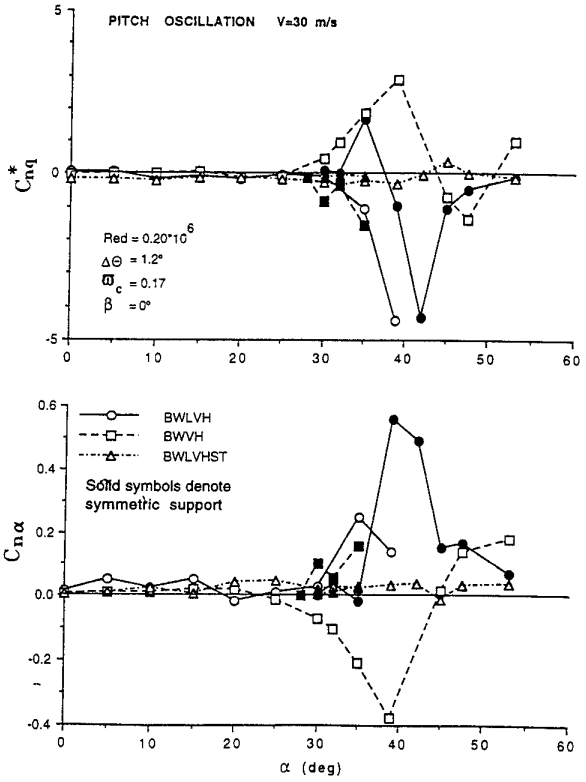

Fig. 5.31 Configurational effects on the derivatives C_{nq}* and $C_{n\alpha}$.

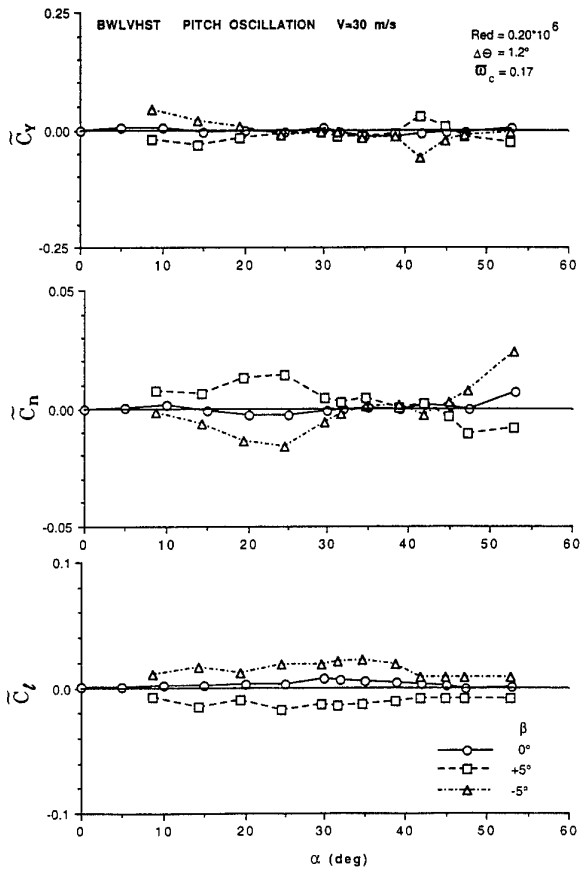

Fig 5.32 The effect of sideslip on the lateral-directional aerodynamic coefficients for BWLVHST configuration in pitch oscillation.

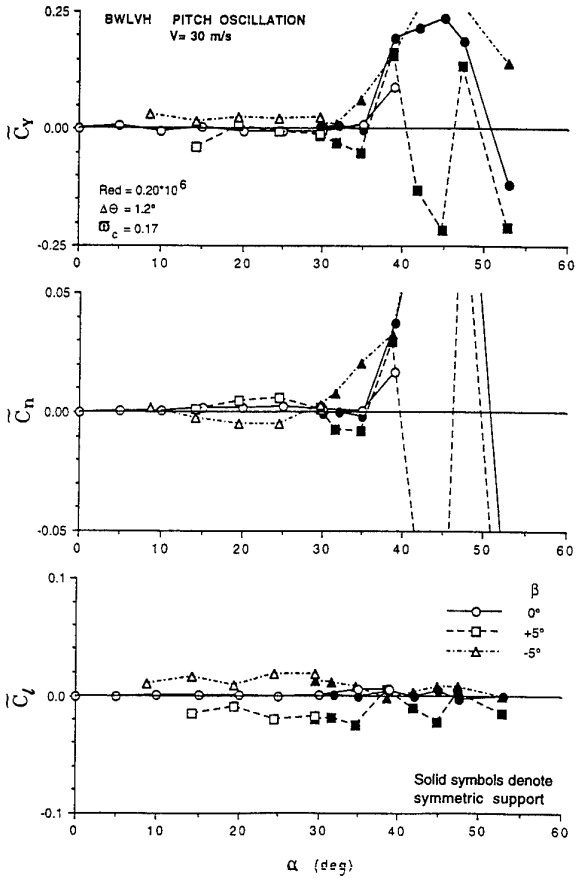

Fig 5.33 The effect of sideslip on the lateral-directional aerodynamic coefficients for BWLVH configuration in pitch oscillation.

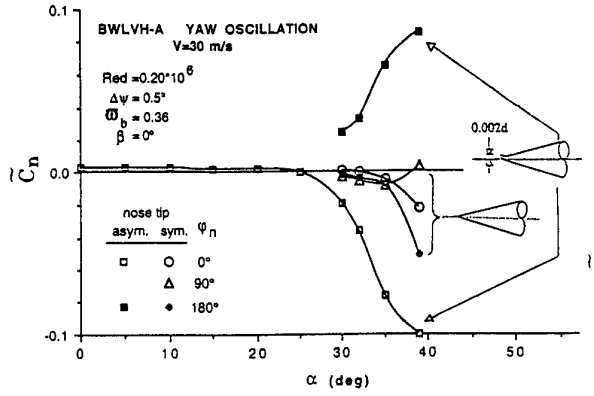

Fig 5.34 Effect of nose tip geometry on $\tilde{C}_n$.

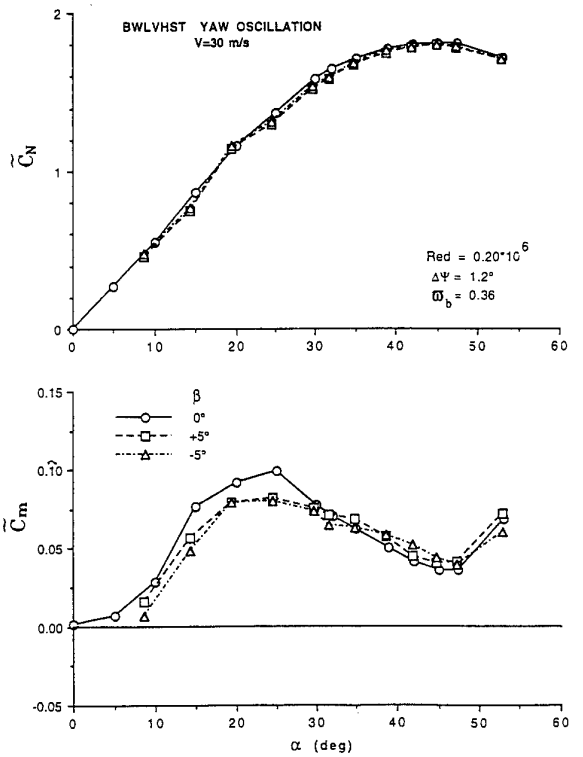

Fig 5.35 The effect of sideslip on the longitudinal aerodynamic coefficients for BWLVHST configuration in yaw oscillation.

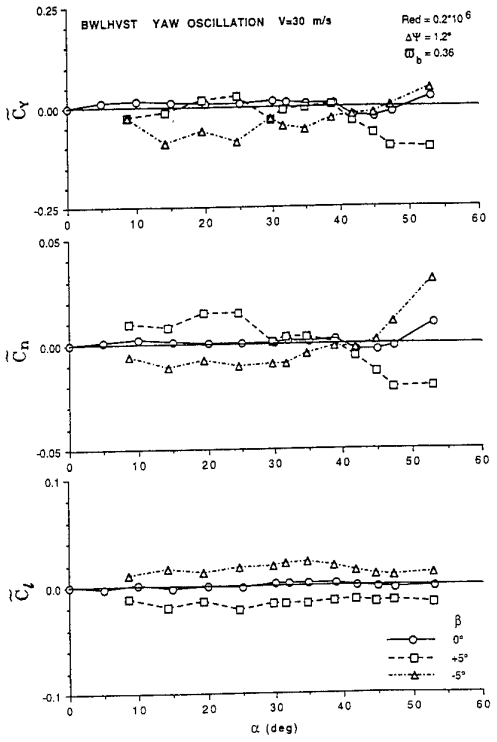

Fig 5.36 The effect of sideslip on the lateral-directional aerodynamic coefficients for BWLVHST configuration in yaw oscillation.

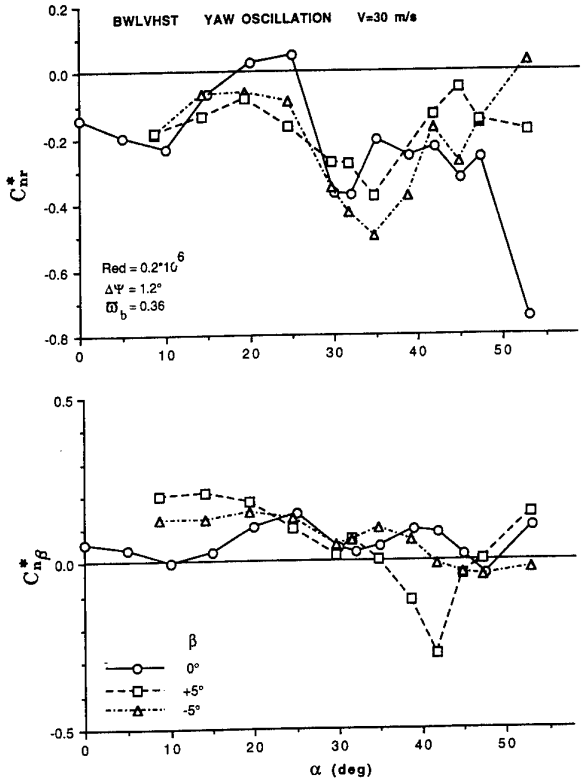

Fig 5.37 The effect of sideslip on derivatives C_{nr}* and $C_{n\beta}$* for BWLVHST configuration in yaw oscillation.

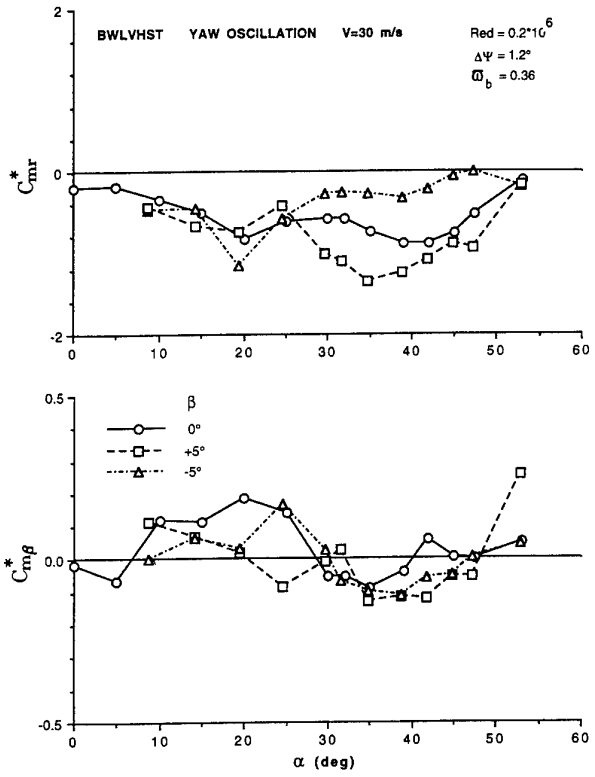

Fig 5.38 The effect of sideslip on derivatives C_{mr}* and $C_{m\beta}$* for BWLVHST configuration in yaw oscillation.

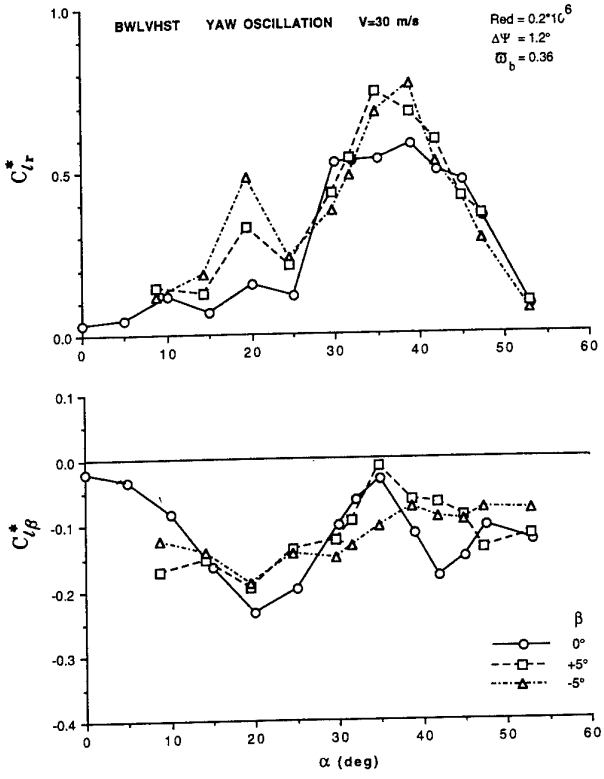

Fig 5.39 The effect of sideslip on derivatives C_{lr}* and $C_{l\beta}$* for BWLVHST configuration in yaw oscillation.

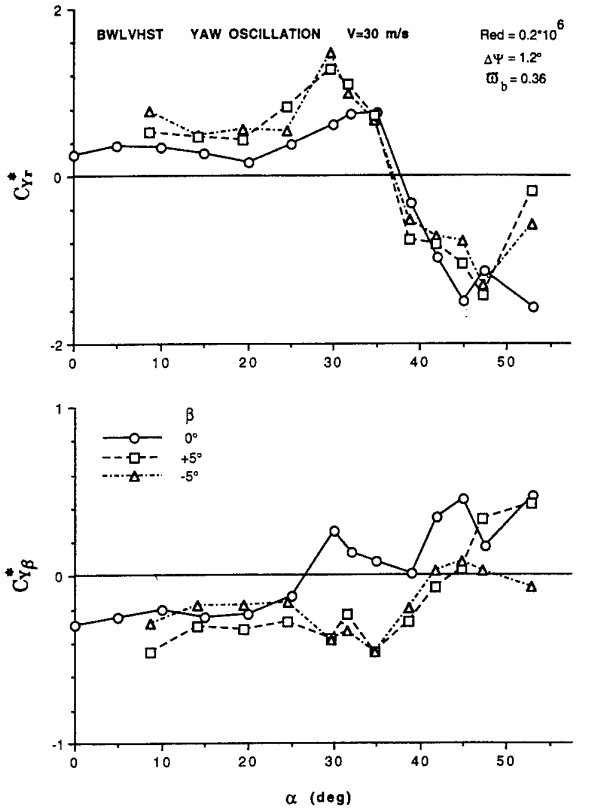

Fig 5.40 The effect of sideslip on derivatives C_{Yr}* and $C_{Y\beta}$* for BWLVHST configuration in yaw oscillation.

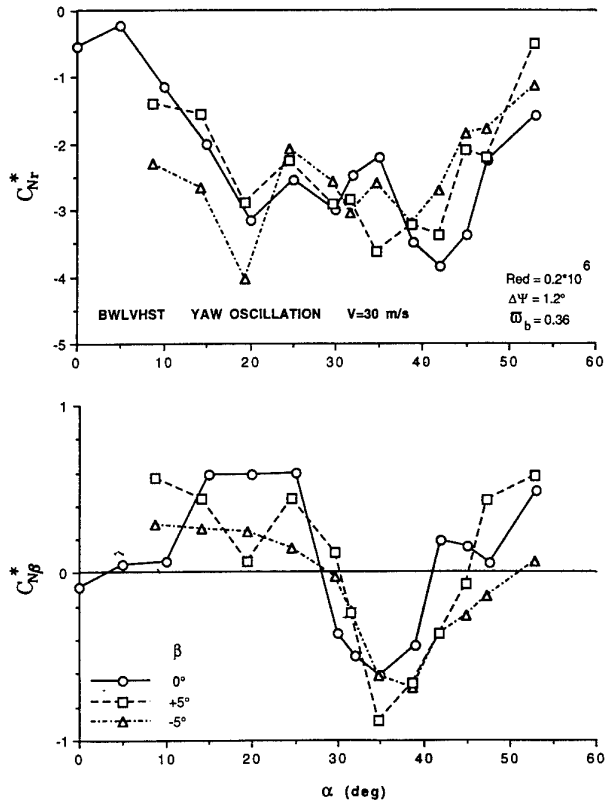

Fig 5.41 The effect of sideslip on derivatives C_{Nr}* and $C_{N\beta}$* for BWLVHST configuration in yaw oscillation.

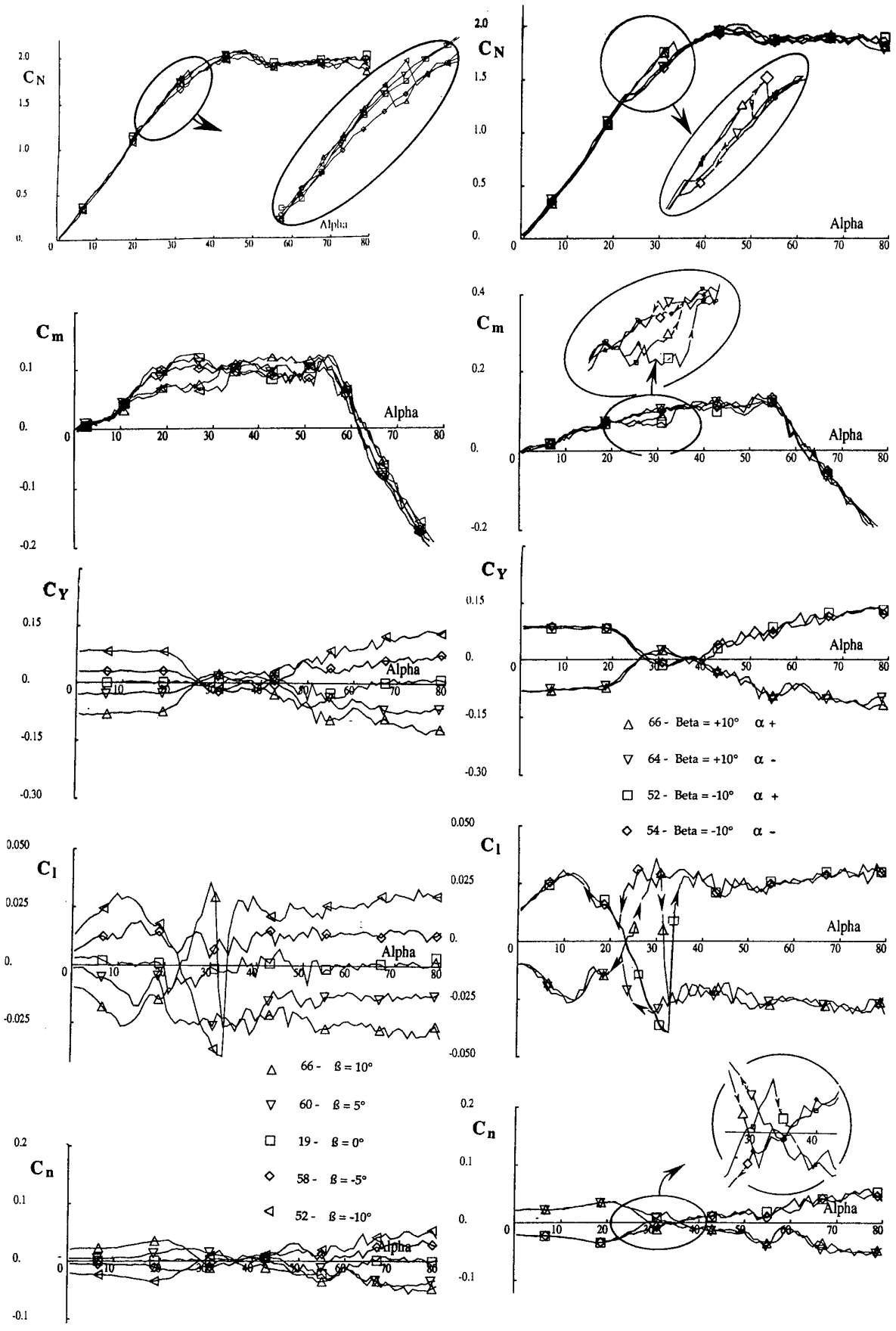

Fig. 5.42 Slow Alpha-sweeps - BWLHVST Configuration - Sideslip effect.

Fig. 5.43 Slow Alpha-sweeps - BWLHVST Configuration Hysteresis effect at β = 10° and -10°.

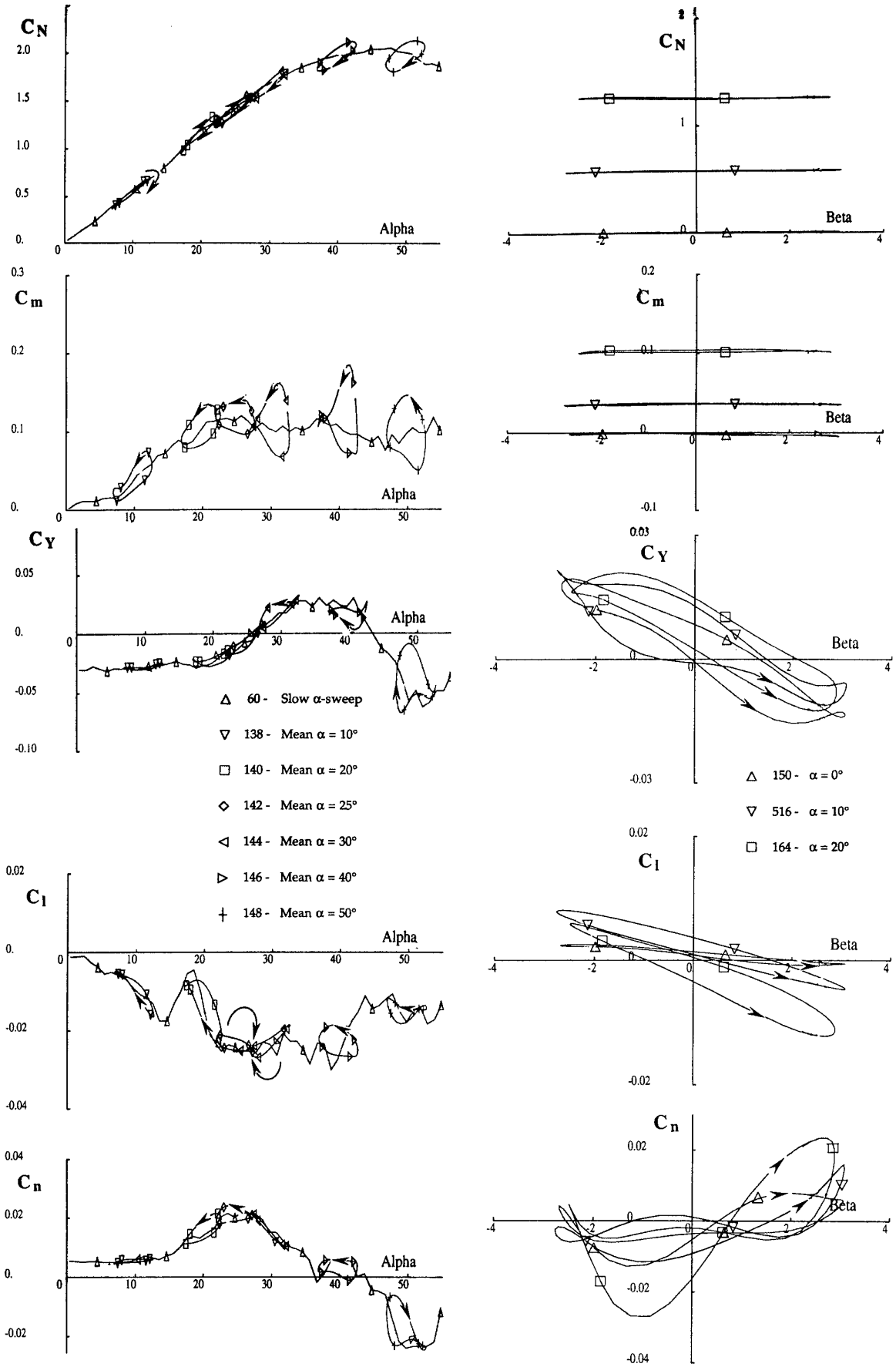

Fig. 5.44 Pitch oscillations at β = 5°, f = 2.5 Hz, Amp. = 2.9° BWLHVST Configuration.

Fig. 5.45 Yaw oscillations at β = 0°, f = 2.5 Hz, Amp. = 2.9° BWLHVST Configuration.

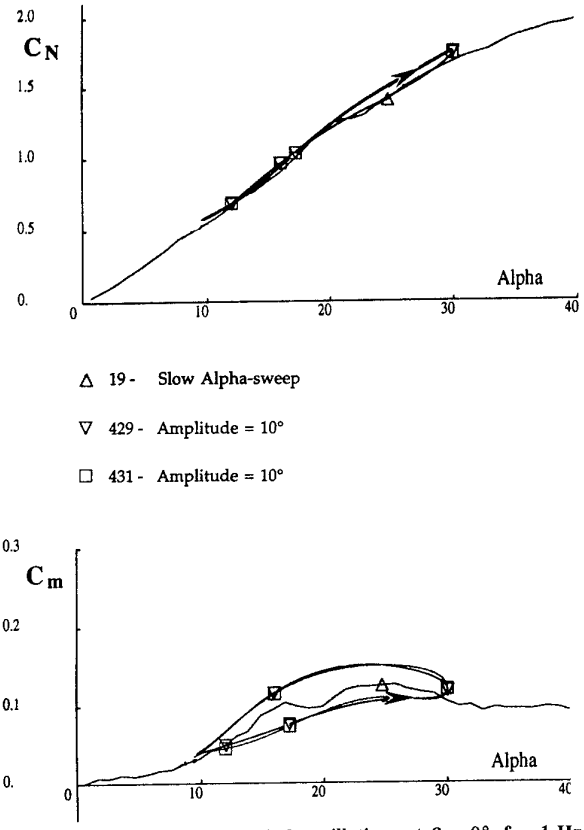

Fig. 5.46 Large amplitude pitch oscillations at β = 0°, f = 1 Hz Repeatibility tests - BWLHVST Configuration.

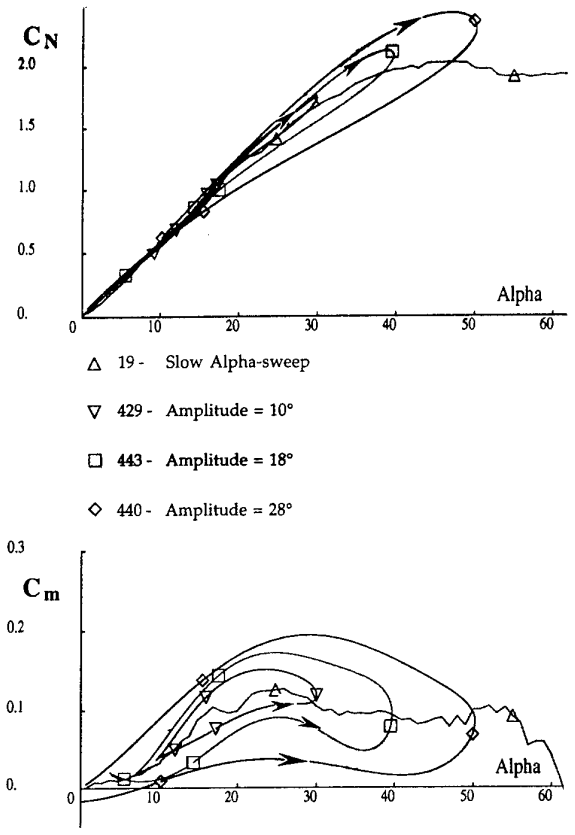

Fig. 5.47 Large amplitude pitch oscillations at β = 0°, f = 1 Hz Amplitude effect Mean α=20° BWLHVST Configuration

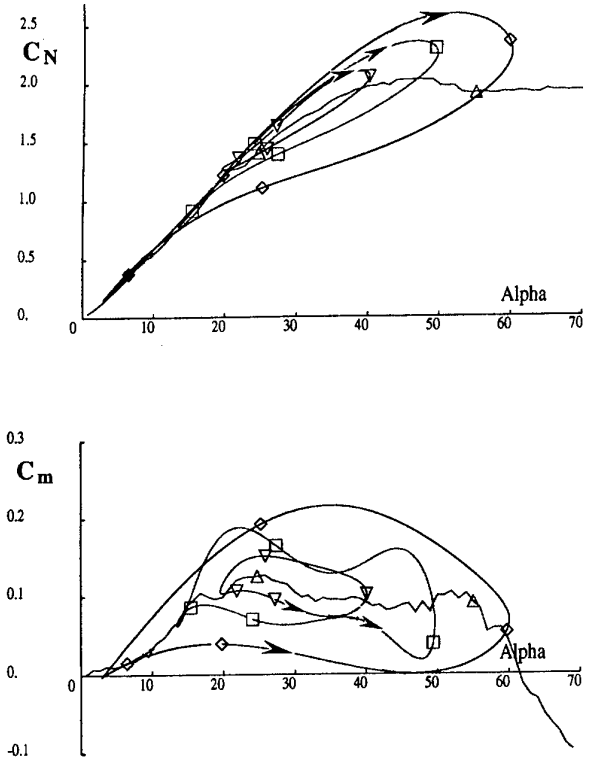

Fig. 5.48 Large amplitude pitch oscillations at β = 0°, f = 1 Hz Amplitude effect - Mean α=30° - BWLHVST Configuration

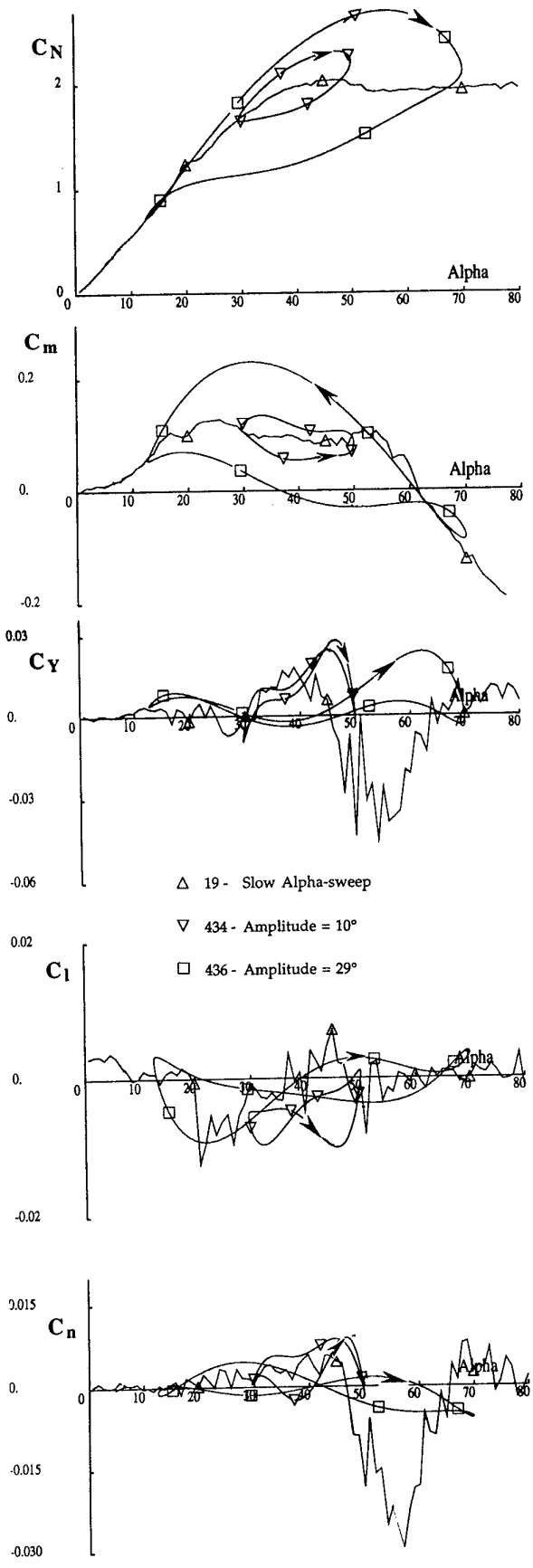

Fig. 5.49 Large amplitude pitch oscillations at $\beta = 0°$, f = 1 Hz
Amplitude effect - Mean $\alpha = 40°$ - BWLHVST Configuration

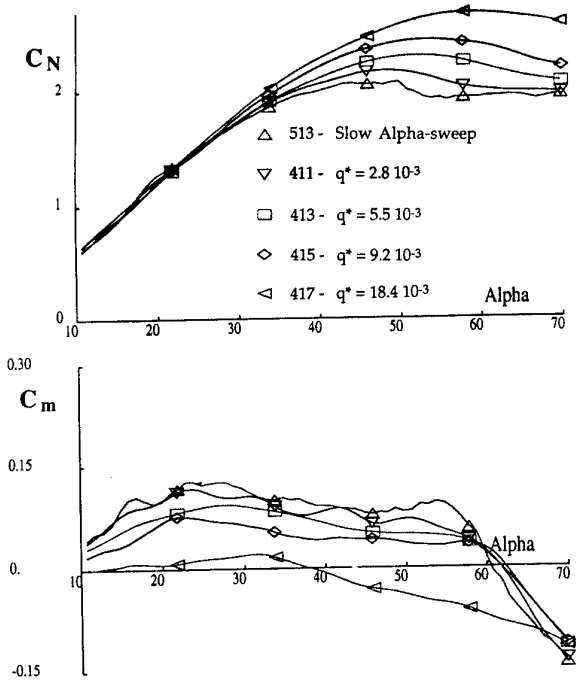

Fig. 5.50 Alpha-ramps - BWLHVST Configuration - $\beta = 0°$.

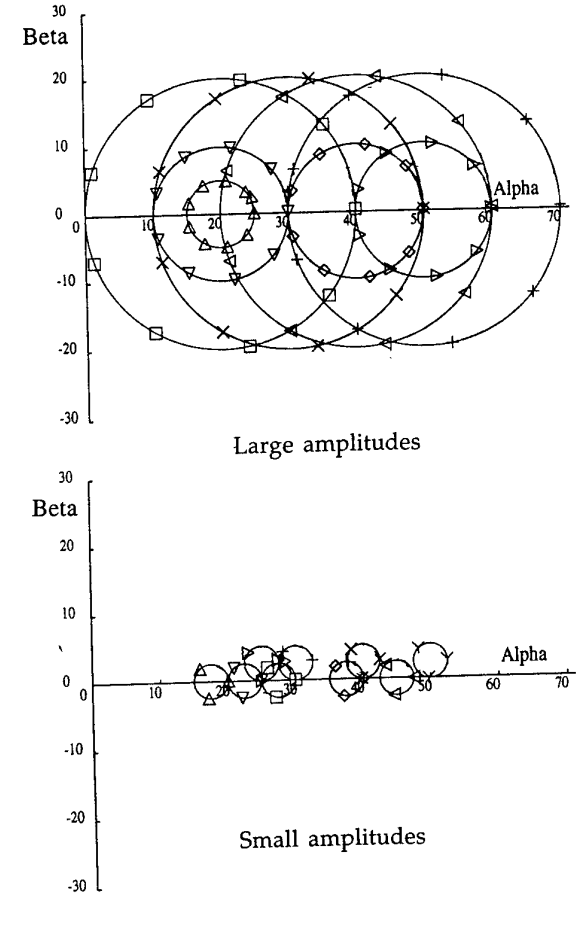

Fig. 5.51 Oscillatory coning tests - Trajectories in { α - β } plane
Large and small amplitudes.

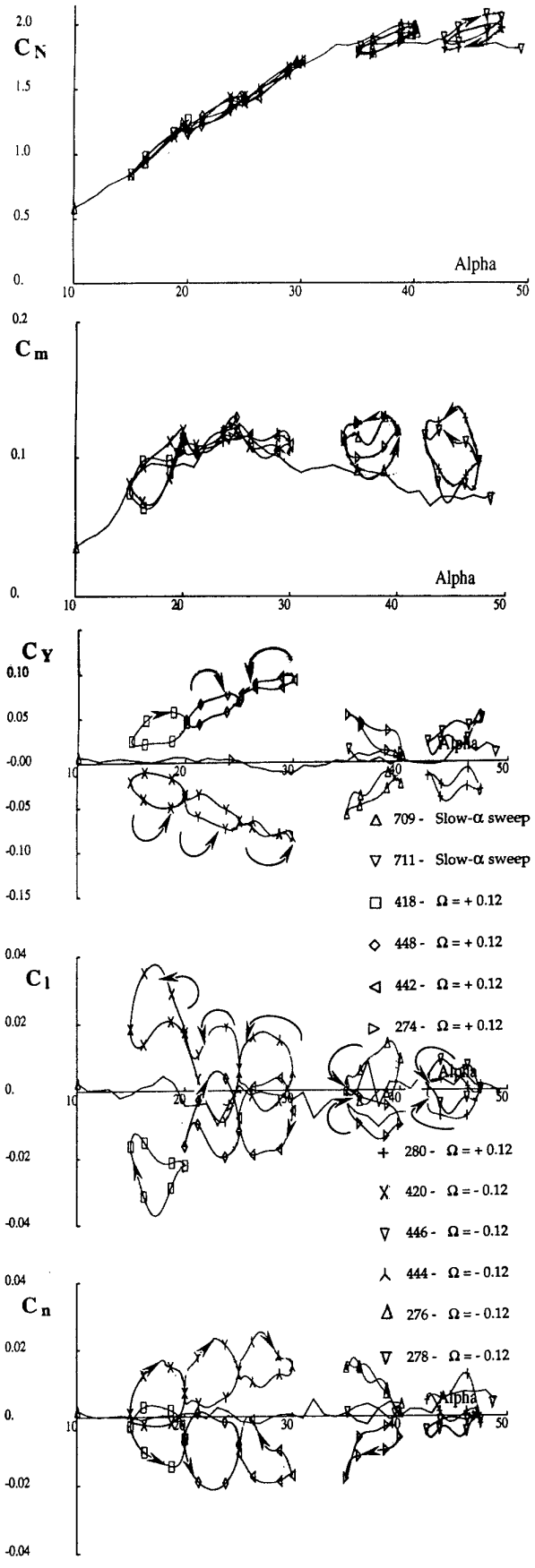

Fig 5.52 Small amplitude oscillatory coning tests BWLHVST Configuration - Mean $\beta = 0°$, $\Omega = \pm 0.12$.

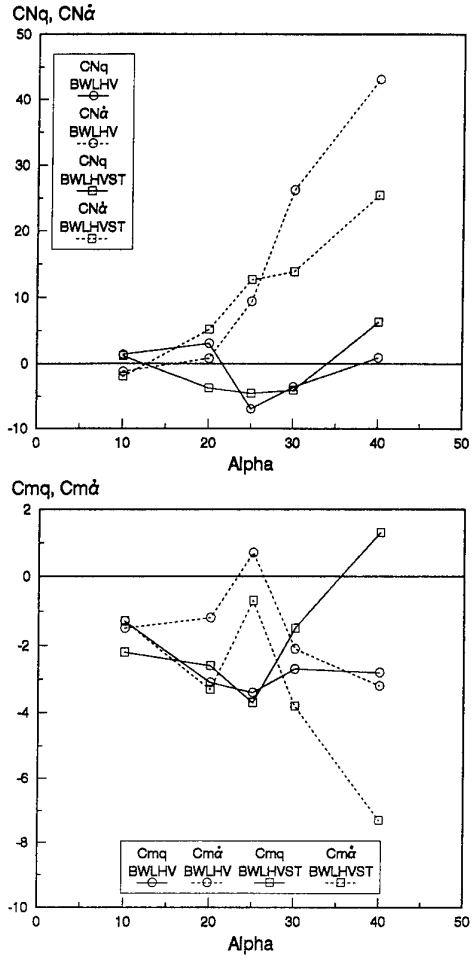

Fig. 5.53 Longitudinal damping derivatives from oscillatory coning tests - BWHLV and BWHLVST configurations.

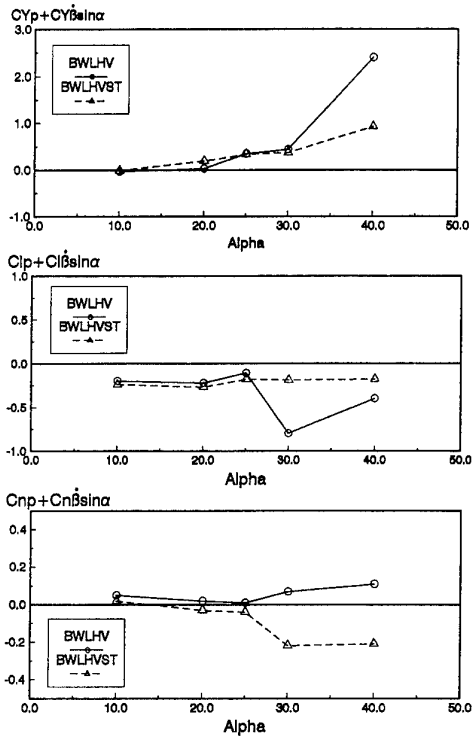

Fig. 5.54 Lateral-directional rolling derivatives from oscillatory coning tests - BWHLV and BWHLVST configurations.

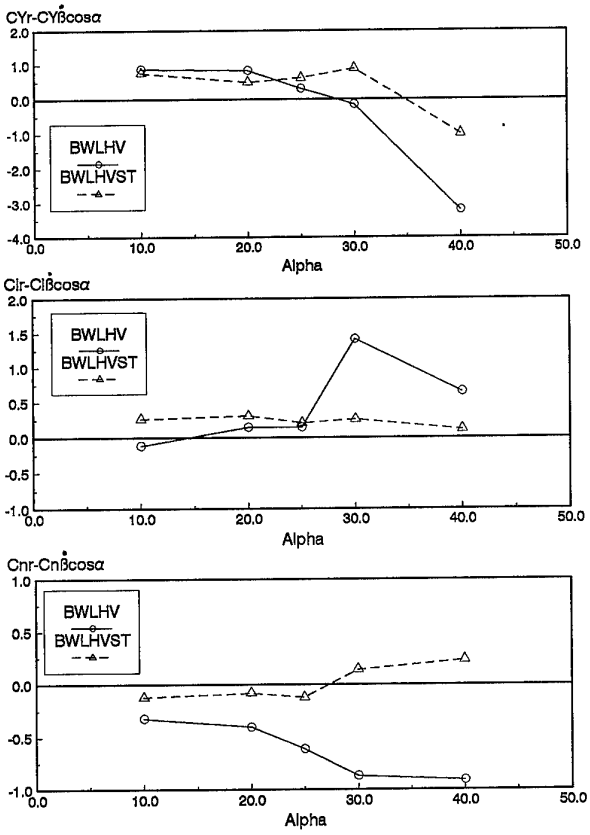

Fig. 5.55 Lateral-directional yawing derivatives from oscillatory coning tests - BWHLV and BWHLVST configurations.

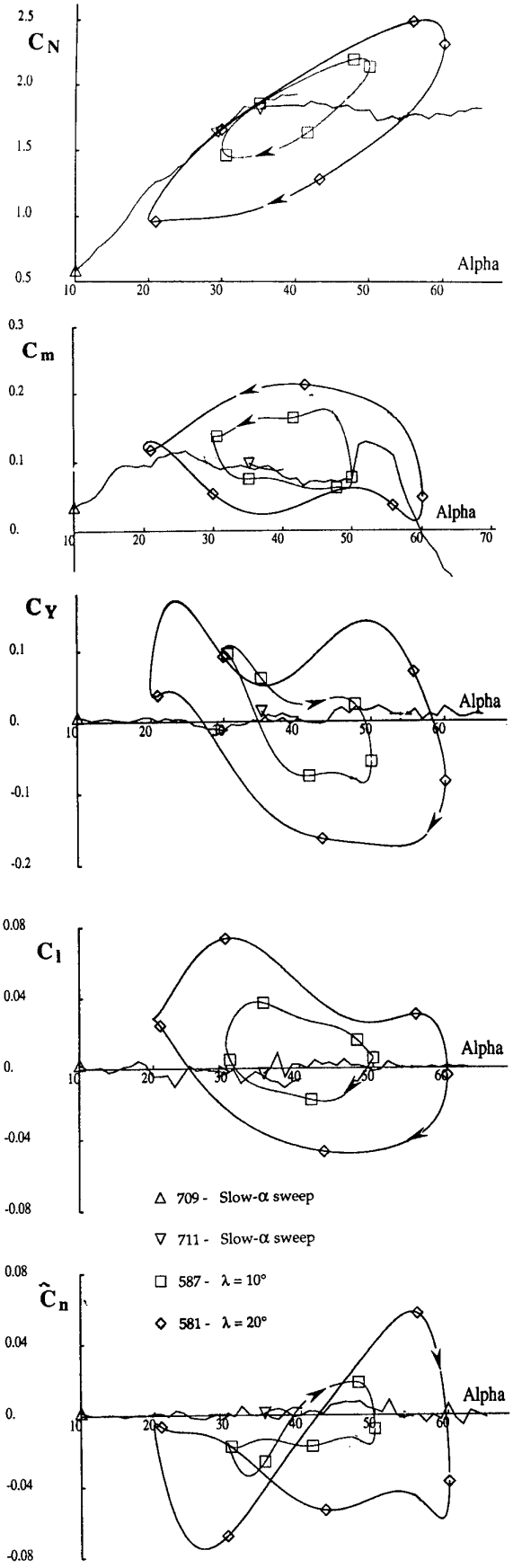

Fig 5.56 Large amplitude oscillatory coning tests Amplitude effect. Mean β = 0°, Ω=0.12 BWLHVST Configuration.

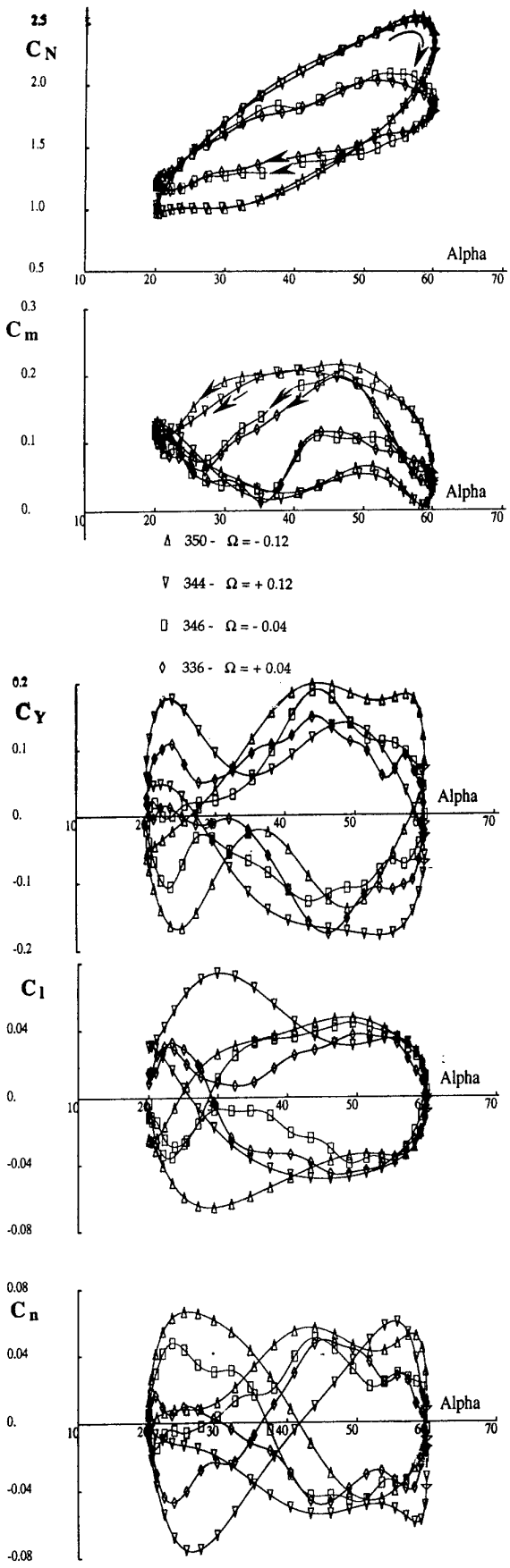

Fig 5.57 Large amplitude oscillatory coning tests - Rate effect
λ = 20°, mean α = 40°, mean β = 0°
BWLHVST Configuration

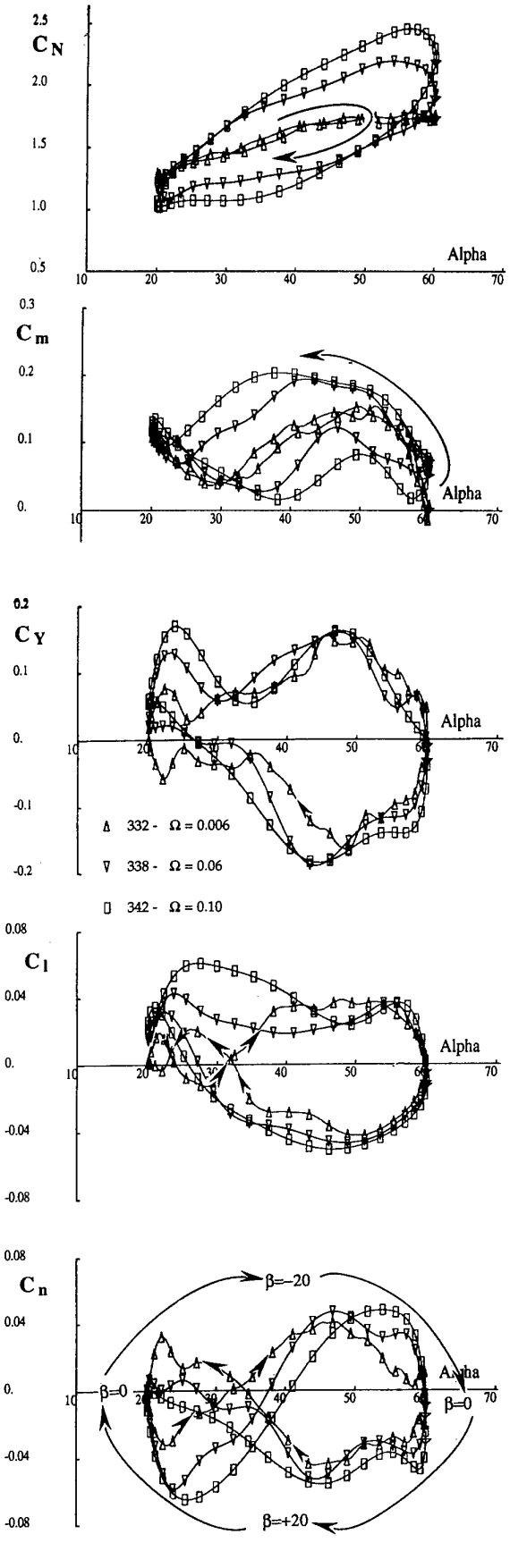

Fig 5.58 Large amplitude oscill. coning tests - Rate effect (cont.)
λ = 20°, mean α = 40°, mean β = 0°
BWLHVST Configuration

CHAPTER 6

CORRELATION OF OSCILLATORY-BALANCE RESULTS

6. 0 INTRODUCTION

This chapter deals with the correlation of oscillatory-balance results, obtained by four organizations: DRA, ONERA/IMFL, TPI and NRC/IAR. The tests were performed using models WG16A and WG16CA. The external shapes of the two models are identical: the former was constructed for the tests in the European facilities and the latter for the tests in North-America.
The influence of various configurational components, such as nose strakes, longitudinal transition strips and LEX, were investigated in each of the facilities mentioned above.

Most of the results are presented as functions of angle of attack, identifying three ranges: linear, stall and post-stall. Some results are also given as functions of angle of sideslip.
The effects of oscillation frequency and oscillation amplitude were also investigated, but the results are discussed in Chapters 5 and 8.

The subject of the present chapter is the correlation of the oscillatory results obtained in each of the four facilities involved, in order to evaluate the influence of:

- different rig support systems,
- dimensions and geometry of the wind tunnel working sections,
- flow characteristics of the wind tunnels,
- data acquisition and data reduction systems.

The repeatability of the results was assessed in all facilities, and was found very satisfactory; this is discussed in the organizational test reports listed in Appendix 1.
As expected, some results were strongly affected by the facility characteristics (the support asymmetry is an important example), as will be shown.

The derivatives considered in the present correlation are summarized in Table 6.1. The ranges of angle of attack and angle of sideslip are given for each facility.
Most derivatives were measured in three or four facilities, providing adequate data for a meaningful correlation.

6. 1 EXPERIMENTAL RESULTS

The primary aim of the correlation is to evaluate the reliability of tests done on the same model configuration in the different facilities, by focusing the analysis on the high angle of attack regime and identifying the sensitivity of coefficients and derivatives to the characteristics of the experimental apparatus.
Results are presented for two configurations: clean, BWLVH (B-body, W-wing, L-LEX, V-vertical tail, H-horizontal tail), and with strakes and transition strips, BWLVHST (S-strakes, T-transition strips). The effects of the LEX on longitudinal stiffness and damping derivatives were also examined.

The available coefficients and derivatives correlated are listed in Table 6.1. The table includes the organizations involved in each correlation, the coefficients and derivatives correlated and the ranges of angle of attack and sideslip considered.
As can be seen, most of the coefficients and derivatives were measured in three or four facilities, which improves the reliability of the correlation.

The first correlation deals with static results obtained on the oscillatory rigs of four organizations (DRA, IAR, IMFL, TPI) in the range of angle of attack 0°- 45° where the largest number of the results were available. The effect of the sideslip angle was also investigated, but the correlation is limited to the longitudinal coefficients C_N and C_m.
The contributions of the strakes and transition strips on the clean configuration were analyzed for the lateral-directional coefficients C_Y, C_l and C_n.

The analysis of the oscillatory results, including static and oscillatory data (stiffness, damping and cross-coupling derivatives) is mainly based on the investigation of the effectiveness of the nose strakes in the high angle of attack regime. The presence of the strakes enhances the cross-correlation of the results obtained in facilities having different flow characteristics because of their symmetrization effect on the forebody vortices. Without strakes the asymmetry of those vortices has a random behaviour, which depends on the microasymmetries of the model nose tip and on the flow field in the wind tunnel.
When using the strakes, together with the transition strips (for the optimization of the position of those devices refer to Chapter 2), the results became coherent, even though the different geometries of the working sections and support rigs, added to the different flow qualities, caused an evident effect for angles of attack above 25°- 30°.

It should be noted that only TPI, among the four organizations involved in the small- amplitude oscillation tests, utilizes a vertical strut support. Nevertheless, with the nose strakes, TPI results are in good agreement with the other data, even at high angles of attack. In this case, and for this test procedure, the results seem not to be affected by the configuration of the model support.

For oscillations in pitch, the stiffness, damping and cross-coupling derivatives were correlated at zero sideslip angle and only the contribution of nose strakes and transition strips was investigated.
As regards the effect of sideslip angle, two values have been evaluated for the oscillations in pitch: 0° and +5°.

The effect of the presence of the LEX on longitudinal stiffness and damping derivatives was illustrated.

The results of the oscillations in yaw were available (at zero sideslip angle) from three organizations (DRA, IAR, IMFL) and correlations were done on stiffness derivatives, damping derivatives and cross derivatives.
According to the test program determined at the beginning of the activity, the oscillations in roll have been carried out only by two organizations (DRA and TPI), but roll derivatives are also available from oscillatory-coning tests at IMFL.
The effect of the Reynolds number is not discussed in this chapter.

Summarizing, this chapter includes:

- static results for the BWLVH (clean) configuration, versus angle of attack, in the range 0°- 45°, where most of the data were available, for five sideslip angles (0°, +5°, -5°, +10°, -10°) and for the BWLVHST (forebody strakes and transition strips) configuration. In the latter case only sideslip angles of 0° and +/- 5° were included in the test program.
  A summary of longitudinal and lateral-directional results is given.
- oscillatory-balance results for pitch, roll and yaw oscillations in the α range 0°- 45°. Three values of the sideslip angle (0°, +5°, -5°) were used in pitch for the BWLVH configuration, two (0°, +5°) for the BWLVHST configuration, and only one (0°) for the clean configuration with LEX removed, BWVH. The lateral-directional oscillatory tests were carried out only at zero sideslip, for both the BWLVH and BWLVHST configurations.

The summaries of the test programs, including organizations, configurations investigated, wind tunnel velocity and values of the sideslip angle, are presented in section 6.2 for static tests, in sub-section 6.3.1 for oscillatory tests in pitch, in sub-section 6.3.2 for oscillatory tests in roll and in sub-section 6.3.3 for oscillatory tests in yaw.

6. 2 STATIC RESULTS

The static test results were available from DRA, IAR, IMFL and TPI, as shown in the following table:

CONFIG.	β	V. (m/s)	DRA	IMFL	IAR	TPI
BWLVH	+0°	30	X	X	X	X
BWLVH	+0°	25		X	X	X
BWLVH	-10°	30		X		X
BWLVH	-5°	30	X	X		X
BWLVH	+5°	30	X	X		X
BWLVH	+10°	30		X		X
BWLVH/S/T	+0°	30	X	X		X
BWLVH/S/T	-5°	30	X	X		X
BWLVH/S/T	+5°	30	X	X		X

The most significant static coefficients obtained with the oscillatory rigs (except for DRA data, which were measured with a static balance) are presented in Figs 6.1 to 6.20. The available data cover the complete range of angle of attack from 0° to 45°. For β= +/- 10°, only two sets of data were available (IMFL, TPI).
Transition strips were used only on the BWLVHST configuration (together with strakes). This topic is discussed in other chapters.
On the whole, there is a good agreement in the linear range of α, from 0° to 25°. In Figs 6.1 to 6.5 the position of the typical kink in the slope of the normal force coefficient C_N is in good agreement, in the proximity of α=22°, for zero sideslip.
The results are not influenced by the support geometries nor by the shape and the dimensions of the working sections of the wind tunnels.
Differences become evident at α larger than 25° for the longitudinal coefficients C_N and C_m (Figs 6.1 to 6.10). Similar differences have been found and discussed in Chapter 4.
Referring to Figs 6.13 to 6.20 it can be seen that supports and wind tunnel characteristics affect the side force coefficient C_Y and the yawing moment coefficient C_n. Even at zero angle of sideslip these coefficients are not zero through the complete angle of attack range; the departure from zero in the non-linear range of angle of attack is caused by the asymmetry of the forebody vortices, which depends on the test apparatus and on the flow characteristics in the wind tunnel. The strakes eliminate the asymmetry of the forebody vortices (Figs 6.14 and 6.20).

The effect of strakes is similar for the rolling moment coefficient. The wider asymmetry in the TPI results is a consequence of the asymmetric shape of the support (roll configuration: see Chapter 3). With the strakes, the flow on the forebody is almost symmetric and the rolling moment is less sensitive to the asymmetries of the support. Hence, the non-linear coupling between separated forebody flows and support is reduced.
Nevertheless, in the non-linear range of α a weakly asymmetric trend is still present for the BWLVHST configuration (Figs 6.11 and 6.12). In Chapter 4 this phenomenon is explained by wing stall asymmetry.

6.2.1 Summary of Longitudinal Results

An overall analysis of the static longitudinal results leads to the following remarks:

- above 25°- 30° of incidence, the pitching moment coefficient C_m is more sensitive to the support geometry than the normal force coefficient C_N.
- a rear sting is recommended for use above α=30°. Above this limit, significant differences in the normal force and, more evidently, the pitching moment trends are found; for the TPI data this is probably caused by the presence of the vertical strut.
- the presence of the ventral strut does not influence the results in the linear range.
- good agreement is present in the whole linear range of α, where the support has a very small effect on the quality of measurements.

6.2.2 Summary of Lateral-Directional Results

The general conclusions for static lateral directional results are:

- as already discussed in Chapter 4, at zero sideslip the side force coefficient C_Y, the rolling moment coefficient C_l and the yawing moment coefficient C_n are zero up to α equal to 25°- 30°.
- in the non-linear range of α, where the asymmetric flow field on the forebody is present, the coefficients depend on the forebody shape as well as on the rig and wind tunnel flow characteristics, both at zero and non-zero sideslip.
- with strakes attached, the coefficients are zero or small through the angle of attack range investigated, due to the effect of the strakes, as explained in Chapter 4.
- the presence of the strakes results in good correlation of the data in stall and post-stall range, even if asymmetric support rigs are used.

- a strong asymmetric trend is present in the rolling moment coefficient in the α range 20°-40°, consistently reduced with strakes attached, due to the sensitivity of rolling moment to wing stall asymmetry.

6. 3 OSCILLATORY RESULTS

The oscillatory-balance test activity was concentrated mainly on comparisons of three configurations, BWLVH, BWLVHST and BWVH.
Twenty two oscillatory derivatives were correlated (see Table 6.1).

As previously mentioned for the static tests, the model was tested with strakes and transition strips. Two different kinds of strips have been used (DRA and AEM), as already mentioned in previous chapters. In the present chapter no distinction is made between them.
Results are available from the four organizations involved in this activity: IMFL measurements refer both to the PQR and TourneBroche apparatus (see Chapter 3).

6. 3. 1 Oscillation in Pitch.

The static derivatives measured are: $C_{m\alpha}$, $C_{N\alpha}$, $C_{Y\alpha}$, $C_{l\alpha}$, $C_{n\alpha}$; the dynamic derivatives: $C_{mq}+ C_{m\dot{\alpha}}$, $C_{Nq}+ C_{N\dot{\alpha}}$ and the dynamic cross-coupling derivatives $C_{yq}+ C_{y\dot{\alpha}}$, $C_{lq}+ C_{l\dot{\alpha}}$, $C_{nq}+ C_{n\dot{\alpha}}$.
The test matrix for pitch oscillatory tests was:

CONFIG.	β	V.(m/s)	DRA	IMFL PQR	IMFL TB	IAR	TPI
BWLVH	+0°	30	X		X	X	X
BWLVH	-5°	30				X	X
BWLVH	+5°	30				X	X
BWLVH/S/T	+0°	30	X	X	X	X	X
BWLVH/S/T	+5°	30		X		X	X

Figures 6.21 to 6.44 present the most significant results. For brevity the superscript * has been used in the titles to indicate combined derivatives, however in the diagrams the complete name of those derivatives is used.
Figures 6.21 to 6.24 show the plots of derivatives $C_{N\alpha}$ and $C_{m\alpha}$ for the BWLVH and BWLVHST configurations at zero sideslip.
Differences in the data measured are evident in the whole range of angle of attack considered. However, the important effect of strakes and transition strips in the non-linear range of α appears, as in the static case.
As a matter of fact, Fig 6.22 shows a similar trend of the curves in the non-linear range of α and this tendency is even more evident for $C_{m\alpha}$, in Fig 6.24.

There are presently some unexplained differences among results from each facility at low angles of attack. The corresponding values calculated for static tests (averaging over 2.5° intervals) are also plotted for comparison (the good agreement of static data in the range 0°- 25° α does not require identification of the different test facilities).
Two different symbols are used to identify the IAR results: they refer to the tests with symmetric and asymmetric supports, as explained in Chapter 5.

The values of the damping derivatives $C_{Nq}+ C_{N\dot{\alpha}}$ and $C_{mq}+ C_{m\dot{\alpha}}$ are fairly coherent below 25° α for the BWLVH configuration (Figs 6.25 and 6.27); with strakes attached and transition strips on (Figs 6.26 and 6.28) only relatively small differences are observed in the complete range of α.

The static derivatives $C_{Y\alpha}$, $C_{l\alpha}$ and $C_{n\alpha}$ (Figs 6.29 and 6.30, 6.33 and 6.34, 6.37 and 6.38) are mostly small in the linear range of angle of attack and remain around zero in the complete range when strakes and transition strips are added.
A similar behaviour characterizes the cross-coupling derivatives $C_{Yq}+C_{Y\dot{\alpha}}$, $C_{lq}+C_{l\dot{\alpha}}$ and $C_{nq}+ C_{n\dot{\alpha}}$ (Figs 6.31 and 6.32, 6.35 and 6.36, 6.39 and 6.40).

In addition to the discussion in Chapter 5, one can also examine the effect of LEX by comparing Figs 6.21, 6.23, 6.25 and 6.27 (BWLVH) with Figs 6.41 to 6.44 (BWVH). The most noticeable is the increase of $C_{N\alpha}$ values in the non-linear α-range, evident from the TPI data and the IAR asymmeric support data.
The presence of the LEX does not affect significantly the results for damping derivatives.

In conclusion, as already seen for static tests, nose strakes and transition strips on the forebody of the model improve the correlation of oscillatory-balance results in pitch for different support and wind tunnel geometries.

6. 3. 2 Oscillation in Roll

This section describes the effect of nose strakes and transition strips determined from oscillatory roll tests: static derivatives $C_{Y\beta}\sin\alpha$, $C_{l\beta}\sin\alpha$ and $C_{n\beta}\sin\alpha$, damping derivative $C_{lp}+ C_{l\dot{\beta}}\sin\alpha$, and cross derivatives $C_{yp}+ C_{Y\dot{\beta}}\sin\alpha$ and $C_{np}+C_{n\dot{\beta}}\sin\alpha$.
The tests matrix is shown in the table below:

CONFIG.	β	V. (m/s)	DRA	IMFL	IAR	TPI
BWLVH	+0°	30	X	X		X
BWLVH/S/T	+0°	30	X	X		X

The oscillatory tests in roll demonstrate that the repeatability of the different tests is good in the linear range of α (Figs 6.45, 6.47, 6.49, 6.51, 6.53 and 6.55), but a wide scatter appears for α above 25°. The forebody strakes (always together with the transition strips) extend the good agreement of the results to the stall and post-stall ranges (Figs 6.46, 6.48, 6.50, 6.52, 6.54 and 6.56).
It should be noted that the excitation system geometry, behind the model wake, is different for pitch and roll case respectively at TPI (Chapter 3).

Due to individual test program, the correlation for direct derivatives is limited to the DRA and TPI data. For damping derivative $C_{lp}+ C_{l\dot{\beta}}\sin\alpha$ and cross derivatives $C_{np}+ C_{n\dot{\beta}}\sin\alpha$ and $C_{yp}+ C_{Y\dot{\beta}}\sin\alpha$ the IMFL data are also available.

6. 3. 3 Oscillation in Yaw

The derivatives evaluated during the yaw oscillatory tests and discussed in this section are: three static derivatives in yaw $C_{Y\beta}$, $C_{l\beta}$ and $C_{n\beta}$, two dynamic derivatives $C_{yr} - C_{y\dot{\beta}}\cos\alpha$ and $C_{nr} - C_{n\dot{\beta}}\cos\alpha$, and the cross derivative $C_{lr} - C_{l\dot{\beta}}\cos\alpha$.
The test matrix is shown in the following table:

CONFIG.	β	V. (m/s)	DRA	IMFL	IAR	TPI
BWLVH	+0°	30	X	X		
BWLVH/S/T	+0°	30	X	X	X	

Each of the static derivatives $C_{Y\beta}$, $C_{l\beta}$ and $C_{n\beta}$ has a different behaviour, specially for the BWLVH configuration. Therefore they must be considered separately. Correlation is not possible, because only DRA data are available for the BWLVH configuration.

$C_{Y\beta}$ is slightly negative for α below 30°; for α above this limit it increases consistently in the negative direction up to 37°, decreasing again to zero for α=42° (Fig 6.57). The BWLVHST configuration maintains the slightly negative value of BWLVH in the linear α range and the results hover around zero up to α=40°. From this point onwards the results of the two sets of tests diverge (Fig 6.58).

The trends of the $C_{n\beta}$ plots are similar, but this derivative stays almost on the zero axis in the linear field (Figs 6.61 and 6.62).
As discussed in Chapter 4, the large negative value of $C_{Y\beta}$ and $C_{n\beta}$ derivatives at angles of attack above 30° (BWLVH) could be the consequence of the micro-asymmetries on the nose tip, which determine, for α above 30°, whether the left or the right forebody vortex is higher at the critical angle of attack, causing a positive or negative yawing moment. With forebody strakes attached, the asymmetry is delayed to higher angle of attack.
The influence of the strakes and transition strips on the $C_{l\beta}$ derivative is insignificant (Figs 6.59 and 6.60).

Plots of the dynamic derivatives C_{Yr}- $C_{Y\dot{\beta}}\cos\alpha$ and C_{nr}- $C_{n\dot{\beta}}\cos\alpha$ show a good agreement even at high angle of attack, with strakes attached (Figs 6.64 and 6.66), but large divergences for the BWLVH configuration (Figs 6.63 and 6.65), confirming the effectiveness of the nose strakes for WG16 model.

The IMFL values in Fig 6.65 are not significantly different from zero, which seems to indicate only a limited asymmetric separation of the forebody vortices. A similar behaviour can be observed for C_{Yr}- $C_{Y\dot{\beta}}\cos\alpha$ only for α below 30° (Fig 6.63).

Finally, the effectiveness of the strakes can also be seen for the cross- derivative C_{lr}- $C_{l\dot{\beta}}\cos\alpha$ with zero sideslip (Figs 6.67 and 6.68), where the results are in good agreement for the BWLVHST configuration (with the exception of the DRA point at α=20°), but not for the BWLVH configuration.

6. 4 CONCLUSIONS

Static aerodynamic coefficients and static and dynamic derivatives were obtained for the WG16 configuration using oscillatory balances in wind tunnel facilities in four countries.

The effect of strakes, transition strips and LEX were examined for angles of attack up to 45°and in some cases, in the presence of sideslip.

With some exceptions, the results were found to be in good agreement in the linear range of α and, for the configuration with strakes and strips, also in the non-linear α range (α>25°).
However, the agreement in the non-linear range for the configuration without strakes and strips was poor. This was attributed to differences in the support systems and in the flow characteristics in the various facilities.
The high number of tests performed supports the validity of the correlations.

6. 5 REFERENCES

Various organizational reports, as listed in Appendix 1.

Coefficient/Derivative	Incidence	Sideslip	DRA	IMFL	IAR	TPI
C_Y	$\alpha = 0°\div45°$	$\beta = -10°\div10°$	X	X	X	X
C_N	$\alpha = 0°\div45°$	$\beta = -10°\div10°$	X	X	X	X
C_l	$\alpha = 0°\div45°$	$\beta = -10°\div10°$	X	X	X	X
C_m	$\alpha = 0°\div45°$	$\beta = -10°\div10°$	X	X	X	X
C_n	$\alpha = 0°\div45°$	$\beta = -10°\div10°$	X	X	X	X
C_{m_α}	$\alpha = 0°\div45°$	$\beta = -5°\div5°$	X		X	X
$C_{m_q} + C_{m_{\dot\alpha}}$	$\alpha = 0°\div45°$	$\beta = -5°\div5°$	X	X	X	X
C_{N_α}	$\alpha = 0°\div45°$	$\beta = -5°\div5°$	X		X	X
$C_{N_q} + C_{N_{\dot\alpha}}$	$\alpha = 0°\div45°$	$\beta = -5°\div5°$	X	X	X	X
C_{Y_α}	$\alpha = 0°\div45°$	$\beta = -5°\div5°$			X	X
$C_{Y_q} + C_{Y_{\dot\alpha}}$	$\alpha = 0°\div45°$	$\beta = -5°\div5°$			X	X
C_{l_α}	$\alpha = 0°\div45°$	$\beta = -5°\div5°$	X		X	X
$C_{l_q} + C_{l_{\dot\alpha}}$	$\alpha = 0°\div45°$	$\beta = -5°\div5°$	X		X	X
C_{n_α}	$\alpha = 0°\div45°$	$\beta = -5°\div5°$			X	X
$C_{n_q} + C_{n_{\dot\alpha}}$	$\alpha = 0°\div45°$	$\beta = -5°\div5°$			X	X
$C_{l_\beta} \sin\alpha$	$\alpha = 0°\div45°$	$\beta = 0°$	X			X
$C_{l_p} + C_{l_{\dot\beta}} \sin\alpha$	$\alpha = 0°\div45°$	$\beta = 0°$	X	X		X
$C_{n_\beta} \sin\alpha$	$\alpha = 0°\div45°$	$\beta = 0°$	X			X
$C_{n_p} + C_{n_{\dot\beta}} \sin\alpha$	$\alpha = 0°\div45°$	$\beta = 0°$	X	X		X
$C_{Y_\beta} \sin\alpha$	$\alpha = 0°\div45°$	$\beta = 0°$	X			X
$C_{Y_p} + C_{Y_{\dot\beta}} \sin\alpha$	$\alpha = 0°\div45°$	$\beta = 0°$	X	X		X
C_{n_β}	$\alpha = 0°\div45°$	$\beta = 0°$	X			
$C_{n_r} - C_{n_{\dot\beta}} \cos\alpha$	$\alpha = 0°\div45°$	$\beta = 0°$	X	X	X	
C_{Y_β}	$\alpha = 0°\div45°$	$\beta = 0°$	X			
$C_{Y_r} - C_{Y_{\dot\beta}} \cos\alpha$	$\alpha = 0°\div45°$	$\beta = 0°$	X	X	X	
C_{l_β}	$\alpha = 0°\div45°$	$\beta = 0°$	X			
$C_{l_r} - C_{l_{\dot\beta}} \cos\alpha$	$\alpha = 0°\div45°$	$\beta = 0°$	X	X	X	

TABLE 6.1

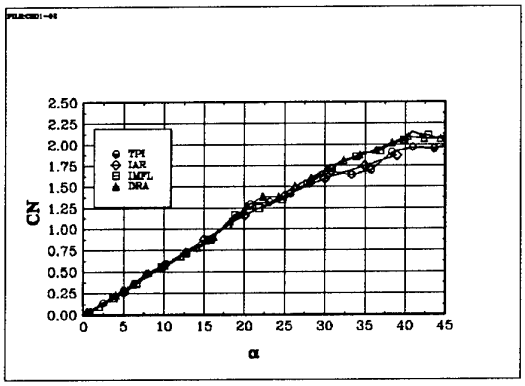

Fig 6.1 The coefficient CN: BWLVH, β= 0°

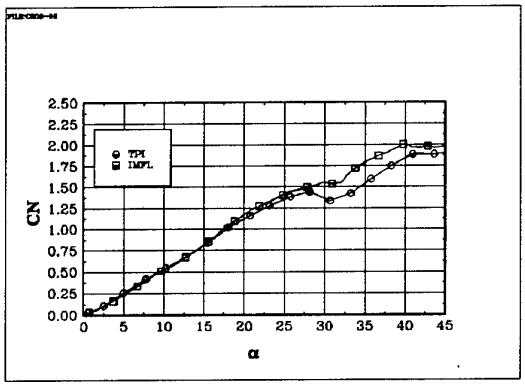

Fig 6.2 The coefficient CN: BWLVH, β= -10°

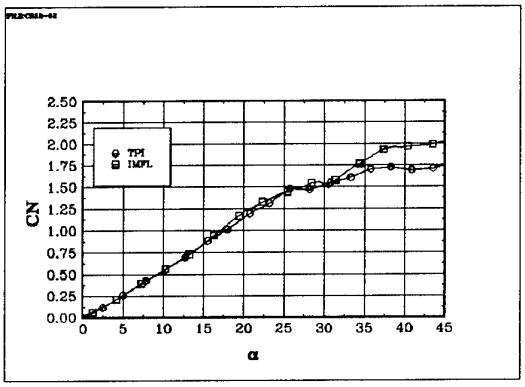

Fig 6.3 The coefficient CN: BWLVH, β= 10°

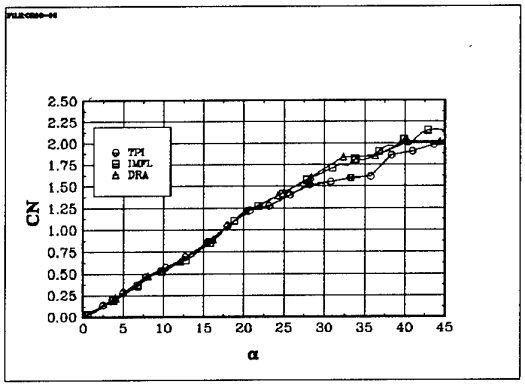

Fig 6.4 The coefficient CN: BWLVH, β= -5°

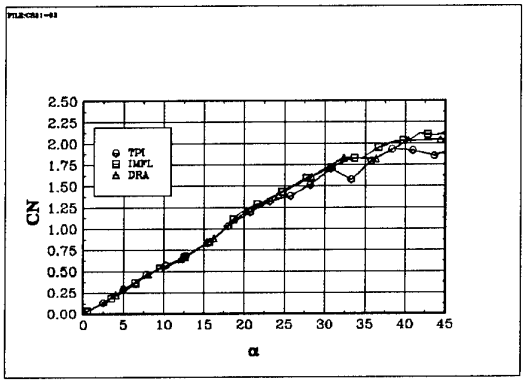

Fig 6.5 The coefficient CN: BWLVH, β =5°

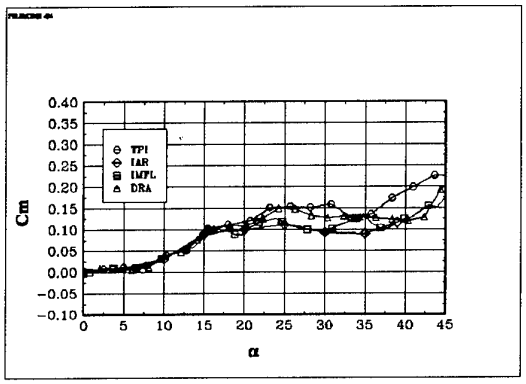

Fig 6.6 The coefficient Cm: BWLVH, β= 0°

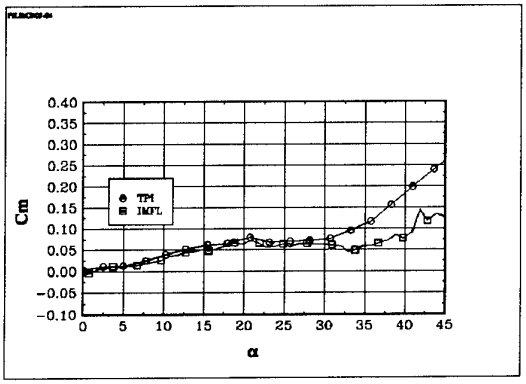

Fig 6.7 The coefficient Cm: BWLVH, β= -10°

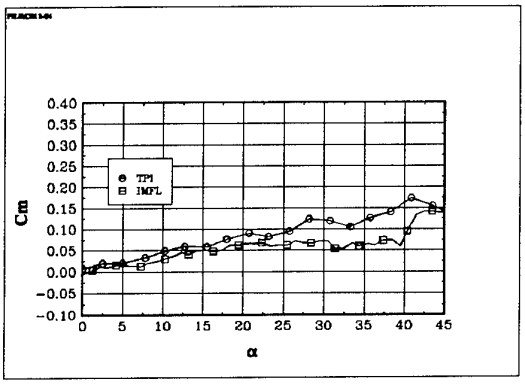

Fig 6.8 The coefficient Cm: BWLVH, β= 10°

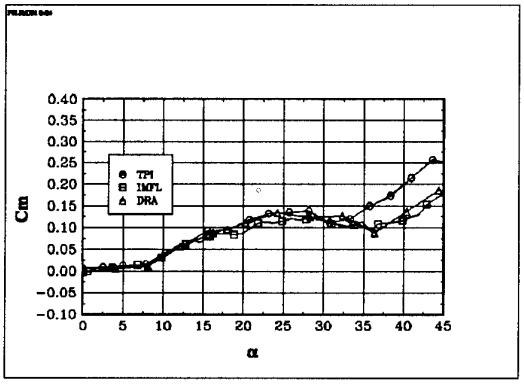

Fig 6.9 The coefficient Cm: BWLVH, β= -5°

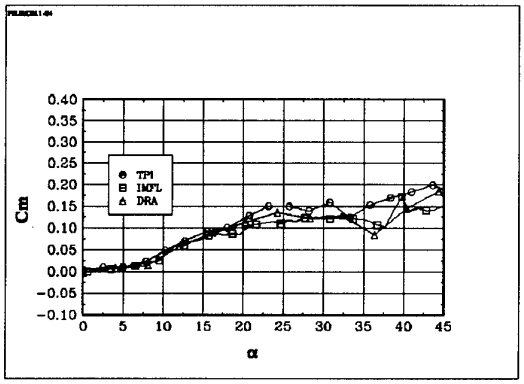

Fig 6.10 The coefficient Cm: BWLVH, β= 5°

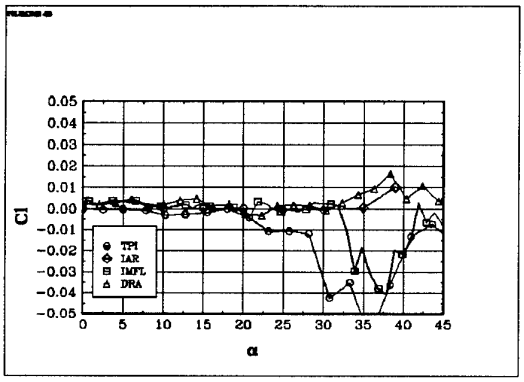

Fig 6.11 The coefficient Cl: BWLVH, β= 0°

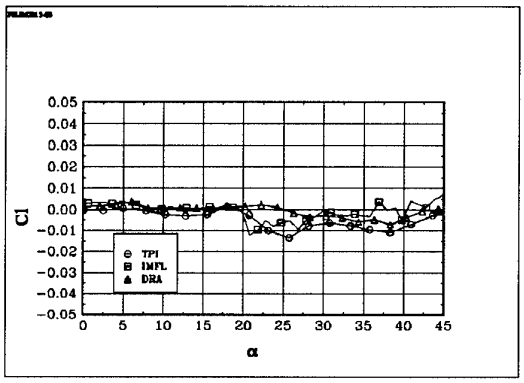

Fig 6.12 The coefficient Cl: BWLVHST, β= 0°

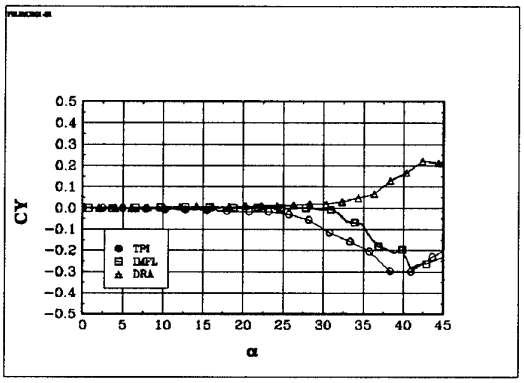

Fig 6.13 The coefficient CY: BWLVH, β= 0°

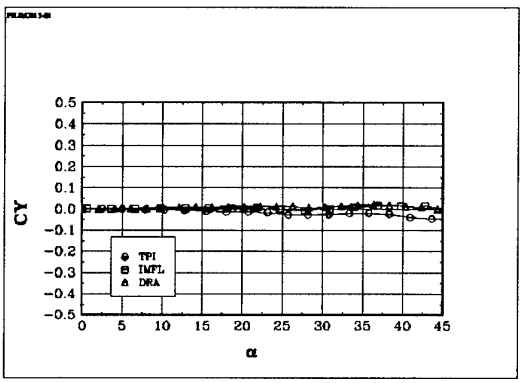

Fig 6.14 The coefficient CY: BWLVHST, β= 0°

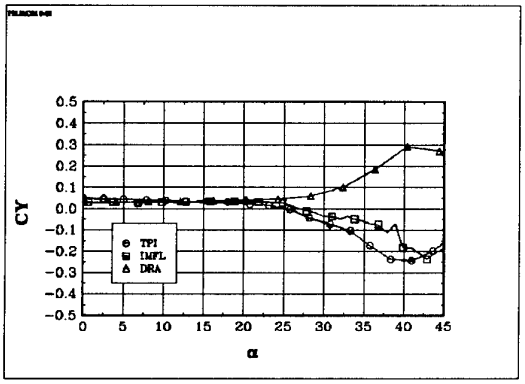

Fig 6.15 The coefficient CY: BWLVH, β= -5°

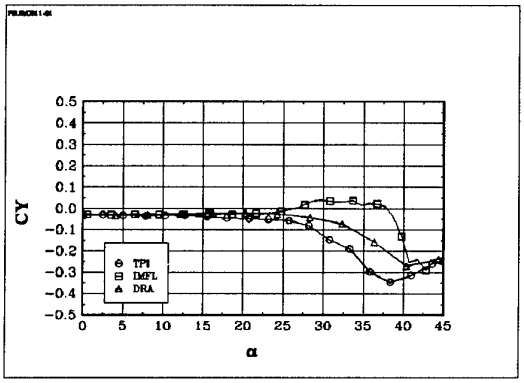

Fig 6.16 The coefficient CY: BWLVH, β= 5°

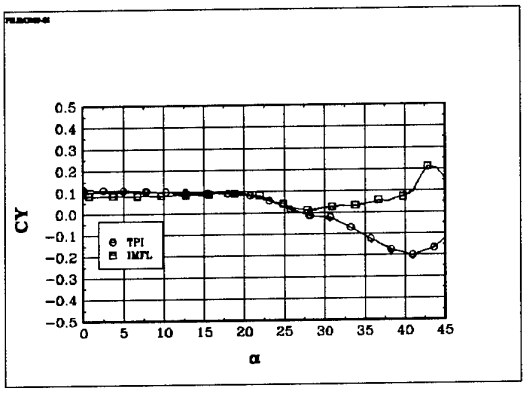

Fig 6.17 The coefficient CY: BWLVH, β= -10°

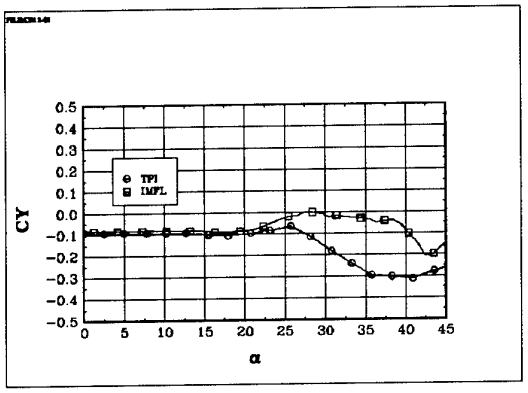

Fig 6.18 The coefficient CY: BWLVH, β= 10°

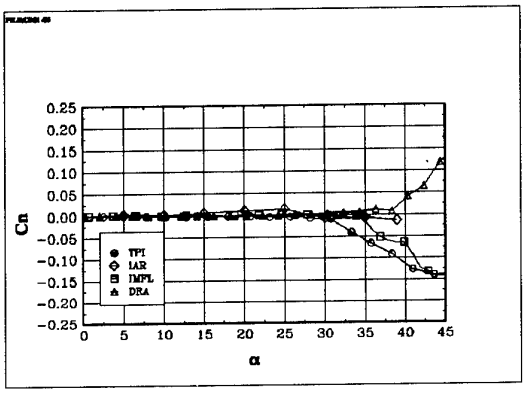

Fig 6.19 The coefficient Cn: BWLVH, β= 0°

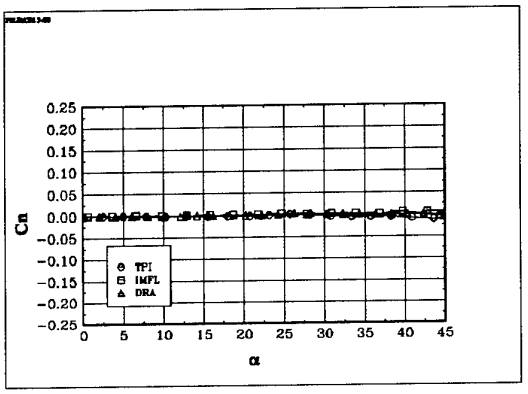

Fig 6.20 The coefficient Cn: BWLVHST, β= 0°

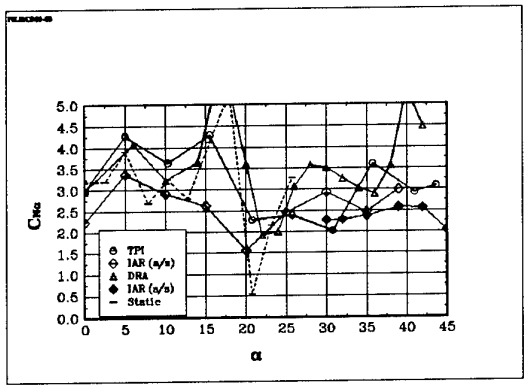

Fig 6.21 The derivative CNα: BWLVH, β= 0°

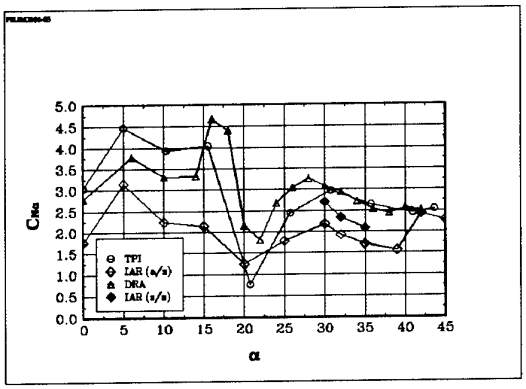

Fig 6.22 The derivative CNα: BWLVHST, β= 0°

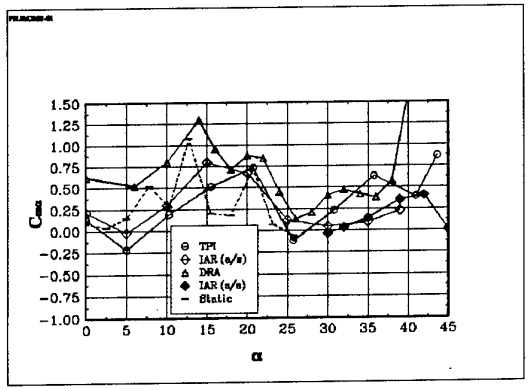

Fig 6.23 The derivative Cmα: BWLVH, β= 0°

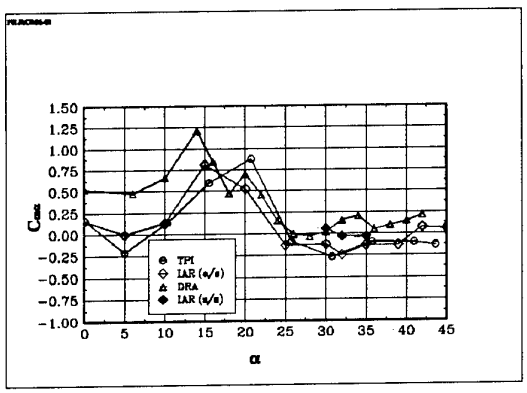

Fig 6.24 The derivative Cmα: BWLVHST, β= 0°

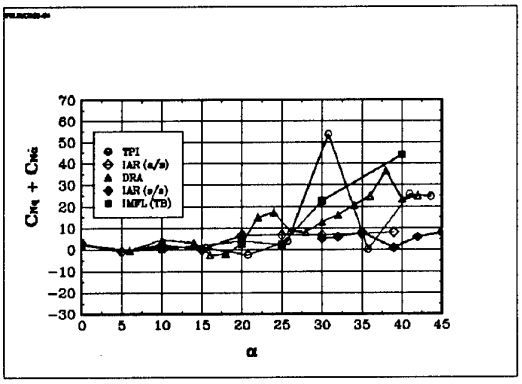

Fig 6.25 The derivative CNq*: BWLVH, β= 0°

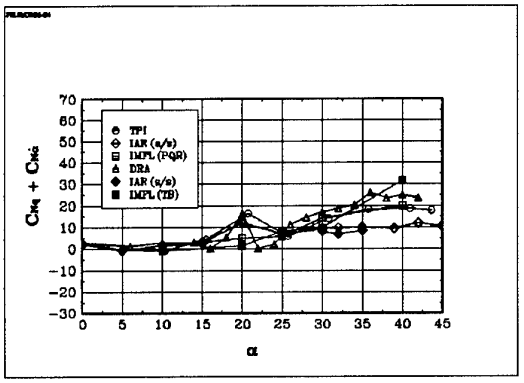

Fig 6.26 The derivative CNq*: BWLVHST, β= 0°

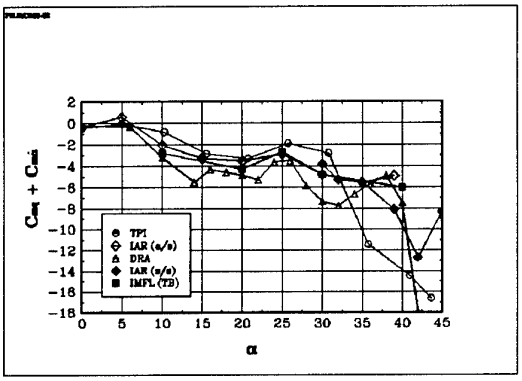

Fig 6.27 The derivative Cmq*: BWLVH, β= 0°

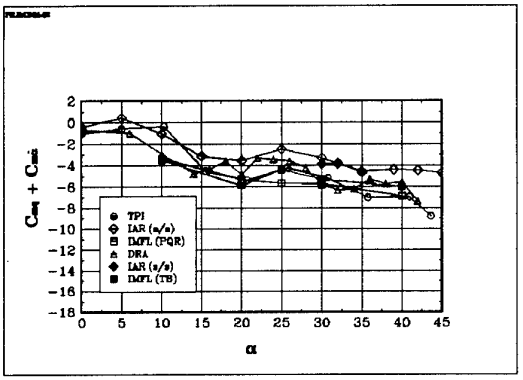

Fig 6.28 The derivative Cmq*: BWLVHST, β= 0°

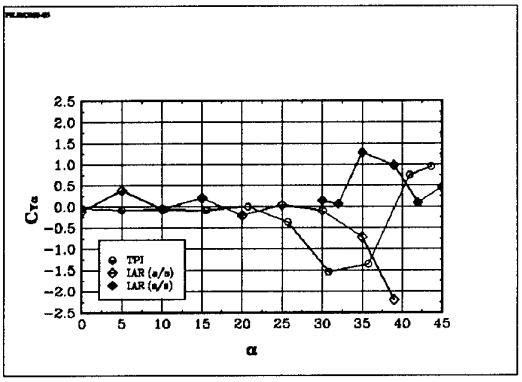

Fig 6.29 The derivative CYα: BWLVH, β= 0°

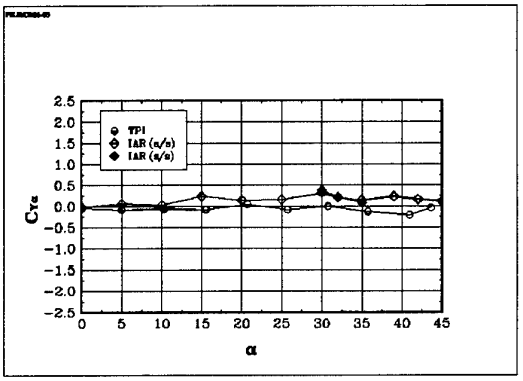

Fig 6.30 The derivative CYα: BWLVHST, β= 0°

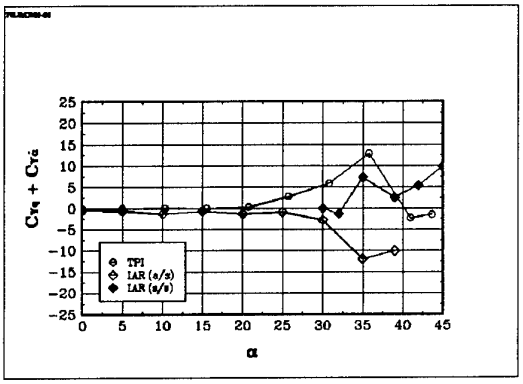

Fig 6.31 The derivative CYq*: BWLVH, β= 0°

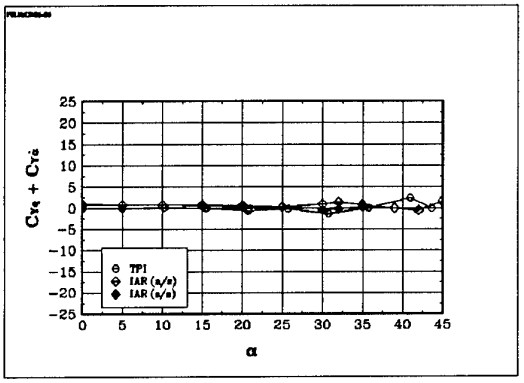

Fig 6.32 The derivative CYq*: BWLVHST, β= 0°

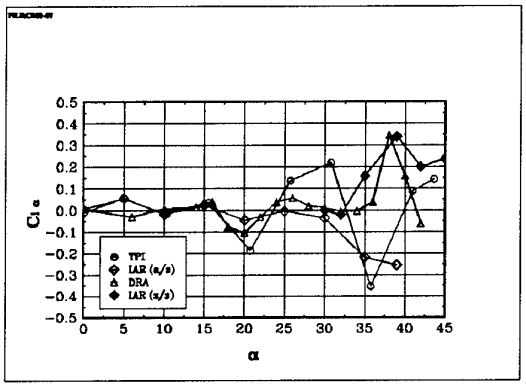

Fig 6.33 The derivative Clα: BWLVH, β= 0°

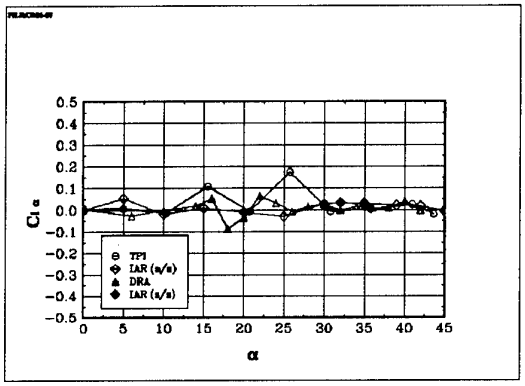

Fig 6.34 The derivative Clα: BWLVHST, β= 0°

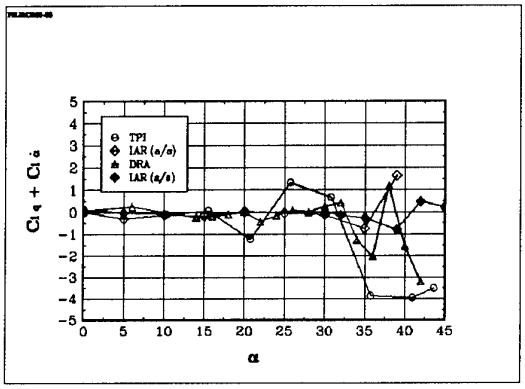

Fig 6.35 The derivative Clq*: BWLVH, β= 0°

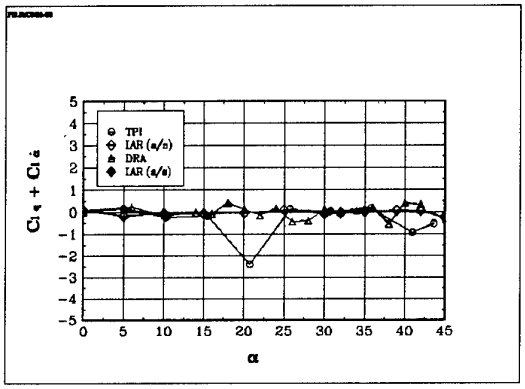

Fig 6.36 The derivative Clq*: BWLVHST, β= 0°

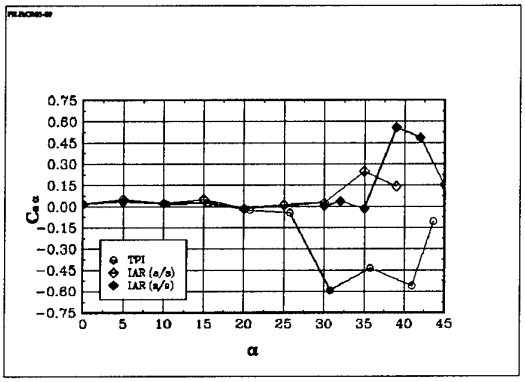

Fig 6.37 The derivative Cnα: BWLVH, β= 0°

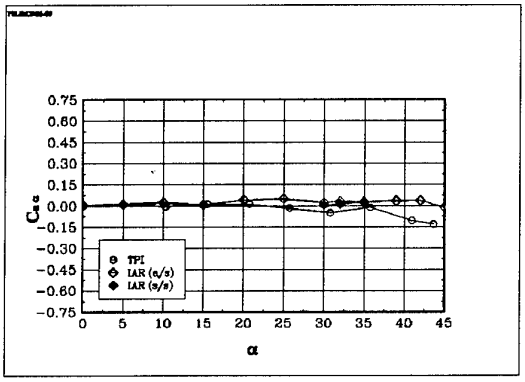

Fig 6.38 The derivative Cnα: BWLVHST, β= 0°

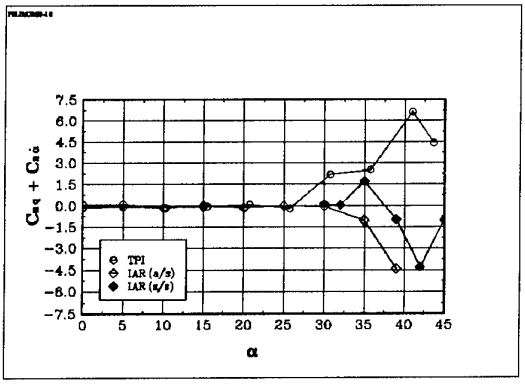

Fig 6.39 The derivative Cnq*: BWLVH, β= 0°

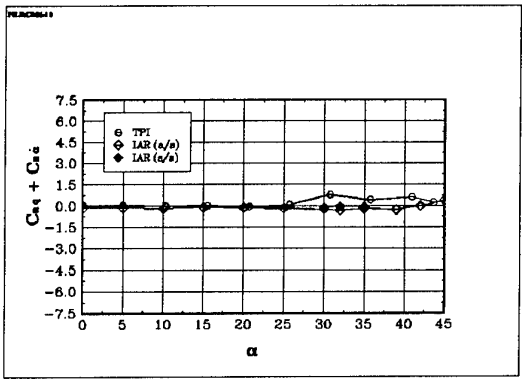

Fig 6.40 The derivative Cnq*: BWLVHST, β= 0°

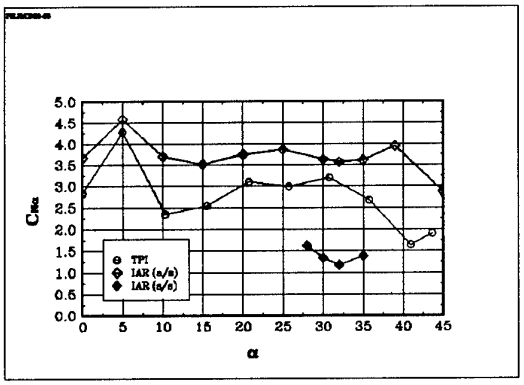

Fig 6.41 The derivative CNα: BWVH, β= 0°

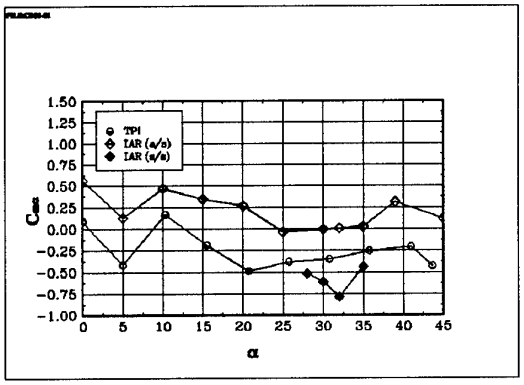

Fig 6.42 The derivative Cmα: BWVH, β= 0°

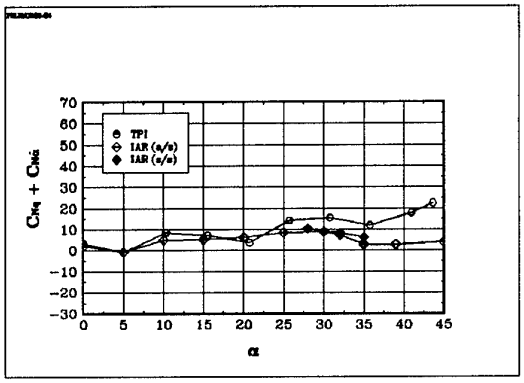

Fig 6.43 The derivative CNq*: BWVH, β= 0°

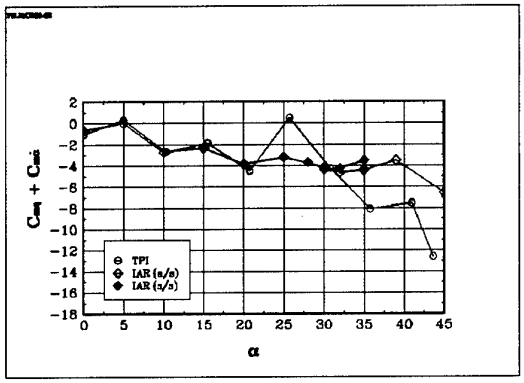

Fig 6.44 The derivative Cmq*: BWVH, β= 0°

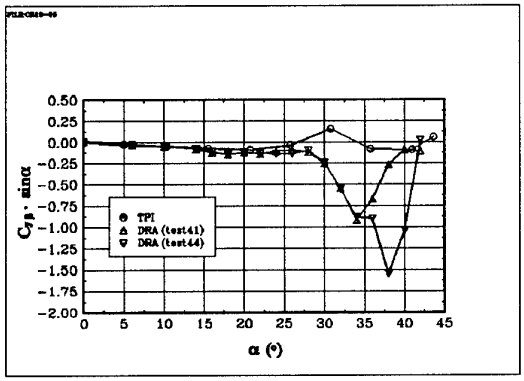

Fig 6.45 The derivative CYβsinα: BWLVH, β= 0°

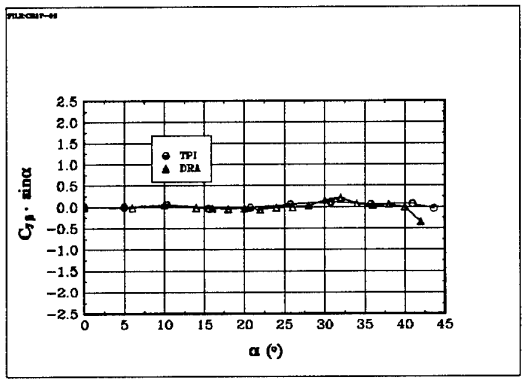

Fig 6.46 The derivative CYβsinα: BWLVHST, β= 0°

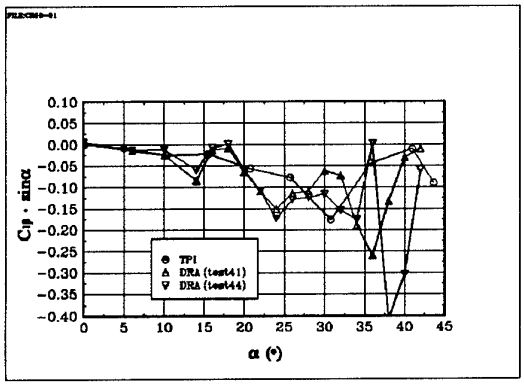

Fig 6.47 The derivative Clβsinα: BWLVH, β= 0°

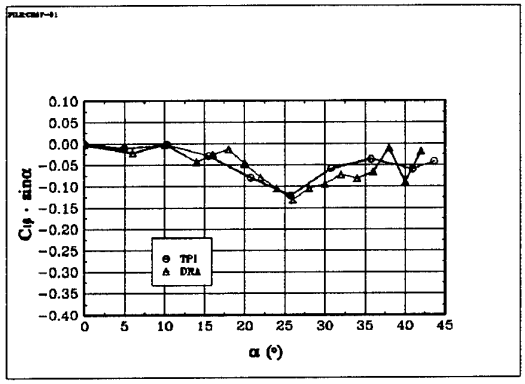

Fig 6.48 The derivative Clβsinα: BWLVHST, β= 0°

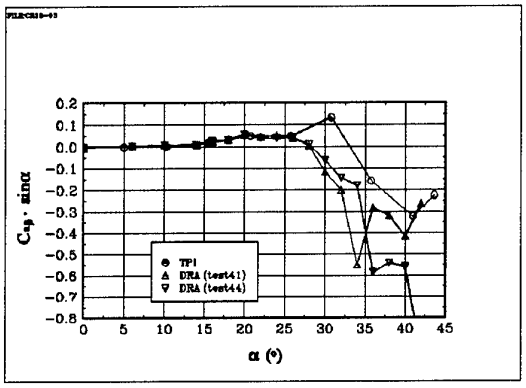

Fig 6.49 The derivative Cnβsinα: BWLVH, β= 0°

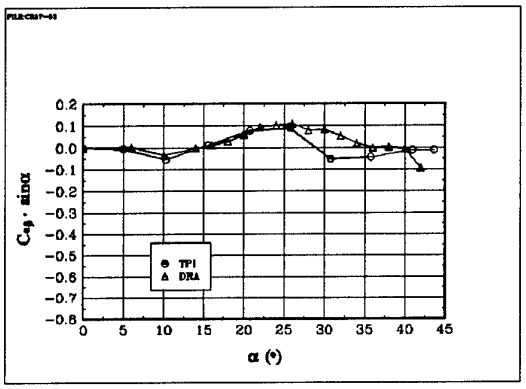

Fig 6.50 The coefficient Cnβsinα: BWLVHST, β= 0°

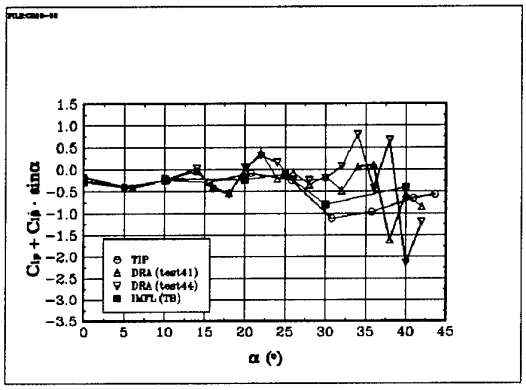

Fig 6.51 The derivative Clp*: BWLVH, β= 0°

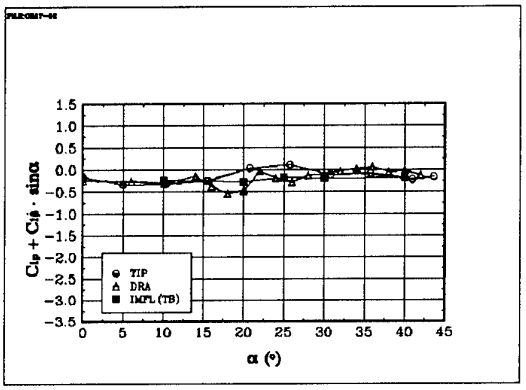

Fig 6.52 The derivative Clp*: BWLVHST, β= 0°

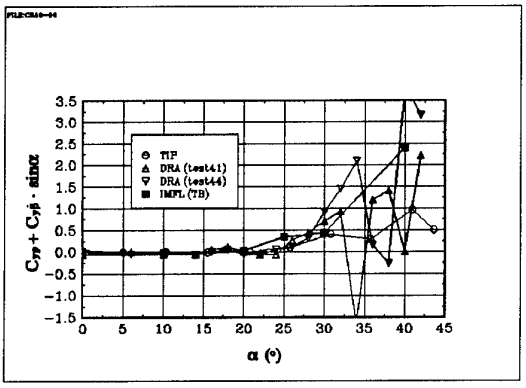

Fig 6.53 The derivative CYp*: BWLVH, β= 0°

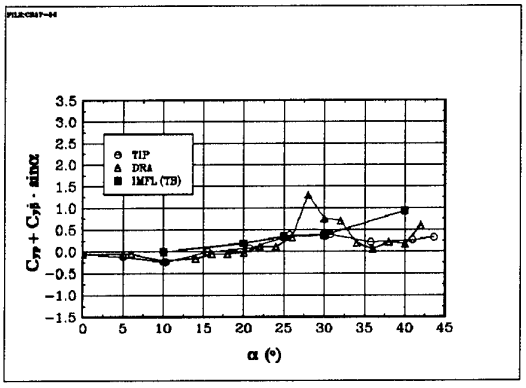

Fig 6.54 The derivative CYp*: BWLVHST, β= 0°

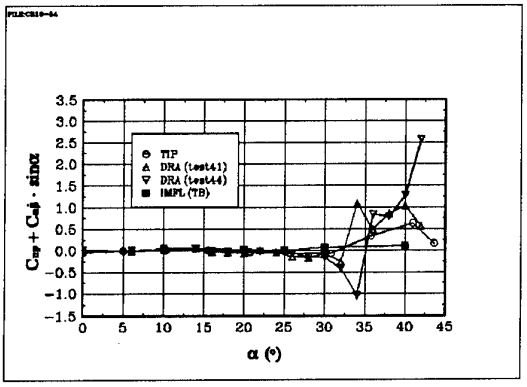

Fig 6.55 The derivative Cnp*: BWLVH, β= 0°

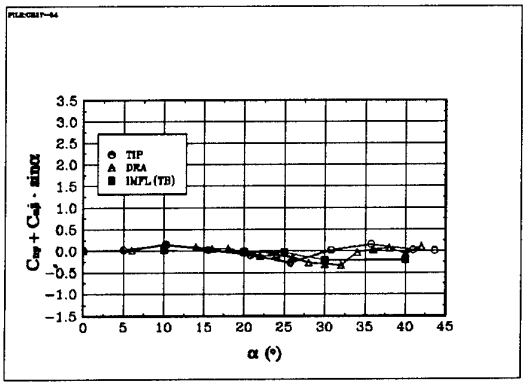

Fig 6.56 The derivative Cnp*: BWLVHST, β= 0°

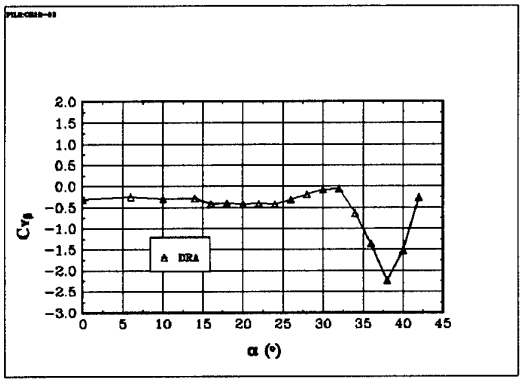

Fig 6.57 The derivative CYβ: BWLVH, β= 0°

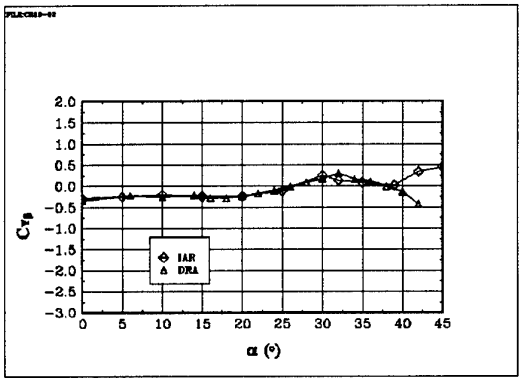

Fig 6.58 The derivative CYβ: BWLVHST, β= 0°

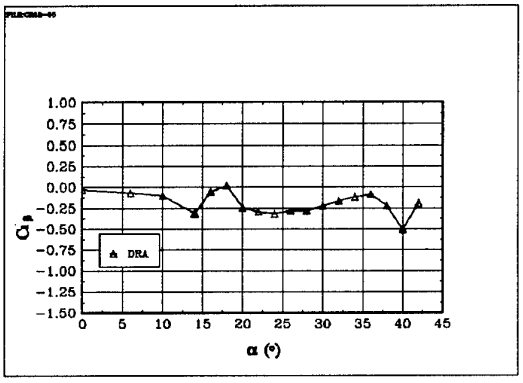

Fig 6.59 The derivative Clβ: BWLVH, β= 0°

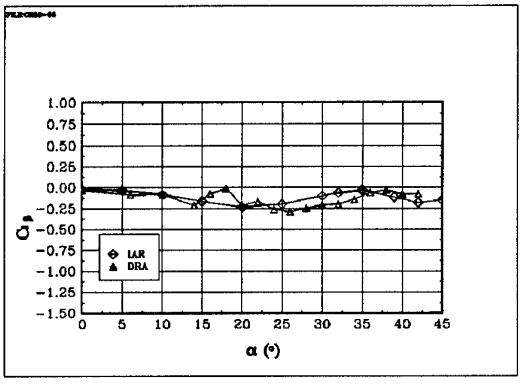

Fig 6.60 The derivative Clβ: BWLVHST, β= 0°

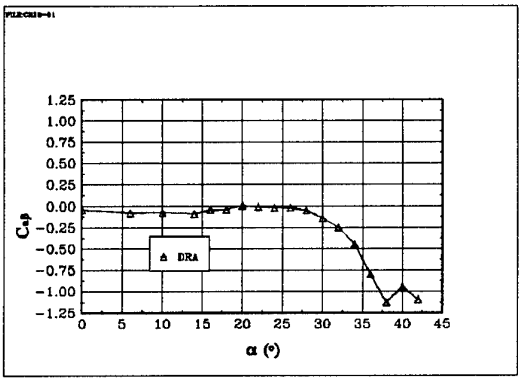

Fig 6.61 The derivative Cnβ: BWLVH, β= 0°

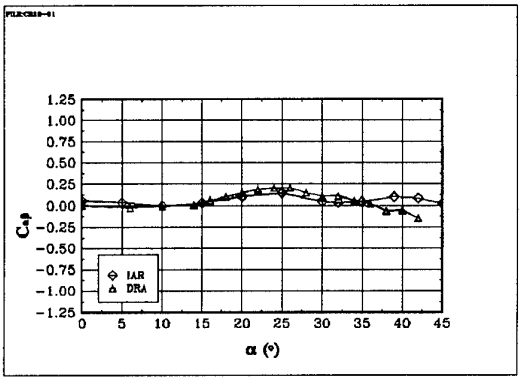

Fig 6.62 The derivative Cnβ: BWLVHST, β= 0°

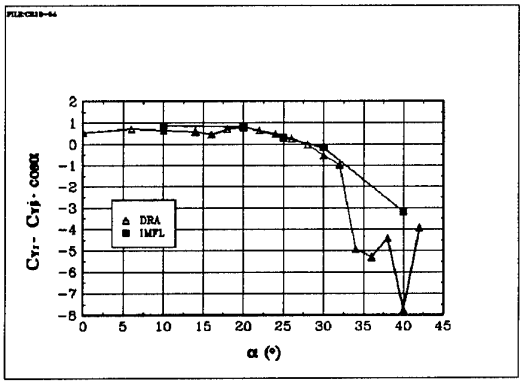

Fig 6.63 The derivative CYr*: BWLVH, β= 0°

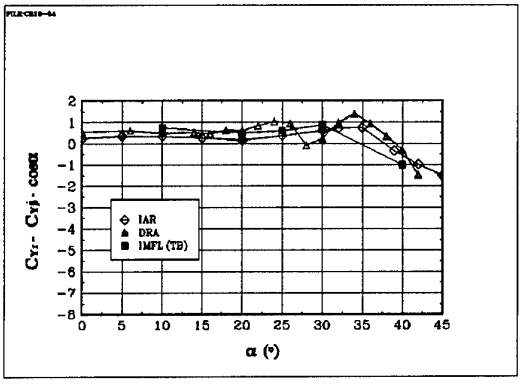

Fig 6.64 The derivative CYr*: BWLVHST, β= 0°

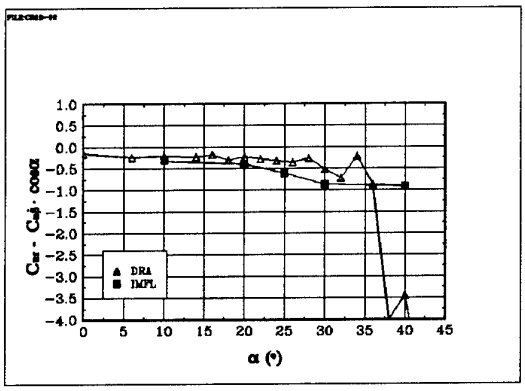

Fig 6.65 The derivative Cnr*: BWLVH, β= 0°

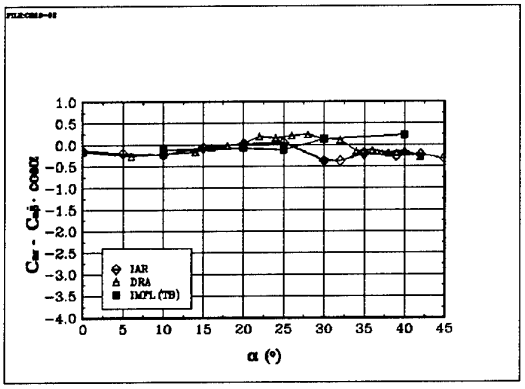

Fig 6.66 The derivative Cnr*: BWLVHST, β= 0°

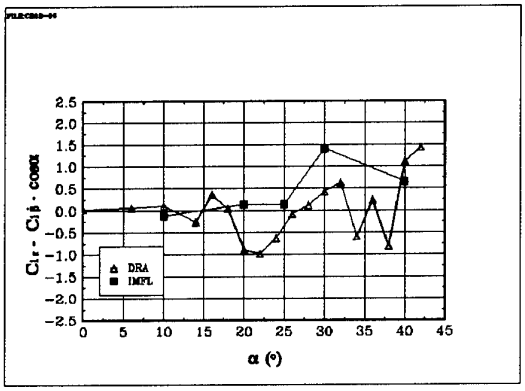

Fig 6.67 The derivative Clr*: BWLVH, β= 0°

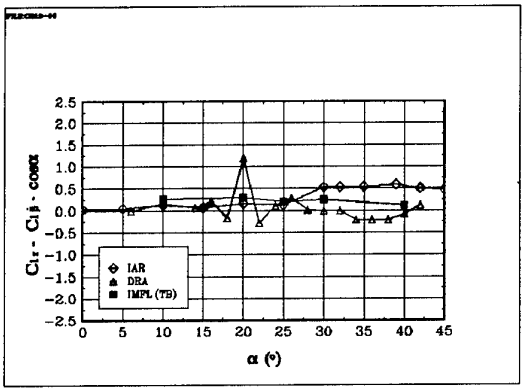

Fig 6.68 The derivative Clr*: BWLVHST, β= 0°

CHAPTER 7

ROTARY RESULTS ON FOREBODY MODELS

7.0 INTRODUCTION

This chapter presents results from rotary testing on generic forebody models conducted by the National Aeronautics and Space Administration (NASA) in the United States and the Defense Research Agency (DRA) in the United Kingdom. Rotary balance experiments were conducted on rectangular and circular ogive forebodies at 60 and 90 degrees angle of attack over a wide range of Reynolds numbers to determine the effects of nose geometry, angle of attack, and rotation on the aerodynamic characteristics of fuselage-type forebodies. These tests successfully measured, for the first time, the surface pressure distribution of these configurations under dynamic conditions in a pressurized tunnel. The results of the tests were to provide an initial exploration of the effects of velocity vector roll rates and Reynolds numbers on simple geometries, as well as to provide a database for the development of high angle of attack computational methods. Analysis of a limited portion of this substantial database is contained in Ref. 1. The facilities, models, and instrumentation used are described in Chapter 2. A schematic of the configurations is shown in Fig. 7.1.

The models were pressure-tapped with six circumferential rows of taps on the forebody and two on the aftbody. All models were 36 inches long, with a diameter of 6 inches. Station zero represented the tip of the forebody, station 12 the forebody break-point, and station 36 the overall length. Taps were located at stations 1, 2, 4, 6, 8, 11, 29, and 32.5. The total number of surface pressure ports was 254 for each configuration. There were 32 pressure taps at each body station except station 1, which only accommodated 30 taps. Trip strips and strakes were tested on the circular ogive configuration at 60 degrees angle of attack. The trip strips were narrow thin pieces of metal with small, raised holes punched in them. One strip was attached on each side of the nose of the circular ogive model, 80° from the bottom centerline, and extended down the sides until about 3 inches from the aft end. The strakes were thin pieces of metal mounted perpendicular to the model surface on either side of the nose, approximately 0.5 inches wide by 4 inches long and placed 135° from the bottom centerline.

This chapter describes the experiments conducted and an analysis of these data, presenting aerodynamic forces and surface pressures for these generic bodies at high angle of attack as a function of Reynolds number and rotation rate from two wind-tunnel test entries. In the discussions in this chapter Re_D is defined as the Reynolds number based on either the maximum diameter of the circular cross section body or the maximum width (referred to as the diameter) of the rectangular cross section. The non-dimensional rotation rate is $\Omega b/2v$ where b is the model reference length and the aerodynamic coefficients are based on a reference area of the maximum body cross section and cross sectional width (diameter) for moment coefficients. The pressure data are presented by assigning color values to the measurements and mapping these values onto a three-dimensional surface model of the configuration.

7.1 RECTANGULAR OGIVE

7.1.1 60° Angle Of Attack

Figure 7.2 shows the Reynolds number sensitivity of the rotational side force and yawing moment characteristics for the rectangular ogive at 60° angle of attack. As seen in Fig. 7.2, increasing Reynolds number has little effect on the yawing moment characteristics at all rotation rates tested. Even as Re_D increased from values normally consistent with laminar flow to those representative of transitional and turbulent flow on a cylinder in cross-flow (α=90°) the basic behavior in yaw for α =60° remained the same: a highly damped configuration with little asymmetric yaw at static conditions except at Re_D =175,000. These results are very similar to results from Ref. 2 (shown in Fig. 7.3) measured in the NASA Ames 12-Foot Pressure Tunnel on a forebody nose with similar cross section on a full body-wing-tail configuration. In the Ames results it was found that at α=60° the boundary layer, even at low Reynolds number, was transitional to turbulent around the corners because of cross-flow instabilities in the boundary layer. The transitional flow allowed the flow to remain attached around the corners even at low Reynolds numbers, resembling the behavior of the flow at higher Reynolds number around a rectangular cross section at α=90° (2-d flow). Pressure data on the present configuration measured at static conditions, shown in Fig. 7.4, indicate that the flow was characterized by attached flow along the four corners of the forebody. The basic surface pressure features remained relatively unchanged as Reynolds number increased to the maximum tested, the most prominent difference being a slight increase in the peak suction values at the nose as Reynolds number was increased.

The imposition of a rotation rate on the forebody resulted in a rotation of the surface pressure distribution commensurate with the movement of the local velocity vector. The net result was a reduction in the local suction

vector. The net result was a reduction in the local suction on the lower windward and upper leeward corners, and an increase in suction on the remaining corners, as illustrated in Fig. 7. 5. The increased crossflow on the advancing upper corner resulted in a more pronounced vortex effect on the upper surface. The mechanism responsible for the yaw damping characteristics was also evident. As rotation rate increased, the rotation of the relative velocity vector produced an increase in pressure on the advancing face of the forebody, with the leeward side surface pressure remaining essentially unchanged from the static case. The net difference in the surface pressure on either side yielded the increase in damped yawing moment as rotation rate increased. As with the static case, the basic surface pressure features were essentially unchanged as Reynolds number increased. Because these differences lie primarily in the longitudinal plane, their effect on the directional characteristics are minimal. The upper surface differences contributed to a static shift in the rotational pitching moment data as shown in Fig. 7.6. The general rotational behavior remained similar, however.

For this configuration, increasing Reynolds number generally made the flowfield features more distinct, yet the basic structures, including the low pressure regions and separation lines, were relatively unaffected by Reynolds number. This apparently is because the key surface pressure features are defined by the corners of the rectangular body and because of the cross-flow instability in the boundary layer at α =60° which promotes a turbulent boundary layer condition at lower Reynolds number than for a cylinder in 2-d cross-flow (α=90°).

7.1.2 90° Angle Of Attack

The effects of Reynolds number on the rotational yawing moment and side force characteristics for the rectangular ogive at 90° angle of attack are shown in Fig. 7.7. At 90° angle of attack, the yawing moment characteristics and the flowfield about the rectangular ogive were strongly influenced by Reynolds number effects and rotation rate. At low Reynolds numbers (Re_D<200,000) the rectangular ogive was typically propelling in yaw, with substantial static offset values occurring at Re_D = 178,000. The offsets were reduced and the yawing moments gradually changed from propelling to damping with increasing rotation rates as Reynolds number was further increased to 500,000 where yawing moment was damped at all rotation rates. This trend with Reynolds number is consistent with earlier experiments discussed in Ref. 2 on a similar rectangular cross section forebody at α =90° (see Fig. 7.8). In the experiments in Ref. 2 the rotation rate was varied as shown in Fig. 7.8 and revealed substantial hysteresis effects caused by the dependency of flow separation at the front leeward corner on whether the rotation rate was increasing or decreasing. No measurements were made in the present experiments to detect hysteresis effects. The extent of forebody flow attachment was highly dependent on Reynolds number because the local Reynolds number varied with the width (diameter) of the forebody cross sections (which varied depending on longitudinal location on the model). By evaluating the pressure data obtained at various cross sections along the forebody under static conditions such as those shown in Figs. 7.9 and 7.10, it was determined that a minimum local sectional Reynolds number (based on local diameter) of at least 200,000 was necessary in order to promote attached flow around the corners of the forebody.

As noted above, the rectangular ogive at 90° was propelling in yaw for Reynolds numbers below 200,000. A transitional region was observed between Reynolds numbers of 200,000 and 500,000, where changes or a jump from propelling to damping in yaw occurred with increasing rotation rate. This separation "jump" is characterized by a discontinuity in the slopes of the yawing moment curves. The propelling moments observed at these Reynolds numbers were a result of the suction produced by a region of attached flow along the windward corner of the forebody nose, as illustrated in Fig. 7.11 which shows the pressure data for Re_D=401,000 at rotation rates of -0.3 (where yawing moment is damped) and -0.4 (where yawing moment is propelling). As Reynolds number increased, transition occurred at higher rates of rotation until there was damping in yaw at all rotation rates for Re_D = 609,000. Damping moments were generated when the cross-flow over the forebody separated and reattached along the leeward side of the aftbody. Correlation between the yawing moments and forebody pressures suggested that transition occurred similarly for Re_D=209,000 at a lower rotation rate of -0.15 Ωb/2V. As rotation rate decreased the flow was less likely to remain attached at the nose tip due to a reduction in the local velocity.

As Reynolds number increased above 500,000 and out of the transitional range, the flow became fully attached on the forebody with damped yawing moments resulting. Fig. 7.7 shows that yaw was similarly damped for post-transitional Reynolds numbers. Correspondingly, the flowfield was relatively independent of Reynolds number once the flow was no longer transitional. Additionally, the strong flow attachment along the leeward side of the aftbody increased the magnitude of the yawing moment.

7.1.3 Correlation Of Yaw And Side Force For 60° And 90° Angle Of Attack

Although past forebody studies have made assumptions about stability characteristics based on side force behavior, the NASA/DRA data showed that side forces, both statically and at rotation rate, are not necessarily indicative of the yawing moment behavior. It should be noted, however, that the degree of correlation (direction and magnitude) between side force and yawing moment is very

dependent upon one's choice of the center of rotation and center of moments. If a forebody contribution to the yawing moment is dominated by the forebody side force applied at a significant distance from the center of rotation, and the aft body contribution is substantially less, then the yawing moment and side force will exhibit very similar characteristics with rotation rate. An example is the data from Ref. 2 shown in Fig. 7.8. In the present experiments the center of rotation is chosen such that there is a direct correlation between the side force and yawing moment for α=60° (i.e., they are the same sign meaning that the center of pressure of the body is ahead of the center of rotation) and for α=90° there is an opposite correlation where the center of pressure of the body is behind the center of rotation (see Fig. 7.12). For a chosen configuration the significance of the yaw characteristics at high angles of attack, particularly the slope of yawing moment curve versus rotation, is of critical importance in determining a configuration's behavior at these angles. Propelling yawing moments versus rotation are indicative of possible departure susceptibility and spin behavior, and in configuration terms is considered adverse. Conversely, damped yawing moments are desirable from both a spin as well as a controlled maneuver standpoint. While previous research efforts have assumed that yaw behavior parallels that seen in side force and have frequently presented only these data, these tests indicated that this was not the case. The assumption that yawing moment has the same characteristics as side force(Ref. 3) is unsatisfactory for static test conditions and can lead to completely erroneous conclusions when evaluating rotational behavior. This is shown graphically in the comparison of aerodynamic characteristics for the rectangular ogive at both 60° and 90° angle of attack, presented in Fig. 7.12. The rotational yawing moment curves for the rectangular ogive configuration at these two angles of attack exhibited very similar slopes, while the slopes of the rotational side force curves for the two angles of attack were opposite. As a result of the numerous differences between yawing moment and side force trends, as well as the fact that side force variation (included here for completeness) has a relatively insignificant contribution to aircraft behavior at high angles of attack, the following discussion will focus primarily on the variation of yawing moment with rotation rate.

7.2 CIRCULAR OGIVE

7.2.1 60° Angle Of Attack

The effects of rotation on the aerodynamic characteristics for the circular ogive at 60° angle of attack are presented in Fig. 7.13 for selected Reynolds numbers. Pressure distributions for selected static and dynamic conditions are presented in Figs. 7.14, 7.15 and 7.16. Section C of Fig. 7.15 and 7.16 is a display of the pressure increments between the two flow conditions which allows a clearer understanding of the vortex behavior. The force and moment data collected during these tests, in correlation with the pressure data, show that the separated vortex flow had a significant influence on the circular ogive at 60° angle of attack. As expected, the rotational yawing moment and side force characteristics of the circular ogive at 60° angle of attack exhibited significant effects due to Reynolds number. At low Reynolds number, yawing moments remained well damped at all rotation rates, as shown in Fig. 7.13. However, an increase in Reynolds number resulted in significant changes to the rotational yawing moment (and side force) characteristics. Yaw damping was reduced in the transitional Reynolds number range, resulting in neutral to slightly propelling characteristics, and further increases in Reynolds number yielded very non-linear results. The rotational yawing moment characteristics were significantly different between Re_D of $1x10^6$ and $2x10^6$. As shown in Fig. 7.13, yawing moments were propelling at a Re_D of 1,400,000, but then became damped again at low rotation rates at a Re_D of 2,080,000. The pressures shown in Figs. 7.15 and 7.16, particularly the increments between the two conditions, clearly demonstrate that these forces come from changes in the forebody flow. This behavior would indicate that either the flowfield was highly unstable at these high Reynolds numbers, or that Reynolds number dependent flowfield changes were still occurring as Re_D was increased through this region.

The characteristics observed on the circular ogive at 60° angle of attack reflected those observed in other rotary studies of the circular tangent ogive configuration, including those presented in this report in Chapter 3. The pressure data clearly showed the influence of different boundary layer separation conditions on the forebody flowfield. As would be expected, rotational yaw damping varied considerably for test data measured throughout a broad transitional Reynolds number region.

7.2.2 90° Angle of Attack

The rotational side-force and yawing-moment characteristics at several Reynolds numbers are presented in Fig. 7.17 for the circular ogive at 90° angle of attack. Note that yawing moments were damped for all Reynolds numbers (Fig. 7.17a) with large static offsets occurring in the transitional Reynolds number region. Note that the offsets were reduced for both low and high Reynolds numbers. However, an increase in the offset occurred at the highest Reynolds number tested (Re_D=2,080,000), indicating that fully turbulent flow conditions had not yet been attained.

As with the rectangular ogive at 90° angle of attack, the flow about the circular ogive forebody at static conditions was two-dimensional and highly dependent on the local Reynolds number. Because of the varying diameter of the forebody, as the freestream Reynolds number was increased the local Reynolds number on the forebody

increased in proportion to the local diameter and to the changing freestream Reynolds number. Therefore, as the Reynolds number increased from 350,000 on the maximum forebody diameter to 2,000,000 the flow on the forebody exhibited delayed separation at body stations progressively towards the tip (Fig. 7.18). Also, at Re_D =350,000 there was a strong suction on the port side of the afterbody (Fig. 7.18a) which in combination with the long moment arm generated a substantial static offset in yawing moment (Fig. 7.17a). As the Reynolds number increased, the flow remained attached further forward until at approximately Re_D =690,000 the flow was attached on nearly the entire forebody and was quite symmetric. At Re_D =2.08×10^6 the flow became somewhat asymmetric again as the vortex pair began to migrate back towards the forebody surface. The starboard vortex appeared to generate greater suction along the right side of the forebody. This vortex asymmetry could explain the static yaw offset seen in Fig. 7.17a for Re_D=2,080,000. The moment and pressure data for the circular ogive at both 60° and 90° angles of attack indicated that there were still some remaining instabilities in the flow as Reynolds number increased from 1×10^6 to 2×10^6. Thus, additional testing at higher Reynolds numbers may be necessary in order to obtain data at fully turbulent flow conditions. Higher Reynolds number testing may help determine if this flow asymmetry exists at fully turbulent conditions as well, or if it is merely an effect of transition.

The rotational flow effects on the forebody pressures are shown in Fig. 7.19 for increasing Reynolds number at a rotation rate of -0.2 $\Omega b/2V$. The effects were noticeable at low Reynolds number in the orientation of the positive pressure region around the bottom of the forebody (Fig. 7.19a). As Reynolds number increased, the rotational effects became more evident in the reorientation of the low pressure lobes on the forebody. This is illustrated in Figs. 7. 19b and 7. 19c as the starboard suction lobe was situated lower on the forebody than the port suction lobe. The vortex asymmetry observed for a Reynolds number of 2×10^6 became exaggerated with rotation as the port vortex was pulled over towards the starboard side of the forebody (Fig. 7. 19d).

The reorientation of the pressure along the bottom of the circular ogive generated damping moments at 90° angle of attack for all Reynolds numbers. This was particularly true at low Reynolds numbers where the flow was fully detached, and the pressures were constant over most of the body. In contrast, yaw was propelling for the rectangular ogive at 90° angle of attack at low Reynolds numbers. The flow was separated on the rectangular ogive at low Reynolds numbers as well, but the positive pressure region along the bottom was constrained by the corners of the rectangular cross-section.

7.3 EFFECT OF FLOW MODIFIERS

Interest in the modification of the forebody flowfield at high angles of attack has ranged from the manipulation of the surface pressure distribution to permit the replication of high Reynolds number characteristics at low Reynolds number test conditions (e.g. Ref. 4), to the outright modification of the flowfield to improve the basic airplane behavior and control characteristics (e.g., Ref. 5). Because of these concerns, a limited attempt was made during the course of these tests to evaluate the influence of Reynolds number and rotation on a typical trip strip and a strake installation on the circular ogive configuration.

7.3.1 Effect of Trip Strips

The installation of flow tripping strips along the lower portion of the body was configured based on DRA experience with similar applications. No attempt was made in these experiments to optimize these strips either for location or size. Different placement of the strips and a change in the roughness height might alter the resulting behavior of the boundary layer. The flow tripping surfaces consisted of the raised edges of small holes punched in a thin metal strip with the dimensions shown in Fig. 7.1. The effect of these devices on the circular forebody's yaw and sideforce characteristics at various Reynolds numbers is shown in Fig. 7.20.

The typical purpose of adding devices such as these to a configuration's forebody is to attempt to stimulate the development of fully turbulent flow conditions at Reynolds numbers below where this flow condition would naturally occur. This technique has been used with some success in other static testing, but as seen in the force and moment data of Fig. 7.21, the application of these devices can be problematic. When applied to this particular configuration, the yaw characteristics were significantly changed from the clean forebody data, at both low and high Reynolds numbers. However, the side force data with the strips applied basically collapsed to a single curve, although with a significant offset even at no rotation rate. With the strips applied, very large asymmetries in yaw developed for all Reynolds numbers tested even with no rotation and the rotational characteristics varied widely with Reynolds number, ranging from highly asymmetric between positive and negative rotation rates, to invariant with rotation. While very carefully applied, some asymmetry in the attachment of the strips was apparently responsible for the pervasive offsets that exceeded the highest values observed with the clean forebody. Assuming the strips were installed to simulate the development of fully turbulent flow conditions at Reynolds numbers below where this flow condition would naturally occur, the purpose would be lost, as seen in Fig. 7.20 when comparing the open circles representing trips-on at the lowest Reynolds number with the solid diamonds representing the highest Reynolds number data without the trip strips applied. The pressure data, shown for various Reynolds numbers at static conditions without the strips in Fig. 7.14 and with trip strips in Fig. 7.21, revealed the expected modification of the forebody flowfield

imposed by the addition of the strips. For the Re_D tested, the strips did provide a relatively invariant forebody surface pressure distribution. For this case, transition strips increased the suction on the starboard side of the body corresponding to the positive yaw offsets seen in the moment data. This region of enhanced attached flow on the starboard side of the body also produced a more pronounced vortex suction peak on that side of the upper body. The effect of rotation rate is depicted in Fig. 7.22 at a Re_D of 2.1×10^6 and shows how the surface pressure distribution was only slightly influenced by increasing rate. As a result, the moment data was essentially unchanged with increasing rate (see Fig. 7.20 at a Re_D of 2.1×10^6). While not evaluated in this particular test, it is likely that a similar situation would have arisen for non-zero sideslip conditions as well.

7.3.2 Effect of Forebody Strakes

Several recent high angle of attack aircraft have utilized the application of forebody strakes to improve their high angle of attack characteristics (e.g., the X-29 and the X-31, as described in Refs. 6 and 7). In both cases the primary function of the strakes was to reduce the incidence of asymmetric yaw offsets that frequently occur on these types of forebodies. Other low Reynolds number test work has shown that when properly located, nose strakes can also have a beneficial influence on the rotational yaw damping (Ref. 8). For these reasons, test data were taken for the strake configuration with the strake mounted at a 45° angle above the maximum half breadth of the local cross section.

The effect of the addition of this strake on the circular forebody's side force and yawing moment characteristics at various Reynolds numbers is shown in Fig. 723. As shown in this figure, the addition of the strake had a pronounced effect on the yaw damping characteristics, substantially increasing the damping for all rotation rates tested, as well as generally reducing the asymmetric yawing moments at static conditions. While there was a static moment displacement between the lower and the highest Re_D curves, the damping slopes remained very consistent throughout the range of Re_D tested. As was the case for the rectangular ogive, the geometric features presented by the strakes resulted in a consistent surface pressure distribution for all tested Re_D as well. At static conditions (e.g. Fig. 7.24) the presence of the strake disrupted the formation of attached flow along the fuselage sides that is characteristic of circular ogive bodies until aft of the strake. Strong vorticity shed from the strake edges resulted in upper surface suction whose peak values decreased slightly with increasing Re_D. For all Re_D, the downstream attached flow regions were less pronounced than that seen on the clean forebody (e.g., Fig. 7.25 comparing the clean forebody pressures with the strake configuration at a Re_D of 2.1×10^6).

The effect of rotation on the surface pressure distribution revealed the source of the Reynolds number independent yaw damping observed in the moment data. As seen in Fig. 7.26, which shows the effect of rotation on the strake configuration at a Re_D of 2.1×10^6, increasing rotation rate skewed the lower surface transition region associated with the development of attached flow towards the windward strake and away from the leeward strake. This resulted in a further reduction of attached flow under the windward strake (and an increase in surface pressure), along with the development of limited attached flow under the leeward strake (a decrease in the surface pressure). This pressure differential between the forebody sides resulted in damped yawing moments with rotation. This reorientation of the surface pressures was essentially the same for all Re_D tested.

These test results revealed that the beneficial effects observed in other low Reynolds number testing for this particular strake configuration are relatively invariant with Reynolds number, and thus may have potential as a device to limit or avoid adverse propelling yaw characteristics. Geometric features that fix vortex development yield configurations that are relatively insensitive to the test Reynolds number. These results also validate the mechanism resulting in the selection of the strakes-on configuration for comparison between facilities testing the WG-16 models reported earlier in this publication.

7.4 CONCLUDING REMARKS

Rotary balance experiments were conducted on circular and rectangular ogive forebodies at 60° and 90° angle of attack over a wide range of Reynolds numbers to determine the effects of nose geometry, angle of attack, and rotation rate on the aerodynamic characteristics of fuselage-type forebodies. Those tests successfully measured, for the first time, surface pressures on rotating models in a pressurized tunnel. The results can be considered as an initial exploration of the effects of velocity vector roll rates and Reynolds numbers on simple geometries and provides a database for the development of high angle of attack computational methods.

7.5 REFERENCES

1. Pauley, H., Ralston, J., and Dickes, E.: Experimental Study of the Effects of Reynolds Number on High Angle of Attack Aerodynamic Characteristics of Forebodies During Rotary Motion, NASA-CR-195033, January 1995.

2. Malcolm, G.N.: New Rotation-Balance Apparatus for Measuring Airplane Spin Aerodynamics in the Wind Tunnel, Journal of Aircraft, Volume 16, Number 4, April 1979, p 264.

3. Clark, W.H.; Peoples, J.R.; and Briggs, M.M.: Occurrence and Inhibition of Large Yawing Moments During High Incidence Flight of Slender Missile Configurations, AIAA Paper 72-968, September 1972.

4. Hall, R.M. et al: A Status Report on High Alpha Technology Program (HATP) Ground Test to Flight Comparisons, NASA-CP-10143 Vol. 1, July 1994.

5. Simon, James M.; LeMay, Scott and Brandon, Jay M.: Results of Exploratory Wind Tunnel Tests of F-16/Vista Forebody Vortex Control Devices, WL-TR-93-3013, January 1993.

6. Croom, Mark A.; Whipple, Raymond D.; Murri, Daniel G.; Grafton, Sue B., and Fratello, David J.: High-Alpha Flight Dynamics Research on the X-29 Configuration Using Dynamic Model Test Techniques, SAE Technical Paper Series 881420, October 1988.

7. Dickes, E.; Kay, J. and Ralston, J.: Validation of the NASA Dryden X-31 Simulation Aerodynamic Math Model and Evaluation of Mechanization Techniques, Bihrle Applied Research Report No. 93-4, June 1993.

8. Ralston, John N.: Rotary Balance Data and Analysis for the X-29A Airplane for an Angle-of-Attack Range of 0° to 90°, NASA-CR-3747, August 1984.

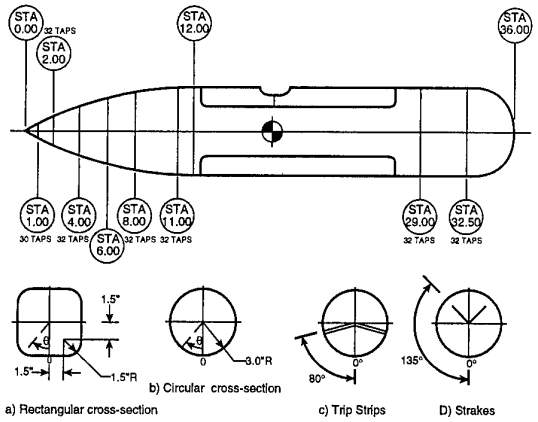

Figure 7.1. Schematic of models

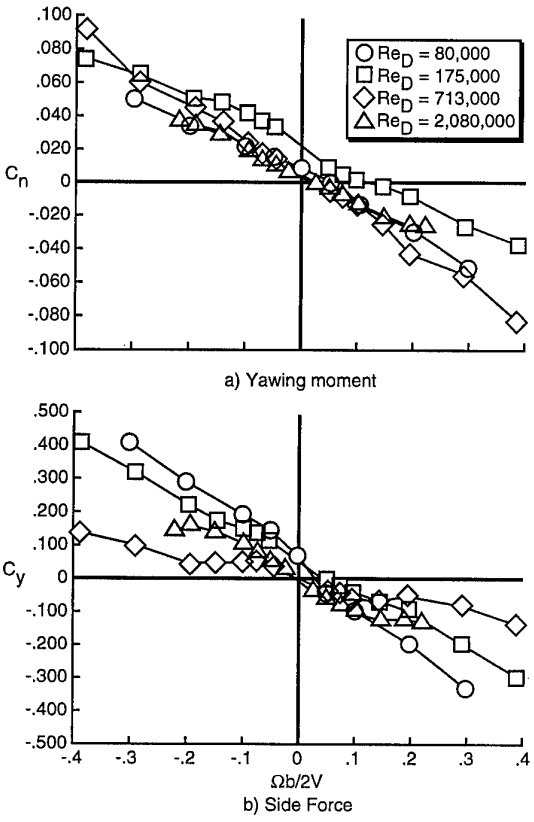

Figure 7.2. Effect of rotation rate and Reynolds number on aerodynamic characteristics for the rectangular ogive at 60° angle of attack.

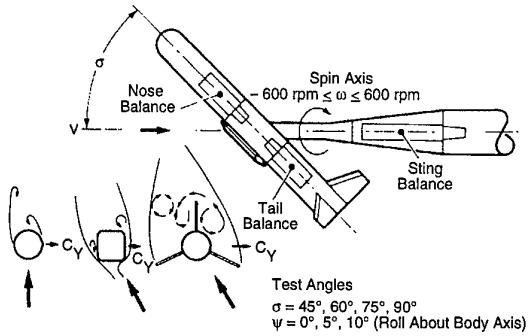

(a) Model and balance combinations and some prospin flow mechanisms.

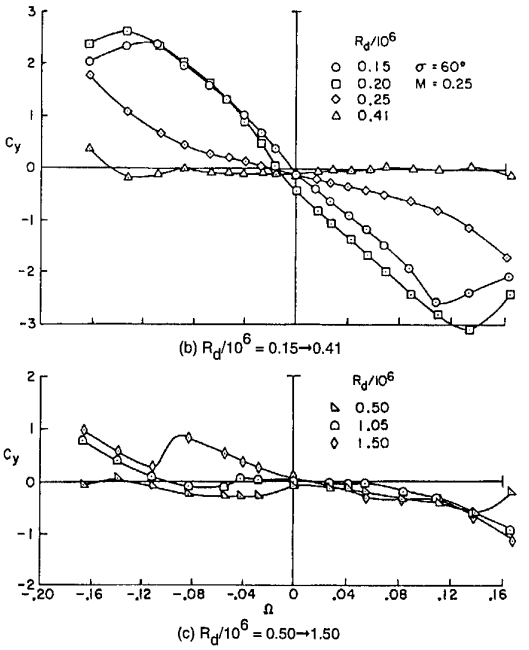

Figure 7.3. Side-force coefficient on the nose section; effect of Reynolds number at σ = 60 deg, M = 0.25.

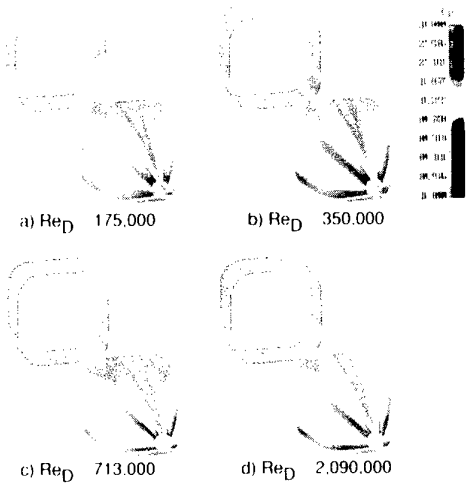

Figure 7.4. Pressure distribution for the rectangular ogive at 60° angle of attack and Ωb/2V = 0.0.

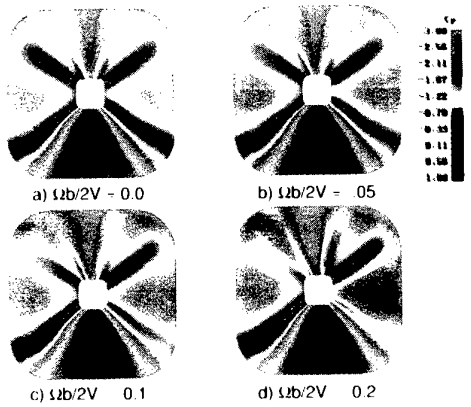

Figure 7.5. Effect of rotation rate on forebody pressure distribution for the rectangular ogive at 60° angle of attack at Re$_D$ = 2,090.

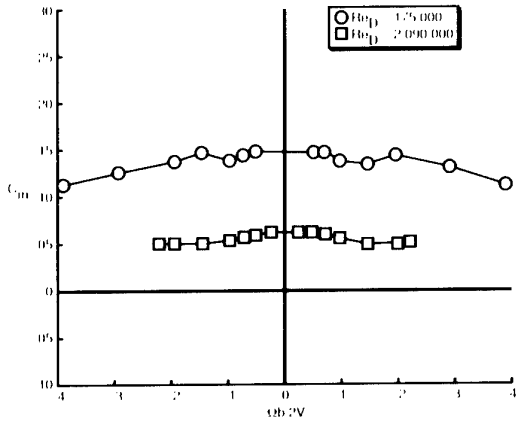

Figure 7.6. Effect of rotation rate and Reynolds number on pitching moment characteristics for the rectangular ogive at 60° angle of attack.

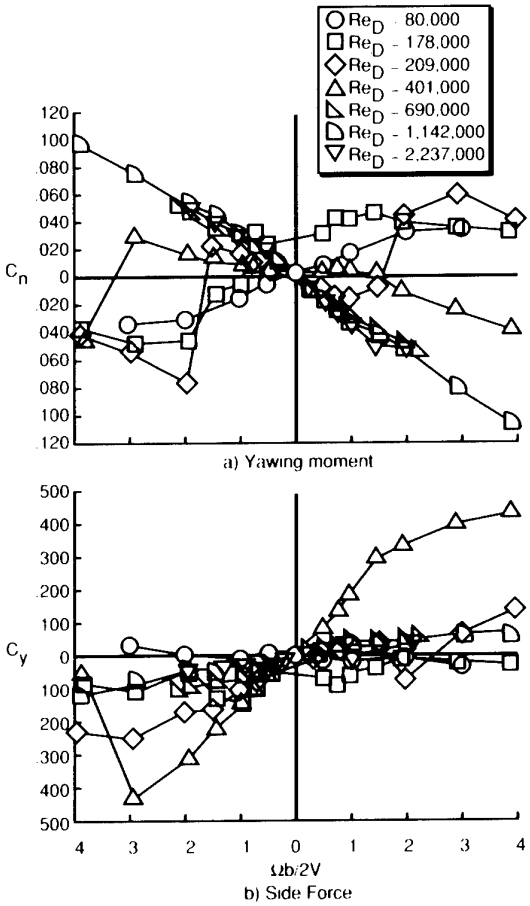

Figure 7.7. Effect of rotation rate and Reynolds number on aerodynamic characteristics for the rectangular ogive at 90° angle of attack.

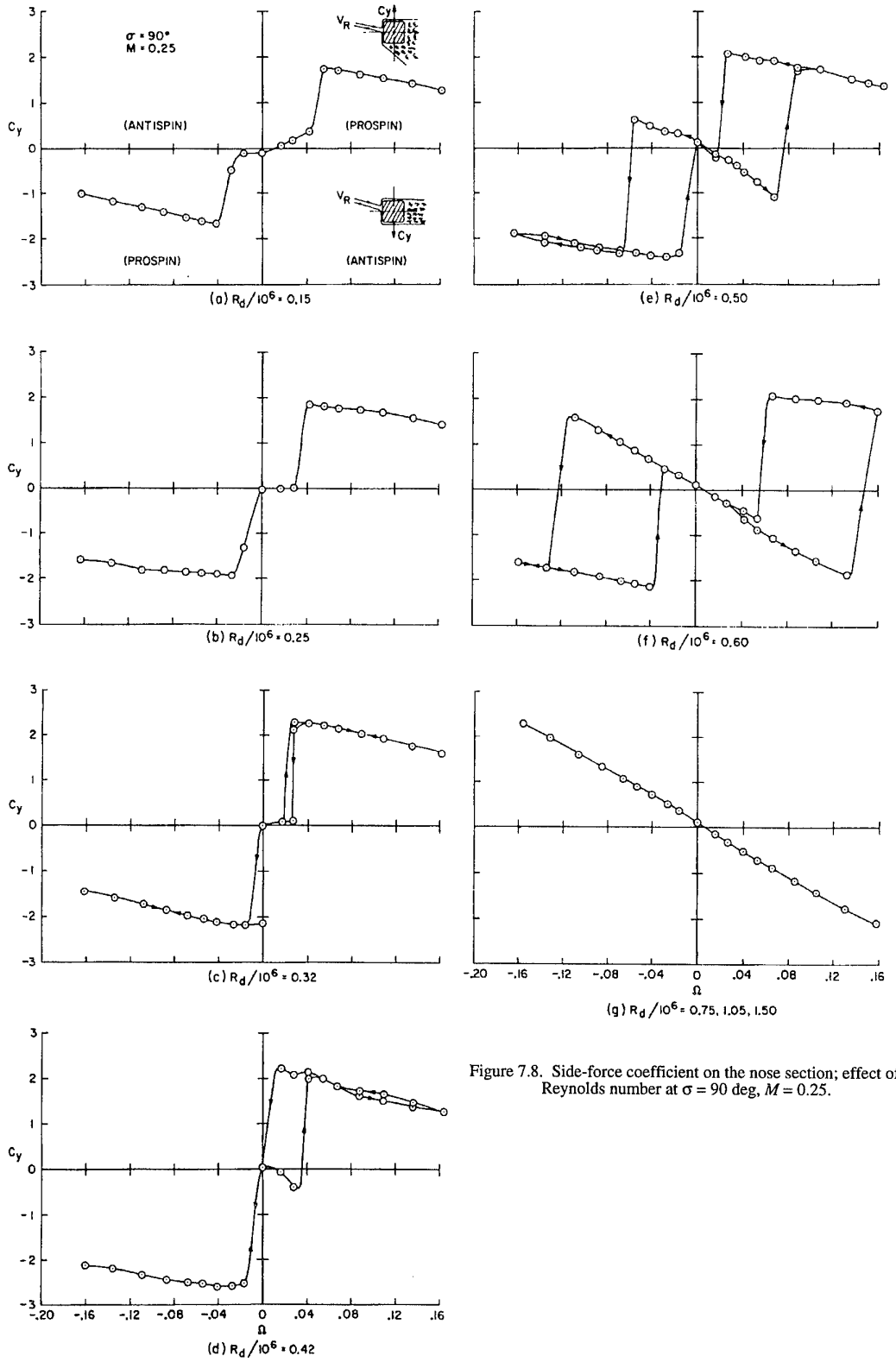

Figure 7.8. Side-force coefficient on the nose section; effect of Reynolds number at $\sigma = 90$ deg, $M = 0.25$.

a) Re_D = 178,000 b) Re_D = 401,000

c) Re_D = 2,237,000

Figure 7.9. Pressure distribution for the rectangular ogive at 90° angle of attack Ωb/2V = 0.0

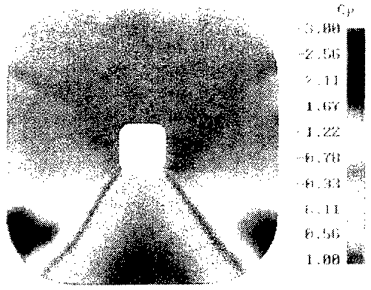

a) Re_D = 401,000

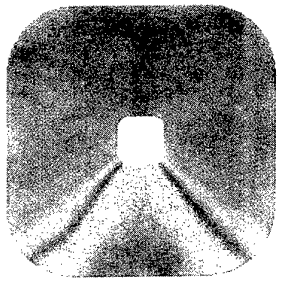

b) Re_D = 178,000

Figure 7.10. Frontal view of pressure distribution for the rectangular ogive at 90° angle of attack and Ωb/2V = 0.0.

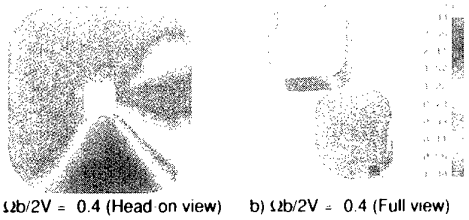

a) Ωb/2V = 0.4 (Head on view) b) Ωb/2V = 0.4 (Full view)

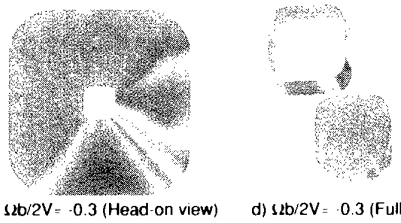

c) Ωb/2V = -0.3 (Head on view) d) Ωb/2V = -0.3 (Full view)

Figure 7.11. Pressure distribution for the rectangular ogive at 90° angle of attack and Ωb/2V = -0.3 and -0.4 for Re_D = 401,000.

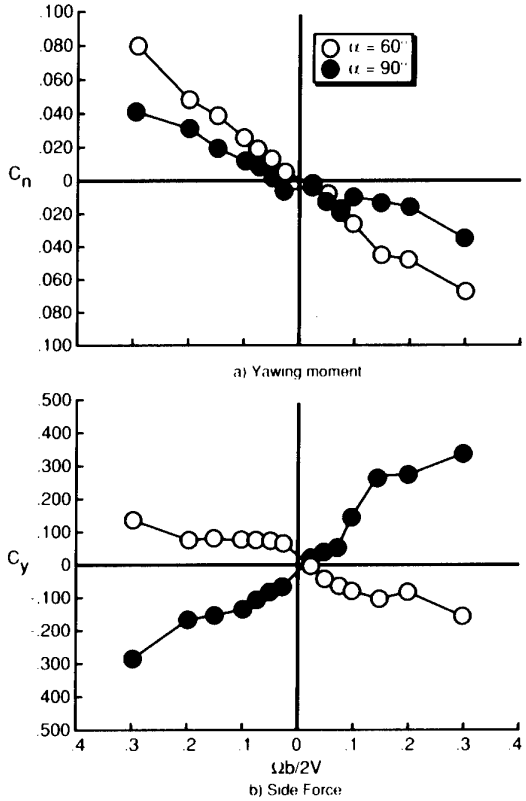

Figure 7.12. Comparison of aerodynamic characteristics for rectangular ogive at 60° and 90° angle of attack.

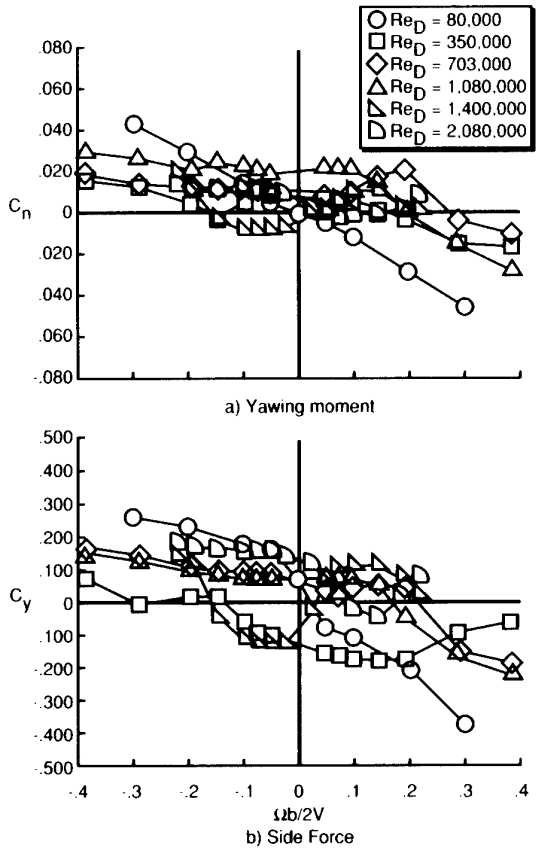

Figure 7.13. Effect of rotation rate and Reynolds number on aerodynamic characteristics for the circular ogive at 60° angle of attack.

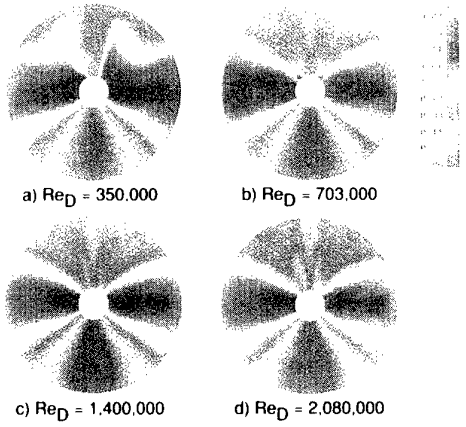

Figure 7.14. Pressure distribution for the circular ogive at 60° angle of attack and Ωb/2V = 0.0.

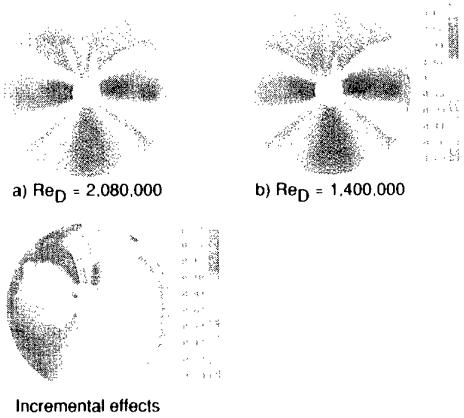

Figure 7.15. Comparison of the pressure distribution at Ωb/2V = -0.1 for the circular ogive at 60° angle of attack for two Reynolds numbers.

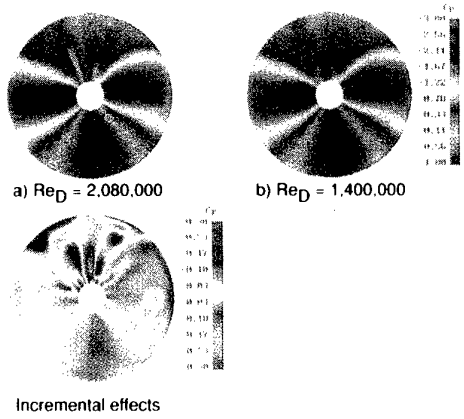

Figure 7.16. Comparison of the pressure distribution at Ωd/2V = -0.2 for the circular ogive at 60° angle of attack for two Reynolds numbers.

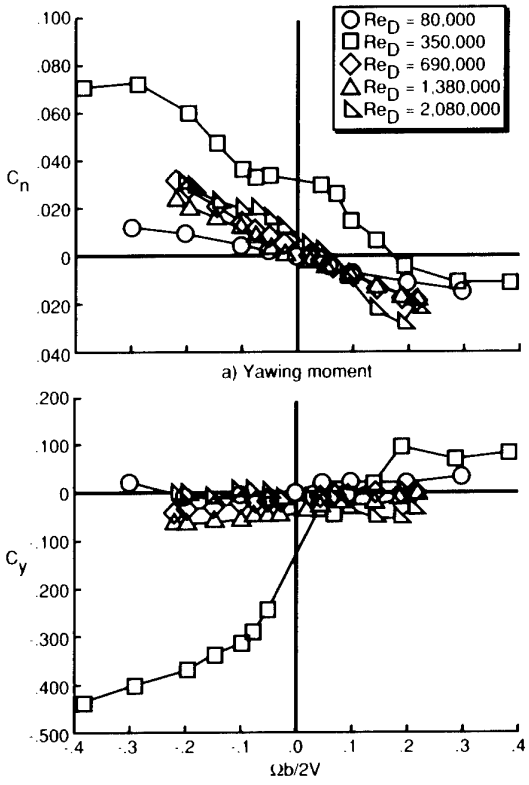

Figure 7.17. Effect of rotation rate and Reynolds number on aerodynamic characteristics for the circular ogive at 90° angle of attack.

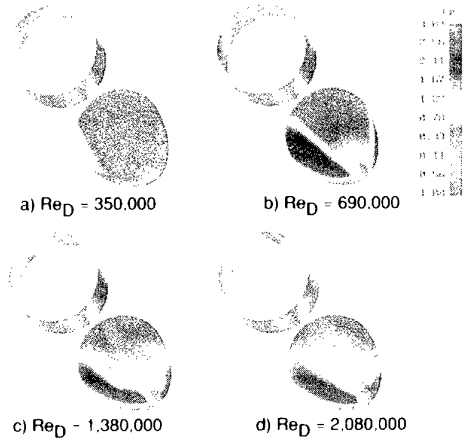

Figure 7.18. Pressure distribution for the circular ogive at 90° angle of attack and Ωb/2V = 0.0.

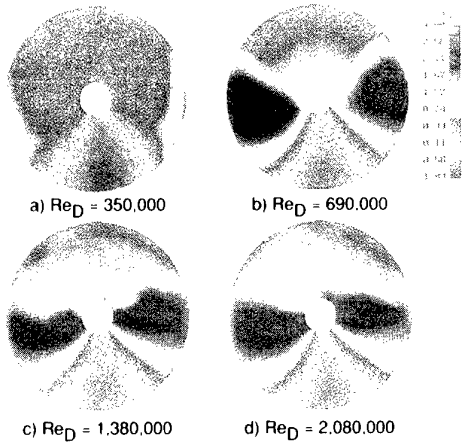

Figure 7.19. Frontal view of pressure distribution for the circular ogive at 90° angle of attack; Ωb/2V = -0.2.

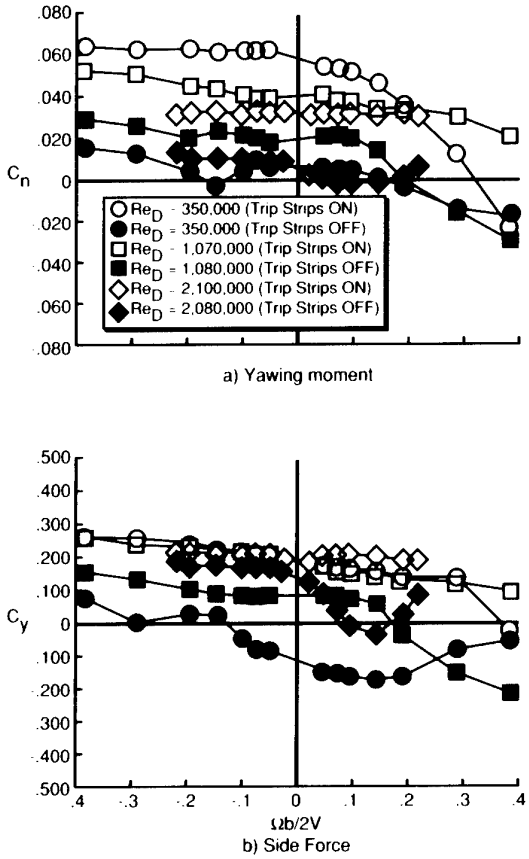

Figure 7.20. Effect of rotation rate and Reynolds number on aerodynamic characteristics for the circular ogive at 90° angle of attack.

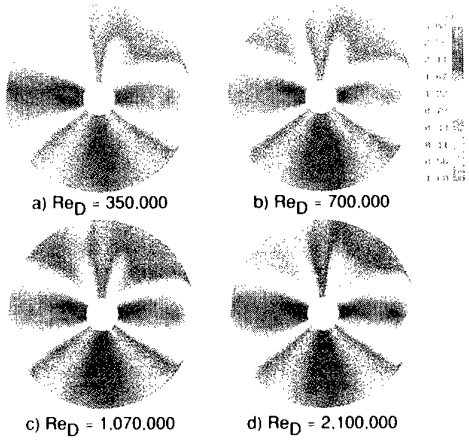

Figure 7.21. Effect of trip strips on forebody pressure distribution at selected Reynolds numbers for the circular ogive at 60° angle of attack and Ωb/2V = 0.0.

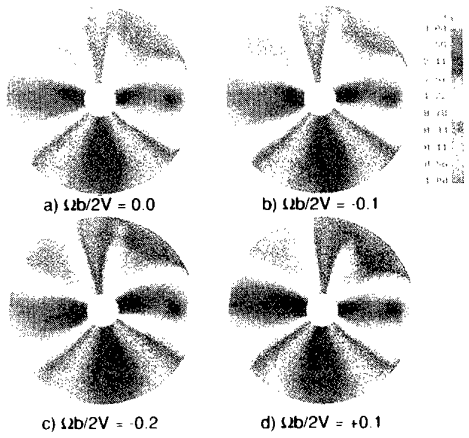

Figure 7.22. Effect of rotation rate on forebody pressure distribution for the circular ogive at 60° angle of attack with trip strips at Re$_D$ = 2,100,000.

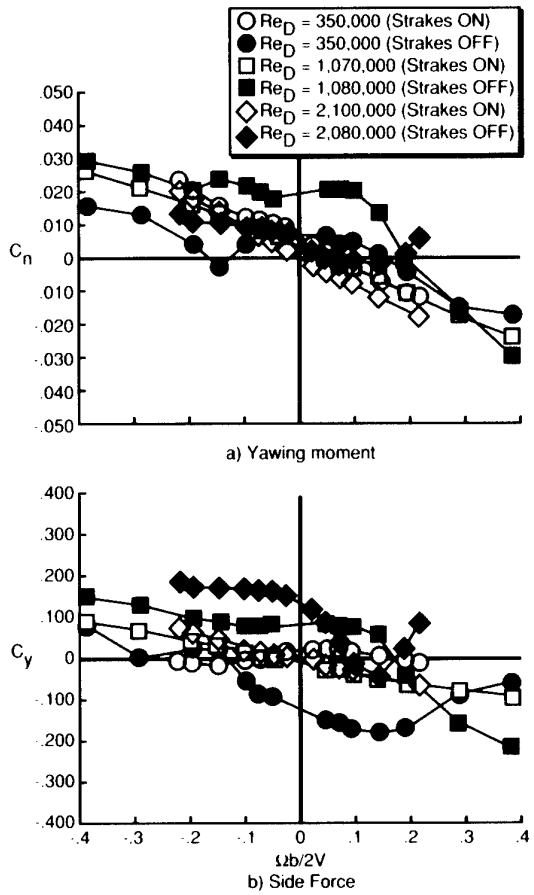

Figure 7.23. Effect of forebody strakes on rotational aerodynamic characteristics at selected Reynolds numbers for the circular ogive at 60° angle of attack.

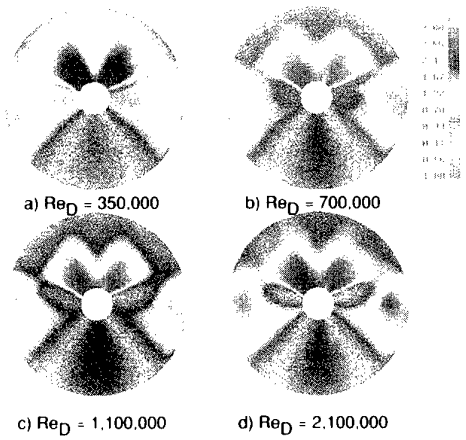

Figure 7.24. Comparison of forebody strakes on and off on forebody pressure distribution for the circular ogive at 60° angle of attack and Ωb/2V = 0.0.

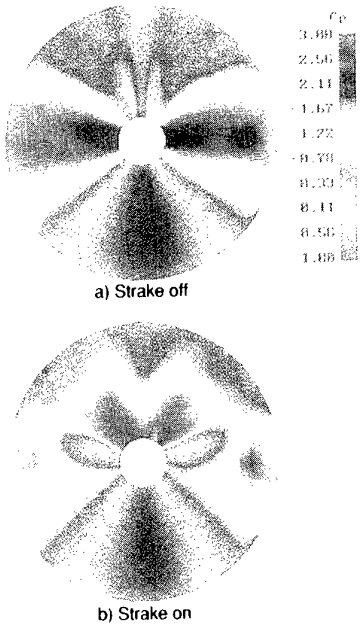

Figure 7.25. Comparison of forebody strakes on and off on forebody pressure distribution for the circular ogive at 60° angle of attack and Re_D = 2,100,000.

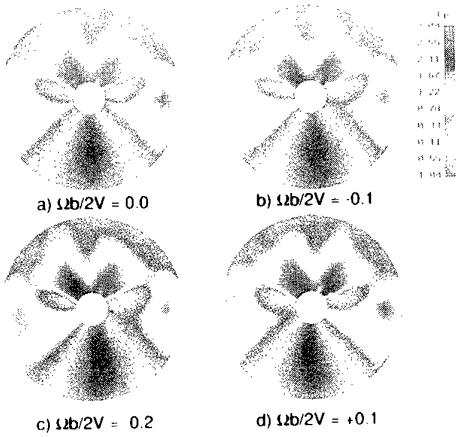

Figure 7.26. Effect of rotation rate on forebody pressure distribution for the circular ogive at 60° angle of attack with forebody strakes at Re_D = 2,100,000.

CHAPTER 8

ANALYSIS OF NON-LINEAR AND UNSTEADY DATA FOR MATHEMATICAL MODELLING

8.0 INTRODUCTION

The FDP Working Group 16 carried out many wind tunnel experiments on a generic combat aircraft configuration. This configuration, described in Chapter 2, comprises a 45° swept wing, tail surfaces, leading edge extensions (LEX) and a high fineness ratio forebody fitted with strakes. The flow pattern on such a configuration is complex. At angle of attack separated flows occur and vortices are generated from the wing, LEX, forebody and strakes. Vortex breakdown or vortex interactions can produce very non linear phenomena like hysteresis, large discontinuities and strong time dependency of aerodynamic loads. Many experiments were conducted at high angles of attack and on dynamic apparatuses like rotary balances or oscillatory rigs, i.e., with dynamic motion of the model with respect to the free stream.

In Chapters 3 and 5 many non-linear and unsteady data have been illustrated. The aim of Chapter 8 is now to analyse the unsteady and non-linear characteristics of these aerodynamic data.

First, in Section 8.1 dynamic derivatives obtained in wind tunnel tests with different dynamic experiments (coning, oscillatory and oscillatory coning) are compared and analysed in order to estimate the sensitivity of dynamic derivatives to the type of motion considered. Effects of motion parameters like frequency, amplitude and mean angle of attack on dynamic derivative calculations are also examined.

In Section 8.2 analysis is focused on time dependency of aerodynamic loads which are encountered during dynamic motions and are due to flow unsteadiness. Time lags of aerodynamic coefficients with respect to time histories of motion parameters are evaluated. It is shown that flow unsteadiness can significantly modify the results of dynamic derivative calculations which assume steadiness and linearity of aerodynamic coefficients during dynamic motion of the model.

Finally, in Section 8.3, some reflections are presented on aerodynamic modelling for some non-linear data. A mathematical model of unsteady and non-linear data is also suggested. Aerodynamic loads obtained during dynamic tests are compared to predictions calculated from both linear and non-linear mathematical modellings.

Except for Subsection 8.1.1, all the data considered in this Chapter were acquired from the dynamic rigs of ONERA-IMFL, namely the "PQR" apparatus (oscillatory tests) and the "TourneBroche" rotary balance (coning and oscillatory-coning tests). This is due to two main reasons. First, because time histories of aerodynamic data are necessary to analyse non linear and unsteady contributions, but such data were available only for IMFL dynamic rigs. Second, within the AGARD FDP-WG16 cooperative programme, large amplitude tests which are closest to high angle-of-attack rapid manoeuvers of a combat aircraft than small amplitude oscillations, were performed only in IMFL facilities.

All the data presented are relative to the BWLHVST configuration (with strakes and transition); these data were obtained at a velocity of 30m/s and a Reynolds number of 655,000 (Re_D= 207,000).

In this Chapter : the derivative $d\alpha(t)/dt$ will be noted :α', the reduced rate of change of angle of attack $d\alpha(t)/dt.c/V$ will be noted: α^*, and the combined derivatives $C_{Nq} + C_{N\alpha'}$ and $C_{mq} + C_{m\alpha'}$ will be respectively noted : $C_{N\alpha^*}$ and $C_{m\alpha^*}$.

8.1 DYNAMIC DERIVATIVE ANALYSIS

8.1.1 Comparison Between Oscillatory, Coning and Oscillatory Coning Derivatives (DRA)

The relationship between derivatives obtained from coning (continuous rotation) and oscillatory tests was discussed in Reference 1. Comparisons were made for the HIRM 1 and HIRM 2 models. Before comparing results from tests on the WG16 model it is convenient to summarize here key points of the discussion in Reference 1.

In a conventional coning test the axis of rotation is coincident with the wind direction. Aerodynamic loads on the model due to steady coning motion are measured by a balance which is aligned along the model body axis. These measurements can be converted to wind axes coefficients and derivatives determined from the gradients of forces with reduced rotation rate. In an oscillatory test, derivatives are obtained directly in body axes but may be converted to wind axes if a complete set has been measured. Thus, derivatives from oscillatory and coning tests are nominally comparable. However, the flow conditions in the tests are different and there is no theoretical basis for agreement. At low angles of attack and sideslip, where there is attached flow over all surfaces of the model, it is possible that there will be agreement between coning and oscillatory derivatives but at high angles of attack, where flow separation, lag and hysteresis effects are present, there may be significant differences.

A comparison of results from coning and oscillatory tests on the WG16 configuration at DRA is made in Fig 8.1. In the DRA tests, model WG16B was tested on the coning balance and WG16A on the oscillatory balance. Results obtained from the oscillatory tests are the body axis derivatives $C_{l_p} + C_{l_\beta}.\sin\alpha$ and $C_{n_p} + C_{n_\beta}.\sin\alpha$ which are converted to wind-axis derivatives $C_{l\Omega}$ and $C_{n\Omega}$ respectively. For the coning tests, the gradients of C_l and C_n vs $\Omega = \omega b/2V$ are measured near the origin, $\Omega = \pm 0.05$, since the reduced roll rate for oscillatory tests was in this range. The variation over this range may not be linear so mean values, using a least squares fit, are determined. Repeatability of coning

data is shown at $\alpha = 32°, 40°, 50°$ and $60°$.

A rolling model induces differential angle of attack on the port and starboard wings. There are positive and negative contributions to the derivative $C_{n\Omega}$ from various sources, including: differential leading edge suction, differential profile drag, induced incidence on the vertical tail and forebody yawing moment due to rotation about the wind axis. These contributions will, of course, vary with configuration and angle of attack. At low angle of attack, $\alpha<25°$, there is fair agreement between the coning and oscillatory data. For $15°<\alpha<35°$ $C_{n\Omega}$ from coning tests is small and positive, whereas oscillatory test measurements are mostly negative. On the WG16 configuration the relative magnitudes of the various contributions to $C_{n\Omega}$ are difficult to predict but it is apparent that there is a negative contribution which is only measured in the small amplitude oscillatory test.

The main contribution to $C_{l\Omega}$ is differential wing lift due to induced differential angle of attack on the outer wing. It is usually negative for well ordered flow. As shown in Fig 8.1 there is agreement between coning and oscillatory data at low angle of attack but the oscillatory data is more positive at higher alpha.

Although coning motion measurements were made at larger intervals of alpha than oscillatory motion measurements, it appears that there is more variation in $C_{l\Omega}$ and $C_{n\Omega}$ from oscillatory tests.

The derivatives $C_{l\Omega}$ and $C_{n\Omega}$ were also obtained from IMFL coning and oscillatory coning tests. The body-axes derivatives $C_{lp} + C_{l\dot{\beta}} \cdot \sin\alpha$ and $C_{np} + C_{n\dot{\beta}} \cdot \sin\alpha$ were measured in oscillatory coning tests but, as for DRA oscillatory results, these were converted to wind axes derivatives $C_{l\Omega}$ and $C_{n\Omega}$. The frequency parameter for the oscillatory coning tests was close to the lower frequency used for the DRA oscillatory tests. These results are shown in Fig 8.2 for the same configuration (BWLHVST) as for the DRA tests. In coning tests, repeat measurements were made at $\alpha = 25°, 40°$ and $50°$. Only six test points were available for comparison.

$C_{n\Omega}$ from IMFL coning and oscillatory coning tests is small for all angles of attack up to $50°$ and in good agreement. Comparison with Fig 8.1 shows that these results are slightly more negative than results from DRA coning tests. $C_{l\Omega}$ from coning tests is less negative than results from oscillatory coning tests for $\alpha>25°$. IMFL results and results from DRA coning tests are of similar magnitude for $\alpha<20°$.

In conclusion, there is fairly good agreement between ONERA-IMFL coning and oscillatory coning measurements for $C_{n\Omega}$ and $C_{l\Omega}$ for $\alpha<25°$ but the comparison of results from oscillatory and coning tests at DRA shows that except at low angle of attack there are substantial differences between these measurements of $C_{n\Omega}$ and $C_{l\Omega}$. This is in contrast to similar comparison made for the HIRM 1 and HIRM 2 models in reference 1 where there was fair agreement, even for $\alpha>20°$. The degree of agreement between results from continuous rotary and oscillatory tests is probably dependent on configuration: particularly wing planform, aspect ratio, leading edge sweep and profile and also on the forebody and presence of a foreplane.

8.1.2 Small / Large Amplitude Comparisons (ONERA/IMFL)

Before dealing with comparisons between derivatives from small and large amplitude motions, some mathematical aspects have to be considered. Common mathematical modellings are based on assumptions that aerodynamic coefficients depend only on the instantaneous values of the motion variables and vary linearly with these variables. For instance the normal force coefficient C_N is often expressed as follows:

$$C_N(t) = C_{N0} + C_{N\alpha}\,\alpha(t) + C_{Nq}\,q(t).c/V + C_{n\alpha'}\,d\alpha(t)/dt.c/V \qquad (1)$$

On the basis of such a mathematical model, dynamic derivatives are usually determined from oscillatory tests by using the "first harmonic method" or an equivalent method. Indeed, during oscillatory tests, $\alpha(t)$ varies as a harmonic signal at a frequency f and amplitude α_A: $\alpha(t) = \alpha_A \sin 2\pi ft + \alpha_0$ (harmonic input). Then, within the linearity assumption, the aerodynamic coefficient (output) is also a harmonic signal at the same frequency.

So, the normal force measurement is considered as a time function including only one harmonic at motion frequency. Mathematically, the general expression of C_N will be $C_N = C_{N0} + A.\sin(\omega t+\phi)$ where A and ϕ are, respectively, the amplitude and phase of the first harmonic. A and ϕ can be directly calculated from measured signals by using a Fourier analysis. Then, considering pitch oscillatory tests ($q=d\alpha/dt$), the first harmonic of the aerodynamic coefficient measurements will provide directly the values of derivatives :

$$C_{Nq} + C_{N\alpha'} = (A \sin\phi) / (\alpha_A\, \omega c/V) \quad \text{and}$$
$$C_{N\alpha} = A \cos\phi / \alpha_A$$

This methodology which is currently used to calculate derivatives of small amplitude oscillatory tests, was also used to calculate the "mean derivatives" for different types of dynamic tests. As aerodynamic coefficient time histories of all the tests carried out at ONERA-IMFL were stored, calculations and comparisons of derivatives could be made off line. These results are presented and discussed hereafter .

8.1.2.1 Pitch oscillatory derivatives of small amplitude

Pitch oscillatory tests of small amplitude (2.9°) were tested at different mean angles of attack (10°, 20°, 25°, 30°, 40° and 50°) and for three values of sideslip (0°, -5° and +5°). Frequency of these tests was 2.5Hz and airspeed was 30m/s.

The dynamic derivatives $C_{N\alpha^*}$ and $C_{m\alpha^*}$ are plotted in Fig 8.3. Sensitivity of results to sideslip is fairly limited except around mean-$\alpha = 25°$ where differences on derivatives are larger.

8.1.2.2 Mean pitch oscillatory derivatives : small/large amplitude comparison

On the PQR apparatus pitch oscillatory tests of large amplitude were carried out at three values of mean angle of attack: 20°, 30° and 40° and for three large amplitudes: 10°, 18° and 28°. In Fig 8.4 are plotted the derivatives $C_{N\alpha^*}$ and $C_{m\alpha^*}$ as function of mean alpha for the different amplitudes. It can be noted that large amplitude tests provide larger values of $C_{N\alpha^*}$ than small amplitude tests. Differences are larger around $\alpha=20°$ than around $\alpha=30°$. The values of $C_{N\alpha^*}$ are more sensitive to test conditions in this α-range. This point has already been noted on different rigs in this α-range. Experiments conducted at DRA with and without the LEX on the model have shown that this effect could be attributed to the LEX. It was suggested it could be due to LEX vortex breakdown or LEX/wing interaction (see Fig 5.4. and Chapter 6). At high angle of attack ($\alpha = 40°$) and for large amplitudes the $C_{N\alpha^*}$ values are larger than for small amplitude tests. As illustrated at length in Chapter 5 (see Figs

5.46 to 5.50) at high angles of attack dynamic stall occurs; this non-linear phenomenon which depends on amplitude motion consequently makes the values of $C_{N\alpha^*}$ derivatives largely biased.

Amplitude effects are lower for $C_{m\alpha^*}$ than for $C_{n\alpha^*}$; the $C_{m\alpha^*}$ derivatives for large amplitude tests are very close or slightly greater than small amplitude derivatives (Fig 8.4). However, at high angle of attack (α = 40°) discrepancies are larger, pitch damping tends to lessen for larger amplitudes.

8.1.2.3 Oscillatory coning derivatives of small amplitude

On the ONERA-IMFL rotary balance called "TourneBroche" the axis of rotation can be tilted through an angle λ relative to the free-stream direction. During such rotary tests, α and β are oscillatory, whereas rotation rate is constant; these tests are referred to as "oscillatory coning". This motion corresponds to a rotary motion of aircraft about an axis not colinear to the velocity vector. Such motion can be encountered in flight during transient phases like loss of control or spin entry, for example. Oscillatory coning tests are also of interest to calculate some specific derivatives. For example, oscillatory coning tests at mean β=0° are rotary tests where the pitch rate q is equal to zero but the angle of attack is oscillatory. Therefore, $C_{N\alpha'}$ and $C_{m\alpha'}$ derivatives can be identified separately from pure pitch rate effects: C_{Nq} and C_{mq} .

In the course of WG16 experiments oscillatory coning tests of small amplitude were performed at mean α= 17°5, 22°5, 27°5, 37°5 and 45° for mean β=0°, and at mean α= 10°, 20°, 25°, 30°, 40° and 50° for mean β=2.5°. Amplitude of α and β oscillations was 2°5 (λ=2.5°) and two rotation rates were tested: Ω=+.12 and -.12.

In Figs 8.5 and 8.6 $C_{N\alpha'}$ and $C_{m\alpha'}$ derivatives are plotted as functions of angle of attack at different rotation rates and mean sideslip angles. No sensitive effect of mean β or rotation rate values can be noted on derivatives; only a slight difference on $C_{N\alpha'}$ derivatives is noticeable between clockwise and counterclockwise rotations, especially for α above 25°. However, effects of angle of attack are very sensitive, in particular for α close to 22° where a spike in normal force derivative is noted. It was previously mentionned (pitch oscillatory tests) that normal force derivatives of the complete configuration fitted with strakes and transition are sensitive in this α-range.

8.1.2.4 Mean oscillatory coning derivatives : small/large amplitude comparison

Large amplitude oscillatory coning tests were carried out at various mean-α : 10°, 20°, 30°, 40° and 50° for 10° and 20° of amplitude, mean β=0° and opposite values of the rotation rate: +.12 and -.12.
In addition at α= 20°, 30° and 40° , high rotation rate .12 and high amplitude 20° tests were repeated during the course of the test series in order to estimate repeatability of results for unsteady tests and at high angles of attack. As shown in Fig 8.7, $C_{N\alpha'}$ and $C_{m\alpha'}$ dynamic derivatives are very similar ; the repeatability of unsteady data can be judged as very satisfactory.

Comparison of derivatives obtained for small and large amplitude tests is provided on Fig 8.8. For the normal force derivative it is surprising to note that results are fairly similar, even at high angles of attack. The situation is different on the pitching moment where some differences appear at high α, especially for larger amplitude tests (20°). At high incidence, values of $C_{m\alpha'}$ are less negative for large amplitude tests than for small amplitude tests. A loss of pitch damping is noted for high amplitude oscillatory coning motions.

8.1.2.5 Mean oscillatory coning derivatives : rotation rate effects

As the rotation rate of oscillatory coning tests is changed, both the coning and the oscillatory rates are changed. At fixed values of mean α and amplitude, the value of rotation rate determine the values of roll, and yaw rates (p and r) and also the frequency of α and β oscillations. During the test series of the WG16 model, tests at mean α= 20°, 30° and 40°, mean β=0 and at 20 degrees of amplitude were carried out for various values of the rotation rate Ω= -.12, -.08, -.04, .02, .04, .06, .08, .10 and .12. The $C_{N\alpha'}$ and $C_{m\alpha'}$ dynamic derivatives were calculated for these different test cases and comparisons are presented on Fig 8.9.
For the normal force derivative $C_{N\alpha'}$, a fairly sensitive effect of the rotation rate can be noted : $C_{N\alpha'}$ values tend to decrease as rotation rate is increased in amplitude. This effect of the rotation rate is more sensitive for higher angles of attack (Fig 8.9). Derivatives calculated for negative rotation rates are not exactly symmetric to those obtained for positive rotation rates. Effect of rotation rate on pitching moment derivative $C_{m\alpha'}$ is less sensitive; nevertheless $C_{m\alpha'}$ tends to be less negative as Ω is increased, in particular at α= 30° and 40°.

8.1.2.6 Comparison between oscillatory and oscillatory coning derivatives

Figure 8.10 presents comparison of oscillatory and oscillatory coning derivatives of small amplitude at mean sideslip equal to zero. To compare with oscillatory derivatives, values of C_{Nq} and C_{mq} derivatives were added to $C_{N\alpha'}$ and $C_{m\alpha'}$ calculated with oscillatory coning tests. Although these tests were not carried out at exactly the same values of angle of attack, it can be concluded that differences are relatively small except perhaps for some discrepancies for the normal force derivative. The spike on $C_{N\alpha'}$ seems precisely located around α= 22°. Oscillatory tests were not carried out at an angle of attack of 22° and therefore the spike was not found.

Figure 8.11 shows the same type of comparison but for large amplitude tests. Differences are larger than for small amplitude tests. The pitch oscillatory tests provide larger values of dynamic derivatives than the oscillatory coning tests. So, it appears that dynamic stall effects are more prevalent in oscillatory motion than in oscillatory coning motion.

8.2 TIME HISTORY ANALYSIS (ONERA/IMFL)

Unsteady and non-linear aerodynamic phenomena associated with oscillatory motion can be strong functions of frequency and amplitude. Consequently, for data analysis, test measurements at high frequency (currently 330Hz) are stored and then analyzed and processed off-line before achieving data reduction. During a dynamic test only one degree of freedom is varying : the pitch angle θ for pitch oscillation or the heading angle ψ for oscillatory coning motion. To obtain time histories of coefficients, aerodynamic data are calculated for an angular sector of the degree of freedom θ or ψ. As motion and signals are periodic, each cycle is divided into angular windows of θ or ψ ; then average values of coefficients and motion parameters

are calculated within each window. A low pass filter with a fast Fourier transform eliminates noise frequencies. The choice of the frequency bandwith is determined by considering the lowest structural frequency due to vibration of the mounting. Practically, only the frequencies above 10Hz were eliminated. Consequently, as small amplitude oscillatory tests are at 2.5Hz and oscillatory coning tests are at 1.6Hz, the aerodynamic coefficients are not limited to the first harmonic as within the linear approach. Thus, aerodynamic contributions of higher frequencies, practically up to 10Hz, can be considered. This procedure, currently used at ONERA-IMFL for small as well as for high amplitude dynamic tests, provides time histories of aerodynamic coefficients which are now presented.

8.2.1 Dynamic Tests of Small Amplitude

In Figs 8.12 and 8.13 the normal force coefficient C_N and the pitching moment C_m are plotted against α for pitch oscillatory tests of small amplitude at 6 values of mean α: 10°, 20°, 25°, 30°, 40°and 50°. A short analysis of such curves can bring out information on dynamic behaviour of aerodynamic coefficients. Indeed, as the motion is periodic, aerodynamic coefficients are also periodic, so curves are closed. Within the linearity assumption, if α is oscillatory, the measured aerodynamic coefficient must also be oscillatory at the same frequency. Therefore, in the linear approach the shape of the curves $C_N(\alpha)$ or $C_m(\alpha)$ should be similar to ellipses; otherwise it means that aerodynamic non-linear or unsteady effects exist. Moreover, the breadth of the closed curves along the ordinate measures the magnitude of dynamic effect. On these curves arrows indicate the time evolution. So if the arrow on the curve is oriented in the clockwise direction, the dynamic derivative is positive and vice versa. Dynamic data can be compared to static data which are plotted with a dashed curve.

Considering data plotted on Figs 8.12 and 8.13, the following points can be noted :

- dynamic effects are larger at high angles of attack, they are very small on C_N at α = 10°
- with regards to the curve shape it is clear that non-linear or unsteady effects are present, in particular at α = 20°, 25°, 40°, 50° for C_N and at every incidence for C_m
- $C_{N\alpha^*}$ is always positive and $C_{m\alpha^*}$ is always negative
- the mean axis of the closed curves is close to the static curve at moderate α, but it is pivoted with respect to the static curve at high angles of attack. As will be shown hereafter, this indicates time lags of the coefficient with respect to the motion.
- $C_N(\alpha)$ at mean α = 20° and 25° show an increase of curve breadth as α approaches 22°. Although the spike on $C_{N\alpha^*}$ could not be identified with oscillatory test results at mean α = 20° (Fig 8.10), time history of the oscillatory test reveals the dynamic increase of C_N as α approaches 22°. It is interesting to note that, in this α-range, there exists a kink on the static data due to the LEX.

Thanks to time histories of coefficients, another alternative to "mean" dynamic derivatives exists to calculate "local" derivatives at constant angle of attack but different from the normal mean angle of attack. Indeed, considering closed curves in Figs 8.12 or 8.13, at a given value of angle of attack the aerodynamic coefficient time histories provide two different values corresponding to opposite values of α^*. Consequently, a "local" dynamic derivative can be calculated as a partial derivative of normal force with respect to α^*. Such calculations of <u>local</u> derivatives have been made with data relative to oscillatory tests of different amplitudes (10°,18° and 28°) at mean α=20°. In Fig 8.14 these results are plotted and compared to small amplitude derivatives. Differences in derivative value are fairly limited for pitching moment except maybe at high α. This is not too surprising because mean α of these tests is equal to 20°, so high values of angle of attack are obtained when α is close to its maximum value, i.e: for small changes in α^*. Therefore accuracy of derivatives is smaller at high α in this case. Discrepancies are a bit larger on normal force; they can be attributed to time dependency effects which are sensitive for this coefficient. However, large amplitude dynamic tests can provide local dynamic derivatives which are comparable to small amplitude derivatives over a large α range.

In order to estimate time dependency of aerodynamic coefficients, "dynamic contributions" have been calculated from the global aerodynamic coefficients obtained during oscillatory tests. These dynamic contributions are considered as the difference between the global coefficient (for instance $C_N(t)$) and the static coefficient corresponding to the angle of attack and sideslip values at the same time t : $\alpha(t)$, $\beta(t)$.

The following notation is introduced :

$$C_{i\,dyn}(t) = \text{global } C_i(t) - \text{static } C_i(\alpha(t), \beta(t)).$$

In Figs 8.15 and 8.16 the dynamic contributions C_{Ndyn} and C_{mdyn} are plotted against $\alpha^*=d\alpha/dt.c/V$. With reference to the instantaneous and linear model (1) the dynamic contribution relative to oscillatory motions is proportional to α^*. Therefore, within this approach, for oscillatory tests, the curves $C_{Ndyn}(\alpha^*)$ and $C_{mdyn}(\alpha^*)$ should be very close to straight lines. It can be noted on Figs 8.15 and 8.16 that the actual situation is completely different, in particular at high angles of attack. The "mean" slope of these dynamic contributions $C_{Ndyn}(\alpha^*)$ and $C_{mdyn}(\alpha^*)$ correspond to the "mean" dynamic derivatives within the linear approach : $C_{N\alpha^*}$ and $C_{m\alpha^*}$. On the normal force this slope enlarges with angle of attack, but the curve breadth enlarges too, indicating a larger time dependency of the coefficient. On the pitching moment the change in slope is not so large with mean α but it can be noted that higher frequencies (non-linearities) are present (see Fig 8.16). At mean α = 20° non-linear behaviour of C_{Ndyn} is also noticeable.

In Fig 8.17 the same coefficients C_{Ndyn} and C_{mdyn} are plotted as functions of time at different values of mean α. With reference to the linear modelling (1) the dynamic contributions should be in phase and proportional to $\alpha^*(t)$ at each time. However, in Fig 8.17 the following points can be noted :

- dynamic contributions comprise higher frequencies than α^* frequency (non-linear contributions), especially on the normal force at mean α= 20° and on the pitching moment at mean α= 20° and 50°. As previously mentionned, around α= 20°, the non-linear behaviour of the aerodynamic coefficients, especially the normal force was attributed to the LEX vortices. On the contrary, non-linearities at high angles of attack (α= 50°) were rather expected.
- time lags of dynamic contributions with respect to $\alpha^*(t)$ are noticeable on both the normal force and pitching moment coefficients,
- time lags are significantly larger at mean α=50° as the flow is completely separated from surfaces,
- the larger mean α, the larger the magnitude of C_{Ndyn} ,
- differences of time lags appear between phases where $\alpha^*(t)$ is positive and those where $\alpha^*(t)$ is negative, in particular on the pitching moment at high incidence.

In conclusion, though these oscillatory tests have a small amplitude, it clearly appears that aerodynamic coefficients are time dependent. In addition, non-linear contributions exist even

at moderate angles of attack. Therefore, dynamic derivatives seem not to be sufficient to correctly describe unsteady aerodynamics on such a generic fighter configuration. Time lags of aerodynamic data with respect to the motion tend to shift values of dynamic derivative calculations.

The analysis of oscillatory coning data time histories is a bit more complicated because both the angle of attack and sideslip are oscillatory. In Fig 8.18 $C_{Ndyn}(t)$ and $C_{mdyn}(t)$ have been plotted with $\alpha^*(t)$ for oscillatory coning tests of small amplitude at mean $\beta=0°$. As for oscillatory tests, time lags are noticeable on normal force. However, data are more non-linear than oscillatory data. For lateral coefficients, the dynamic contributions in roll: C_{ldyn} and in yaw: C_{ndyn} have also been calculated and plotted on Fig 8.19 with β^*: the reduced rate of change of sideslip. Time histories show that higher frequencies than motion frequency are present, in particular on the rolling moment, and it can be concluded that large non-linear effects exist. Effects of $\alpha^*(t)$ on lateral coefficients could probably explain some of these non-linearities.

8.2.2 Dynamic Tests of Large Amplitude

To illustrate unsteadiness and non-linearity of dynamic contributions, Fig 8.20 presents at mean $\alpha= 40°$ time histories of C_{Ndyn} for three values of large amplitude : 10°, 18° and 28°. On these curves time lags of $C_{Ndyn}(t)$ with respect to $\alpha^*(t)$ have been roughly estimated between .1 and .2 sec. High amplitude tests were performed at a frequency of 1Hz, so these time lags are not negligible with respect to the period of a complete cycle which lasts one second. Indeed, during this same period of time the angle of attack can vary approximately ten degrees. Maximum values of dynamic contributions are also quite dependent on amplitude of oscillatory tests. It will be also noted that time lags are significantly smaller as angle of attack decreases ($\alpha^*<0$). Figure 8.21 presents rough estimates of reduced time lags of normal force ($\tau^*= \tau.c/V$) against mean-α for different values of amplitude. These time lags were calculated only for positive α^* phases. In comparison with small amplitude test data, time lags of high amplitude tests are much larger. On this figure the maximum values of normal force dynamic contribution are also plotted. These dynamic contributions can be very large, up to 0.80 in normal force coefficient. This maximum value obtained during an oscillatory cycle is quite dependent on mean α and amplitude (or α^*).

Another example of illustrative data is presented in Fig 8.22 where $C_{Ndyn}(t)$ and $C_{mdyn}(t)$ are plotted with $\alpha^*(t)$ for large amplitude oscillatory coning motions ($\lambda=20°$) at opposite values of the rotation rate (+.12 and -.12) and at mean $\alpha= 50°$. The good symmetry of dynamic contributions with respect to the sign of the rotation rate is noticeable for the normal force as well as for the pitching moment. Futhermore, on $C_{mdyn}(t)$ strong non-linear contributions are noted. Dynamic behaviour of pitching moment appears to be complex at high α. Although static effects due to sideslip have been substracted from time history of the pitching moment measurement, dynamic effects of sideslip, due for instance to $\beta^* = d\beta/dt.b/V$ could be envisaged in order to represent pitching moment behaviour.

8.3 UNSTEADY AND NON LINEAR MATHEMATICAL MODELLING (ONERA/IMFL)

To predict aircraft motions a mathematical model of the aerodynamics is necessary. Commonly the formulation of mathematical models is instantaneous and linear. At high α, flight dynamicists have to modify this formulation in order to produce non-linearities of aerodynamic coefficients. In this endeavor the different derivatives are usually expressed as functions of the motion variables : angle of attack, sideslip, or rates. These derivatives are either tabulated or expressed as polynomials of motion variables. Such formulations are non-linear, but nevertheless they are instantaneous. Each aerodynamic coefficient $C_i(t)$ is only a function of variables at the current time t : $\alpha(t)$, $\beta(t)$.... Therefore, this formulation is inadequate to produce dynamic manoeuvers of combat aircraft when the flow is unsteady and aerodynamic coefficients are time dependent. Moreover, it was shown in the previous section 8.2 on time history analysis that time lags of coefficients had to be taken into account in order to correctly represent aerodynamics for dynamic motions. For this goal a realistic mathematical formulation of unsteady and non linear model is proposed below.

Within the instantaneous and linear modelling (1) the dynamic contribution is : $C_{Ndyn}(t) = C_{N\alpha'} .\alpha^*(t)$. In order to produce time dependency of aerodynamic coefficient, a more general mathematical formulation could be the following :

$$C_{Ndyn}(s) = H(s) . A^*(s) \quad (2)$$

where : s is the Laplace variable,

$C_{Ndyn}(s)$ is the Laplace transform of the dynamic contribution $C_{Ndyn}(t)$,

$A^*(s)$ is the Laplace transform of $\alpha^*(t)$,

H(s) is a transfer function relating the motion variable $\alpha^*(t)$ to the aerodynamic response.

Then the aerodynamic effect is not limited to an instantaneous response but the unsteady coefficient at time $t - \delta t$, $C_N(t - \delta t)$ may influence $C_N(t)$.

As a first step, the simpler formulation of type (2) is a first order transfer function. Thus, two dynamic parameters characterize the unsteady aerodynamic response, a gain G which is relative to the instantaneous contribution and a time constant T which is relative to the time lag contribution. In this case the mathematical formulation is:

$$C_{ndyn}(s) = \frac{G}{(1+T.s)} . A^*(s)$$

This formulation is also equivalent to the first order differential equation :

$$C_{ndyn}(t) = G.\alpha^*(t) - T.dC_{Ndyn}(t)/dt \quad (3)$$

With this formulation, at any time t, the dynamic contribution $C_{Ndyn}(t)$ is the solution of the differential equation referenced as (3). The instantaneous dynamic contribution to normal force coefficient has two components which are respectively proportional to the rate of change of angle of attack $\alpha^*(t)$ and to the rate of change of dynamic contribution to normal force $dC_{Ndyn}(t)/dt$. If time lags are neglegible, the time constant T is equal to zero and the formulation (3) is identical to the instantaneous modelling (1) with $G = C_{N\alpha'}$. In that case the gain G corresponds exactly to the linear dynamic derivative $C_{n\alpha'}$.

Such a mathematical modelling has already been applied to unsteady data of an Alphajet model at high angles of attack on the IMFL rotary balance (Ref 2). Correlation with flight test data was very good and showed the importance of correctly representing the unsteady aerodynamic contributions at high

angles of attack (see Ref 3). A similar mathematical model, but using internal dynamic variables to represent unsteady aerodynamic coefficients of separated and vortical flows, is also proposed by Goman and Khrabrov (Ref 4).

Formulation (3) is not instantaneous and can properly take into account some unsteady effects which have been noted through WG16 model data analysis. Moreover, if the parameters are not constant but depend on motion variables, non-linear effects can be expressed in this formulation. The parameters are evidently function of angle of attack. Futhermore, it has been properly noted in the previous section on time history analysis that time lags of the aerodynamic coefficients could be different according to the sign of $\alpha^*(t)$: increasing-α (i.e: $\alpha^*(t)>0$) or decreasing-α (i.e: $\alpha^*(t)<0$). Consequently, the mathematical formulation was chosen as follows:

$$C_{Ndyn}(t) = G(\alpha(t), \text{sign}(\alpha^*(t))) \cdot \alpha^*(t) - T(\alpha(t), \text{sign}(\alpha^*(t))) \cdot dC_{Ndyn}(t)/dt \quad (4)$$

To compare predictions obtained with such a mathematical model with those obtained with a "classical" linear formulation, the parameters G and T have been calculated with pitch oscillatory data from tests at small amplitude and at a frequency of 2.5Hz. These results are presented on Fig 8.23 for the normal force and the pitching moment. The gains and time constants have been calulated for different mean α and separately for positive and negative α^*. On the base of such a mathematical model, global aerodynamic coefficients have been calculated as functions of time histories of oscillatory test variable $\alpha(t)$. This prediction of normal force coefficient during oscillatory tests has been compared to test data and to the prediction obtained with a "classical" model ; i.e. a model comprising only static data and dynamic derivatives. These comparisons are presented for the small amplitude pitch oscillation tests.

In Figure 8.24, normal force predictions obtained with these two types of mathematical model are plotted against α and compared to experimental data. In addition, static data have also been plotted to provide a qualitative estimation of dynamic effects. It can be noted that results obtained with transfer functions are better than those obtained with derivatives, in particular at high angles of attack. Above α=30°, in comparison with test data, predictions obtained with dynamic derivatives are very poor; the shape and the orientation of C_N curves are significantly different from experiments. Oppositely, results from the transfer function model are close to experimental data at high angles of attack. Taking time lags into account significantly improves accuracy of predictions. Figure 8.25 presents the same comparisons plotted as functions of time. With the transfer function model results are better, notably in terms of phase and amplitude; the transfer function model can be judged as quite satisfactory.

In Fig 8.26 comparisons are presented for the pitching moment C_m. Results are not as satisfactory as for the normal force. Indeed, through data analysis more non-linear effects had been noted (Fig 8.17). A more sophisticated model would be necessary to produce these non-linearities. However, improvements in predictions obtained with first order transfer functions are also noticeable.

It can be concluded that time dependency of aerodynamic coefficients can be taken into account with only a first order transfer function formulation. Predictions with such a model are satisfactory and/or are largely improved with respect to dynamic derivative predictions, especially at high angles of attack.

The same type of mathematical modelling has also been realised for the yawing moment C_n. The formulation is similar to formulation (4); however, the variable α^* has been replaced by β^*. Thus, the mathematical model of yawing moment is expressed below :

$$C_{ndyn}(t) = G(\alpha(t), \text{sign}(\beta^*(t))) \cdot \beta^*(t) - T(\alpha(t), \text{sign}(\beta^*(t))) \cdot dC_{ndyn}(t)/dt$$

Parameters of this formulation are shown in Fig 8.27a. Comparisons between test data and predictions with a first order transfer function model or derivatives have been made for small amplitude oscillatory coning tests at mean $\beta = 0°$ and Ω =+.12. They are presented in Fig 8.27b. From a general point of view the transfer function model improves predictions of yawing moment measurements; however, some discrepancies with experimental data still exist. Achieving accurate yawing moment modelling appears more difficult and would probably require more complex transfer functions. Moreover, oscillatory coning testing produces motion where oscillations of angle of attack and sideslip are superimposed to roll and yaw rates. Inclusion into the yawing moment model formulation of supplementary dynamic terms, due to $\alpha^*(t)$ for instance, could also be of benefit to predict with a better accuracy such a non linear behaviour of the yawing moment coefficient .

8.4 REFERENCES

1. O'Leary, C.O., "Relation between Rotary and Oscillatory Test Results", Chapter 10, AGARD-AR-265, Dec 1990, pp. 209-212

2. Tristrant, D., "Use of Rotary-Balance Data in the Prediction of Aircraft Dynamics", Chapter 9.3, AGARD-AR-265, Dec 1990, pp.189-192

3. Tristrant, D., "Correlation with Flight Tests", Chapter 11.3, AGARD-AR-265, Dec 1990, pp.217-218

4. Goman, M. and Khrabrov, A., "State-Space Representation of Aerodynamic Characteristics of an Aircraft at High Angles of Attack", J. Aircraft, Vol.31, No. 5, Sept.-Oct. 1994, pp.1109-1115

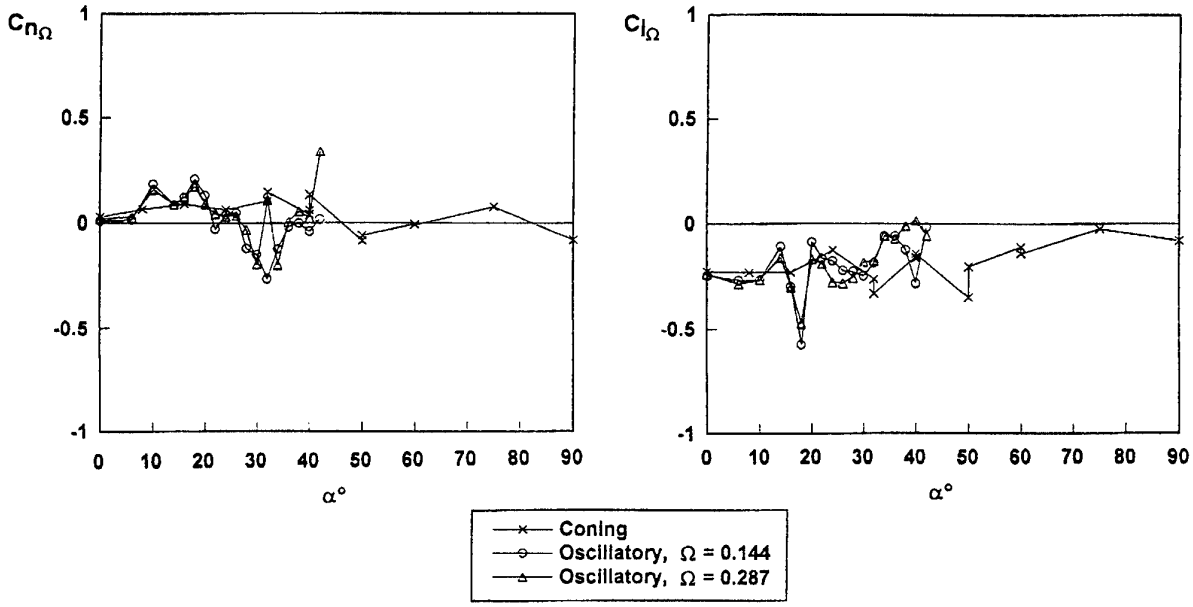

Fig 8.1 Comparison of oscillatory and coning derivatives from DRA tests.

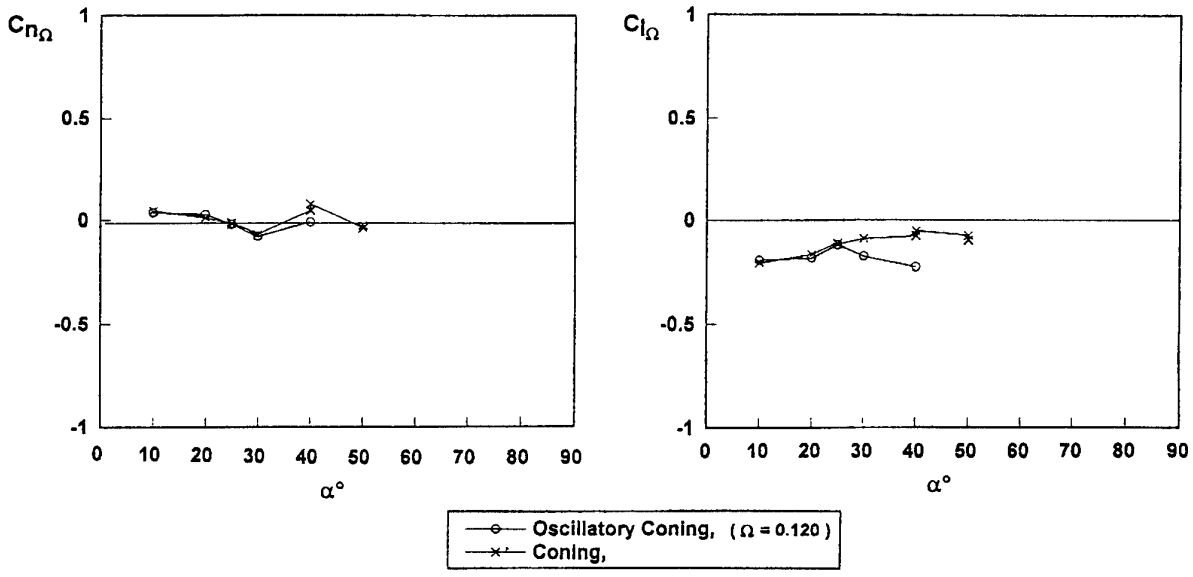

Fig 8.2 Comparison of coning and oscillatory coning derivatives from ONERA-IMFL tests

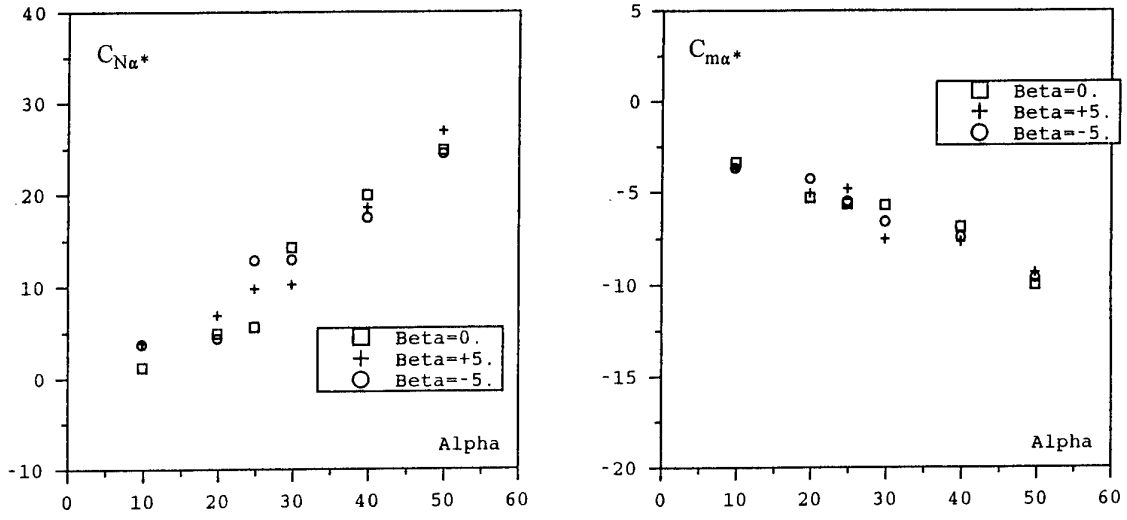

Fig 8.3 Small amplitude oscillatory derivatives

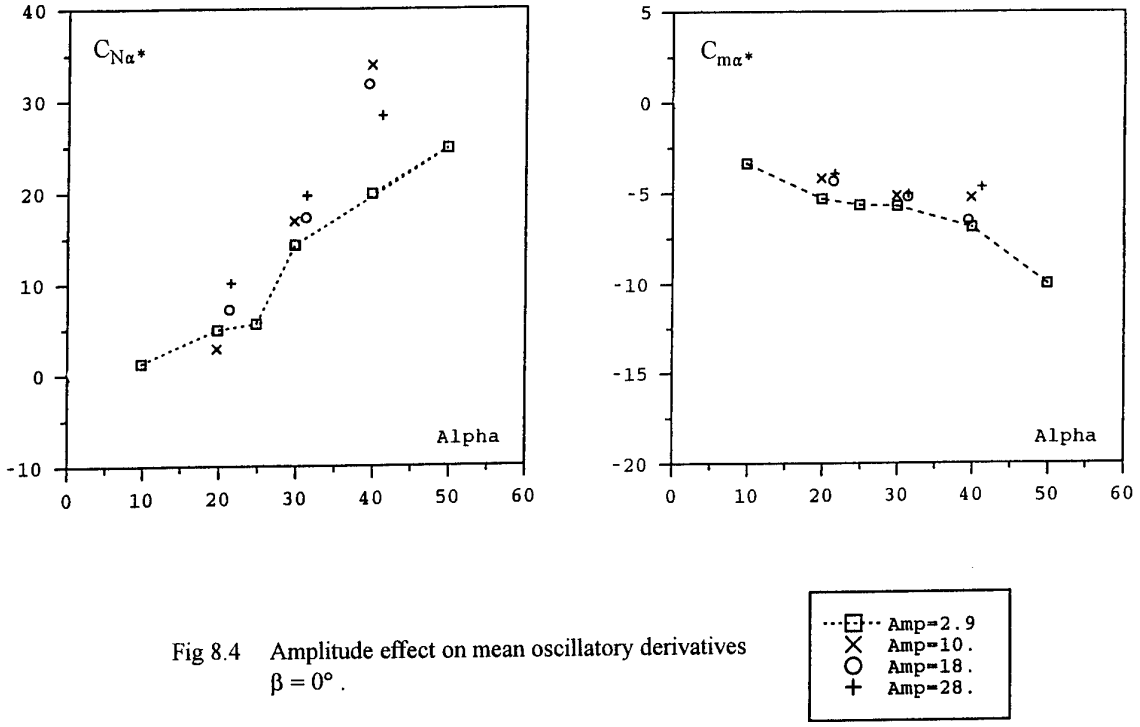

Fig 8.4 Amplitude effect on mean oscillatory derivatives $\beta = 0°$.

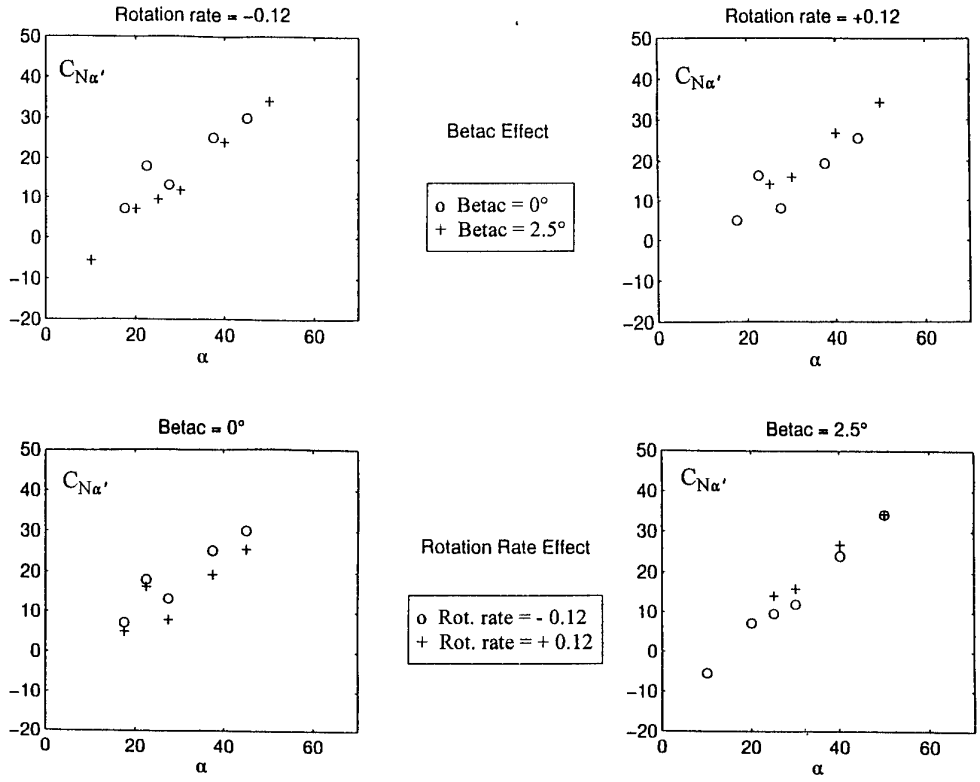

Fig 8.5 Small amplitude oscillatory coning derivatives.
Sideslip and rotation rate effects on $C_{N\alpha'}$.

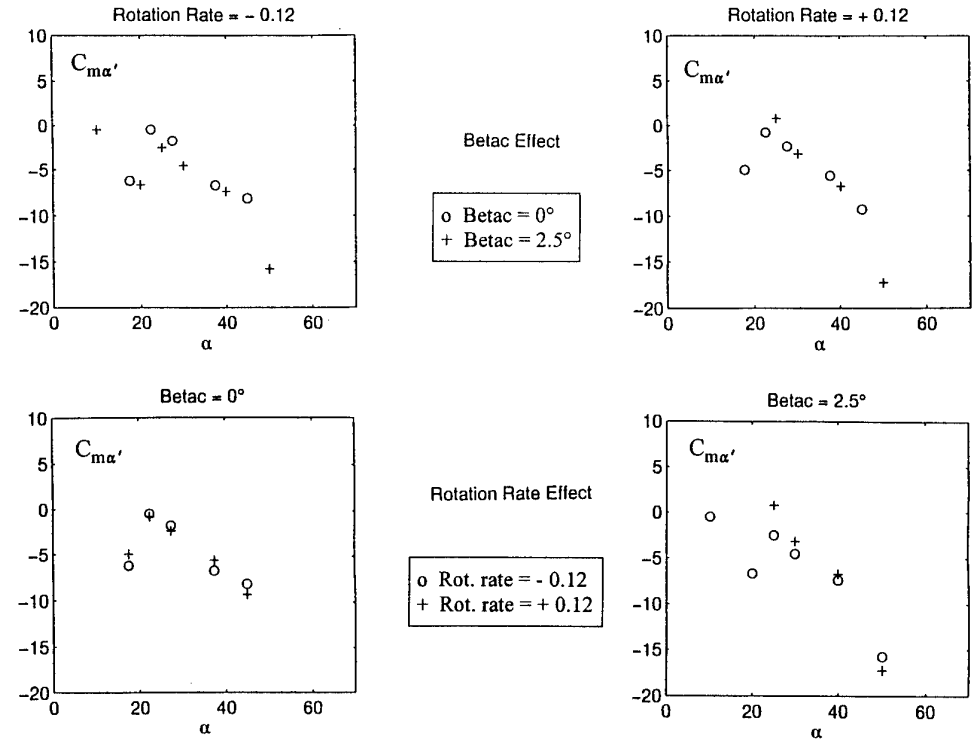

Fig 8.6 Small amplitude oscillatory coning derivatives.
Sideslip and rotation rate effects on $C_{m\alpha'}$.

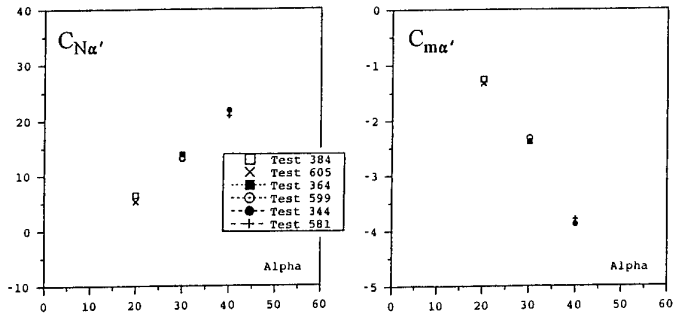

Fig 8.7 Repeatability of mean oscillatory coning derivatives. Amplitude = 20°.

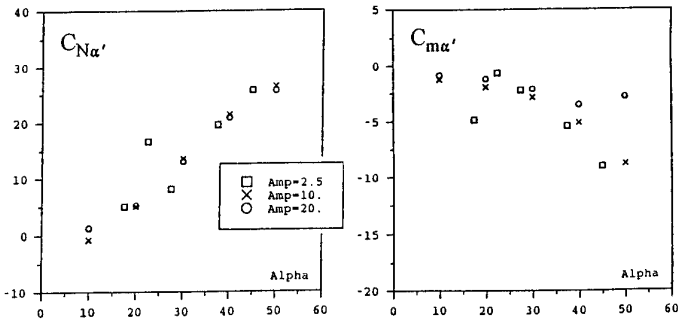

Fig 8.8 Amplitude effect on mean oscillatory coning derivatives

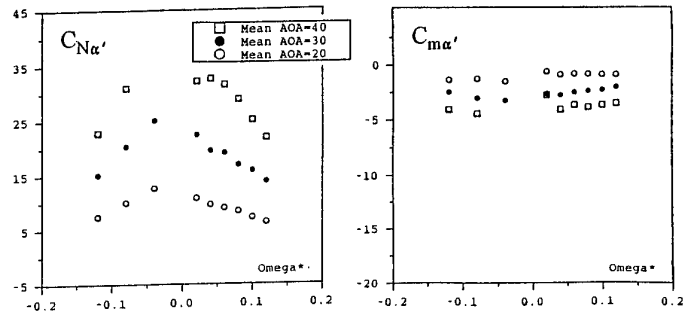

Fig 8.9 Rotation rate effect on mean oscillatory coning derivatives. Amplitude = 20°.

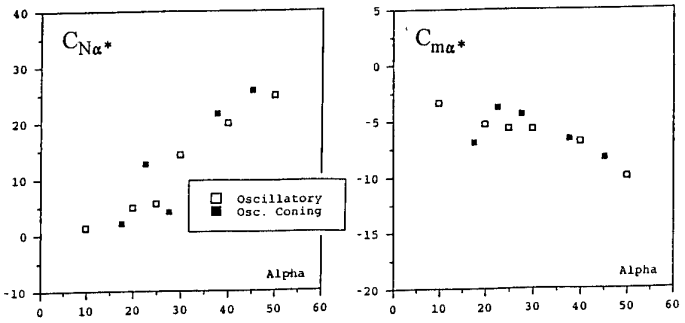

Fig 8.10 Comparison of small amplitude oscillatory and oscillatory coning derivatives

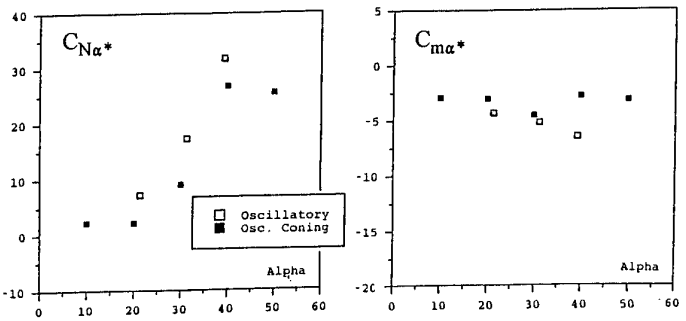

Fig 8.11 Comparison of oscillatory and oscillatory coning derivatives. Amplitude = 20°.

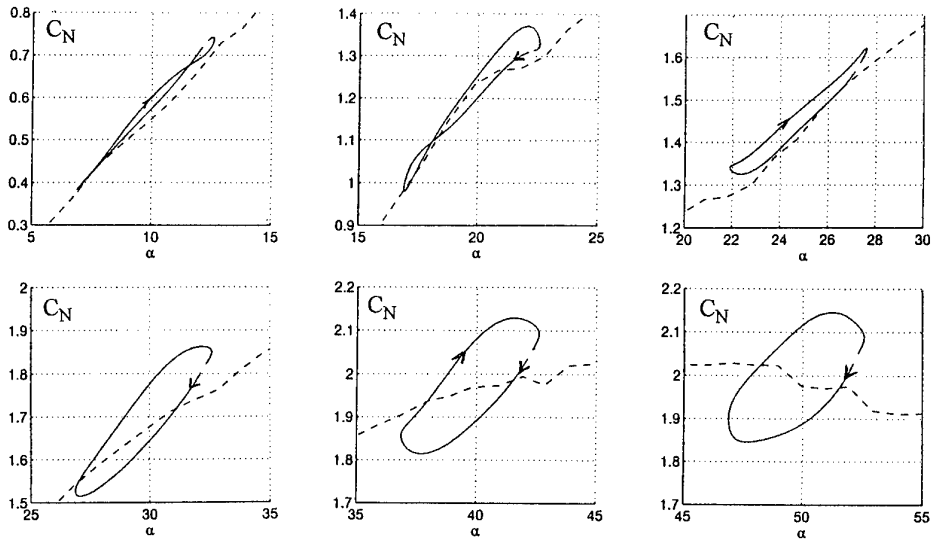

Fig 8.12 Normal force time histories of small amplitude oscillatory tests

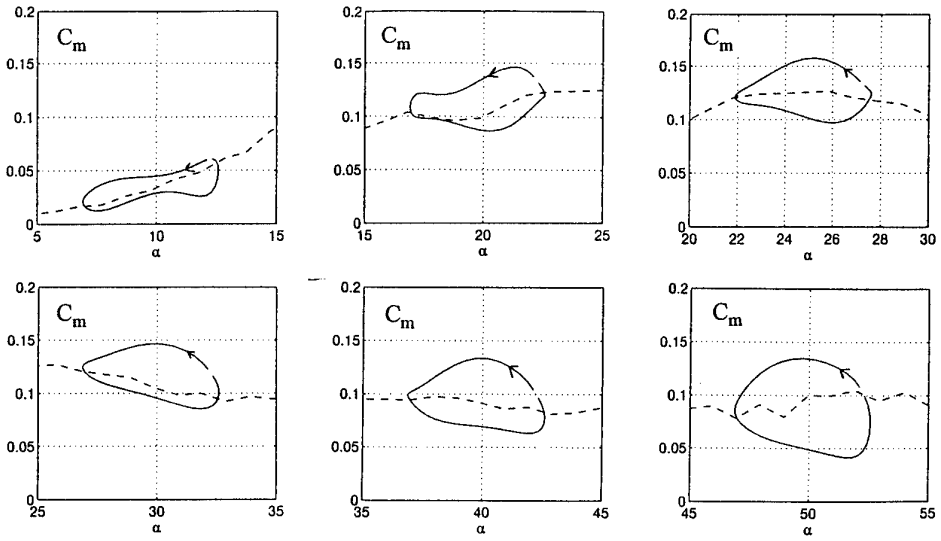

Fig 8.13 Pitching moment time histories of small amplitude oscillatory tests

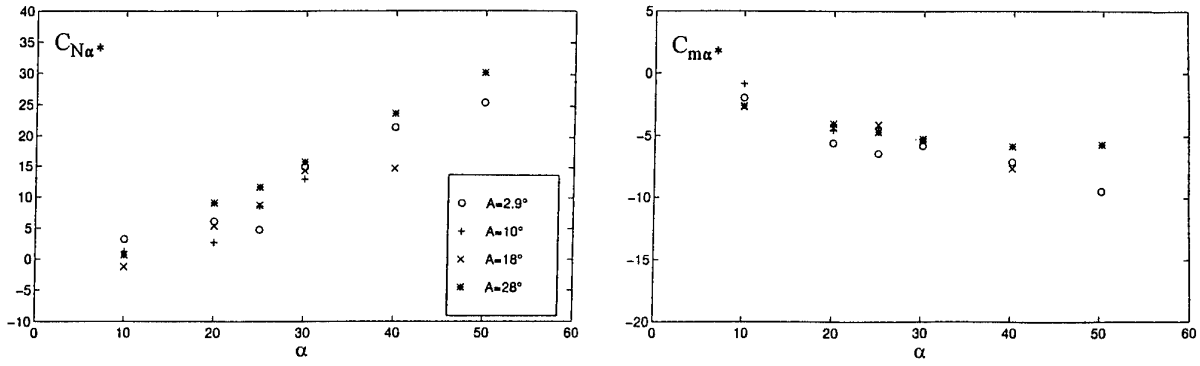

Fig 8.14 Comparison between small amplitude derivatives and local derivatives calculated from 20° amplitude oscillatory tests.

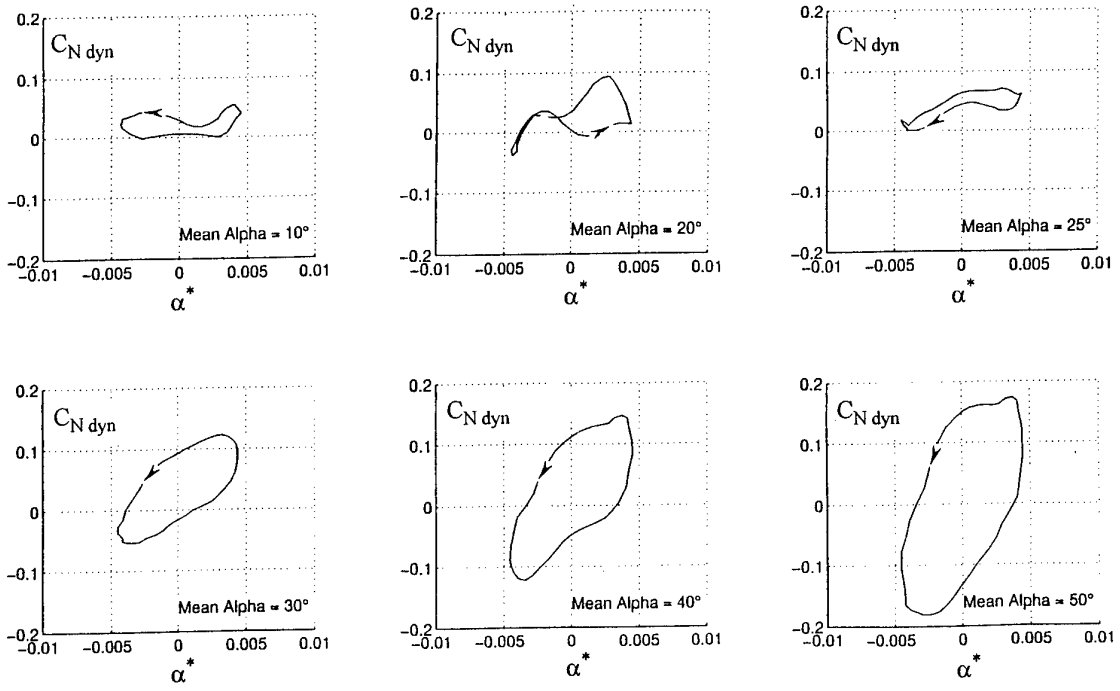

Fig 8.15 Dynamic contribution in Normal force : C_{Ndyn}
Small amplitude oscillatory tests

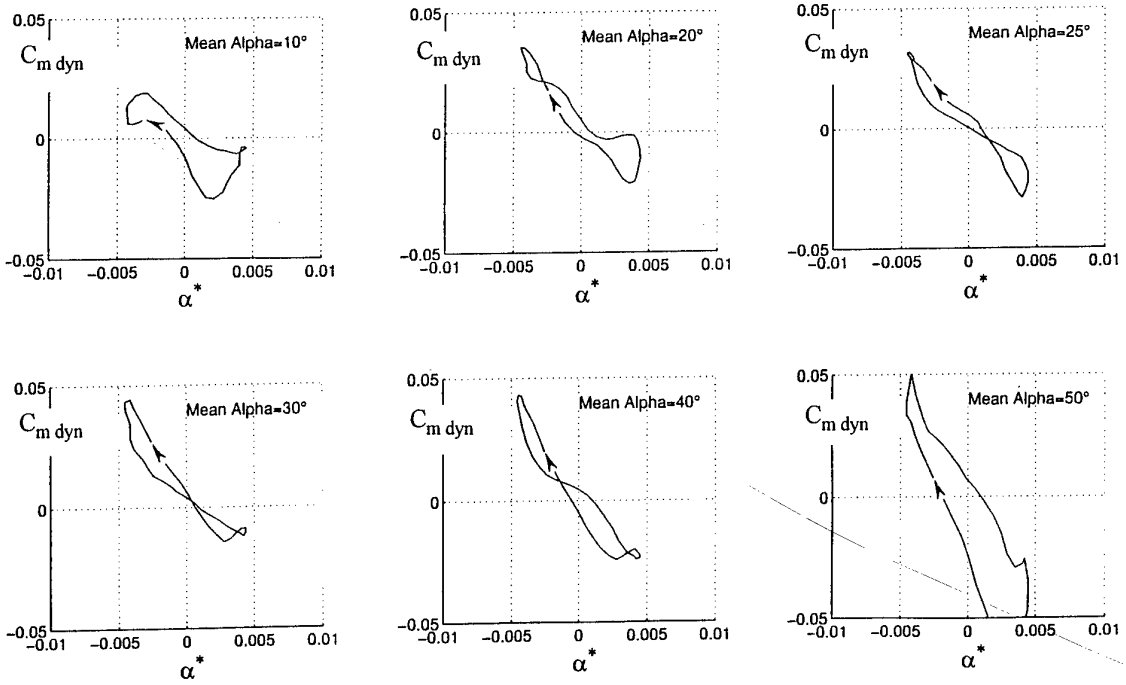

Fig 8.16 Dynamic contribution in pitching moment : C_{mdyn} .
Small amplitude oscillatory tests .

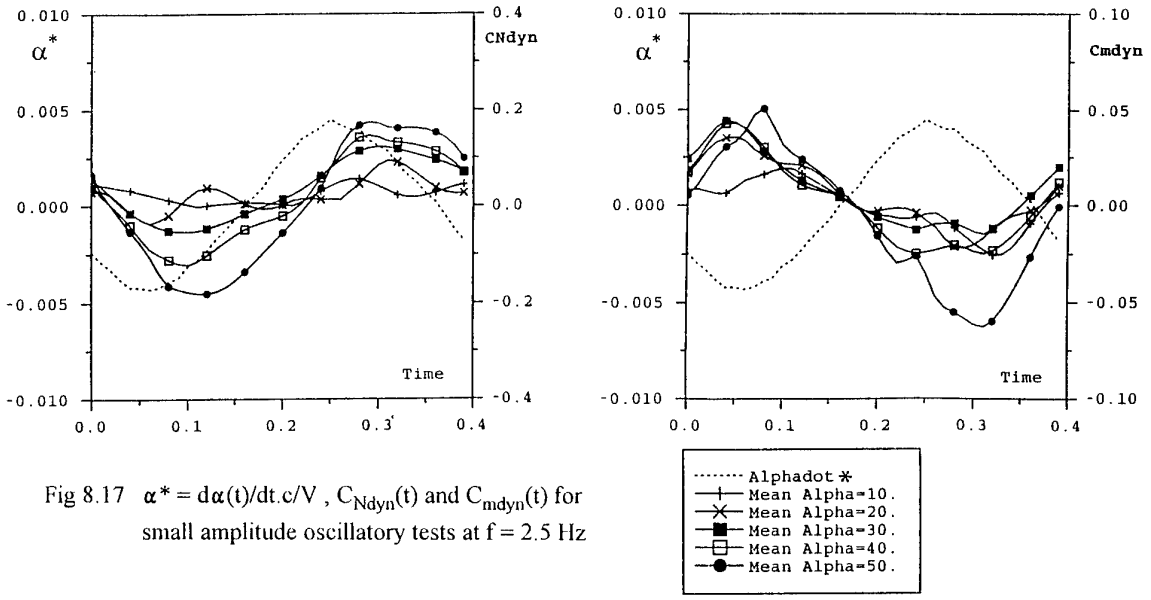

Fig 8.17 $\alpha^* = d\alpha(t)/dt.c/V$, $C_{Ndyn}(t)$ and $C_{mdyn}(t)$ for small amplitude oscillatory tests at f = 2.5 Hz

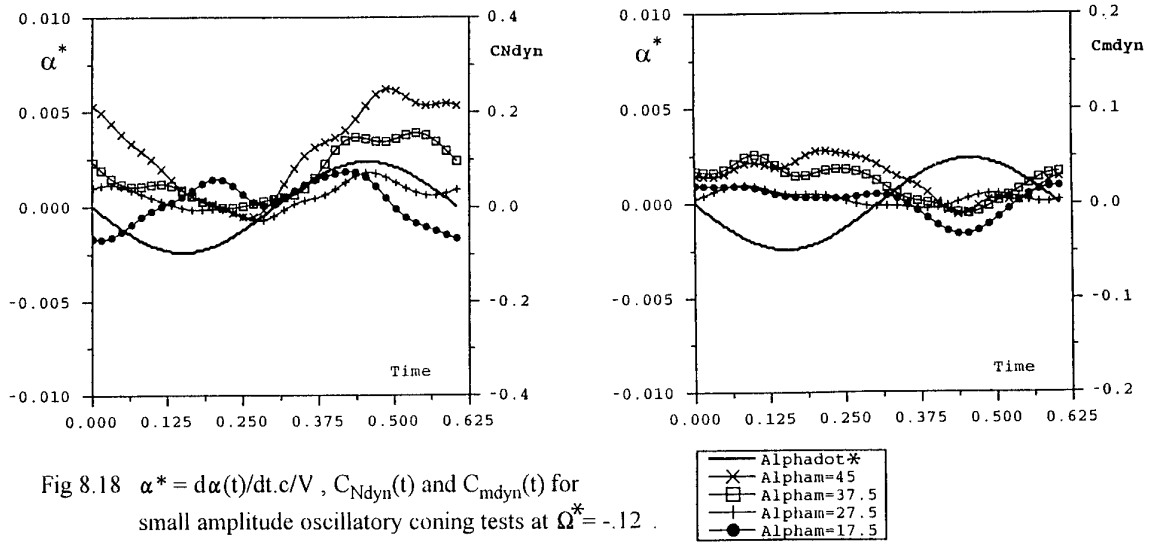

Fig 8.18 $\alpha^* = d\alpha(t)/dt.c/V$, $C_{Ndyn}(t)$ and $C_{mdyn}(t)$ for small amplitude oscillatory coning tests at $\Omega^* = -.12$.

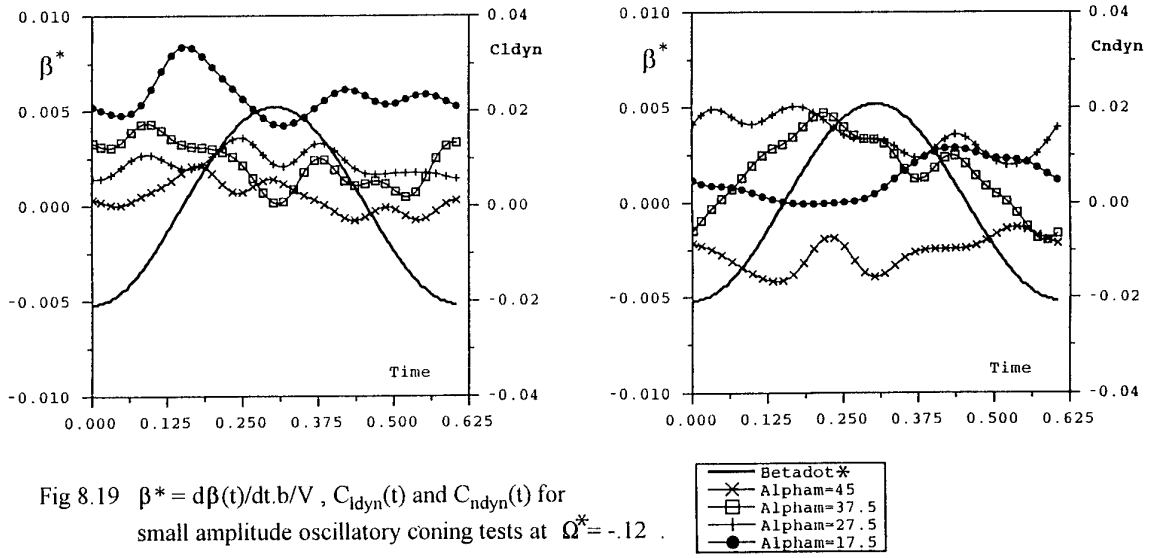

Fig 8.19 $\beta^* = d\beta(t)/dt.b/V$, $C_{ldyn}(t)$ and $C_{ndyn}(t)$ for small amplitude oscillatory coning tests at $\Omega^* = -.12$.

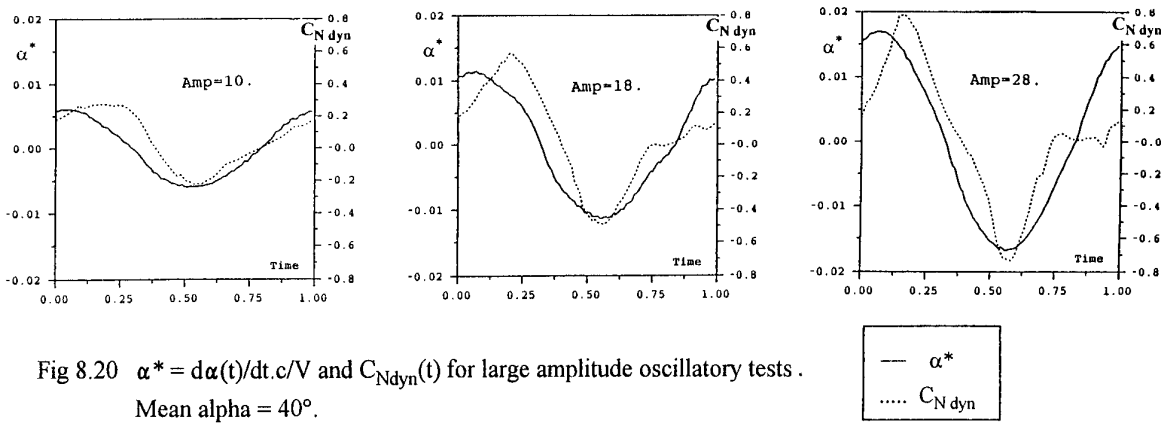

Fig 8.20 $\alpha^* = d\alpha(t)/dt.c/V$ and $C_{Ndyn}(t)$ for large amplitude oscillatory tests . Mean alpha = 40°.

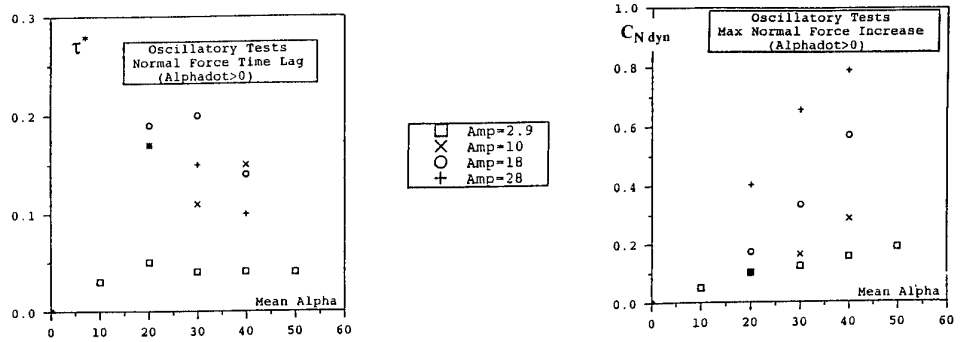

Fig 8.21 Rough estimates of reduced time lags and maximum increase of dynamic contributions in Normal force for pitch oscillatory tests.

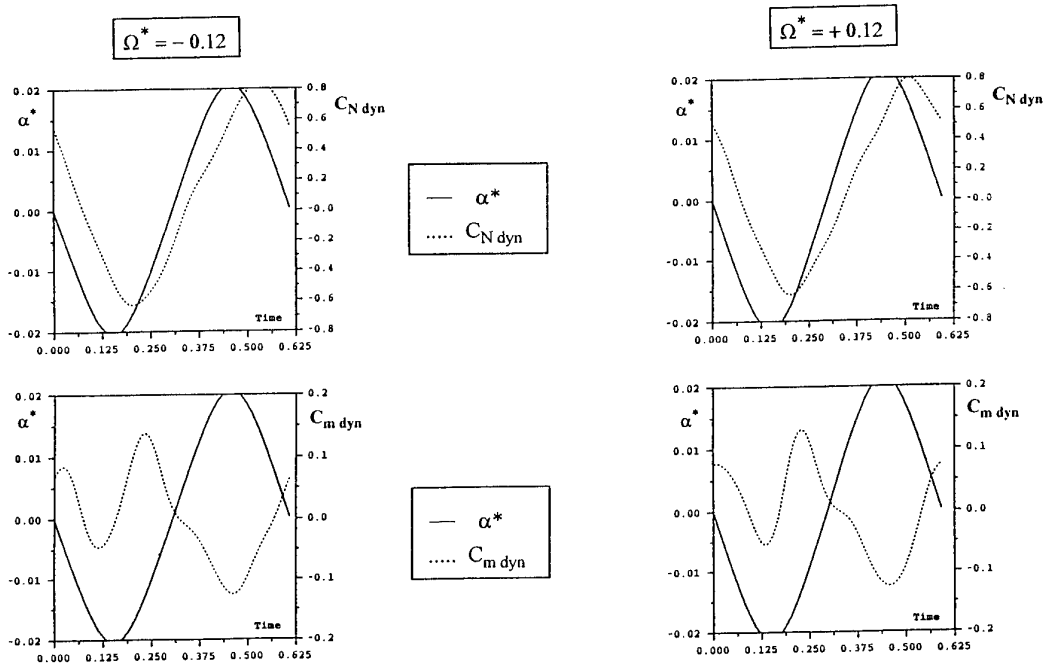

Fig 8.22 Time histories of dynamic contributions in Normal force and pitching moment for large amplitude oscillatory coning tests ($\lambda = 20°$, mean $\alpha = 50°$).

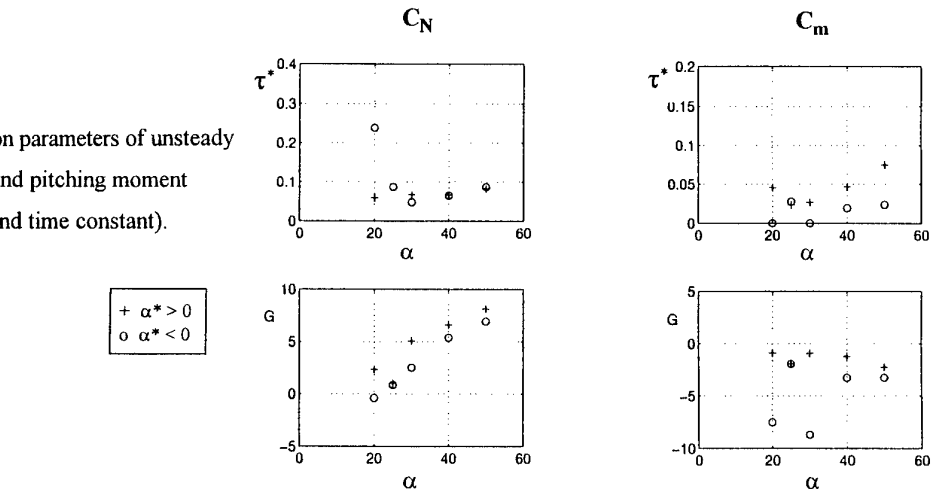

Fig 8.23 Transfer function parameters of unsteady Normal force and pitching moment models (gain and time constant).

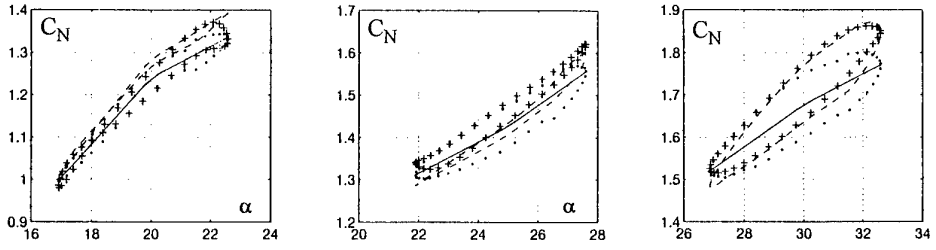

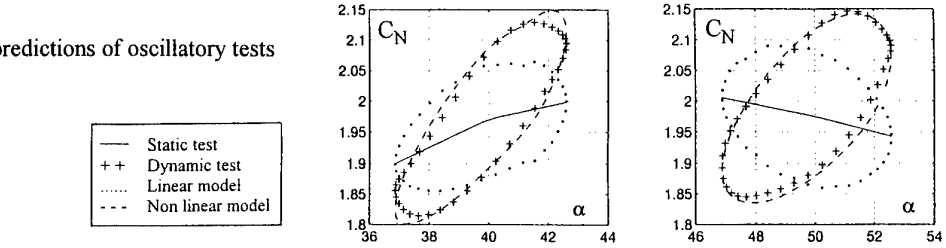

Fig 8.24 Normal force predictions of oscillatory tests (f = 2.5 Hz).

Static test
Dynamic test
Linear model
Non linear model

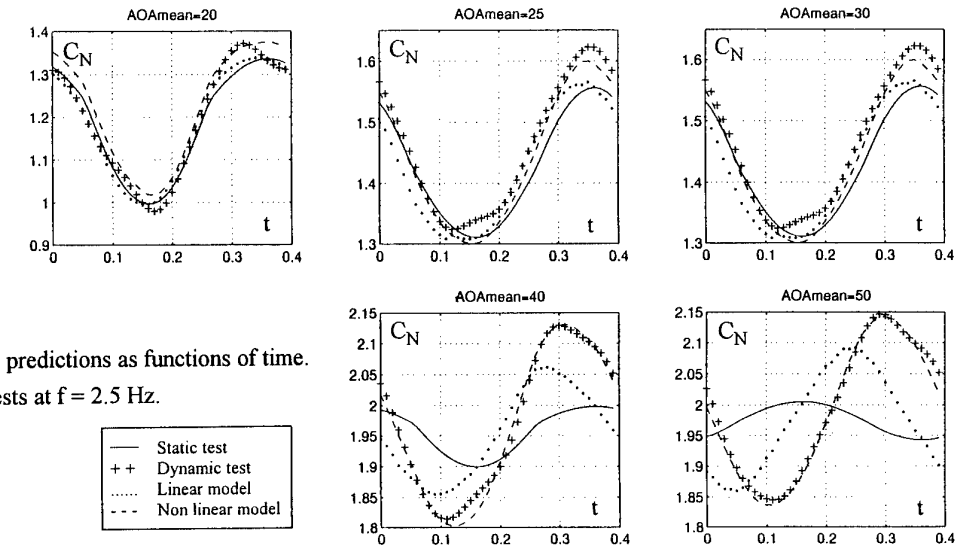

Fig 8.25 Normal force predictions as functions of time. Oscillatory tests at f = 2.5 Hz.

Static test
Dynamic test
Linear model
Non linear model

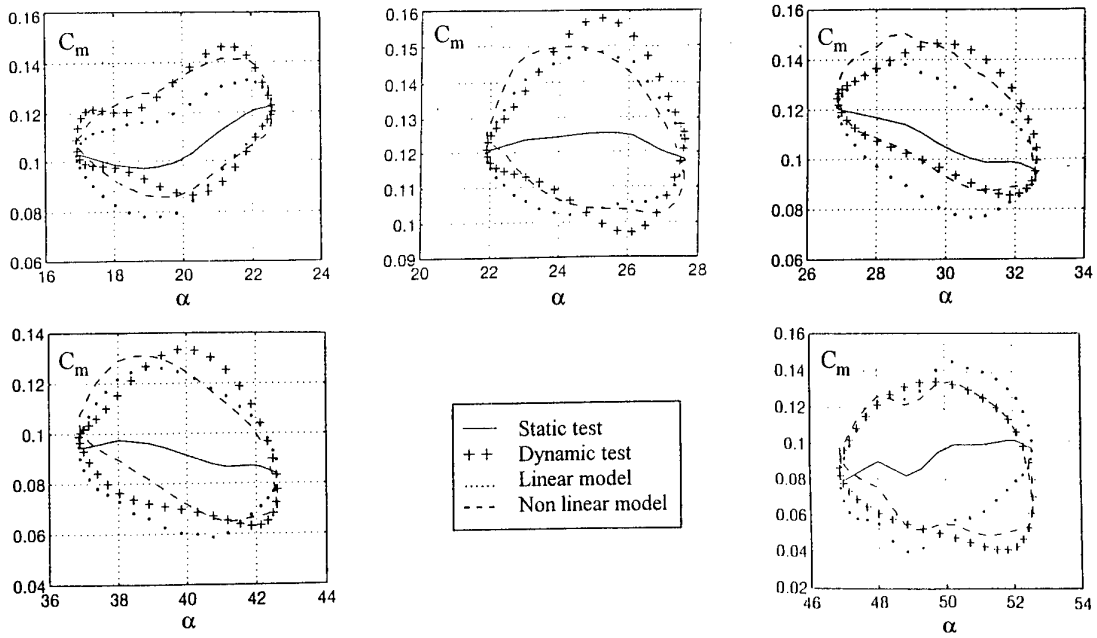

Fig 8.26 Pitching moment predictions of oscillatory tests (f = 2.5 Hz).

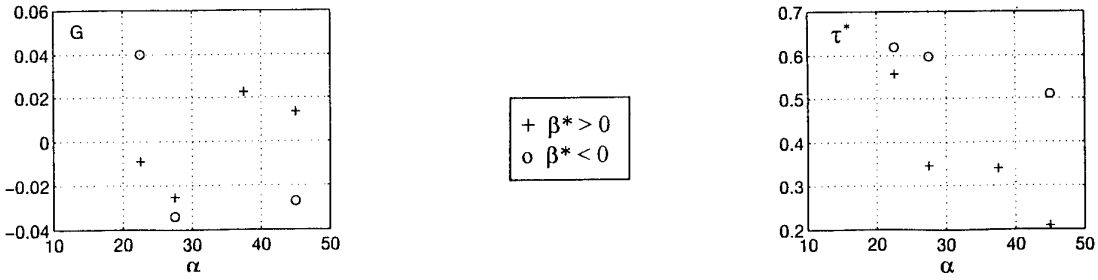

Fig 8.27a Transfer function parameters of unsteady yawing moment model

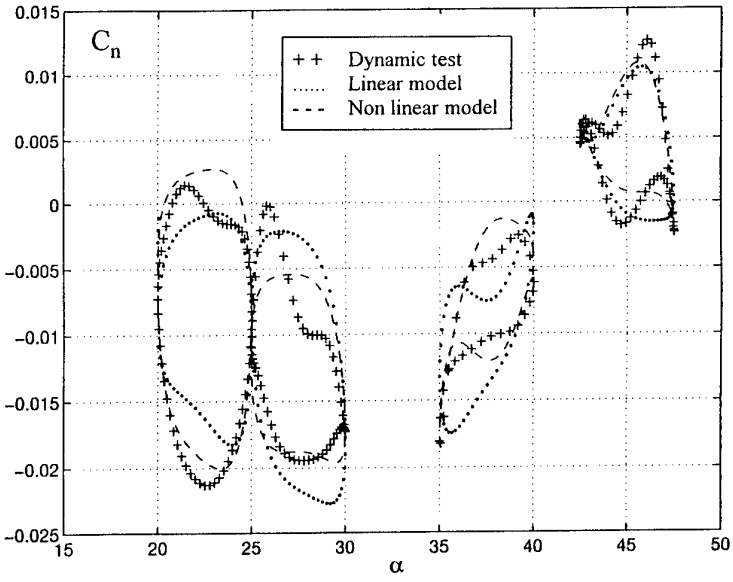

Fig 8.27b Yawing moment predictions of oscillatory coning tests (Ω = + .12).

CHAPTER 9

SUMMARY AND CONCLUSIONS

9.0 BACKGROUND

There is now considerable interest in highly agile fighter aircraft, capable of flying at high angles of attack and of performing rapid, large-amplitude manoeuvres under such conditions. Such manoeuvres result in highly non-linear, asymmetric and unsteady flows, which also usually contain several systems of vortices. To correctly and efficiently predict such high angle-of-attack (high alpha) manoeuvres, the structure of these very complex flows must be properly understood and the resulting aerodynamic loads must be accurately determined. At the present time, the best way to achieve this is by conducting appropriate wind-tunnel experiments at high alpha, with aircraft models performing rotary or oscillatory motions, or - if feasible - a representative combination of these motions.

Although rotary and oscillatory experiments have been performed almost since the beginning of the century, their application to high-alpha manoeuvres has opened up a new era in the history of these experiments, resulting in new performance requirements and an expanded range of test conditions. In the case of *rotary* experiments this means a requirement for improved data accuracy and a better understanding of any interference effects that may be present in the rotary data. In the case of *oscillatory* experiments this means the necessity of performing them at much higher alpha than ever before, often with much larger amplitudes than those that were of interest in the past and in the presence of very significant unsteady and non-linear effects. For both types of experiments there is a requirement for a much better understanding of the resulting complex flow fields, which often may necessitate additional flow field measurements and flow visualization studies, such as those involving surface-flow or laser-sheet experiments or water-tunnel investigations. A good insight into the state of the boundary layer and into the effects of time lags and time histories is usually required before wind-tunnel data can be applied to full-scale free-flight conditions. In many cases this latter objective can still not be satisfactorily achieved.

In recognition of these new requirements for wind-tunnel dynamic tests, the Fluid Dynamics Panel of AGARD has set up the present Working Group to assess the reliability of dynamic test methodology in this new, expanded range of test conditions and to provide a data base for dynamic experiments, which would illustrate the effects of systematic variation of some of the many geometric and fluid dynamics parameters involved.

To perform this mission, a cooperative experimental programme was set up involving 10 wind tunnel facilities in 7 countries in Europe and North America. Most of the experiments were carried out using three conformal models of a schematic fighter configuration ("WG16 configuration"). In addition, a smaller experimental programme was carried out using two generic forebody models.

For the purpose of interfacility comparison, the WG16 models were equipped with strakes and transition trips to make the flow over the model predictable and repeatable. However, the same models were also tested with the basic clean forebody to study the effects of model nose microasymmetries and boundary layer separation and transition. Interfacility comparisons were mostly done for Reynolds numbers ranging from 875,000 to 950,000, although results were also obtained for Reynolds numbers as low as 475,000 (based on wing mean aerodynamic chord). The corresponding values of Reynolds number based on body diameter were 275,000, 300,000 and 150,000. With respect to critical Reynolds number for the forebody cross flow, the above range covered part of the transitional regime and extended down to the laminar/transitional boundary. Even with transition trips on the WG16 configuration, a complete turbulent boundary layer was probably not established for any of the test Reynolds numbers.

The dynamic tests included rotary, oscillatory and, in one case, oscillatory-coning experiments. In several facilities this was complemented by static and, in some cases, also dynamic flow visualization experiments in water tunnels. The forebody experiments included extensive surface pressure measurements under rotary conditions, carried out in a pressurized wind tunnel.

9.1 STATIC EXPERIMENTS

Static tests are an integral part of any dynamic wind-tunnel test programme. As a result of the present study, the following two recommendations can be made:

- It is important to obtain static data on dynamic rigs (by taking isolated data points at zero rotation rate or by conducting slow alpha sweeps, where possible) and compare the results with static reference data. If such static results disagree, the reason should be investigated and steps taken to minimize any differences. Such a procedure is considered to be an important and prudent first step in gaining confidence in the subsequent dynamic results.

- Static tests on rotary or oscillatory rigs should be conducted to detect possible occurrences of flow instability at different combinations of test conditions, such as defined by angles of attack and sideslip and Reynolds number. Such tests should preferably be carried out in advance of the dynamic tests,

especially at high alpha, to avoid subsequent misinterpretation of dynamic results.

9.2 ROTARY EXPERIMENTS ON WG16 CONFIGURATION

Rotary-balance results for the WG16 configuration were obtained in five facilities with different rigs and support systems, different test section geometries, open and closed test sections, different data acquisition and reduction systems and two model sizes. The main objective was to compare results from the different facilities in order to assess the repeatability and reliability of the experiments and to identify those test and facility parameters that had the most significant effect on the aerodynamic results. The underlying assumption was that if the results from many different facilities are similar then there is a good probability (although still no certainty) that the test methodology is reliable. This is similar to the well known, time-honoured method of performing static tests in different wind tunnels using the same ("standard") model to assess the reliability of a particular static test technique, or the quality of flow in wind tunnel.

The agreement of results from the various facilities was found to depend strongly on the presence or absence of strakes and transition trips. The model with strakes could be considered to be representative of some of the more advanced fighter configurations because the sharp-edged strakes behave much like the chine cross section often associated with these newer aircraft, creating a well-defined flow separation. The other extreme was a configuration with a clean circular cross section which allowed crossflow separation to take place asymmetrically at certain flow conditions. As a result, asymmetric vortices were shed from the forebody, affecting the flow field on the afterbody and generating side loads. The differences in sensitivities of the model flow fields to various effects, including support interference, wall effects, open and closed test sections, etc, for different models showed that the reliability of test results can be influenced significantly by the geometry of the model being tested.

A major and not necessarily fully expected finding of this Working Group activity was that, for models with strakes and transition trips, there was an overall consistency of data regardless of test facility or model size. There were only minor differences due to the proximity of the sting and/or support system to the model. However, for models without strakes, at angles of attack where unstable flow conditions existed, there was a wide variation in the results, not only between facilities but also in the same facility with changes to the overall test setup, particularly with top-mounted sting. Some of the variations, in particular at an angle of attack of 40°, were of a clearly bi-stable character. This is typical of pointed slender configurations where the flow field is determined by small variations in the flow near the tip (effect of nose microasymmetries), often magnified by induced pressure gradients in the leeward-side flow field due to the proximity of test support hardware.

Despite the wide variation in the geometry of the rotary-balance rigs used for these comparative tests, all the rigs appeared to the capable of producing reliable data for configurations where the flow was not unusually sensitive to small variations in the local flow conditions. In general, for any test setup, the farther the model could be located from the support system, the better. It is good practice to test, where practical, a particular model with more than one sting/support arrangement, particularly with top-mounted versus rear-mounted models. Also, efforts should be made to minimize effects of longitudinal pressure gradients on the vortex flow over the model. Such gradients may be associated with the test section geometry or be caused by the model support structure.

Additional information on the differences in the wind tunnel data observed for the model without strakes was obtained from flow visualization studies performed in water tunnels. It is certainly clear that the presence of the sting and arc (the so called C-strut) can have an effect on the forebody vortices, particularly on burst location, which in turn affects the forces and moments. The degree of interference is very dependent upon the particular test conditions, especially rotation rate and angle of attack. The critical factor appears to be whether the combination of angle of attack and rotation rate can produce vortices which break down over the aft part of the model and thus are sensitive to the proximity of the support system.

It is also revealing that adding the forebody strakes resulted not only in stabilizing the vortices but also in causing them to burst well upstream of the sting and arc and minimizing the effect of the hardware on the vortex structure. The most troublesome component appears to be the top-mounted sting. If there is a means of reaching the desired angles of attack without resorting to a top-mounted sting, at least in the 40° to 50° alpha range, a rear-mounted sting is preferable. Cranks should be carefully designed, taking into account their proximity to the model and blockage effects. Also, when changing mounting configurations on any rig it is desirable to have an overlap in angle of attack of at least 10°.

In general, it has to be realized that in *any* wind-tunnel work there are, of course, *some* interference effects. The question is, when do these effects become significant enough to render the results unreliable for practical applications.

For example, for the *straked* WG16 configuration almost all results fall into well defined bands, and it may be reasonable to expect that it is only the general behaviour of these bands, rather than the small, often irregular variations in the individual curves, that may be of practical interest for the flight dynamics simulation. On the other hand, for the *unstraked* WG16 configuration, most of the results in the critical $40° < \alpha < 60°$ range have a distinct bistable character, obviously reflecting the direction of the instantaneous flow asymmetry and often displaying sudden jumps from one extreme position to the other. In such cases it may be reasonable to expect that it is only the envelopes of pertinent

curves rather than the detailed variations withing the envelopes that may be of interest when designing a flight control system capable of overcoming these asymmetric effects.

The results obtained in the present cooperative programme on the WG16 models are given in data reports prepared by the participating organizations. These data reports, together with the pertinent test matrices, are listed in Appendix 1. Thus a unique, comprehensive dynamic data base is presented, which can be used to illustrate the effect of various configurations, facility parameters and aerodynamic test conditions. For the rotary experiments, some of the parametric effects discussed in the present report include, inter alia, effects of forebody configuration, transition fixing, Reynolds number, model size, configuration build-up, nose strakes position, angle of attack, angle of sideslip, model distance to the support arc, type of sting support and type of test-section wall (open versus closed). These effects are too numerous to be described here, and the reader is referred to Chapters 3 and 4 of the present volume.

9.3 ROTARY EXPERIMENTS ON FOREBODIES

Rotary-balance experiments were conducted on rectangular and circular ogive forebodies at angles of attack of 60° and 90° and over a wide range of Reynolds numbers to determine the effects of nose geometry, angle of attack and rotation rate on the aerodynamic characteristics of fuselage-type forebodies. In these tests, for the first time, a large number of surface pressures were measured on rotating models in a pressurized wind tunnel. The resulting comprehensive data base can also be applied for future development and validation of pertinent high angle-of-attack computational methods.

One of the objectives of these tests was to identify the capabilities and limitations of using low Reynolds number data to simulate high Reynolds number characteristics. For the data base examined it appears that, with some restrictions, the data obtained at laminar separation conditions can be used to predict the turbulent Reynolds number characteristics. For example, on the circular ogive at angle of attack of 60°, although the surface pressure data showed significant structural differences in the flow field between low and high Reynolds numbers, the yaw damping at low rotation rates was similar for both the laminar and the fully turbulent flow conditions. However, as could be expected, the yaw damping varied considerably for test data measured throughout the broad transitional Reynolds number region. More details can be found in Chapter 7.

9.4 OSCILLATORY EXPERIMENTS

9.4.1 Small-Amplitude Oscillation

Small-amplitude oscillatory data were obtained for the WG16 configuration in wind tunnel facilities in four countries. The experiments were conducted using conventional angular-oscillation rigs (for pitch, yaw and roll), as well as the DRA 5 degree-of-freedom (which includes heave and sway) rig and the ONERA-IMFL oscillatory-coning rig (for various angular degrees of freedom in the presence of coning). Both rear stings and ventral struts were used. Static aerodynamic coefficients and static and dynamic derivatives were obtained and the data correlated. The following observations can be made:

- With some exceptions the results were found to be in good agreement in the linear alpha range and, for the configuration with strakes and trips, also at angles of attack from 25° to 45°. However, the agreement in the non-linear range for the configuration without strakes and trips was poor.

- It was found that the various dynamic cross and cross-coupling derivatives were very small for models in symmetric flow conditions (i.e. models with strakes), but became large and irregular in asymmetric flow conditions (i.e. for models without strakes).

- It was possible, using the unique capabilities of the advanced oscillatory rigs at DRA and ONERA IMFL, to separate the dynamic derivatives due to pure rotation (i.e., due to p, q, and r) from the derivatives due to vertical or lateral acceleration (i.e., due to $\dot{\alpha}$ or $\dot{\beta}$). As is well known, in conventional oscillatory tests only composite derivatives, which include a combination of these two effects, can be measured. It was demonstrated that at high angles of attack the $\dot{\alpha}$ and $\dot{\beta}$ derivatives constituted the dominant part of such composite derivatives. This should be reflected in the way these derivatives are used in the equations of motion (which, at the present time, is often done incorrectly).

- It was found that at high angles of attack the aerodynamic coefficients are not only non-linear but include effects of higher harmonics and time lags. It was shown that in such conditions the aerodynamic coefficients can be predicted better by non-linear transfer functions than by the "classical" linear formulation that uses stability derivatives. This finding is of large interest for predicting aerodynamics of aircraft manoeuvring at high angles of attack.

- The large oscillatory data base accumulated during this programme clearly illustrates the effect of various test conditions and the contributions of different model components. For further details the reader is referred to Chapters 5 and 6.

9.4.2 Large-Amplitude Oscillation

Oscillatory data were obtained at large amplitudes for oscillation in pitch and for a combined oscillation in pitch and yaw in the presence of rotation. It was found that

- Large-amplitude data are non-linear and strongly time-dependent. At high angles of attack they cannot, as a rule, be extrapolated from small-amplitude tests and cannot be adequately represented by stability derivatives. One possible

approach is the use of non-linear transfer functions. This is discussed in some detail in Chapter 8.

- The pitch and yaw rates can have important effects on the lateral-directional coefficients. It was found in particular, that at high angles of attack the pitch rate could greatly reduce the magnitude of asymmetric forces at zero sideslip. Also, in the presence of coning, the change of sign of directional stability was delayed to higher angles of attack and there was no loss of lateral stability in the 25° to 35° range. Such effects are described in detail in Chapter 5. Since the lateral-directional stability characteristics of manoeuvring aircraft are normally assessed on the basis of static tests, the appreciation of such dynamic effects may be helpful in understanding the actual behaviour of aircraft at high angles of attack.

9.5 GENERAL CONCLUSIONS AND RECOMMENDATIONS

For configurations with stable flow characteristics the dynamic results, for all practical purposes, were consistent. Thus, as far as the majority of the Working Group members were concerned, such results were considered reliable.

For configurations, which in a certain range of angles of attack had bi-stable flow characteristics, the dynamic results in that range were scattered or displayed a bi-stable character. However, despite the unpredictability of the flow, the tests could still provide a control-system designer with the absolute magnitude of the design loads that could be expected, and the threshold angle of attack at which the flow could become bi-stable.

Flow visualization in water tunnels and in wind tunnels is highly recommended for studying the various features of the vortex flow over a configuration and to indicate possible interference effects.

All dynamic tests in wind tunnels are presently performed at either fully laminar or transitional flow conditions. This is not likely to change in the near future. Two schools of thought presently exist regarding the application of such subscale data to full-scale flight conditions. One option is based on the demonstrated qualitative analogy between laminar and turbulent flow patterns over tangent-ogive bodies. This option consists of testing at laminar flow conditions and assuming that the test results apply to full-scale conditions or, possibly, of using analytical extrapolation guided by a physical interpretation of both dynamic and static test results. The second option is to perform the tests at the highest available Reynolds number, visualize the structure (state) of the boundary layer and use carefully designed transition tripping to change the boundary layer to turbulent as may be required to simulate full-scale conditions. These two options are discussed in the appendices. In this connection, there is a definite need for benchmark experiments that could be used to verify the effect of full-scale Reynolds number on dynamic results for a realistic aircraft configuration (as opposed to simple bodies).

APPENDIX 1

TEST REPORTS and TEST MATRICES

A1.0 INTRODUCTION

The overall test activity performed under the auspices of the AGARD FDP Working Group 16 constitutes a large wealth of data which in many respects is unique in terms of completeness and consistency, number of variables investigated, number of different rigs used, etc. The present report highlights and summarizes all major effects and presents data analyses aiming at answering the fundamental questions which gave origin to the activity of the working group.
In addition to what is collected here, each organization performed a more detailed presentation and analysis of its own data. For a complete presentation of all results the reader should consult the following reports:

AerMacchi:
- R. Pertile, "AGARG WG16 Reference Models: Static and Rotary Balance Tests in AerMacchi Wind Tunnel", AeM rept. 567-ANG-292, Nov. 1993.

DRA:
- C.O'Leary, B. Weir, J.M. Walker, "Continuous Rotation Tests of a Generic Combat Aircraft Model in a Low Speed Wind Tunnel", DRA TechMemo Aero/Prop 42 (1993).

- C.O'Leary, B. Weir, J.M. Walker, "Static and Forced Oscillation Tests on a Generic Combat Aircraft Model (AGARD-FDP WG16A)", DRA/AS/HWA/TR94066/1.

EI/NASA Ames:
- G.N. Malcolm, B.K. Kramer, C.J. Suarez, B.F. Ayers, K.D. James, "Rotary Balance Tests in NASA-Ames 7x10-ft Wind Tunnel with AGARD Generic Fighter Model", Eidetics report TR93-004, March 1993.

IAR/NRC:
- H.J. Cai, M.E. Beyers, S. Elias, "Oscillatory Experiments on the AGARD WG16CA Model", NRC IAR-AN-83.

ONERA/IMFL:
- D.R. Tristrant, F.F. Gauthier, M.G. Vanmansart, "Dynamic Tests in ONERA/IMFL Wind Tunnels with AGARD Generic Fighter Model", IMFL rept. 94113, nov. 1994.

TPI:
- F.B. Quagliotti, G. Guglieri, "Static and Oscillatory Tests on a Generic Combat Aircraft Model in a Low Speed Wind Tunnel", Dip. Ing. Aerospaziale, Politecnico di Torino, Nota Tecnica NT75-1993.

FFA:
- F. Rafatnia, "Rotary Balance Tests with AGARD Generic Fighter Model in FFA Low-speed Wind Tunnel LT1", FFA TN-1994-15.

DRA/BAR/NASA-Langley:
- H. Pauley, J. Ralston, E. Dickes, "Experimental Study of the Effects of Reynolds Number on High Angle of Attack Aerodynamic Characteristics of Forebodies during Rotary Motion", NASA CR-195033, Jan. 1995, also published as DRA/AS/HWA/TR96007/1.

In addition to the above reports, papers were presented at various meetings presenting a few aspects of the ongoing work.
Such papers are the following:

- G.N. Malcolm, B.R. Kramer, C.J. Suarez, B. Ayers, C.O. O'Leary, B. Wier, J.M. Walker, "US/UK Rotary-Balance Test Comparisons with a Generic Fighter Model" AIAA Paper 94-0196.

- G. Guglieri, F.B. Quagliotti, "Static and Oscillatory Tests on a Generic Combat Aircraft Model in a Low Speed Wind Tunnel", 19th ICAS Congress, Anaheim CA (USA), 1994, Paper 3.6.1.

- G.N. Malcolm, B.R. Kramer, C.J. Suarez, C.O. O'Leary, B. Wier, J.M. Walker, L. Visintini, F. Rafatnia, L. Fernkrans, "Rotary-Balance Test Comparisons with AGARD WG-16 Generic Fighter Model", 19th ICAS Congress, Anaheim CA (USA), 1994, Paper 3.8.2.

A summary description of test programs performed by each organization is included in Chapter 2. The present appendix presents the complete test matrices, thus allowing a more detailed information about the complete set of available results. The tests variables are presented, as well as reference to run numbers for test identification.
All test data are available in digital form (data tables formatted as ASCII files). All data are unclassified and available to researchers interested in making further analysis or for purpose of validation of CFD or engineering methods. The organization originating the data should be contacted for further details.

A1.1 AERMACCHI (Rotary tests - models WG16A and B)

A1.1.1 Rotary tests

RUN N.	MODEL	CONFIGURATION	OPEN/CLOSE Test Sect.	Beta (deg.)	Alfa (deg.)	STING	V (m/s)	REc,REd (/10E6)
R25527	A	BWLWH	OPEN	0	0	REAR	44	.95,.3
R25528	"	"	"	"	8	"	"	"
R25530	"	"	"	"	24	"	"	"
R25531	"	"	"	"	40	"	"	"
R25537	A	BVLVHT	OPEN	0	0	"	"	"
R25536	"	"	"	"	8	"	"	"
R25534	"	"	"	"	24	"	"	"
R25532	"	"	"	"	40	"	"	"
R25564	"	"	"	"	50	TOP	"	"
R25563	"	"	"	"	60	"	"	"
R25538	A	BWLVHST	OPEN	0	0	REAR	"	"
R25539	"	"	"	"	8	"	"	"
R25540	"	"	"	"	10	"	"	"
R25541	"	"	"	"	15	"	"	"
R25542	"	"	"	"	20	"	"	"
R25543	"	"	"	"	24	"	"	"
R25544	"	"	"	"	30	"	"	"
R25545	"	"	"	"	40	"	"	"
R25558	"	"	"	"	30	TOP	"	"
R25559	"	"	"	"	40	"	"	"
R25560	"	"	"	"	50	"	"	"
R25561	"	"	"	"	60	"	"	"
R25562	"	"	"	"	70	"	"	"
R25554	A	BWLVHST	OPEN	-10	8	REAR	"	"
R25550	"	"	"	"	24	"	"	"
R25546	"	"	"	"	40	"	"	"
R25556	A	BWLVHST	OPEN	-5	8	REAR	"	"
R25552	"	"	"	"	24	"	"	"
R25548	"	"	"	"	40	"	"	"
R25557	A	BWLVHST	OPEN	+5	8	REAR	"	"
R25553	"	"	"	"	24	"	"	"
R25549	"	"	"	"	40	"	"	"
R25555	A	BWLVHST	OPEN	+10	8	REAR	"	"
R25551	"	"	"	"	24	"	"	"
R25547	"	"	"	"	40	"	"	"
R25579	A	BWLVHT	CLOSE	0	0	REAR	"	"
R25578	"	"	"	"	8	"	"	"
R25577	"	"	"	"	24	"	"	"
R25576	"	"	"	"	40	"	"	"
R25565	"	"	"	"	50	TOP	"	"
R25566	"	"	"	"	60	"	"	"
R25572	A	BWLVHST	CLOSE	0	0	REAR	"	"
R25573	"	"	"	"	8	"	"	"
R25574	"	"	"	"	24	"	"	"
R25575	"	"	"	"	40	"	"	"
R25568	"	"	"	"	50	TOP	"	"
R25567	"	"	"	"	60	"	"	"
R25721/22	B	BWLVHT	OPEN	0	40	REAR	60	.95,.3
R25728	B	BWLVHST	"	"	8	REAR	30	.475,.15
R25726	"	"	"	"	24	"	"	"
R25724	"	"	"	"	40	"	"	"
R25729	B	BWLVHST	OPEN	0	0	REAR	60	.95,.3
R25727	"	"	"	"	8	"	"	"
R25725	"	"	"	"	24	"	"	"
R25723	"	"	"	"	40	"	"	"
R25584	B	BWLVHT	CLOSE	0	24	REAR	"	"
R25583	"	"	"	"	40	"	"	"
R25580	B	BWLVHST	CLOSE	0	0	REAR	60	"
R25581	"	"	"	"	24	"	"	"
R25582	"	"	"	"	40	"	"	"
R25570	"	"	"	"	50	TOP	"	"
R25571	"	"	"	"	60	"	"	"

A1.1.2 Static tests

RUN N.	MODEL	CONFIGURATION	OPEN/CLOSE Test Sect.	Beta (deg.)	Alfa (deg.)	STING	V (m/s)	REc,REd (/10E6)
C25718	B	B	OPEN	0°	0/45°	REAR	60	.95,.3
C25719	"	BW	"	"	"	"	"	"
C25720	"	BWL	"	"	"	"	"	"
C25717	"	BWLVH	"	"	"	"	"	"
C25716	"	BWLVHT	"	"	"	"	"	"
C25714	"	BWLVHST	"	"	"	"	"	"
C25715	"	"	"	"	"	"	30	.475,.15

A1.2 DRA (Rotary and oscillatory tests - models WG16A and B)

A1.2.1 Rotary tests - Model WG16B - 13ft x 9ft Wind Tunnel - Bedford

Run	Config.	Grit	Strks	AOA	Crank	Vel.	Comments
2	B	OFF	OFF	20	60	60	
4	B	"	"	40	"	"	
6	B	"	"	60	"	"	
8	B	"	"	50	"	"	
10	B	"	"	30	"	"	
11	B	70	"	60	"	"	
12	B	"	"	"	"	"	Repeat
13	B	"	"	50	"	"	
14	B	"	"	40	"	"	
15	B	40	"	40	"	"	
16	B	"	"	50	"	"	
17	B	"	"	"	"	"	Repeat
18	B	"	"	60	"	"	
19	B	"	"	"	"	"	Repeat
21	B	"	"	20	"	"	
23	B	"	"	"	"	"	Repeat
25	B	"	"	40	"	"	new grit
26	B	"	"	"	"	"	Repeat
27	B	"	"	50	"	"	
29	B	"	"	"	"	"	Repeat
30	B	"	"	30	"	"	
31	B	"	"	"	"	"	Repeat
32	B	"	"	60	"	"	
33	B	"	"	"	"	"	Repeat
35	BWL	"	"	"	"	"	
38	BW	"	"	"	"	"	
40	BW	"	"	40	"	"	
42	BWL	"	"	"	"	"	
44	BWLVH	"	"	"	"	"	
46	BWLVH	"	"	60	"	"	
48	BWLVH	"	"	50	"	"	
50	BWLVH	"	"	32	"	"	
52	BWL	"	"	0	40	"	
54	BW	"	"	"	"	"	
56	BW	"	"	8	"	"	
58	BWL	"	"	"	"	"	
60	BWL	"	"	16	"	"	
62	BW	"	"	"	"	"	
64	BW	"	"	24	"	"	
66	BWL	"	"	"	"	"	
68	BWL	"	"	32	"	"	
70	BW	"	"	"	"	"	
72	BW	"	"	40	"	"	

Run	Config.	Grit	Strks	AOA	Crank	Vel.	Comments
73	BW	40	OFF	40	40	60	Repeat
75	BWL	"	"	"	"	"	
77	B	"	"	"	"	"	
79	BWLVH	"	"	"	"	"	
80	BWLVH	"	"	32	"	"	
82	BWLVH	"	ON	"	"	"	
84	BWLVH	"	"	40	"	"	
87	B	"	"	"	"	"	
88	B	OFF	"	40	"	"	
89	BWLVH	OFF	ON	40	40	60	
90	BWLVH	40	"	"	"	"	new grit
92	BWLVH	"	"	"	"	"	new grit
93	BWLVH	"	"	"	"	"	
95	BWLVH	"	"	"	"	"	
97	BWLVH	"	"	24	"	"	
99	BWLVH	"	"	16	"	"	
101	BWLVH	"	"	8	"	"	
103	BWLVH	"	"	0	"	"	
104	BWL	"	"	40	"	"	
107	BW	"	"	"	"	"	
109	B	"	"	"	"	"	
111	B	"	"	40	60	"	
113	B	"	"	50	"	"	
115	BWLVH	"	"	"	"	"	
117	BWLVH	"	"	60	"	"	
119	BWLVH	"	"	40	"	"	
121	BWLVH	"	"	32	"	"	
122	BWLVH	"	"	50	90	"	
125	BWLVH	"	"	60	"	"	
127	BWLVH	"	"	75	"	"	
129	BWLVH	"	"	90	"	"	
131	B	"	"	"	"	"	
132	B	"	"	"	"	30	
134	B	"	"	50	"	60	
135	B	"	"	"	"	30	
137	BWL	"	"	"	"	60	
138	BWL	"	"	"	"	30	
140	BW	"	"	"	"	60	
142	BWL	"	"	8	40	"	
143	BWL	"	"	"	"	30	
145	BW	"	"	"	"	60	
147	BWLVH	"	"	40	"	"	

Configs : B = Body Only.
BW = Body/Wing.
BWL = Body/Wing/LEX.
BWLVH = Body/Wing/LEX/Vert. & Hor. Tails

Grit: 0.2mm diam grit, strips at ±40° from windward,3mm wide,from nose tip to LEX apex.

Strks: Forebody strakes mounted at ±105° from windward, 1.0d long, 0.1d height (d=73mm)

AOA: Angle of attack

VELOC: Tunnel wind velocity (m/s)

A1.2.2 Static tests - Model WG16A - 13ft x 9ft WT - V=30 m/s

Results File	Model Config.	Alpha	Beta
RES1	B	✓	✓
RES3	BWL	✓	
RES5	BWLHV	✓	✓
RES6	BT	✓	
RES8	BWLT	✓	
RES9	BST	✓	
RES11	BWLST	✓	
RES13	BWLHST	✓	✓

A1.2.3 Oscillatory tests - Model WG16A - 13ft x 9ft WT - V=30 m/s

Results File	Model Config.	Mode	Frequency (Hz)	Ampl.
RES10	BWLHST	Roll	2	±2°
RES11	"	"	4	"
RES12	"	"	6	"
RES13	BWHVST	"	2	"
RES14	"	"	4	"
RES15	BWLV	"	2	"
RES16	"	"	4	"
RES20	BWLHVST	Yaw	2	"
RES21	"	"	4	"
RES22	BWHVST	"	2	"
RES23	"	"	4	"
RES25	"	Pitch	2	"
RES26	BWLHVST	"	2	"
RES27	"	"	4	"
RES30	"	Plunge	2	±50mm
RES31	"	"	4	"
RES32	BWHVST	"	2	"
RES33	"	Sway	2	"
RES34	BWLHVST	"	2	"
RES35	"	"	4	"
RES36	BWLH	"	2	"
RES37	BWLHV	"	2	"
RES38	"	Plunge	2	"
RES39	"	Pitch	2	±2°
RES40	"	Yaw	2	"
RES41	"	Roll	2	"
RES42	BWHV	"	2	"
RES43	"	"	2	"
RES44	BWLHV	"	2	"
RES45	"	"	4	"

A1.3 EIDETICS/NASA-AMES (Rotary tests - model WG16B)

Run no.	CONF	STRKS	AOA	VELOC	Re/10^6
2004	B	ON	51	100	0.478
2005	B	ON	5	150	0.720
2007	B	ON	5	200	0.955
2010	B	ON	39	100	0.478
2011	B	ON	39	150	0.720
2012	B	ON	39	200	0.955
2014	B	ON	24	100	0.478
2015	B	ON	24	150	0.720
2016	B	ON	24	200	0.955
2019	BW	ON	24	200	0.955
2021	BWL	ON	24	200	0.955
2023	BWL	ON	39	100	0.478
2024	BWL	ON	39	200	0.955
2026	BW	ON	39	100	0.478
2027	BW	ON	39	200	0.955
2029	BW	ON	51	100	0.478
2030	BW	ON	51	200	0.955
2032	BWL	ON	51	100	0.478
2033	BWL	ON	51	200	0.955
2036	BWLVH	ON	51	100	0.478
2037	BWLVH	ON	51	150	0.720
2038	BWLVH	ON	51	200	0.955
2040	BWLVH	ON	24	100	0.478
2041	BWLVH	ON	24	150	0.720
2042	BWLVH	ON	24	200	0.955
2045	BWLVH	ON	39	100	0.478
2046	BWLVH	ON	39	150	0.720
2047	BWLVH	ON	39	200	0.955
2050	BWLVH	LEFT	39	150	0.720
2052	BWLVH	OFF	39	100	0.478
2053	BWLVH	OFF	39	200	0.955
2055	BWLVH	OFF	51	100	0.478
2056	BWLVH	OFF	51	200	0.955
2058	BWLVH	OFF	24	200	0.955
2060	BWL	OFF	24	200	0.955
2060	BWL	OFF	24	200	0.955
2062	BW	OFF	24	200	0.955
2064	BW	OFF	39	100	0.478
2065	BW	OFF	39	200	0.955
2067	BWL	OFF	39	100	0.478
2068	BWL	OFF	39	200	0.955
2070	BW	OFF	5	100	0.478
2071	BWL	OFF	51	200	0.955
2073	BW	OFF	51	100	0.478
2074	BW	OFF	51	200	0.955
2076	B	OFF	51	100	0.478
2077	B	OFF	51	200	0.955
2079	B	OFF	39	100	0.478
2080	B	OFF	39	200	0.955
2082	B	OFF	24	200	0.955
2084	BWLVH	ON	60	200	0.955
2085	BWLVH	ON	60	100	0.478

CONF: B-body only
BW-body/wing
BWL - body/wing/Lex
BWLVH - body/wing/Lex/vertical and horizontal tails.

STRKS: Forebody strakes mounted at +/- 105° from windward, 1.0d length, 0.1d height (d = diameter of fuselage, 73 mm).

AOA: Angle of attack.

VELOC: Tunnel wind velocity (ft/s).

Re: Reynolds number based on wing mean aerodynamic chord.

Grit on all runs, 0.2mm diam grit strips at +/- 40° from windward, 3 mm wide, from nose tip to LEX apex.

Rotation rates: 0, 40, 80, 120, 160, 200, 240, 280, 320, 350 rpm, clock wise and counter-clock wise directions.

A1.4 IAR/NRC (Oscillatory tests - model WG16CA)

Pitch Oscillation Test Matrix

mode	conf.	supp.	σ (deg)	β (deg)	V_∞ (m/s)	φ_s (deg)	ϖ_c	$\Delta\theta$ (deg)
static	BWLVH	A	0-39	0	20-70	0		0
pitch	BWLVH	A	0-39	0	70	0	0.07	1.2
dynamic			0-39	0	30	0	0.17	
			10-39	±5				
		S	30-53	0, ±5				
		A	0-39	0	30	0, 90, 180	0.17	1.2
		S	30-39					
	BWLVHST	A	0-53	0	30	0	0.17	1.2
			10-45	±5				
		S	30-35	0, ±5				
	BWVH	A	0-53	0	30	0	0.17	1.2
		S	0-39	0	30	0, 90		
					70		0.07	

Yaw Oscillation Test Matrix

mode	conf.	supp.	σ (deg)	β (deg)	V_∞ (m/s)	φ_s (deg)	ϖ_b	$\Delta\psi$ (deg)
static	BWVH	A	0-39	0	30,70	0	0	0
yaw	BWLVHA	A	0-53	0	70	0	0.15	1.2
dynamic			0-53	0	30	0, 90	0.36	
		S	10-53	±5	30	0	0.36	1.2
			15-53	0	30	0, 90		
			32-51	0, ±5, ±10	30	0, 90		
	BWLVH	A	0-39	0	70	0	0.15	1.2
			0-39	0	30	0	0.36	
			30-39	0	30	0, 90, 180		
	BWLVHST	A	0-39	0	70	0	0.15	1.2
			0-53	0	30	0	0.36	
			10-53	±5	30	0		
			32	0, ±5, ±10	30	0		
		S	32	0, ±5, ±10	30	0	0.36	
			16-20	0	70	0	0.15	
	BWLVHST $\delta_e = \pm 30$	A	0-53	0	30	0	0.36	1.2
	BWVH	A	0-39	0	70	0	0.15	0.5
			0-39	0	30	0	0.36	

A - asymmetric strut
S - symmetric strut

Unless otherwise specified conditions are normal:

velocity: $V_\infty = 30$ m/s

amplitude: $\Delta\theta$ (or $\Delta\psi$)=1.2°

reduced frequency: $\varpi_c = 0.17$ for pitch oscillation mode

$\varpi_b = 0.36$ for yaw oscillation mode

(frequency: $f = 5$ Hz)

sideslip angle: $\beta = 0°$

support: asymmetric support (without the dummy strut)

A1.5 ONERA-IMFL (Oscillatory, rotary and large amplitude tests - model WG16A)

A1.5.1 Tests on the "PQR" rig - Model WG16A

Static Tests

Increasing AOA Sweeps **Decreasing AOA Sweeps**

		25 m/s 545,000	30 m/s 655,000	40 m/s 875,000	Velocity Reynolds Nb	25 m/s 545,000	30 m/s 655,000	40 m/s 875,000
Beta :	10°		34		BWLHV Configuration		41	
	5°		39					
	0°	32	31	30			27	28
	- 5°		45					
	- 10°		47				49	
Beta :	10°		66		BWLHVST Configuration		64	
	5°		60					
	0°	18	19 - 67	20			23	22
	- 5°		58					
	- 10°		52				54	

Dynamic Tests On The BWLVHST Configuration

V = 30 m/s **Reynolds Nb = 655,000**

Yaw Oscillations	Pitch Oscillations							A O A Ramps (0° -> 80°)			
(Small Amplitudes)	(Large Amplitudes)										
2.9° 2.5 Hz	2.9° 2.5 Hz	10° 1 Hz	13° 1 Hz	18° 1 Hz	28° 1 Hz	29° 1 Hz	<-- Amplitude <-- Frequency				
							d Alpha / dt --> q° rd -->	30°/s 2.8 10-3	60°/s 5.5 10-3	100°/s 9.2 10-3	200°/s 1.8 10-2
							Mean AOA				
150							0° at Beta = 5°				
152							0° at Beta = 0°				
	138						0° at Beta = -5°				
516	114						10° at Beta = 5°				
	126						10° at Beta = 0°				
	140						10° at Beta = -5°				
164	116	429 , 431	427	443	440		20° at Beta = 5°				
452	128						20° at Beta = 0°				
	142						20° at Beta = -5°				
	118						25° at Beta = 5°				
	130						25° at Beta = 0°				
	144						25° at Beta = -5°				
	120	432		445	438		30° at Beta = 5°				
	132						30° at Beta = 0°				
	146						30° at Beta = -5°				
	124	434				436	40° at Beta = 5°	419	421	423	425
	134						40° at Beta = 0°	411	413	415	417
	148						40° at Beta = -5°				
	122						50° at Beta = 5°				
	136						50° at Beta = 0°				
							50° at Beta = -5°				

A1.5.2 Tests on the "TourneBroche" rotary balance - Model WG16A

V = 30 m/s Reynolds Nb = 655,000

Configuration	Beta	Static Tests: AOA Sweep 10° to 40°	Static Tests: AOA Sweep 35° to 65°	Coning Tests: AOA 10°	20°	25°	30°	40°	50°
BWLVH	0°	659 818	663 820		691	693	695	697	699
BWLVHT	0°	642 762 1103	644 760 1101						
BWLVHST	10°			408	406	396	262	260	250
	5°			410	404	394	264	258	252
	0°	209 500 709	203 211 711	414	400	398 721	268	270 719	248 756
	-5°			412	402	392	266	256	254

Oscillatory Coning Tests

Configuration	Mean Beta	Ω *	Mean A O A	Lambda

Small Amplitude Tests

Configuration	Mean Beta	Ω *	17.5°	22.5°	27.5°	37.5°	45°		Lambda
BWLVHST	0°	.12 rd	418	448	442	274	280		2.5°
		.006 rd	416	450	440	272	282		
		-.12 rd	420	446	444	276	278		
	2.5°	.12 rd	10°	20°	25°	30°	40°	50°	2.5°
		.006 rd	454	472	508	286	292	298	
		-.12 rd	452	474	506	284	294	296	
			456	470	511	288	290	300	

Large Amplitude Dynamic Tests

Configuration	Mean Beta	Ω *	5°	10°	15°	20°	25°	30°	40°	50°	Lambda
BWLVHST	0°	.12 rd	466		424	430	436				5°
						611		593	587	569	10°
		.10 rd				384		364	344		20°
		.08 rd		623		605		599	581	575	
		.06 rd				382		362	342		
		.04 rd				380		360	340		
		.02 rd				378		358	338		
		.006 rd				376		356	336		
						374		354	334		
		- .04 rd	464		426	428	438				5°
		- .08 rd				613		591	589	567	10°
		.12 rd		625		372/603		352/601	332/579	577	20°
						386		366	346		
						388		368	348		
						390		370	350		
				621		607		597	583	573	
						609		595	585	571	10°
			468		422	432	434				5°

A1.6 TPI (Oscillatory tests - model WG16A)

A1.6.1 Static tests

α-range (deg)	β (deg)	V (m/s)	Re	Configuration
0°÷45°	0°	25.	525000	BWLVH
0°÷45°	0°	30.	630000	BWLVH
0°÷45°	+5°	"	"	"
0°÷45°	-5°	"	"	"
0°÷45°	+10°	"	"	"
0°÷45°	-10°	"	"	"
0°÷45°	0°	30.	630000	BWLVH - δ_e=30°
0°÷45°	0°	"	"	"
0°÷45°	0°	40.	840000	BWLVH
0°÷45°	0°	"	"	BWLVH-repeat
0°÷45°	0°	30.	630000	BWVH
25°÷45°	0°	30.	630000	BWLVH-roll support
25°÷45°	+10°	"	"	"
25°÷45°	-10°	"	"	"
0°÷45°	0°	30.	630000	BWLVHT
0°÷45°	+5°	"	"	"
0°÷45°	-5°	"	"	"
0°÷45°	+10°	"	"	"
0°÷45°	-10°	"	"	"
0°÷45°	0°	40.	840000	BWLVHT
0°÷45°	0°	30.	630000	BWLVHST
0°÷45°	+5°	"	"	"
0°÷45°	-5°	"	"	"

A1.6.2 Oscillatory tests - pitch mode

α-range (deg)	β (deg)	V (m/s)	f (Hz)	fc/2V (-)	θ (deg)	Model Config.
0°÷42.5°	0°	30	2.5	0.083	±1°	BWLVH
0°÷42.5°	+5°	30	2.5	0.083	±1°	BWLVH
0°÷42.5°	-5°	30	2.5	0.083	±1°	BWLVH
0°÷42.5°	+10°	30	2.5	0.083	±1°	BWLVH
0°÷42.5°	-10°	30	2.5	0.083	±1°	BWLVH
0°÷25°	0°	40	2.5	0.062	±1°	BWLVH
0°÷42.5°	0°	30	2.5	0.083	±1°	BWVH
0°÷42.5°	0°	30	2.5	0.083	±1°	BWLVHST
0°÷42.5°	+5°	30	2.5	0.083	±1°	BWLVHST

A1.6.3 Oscillatory tests - roll mode

α-range (deg)	β (deg)	V (m/s)	f (Hz)	fb/2V (-)	Ampl. (deg)	Model Config.
0÷42.5	0	30	2.5	0.180	±1	BWLVH
0÷42.5	+5	30	2.5	0.180	±1	BWLVH
0÷42.5	0	40	2.5	0.135	±1	BWLVH
0÷42.5	+5	40	2.5	0.135	±1	BWLVH
25÷42.5	0	30	2.5	0.180	±2	BWLVH
0÷42.5	0	30	2.5	0.180	±1	BWLVHST
0÷42.5	+5	30	2.5	0.180	±1	BWLVHST

Transition strips were obtained in accordance with suggestions of Aermacchi, using several grit disks (thickness = 0.2 mm) bonded to the forebody by means of a thin adhesive film (φ_T = 40° and l_T = 400 mm).

A1.7 FFA (Rotary tests - model WG16B)

Run nr.	Conf	V	AOA	Mounting	Transition	Comments
4068	B	30	40	Rear	BT	
4070	B	60	40	Rear	BT	
4072	BS	60	40	Rear	BT	
4073	BS	60	32	Rear	BT	
4079	BWLHVS	60	32	Rear	BT	
4080	BWLHVS	60	8	Rear	BT	
4081	BWLHVS	60	16	Rear	BT	
4083	BWLHVS	60	24	Rear	BT	
4084	BWLHVS	60	32	Rear	BT	
4085	BWLHVS	30	32	Rear	BT	
4086	BWLHVS	60	40	Rear	BT	
4087	BWLHVS	30	40	Rear	BT	
4089	BWLHV	60	32	Rear	BT	
4090	BWLHV	60	40	Rear	BT	
4092	BWLS	60	40	Rear	BT	
4093	BWLS	30	40	Rear	BT	
4096	BWS	60	40	Rear	BT	
4097	BWS	60	32	Rear	BT	
4828	BS	60	40	Rear	IT	
4830	BWS	60	40	Rear	IT	
4831	BWLS	60	40	Rear	IT	
4832	BWLHVS	60	40	Rear	IT	
4833	BWLHVS	30	40	Rear	IT	
4835	BWLHVS	60	40	Rear	IT	
4836	BWLHVS	30	40	Rear	IT	
4837	BWLHVS	60	30	Rear	IT	
4838	BWLHVS	60	32	Rear	IT	
4839	BWLHV	60	40	Rear	IT	
4841	BWLHV	60	40	Rear	IT	0.5 m extension
4842	BWLHVS	60	40	Rear	IT	0.5 m extension
4844	BWLHVS	30	40	Rear	IT	0.5 m extension
4845	BWLS	60	40	Rear	IT	0.5 m extension
4846	BWS	60	40	Rear	IT	0.5 m extension
4848	BWS	60	40	Rear	IT	0.5 m extension
4849	BS	60	40	Rear	IT	0.5 m extension
4852	BS	60	α1	Rear	IT	0.5 m extension
4853	BS	60	α1	Rear	IT	0.5 m extension
4854	BS	60	α1	Rear	IT	
4855	BS	60	α1	Rear	IT	
4857	BWLHVS	60	α1	Rear	IT	
4859	BWLHVS	60	α1	Rear	IT	
4860	BWLHVS	60	α1	Rear	IT	strake angle 95°
4861	BWLHVS	60	40	Rear	IT	strake angle 95°
4862	BWLHVS	60	α1	Rear	IT	strake angle 85°
4863	BWLHVS	60	40	Rear	IT	strake angle 85°
4866	BWLHVS	60	40	Rear	IT	strake angle 90°, same as 4835, but strakes off and on once
4867	BWLHVS	60	40	Rear	IT	
4869	BWLHVS	60	32	Top	IT	
4871	BWLHVS	60	40	Top	IT	
4872	BWLHVS	60	50	Top	IT	
4873	BWLHVS	60	60	Top	IT	
4874	BWLHVS	60	69	Top	IT	
4875	BWLHVS	30	69	Top	IT	
4876	BWLHVS	30	60	Top	IT	
4877	BWLHVS	30	50	Top	IT	
4879	BWLHVS	30	40	Top	IT	
4880	BWLHVS	30	32	Top	IT	
4882	BWLHVS	60	32	Top	IT	
4883	BWLHVS	30	40	Top	IT	
4884	BWLS	60	40	Top	IT	
4885	BWLS	60	50	Top	IT	

Run nr.	Conf	V	AOA	Mounting	Transition	Comments
4886	BWLS	60	60	Top	IT	
4888	BWLS	30	60	Top	IT	
4889	BWLS	30	50	Top	IT	
4890	BWLS	30	40	Top	IT	
4891	BWLHVS	15	40	Top	IT	
4892	BWS	60	40	Top	IT	
4893	BWS	60	50	Top	IT	
4894	BWS	60	60	Top	IT	
4896	BWS	30	40	Top	IT	
4897	BWL	60	40	Top	IT	
4898	BWL	60	50	Top	IT	
4899	BWL	60	60	Top	IT	
4901	BWLHV	60	32	Top	IT	
4902	BWLHV	60	40	Top	IT	
4903	BWLHV	60	50	Top	IT	
4905	BWLHV	60	60	Top	IT	
4906	BWLHV	60	69	Top	IT	
4910	BWLHV	60	$\alpha 2$	Top	IT	
5049	BWLHVS	60	0	Rear	IT	
5050	BWLHVS	60	30	Rear	IT	
5051	BWLHVS	60	32	Rear	IT	
5052	BWLHVS	60	40	Rear	IT	
5054	BWLHVS	30	40	Rear	IT	
5061	BWLHVS	30	40	Rear	IT	with extension
5062	BWLHVS	30	40	Rear	IT	with extension
5063	BWLHVS	60	40	Rear	IT	with extension
5065	BWLHVS	60	40	Rear	IT	with extension, port strake moved 2mm backwards
5066	BWLHVS	60	40	Rear	IT	with extension, port strake moved 2mm back and 2mm up
5068	BWLHVS	60	40	Rear	IT	with extension, strakes slightly asymmetrical at the nose, port over starboard at the apex

AOA sweeps:

$\alpha 1 = 0° \rightarrow 40°$ $\alpha 2 = 30° \rightarrow 70°$

IT=Italian Transition strips BT=British Transition strips

A1.8 DRA/BAR/NASA-LANGLEY (Rotary tests - forebody models)

A1.8.1 8ft x 6ft Wind Tunnel,DRA Bedford, June 1992

Configuration 1 = Hemisphere (Rectangular / Circular)
Configuration 2 = Ogive (Rectangular / Circular)
Configuration 3 = Transition Strip at 80° from bottom centre line
Configuration 4 = 1.5" Height x 4" Length nose strakes

MODEL	RUN	1st DP	Last DP	CONFIG	MACH No	ATM	ALPHA
2318	21	296	310	1	0.105	3	90
	5	60	73			2	
	3	29	43			1	
	7	91	105			0.5	
	20	280	293		0.21	3	
	6	75	89			2	
	4	45	59			1	
	8	107	121			0.5	
	12	168	182	1	0.105	3	60
	13	184	198			2	
	15	216	230			1	
	17	248	261			0.5	
	11	152	166	1	0.21	3	
	14	200	214			2	
	16	232	246			1	
	18	264	278			0.5	
	24	340	354	2	0.105	3	90
	26	370	384			2	
	28	402	416			1	
	30	434	448			0.5	
	25	356	368	2	0.21	3	
	27	386	400			2	
	29	418	432			1	
	31	450	464			0.5	
	34	494	508	2	0.105	3	60
	36	526	540			2	
	38	558	572			1	
	40	590	604			0.5	
	35	510	524	2	0.21	3	
	37	542	556			2	
	39	574	588			1	
	41	606	620			0.5	
2317	44	650	663	1	0.105	3	60
	46	683	698			2	
	48	716	730			1	
	45	666	682	1	0.21	3	
	47	700	714			2	
	49	732	746			1	
	52	776	790	1	0.105	3	90
	54	806	821			2	
	56	839	853			1	
	53	791	805	1	0.21	3	
	55	823	837			2	
	57	855	869			1	
	60	899	913	2	0.105	3	90
	62	931	945			2	
	64	963	977			1	
	61	915	929	2	0.21	3	
	63	947	961			2	
	65	979	993			1	
	68	1023	1037	2	0.105	3	60
	70	1054	1069			2	
	72	1087	1101			1	
	69	1039	1053	2	0.21	3	
	71	1071	1085			2	
	73	1103	1117			1	
	77	1167	1181	3	0.105	3	60
	78	1183	1197			2	
	74	1119	1133			1	
	76	1151	1165	3	0.21	3	
	79	1199	1213			2	
	75	1135	1149			1	
	80	1215	1229	4	0.105	3	60
	82	1246	1260			2	
	84	1278	1292			1	
	86	1310	1323			0.5	
	81	1231	1244	4	0.21	3	
	83	1262	1276			2	

MODEL	RUN	1st DP	Last DP	CONFIG	MACH No	ATM	ALPHA
	85	1294	1308	4	0.21	1	
	87	1326	1340			0.5	
	90	1370	1384	4	0.105	1	70
	91	1386	1400	4	0.21	1	
	92	1402	1416	2	0.105	1	70
	93	1418	1432	2	0.21	1	

A1.8.2 13ft x 9ft Wind Tunnel,DRA Bedford, February 1992

Configuration 1 = Hemisphere (Rectangular / Circular)
Configuration 2 = Ogive (Rectangular / Circular)

MODEL	RUN	1st DP	Last DP	CONFIG	V (m/s)	Q(psf)	ALPHA
2318	1	2	21	1	20	247	90
	3	49	66	1	20	247	
	4	68	81	1	20	247	
	5	84	98	1	70	3000	
	6	100	114	1	60	2210	
	7	116	130	1	50	1530	
	8	132	146	1	40	986	
	9	148	162	1	30	555	
	10	164	178	1	35	753	
	11	180	194	1	33	668	
	12	197	208	1	8.2	42	
	15	241	255	1	40	986	60
	16	257	271	1	70	3000	
	18	292	307	1	40	962	
	19	309	323	1	70	3000	
	20	325	339	1	60	2210	
	21	341	355	1	50	1530	
	22	357	371	1	30	555	
	23	373	387	1	20	225	
	24	389	401	1	8	41	
	26	423	437	2	20	245	60
	27	439	453	2	30	560	
	28	455	469	2	40	987	
	29	470	485	2	50	1530	
	30	487	501	2	60	2210	
	31	504	515	2	8	41	
	32	516	531	2	70	3000	
	34	553	567	2	40	983	90
	35	569	583	2	50	1530	
	36	585	599	2	70	3000	
	37	601	615	2	60	2250	
	38	617	631	2	30	569	
	39	632	647	2	20	245	
	40	649	661	2	8	48	
2317	41	663	677	1	30	568	90
	42	679	693	1	40	995	
	43	695	709	1	50	1530	
	44	711	724	1	60	2240	
	45	726	740	1	70	3000	
	46	742	756	1	30	568	
	47	758	772	1	20	243	
	48	774	786	1	8	41	
	51	828	842	1	30	566	60
	52	844	858	1	40	995	
	53	860	874	1	50	1535	
	54	876	890	1	60	2248	
	55	892	906	1	70	3000	
	56	908	922	1	20	248	
	57	925	937	1	8	41	
	58	939	953	2	30	568	60
	59	955	969	2	40	993	
	60	971	985	2	50	1543	
	61	987	1001	2	60	2250	
	62	1003	1017	2	70	3000	
	64	1040	1054	2	20	248	
	65	1056	1068	2	8	42	
	67	1090	1104	2	30	568	90
	68	1106	1120	2	40	994	
	69	1123	1137	2	50	1535	

APPENDIX 2 - ROTARY BALANCE APPARATUS

(Representative Values Indicated)

Country	Apparatus Name	Facility	Facility Size	Max Velocity or Mach	Max RN $x10^{-6}/m$	Max Model Span, m	Max Ω rpm	Typical max $\frac{\Omega b}{2V}$	α Range, degrees	β Range, degrees	Model Mass, kg	Inclined Axis Capability	Spin Radius
USA	NASA-Langley Spin Tunnel Rotary Balance	Langley Spin Tunnel	6.7m	30 m/sec	1.8	2.0	90	1.0	-90 to 90	-30 to 30	5	No	Yes
USA	NASA-Ames Rotary Balance	Ames 7 ft x 10 ft Low-Speed Tunnel	2.1m x 3.05m	60 m/sec	3.3	0.7	300	0.2	-60 to 60	-60 to 60	15	No	No
ITALY	AerMacchi 6CR	AerMacchi Low-Speed Wind Tunnel	2m	70 m/sec	3.3	1.3	300	0.3	-180 to 180	-30 to 30	20	No	Yes
UNITED KINGDOM	British Aerospc Low-Speed Rolling Rig	Warton 5.5 m Low-Speed Wind Tunnel	5.5m	22 m/sec	1.5	2.0	60	0.2	0 to 90	-90 to 90	60	No	No
UNITED KINGDOM	British Aerospc Multifacility Derivative Rig	Warton 1.2 m High-Speed Blowdown	1.2m	M = 0.4 to 0.86	30 - 65	0.6	300	0.3	0 to 90	-90 to 90	30	No	No
UNITED KINGDOM	RAE-Bedford Rotary Balance	DRA-Bedford Low-Speed Tunnel	4m x 2.7m	90 m/sec	6.0	0.7	400	0.2	-20 to 60	-60 to 60	15	No	No
GERMANY	DLR Rotary Balance	DLR 3 m Low-Speed Tunnel	3.25m x 2.8m	80 m/sec	5.5	1.0	300	0.3	-30 to 90	-90 to 90	20	No	No
FRANCE	ONERA-IMF Lille Tournebroche Rotary Balance	SV4 Vertical Wind Tunnel	4m	50 m/sec	2.0	1.0	120	0.6	-135 to 135	-90 to 90	10	Yes (20 deg)	Yes
SWEDEN	FFA L2 Rotary Rig	FFA Low-Speed Tunnel L2	2m x 2m	65 m/sec	3.5	0.6	600	0.3	-40 to 40	-40 to 40	5	No	No
SWEDEN	FFA LT1 Rotary Rig	FFA Low-Speed Tunnel LT1	3.6m	70 m/sec	6.0	1.0	360	0.3	-150 to 150	-10 to 10	10	No	No
SWEDEN	FFA S4 Rotary Rig	FFA Transonic-Supersonic Tunnel S4	1m x 1m	M = 0.5 to 2.0	14.0	0.4	600	0.2	0 to 25	0	5	No	No
CHINA	CARDC Rotary Balance	CARDC 4m x 3m Low-Speed Tunnel	4m x 3m	100 m/sec	6.0	1.0	330	0.2	-135 to 135	-45 to 45	15	No	No
CHINA	Chinese Aero-nautics Estab. HARI RB-1	FL-8 Low-Speed Tunnel	3.5m x 2.5m	N/A	N/A	N/A	300	0.2	-126 to 126	-36 to +36	N/A	Yes	No
USA	WPAFB Rotary Balance	Wright Labs Spin Tunnel	3.7m dia.	50m/sec	3.4	1.2m	130	0.6	-90 to +90	-30 to +30	12	No	No
GERMANY	BAR Rotary Balance	Large Amplitude Multi-Purpose Facility	3.3m dia.	40m/sec	2.0	1.0	150	0.5	-180 to +180	±32	10	No	Yes

APPENDIX 3

REYNOLDS NUMBER SIMULATION IN HIGH-ALPHA TESTS

A3.0 RATIONALE

The existence of significant Reynolds number effects for high angle of attack flows is now well established, both for static and dynamic conditions. For static conditions, such Reynolds number effects have been extensively studied for simple shapes, such as tangent-ogive cylinders (see for example Refs 1-2) and a number of excellent review papers exist, such as Ref 3. Also, the extensive research work conducted by NASA both in wind tunnels and in flight using the F-18 HARV, has highlighted the significant impact of scale effects on lateral-directional behaviour of aircraft configurations and problems related to wind tunnel measurements at sub-scale Reynolds numbers[4-5]. For dynamic conditions and for rotary testing in particular, available information is still quite limited, but clear evidence exists for some families of simple shapes[6-7], for the F-15 aircraft[8], and from the tests reported in Chapter 7 of the present report.

In fact, for many reasons, the largest part of the high angle of attack testing used for the development of aircraft configurations is done at low to moderate Reynolds numbers, and almost all dynamic testing, either rotary or oscillatory, is done at low Reynolds numbers because of the unavailability of dynamic testing facilities in high-Re tunnels, the difficulty in their realization and limited past interest in this issue.

A significant level of uncertainty is thus included in all such data when applied to a full scale aircraft. There is significant interest in any technique that may allow a more confident extrapolation of data to higher Reynolds numbers.

Two definitely different approaches exist within the scientific community about the problem of extrapolation to full scale of dynamic test results. The first approach chooses to perform all testing at subcritical (i.e. laminar) flow conditions and assume that such results can be directly applied to full scale. Such approach is based on the well demonstrated analogy existing for tangent-ogive circular forebodies. For such bodies the onset angles of asymmetric flows and the magnitude of asymmetric side forces are very similar at subcritical and supercritical Reynolds numbers. Also, the approach is justified by the experience of good correlation between spin behaviour predicted by rotary balance testing at laminar flow conditions and full scale. When a good physical insight exists about the governing flow phenomena, some kind of "analytical extrapolation" can be applied, guided by static test data at subcritical and supercritical flow conditions. In fact no general theory exists and such extrapolation normally consists in qualitative adjustments of data based on good judgement.

A number of objections exist to such an approach, the most obvious ones are the following:
- there exists a number of demonstrated cases, as reported in the references mentioned above, which show that results of testing at laminar flow conditions do not correlate with results at turbulent flow conditions;
- the analogy of laminar and turbulent flows is only valid as far as the side force on isolated tangent ogive forebodies is concerned. On complete and complex configurations the difference in flow separation positions may lead to different vortex positions, and thus different interaction with downstream model components.

A second approach which is getting attention is based on the concept of performing tests at the highest available Reynolds number and make use of boundary layer manipulation in order to obtain a better approximation to full scale conditions. Reference 9 is an example of a very detailed attempt to establish guidelines and methodology for Reynolds number simulation in wind tunnel testing. Although the methodology is devoted to transonic flows over wings and wing sections, the general framework and some useful concepts can be extrapolated to other types of flow. One useful concept is the classification of Re-effects in terms of:

(i) "Direct" Re-number (i.e. viscous) effects, which arise as a result of changes in the boundary layer (and wake) development for a fixed or "frozen" pressure distribution;
(ii) "Indirect" viscous effects, associated with changes in pressure distribution resulting from changes with Re-number in the boundary layer state and wake development.

Examples of direct effects are changes with Re-number of thickness or friction in a turbulent boundary layer; an example of indirect effects is the change of drag of a cylinder related to the presence of a laminar or turbulent separation. Indirect viscous effects are normally related to the presence of "critical" phenomena, which lead to a change in flow structure.

It is quite clear that the important Re-effects on forebody flows are of the indirect type and are related to the transition

mechanism. Boundary layer transition mechanisms on a body at incidence have been classified by Poll[10] in terms of:

- free shear layer instability, i.e. transition in a separation bubble;
- contamination along the attachment line;
- cross-flow instability;
- streamwise-flow instability (i.e. classical Tollmien-Schlichting 2D transition).

Depending on cross-sectional shape, onset boundaries of angle of attack and Re-number can be established for each transition mechanism. For a circular cylinder such boundaries are represented in Fig A3.1 from Ref 10. On such boundaries onset of transition will generate "critical" phenomena, leading to changes in position of separation lines, changes in pressure distributions, and thus changes in position, strength and interactions of forebody vortices. Such (indirect) scale effects can be avoided in testing at lower Re-numbers if the boundary layer can be manipulated by forcing transition so that the boundary layer state at separation is the same as in full scale. Fortunately, the size and flight conditions of most aircraft and missiles are such that the flow will be fully turbulent.

Of course, a test technique aimed at simulating higher Reynolds numbers by forcing boundary layers to be turbulent does have some obvious limitations, such as:

- "direct" Re-effects will not normally be simulated (i.e. effects due to actual thicknesses of boundary layer). At the present level of knowledge, this is considered to be a secondary effect;

- due to the wide range of attitudes (angles of attack and of sideslip) where testing is normally performed, and the variation of transition mechanisms and flow topology over this range, it will normally be difficult to devise a single tripping configuration that may be effective in the complete range of interest;

- the test Re-number must be high enough that effective tripping can occur. Limits exist to the lowest Re-number where boundary layer can be tripped to a turbulent state;

- for pointed forebodies, local Re_d is very small near the tip. A small amount of laminar flow cannot be ruled out at full scale, and boundary layer tripping will not be possible very near to the leading edge. This leaves a margin of uncertainty for flow conditions dominated by phenomena occurring at the very tip of the nose (such as onset of asymmetric flow);

- the technique is only applicable to cases when the full-scale boundary layer state and flow separation are of known and constant character. Thus it is applicable to conventional steady tests, to rotary tests (which are aerodynamically steady) and to oscillatory tests only in situations when effects of unsteady transition movement can be excluded.

The possibility of Re-number simulation for high angle-of-attack flows on forebodies was suggested by Poll[10-11] and is supported by Haines[3] and other authors. Although some kind of transition tripping has been often used in the past in everyday test practice, this is often done somewhat "blindly" without much attention to proper trip sizing, position and verification of desired effect within the test envelope. It is the purpose of the present appendix to describe a systematic approach to the problem which can be used as a starting point for further investigations.

Also, most of what will be described pertains to static tests, but it is considered to be of importance for dynamic tests as well, for the following reasons:

- due to the highly non-linear nature of vortex interactions, it is definitely important that static coefficients of the model on the installation to be used for dynamic tests be representative of a correct behaviour;
- rotary tests, although performed in dynamic conditions, create a steady flow condition on the model. Concepts applicable to, say, static tests at sideslip can be transferred to rotary tests as well;
- a large contribution to "unsteady" effects measured in oscillatory tests is often generated by "quasi-steady" phenomena. Such phenomena will also be better simulated if the initial flow condition is correct.

A3.1 REVIEW OF SOME AVAILABLE TEST EVIDENCE

Although usage of some form of transition tripping is an often used practice in high-alpha and dynamic tests, very few dedicated and careful experiments have been reported having the specific aim of assessing the success of the technique in simulating flow at higher Reynolds numbers. Results of two such systematic experiments[12-13] will be briefly reviewed in the following.

A3.1.1 NASA-Langley experiment

The effectiveness of different transition tripping strategies was tested on a fineness ratio 3.5 ogive-cylinder model, with a cylindrical length of 7 diameters[12]. The model was instrumented with 14 rows of 30 pressure ports so that detailed pressure distributions could be measured, and total forces were computed from integration of pressures. Tests were performed in three wind tunnels, namely the Langley 7 by 10-Foot High Speed Wind Tunnel, the Langley 14 by 22-foot Subsonic Tunnel and the Langley Low-Turbulence Pressure Tunnel, covering a Re-number range between 0.27 to 5.5 millions based on body diameter. All tests were run at an angle of attack of 40°.

Two transition tripping techniques were tested. The first one makes use of distributed roughness elements equally dispersed on the whole model surface, with the exception of the pressure hole rings and of the model tip. Carborundum #80 grains (average 0.2 mm size) were used. The second technique utilizes two strips of the same carborundum grains placed along two body meridians at 54° from the bottom symmetry line. Again such strips were stopped at some distance from the ogive tip. Such placement is justified by the fact that at high angles of attack an attachment line occurs at the windward centerline and that streamlines are much more oriented in a cross-flow direction. It is this cross-flow that has to be tripped.

Figures A3.2 and 3 show a comparison of normal and side force distributions (integrated from pressure distributions) for the three cases:
- low Re-number natural transition (Re_D=0.6 million)

- high Re-number natural transition (fully turbulent at Re_D=5.5 million)
- low Re-number (Re_D=0.6 million) with tripped boundary layer.

The figures clearly show that transition tripping is quite effective and that the higher Re-number condition is quite well represented from a qualitative as well as quantitative point of view, although with some approximation. In terms of overall integrated normal and side forces Figs A3.4-5 show that the model with fixed transition does not exhibit any significant Re-number sensitivity. For a "long" (6 diameters) cylindrical body the quality of simulation is excellent, with the distributed roughness showing some excess normal force, which is attributed by the author to cross flow drag generated by the roughness in the turbulent boundary layer. For a "short" body some discrepancy is evident, mainly on side force values, probably because of the absence of the trip near the ogive tip. In any case the simulation is significantly improved, especially at intermediate, transitional, Reynolds numbers.

A3.1.2 AEM/NLR experiment

Although devised independently, the purpose and rationale of this test[13-14] were very similar to the Langley test. The configuration selected was that of a realistic aircraft front fuselage, featuring a 2.3 fineness ratio forebody, a canopy and Leading Edge Extensions (Fig A3.6). The model was tested in NLR-HST wind tunnel at a Mach number of 0.3 and total pressures from 0.5 to 4 bar giving a Re range between 0.34 to 2.8 millions based on body equivalent diameter at the forebody-canopy intersection. Angles of attack were varied between 30° to 70° and angles of sideslip up to -30 to 30° depending on total pressure. The model was instrumented with a balance for measurement of total forces, as well as with pressure measurements at five stations. Visualizations with liquid crystals were also performed in order to highlight the boundary layer state.

Similarly to the Langley test two transition tripping configurations were tested, namely a distributed roughness, i.e. 0.2 mm "ballottini" dispersed over the whole model surface except LEX's, and transition strips, i.e. two strips of 3-D approximately cylindrical roughness elements of 0.8 mm diam. and 0.25 to 0.3 mm height. The position of such strips, approximately located at the 45° meridian from the bottom centerline, was in fact determined on the basis of flow visualizations at low Re-number in order to guarantee that transition strips be located in front of the laminar separation lines of the untripped boundary layer for all attitudes of interest.

In the analysis of results, attention was given primarily to the forebody contribution to aircraft directional stability, represented either by yawing moment or side force, since center of pressure of side force was shown to be quite constant. Such contribution is characterized by $C_{n\beta}$ or $C_{Y\beta}$ derivatives, as well as onset and intensity of asymmetric forces.

Significant Re-number effects were found, as demonstrated by Figs A3.7-8. At high Re-number the onset of asymmetric side force shifts from 56° to 47° and intensity of asymmetric forces is much larger. At high Re-number the unstable $C_{Y\beta}$ contribution of the forebody is larger and it increases with angle of attack. Consistently with the onset of asymmetric forces, such contribution becomes stabilizing at 48° with a much larger value than shown by low-Re tests.

The effectiveness of transition tripping in simulating the asymmetric side forces is shown in Fig A3.9. With transition tripping, the maximum intensity of asymmetric forces is correctly reproduced, although the onset angle is still delayed by 5 to 7°. The fixed transition strips appear to be preferable from this point of view. In terms of $C_{Y\beta}$ below asymmetry onset, Fig A3.10 shows that in both cases transition tripping improves the simulation significantly, with the distributed transition being preferable.

The indicated conclusions are confirmed by detailed analysis of the pressure distributions, which show, in the presence of transition tripping, the elimination of the laminar separation, the attainment of correct levels of maximum suctions on the forebody sides and the different position of the turbulent separations compared to the laminar ones (see Figs A3.11-12).

A3.2 PROCEDURES AND CRITERIA FOR TRANSITION TRIPPING

As illustrated in the description of the two experiments, two main strategies exist for boundary layer tripping in high-alpha tests, i.e. use of distributed roughness and use of discrete transition strips. The two experiments were not conclusive in defining a preferable alternative, although in principle each procedure has its own benefits and drawbacks. Distributed roughness:
- does not require previous knowledge of separation lines positions;
- may cause transition of reattachment flows and thus of secondary separations as well as primary ones;
- allows for more complex flow topologies;
- would properly work for any angle of attack/sideslip combination;
- introduces an undesirable disturbance to the velocity profiles and some thickening of the turbulent boundary layer, which will be different from those typical of a smooth surface and may cause premature separation.

Other combined strategies, such as usage of distributed roughness on the full windward surface of the forebody or on parts of the surface can be devised, although no experience about their use is known to the author.

A3.2.1 Roughness sizing.

A wealth of information exists about effectiveness of 2D or 3D isolated roughness elements and distributed roughness on transition. The two best known and often used criteria are the Braslow-Knox[15] and Potter-Whitfield[16]. It must be recalled that such criteria, as well as most of the available evidence on transition tripping, have been developed for flat plate flow where the dominant transition mechanism is Tollmien-Schlichting instability. No information exists about sizing criteria in the presence of significant cross-flows, where cross-flow instability is the dominant transition trigger and possibly smaller roughness sizes may be sufficient. Also, only limited information exists about effects of pressure gradients on the effectiveness of the strips[17]. While strips can be located near to pressure peaks, where gradients are small, very often they

will operate in a favourable pressure gradient that may produce re-laminarization.

In the context of high-alpha tests, it is felt that use of 2D transition trips such as wires is not advisable because, at the lowest Re-numbers, when size of the trip is relatively large compared to the local laminar boundary layer thickness, transition would be promoted by creating a local separation bubble. If the bubble flow fails to reattach, the trip would act as a strake, fixing separation position and thus effectively altering the flow.

A limit also exists to the minimum test Re-number where transition can be effectively tripped. Reference 13 indicates such limit at about $Re_x=1.x10^5$ although lower values, as low as 20000 can be achieved. At the lowest Re-numbers the size of the disturbance becomes significant compared to the thickness of the laminar boundary layer, so that intrusive effects may appear.

A3.2.2 Strip placement

If discrete strips are used, their proper positioning requires much care. Because of the cross-flow character of forebody flows at high angles of attack, it is quite obvious that the reasonable distribution of the roughness strips is in the form of longitudinal lines. The placement of such strips is subject to conflicting requirements. In fact they should be placed in front of any laminar separation line (or laminar bubble) at a minimum distance of 10 to 20 roughness heights, in order to guarantee that transition is complete. Also, they should be placed as near as possible to the pressure peaks, in order to work in a constant or adverse pressure gradient and avoid strong favourable pressure gradients as occurring near to the attachment line. Finally, if a range of model attitudes has to be tested, the selected position must compromise the above requirements for a range of attitudes, and different positions may be required to cover the complete range of interest.

Surface flow visualizations should be systematically used as a support in defining strip positions and in assessing their correct placement and effectiveness in promoting transition. For unconventional cross sectional shapes, simple computational tools (such as surface panel or slender-body programs) may be of help in defining inviscid pressure distributions which will be reasonably valid for the windward side of the model and help defining local external flow conditions for roughness sizing and identification of pressure peaks.

A3.3 REFERENCES

1. Lamont P.J. Pressures around an inclined Ogive-Cylinder with Laminar, Transitional or Turbulent Separation, AIAA Journal 20, 11, pp 1492-1499, Nov. 1982

2. Champigny, P. Reynolds number effect on the aerodynamic characteristics of an ogive-cylinder at high angles of attack, AIAA paper 84-2176

3. Haines, A.B., Scale effects on Aircraft and Weapon Aerodynamics, AGARDograph 323, 1994.

4. Erikson G.E., Hall R.M. Banks D.W., Del Frate J.H., Schreiner J.A., Handley R.J., Oulley C.T., Experimental investigation of the F/A-18 Vortex Flow at Subsonic through transonic speeds, AIAA 89-2222

5. Del Frate J.H., Zuniga F.A., In flight analysis on the NASA F-18 HARV with comparisons to ground facility data, AIAA-90-0231, Jan 1990.

6. Polhamus F. C., A review of some Reynolds number effects related to bodies at high angles of attack, NASA CR 3809, 1984.

7. Clarkson, M.H., Malcolm, G.N., Chapman, G.T.: Experimental Poststall Aerodynamic Coefficients for Airplane-Like Configurations. J. of Aircraft, Vol 13, No 8, pp 565-570, August 1976.

8. Malcolm, G.N.: Rotary-Balance Experiments on a Modern Fighter Aircraft Configuration at High Reynolds Numbers. AIAA-85-1829, August 1985.

9. Boundary Layer Simulation and Control in Wind Tunnels, AGARD AR-224, 1988.

10. Poll. D.I.A., On the effects of boundary layer transition on a cylindrical afterbody at incidence in low-speed flow, Aeronautical Journal, Oct. 1985.

11. Poll D.I.A., Some effects of boundary layer transition on slender axi-symmetric bodies at incidence in incompressible flow, AGARD CP-336, Missile Aerodynamics, Sept. 1982.

12. Hall R.M., Banks D.W., Progress in Developing Gritting Techniques for High Angle of Attack flows, AIAA paper 94-0169, Jan. 94.

13. Heppe G.J.T., Investigation on AEM Forebody Model 4 in the High Speed Wind Tunnel HST, NLR TR 94325 C, Dec. 94.

14. Pertile R., Cooperative AEM/NLR research on scale effects on a generic fighter forebody - Analysis of test results, AEM report 567-ANG-339, Feb. 95.

15. Braslow A.L., Knox E.C., Simplified Method for Determination of Critical Roughness Height of Distributed Roughness Particles for Boundary Layer Transition at Mach Numbers from 0 to 5, NACA TN-D-4363, Sept. 1958.

16. Potter L.L., Whitfield J.D., Effects of Unit Reynolds Number, Nose Bluntness and Roughness on Boundary Layer Transition, AEDC-TR-605, March 1960.

17. Michel R., Arnal D., Investigations of the conditions fro Tripping Transition with Roughness Elements and their Influence on Boundary Layer Development, in "Boundary Layer Control by Transition Fixing", DFVLR-Mitt-84-17

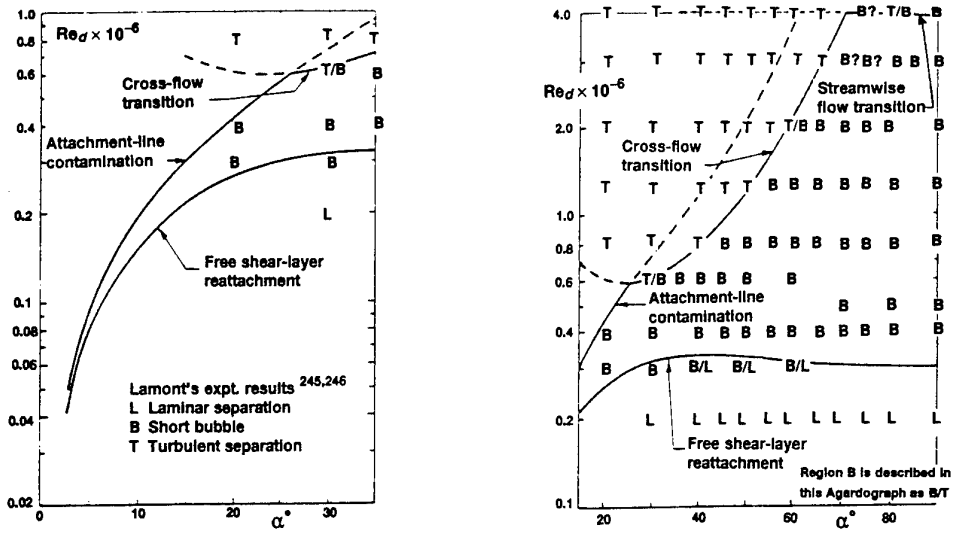

(a) Incidences up to 35°

(b) Incidences from 20° to 90°

Fig A3.1 - Illustration of the types of transition on cylindrical bodies and a comparison of predicted and measured results (from Ref 10).

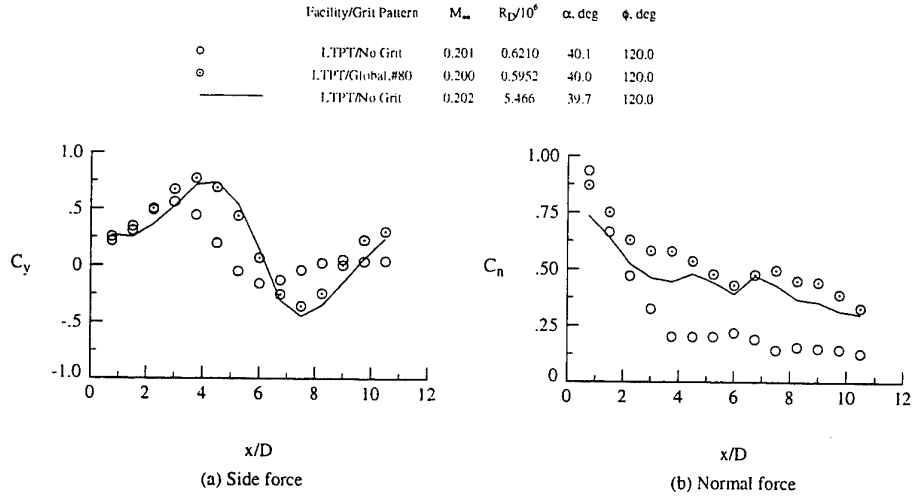

(a) Side force

(b) Normal force

Fig A3.2 - NASA Langley experiment - Effect of distributed roughness on force distributions for ogive/cylinder model.

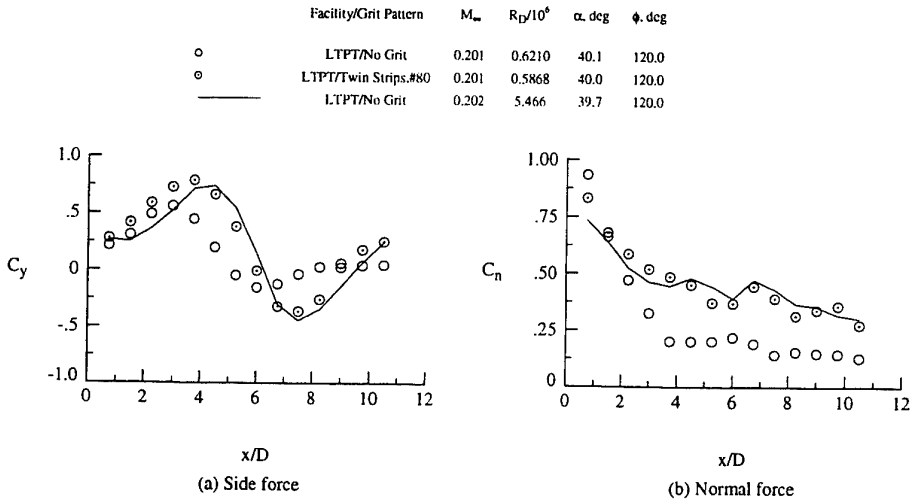

(a) Side force

(b) Normal force

Fig A3.3 - NASA Langley experiment - Effect of twin transition strips on force distributions for ogive/cylinder model.

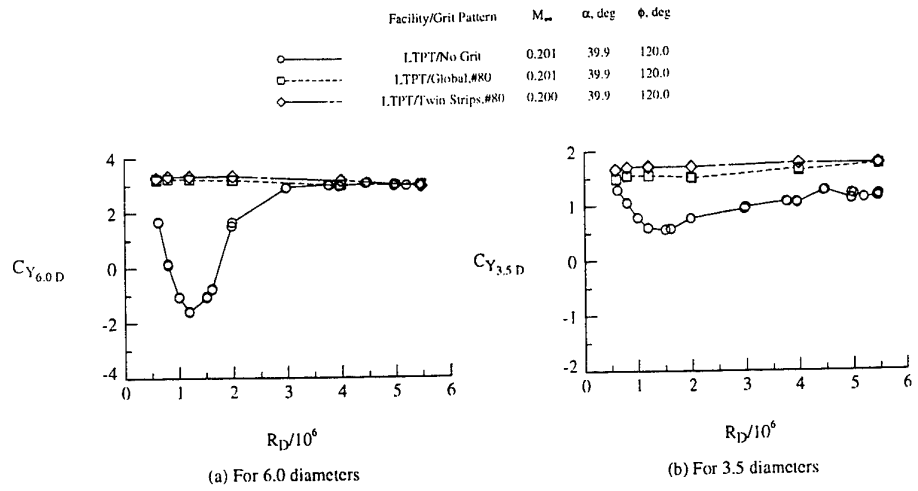

(a) For 6.0 diameters

(b) For 3.5 diameters

Fig A3.4 - NASA Langley experiment - Effect of transition tripping pattern on variation of total integrated side force with Reynolds number for ogive/cylinder model and two model lengths.

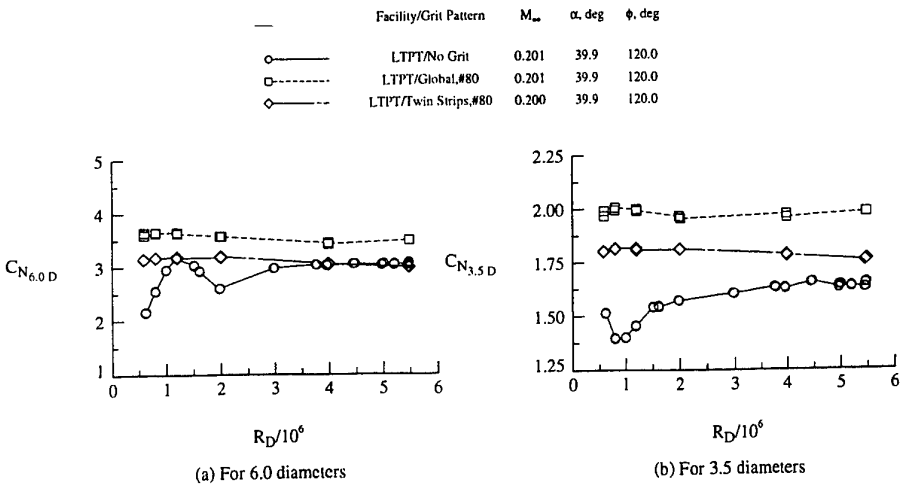

(a) For 6.0 diameters

(b) For 3.5 diameters

Fig A3.5 - NASA Langley experiment - Effect of transition tripping pattern on variation of total integrated normal force with Reynolds number for ogive/cylinder model and two model lengths.

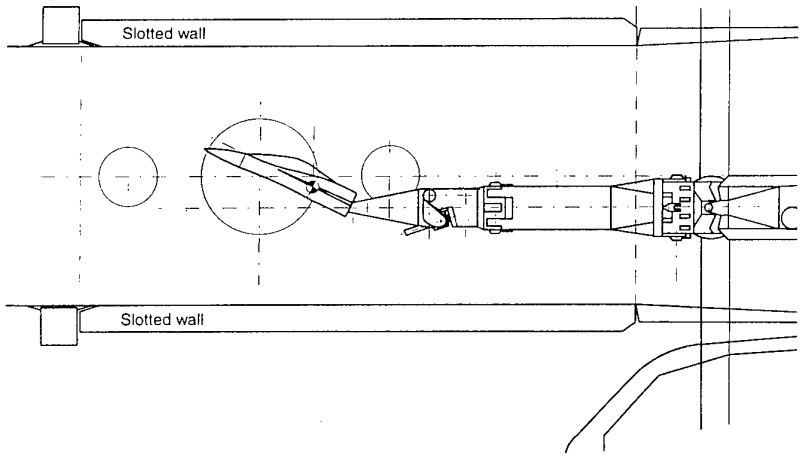

Fig A3.6 - AEM/NLR forebody model in NLR/HST wind tunnel on articulated boom support.

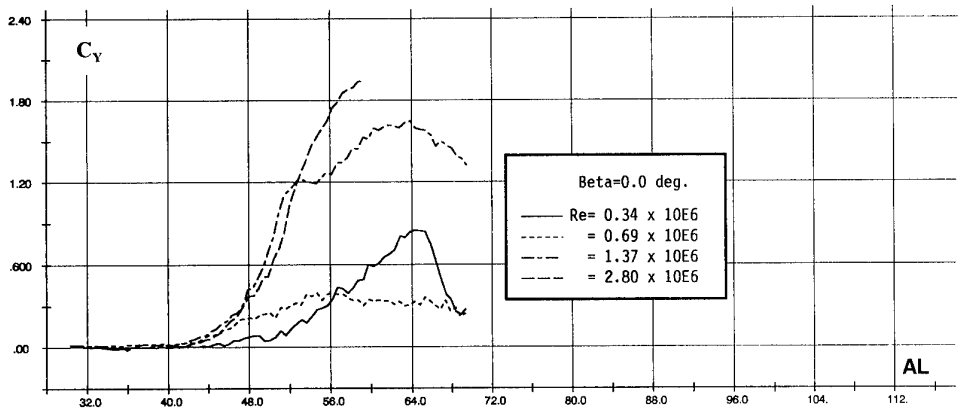

Fig A3.7 - AEM/NLR experiment - Re-number effect on side force at zero sideslip, free transition.

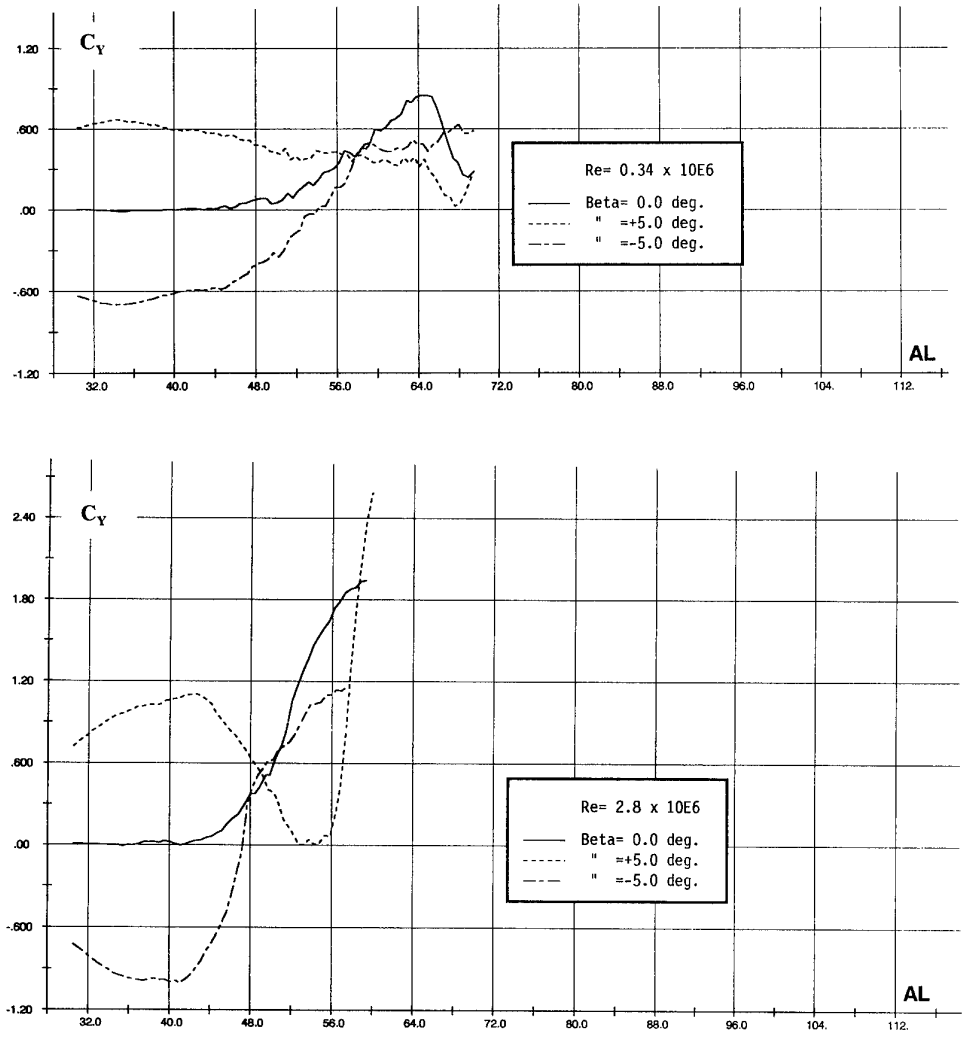

Fig A3.8 - AEM/NLR experiment - Re-number effect on side force variation with sideslip, free transition.

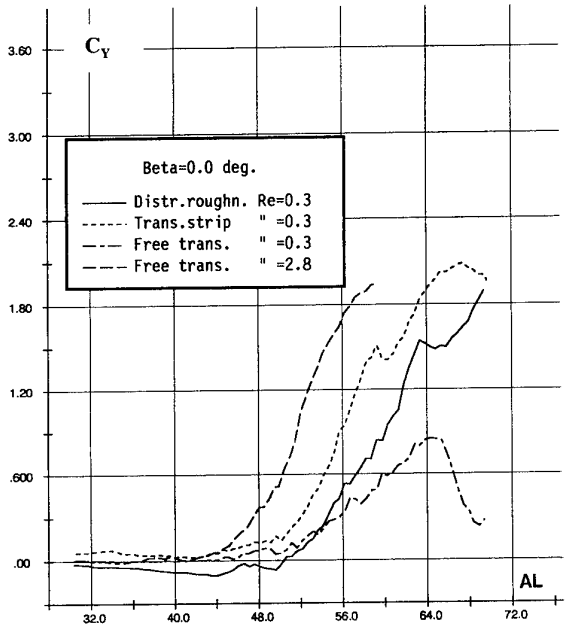

Fig A3.9 - AEM/NLR experiment - Effectiveness of transition tripping techniques in simulating Re-number effects on side force at zero sideslip.

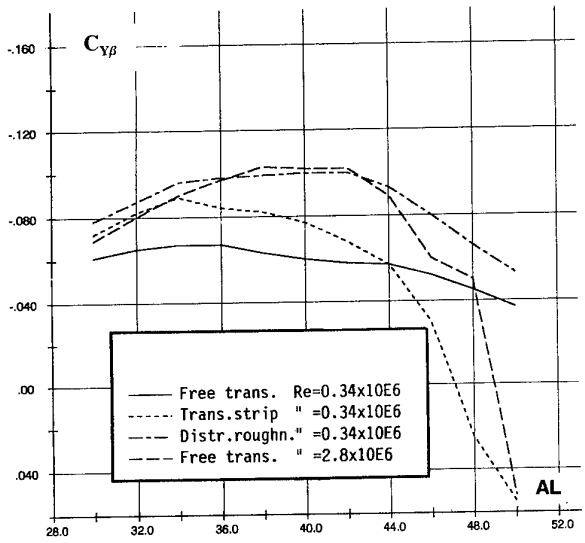

Fig A3.10 - AEM/NLR experiment - Effectiveness of transition tripping techniques in simulating Re-number effects on side force gradient due to sideslip.

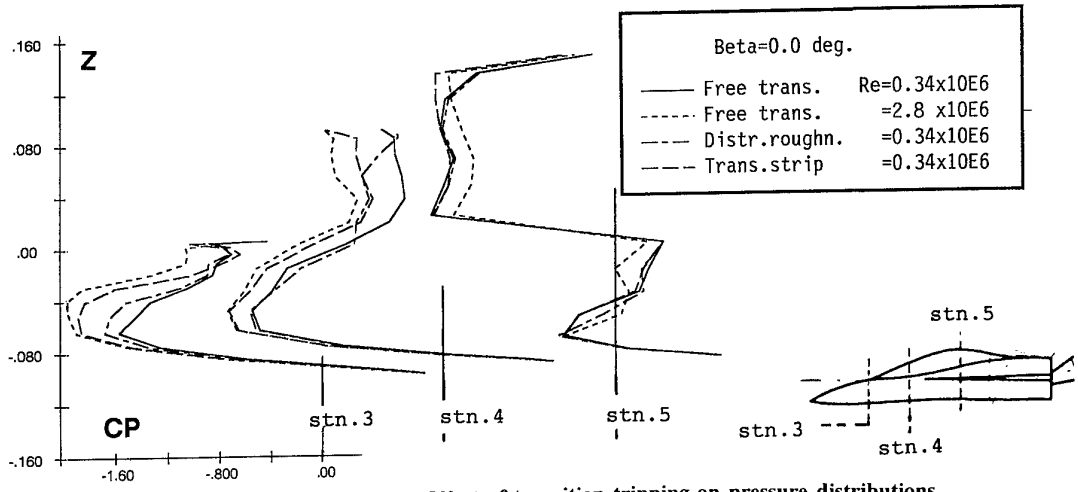

Fig A3.11 - AEM/NLR experiment - Effect of transition tripping on pressure distributions. Asymmetric flow condition at α=58°, β=0°, starboard side.

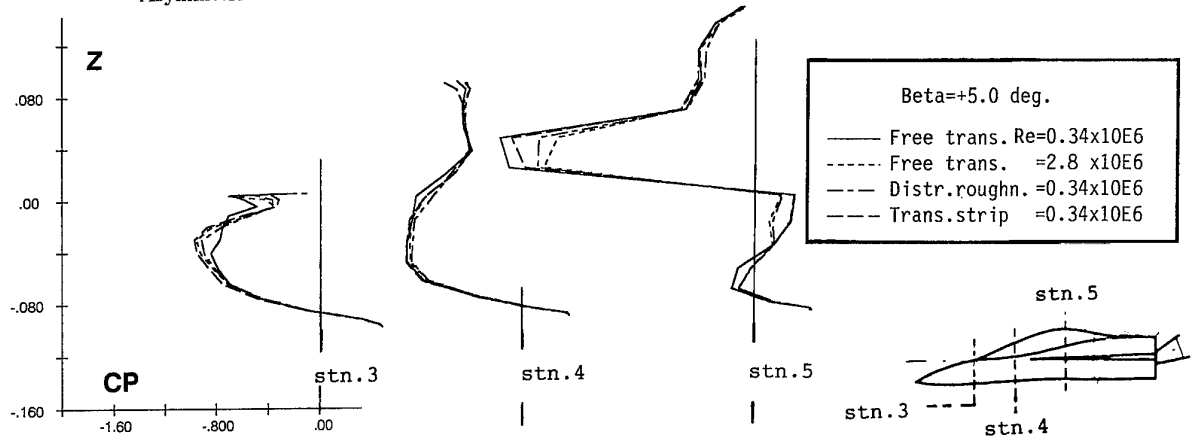

Fig A3.12 - AEM/NLR experiment - Effect of transition tripping on pressure distributions. α=40°, β=5°, starboard side.

Appendix 4

This appendix is reproduced directly as received from the authors. It does not represent the views of the Working Group as a whole. Nevertheless, because of its high relevance to the field, it is included in this volume, with the understanding that, in the opinion of the Working Group, the authors' analysis and conclusions are open to other interpretations.

AERODYNAMIC ANALYSIS AND INTERPRETATION OF WG16 RESULTS

by

M.E. Beyers and L.E. Ericsson

A4.0 INTRODUCTION

Increasingly high-quality rotary and oscillatory data are needed to advance the understanding of manoeuvring aerodynamics at high angles of attack, which is the principal objective of AGARD FDP WG16[1]. To reach that goal requires extensive analysis of the experimental results.

A cursory perusal of the steady and unsteady force and moment data presented in Chapters 3 to 6 gives an appreciation of the complexity of the aerodynamics of the WG16 configuration. An adequate understanding of the physics of rotary and oscillatory flows is a prerequisite for the correct interpretation of these high-α nonlinear data. Issues that have a bearing on the analysis include Reynolds number scaling, and, in particular, Reynolds number criticality in the presence of motion, and diverse experimental constraints associated with the different experimental facilities and test apparatuses. Scaling problems associated with boundary layer simulation and support and wall interference effects need to be investigated for both the basic and the straked configuration. As a result, the wind tunnel aerodynamics of the model are generally more complex than those of the full-scale aircraft in free flight and must, therefore, be understood before flight predictions can be made.

The effects of ground facility interference have to be dealt with first as they are often the dominant source of uncertainty in rotary tests. The assessment of these effects is complicated by the coupling with motion-induced viscous effects. The nature of the fluid/motion coupling is largely determined by forebody geometry. For specific configurations the coupling is alleviated, resulting in predictable aerodynamic characteristics under certain conditions.

Good correlations of the rotary characteristics were obtained for the BWLVHST configuration at low to moderate angles of attack ($\alpha < 40°$) in the different facilities. This is to be expected for a model in steady motion where the primary flow separations are fixed. The results demonstrate the correct functioning of the measurement systems, and show the relative insensitivity under these conditions to model size and support geometry (Figs 4.7 and 4.8). As the angle of attack is increased above 45 deg, however, the sensitivity of the results to support geometry appears to increase, as can be seen in Figs 4.9 and 4.10.

In this chapter an analytic approach is followed which can provide a realistic assessment of the prevailing flow mechanics revealed by the wind tunnel experiments. Support interference contributions, for instance, can be identified, indicating the kinematic and aerodynamic conditions under which the dynamic results can be applied with confidence. The degree to which the facility interference can be quantified and, thereby, the veracity of the free-flight vehicle aerodynamics extracted, depends on the complexity of the experiments. For configurations that do not have boundary layer trips, the unsteady aerodynamics are reasonably well understood and the procedure is quite straightforward, even routine at subcritical Reynolds numbers. In contrast, the high-α aerodynamics of configurations with trips are highly complex, and the equivalent analysis requires very comprehensive flow field information. In such cases the analysis of the rotary and oscillatory results in Chapter 3-6 is based upon conceptual models. Where limitations exist, solutions are proposed for future application.

A4.1 BACKGROUND

The rotary balance provides a natural analogue to aircraft spinning. However, it has a wider significance, as the coning motion generated at high angles of attack is the elementary characteristic motion prescribed by many mathematical models of aircraft dynamics. Because of the kinematic similitude provided, rotary data are directly useful in the prediction of steady spin rates, but generally require extensive analysis before predictions of manoeuvring flight can be made. Support interference, Reynolds-number-critical behavior and free-stream turbulence are some of the factors that determine under which conditions the measured rotary characteristics are directly applicable to flight prediction. Additional information is obtained from test results for small- and large-amplitude oscillations in pitch, yaw and roll, alone as well as in combination with a basic coning motion.

In selecting a test model for the development of rotary testing techniques, there are several choices to be made. When a configuration such as BWLVHST is chosen, the flow separations are fixed at moderate angles of attack. Consequently, the rotary characteristics are much less sensitive to support interference, Reynolds number, and free-stream turbulence up to a point ($\alpha < 45°$). This has some relevance for current low-observables configurations at moderate angles of attack. However, in general, advanced aircraft are sensitive to these variables and prediction of their characteristics requires data as closely allied to the case under consideration as possible. Perhaps of more immediate importance is the need to validate the rotary balance results that have been accumulated for existing aircraft configurations. With the possibility of quantifying the effects of facility interference and scale effects, data for configurations such as BWLVH on which boundary layer transition effects played an important role could be cleared of the cloud of uncertainty presently existing. The additional efforts needed to determine the effects of support interference in many cases add valuable information about the flow physics not obtained under interference-free test conditions. For this reason, constructive methods of dealing with these configurations are introduced and developed. This rationale is equally applicable to the straked configuration in the absence of boundary layer trips at conditions for which viscous flow effects become important, such as at $\alpha > 45°$ for BWLVHS, where evolving vortex interactions are dominated by viscous flow effects on the forebody aft of the strakes.

Thus, it is of fundamental importance to demonstrate the viability of test techniques in situations where significant viscous flow effects exist, and in particular in cases where boundary layer transition plays an important role. Specifically, it is necessary to document how the flow separation characteristics and vortex interactions in rotary motion are affected by model scale and facility interference effects. At high angles of attack this need exists also for models with forebody strakes, because of the crossflow separation and associated development of a second vortex pair observed to take place on the BWLVHST configuration aft of the strakes.

As noted in the Introduction, because of the complexity of the aerodynamics of configurations with boundary layer trips highly detailed flow-field information is required if such quantitative analyses are to be undertaken. In the present programme such data are not available and BWLVHST can be analyzed on the basis of phenomenological considerations only. Accordingly the discussion in Section A4.4 will be focussed on the straightforward case of BWLVH with quantification of the effects concerned to the extent permitted by a sparse data base. Any analysis of the large data base of the configurations with trips BWLVHT and BWLVHST would have to be based on the understanding of the baseline aerodynamics, and of the effects of trips, which are discussed in Section A4.3.

A4.2 ANALYSIS OF DYNAMIC EXPERIMENTS

To develop an understanding of the aerodynamics of the WG16 model the surface flow patterns are analyzed. With the benefit of a knowledge of the topological changes in the flow field and previous experiences of facility interference and Reynolds number sensitive behavior the rotary and oscillatory aerodynamic characteristics can be identified.

A4.2.1 Flow Field Analysis

The IAR oil flow visualization results[2] for BWLVH shown in Figs A4.2.1-A4.2.9 and A4.2.13 were obtained on the symmetric support (Fig 2.23) at the nominal freestream velocity 30 m/s, corresponding to $Re_d = 0.2 \times 10^6$. The ranges of angle of attack covered were 25° - 53° for the forebody, and 17° - 53° for the LEX and wing.

Forebody - LEX (Baseline Configuration)

The leeside skin friction lines obtained at the azimuth angle $\phi_m = 180°$ in Fig A4.2.1 show symmetric flow separation on the forebody at $\alpha < 30°$. Fully developed secondary separation lines and vortex flow patterns exist up to the nose tip. The primary laminar separations are symmetrical over the full length of the forebody, at $\phi_m < 90°$, and the primary vortex reattachment line is straight, along $\phi_m = 180°$.

At $\alpha > \alpha_{on} \approx 30°$ the asymmetry of the primary separation lines developed, increasing with increasing α (see Fig A4.2.2). At $\alpha = 41°$ the primary separation lines were located at $\phi_m \approx 98°$ on the starboard side (Fig A4.2.3) and $\phi_m = -76°$ on the port side[2]. The average displacement of these separations from the stagnation line is about 87°. The topology is developed in Fig A4.2.4.

At $\alpha \geq 45°$ a dramatic change in the flow topology occurs, with the shedding of a second pair of vortices. Figure A4.2.5 shows the second vortex pair to be starting at about two diameters from the tip, at $\alpha = 46°$, seen from a viewing angle of about $\phi_m = 290°$. This appears to be near a critical condition as the second vortex pair was found to be absent in at least one repeat run. In the absence of forced oscillation the amplitudes of sting oscillation were considerable at this angle of attack, suggesting that oscillatory fluid/motion coupling could have determined the final flow separation topology. The asymmetry is accentuated and becomes a permanent feature as α is increased to 47° (Fig A4.2.6). The surface flow and cross flow topologies in Fig A4.2.7 show the formation of the second vortex pair.

In the presence of vortex asymmetry at elevated angles of attack the attached vortex moves inboard generating a downwash/sidewash field on the opposite side, energizing the LEX vortex. This can be seen in Fig A4.2.8, which shows the

LEX/wing junction region at $\alpha = 49°$. As a result of the vortex-induced downwash the starboard LEX vortex remains intact and the joined vortex system breaks down downstream of the LEX/wing junction. The sidewash is strongest when the inboard vortex is shed near the LEX as it is then close to the surface. Therefore, this flow mechanism is most effective in the α range where two vortex pairs are shed from the forebody.

At higher α the vortex burst has moved up to near the LEX apex on the side of the attached LEX so that the influence of the sidewash on the flow field diminishes. Similar flow structures were present upstream of the LEX at angles of attack up to 53° (see, for instance, Fig A4.2.9). The flow topology shown in Fig A4.2.7 was found to prevail at $46° \leq \alpha \leq 53°$ in the IAR experiments. The data at $\alpha = 53°$ are omitted for brevity.

The IAR results are confirmed by the IMFL oil flow visualization[3] on BWLVH (Model WG16A) at $U_\infty = 30$ m/s and $\alpha = 53°$ (Fig A4.2.10). Traces of the secondary vortex on the left hand side are not very clear, due possibly to the conditions of the oil. However, the secondary separation-line asymmetry is the same as that in Fig A4.2.11, which clearly shows the secondary vortex.

In all cases where adequate photographic records are available the surface flow results show how the crossflow separation asymmetry generates the vortex asymmetry. Without exception symmetric support systems were used, ruling out the possibility that support interference could have promoted the onset of vortex asymmetry at $\alpha = 41°$ in the IAR experiment. At $\alpha = 41°$ the skin friction pattern is clearly asymmetric along the full length of the forebody (Fig A4.2.4), consistent with the large side forces measured (Fig 3.10). At $\alpha = 47°$ and 51° the flow state depicted in Fig A4.2.7 prevails. The real crossflow asymmetry (pronounced three-dimensionality) appears with the formation of the second cell of separation and associated second upwind vortex on the aft forebody. Since the separation line curves up quite far downstream, the side force generated diminishes rapidly as α increases above about 45°. Note that the IMFL result in Fig A4.2.10 corresponds to the $\phi_m = 270°$ position in Fig A4.2.7, showing a straight separation line at $\phi_m > 270°$; the view from the opposite side was not available.

Forebody (Configuration with Trips)

IMFL flow visualization[3] on BWLVHT (model A) at $\alpha = 53°$ with oil (Fig A4.2.11) and with acenaphtene at $U_\infty = 30$ m/s (Fig A4.2.12) clearly show the relaminarization of the flow downstream of the boundary layer trips, and the subsequent laminar separation. At this angle of attack the flow over the forebody with trips produced the same final separation pattern as the clean forebody. This can be seen by comparing Fig A4.2.11 with A4.2.5. The traces of the secondary vortices associated with the second cell of separation, present in the α range spanned by the two figures, $46° \leq \alpha \leq 53°$, are in good agreement in the two cases.

Wing - LEX

At lower angles of attack the primary LEX and wing vortices are fully formed and separated by an attachment line (Fig A4.2.13a). As α is increased to about 19° the two co-rotating pairs of vortices start to merge near the trailing edge (Fig A4.2.13b). From the laser sheet results it appears that the interaction involves lateral merging of the wing and LEX vortices with coiling occurring before breakdown. Evidence of vortex breakdown can be seen at $\alpha = 20°$ (Ref. 2).

Figure A4.2.14 shows the skin-friction line topology of the wing and the laser sheet video image at a station near the wing apex, at $\alpha = 20°$. The joined LEX and wing leading edge vortices are seen to burst at the wing trailing edge. The effect of the chamfered edge is apparent at the wing tip, giving rise to a node of attachment (Fig A4.2.14b). Oil flow visualization results at higher α show the upstream progression of vortex burst with alpha[2].

Vortex breakdown on the LEX in the range $40° < \alpha < 53°$ is strongly controlled by forebody flow separation asymmetries, which in the static case are determined by micro-asymmetry and lateral support oscillation, as sideslip angle and support asymmetry are not a factor here. Depending on forebody flow asymmetries both intact and burst vortex conditions could be observed on the LEX in this range (see, for instance, Fig A4.2.8).

The oil surface flow pattern on the starboard wing and the off-body video image for section B-B at $\alpha = 39°$ is presented in Fig A4.2.15, showing the asymmetric forebody vortex pair and symmetric LEX vortices. The LEX vortex breakdown location is in the vicinity of the LEX/wing junction on this LEX/wing half.

Off-Surface Flow

The rotational flow fields of the baseline configuration BWLVH at $\alpha = 40°$ were analyzed using the AerMacchi and Eidetics water tunnel results presented in Ch. 4.3. Limited results for BWLVHS are also available but are not studied here. The crossflow structure is shown schematically with reference to sections near the nose tip, on the aft forebody and at a section downstream of the LEX apex (Figs A4.2.16 and A4.2.17).

The main flow features visible in the photographs in Figs 4.16, 4.17a, 4.21 and 4.22 show a near-symmetric vortex pair at A-A, development of a second vortex pair at B-B and various types of interactions with the LEX vortices at section C-C (see Figs A4.2.16 - A4.2.18). For the stationary model at $\alpha = 40°$ the entire flow field is essentially symmetrical in the absence of significant support or wall interference effects (Figs 4.16, 4.21 and 4.22). The differences between the locations of the vortices in the cross-flow plane as shown in Fig A4.2.16 are subtle when no change of state occurs (compare for instance Figs 4.21 and 4.22). However, the respective differences in the vortex interactions are clearly visible from the water tunnel results.

Laser sheet flow visualization was conducted at laminar conditions (Re_d = 0.2 x 10^6) in the IAR 2m x 3m low speed wind tunnel. At $\alpha = 39°$ the forebody vortices are asymmetric (Fig A4.2.15), in contrast to the water tunnel results. Force measurements revealed a side force asymmetry, even when the symmetric strut system was used[2] (Fig 5.29). The delay in crossflow asymmetry to $\alpha > 40°$ at the much lower Reynolds numbers of the water tunnel tests is consistent with flow visualization results on a 15°-half-angle cone-cylinder model[4] (for the WG16CA model $\theta_A = 14.25°$).

Returning to the water tunnel tests at $\alpha = 40°$, Fig A4.2.16 shows that in the presence of coning motion the flow field becomes asymmetrical with the formation of a second vortex beneath the lifted, upwind vortex, which is clearly visible in section C-C (Figs 4.21, 4.22 and 4.24). At C-C the inboard primary vortex interacts with the LEX vortex to a greater or lesser extent. Note that the positions of vortices obscured by the body are inferred, not observed. However, the second upwind vortex is always visible in Figs 4.21 - 4.24 and the positions of the inferred vortices are validated by the flow topology identity. A close inspection of the results at section C-C (inset in Figs A4.2.16 and A4.2.17) shows a larger vortex asymmetry in the absence of the conventional C-strut (Fig A4.2.16). As discussed in Section A4.3 and A4.4 it is the differential LEX upwash due to coning-induced changes in the effective leading edge sweep that produces the vortex asymmetry on the WG16 configuration. The conditions at Section A-A near the nose tip are difficult to discern from these flow visualizations but are included for completeness. Also, it is the asymmetry associated with the lifted upwind vortex that yields the aerodynamic damping moments characteristic of this configuration.

Various C-strut geometries were simulated in the AerMacchi tests. The tests performed with an extended sting support to simulate low-support-interference conditions (Fig 4.21) are essentially consistent with the standard C-strut configuration as used by AerMacchi (Fig 4.22) and Eidetics (Fig 4.16). See Fig A4.2.18. In these examples $b_c/w = 0.63$ (Fig 4.22) and $b_c/w = 0.51$ (Fig 4.16), where b_c is the span of the C-strut and w the minimum dimension of the test section. Previous analysis[5] has shown that unsteady wall interference will become significant when $b_c/w \geq 0.6$. Thus, the Eidetics results may be considered free of unsteady wall interference, while some effects may be present in the results shown in Fig 4.22. In the vertical orientation the tunnel dimension h = 1.5w, and such effects are not visible. In contrast, the larger C-strut used in Fig 4.24, which gives $b_c/w = 0.744$, shows evidence of both unsteady wall interference, manifested in the lack of mirror symmetry in clockwise and anticlockwise rotation, and static support interference seen in the asymmetric flow at $\Omega = 0$. Note again that the positions of vortices obscured by the body are inferred from the flow field analysis. The unsteady interference effect is evident in the time history of the flow field at $|\Omega b/2U_\infty| = 0.1$ (not always visible at the vertical position, where $b_c/h < b_c/w$ is the relevant parameter). For this reason this particular case cannot be further analyzed (see also, comments in Section A4.4).

The test simulating the top sting mount (Fig 4.23) shows clear evidence of support interference, which is probably the main source of interference as $b_c/w = 0.63$ and transition does not play a role. The structure of the vortex system is different for $\Omega b/2U_\infty = 0.1$ than for $\Omega b/2U_\infty = -0.1$ (Fig A4.2.17). Neither of the two cases agrees with the results in Fig A4.2.16, indicating that support interference is significant.

When α is increased to 50° (Fig 4.17) the flow field structure changes to that shown in Fig A4.2.18. For $\Omega \neq 0$ the second up-wind vortex crosses over in response to the sidewash generated by the leeward primary vortex. In this case, the photographic evidence was not very clear, and only the vortex locations at B-B could be discerned. The flow structure at C-C was deduced, in part, from the surface flow visualization data (Fig A4.2.5 - A4.2.11).

The analysis of the water tunnel results shows that the basic upwash-induced vortex asymmetry associated with BWLVH is not disrupted by support interference at very low Re_d. Only in the case of the strong unsteady wall interference of Fig 4.24 was there a tendency for the LEX/forebody interactions to depend on the direction of rotation. As a result the magnitude of the asymmetry is affected cyclically, but it is unlikely that a switch in the primary asymmetry could have taken place during the rotation cycle.

The flow field analysis of the baseline configuration is taken a step further in Section A4.4. Although a detailed analysis of the configurations with forebody strakes and trips could not be included in this report, their effects on the flow field are discussed in Sections A4.3 and A4.4.

A4.2.2 Rotary Experiments

Rationale. The key to the analysis of rotary experiments is an understanding of the fluid/motion coupling mechanisms involved, and in particular, how such flow mechanisms establish the prevailing ground facility interference, including dynamic support interference and unsteady wall interference. Progress has been made in the understanding of the underlying flow physics[5-10]. Some examples are given here to illustrate the concepts involved, while the detailed analysis appears in Section A4.4.

Ground facility interference in high-α experiments produces effects characterized by (a) strong interactions causing structural flow field changes and (b) weak interactions that do not involve a change in flow state[10]. The large effect of the former is naturally easier to detect, particularly when available flow field data are limited. However, the weak interactions can also have a significant effect. A factor complicating the identification of facility interference effects is the degree of symmetry of the support and tunnel walls. For instance, interference effects produced by an asymmetric support are readily revealed by asymmetry in aerodynamic characteristics that are expected to be symmetrical[9]. In contrast, a similar level of interference due to a symmetric support may not be apparent unless strong interactions are present, when the severity of the effects can be gauged on the basis of the propensity for the interference to change the flow state[10].

In the case of rotary balance experiments on configurations that do not have boundary layer trips, the circumstances are usually such that the interference effects can readily be identified. Although the rotary balance support, comprising a sting and C-strut, is geometrically symmetric, the rotational flow field causes the interference effects to be asymmetrical. Moreover, when wall interference is present it will be coupled with the support interference, irrespective of the test section geometry. Consequently, when the wall interference is unsteady, as in a rectangular test section, the effects on the model become unsteady even though the coning motion is steady[5]. As shown in Section A4.2.1 such effects can readily be detected in flow visualization results when strong interactions are present. The manifestations of facility interference in rotary balance force and moment characteristics at high α include (i) modification of the static offsets, (ii) appearance or modification of discontinuities associated with jump phenomena and (iii) introduction of asymmetry with respect to rotation direction.

In each of these manifestations it is the distortion of the free-flight aerodynamics that has to be extracted from the wind-tunnel determined characteristics. Since the free-flight characteristics are not known a priori, knowledge of the physics of both free-flight and facility interference mechanisms is necessary. The orbital platform technique[4,11] makes it possible to measure directly the essential sub-scale free-flight characteristics[5] at high α.

While similar considerations could, in principle, apply when boundary layer tripping devices are used, in practice a quantitative analysis of facility interference is not possible in the absence of highly detailed flow field information. Thus, in view of the difficulties in determining boundary layer characteristics when trips are present, the identification of the free-flight characteristics would at best be ambiguous.

Although the flow is stationary in nature in rotary experiments it is important to realize that the coning-induced displacement of the crossflow stagnation point strongly influences how boundary layer trips and nose strakes affect the rotary aerodynamics. The rotation of the flow stagnation point due to the coning-induced lateral velocity component at x is, for modest sideslip angles, $\beta < 20°$, determined as follows to within 6%

$$\phi_m \approx \tan^{-1}[2(x_{CG}/b - x/b)(\Omega b/2U_\infty)] \qquad \text{(A4.1)}$$

At the base of the ogival nose, $x = x_{CG}/4$, Eq. (A4.1) gives $\phi_m = 10°$ for $(\Omega b/2U_\infty) = 0.1$ and $\phi_m = 28°$ for $(\Omega b/2U_\infty) = 0.3$.

The problem is greatly simplified if the facility interference effects can be uncoupled from the free-flight high-α aerodynamics[10]. Again, this would require an approach such as the orbital platform technique (at present available in only one wind tunnel and one water tunnel), but since conventional rotary results only could be obtained in the WG16 programme more emphasis will be placed on the understanding of the flow physics of the configurations with trips, first in Section A4.3 and then in A4.4.

Support Interference. The direct effect of an obstacle positioned downstream of a model at high α was demonstrated in Hummel's classic experiment[12]. Vortex breakdown was promoted significantly in the presence of the obstacle. Another manifestation of such direct interference is found in asymmetry switching under conditions of asymmetric vortex shedding from a slender forebody[13]. The counterpart of this static support interference can be found in rotary balance experiments as illustrated in tests using alternative support geometries[14,15].

As in Hummel's experiment, it is the proximity of the obstacle presented by the support to the flow separation region that is a critical factor in determining the severity of the support interference. The ability of the obstacle to influence the forebody vortex system diminishes if located downstream of the breakdown region. Generalizing, it may be said that the ability of the support to cause significant interference depends on the presence of organized flow structures near the obstacle. When a top-mounted strut is used the obstruction is closest to the forebody and is often the dominant source of interference on forebody flow separation. However, there are cases where the basic C-strut remains most damaging, even in the presence of a dorsal dummy strut[5].

In a conventional rotary balance it may, however, not be possible to increase the distance to the C-strut to the point of negligible support interference, because of the increased bulkiness of the sting carrier needed to maintain adequate stiffness. The results for BWLVHT shown in Fig 3.46 demonstrate that the loads were essentially unchanged by the addition of an extension that moved the model 0.5m forward. That this cannot be interpreted to mean that the support interference was negligible is demonstrated by the discontinuity at $\Omega b/2V > 0.10$. The Ω-location of the discontinuity is not determined solely by support interference[6] but is also the result of the dependence of the trip effect on its location relative to the crossflow stagnation point, Eq. (A4.1), which will be discussed in Section A4.4.3.

This example illustrates how complex support interference can be in the presence of trips (see Sections A4.3 and A4.4). Similarly, for the body with trips at $\phi_t = \pm 40°$ large differences can be seen between the data obtained with the 60°-crank and 40°-crank stings at DRA (Figs 3.1 and 3.2, respectively). These results show that the opposite types of behaviour are possible with trips for relatively minor changes in support geometry.

In contrast, for a clean configuration the support interference mechanisms are quite straightforward. Figure 3.1 shows that at $\alpha = 50°$ the moving wall effect is large enough to overcome the support interference bias and switch the asymmetry, while at $\alpha = 40°$ the bias is large enough to prevent this from occurring at the rotation rates tested. Because the support interference mechanism is well understood the quantitative assessment of its impact is possible (see Section A4.4.2).

In the case of the complete configuration BWLVHST at $\alpha = 40°$ and $Re_d = 0.3 \times 10^6$, in the DRA 4m x 2.7m wind

tunnel the C_Y and C_n characteristics showed mildly destabilizing trends (Fig 3.50b), unlike their counterparts in the FFA tunnel, which were stabilizing outside the range $-0.05 \leq \Omega b/2U_\infty \leq 0.02$ (Fig 3.47). This result was unaffected by the change from 40° to 60° sting crank in the former case. The conclusion which may be drawn is that the facility interference for the C-strut with 40° carrier was as large as with the 60° carrier, while the model supports in the two facilities were sufficiently different that the results were quite dissimilar.

Unsteady Wall Interference. The main sources of unsteady wall interference in rotary tests at high α include vortex-wake/wall interference and the fluctuating pressure gradients due to unsteady separation in the diffuser or on the walls downstream of the support[5]. When the unsteady flow fields near the model, the tunnel walls, and around the support are coupled, the individual interference elements cannot be distinguished.

When the span b_c of the rotor arm or C-strut is large the trailing tip vortices will be the prime source of vortex-wake/wall interference. As the vortex trails move towards or away from a point on the wall, boundary-layer separation could occur on the wall or further downstream, in the diffuser, oscillating longitudinally while travelling in the direction of the rotation.

An example of this phenomenon is provided by tests conducted with the HIRM 2 model on the same apparatus in a 4 x 2.7m low-speed wind tunnel, and in a 2.4 x 1.8m transonic wind tunnel[15]. The analysis of Ref. 5 showed that, in addition to differences in turbulence levels, unsteady coupled support/wall interference could have been a factor in the latter facility, where $b_c/w = 0.6$, but not in the large tunnel, where $b_c/w = 0.4$ (w is the minimum test section dimension).

Such facility interference mechanisms may be complicated by static wall effects on the test section flow field. The longitudinal dynamic pressure gradient due to blockage effects of the rotary rig can have a significant effect on boundary layer transition, flow separation, and vortex breakdown[16]. Such effects cannot be corrected for but can be alleviated by adjusting the divergence/contraction of the walls. For instance, using a slight area contraction over the length of the open test section in the IMFL vertical wind tunnel, the blockage of the rig could be compensated for[17]. These effects could have significantly complicated the facility interference in one case, discussed in Ref. 36, where the necessary adjustment had not been made.

Unsteady wall interference in rotary tests is for practical purposes an insoluble problem because of the coupling with support interference. Its presence can be detected but not corrected for. This is not expected to be a problem in the WG16 wind tunnel tests where trips were not used.

It should be noted that the comparison of Model A versus Model B results does not yield information that isolates the effects of wall interference. For instance, in Figs 3.25 and 3.26 the major contributions to the discrepancies shown are from differences in support interference, while the possibility of a contribution due to coupling with unsteady wall interference is unlikely, as b_c/w was the same in the two cases.

A4.2.3 Oscillatory Experiments

It is generally recognized that the presence of support struts and stings can introduce appreciable interference in dynamic tests at high α[18]. Again, the problem is compounded when coupling occurs between support and wall interference[5,10]

As before, ground facility interference effects in oscillatory tests fall into the general categories of strong or weak interactions[10]. While evidence of the former can be found in flow visualization results the latter have to be inferred from flow field measurements[10,19]. When symmetric test installations are used at high α the effects might be significant, yet difficult to detect[9]. One exception is the case where vortex burst is promoted by adverse pressure gradients produced by the associated weak interactions. In contrast, the strong interactions associated with asymmetric support systems are explicitly manifested in changes in flow state, such as onset of vortex asymmetry or vortex branching. Where the expected symmetry of the aerodynamic characteristics with symmetric β deflections is not realized, strong and/or weak interactions could be indicated.

Support Interference. Three types of support have to be considered in the present analysis; symmetric and asymmetric aft sting/strut, and symmetric ventral strut supports. As already noted, the support interference problem is more difficult when the sting or strut offset is in the plane of total angle of attack[9].

The presence of ventral support mechanisms require attention as even small protuberances on the windward side of delta wings are known to produce significant interference. For instance, Lambourne et al[20] observed a profound effect of small protuberances on the vortex pattern of a 70 deg delta wing. A small protrusion on the bottom surface caused the leading-edge vortex to degenerate into a partial-span leading-edge vortex, while a new leading-edge vortex started to develop downstream of the protrusion.

When comparing the aerodynamic characteristics obtained for BWLVH on a ventral strut support at TPI with those measured on sting supports, differences are found in the pitching moment and pitch damping at medium and high α (see Chapter 6). The increased adversity of the pressure gradient results in earlier vortex breakdown for $20° < \alpha < 30°$ downstream of the rotation centre, resulting in a nose-up pitching moment increment (Fig A4.2.19 and 6.2.6). As α increases above $\alpha = 35°$, where the vortex breakdown has moved up to the wing apex, the downwash from the wing decreases and is further decreased by the upwash generated by the strut. The decreased lift on the horizontal tail yields $\Delta C_m > 0$. Because of the convective time lag this statically destabilizing increment results in a dynamically stabilizing pitch damping increment $\Delta C_{mq} < 0$ (Fig 6.3.3).

To investigate the effects of support asymmetry a non-structural image strut was installed in the IAR 2m x 3m wind tunnel (Fig 2.23). Figure A4.2.20 shows how the onset of unsteady side force is promoted by the presence of strut asymmetry to occur at $\alpha_{on} \approx 30°$ compared to $\alpha_{on} \geq 32°$ with the image strut in place. This tendency was found to be consistent throughout the present test series. In the region of incipient asymmetric vortex shedding the natural unsteadiness in the flow field gives way to the steady asymmetric vortex configuration corresponding to the flow field bias associated with the support asymmetry. Thus the random fluctuations in the time-averaged unsteady loads tend to return when the symmetric support is used. Derivatives obtained on the asymmetric support for BWLVH and BWVH show this trend clearly, following the envelope for maximum vortex asymmetry (see Fig 5.31). Similar behaviour is expected near $\alpha = 46°$ with the formation of the second forebody vortex pair (Section A4.2.1) but no pitch oscillation data on BWLVH are available with the asymmetric strut at $\alpha > 39°$.

Unsteady Wall Interference. The configuration with strakes is characterized by a delta-wing-like flow field (see Section A4.4.4). Wall interference on delta wing vortex burst can be significant.

The centrebody or fuselage generates an upwash at the leading edge that decreases with increasing downstream distance from the apex[21]; the resulting negative camber effect promotes vortex breakdown[22]. Weinberg[23] has shown that tunnel wall interference generates an upwash distribution along the leading edge that is of the opposite type, creating a positive camber effect. For b/w = 0.44, the induced upwash along the leading edge on a 70 deg delta wing was computed[23] to increase from 1.5 deg at the apex to 4.7 deg at the trailing edge. The induced camber effect delays vortex breakdown, the more the larger the ratio b/w is (Fig A4.2.21).

Pitching moment data obtained for BWLVHST at finite sideslip angles exhibit wall interference effects. In comparing the $\widetilde{C}_m$ data for oscillation in pitch and in yaw (Fig A4.2.22) it can be seen that there is a nose-down increment at $\beta \geq 0°$ and $\alpha > 40°$ in the former case. This is believed to be the result of unsteady wall interference, which is absent in yaw oscillation, where the distance of the nose to the wall is invariant. The wall interference results from the upwash at the nose strakes, which is determined by the ratio b/w and their proximity to the wall.

A4.2.4 Quantification of Support Interference

As noted in the Introduction a desirable objective is to quantify facility interference contributions in the experimental data to the extent that the free-flight high-α aerodynamics can be determined explicitly. For clean configurations this is a perfectly realistic objective provided that detailed parametric effects have been explored in the experiments, accompanied by comprehensive flow field investigation. The former type of data is not available from the WG16 test programme.

An approach involving far less effort would be to perform low interference experiments, for instance, using the orbital platform (or OPLEC) apparatus[4,5,11] (Fig A4.2.23) to determine the regions in the α–Ω space for which support and/or wall interference becomes severe[4].

By eliminating the need for using a top-mounted support and the associated C-strut structure, OPLEC eliminates the prime source of high-alpha support interference. OPLEC allows the use of a regular sting support up to 90 deg angles of attack. Tests on an ogive-cylinder body[24] have shown that at high angles of attack even a sting diameter equal to the body diameter causes no measurable interference effects. Thus, the sting support in Fig A4.2.23 causes no appreciable high-alpha support interference. OPLEC tests[4] of the cone-cylinder used in coning tests by Yoshinaga et al[25] gave the results shown in Fig A4.2.24. The figure exhibits the incremental effect of the C-strut support structure on the location of vortex breakdown in the form of a contour plot that shows $\Delta x_B/l = [(x_B)_{no\ support} - (x_B)_{support}]/l$, where l is the body length. It can be seen how for some combinations of coning rates and angles of attack the support has minimal interference, consistent with earlier observations for slender aircraft models[6].

The orbital platform approach can therefore give a quantitative measure of the type of support interference experienced in wind tunnel tests of an advanced aircraft model. A sophisticated orbital platform apparatus is currently in use in the IAR water tunnel for this purpose. In this case, the criteria for acceptable levels of support interference will be based primarily on the effects on the lateral-directional rate-dependent aerodynamic characteristics rather than on the effect on vortex breakdown, as in Fig A4.2.24. Equally important will be the opportunity to observe the unobstructed rotary flows in the wake of the aircraft model, which could improve the understanding of its free-flight high-α aerodynamics needed in the interpretation of the wind tunnel data.

In the case of oscillatory experiments the quantitative analysis of support and unsteady wall interference can be accomplished through diagnostic experiments employing alternative support structures/orientations and/or test section locations[5,10]. This approach has been followed in the WG16 programme and some of the results obtained are analyzed in Section A4.4.

A4.3 SCALING ISSUES

One of the problems that the test engineer faces when trying to simulate full-scale vehicle aerodynamics in a wind tunnel test is the fact that the test usually will be performed at Reynolds numbers far below those for the full-scale vehicle. The strong coupling existing between boundary layer transition and vehicle motion can cause the subscale test results to be very misleading. This is especially true in cases where flow separation occurs in combination with boundary layer transition[26]. If the flow physics are well understood it is sometimes possible to predict the full-scale vehicle dynamics through analytic extrapolation[27,28].

A4.3.1 Effects of Boundary Layer Trips.

It has long been common practice to use boundary layer trips on subscale models in the attempt to simulate full-scale flow conditions. This method has, however, very limited success in cases where the aerodynamic characteristics are dominated by the effects of separated flow, as in the present case of the WG-16 model.

The body-alone results in Fig 3.1 show that the measured rotary characteristics depend strongly on whether transition is free or fixed, and also upon the location of the grit strips. The huge difference between Fig 3.1 and Fig 3.2 in the strakes-off data at $\alpha = 40°$ with trips at $\phi_t = \pm 40°$ was caused by different sting crank angles, 60° versus 40°, respectively. The results for $\alpha = 40°$ in Fig 3.3 show that the use of trips changes the effect of the nose strakes, even changing the sign of the roll damping for the complete configuration BWLVHS. The fact that removing the trips for strakes-on had no effect on C_n but a large effect on C_Y in Fig 3.3 indicates that it is the flow conditions at the LEX, close to x_{CG}, that are affected by the presence of the trips.

The different effects of trips and/or strakes for positive and negative coning rates in Figs 3.1-3.5 reveal the existing strong coupling between the viscous flow conditions and the prevailing ground facility interference[6,9,26,29,30]. The extensive analysis leading to this conclusion is contained in Sections A4.4.2 and A4.4.3. Figure 3.3 shows that at $\alpha = 40°$ the presence of the trips influenced greatly the effect of strakes on C_Y for $\Omega b/2U_\infty > 0.1$, but did not affect C_n. This indicates that the forebody vortices have a significant effect on downstream wing and tail surfaces, as is verified by the C_l characteristics. This downstream effect of forebody vortices is, of course, likely to be subject to support interference effects. Figures 3.4 and 3.5 show that at $\alpha = 50°$ and 60°, where strakes-on prevented the development of the primary asymmetric flow separation at the nose tip, the (secondary) asymmetric flow separation aft of the strakes (Fig A4.2.5) still produced significant forebody side forces.

The simulation of turbulent crossflow conditions by the use of boundary layer transition trips is difficult even in the case of static tests. In dynamic tests it is much more difficult. Full simulation in dynamic tests with subscale models is only possible if the full-scale Reynolds number is simulated by the use of a pressurized test section or a cryogenic wind tunnel[26]. Of course, in the present case of interest the incident flow conditions are steady rather than unsteady, and one would think that the simulation problem could be solved. However, a careful analysis shows that this would be possible only if the large parameter space in the present tests were adequately populated.

For zero sideslip the rotation of the flow stagnation point due to the coning-induced lateral velocity component at x is given by Eq. (A4.1). For $\beta = 0$, $\sigma = 40°$ and $\Omega b/2U_\infty = 0.15$, Eq. (A4.1) gives $\phi_m = 19°$ at the nose tip, and $\phi_m = 10°$ at the LEX-apex. In the sketches of the crossflow geometries to be discussed shortly the value $\phi_m = 15°$ is used for the cross-section translating in the starboard direction. It corresponds to the crossflow geometry aft of the nose strakes for $\Omega b/2U_\infty = 0.1$.

Figure A4.3.1a illustrates how the body-alone crossflow characteristics would look for turbulent crossflow conditions. The moving wall effects in the stagnation region will cause the flow separation to be delayed on the advancing side and promoted on the receding side[26,31-33], generating a pro-spin force, as indicated in the figure. In the absence of moving wall effects the crossflow separation would be symmetric relative to the crossflow velocity vector at $\alpha < 2\theta_A$, and asymmetric at $\alpha > 2\theta_A$, with the direction of the resulting side force determined by nose microasymmetry[13]. At $\theta_A < \alpha < 2\theta_A$, the moving wall effect acts as the nose microasymmetry at $\alpha > 2\theta_A$, determining the direction of the side force. Figure A4.3.1b shows that a separation geometry exists for purely laminar flow conditions that is similar to that for turbulent flow conditions, also resulting in a pro-spin force, as has been demonstrated[25,34] (Fig A4.3.2). Experimental results for a fighter aircraft model[35] (Fig A4.3.3) showed that body-alone aerodynamics could in that case represent the essential high-alpha $C_n(\Omega)$ characteristics of the complete aircraft. However, the WG16 model has LEX surfaces extending all the way to the base of the slender forebody. As will be shown later, the LEX-induced upwash dominates over the moving wall effects, reversing the $C_n(\Omega)$ trend from being pro-coning to anti-coning. However, many of the existing aircraft, such as the F-14 with its flat-spin problem, discussed in Section A4.5, have geometries similar to that shown in Fig A4.3.3. Hence, it is still worthwhile to pursue the case in which the forebody crossflow asymmetry and associated vortex asymmetry is determined by the moving wall effects.

In contrast to the crossflow characteristics for a clean forebody illustrated in Fig A4.3.1, the trips at $\phi_t = \pm 40°$ will at subcritical flow conditions generate the crossflow characteristics shown in Fig A4.3.4a. On the advancing side the trip at $\phi_t = 40°$ is close to the stagnation point and there is a long run of favorable pressure gradient after the trip. This could result in relaminarization before flow separation. At $Re_d = 0.3 \times 10^6$ in Fig 3.1 to 3.3 this is likely to have occurred on the forward portion of the nose. In contrast, on the receding side the trip is farther away from the stagnation point and the trip could cause a transition to turbulent flow conditions before separation, resulting in a substantial delay of the crossflow separation compared to the other side. The end result would be the generation of an anti-spin force, as illustrated in Fig A4.3.4a. For the trips at $\phi_t = \pm 70°$ (Fig A4.3.4b), it is unlikely that relaminarization occurs on the advancing side. However, because of the closeness of the trip to the lateral meridian it will be difficult for turbulent flow separation characteristics to be established. It is possible that the trip could promote the laminar flow separation on the advancing side.

The detailed body-alone crossflow characteristics in Fig A4.3.4 depend on both the Reynolds number and the coning rate. Figure 3.1 shows that at $\alpha = 40$ and 50 deg discontinuous changes of $C_n(\Omega)$ take place at certain values of

the coning rate, indicating the possible existence of threshold values which the rate has to exceed before the flow geometries sketched in Fig A4.3.4 can result. The experimental results in Fig 5.2 show the grit strips to have very large effects on the static characteristics $C_N(\alpha)$, $C_Y(\alpha)$, $C_m(\alpha)$, and $C_n(\alpha)$, indicating that these characteristics could be very sensitive to sideslip. The existence of a ϕ_m threshold is discussed briefly in Section A4.4 and analyzed in detail in Ref. 36.

From the experimental results for body alone in Fig 3.1 for $\alpha = 40°$ it appears that both trip locations generated anti-spin forces at $\Omega b/2U_\infty < -0.05$, in agreement with the flow sketches in Figs A4.3.4a and b, respectively. The discontinuity at $\Omega b/2U_\infty > -0.05$, is produced by support interference. At $\alpha = 50°$ and $\alpha = 60°$ the additional asymmetric crossflow separation aft of the nose tip (Fig A4.2.5) complicates the flow picture, particularly as relaminarization is more likely to occur at these angles of attack.

Considering the lessons learned when attempting to influence asymmetric crossflow separation by the use of body trips in the case of static tests[13] it is expected that it would be very difficult to use tripping devices in the present tests. Even when they used distributed roughness, Hall and Banks[37] concluded that "The sectional side forces produced by the gritting patterns were 50% larger than the grit-free data. This overshoot in the gritted data is attributable to improper modeling, at low Reynolds number, of the vortex shedding near the apex that occurs at high Reynolds numbers." That "further work is necessary----" is a foregone conclusion. The greatest difficulty is to determine to what extent asymmetric boundary layer transition in the near-tip region affects the crossflow separation and associated vortex shedding[13]. The tests performed by Rao[38] with helical trips of relatively large diameter illustrate the difficulties involved (Fig A4.3.5). The trips were found to be effective in reducing the side force, but the usually effective straight trips were not. Whereas a nose strake generates its own crossflow separation and associated vortex geometry independently of the Reynolds number, the body trip acts only via its local action on the boundary layer over the forebody. Its location relative to the natural separation line is therefore crucial. The straight trip, located at the lateral meridian, is not effective at the critical flow conditions ($Re_d = 0.47 \times 10^6$) of Rao's test[38]. Instead of eliminating the side force it amplifies it, starting to generate it at a lower alpha and producing a side force of as large a magnitude as that measured without any trips (Fig A4.3.5). The sketches in Fig A4.3.6 illustrate how the helical trip might work to alleviate the separation-induced side force at critical flow conditions. Without a trip the critical flow conditions are expected to be as sketched in the left part of the figure. The middle part of the figure illustrates how the helical trip might work. Forward of section A-A it acts as a separation device, forcing separation to take place at the trip. However, at and behind section A-A it acts as a preseparation device[39]. In the present case it is not delaying separation but delaying boundary layer transition. The effective Reynolds number of the reattaching flow is lessened through the shortened approach length between reattachment and the lateral meridian, causing symmetric subcritical flow separation similar to that forward of section A-A.

The straight longitudinal trip in the right hand sketch of Fig A4.3.6 may have been ineffective because of the critical Reynolds number. The trip could reinforce the subcritical flow separation already established but may not be able to move the supercritical separation on the opposite side, as was the case for the helical trip, because the trip is not far enough upstream to affect transition. Its preseparation effect will instead be to strengthen the turbulent boundary layer, thereby delaying separation on this side. That is, the straight trip would, if anything, aggravate the separation asymmetry. Something similar happens also if the helical trips are inverted, rotated 180 deg (Fig A4.3.5). Truncating the helical trips did not decrease their effectiveness as much as decreasing the trip diameter from 3.18 mm to 1.59 mm. The variation of side force characteristics in Fig A4.3.5 gives ample warning that one should expect the grit strips on the WG16 model to have local tripping effects that will vary greatly along the length of the forebody. Adding this to the effects of coning rate, Reynolds number, wind tunnel turbulence, and ground facility interference one must realize how difficult it would have been to simulate high-Re characteristics in the test of the WG16 model.

Experimental results at $Re_d = 0.205 \times 10^6$ for the basic configuration without trips[40] (BC in Fig A4.3.7) show $C_n(\Omega)$ characteristics with anti-spin tendencies that increase with α; up through $\alpha = 30°$. At $\alpha = 40$ and 50 deg the data trend is reversed and also becomes very erratic (Note the changing ordinate scale between α s). That the anti-spin data trend is strongest at $\alpha = 30°$ is no surprise[41]. As $\theta_A = 14.25°$, the static asymmetry is expected to start at $\alpha > 28.5°$. Thus, at $\alpha > 30°$ the LEX-induced upwash has to overpower the static microasymmetry[13]. This explains the lessened C_n magnitude at $\alpha = 40°$ and 50°, as well as the erratic effect of the coning rate, at least at $\alpha = 40°$. At $\alpha = 50°$ the combined effect of support interference and microasymmetry initially dominates. The $|C_n|$ value agrees with the static results for $40° < \alpha < 60°$ in Fig A4.3.8. The discontinuity is likely to be the result of support interference.

A4.3.2 Laminar Test Results

The test Reynolds number, $Re_d = 0.205 \times 10^6$, would be expected to produce laminar crossflow conditions, especially when considering that this is the upper Re_d limit on the slender nose. Of course, tunnel turbulence could possibly cause crossflow conditions to become of the critical type even at this low Reynolds number. In that case the upstream moving wall effects would promote transition[26,31], resulting in the crossflow geometry sketched in Fig A4.3.9, producing anti-spin forces on the forebody, in agreement with the experimental results in Fig A4.3.7. The test[40] provides results that make it possible to

determine if the crossflow conditions were in or near the critical range. Ref. 13 shows conclusively that the experimental results for $U_\infty = 30$ m/s in Fig A4.3.7 were well below the critical range (see also, Section A4.4.1). Otherwise huge variations of the side force and yawing moment would have been observed in Fig A4.3.8 for the Reynolds number range tested[13]. The results in Fig A4.3.8 also illustrate the point made earlier that when $\alpha \geq 40°$ the effects of static microasymmetry become large.

The water tunnel flow visualization results at $\alpha = 40°$ in Fig 4.21a for BWLVH show the forebody vortices to be symmetric for $\Omega = 0$. In this case the Reynolds number is far below that for BWLVH in Fig A4.3.8. The Reynolds number difference could account for the delay of crossflow asymmetry to $\alpha > 40°$ in Fig 4.21a. Of course, the support interference is also different in the two cases. Figure 5.31 shows that a change from asymmetric to symmetric support structure through the addition of a dummy strut delayed the start of asymmetry by 5 deg. In Section A4.4 it is shown that the results in Fig 4.21a are consistent with those in Fig A4.3.8. It still remains to explain the anti-spin characteristics in Fig A4.3.7.

As the crossflow conditions in Fig A4.3.7 are laminar, the crossflow separation would be similar to that shown in Fig A4.3.1b, producing a pro-spin yawing moment. This is certainly true for body alone (Fig A4.3.2) and for a fighter aircraft model (Fig A4.3.3). Why, then, is the WG-16 model producing anti-spin $C_n(W)$ characteristics (Fig A4.3.7)? One difference between the aircraft geometries in Figs A4.3.3 and A4.3.7 is the presence of the LEXs on the WG-16 model. The wing rock observed in tests with another generic aircraft model[42] (Fig A4.3.10) was caused by moving wall effects generated by a rolling motion rather than coning[43]. Moving the wing forward to the base of the slender nose eliminated the wing rock existing for the wing in the aft position. It was suggested in Ref. 44 that the reason for this was that in the forward position the wing-induced upwash overpowered the moving wall effects, thereby eliminating the flow mechanism driving the wing rock. The question is whether the shaded LEX surfaces, added in the right hand sketch of Fig A4.3.10, would not have accomplished the same thing. Experimental results[2] indicate that this would indeed have been the case. The LEX surfaces delayed the occurrence of asymmetric crossflow from the expected value[13] $\alpha = 2\theta_A = 28.5°$ to $\alpha > 40°$.

Figure A4.3.11 illustrates the effect of the LEX-induced upwash on the forebody in the case of a coning motion. The coning rate generates a sideslip that decreases the effective leading-edge sweep of the LEX surfaces on the advancing side and increases it on the receding side[45]. This results in a stronger LEX-induced upwash on the advancing side than on the receding side, as indicated in Fig A4.3.11b. As a consequence of the dominance of the LEX-induced upwash over the moving wall effects, discussed earlier, the crossflow separation and associated vortex shedding on the slender forebody is affected as sketched in Fig A4.3.11. That is, instead of generating a pro-spin force as in the case of no LEX surfaces (Fig A4.3.11a), the LEX-induced upwash causes the crossflow separation to generate an anti-spin force on the forebody (Fig A4.3.11b). This probably requires that the coning-induced sideslip has to exceed a certain threshold value. The nose strakes eliminated this LEX-induced crossflow asymmetry, resulting in the measured large reduction in the magnitude of the anti-spin moment (Fig A4.3.7).

Combining the flow sketches in Fig A4.3.4a and A4.3.11b, one concludes that the effect of the trips would be to amplify the asymmetry of the crossflow separation and vortex shedding shown in Fig A4.3.11b. Thus, the measured $C_n(\Omega)$ trend in Fig 3.3 is in agreement with expectations. The zero-offset is probably an effect of support interference. Strakes eliminated the forebody flow asymmetry and, thereby, the non-zero $C_n(\Omega)$. However, the strakes had no such effect on $C_Y(\Omega)$ or $C_l(\Omega)$, indicating that downstream vortex interactions generate significant loads. Based upon the flow visualization in Fig 4.21, one obtains the picture of the forebody/LEX vortex interaction sketched in Fig A4.3.12, where the sidewash induced by the high, lifted-off forebody vortex causes the low, attached forebody vortex to move across laterally to interact with the LEX vortex on the opposite side. Apparently, the nose strakes could not eliminate forebody-LEX vortex interaction effects entirely, judging by the $C_Y(\Omega)$ and $C_l(\Omega)$ results in Fig 3.3.

A4.3.3 Trip Effects on Strake-on Characteristics

The use of the trips gave the crossflow separation geometry sketched in Fig A4.3.4, in sharp contrast to the one existing in full-scale flight (Fig A4.3.1a). Not using any trips at all would have given the crossflow geometry shown in Fig A4.3.1b, which is in qualitative agreement with the full-scale case in Fig A4.3.1a. At $\alpha > 46°$ one can expect this effect of the trips also for the strake-on configuration, because of the secondary asymmetric flow separation discussed earlier. For $\alpha < 46°$, the trips could affect the primary crossflow separation for strake-on to change the vortex geometry as shown in Fig A4.3.13. Figure A4.3.13a shows the expected full-scale flow geometry for turbulent flow conditions (the one for incident laminar flow conditions would be qualitatively similar). Figure A4.3.13b shows the crossflow geometry for incident laminar flow conditions. The adverse moving wall effect on the receding side reinforces the trip effect causing turbulent crossflow separation. On the advancing side the downstream moving wall effect facilitates relaminarization. That is, even at $\alpha < 46°$ the trips will not be able to provide full simulation of the full-scale crossflow conditions for the strake-on configuration. A similar situation will result also in the absence of strakes at moderately high angles of attack, $\theta_A < \alpha < 2\theta_A$ ($\theta_A = 14.25°$), when the forebody vortices are symmetric at $\Omega = 0$ (Ref. 13).

As Fig A4.3.13 indicates and the strake-on $C_n(\Omega)$ characteristics in Figs 3.3 and 3.21 confirm, the trip effect on the local forebody side force is probably insignificant. However, the difference in forebody vortex geometry will have

a significant effect on the $C_l(\Omega)$ characteristics through the forebody-LEX vortex interaction discussed earlier (Fig A4.3.12).

Because of the dominating effect of the upwash induced by the LEX on the adjacent slender nose, the consequences of the adverse trip effects are not as powerful as they would have been if the LEX surfaces had been located downstream of the nose, or had been absent, as in the case of the fighter configuration in Fig A4.3.3. However, Figs 3.17-3.20 show a large Re_d sensitivity of the $C_Y(\Omega)$ and $C_n(\Omega)$ characteristics even in the presence of the trips. When nose strakes are added (Fig 3.21), this Re_d sensitivity disappears for the $C_Y(\Omega)$ and $C_n(\Omega)$ characteristics. However, for the $C_l(\Omega)$ characteristics it becomes even stronger, demonstrating that to simulate Reynolds number effects by the use of boundary layer trips is not possible, even for the present case of steady rotations with fixed forebody flow separation. The large effect of trips on $C_m(\Omega)$ for strakes-on in Fig 3.3 illustrates the complexity of the flow physics.

The use of distributed roughness in lieu of boundary layer trips avoids the situation sketched in Fig A4.3.4b, where the trip may initiate the crossflow separation. However, simulation of full-scale flow conditions would require the circumferential roughness distributions in the forebody cross-sections to be changed every time the crossflow stagnation point moved in response to a change of the coning rate, as the correct roughness height varies with the local boundary layer thickness. It should be emphasized that neither trips nor distributed roughness can provide simulation of time-history effects, which to a large extent determine the aerodynamic characteristics of a manoeuvring aircraft. However, it should also be emphasized that the results obtained in the absence of trips (Fig A4.3.7) provide an approximation of the full-scale characteristics, offering the possibility to predict the full-scale characteristics through analytic extrapolation.

A4.3.4 Analytic Extrapolation to Full-Scale Characteristics

With a flow field as complex as that existing on the WG16 geometry at high angles of attack it is to be expected that to extract the full-scale vehicle dynamics from subscale tests is going to be difficult. The present analysis and past experience has led to the following conclusions.

Straightforward simulation of full-scale vehicle dynamics requires the subscale test to be performed at full-scale Reynolds numbers. Although test facilities exist in which the full-scale Reynolds number can be simulated, it will rarely be possible to perform the needed tests in such facilities; for the following reasons: a) the access to such facilities is very limited and b) they presently cannot perform dynamic tests of the nature discussed in this report. Consequently, a different approach is needed in most cases.

A practical means of obtaining the full-scale dynamic characteristics is through analytic extrapolation from subscale rotary test results. However, this requires a satisfactory understanding of the flow physics involved. The procedure is as follows:

1. Determine, based upon past experience, whether or not coupling between vehicle motion and boundary layer transition will play an important role in full-scale flight. If the answer is negative, and support interference is not a factor (eg. by the use of OPLEC[10,11]) one can proceed as follows:

A. Perform subscale rotary tests at subcritical Reynolds numbers and extrapolate analytically to full-scale vehicle dynamics.

2. If simulation of the coupling between vehicle motion and boundary layer transition is deemed important one should proceed in the following fashion:

a. Determine where on the full-scale configuration the important motion/transition coupling occurs. That region is likely to be located near the nose of the fuselage (or the leading edge of the wing). As this usually is only a small part of the overall vehicle, a relatively large scale partial model of the full-scale vehicle can often be built and tested in a pressurized wind tunnel at a high enough Reynolds number to provide substantial information about the transition/motion coupling.

b. Perform rotary tests with the partial model over the Reynolds number range.

c. Perform static tests of the partial model to extend the Reynolds number range.

d. Use the information gained in (a) - (c) to extrapolate analytically to the full-scale Reynolds number.

In all cases of complicated flow physics, as in the case of the WG16 model, it is important to start with flow visualization tests, such as used in the present analysis, and to proceed from there following the steps outlined above.

A4.4 INTERPRETATION OF WG16 HIGH-ALPHA AERODYNAMICS

From the preceding discussion it is clear that the primary concern in the analysis of the WG16 rotary data is the complexity of the interactions due to viscous-flow/motion coupling for the configurations with boundary layer trips, BWLVHT and BWLVHST. Such interactions are, of course, even more complex in oscillatory motions but the interpretation of the oscillatory data base as a whole is less of a problem owing to the greater availability of data on the baseline or "clean" configuration (BWLVH) in these experiments. In both cases, however, Sections A4.2 and A4.3 provide the basis for the analysis in this section.

The analysis in Section A4.3 shows that high-Reynolds number conditions cannot be simulated by means of trips. The complexity of the flow physics makes it clear that the results will be indeterminate unless highly detailed flow-field information is available, which is not the case here. In the absence of such information direct correlations of results for configurations with trips are not expected to contribute much to the understanding of the flow physics.

To advance the objectives of the WG16 programme a delimitation of the parameter space defining the data base is needed. However, analysis of the reduced data based on phenomenological considerations can potentially contribute to the understanding of high-α manoeuvring aerodynamics.

A4.4.1 Identification of Aerodynamic Parameters

The analysis of the high-α aerodynamics of the baseline or "clean" configuration BWLVH is relatively straightforward as the fluid dynamics processes are quite well understood. Here the key aerodynamic parameters are Re_d and the geometric parameters determining support interference and unsteady wall interference[7,10]. According to the discussion in Section A4.2, the latter source of interference is, in general, not a major concern in the BWLVH experiments. The remaining factors, Re_d and support interference, result in complex interactions as they are coupled, but do not present an insurmountable problem as has been shown previously[6,8,10].

In contrast, for the configurations with forebody trips BWLVHT and BWLVHST the wind-tunnel determined high-α aerodynamics are generally exceedingly complex[26] as the coupled fluid dynamics[46] mechanisms now include those due to Reynolds number and motion time history effects[47], support interference[8-12], unsteady wall interference[7] and boundary-layer/trip interactions[26,40].

Flow Conditions

At the nominal test conditions, $U_\infty = 30$ m/s, $Re_d = 0.20 \times 10^6$, the basic forebody exhibits laminar separation along its full length. The primary separation lines are located at ±87° for $\alpha = 39°$ and $\alpha = 41°$ (see Fig A4.2.3). In the IAR tests the conditions were just below the laminar/transitional boundary. This is true of the low-Re tests of model WG16A in most of the facilities concerned, while the low-Re WG16B tests at Eidetics were even further into the laminar regime, at $Re_d = 0.15 \times 10^6$ (Section 3.3). Figure A4.4.1 shows that as α increases the laminar/transitional boundary moves to higher Re_d (Ref. 48). At the higher Reynolds numbers $Re_d \geq 0.3 \times 10^6$, the separations were clearly transitional. Fully turbulent flow could not be achieved at the Reynolds numbers covered in the WG16 tests (see Fig A4.4.1).

Effects of roughness and freestream turbulence. It is well known that the effects of freestream turbulence on the drag characteristics of a circular cylinder are significant, shifting the Reynolds number critical behaviour in the direction of decreasing Re_d[49]. This complicates the comparison of results from different facilities[50] (Fig A4.4.2) even when the same model is used, and even more so when different models are used since the effects on drag measurements of turbulence and surface roughness are generally indistinguishable in this flow regime. In the presence of lateral motion the effects on the lateral-directional characteristics are expected to be larger. The problem of interfacility correlation is compounded in the dynamic case when coupling exists between boundary layer transition and vehicle motion[30,46].

For the facilities used in the present investigation significant effects of dissimilar turbulence levels can be expected (Fig A4.4.2). Thus, it is important to conduct a correlation of results at subcritical Reynolds numbers. In the present tests the agreement between IMFL and IAR surface flow visualization results at $Re_d = 0.2 \times 10^6$ obtained on BWLVH at $\alpha = 53°$ is encouraging as it shows that the combined effects of dissimilar turbulence levels, roughness and facility interference are not large in these two facilities at subcritical conditions.

Effects of boundary layer trips. The discussion of Section A4.3 shows that at the laminar/ transitional Reynolds numbers the effects of the trips are not straightforward. Static aerodynamic data on BWLVHST demonstrate a sensitivity to Re_d at $Re_d \leq 0.28 \times 10^6$; see, for instance, the IMFL C_n data at $45° < \alpha < 64°$ (Fig 4.1). From the results in Fig 3.9 for BWLVHST it is not possible to tell conclusively what type of separation the trips produced; only that the separation characteristics were different at the two Reynolds numbers. However, flow visualization results showed that the boundary layer trips were not effective in producing turbulent flow separation (Section A4.2.1). For instance, for BWLVHT at $\alpha = 53°$ (Fig A4.2.12) relaminarization occurred, resulting in a final laminar crossflow separation at $\phi_m \approx 85°$. Under such conditions the effect of local moving wall effects will likely be to prevent the laminar separation from occurring on the side away from the stagnation point (Fig A4.3.4a). The resulting flow asymmetry results in an antispin yawing moment, amplifying the LEX-induced damping trend at $|\Omega b/2U_\infty| > 0.1$ (Fig 3.9b).

In general, it would not be possible to match higher Reynolds number data in the critical range over a range of rotation rates. The effects of the trips is generally to shift the critical Reynolds number regime to a lower test Re_d but other scenarios are also possible. As a result of the trips, relaminarization, if present, will occur at higher Re. In this case the trend may be reversed. When the coning induced rotation of the stagnation point is large enough the trips are likely to act as a separation device near the tip[51], resulting in a radical switch in the separation asymmetry. The correlation in Ch. 4 was done for the highest Reynolds numbers available ($Re_d = 0.276 \times 10^6$ to 0.302×10^6), which are all in the critical range. The correlation at the higher Reynolds numbers is appropriate for BWLVHST, since for much of the α range ($\alpha \leq 45°$) the associated separations are supercritical, and an increase in Re_d would only serve to delay the angle of attack for onset of viscous interactions on the aft forebody. At higher α this holds only for low $\Omega b/2U_\infty$. On the other hand, for BWLVHT (Figs 4.11 to 4.14) the increase to higher Re_d in the

presence of trips drives the flow conditions alternatively further into the critical range or into the laminar range (Fig A4.3.4a). As a result the separations become more sensitive to sideslip/rate induced effects and facility interference effects.

Flow Conditions for Straked Forebody

Forebody strakes have a symmetrizing effect at $\alpha < 45°$. For BWLVHST at $\alpha > 30°$ this is due to a structural change to the entire flow field, in which the beneficial, stabilizing effect of the coning-induced LEX upwash associated with BWLVH is lost. At $\alpha = 39°$ the moving wall effect is all but eliminated (Fig 3.21) and no significant side forces are generated on the forebody. (Note that the ordinate scale is much smaller in Fig 3.9 than in Fig 3.21). This means that the viscous flow interactions on the aft forebody have relatively little effect until after the second cell of separation asymmetry with associated vortex pair[13] is formed, at, for instance, $\alpha = 51°$ (Fig 3.22).

At finite coning rates the induced sideslip angle at the nose tip given by Eq. A4.1 results in a flow separation geometry as before. The flow separation topology at $\Omega b/2U_\infty \geq 0.2$ is conceptualized in Fig A4.3.13b, showing that the side force generated by the straked section is in the same direction as that produced by the aft forebody (Fig A4.3.4). However, the former topology is not likely to change significantly with Reynolds number in the range studied at $\alpha = 39°$, explaining the Reynolds number insensitivity of C_n and C_Y in Fig 3.21.

On the other hand, the flow field on the wing is strongly affected by coupling with LEX vortices and breakdown characteristics which are dependent on the Reynolds number sensitive flow on the aft fuselage. Hence C_l is sensitive to Reynolds number (Fig 3.21) and to support interference. At $\alpha = 51°$ the LEX flow is even more sensitive to Re effects on the separation producing the second vortex pair, but now the wings are separated and the LEX effects can not produce much of a ΔC_l.

The strakes produce unwanted effects on crossflow separation. However, the effects of this sensitivity to β on the static aerodynamic characteristics are generally small. On the other hand, the sensitivity of BWLVHST to Reynolds number, coning-induced sideslip, and facility interference can be quite large under dynamic conditions as evidenced by the rotary data at $\alpha = 50°$ (Fig 4.9). Here the moving wall effect on the aft forebody is large enough to switch the vortex asymmetry at the transitional Reynolds number, overpowering the support interference effect. This flow mechanism is coupled with the influence of LEX-induced forebody flow asymmetry, controlling the development of the second vortex pair.

In the case of oscillatory motions the effects are already apparent at slightly lower angles of attack, $\alpha \approx 42°$ (Ref. 2). This is attributed to the effects of rate-induced camber.

Scaling and Time History Considerations. Dynamic data for models of different sizes can be correlated in the case of the clean configuration BWLVH. For configurations with boundary layer trips (BWLVHT and BWLVHST) at high α, however, the flow physics become very complicated, as was discussed in Section A4.3, and direct correlation of results from different facilities and/or different model sizes should not be attempted. If the test conditions traverse part of the critical Reynolds number range, changes in flow topology may occur within the $\bar{\Omega}$-range tested, greatly amplifying the effects of time history. When hysteresis is present, rotation directions should be consistent in the correlation of experimental results from different facilities.

Facility Interference. The starting point for correlating facility interference is the parameterization of support geometry and wall constraints. In the latter case the relevant parameters are b/w (or b/h) and b_c/w for oscillatory and rotary tests, respectively[5]. The key factor defining support interference in all dynamic tests is the location of the obstacle downstream of the primary flow separation on the forebody. To simplify the analysis the support dimensions are referred to the model measurement centre (Fig A4.4.3), which is typically located just downstream of the forebody-LEX interaction region. Accordingly, the salient parameters for a rotary rig are θ_s, R_c/L_n, $b_c/2L_n$ and R_s/L_n.

In general, support interference will increase with increasing θ_s and $b_c/2L_n$ and with decreasing R_c/L_n and R_s/L_n. When R_c/L_n is large θ_s may become the determining parameter. By way of illustration, two extreme examples of rotary rig test installations are top mounted stings, with $\theta_s \rightarrow 90°$, $R_s/L_n = 0$, and the orbital platform system, with $\theta_s \rightarrow 0$, $R_c/L_n \rightarrow \infty$ and $R_s/L_n \rightarrow \infty$ (Fig A4.4.4). Since only a small number of different test installations were used, consistent correlations are not possible for all of these parameters. Thus, it is necessary to determine which parameters are most important to match.

In this regard the rotary balances described in Ch. 2 generally follow one of two design philosophies. A relatively short, rigid sting and small sector typifies the AerMacchi, DRA and Eidetics apparatuses, while in the IMFL and FFA school of thought longer stings and larger sectors are used, with larger values of R_c/L_n. However, in the latter cases larger structures are required to provide the necessary rigidity. Thus, the resulting pressure gradients due to the C-strut are not too different for the two types of apparatus. Moreover, when top mounts are used the effect of the C-strut is secondary in both cases ($R_s = 0$) so that results from different top-mounted models can be correlated directly.

A4.4.2 Aerodynamics of Baseline Configuration

Body-Alone Aerodynamics

On the body alone (configuration B) coning at subcritical Reynolds numbers the moving wall effect acts on the boundary layer to create the crossflow separation asymmetry in Fig A4.3.1b, resulting in autorotative yawing moments[52]. At

critical Reynolds numbers the moving wall effect[31] will advance transition on the receding side of the coning body, delaying separation, with the reverse effect on the advancing side (Fig A4.3.9). The DRA results[53] obtained at $Re_d = 0.3 \times 10^6$ show the expected anti-coning moments through the range $30° \le \alpha \le 60°$ (Fig A4.4.5).

It is well known that the onset of steady asymmetric vortex shedding from a pointed slender body[13] appears at $\alpha > \alpha_{on} \approx 2\theta_A$ (θ_A = 14.25° for WG16 models), and with it the occurrence of static offsets in C_n and C_Y (at $\alpha > 30°$ in Fig A4.4.5). What is less obvious is how the presence of support interference modifies these characteristics in the critical Reynolds number region.

For the clean, pointed body in free flight at these conditions the moving wall effect on boundary layer transition is almost instantaneous when the rotation is initiated[52]. Consequently, the threshold coning rate $\bar{\Omega}_M$ at which the switch in the side force asymmetry occurs is vanishingly small, $\bar{\Omega}_M \to 0$. On the other hand, in the wind tunnel test the moving wall effect has to overcome the flow field bias due to the presence of the support before the switch to the opposite C_n branch can occur at a finite value of $\bar{\Omega}$. The separation asymmetry is initially set by the combined effect of microasymmetry and interference of the sting support and C-strut at $\Omega = 0$. At $\Omega \neq 0$ the switch will occur only when the asymmetry dictated by the moving wall effect is opposite to the static asymmetry, and of sufficient magnitude.

In Figure A4.4.5 at $\alpha = 50°$ the initial rotation direction was clockwise $\Omega > 0$ resulting in flow separation asymmetry in the same direction as the static asymmetry, with $\Delta C_n < 0$. After deceleration to $\Omega = 0$ the model was rotated in the negative Ω direction resulting in moving wall effects favoring the opposing asymmetry. However, the moving wall effects were able to overpower the support-induced flow field bias only after the threshold $\bar{\Omega}_s = -0.5$ was exceeded. At $\alpha = 40°$ the threshold, if it existed, lay outside the range tested $\bar{\Omega}_s \le -0.15$; ie. C_n vs $\bar{\Omega}$ remained on the branch set by static asymmetry. At $Re_d = 0.2 \times 10^6$ the maximum asymmetry for the clean body occurs at $\alpha = 47°$ (Fig 5.2). Judging by the BWLVH data (Fig 3.10) the C_n peak is quite broad, extending from $\alpha = 45°$ to 55° in the low transitional range. Therefore, the reason for the insensitivity of C_n to $\bar{\Omega}$ at $|\bar{\Omega}| < 0.05$ and $\alpha = 50°$ is that the maximum asymmetry has been established at that Reynolds number. Note that weak-interaction support interference could have influenced the characteristics at $|\bar{\Omega}| < |\bar{\Omega}_s|$. The support interference is of the strong interaction type at both $\alpha = 40°$ and 50°, causing structural changes in the flow field. At $\alpha = 60°$ the side force is reduced and with it the static offset, but the yaw damping is maintained at up to $|\bar{\Omega}| \approx 0.11$.

Baseline Configuration - Static Data

Static high-α tests on BWLVH were conducted at low-interference conditions on the IMFL PQR apparatus ($R_c/L_n \to \infty$). The results in Fig 3.10 show no significant sensitivity to Reynolds number in the transitional range, at $\alpha \ge 43°$. The good agreement between aerodynamic data at $Re_d = 0.17 \times 10^6$ and 0.21×10^6 ($Re_c = 0.545$ and 0.655×10^6) is to be expected as both conditions are in the subcritical range (see Section A4.4.1). The lower normal force and pitching moments at $Re_d = 0.28 \times 10^6$ (Section 3.3.1) associated with reduced vortex asymmetry in the transitional range was also observed in their time-averaged oscillatory counterparts, $\bar{C}_N$ and $\bar{C}_m$ (Ref. 2). The earlier onset of side force asymmetry at the transitional Reynolds number, $\alpha_{on} \approx 30°$ compared with $\approx 32°$ for the laminar case, is consistent with IAR symmetric-strut data[2].

In Fig 3.10 C_n appears to be roughly constant for $45° < \alpha < 55°$, whereas in the IAR tests there appears to be a distinct peak near $\alpha = 45°$. However, the data in Fig 3.10 do not give an absolute measure of the maximum asymmetric loads C_{nmax} and C_{Ymax} as the nose tip was not rotated in that experiment. Nevertheless, Fig 3.10 shows that large static side-force asymmetries are maintained in the range of steady asymmetric vortex shedding at subcritical conditions. Similar levels of C_n and C_Y are expected in the offsets in the rotary balance data at $\Omega = 0$.

Rotary Data at Subcritical Conditions

Rotary balance data obtained at IMFL for BWLVH at $\alpha = 40°$ and 50° are shown in Fig A4.4.6 and A4.4.7, respectively. At $\alpha = 40°$ the wind tunnel data ($Re_d = 0.2 \times 10^6$) could be compared with Eidetics water tunnel data at $Re_d = 2800$ (Fig A4.4.6). Large fluctuations in the wind tunnel data are not present in the water tunnel measurements, or for that matter, in AerMacchi data on BWLVH at higher Re_d. Possible reasons for the fluctuations include natural flow field unsteadiness, and the effect of sting oscillation on stability of the vortex system[54]. Such fluctuations can be detected only when the cut-off frequency of the flow-pass filtering is not too low, as in the IMFL tests (Section 2.7.2). Whatever the complete explanation might be this aspect of the IMFL results is particularly valuable as it illustrates the fluid dynamic instabilities under the conditions of the experiment.

Flow Field Unsteadiness

To understand the nature of the flow field unsteadiness a knowledge of the flow states that can occur within this $\alpha - \Omega b/2U_\infty - Re_d$ domain is required. Although it is recognized that flow field characteristics are Reynolds-number dependent in the laminar flow regime the vortical flow states

per se, at the low subcritical conditions of the water tunnel tests, are representative of the more prevalent states existing at higher $Re_d < Re_{dcrit}$, albeit at somewhat different values of α_{on} and ξ_{VB}. Analysis of the water tunnel flow visualization data in Section A4.2.1 revealed a variety of off-surface flow structures, that were corroborated by the surface flow topologies observed in the IAR and IMFL wind tunnels at $Re_d = 0.2 \times 10^6$.

The asymmetric vortex flow topology is shown in Fig A4.4.8. A topological fluid mechanics analysis of the data in Figs 4.21 and 4.17 gave the crossflow separation types represented by the corresponding vortex flow topologies shown in Figs A4.4.9 and A4.4.10, respectively. The prevailing flow states are denoted flow state "A", "B" and "C", respectively. State C is an evolved structure developed from B. Flow state A is associated with a one-cell side-force asymmetry, and B and C with a two-cell side-force asymmetry[13].

As noted in Section A4.1 the subcritical moving wall effect sets the asymmetry at the nose tip, but further downstream the asymmetry is reversed by the coning-rate-induced LEX upwash differential (see also, Section A4.3). For the low-interference case in Fig 4.21 ($R_c/L_n = 3.5$) section B-B in Fig A4.4.9 shows the presence of the second upwind vortex[2] formed under the influence of increased upwash on that side. The reduced upwash on the opposite side permits the interaction of the inboard body vortex with the downwind LEX vortex at C-C. In contrast, with the conventional C-strut in place, $R_c/L_n = 1.3$, the effect of the increased upwash from the upwind LEX was reduced and the second upwind body vortex was not observed (Fig 4.22). With the relatively larger upwash from the downwind LEX the forebody/LEX vortex interaction has not occurred at C-C (Fig A4.4.8).

At $\alpha = 40°$ the conditions are near the onset of the secondary separation cell and associated shedding of the secondary vortex pair, ie. $\alpha \approx \alpha_{on2}$, which becomes a permanent feature at $\alpha \approx 45°$ (Section A4.2). Thus, there is a tendency for the flow field to switch between the flow states in Figs A4.4.8 and A4.4.9 in the presence of ambient unsteadiness. An example of such flow field modulation is provided by the effects of unsteady wall interference associated with the tests in Fig 4.22 and 4.23 (b/w = 0.6 and 0.744), respectively. As noted in Section A4.2.1 periodic lifting and subsidence of the upwind vortex in synchronism with the change in roll angle between the symmetry planes of the C-strut and test section was observed. While these observations were not sufficiently well documented to justify a detailed analysis, it is clear that, as in the case of the support interference in Fig 4.22 and 4.16 that suppressed the onset of the second cell of separation, the modulation due to wall constraints was not sufficiently intense to change the orientation of the primary vortex asymmetry. That is, in all cases for which off-surface flow visualization results were available on the coning BWLVH configuration, at $|\Omega b/2U_\infty| = 0.1$ and 0.15, the LEX upwash effect dominated over the coupled moving wall and facility interference effects. However, this was not the case with the water-tunnel rotary balance data (Fig A4.4.6), which shows that C_n - ($\Omega b/2U_\infty$) remained on the upper branch. Thus, in this instance the threshold coning rate of the bifurcation was not encountered, $\bar{\Omega}_s > 0.15$. This could be attributed to possible small geometric differences between the test set-ups in the flow visualization and force balance measurements.

For BWLVH the peak static side force is generated at near $\alpha = 41°$ (Fig 3.10). The side force diminishes rapidly as α is increased, accompanying the onset of the second asymmetric separation cell and vortex pair. On the other hand, the maximum C_n is maintained at up to $\alpha \approx 55°$. This is the expected data trend for multi-cell asymmetric crossflow separation and vortex shedding[13] as has been demonstrated[55]. The vortex asymmetry is accentuated by the new flow structure (Fig A4.4.9). This region of incipient secondary vortex shedding is accompanied by considerable unsteadiness generated by the fluctuation of the asymmetric separation and vortex structure between the two stable states. As α is increased the second separation cell will spend progressively more time in residence until, at near $\alpha \approx 45°$, it becomes a permanent feature. The time-averaged loads show a continuous drop in side force generated by the forebody at $\alpha > 41°$ (Fig 3.10). Thus, at $Re_d = 0.2 \times 10^6$ the single-cell side force asymmetry peaks at near $\alpha = 41°$, indicating that the bistable condition prevailing at static conditions in the range $\alpha_{on} \le \alpha \le 41°$ is the primary flow separation asymmetry (Fig A4.4.8). On the other hand, the coning test results discussed above and in Section A4.2 demonstrate that in the presence of coupled coning-induced and support interference effects the bistable condition associated with the two-cell asymmetry exists. The unsteadiness associated with the jump to the opposing orientation of the secondary asymmetric vortex system can be seen near the threshold condition $\bar{\Omega}_s \approx -0.02$ (Fig A4.4.6). Once the switch has occurred the unsteadiness due to the incipient secondary vortex asymmetry reappears.

General unsteadiness initially persists but then diminishes as the angle of attack is increased to $\alpha = 50°$ (Fig A4.4.7). At this point a further change in the flow structure has taken place, wherein the inboard upwind vortex has crossed over under the influence of the sidewash generated by the inboard primary vortex. The flow topology shown in Fig A4.4.10 was deduced from observations in Figs 4.17, A4.2.5 and A4.2.6. Direct interaction of the primary, inboard and LEX vortices was observed at C-C. Unlike the case at $\alpha = 40°$ there is only one set of bistable states at $\alpha = 50°$, resulting in relatively steady lateral-directional characteristics at low rotation rates.

That the fluctuations in Fig A4.4.6 and A4.4.7 are not simply due to random experimental error but signal discrete jumps between bistable flow states can be appreciated when it is noted that the peak values of the C_n and C_Y fluctuations correspond to the associated asymmetric loads. Thus, at $\alpha = 40°$, for instance, (Fig A4.4.6) the highest of the two limiting envelopes intersects the $\Omega = 0$ axis at a point which is in agreement with the maximum static offset.

Lateral Directional Characteristics ($\Omega = 0$)

The maximum side force is generated by the crossflow separation resulting in the primary vortex asymmetry depicted in Fig A4.4.8. With the onset of the secondary asymmetric separation cell the side force is reduced due to associated increased suction on the windward side (Fig A4.4.9) in spite of the leeward vortex interaction. In the static test at $Re_d = 0.2 \times 10^6$, $\alpha_{on2} \geq 42°$, a sharp drop in side force occurred with increasing α. On the other hand, the peak C_n is maintained as the contribution to C_n of the second vortex pair, closer to the CG, is small. In the water tunnel the secondary vortex asymmetry was not observed under static conditions, ie. $\alpha_{on2} > 40°$.

Figure A4.3.8 shows nearly discontinuous increases in C_Y and C_n near $\alpha = 40°$ until the side force levels off at $C_{Ymax} = -0.26$ at $\alpha \approx 41°$ and the yawing moment at $C_{nmax} = -0.15$ at $\alpha \approx 44°$. This is accompanied by significant flow unsteadiness. With the onset of the secondary cell of separation, with its flow separation asymmetry in the opposite direction to that of the primary cell[13], the total forebody side force rapidly diminishes as α is increased. In the wind tunnel coning tests at $\Omega = 0$ the C_n and C_Y offsets are in agreement with the PQR static tests although slightly lower in magnitude (C_n = -0.0615 vs -0.064 and C_Y = -0.1821 vs -0.1964, respectively). This suggests that the onset of the secondary cell of separation is promoted in the presence of the adverse pressure gradient associated with the Tournebroche C-strut, causing the flow field to spend progressively more time in flow state B. The existence of this tendency is substantiated by the water tunnel flow visualization results which demonstrate the presence of the second upwind vortex associated with the second cell separation.

In the water tunnel the support interference was large enough to prevent the switch to the negative branch at $\Omega > 0$, but the time-averaged C_n was consistent with the wind tunnel data at $\Omega < 0$, ie. close to the mean level between the limiting envelopes (see previous section). The discrepancy between the C_l - $\Omega b/2U_\infty$ data in the two cases (Fig A4.4.6) may be attributed to the delay in LEX vortex burst in the water tunnel relative to the wind-tunnel case at higher Re_d.

Rotary/Oscillatory Analysis

The combination of rotary and oscillatory data[56,57] through the Tobak-Schiff model[58] facilitates the interpretation of the dynamic test results[15]. Thus, formulated in the body axes system[58] and expressed in terms of aircraft motion variables[59], α, β, and $V = U_\infty$, for linear motion-rate dependence, the aerodynamic coefficient expansion becomes,

$$C_k(t) = C_k(\infty;\alpha,\beta) + \tfrac{1}{\gamma}\tfrac{pl}{V}C_{k\dot{\phi}}(\infty,\alpha,\beta) + \left(\dot{\alpha} - \dot{\beta}\tan\alpha\tan\beta\right)\tfrac{l}{V}C^*_{kq}(\alpha,\beta) - \tfrac{1}{\cos\alpha}\tfrac{\dot{\beta}l}{V}C^*_{kr}(\alpha,\beta); \qquad \text{(A4.2)}$$

where

$$\begin{aligned} C^*_{kp} &= C_{kp} + C_{k\dot{\beta}}\sin\alpha - C_{k\dot{\alpha}}\cos\alpha\tan\beta \\ C^*_{kr} &= C_{kr} - C_{k\dot{\beta}}\cos\alpha - C_{k\dot{\alpha}}\sin\alpha\tan\beta \\ C^*_{kq} &= C_{kq} + C_{k\dot{\alpha}}; \qquad k = X, Y, Z, l, m, n \end{aligned} \qquad \text{(A4.3)}$$

Linking the reactions in the aerodynamic and body-axes systems[58] yields an identity written here in the composite derivative notation[59] (Eq. (A4.3)), where $\gamma = \cos\sigma$ and $\delta = \sin\sigma$,

$$C_{n\dot{\phi}} - \gamma\left(C^*_{np}\cos\hat{\phi} + C^*_{mp}\sin\hat{\phi}\right) = \delta\left(C^*_{nr} + C^*_{mq} - \hat{C}_{m\dot{\sigma}}\right) \qquad \text{(A4.4)}$$

Expressed in body axes, for $\beta = 0$ Eq. (A4.4) reduces to[59]

$$C_{n\dot{\phi}} = \delta C^*_{nr} + \gamma C^*_{np} \qquad \text{(A4.5)}$$

The available yaw damping data for BWLVH at $Re_d = 0.2 \times 10^6$ appear in Fig 6.3.39. The IAR data for BWLVHA (or BC-A) (Fig A4.4.11) have the characteristics of a directional derivative[56,59] as the orientation of the primary vortex asymmetry (if not the secondary separation) is set by the nose tip asymmetry[2]. These data were obtained on the asymmetric strut system. For consistency, the C^*_{np} data should also have been determined in the absence of a downstream symmetric strut. Accordingly, the TPI data (Fig 6.3.31) measured on a ventral strut at $\beta = 0$ were used. The oscillation frequencies differed in the IAR and TPI tests (5 vs 2.5 Hz, respectively) but this is not a concern as the locally-linear aerodynamics are being evaluated.

The derivative $C_{n\dot{\phi}}$ given by Eq. (A4.5) is shown in Fig A4.4.11 together with the measured and interpolated oscillatory derivatives. Since C^*_{np} and C^*_{nr} are only weakly dependent on the forebody flow separation asymmetry at $\alpha > \alpha_{on}$, and C^*_{nr} is a quasi-directional derivative, $C_{n\dot{\phi}}$ provides a measure of the C-strut-interference-free damping due to coning rate at $\Omega = 0$. In the case of the Standard Dynamics Model (SDM)[60] the analysis gave good results at $\alpha \leq 20°$ and qualitative agreement between the rotary and oscillatory terms at $20° \leq \alpha \leq 30°$ (Ref. 57). However, for WG16A the uncertainty in C^*_{np} seems larger than that in the SDM data base. Nevertheless, the analysis is expected to provide qualitatively representative results in the absence of bifurcation at $\Omega = 0$ and at high α, $\alpha \geq 35°$, where the coning and yaw-oscillation characteristic motions are geometrically similar[59].

At $\alpha = 30°$ Eq. (A4.5) yields $C_{n\dot{\phi}} = 0.2$, compared with $\partial C_n/\partial(\Omega b/2U_\infty) \approx 0.4$ at $\Omega = 0$ for the IMFL data[40]. The discrepancy is not surprising considering the nonlinearity associated with the onset of asymmetric forebody vortex shedding. What is more interesting is the predicted loss of damping in the range $35° \leq \alpha \leq 45°$, consistent with the wind tunnel data in Fig A4.4.6. This confirms that at $\alpha = 40°$ C_n is relatively insensitive to both α and $\Omega b/2U_\infty$ when $|\Omega| \to 0$. At $\alpha = 50°$ the damping given by Eq. (A4.5) increases to $C_{n\dot{\phi}} = 0.32$, again consistent with the results in Fig A4.4.7.

Static and Dynamic Support Interference

The larger side force and yawing moment measured on the PQR apparatus at $\alpha = 44°$ (Fig 3.10), $C_{nmax} = -0.15$, is evidence of the existence of flow state A (Fig A4.4.8), which produces the maximum side force associated with the single cell topology. In this case the support interference is very low, deriving from the sting alone[18] (Fig 2.26), and the direction is set by the nose microasymmetry. In contrast, in static measurements on rotary balances the initial direction is determined by the combined effect of microasymmetry and support asymmetry. The somewhat smaller C_n offsets obtained on the C-strut at $\Omega = 0$ are associated with the two-cell structure of the alternative flow state B (Fig A4.4.9), where the second vortex pair has appeared together with the downwind LEX/primary vortex interaction. This effect, due to the combination of wake deflection and adverse pressure gradient produced by the C-strut, is present in both the IMFL and EI data (Fig A4.4.6).

The severity of the support interference is measured in terms of its capacity for changing the flow state. For the clean configuration coning at subcritical Re_d the switch in asymmetry should occur at a small rotation rate determined by the motion, through the coning-induced LEX upwash differential. This is an example of interference of the strong interaction type[10] (Section A4.2). Weak interactions would be produced by the C-strut induced pressure gradients when, at the prevailing motion conditions Ω, $\dot{\Omega}$ the vortex system resides in the preferred orientation relative to the plane of the symmetric support. The sting or C-strut interference competes with the LEX upwash differential to switch the asymmetry of the vortex system.

From Figs A4.4.6 and A4.4.7 it is clear that strong interaction interference is present in both the wind tunnel and water tunnel data, albeit different in the two cases. The effect of the motion variables Ω and $\dot{\Omega}$ on the support interference is considered next in the interpretation of the rotary aerodynamics.

Interpretation of Subcritical Rotary Data

As noted in the preceding paragraphs the available flow field data at $\alpha = 40°$ (Figs A4.2.16 and A4.2.17) have shown that flow state A cannot exist near $\Omega = 0$ in the presence of a C-strut. At the onset of asymmetry the flow state goes directly from the symmetric configuration to flow state B. In the presence of a dorsal sting the symmetric condition is not possible and the flow state changes from an asymmetric single-pair system to an asymmetric two-pair system (Fig A4.2.17).

Confining the discussion to aft-sting systems it is, therefore, known that in the absence of significant C-strut interference state A will prevail and B cannot occur in a stable configuration. Conversely, when C-strut interference is present, the reverse is true. States A and B generate the higher and lower limits in the maximum side force on the forebody at static conditions. That the maximum side force occurred in Fig 3.10 is confirmed by the value $\tilde{C}_{n\max} = 1.5$ obtained for the time-averaged oscillatory coefficient by rotating the nose tip[2]. In this case, however, the oscillatory moving wall effects delayed the peak asymmetry to near $\alpha = 45°$.

Since the forebody side force maxima and, therefore, C_n maxima are identified with the two flow states, and the slope of the $C_n - \Omega b/2U_\infty$ characteristics at $\Omega = 0$ in the absence of C-strut interference is available from Eq. (A4.5), the idealized rotary characteristics of the clean configuration at $\alpha = 40°$ can be constructed as shown in Fig A4.4.12. The measured static data and their mirror image values are denoted by solid and open symbols, respectively. The upper and lower C_n branches are represented by dashed and dot-dashed lines, respectively, as determined by the static offsets and slope of the dynamic characteristic.

As already noted, the initial orientation of the flow separation asymmetry is set by the combined effect of microasymmetry and support-induced flow asymmetry. Thus, the vortex system is in the preferred condition at $\Omega = 0$. In the IMFL wind tunnel rotary test[40] the initial rotation direction is clockwise, $\Omega > 0$, $\dot{\Omega} > 0$ (see point $\left(\vec{1}\right)$ in Fig A4.4.12). In this condition the coning-induced LEX upwash differential reinforces the asymmetry. The threshold rotation rate $\bar{\Omega}_A$ has to be exceeded before state A can be reached from B. Owing to the sparseness of the data available it is not possible to determine the threshold rate precisely but for the purposes of this analysis it is sufficient to identify $\bar{\Omega}_A$ with the first measured occurrence of the upper state, namely $\bar{\Omega}_A \approx 0.035$. At $\bar{\Omega} \geq \bar{\Omega}_A$ both states are possible, explaining the fluctuations between the upper and lower limits seen in the measured data. The level recorded in the rotary balance measurements is determined by the time spent proportionately with the separation asymmetry corresponding to the vortex system in states A and B, respectively. Thus, the actual values recorded would be a strong function of the data sampling rate.

As the rotation rate is reduced to zero $\dot{\bar{\Omega}} < 0$ $\left(\overleftarrow{3}\right)$ the vortex system returns to state B and C_n remains on the lower branch, passing through the static condition. There is some difference between the $\Omega = 0$ values reached from $\dot{\bar{\Omega}} < 0$ as compared with $\Omega = 0$, attributed to time history effects. When the direction of rotation is reversed $\Omega < 0$, $\dot{\Omega} < 0$ $\left(\overleftarrow{4}\right)$, the upwash differential is reversed, but the separation asymmetry is not immediately reversed. The coning-induced effect has first to overpower the bias due to support interference. According to Fig A4.4.6 the switch to condition $\overleftarrow{5}$ occurs in the range $-0.04 \leq \bar{\Omega} \leq -0.21$. It appears that the switch to state A will occur only after the lower level B has been reached, $|\bar{\Omega}_A| > |\bar{\Omega}_B|$. Thus, it is reasonable to assume that $\bar{\Omega}_A = -0.04$ as indicated in Fig A4.4.12. The threshold rate for transition to state A at $\Omega < 0$ is denoted $\bar{\Omega}_{A^-}$. When this threshold has been exceeded $\left(\overleftarrow{6}\right)$, $\bar{\Omega} < \bar{\Omega}_{A^-}$, both states are again possible and the fluctuations in C_n are similar to those at $\Omega > \bar{\Omega}_{A^+}$. In general, the opposing threshold rates are expected to be slightly different, $|\bar{\Omega}_{A^+}| \neq |\bar{\Omega}_{A^-}|$, because of the

support interference bias. The important point is that the switch in asymmetry occurs in the state B domain so that $\bar{\Omega}_s = \bar{\Omega}_B$.

A similar switch in asymmetry does not occur in the EI water tunnel data, at least not in the $\bar{\Omega}$ range tested (Fig A4.4.13). The data acquisition procedure was quite different in this case. The rotation direction was alternated, starting with maximum negative rotation rate, in the order of decreasing $|\bar{\Omega}|$. Thus, the initial direction was anti-clockwise $\overleftarrow{1}$, during which the data at maximum negative rate were recorded. As before, the offset was in the preferred direction reinforced by the coning-induced upwash effect. However, when rotating to maximum positive rate to record the second data point $\vec{2}$ the threshold rate for asymmetry switching was not reached, $\bar{\Omega}_s > \bar{\Omega}_{max}$. Thus, at $R_c/L_n = 1.32$ the differential LEX upwash effect was unable to overpower the support interference effect in this $\bar{\Omega}$ range. At $\bar{\Omega}_{B^+} \geq 0.1$ flow state B^- (state B at $\Omega < 0$) appears to occur intermittently. The apparent slope of the $C_n - \bar{\Omega}$ characteristic measured was larger than that in the wind tunnel data. This could possibly be a consequence of the time in residence in state A increasing proportionately with increasing $|\bar{\Omega}|$. The results in Fig A4.4.13 suggest that at $\bar{\Omega} = -0.15$ the support interference has decreased sufficiently that flow state A can prevail. This is consistent with the findings of Ref. 8. Nevertheless, the levels of C_n recorded at $\Omega < 0$ in the water tunnel experiment, determined as a time average at a lower sampling rate, are qualitatively in agreement with the mean levels of the wind tunnel data.

At $\alpha = 50°$ only one flow topology was observed in the water tunnel experiment (Fig A4.2.18), referred to as state C (Fig A4.4.10). Using the static offset from the IMFL test and slope at $\Omega = 0$ from Eq. (A4.5), the idealized characteristic matches the rotary data well for $\bar{\Omega} \leq 0.05$ when the threshold is assumed to exist at $\bar{\Omega}_s = -0.05$ (see Fig A4.4.14). The damping generated in the evolved state C is larger than that in state B (Fig A4.4.11) owing to the constriction of the downwind vortex interaction (Fig A4.4.10). In this case there is only one threshold coning rate $\bar{\Omega}_s = \bar{\Omega}_{c^-}$. As expected, the static offset is in the same direction as that at $\alpha = 40°$ so that the coning-induced upwash effect again reinforces the asymmetry. However, at higher coning rates $\bar{\Omega} > 0.05$ the rotary balance data depart from the idealized characteristic, indicating that a bifurcation has occurred. This is associated with another flow state change which cannot be analyzed for lack of supporting flow field data. However, the destabilizing tendency at $\bar{\Omega} > 0.05$ may be tentatively attributed to the reduced LEX induced upwash on the upwind side due to LEX vortex burst moving towards the apex. While the leading edge sweep differential increases with increasing coning rate (Section A4.3.2) the sidewash associated with the second cell of separation increases in strength, delaying vortex burst on the leeward side and promoting it on the windward side (see Fig A4.2.8). As the movement of vortex burst towards the apex on the windward side is accelerated the upwash effect weakens and the moving wall effect increases in strength, producing the undamping tendency seen at $\bar{\Omega} > \bar{\Omega}_m \approx 0.045$ in Fig A4.4.14. Finally, when vortex burst reaches the apex the lift on the windward LEX is wiped out (see Section A4.4.4).

Free-Flight Aerodynamics

Having reached an understanding of the aerodynamics of the baseline configuration in rotary and oscillatory experiments an interpretation of the free-flight aerodynamics is possible. Because of the dominance of the LEX upwash effect a single fluid mechanics mechanism governs the forebody/LEX flow separation asymmetry in the absence of facility interference. This means that the threshold for asymmetry switching $\bar{\Omega}_s$ will be determined by flow-field inertia, or the resistance to change of flow state. Thus, when the differential upwash is reversed through a change in yaw direction, $\bar{\Omega}_s \rightarrow 0$, the switch in asymmetry will occur after a time Δt determined by the convective flow-field time lag.

The progressive changes in flow state will generally occur at higher α in the absence of support interference and could be further delayed or promoted by motion coupling. The key point is that the jump phenomena can often be captured in the wind tunnel simulations but will not occur at the correct motion conditions when appreciable facility interference is present. However, if the threshold rates $\bar{\Omega}_s$ and $\bar{\Omega}_m$ in free flight can be identified and the facility dependent thresholds $\bar{\Omega}_A, \bar{\Omega}_B$ and $\bar{\Omega}_c$ are understood, the wind tunnel data become useful. The application to full-scale free flight is discussed in more detail in Section A4.5.

A4.4.3 Extension to Complex Configurations

The approach to the analysis of rotary experiments introduced in Section A4.4.2 is being extended to the WG16 configurations having boundary layer trips and/or forebody strakes. This study is not included in the present report and will appear in a separate publication[36]. A few general comments are made here to outline the direction which has to be taken.

As noted on several occasions, the analysis of the rotary aerodynamic data base on configurations such as BWLVHT and BWLVHST becomes possible only in the event that the implied parameter space is comprehensively populated. In the WG16 programme the data base is adequate in some respects but in others the information needed is not available. This increases the reliance on phenomenological modelling and diminishes the conclusiveness of the results. Notwithstanding this situation, considerable progress can be made by virtue of a redeeming aspect of the aerodynamics of the WG16 configuration.

The dominance of the coning-induced differential LEX upwash over the viscous fluid/motion coupling on the forebody has the effect of structuring the rotary flow field and reducing the sensitivity to Reynolds number in the region of incident subcritical to critical flow. The resulting dynamically stable behaviour over much of the high-α domain is characteristic of a class of LEX-dominated aircraft. However, nothing could be further from the truth in the case of forebody dominated configurations (eg. Fig A4.3.3), which is characterized by coning-induced moving wall effects that are damped only in the critical range. When aerodynamic jump phenomena are governed by viscous fluid/motion coupling the

chances of successfully implementing the type of analysis expounded in Section A4.4.2 would be rather slim.

In spite of the additional complexity introduced by wind tunnel facility interference it could be shown that for the clean configuration, the observed behaviour is not completely random, being governed by definitive physical mechanisms in the free-flight case. For the configuration with trips BWLVHT the aerodynamics are far more complex but can still be reduced to coning-rate-threshold dependent behaviour. The main difference is that instead of three thresholds, $\bar{\Omega}_s, \bar{\Omega}_A$ and $\bar{\Omega}_B$, there are then twice that number. The definitions of the trip-induced threshold rates follows from the considerations of Sections A4.3, A4.4.1, and A4.4.2.

Extraction of Subscale Free-Flight Aerodynamics

In Section A4.3 it is concluded that full-scale flight characteristics cannot be simulated by means of boundary layer trips. A more immediate question posed in this section is whether or not the rotary balance measurements can reveal the free-flight characteristics of a configuration incorporating forebody roughness elements. More specifically, can the facility-interference-free aerodynamics *at the test scale* be extracted from the rotary balance measurements? To answer this question, a typical example is analyzed and an explanation offered. Since no off-surface flow visualization data were available for the configurations with trips the analysis of BWLVHT had to be based on the knowledge gained from the study of the clean configuration, and is therefore of a tentative nature. Nevertheless, the hypothesis that follows is considered plausible as it is the only explanation available that fits the facts. As a result of careful experiments at FFA that introduced a new parameter, ie. the separation distance between model and C-strut, a form of support interference specific to configurations having boundary layer trips could be studied (see Section 3.9).

The forebody crossflow conditions for BWLVHT are conceptualized in Fig A4.4.15 and A4.4.16. Although off-surface flow visualization results are not available to confirm this it appears that forebody states F and G lead to LEX/body topologies similar to states A and B[36]. Evidence for the existence of state G is provided by the good agreement between the surface flow patterns obtained for BWLVH at $\alpha = 51°$ and BWLVHT at $\alpha = 53°$ (Fig A4.2.9 and A4.2.11, respectively). For comparison the same view of the trace of the second upwind vortex can be seen in Figs A4.2.5 ($\alpha = 46°$) and A4.2.11. The FFA data for BWLVHT at $\alpha = 40°$ in Fig 3.46 were obtained at transitional incident flow conditions, $Re_d = 0.28 \times 10^6$. At $\Omega = 0$ a flow state G exists intermittently on the forebody (Fig A4.4.16a), which leads to a topology B^- similar to state B (Fig A4.4.9), resulting in a C_n offset somewhat similar to that in Fig A4.4.6 for the clean configuration. It appears that the support interference, which promotes the occurrence of a state G (Fig A4.4.16a), is produced, in part by the C-strut even when a sting-carrier strut extension is added ($R_c/L_n = 2.64$ without extension). The AerMacchi water tunnel results showed that even with $R_c/L_n = 3.5$ the adverse pressure gradient caused by the C-strut was strong enough to maintain state B (Section A4.2.1).

The initial rotation direction is clockwise in the FFA test (Fig 3.4.6), $\left(\vec{1}\right)$ in Fig A4.4.17, so that the LEX upwash reinforces the separation asymmetry. When the rotation direction is reversed the asymmetry should switch at $\Omega = \bar{\Omega}_s$. If state G is qualitatively similar to state B, $\bar{\Omega}_s \approx 0.035$. However, the support interference prevents this from happening. In coning motion the flow separation asymmetry shown in Fig A4.4.15b is produced for $\bar{\Omega} < 0.11$, under the influence of the coning-induced LEX upwash differential. On the advancing side relaminarization is promoted and separation occurs at $\phi_m \approx 100°$. On the receding side turbulent separation occurs at near $\phi_m = 110°$. Assuming that the flow topology approximates the laminar case the damping constant available for that case can be used.

The insensitivity of the lateral-directional characteristics to the presence of the strut extension gives a clue as to the source of the bifurcation $\left(\vec{2},\vec{3}\right)$ at $\bar{\Omega}_H = 0.11$ (Fig A4.4.17). While the C-strut interference is greatly reduced in the FFA installation ($R_c/L_n \geq 2.64$) the angle θ_s (Fig A4.4.3) is relatively large, $\theta_s = 28°$, and the same with the extension in place (Fig 3.45). Thus, the sting carrier strut presents an obstruction to the inboard, attached vortex. Under the combined influence of the increased adversity of the pressure gradient and flow deflection on the receding side (Fig A4.4.16b) at $\Omega > 0$ the turbulent shear layer will fail to reattach at about 60° from the stagnation point, resulting in state H. Thus, the retreating trip strip acts as a separation device near the tip (see Section A4.3.1), overpowering the otherwise dominant LEX-upwash effect and thereby switching the vortex asymmetry as shown in Fig A4.4.16b. Upon reversing the rotation direction $\left(\overleftarrow{4}\right)$ the expected jump to state G^+ does not occur under the influence of support interference, within the $\bar{\Omega}$-range tested.

This analysis shows that the rotary aerodynamics measured in the presence of support interference in this example do not resemble the free-flight aerodynamics even though the static offsets are not strongly affected. This conclusion is supported by rotary tests of BWLVHT on other rotary balances, which showed similar levels of support interference. The more detailed analysis of Ref. 36 demonstrates that flow mechanisms governed by trip effects are much more sensitive to facility interference than the clean configuration, generally resulting in coning-direction-dependent hysteresis. Since the lateral-directional characteristics may be seriously distorted by support interference in several of the examples considered[36] it must be concluded that it is, in general, very difficult to determine the free-flight (interference-free) sub-scale rotary aerodynamics of models having forebody roughness elements on conventional rotary balances. In such cases, the only recourse is to resort to low-interference tests involving apparatuses such as OPLEC and PQR within large test sections. However, it should be remembered that, as noted earlier, the problem is much more manageable for models without roughness elements.

Configurations with Strakes and Trips

When strakes are added double-delta-wing like flows are obtained, characterized by low aerodynamic efficiency at $\alpha < 45°$ in the case of BWLVHST, and nonlinear responses at higher α. In this case the nose tip preseparation and separation effects of the trips are eliminated, but new coning-rate threshold behaviour is introduced by the re-emergence of the moving wall effect on the aft forebody at $\alpha > 45°$. The static offsets, and therefore the primary switch in asymmetry, are eliminated in the rotary experiments but this is the least of the concerns as the occurrence of static offsets is well understood (Section A4.4.2). The problem that has to be dealt with in the case of BWLVHST is the complexity introduced by competing viscous (moving wall) effects and kinematic coupling (due to LEX upwash effects) at $\alpha > 45°$. The consequence of this complexity is that the potential uncertainty due to facility interference is larger for BWLVHST at high α than for the other configurations, making it difficult to predict, for instance, whether the yawing and rolling moments are dynamically stabilizing or destabilizing in a manoeuvre.

The preliminary analysis of BWLVHT and BWLVHST has shown that consistent correlations can be obtained in the presence of trips when the parameter space is reduced[36]. Since the rationale for the reduction of the parameter space is based on geometric similarity parameters for the support structure and test section walls it follows that the collapse of rotary data from different facilities for BWLVHT, in particular, is indicative of consistent levels of support interference. However, although the analysis confirms the presence of support interference at high-α conditions ($\alpha \geq 45°$) in the BWLVHST data, the threshold coning rates cannot be unambiguously determined because of the large size of the parameter space even after reduction. Again, if the elucidation of this question is desired, it would be necessary to resort to low-interference rotary tests, eg. using the OPLEC approach.

As noted earlier, the interpretation of the aerodynamics of configurations with trips hinges largely on correct phenomenological analyses when insufficient experimental or computational flow field data are available. It is, therefore, encouraging that the preliminary flow physics analyses of Ref. 36, while corroborating the findings and conclusions of Section A4.3, also improve the WG16 rotary data correlations.

A4.4.4 Effect of Coning Rate and Oscillation Amplitude

Up to this point the discussion has been restricted to steady, lunar coning and small amplitude oscillatory motions. In this section the aerodynamic measurements for large-amplitude pitch oscillations separately or in combination with lunar motion are analyzed.

Separated flow effects make the high-alpha aerodynamics of the WG16 model highly nonlinear. This together with significant time-history effects caused the unsteady aerodynamics to be hard to interpret. In what follows one interpretation, based upon an extension of the analysis in Ref. 34, will be presented.

The nonlinear alpha effects exhibited by BWLVHST at $20° < \alpha < 40°$ (Fig A4.4.18 from Fig 5.43) can be explained by applying the flow-physics concepts presented in Ref. 61. At $|\beta| = 10°$, the effective sweep angle of the leeward side (in the lateral sense) of the 45 deg delta wing becomes 55 deg. Experimental results[62] (Fig A4.4.19) show that for that sweep angle a leading-edge vortex exists on a pure delta wing. Considering the effect of the Gothic LEX, the effective sweep would be much larger than 55 deg, indicating that the vortex breakdown would probably not reach the effective wing apex, represented by the wing-LEX juncture, until a substantially higher angle of attack than the value $\alpha \approx 25°$ shown for $\Lambda = 55°$ in Fig A4.4.19, eg. $\alpha \approx 35°$ (Fig A4.4.18). It is true that in the case that a full leading-edge vortex exists at $\beta = 0$, the vortex-induced load is statically stabilizing[63], ie. $C_{l_\beta} < 0$. However, in the present case no vortex exists at $\beta = 0$, and the "sudden" appearance of vortex-induced lift on the leeside wing half at $|\beta| = 10°$ is statically destabilizing, in accordance with the experimental results at $20° < \alpha < 30°$ in Fig A4.4.18. When the angle of attack is increased beyond $\alpha = 30°$, the vortex breakdown moves to the effective wing apex. This causes the lift generated by the vortex upstream and downstream of a spiral breakdown to be wiped out[64] (Fig A4.4.20). This sudden loss of lift constitutes one of the critical states for delta wings at high alpha[65]. In the present case (Fig A4.4.18), this critical state is encountered at $\alpha > 30°$, causing a complete loss of lift on the leeside wing half, thereby eliminating the statically destabilizing rolling moment. The α-hysteresis in Fig A4.4.18 is of the usual type, showing flow reattachment to take place at an angle of attack far below that for flow separation. For increasing angle of attack, "three-dimensional stall", the terminology suggested by Hummel for the flow conditions existing on a delta wing when the vortex breakdown has reached the apex, occurs at $30° < \alpha < 40°$. For decreasing angle of attack only the fully attached flow condition occurs, i.e. the establishment of an unburst leading-edge vortex on the leeside wing half at $\alpha < 25°$. The partial flow separation type, represented by the spiral vortex breakdown downstream of the apex, can apparently not be established for decreasing angle of attack. As a consequence, the rolling moment does not change sign for decreasing angles of attack in Fig A4.4.18.

Figure A4.4.21 (from Fig 5.58) shows that the statically destabilizing $C_l(\beta)$ characteristics, existing at $20° < \alpha < 30°$ for $\bar{\Omega} = 0$ (Fig A4.4.18) and for $\bar{\Omega} = 0.006$ (Fig A4.4.21), are wiped out when the rotation rate is increased to and beyond $\bar{\Omega} = 0.06$. The likely reason for this is that the coning-induced sideslip changes the effective leading-edge geometry[45] (Fig A4.4.22). The rate-induced effects will be largest close to the upper and lower ends of the tested α-range, where $|\dot{\beta}|$ is largest for oscillatory coning (see the sketched β envelope in Fig A4.4.21). This explains the dramatic Ω-effects on the rolling moment at $\alpha > 20°$, completely eliminating the "static" nonlinear $C_l(\alpha)$ loops existing for $\bar{\Omega} = 0.006$. As $\beta < 0$ in the α-range $20° < \alpha < 40°$ in Fig A4.4.21, the flow physics depicted in Fig A4.4.22 apply. The negative yawing rate should generate an increment $\Delta C_l > 0$ relative to the "static" rolling moment at $\bar{\Omega} = 0.006$. This explains the elimination of

the negative $C_l(\alpha)$ loops existing for $\bar{\Omega} = 0.006$. The experimental results in Fig A4.4.21 also show the expected increase of the rate-induced ΔC_l with increasing $\bar{\Omega}$. The analysis of the experimental results in Figs A4.4.18 and A4.4.21 indicate that a manoeuvring BWLVHST is likely to experience significant motion-induced coupling effects[45] at moderately high angles of attack.

The complicated nature of the loads induced on a slender forebody are well illustrated by the C_n results for the pitching AGARD WG16 model (Fig A4.4.23, from Fig 5.49). They are unusual in two respects. First, a static yawing moment, $|C_n| > 0$, is measured at $\beta = 0$ even though the strakes force the flow separation to be symmetric at the nose tip. The nose strakes only delay the occurrence of the separation asymmetry, from $\alpha > 30°$ (Fig 5.29) to $\alpha > 45°$ (Fig 5.49). This is in agreement with flight test results for the X-31 aircraft[66], indicating that a limited α-range exists below $\alpha = 90°$ in which asymmetric crossflow separation can develop aft of the nose region affected by the strakes. Flow visualization results at $\alpha = 46°$ for the AGARD WG16 model with a clean forebody[2] (Fig A4.2.5) show that a new asymmetric vortex pair is being generated two calibers downstream of the nose tip. This is in basic agreement with existing experimental evidence[13]. There is no reason to believe that the second vortex pair will not form in the presence of a symmetric first vortex pair, produced in the presence of the strakes. The location where the second vortex pair starts on the clean forebody (Fig A4.2.5) would be one strake length behind the trailing edges of the strakes.

More challenging is to explain the other result in Fig A4.4.23, i.e. the capability of a very modest pitch rate to eliminate the asymmetric crossflow separation existing at $45° < \alpha < 65°$ for essentially static flow conditions. As the $C_n(\alpha)$ loops above and below $\alpha = 40°$ are very similar for the 29 deg amplitude oscillation, there cannot be any significant effect of forebody flow asymmetry at $\alpha > 40°$. The test Reynolds number was $Re = 0.2 \times 10^6$, ie. the crossflow Reynolds number could have been close to the critical range (Fig A4.3.9). However, flow visualization results[3] show that the trips, located at ±40 deg azimuth, were ineffective; and the crossflow separation at $Re = 0.2 \times 10^6$ was of the subcritical type. Because of their location the trips could even have had an effect opposite to that intended. That is, the relaminarized boundary layer could have been more resistant to transition than in the absence of the trips. That is, the effect could be similar to that for the reattaching turbulent boundary layer aft of a separation bubble, which is more resistant to flow separation.

Experimental results for an ogive-cylinder[67,68] show that pitch-rate effects are in themselves usually not capable of changing the crossflow separation asymmetry. This is to be expected as the moving wall effect[31]in the case of a pitching motion is all but nonexistent in the flow stagnation region, where it is most effective because the crossflow boundary layer is initiated there. The exception to this general rule is the case of critical flow conditions, when also the pitch-rate-induced symmetric moving wall effect[69] can cause a dramatic change of the separation-induced loads at high angles of attack[67] (Fig A4.4.24). The very modest pitch-up rate $\dot{\alpha}d/U_\infty = 0.0027$ changed the supercritical or critical separation existing at $\dot{\alpha} = 0$ for $Re_d = 0.08 \times 10^6$ to the subcritical type existing at $\dot{\alpha} = 0$ for $Re_d = 0.05 \times 10^6$ (the quoted 6 % oscillatory variation of the freestream speed may have been responsible for the early subcritical/critical transition). The moving wall effect delays transition and causes a change somewhat similar to the relaminarization effect illustrated in Fig A4.3.4a.

Considering the fact that the critical Reynolds number can vary by almost an order of magnitude between test facilities[50] (Fig A4.4.2), and that the flow visualization results[2] did not cover the α-region of concern, $53° < \alpha < 60°$ in Fig A4.4.23, one cannot a priori eliminate the possibility that critical crossflow conditions indeed could have existed in that α range. With the forebody vortex pair starting behind the strakes, at least two calibers aft of the nose tip[2] (Fig A4.2.5), the generation of the forebody crossflow separation and associated vortices takes place over the remaining less than two calibers extent of the forebody ahead of the LEX surfaces. Even without considering the wing wake blockage effect, one is inclined to conclude that the crossflow conditions must correspond to an effective angle of attack substantially larger than the nominal value. Hence, in the α-range $50° < \alpha < 60°$ the crossflow conditions are likely to have been those for angles of attack substantially above 60°, and, therefore, similar to those for flat spin.

Based upon the experimental results[70] in Fig A4.4.25, to be discussed further in Section A4.5, one can (for $\alpha > 50°$ in Fig A4.4.23) construct the conceptual crossflow geometries shown in Fig A4.4.26. At $\dot{\alpha} = 0$, the crossflow geometry giving the pressure distribution at point C in Fig A4.4.25 is established. This subcritical/critical separation asymmetry generates the largest possible side force on the forebody[13], producing a yawing moment of large magnitude (Fig A4.4.23 for the slow α-sweep). Figure A4.4.25 (point C) shows that it takes a minute change of the crossflow Reynolds number to go back to the subcritical/subcritical (point B) or move forward to the critical/critical (point D) symmetric crossflow separation geometries. As discussed earlier, a very modest moving wall effect can cause a complete change of flow separation geometry at critical flow conditions. Thus, at point C in Fig A4.4.25 the pitch-rate-induced moving wall effect near the crossflow stagnation point could cause a change of separation geometry (from point C in Fig A4.4.25 to points B or D).

Thus, during the upstroke ($\dot{\alpha} > 0$), the moving wall effect will delay transition, changing the critical separation in Fig A4.4.26a back to a subcritical flow separation, resulting in the subcritical/subcritical crossflow separation shown in Fig A4.4.26b. During the downstroke ($\dot{\alpha} < 0$), on the other hand, the adverse moving wall effect will promote transition, changing the subcritical/critical separation at $\dot{\alpha} = 0$ to a critical/critical crossflow geometry (Fig A4.4.26c). As has been discussed earlier, the subcritical flow separation occurs at 90 deg meridian or earlier, whereas the critical separation occurs at roughly 140 deg. As a consequence, the local normal force generated by the forebody would be reduced below the static value during the upstroke, $\dot{\alpha} > 0$, and increased above it during the downstroke, in agreement with

the experimental C_m results (Fig A4.4.27, from Fig 5.49). The dominant effect on C_m for the present model geometry will be the change of the forebody normal force through the change of flow separation geometry, whereas the downstream vortex-induced loads, which contribute significantly to C_N in Fig A4.4.24 have negligible effect on C_m in Fig A4.27 or C_n in Fig A4.23.

A4.5 APPLICATION TO FULL-SCALE FLIGHT

When pursuing the objective of advancing the understanding of high-alpha manoeuvring aerodynamics both the applicability of unsteady aerodynamic data from available sources and the relevance to high-performance aircraft design have to be established. The viability of current sub-scale dynamic test techniques was assessed in earlier sections.

To provide the vehicle designer with increased insight into the flow physics the fluid/motion coupling prevailing in high-alpha manoeuvres is discussed in this section. There are three fundamentally different classes of advanced aircraft; (a) those that have a long slender forebody with wing and/or LEX well downstream, exemplified by the WG16 configuration BWVH, (b) those with wing and/or LEX near the base of the slender forebody, exemplified by the WG16 configuration BWLVH, and (c) delta wing aircraft. For the purpose of discussion, WG16 configuration BWLVHS(T) can be considered to have some of the characteristics of a double-delta wing aircraft at low alpha ($\alpha < 45°$). The nature of the coupling between control input and vehicle dynamics for these different aircraft categories is discussed in the context of conceptual supermanoeuvres.

The classic supermanoeuvre concept introduced by Herbst[71] is an appropriate model for this discussion (Fig A4.5.1). Quoting Herbst[71]: "One of the most applicable analytic maneuvers, for example, is that of an 180° change of heading with the additional constraint of returning to the point of departure at initial speed and altitude." The aerodynamic control/vehicle dynamics coupling in such a manoeuvre will be very sensitive to the vehicle geometric characteristics, such as delta wing planform and slender forebody geometry, typical characteristics of many advanced aircraft.

A4.5.1 Analysis

The unsteady aerodynamics producing the fluid/motion coupling in a supermanoeuvre are distinctly different for the three categories of advanced aircraft geometries. For the delta wing aircraft[71] (Fig A4.5.1) the high-alpha aerodynamics are dominated by the loads induced by wing leading-edge vortices, whereas for the two types of slender-nosed aircraft, large asymmetric loads are generated by the slender forebody.

A4.5.1.1 Delta-Wing Aircraft

On a supermanoeuvring slender delta wing the vortex-induced normal force C_{NV} will dominate over the potential, attached-flow force $C_{N\alpha}$. The relationship between these force contributions is[72]

$$C_{NV}/C_{N\alpha} = 1.10 \tan \alpha/\sin 2\theta_A \qquad (A4.6)$$

Based upon experimental results[62], Eq. (A4.6) shows that below the angle of attack for starting vortex breakdown on delta wings $C_{NV}/C_{N\alpha} > 1$ for $\theta_A < 19°$. In the high alpha range encountered in the Herbst supermanoeuvre[71] (Fig A4.5.1), the effects of vortex breakdown will dominate the aircraft loads. Thus, the effect of the aircraft motion on the vortex breakdown becomes of concern. The manoeuvres[71,73] shown in Figs A4.5.1 and A4.5.2 involve a coning motion near the completion of a rapid pitch-up motion. This is kinematically similar to a yawing motion (Fig A4.5.3) at high alpha, otherwise known as a velocity vector roll. No significant body-axis rolling motion is involved in the heading change.

In the case of the trajectory shown in Fig A4.5.1, the required yawing motion takes place at or near the completion of a rapid pitch-up motion, which in itself delays vortex breakdown on a delta wing, as discussed in Ref. 74. Thus, at the higher angles of attack of the supermanoeuvre, the yawing moment and the coning motion characteristics are dependent upon the preceding pitch-up time history. Of course, the pitch-up motion will through its delay of vortex breakdown[74] generate a pitching moment that resists the pitch-up motion, but aids in the initiation of the pitch-down motion needed for completion of the supermanoeuvre.
The analysis in Ref. 45 showed that the potential for significant adverse control/vehicle-dynamics coupling does not appear to be great for delta-wing aircraft. The addition of a fuselage (Fig A4.5.2) will introduce the problems associated with a slender forebody. The present analysis is restricted to the WG-16 configuration, whose slender-nosed aircraft geometry is typical of many of the existing advanced fighters.

A4.5.1.2 Double-Delta Aircraft

As indicated in Section A4.4.3 one of the WG16 configurations, BWLVHS(T) has some of the characteristics of double-delta type aircraft. At lower angles of attack $\alpha < 45°$ the forebody crossflow separation is eliminated and replaced by a slender delta-wing vortex flow that interacts with the LEX-wing vortex system. At $\alpha > 45°$ asymmetric crossflow separation on the aft forebody becomes dominant (Sections A4.4.2 and A4.4.3) changing the aerodynamic characteristics completely. In this region both the coning-induced moving wall and LEX upwash effects become important, introducing the potential for aerodynamic cross-coupling.

The small-amplitude forced-oscillation data do not give much of an indication of the nature of the cross-coupling. In fact, except for the modest effect on α_{on} there is little effect of the LEX on C^*_{nq} without strakes (Fig 5.31), while with strakes the levels of the derivative are very small. The important aerodynamic cross-coupling effects are revealed only at large amplitudes and rates discussed in Section A4.4.4. The relevant parameters, coning rate, pitch rate and oscillation amplitude, were studied in Ch. 8.

The highly nonlinear effects of induced sideslip in static (Fig A4.4.18) and oscillatory-coning (Fig A4.4.21) rolling moment data show that an aircraft configuration similar to BWLVHST is likely to experience significant motion-induced coupling effects at moderately high α (see also, Section A4.5.2.3).

Similarly, the large pitch rate effects on BWLVHST (Fig A4.4.23 and A4.4.27) govern the flow separation asymmetry and will therefore result in significant aerodynamic cross-coupling during pitch-up to $\alpha = 90°$. Thus, it could be concluded that aircraft configurations characterized by multiple vortex interactions would not display the obvious advantages for combat manoeuvring associated with pure-delta-wing aircraft[71].

A4.5.2 Slender-Nosed Aircraft

When the aircraft has a slender nose, as in the case of the X-31 aircraft shown in Fig A4.5.2, the coupling between control demands and vehicle dynamics becomes very different from that for a delta-wing aircraft. The flow separation of concern is no longer fixed at the more or less sharp leading edges of the wing but occurs instead on a slender nose. When wing and LEX surfaces are located far behind the slender nose, as in the case of the F-14 Tomcat (Fig A4.5.4), the forebody crossflow separation depends strongly on the vehicle motion through moving wall effects[31], discussed in Section A4.3 in connection with Figs A4.3.2 and A4.3.3. When the wing and/or LEX surfaces start at the base of the slender forebody, as in the case of the F-16 Fighting Falcon[75] (Fig A4.5.5), the wing-induced upwash often overpowers the moving wall effect, as was discussed in Section A4.3 in connection with Figs A4.3.7-A4.3.11. Both aircraft geometries will be analyzed briefly in this section.

A4.5.2.1 Wing and LEX Well Downstream of a Slender Forebody

Tests of a wind tunnel model with this type of aircraft geometry[35] have demonstrated that the huge, rate-induced yawing moments measured at high angles of attack are largely generated by the loads on the slender forebody (Fig A4.3.3), and body-alone aerodynamic results are in this case representative of the high-alpha yaw dynamics of the complete aircraft (Section A4.3.1).

It is well known that nose microasymmetries affect the high-alpha crossflow separation on a slender, axisymmetric body[13]. In view of this fact, the experimental results for a cone-cylinder body, free-to-roll around the velocity vector[25] (Fig A4.3.2), are of considerable interest. The test results demonstrate that, during the initial "spin-up" of the coning motion, the effect of roll-angle, which is large in static tests at similar, laminar test conditions[13], is completely over powered by the moving wall effect[34]. On a full-scale aircraft laminar flow conditions will only exist in a small region near the nose tip. The significant regions of crossflow separation occur for critical or supercritical flow conditions. In the former case the separation is controlled by the coupling between crossflow boundary layer transition and vehicle motion[30,76].

On an advanced aircraft performing a high-alpha manoeuvre, it is the moving wall effect acting in the boundary layer build-up region, near the flow stagnation point on the nose, that determines the flow separation asymmetry. Furthermore, the coning associated with the supermanoeuvre will occur at high angles of attack, $45° < \alpha < 90°$. Consequently, flat-spin results for axisymmetric bodies[77] provide useful information. The static experimental results at $\alpha = 90°$ for a 5.4 deg cone-cylinder[70] (Fig A4.4.25) show that the local crossflow Reynolds number is a good indicator of when symmetric or asymmetric separation of various types will occur. The figure shows that the first side-force peak, point C, is caused by subcritical/critical flow separation. In the static case the force can be positive or negative. However, in the flat-spin case the force establishes itself in a direction that produces an anti-spin moment[31] (Fig A4.5.6). At points D and E, the two-bubble, symmetric, critical/critical separation geometry is established. When perturbed by a translatory motion of the cross-section, this separation type also produces an anti-spin moment, as is demonstrated by Polhamus' experimental results[46,77] in Fig A4.5.7 for $\Omega < 0.25$. Finally, when the Reynolds number has been increased to point F in Fig A4.4.25, the pro-spin supercritical/critical crossflow separation is established[77], obtained at $\Omega > 0.5$ in Fig A4.5.7.

While the flat spin characteristics of advanced aircraft are very similar to those of axisymmetric bodies, the mechanisms initiating the flat spin are quite different. In the case of the axisymmetric body the flat spin was initiated by a static moment generated at $\alpha = 90°$ through the effects of asymmetrically distributed body-roughness[77]. The large static moment is able to accelerate the flat spin through the spin-resisting subcritical/critical (Fig A4.5.6) and critical/critical (Fig A4.5.7 for $\Omega < 0.5$) regions of crossflow separation to the final pro-spin supercritical/critical separation, shown in Fig A4.5.7 for $\Omega > 0.5$. This results in the experimentally observed flat-spin characteristics[78] (Fig A4.5.8). In the case of the supermanoeuvre, the initiation of the translatory motion of the circular cross-section is driven by the control-induced moment. As a rapid roll around the velocity vector is demanded, the supercritical/critical flow separation is established directly. This would occur not only at $\alpha = 90°$ but in the whole range $45° < \alpha < 90°$. Thus, the dynamic vehicle response will significantly amplify the control-induced yawing moment.

In addition, a jumpwise increase of the pitch-up moment will be generated by the change to an asymmetric crossflow separation geometry. The experimental results for a 5 caliber long tangent-ogive[69,79] (Fig A4.5.9) show how the separation asymmetry in addition to generating a side force C_Y also produces an increase of the normal force C_N. Experimental results for the effect of a nose strake[80] indicate that the normal force can be increased substantially through the change from symmetric to asymmetric crossflow separation. The experimental results for the WG-16 model for body-alone (Fig 5.2) show also such an increase of the forebody normal force, manifested by the large difference in C_m for strake-on and strake-off. Even for the complete configuration in Fig 5.3 such a strake effect on C_m was measured. The difference was

that, judging by the C_n data, with the LEX surfaces present (Fig 5.3), the forebody crossflow asymmetry started at $\alpha \approx 40°$ rather than at $\alpha \approx 30°$, as for body-alone in Fig 5.2. It is clear that in the case of the F-14 aircraft (Fig A4.5.4) the pro-spin forebody crossflow loads generated in response to a sharp turn, coupled with the associated nose-up pitching moment, could have driven the aircraft into a stable spin mode at very high angles of attack[77,81], resulting in the loss of 31 aircraft[82] (Fig A4.5.10).

A4.5.2.2 Wing and/or LEX Located Close to a Slender Forebody

The F-16 aircraft[75] (Fig A4.5.5) is not known to have experienced the flat-spin problem plaguing the F-14 aircraft. The key difference between the two aircraft geometries is the presence of LEX surfaces on the F-16 aircraft (Fig A4.5.5). The wing rock observed in tests with a generic aircraft model[42] (Fig A4.3.10) was caused by moving wall effects generated by a rolling motion rather than coning[43]. Moving the wing forward to the base of the slender nose eliminated the wing rock existing for the wing in the aft position. It was suggested in Ref. 44 that the reason was that in the case of the forward wing position the wing-induced upwash overpowered the moving wall effects, thereby eliminating the flow mechanism driving the wing rock. The question is if not the shaded LEX surfaces, added in the right hand sketch of Fig A4.3.10, would have accomplished the same thing. Experimental results for the WG16 model indicate that this would indeed have been the case. The LEX delayed the occurrence of asymmetric forebody crossflow from the expected value $\alpha = 2\theta_A = 28.5°$ in Fig 5.2 to $\alpha \approx 40°$ in Fig 5.3.

Figure A4.3.11 illustrates the probable effect of the LEX-induced upwash on the forebody in the case of a coning motion. The coning rate generates a sideslip that decreases the effective leading-edge sweep of the LEX surfaces on the advancing side and increases it on the receding side. The result is a stronger LEX-induced upwash on the advancing side than on the receding side, as indicated in Fig A4.3.11b. This situation prevails until vortex breakdown moves to the LEX apex, at which time the spiral vortex and associated upwash effect on the forebody is lost (Fig A4.4.20). As a consequence of the dominance of the LEX-induced upwash over the moving wall effects, discussed earlier, the crossflow separation and associated vortex shedding on the slender forebody is affected as sketched in Fig A4.3.11. That is, instead of generating a pro-spin force as in the case of no LEX surfaces (Fig A4.3.11a), the LEX-induced upwash causes the crossflow separation to generate an anti-spin force on the forebody (Fig A4.3.11b), as has been discussed earlier. At high angles of attack where the LEX-induced upwash has lost its dominant effect, at $\alpha > 45°$ (see Section A4.4.2), the WG16 configuration would be subject to the same aerodynamic yaw-pitch cross-coupling effect as the F-14 aircraft.

The fundamental difference between the high-α flight characteristics of the WG16-type and the F-14 type aircraft is that the tendency towards departure in the latter case starts already at $\alpha \approx 30°$, as compared to $\alpha \approx 45°$.

A4.5.2.3 Manoeuvre Time History

Even in the absence of a control-induced input the forebody flow is likely to be asymmetric up to alphas approaching 90 deg in a supermanoeuvre, because of the flow field time lag. For initially supercritical flow conditions the supercritical/critical separation asymmetry (point F in Fig A4.4.25) could be established as α approaches 90 deg. Thus, departure into flat spin is possible. This development of flat spin may be delayed by the presence of nose strakes, but will not be prevented, as at these high angles of attack asymmetric crossflow separation will develop on the forebody aft of the strakes. This behaviour has been observed for the X-31 at $\alpha \geq 60°$ (Ref. 66) as well as for the AGARD WG16 model at $\alpha \geq 45°$ (Fig A4.2.5). Manoeuvre-control effects, such as forebody blowing[83], will be ineffective at angles of attack above the range for asymmetric forebody-crossflow separation.

As already noted, in the case of the supermanoeuvre a large control-induced yaw rate will be generated, favoring departure into flat spin. In the case of pitch-up to $\alpha \approx 70°$, the steep spin that might result at equilibrium conditions will occur at a lower rotation rate because of the reduced pitch-down moment in the presence of asymmetric crossflow separation. On the other hand, if the aircraft is pitched up towards $\alpha = 90°$, the full negative pitching moment has to be balanced, leading to a fast flat spin that is generally not recoverable. The conditions for spin equilibrium also require a balance of lateral forces, which is provided at finite sideslip. The free-flight behaviour of a subscale model[84] similar to the WG16 BWLVH demonstrated high-α departure following stall, resulting in an oscillatory spin. As the flow conditions were subcritical a flat spin could not develop.

For an aircraft with complex forebody geometry a relatively small altitude change could result in a switch of the flow separation topology. At the low end of the critical Reynolds number range this is illustrated[5] by the results obtained on HIRM II (Ref. 15). This configuration has a forebody shape which transitions from a circular to a rounded-square section. At moderate angles of attack, $45° < \alpha < 60°$, the flow is critical on the circular section and subcritical on the rounded-square section in the test at $Re = 0.4 \times 10^6$. This results in bistable $C_n(\Omega)$ characteristics at $\alpha = 60$ deg[5]. Considering time-history effects, in full-scale flight at high altitude the crossflow conditions on the rounded-square section would be supercritical at $\alpha = 60°$ but critical at $\alpha \rightarrow 90°$. This means that in actual flight there could be a tendency to depart when approaching the supercritical/critical boundary. In the case of the Herbst supermanoeuvre the initial conditions involve high subsonic Mach numbers at moderate altitudes. Thus, the conditions are initially supercritical, with considerable compressibility effects, and subsequently traverse the transitional flow region (Fig A4.5.11), as the speed drops during the pitch-up.

As noted in Section A4.4.4, a configuration such as BWLVHST is likely to experience significant motion-induced coupling effects already at moderately high angles of attack

($20° \leq \alpha \leq 35°$). The nonlinear behaviour expected in the presence of such coupling effects is apparent in the large-amplitude oscillatory results (Fig 5.49). Besides introducing these vortex interactions the strakes also eliminate the beneficial LEX-induced upwash effect as noted in Section A4.4. Thus, for configurations dominated by multiple vortex interactions, such as low-observables aircraft, control/vehicle dynamics coupling problems are to expected in this range.

The conditions associated with fluid/motion coupling at lower altitudes are dangerous to cover in flight tests and difficult to investigate in wind tunnels because of the high Reynolds numbers that have to be simulated. As a result, very little data is available for these flow conditions. Consequently, more analysis is needed of fluid/motion coupling at high subsonic Mach numbers and high Reynolds numbers.

A4.5.3 Summary

An analysis of conceptual supermanoeuvres by an aircraft configuration such as the WG-16 model shows that the principal source of the highly nonlinear control/motion coupling effects at high angles of attack is the effects of the vehicle motion on the asymmetric crossflow separation and vortex shedding on a slender forebody. The potential for adverse control/motion coupling is a strong function of aircraft geometry, altitude, and manoeuvre characteristics. The presence of LEX surfaces are found to have a profound effect on the manoeuvre characteristics of a slender-nosed aircraft. The nature of, and response to, the fluid/motion coupling effects are governed by the manoeuvre-time history.

A4.6 CONCLUSIONS

1. For the clean forebody-dominated classes of aircraft (with and without LEXs) conventional dynamic tests performed at laminar flow conditions can provide information from which the free-flight characteristics can be deduced.

2. When boundary layer transition effects are important it is much more difficult to derive useful information from the tests, necessitating a greater reliance on the flow physics analysis.

3. In the presence of significant LEX/wing-induced upwash effects the forebody crossflow separation caracteristics become far less sensitive to viscous fluid/motion coupling effects. This facilitated the analysis of the WG16 rotary aerodynamics, notwithstanding the presence of significant facility interference.

4. It is for all practical purposes impossible to simulate the full-scale high-Re flow conditions by using boundary layer tripping in rotary tests. In fact, it is in general not possible to determine even the sub-scale free-flight aerodynamics of models having forebody roughness elements.

5. With the knowledge gained from the analysis of the WG16 dynamic experiments it is possible to greatly improve rotary test techniques.

6. The forebody-dominated type of aircraft experience a larger α range of departure-prone behaviour than their LEX-dominated counterparts.

7. In all cases of complicated flow physics, it is important to start with comprehensive flow visualization tests.

A4.7 ACKNOWLEDGMENTS

This manuscript benefited greatly from the comments made by members of AGARD WG16. The authors gratefully acknowledge the contributions of Hui Juan Cai, in the flow field analysis and computer graphics, and Roxanne Preseault in computer graphics and word processing.

A4.8 REFERENCES

1. O'Leary, C.O., Weir, B. and Walker, J.M., "Static and Forced Oscillation Tests on a Generic Combat Aircraft Model", Defence Research Agency, DRA/AS/HWA/ TR94066/1, Jan. 1995.

2. Cai, H.J. and Beyers, M.E., "Oscillatory Experiments on the AGARD WG16CA Model", National Research Council Canada, IAR-AN-83, Sept. 1995.

3. Tristrant, D., Private Communication, Oct. 1995.

4. Penna, P.J. and Beyers, M.E., "Support Interference Assessment in Rotary Experiments Using the Orbital Platform Concept", National Research Council Canada, IAR-AN-79, April 1994.

5. Beyers, M.E., "Unsteady Wind Tunnel Interference in Aircraft Dynamic Experiments", J. Aircraft, Vol. 29, No. 6, 1992, pp. 1122-1129.

6. Ericsson, L.E., "Reflections Regarding Recent Rotary Rig Results", Journal of Aircraft, Vol. 24, No. 1, Jan. 1987, pp. 25-30.

7. Beyers, M.E., "Unsteady Wall Interference in Rotary Tests", AIAA Paper 89-0046, Jan. 1989.

8. Ericsson, L.E., "Another Look at High-Alpha Support Interference in Rotary Tests", Journal of Aircraft, Vol. 28, No. 9, Sept. 1991, pp. 584-591.

9. Beyers, M.E. and Ericsson, L.E., "Ground Facility Interference on Aircraft Configurations with Separated Flow", Journal of Aircraft, Vol. 30, No. 5, Sept.-Oct. 1993, pp. 682-688.

10. Beyers, M.E., "Interpretation of Experimental High-Alpha Aerodynamics - Implications for Flight Prediction", Journal of Aircraft, Vol. 32, No. 2, March-April 1995, pp. 247-261.

11. Beyers, M.E. and Huang, X.Z., "The Orbital-Platform Concept for Nonplanar Dynamic Testing", National Research Council Canada, NAE-AN-52, May 1988.

12. Hummel, D., "Untersuchungen über das Aufplatzen der Wirbel an schlanken Delta Flügeln", Z. für Flugwissenschaften, Vol. 3, Heft. 5, 1965, pp. 158-168.

13. Ericsson, L. E. and Reding, J. P., "Asymmetric Flow Separation and Vortex Shedding on Bodies of Revolution," Progress in Astronautics and Aeronautics, Vol. 141, 1992, pp. 391-452.

14. Malcolm, G.N., "Rotary-Balance Experiments on a Modern Fighter Aircraft Configuration at High Reynolds Numbers", AIAA Paper 85-1829, Aug. 1985.

15. O'Leary, C.O. and Weir, B., "Effects of Reynolds Number, Mach Number and Sting Geometry on Rotary Rig Measurements", ICAS Paper 90-3.8.1, Sept. 1990.

16. Ericsson, L.E., "Aerodynamic Support Interference", Ch. 5, Special Aerodynamic Considerations, AGARD-AR-265, Dec. 1990, pp. 77-79, 85-93.

17. Verbrugge, R.A., "Balance Rotative de l'I.M.F.L. et Techniques Expérimentales Associées", Sept. 1979.

18. Ericsson, L.E. and Reding, J.P., "Dynamic Support Interference in High-Alpha Testing", J. Aircraft, Vol. 23, No. 12, 1986, pp. 889-896.

19. Beyers, M.E., Cai, H.J., and Penna, P.J., "Flow Field Interference Produced by an Asymmetrical Support Strut", National Research Council Canada, IAR-AN-75, Jan. 1993.

20. Lambourne, N.C., Bryer, D.W., and Maybrew, J.F.M., "Pressure Measurements on a Model Delta Wing Undergoing Oscillatory Deformation", NPL Aero Report 1314, Aeronautical Research Council, Great Britain, March 1970.

21. Ericsson, L.E., "Comment on 'Effect of Fuselage on Delta Wing Vortex Breakdown'", Journal of Aircraft, Vol. 31, No. 4, July-Aug. 1994, pp. 1006-1007.

22. Straka, W.A. and Hemsch, M.J., "Effect of Fuselage on Delta Wing Vortex Breakdown", Journal of Aircraft, Vol. 31, No. 4, July-Aug. 1994, pp. 1002-1005.

23. Weinberg, Z., "Effect of Tunnel Walls on Vortex Breakdown Location over Delta Wings", AIAA Journal, Vol. 30, No. 6, June 1992, pp. 1584-1586.

24. Keener, E.R., Chapman, G.T., and Kruse, R.L., "Effects of Mach Number and Afterbody Length on Onset of Asymmetric Forces on Bodies at Zero Sideslip and High Angles of Attack", AIAA Paper 76-66, Jan. 1976.

25. Yoshinaga, T., Tate, A., and Inoue, K., "Coning Motion of Slender Bodies at High Angles of Attack in Low Speed Flow", AIAA Paper 81-1899, Aug. 1981.

26. Ericsson, L. E., "Effects of Transition on Wind Tunnel Simulation of Vehicle Dynamics," Prog. Aerospace Sci., Vol. 27, 1990, pp. 121-144

27. Ericsson, L. E. and Reding, J. P., "Dynamic simulation Through Analytic Extrapolation," J. Spacecraft and Rockets, Vol. 19, March-April 1982, pp. 160-166.

28. Ericsson, L. E. and Reding, J. P., "Analytic Extrapolation to Full Scale Aircraft Aerodynamics," J. Aircraft, Vol. 21, March 1984, pp. 222-224.

29. Ericsson, L. E. and Beyers, M. E., "Ground Facility Interference on Slender Vehicle Dynamics," Journal of Aircraft, Vol. 33, No. 1, 1966, pp. 117-124.

30. Ericsson, L.E. and Beyers, M.E. "Special Aerodynamic Considerations", Ch. 5, AGARD-AR-265, Dec. 1990, pp. 88-97.

31. Ericsson, L. E., "Moving Wall Effects in Unsteady Flow," J. Aircraft, Vol. 25, No. 11, Nov. 1988, pp. 977-990.

32. Ericsson, L. E., "A Critical Look at Dynamic Simulation of Viscous Flow," Paper 6, AGARD CP-386 (1985).

33. Ericsson, L. E., "Is Any Free Flight/Wind Tunnel Equivalence Concept Valid for Unsteady Viscous Flow?", J. Aircraft, Vol. 22, Oct. 1985, pp. 915-919.

34. Ericsson, L. E., "Prediction of Slender Body Coning Characteristics," J. Spacecraft and Rockets, Vol. 28, No. 1, Jan,-Feb. 1991, pp. 43-49.

35. Grafton, S. B., Chambers, J. R., and Coe, Jr., P. L., "Wind Tunnel Free-Flight Investigation of a Model of a Spin Resistant Fighter Configuration," NASA TN D-7716 (1974).

36. Beyers, M.E., "Consolidating Critically Contaminated Coning Characteristics", to be published.

37. Hall, R.M. and Banks, D.W., "Progress in Developing Gritting Techniques for High Angle of Attack Flows", AIAA Paper 94-0169, Jan. 1994.

38. Rao, D.M., "Side Force Alleviation on Slender, Pointed Forebodies at High Angles of Attack", Journal of Aircraft, Vol. 16, No. 11, 1979, pp. 763-768.

39. Ericsson, L.E., "Aeroelastic Instability Caused by Slender Payloads", J. Spacecraft and Rockets, Vol. 4, No. 1, 1967, pp. 65-73.

40. Tristrant, D. R., Gauthier, F. F., and Vanmansart, M. G., "Dynamic Tests in ONERA-IMFLille Wind Tunnels with AGARD Generic Fighter Model," Preliminary Report, IMFL 94113, Nov. 1994.

41. Ericsson, L.E., "Unsteady Flow Separation on Slender Bodies at High Angles of Attack", J. Spacecraft and Rockets, Vol. 30, No. 6, 1993, pp. 689-695.

42. Brandon, J. M. and Nguyen, L. T., "Experimental Study of Effects of Forebody Geometry on High Angle-of-Attack Stability," J. Aircraft, Vol. 25, No. 7, July 1988, pp. 591-597.

43. Ericsson, L. E., "Wing Rock Generated by Forebody Vortices," J. Aircraft, Vol. 20, No. 2, Feb. 1989, pp. 110-116.

44. Ericsson, L. E., "Further Analysis of Wing Rock Generated by Forebody Vortices." J. Aircraft, Vol. 20, No. 12, Dec. 1989, pp. 1089-1104.

45. Ericsson, L.E. and Beyers, M.E., "Fluid/Motion Coupling in Conceptual Supermanoeuvres," AIAA Paper 96-0787, Jan. 1996.

46. Ericsson, L.E. and Beyers, M.E., "Viscous-Flow/ Vehicle-Motion Coupling", Ch. 8, Fluid Dynamics of Rotary Flows, Rotary Balance Testing for Aircraft Dynamics, AGARD-AR-265, Dec. 1990, pp. 164-167, 183-187.

47. Ericsson, L.E., Mendenhall, M.R. and Perkins, S.C., Jr., "Review of Forebody-Induced Wing Rock", Journal of Aircraft, Vol. 33, No. 2, 1996, pp.

48. Lamont, P.J., "The Effect of Reynolds Number on Normal and Side Forces on Ogive-Cylinders at High Incidence", AIAA 85-1799, Aug. 1985.

49. Fage, A. and Warsap, J.H., "The Effect of Turbulence and Surface Roughness on the Drag of a Circular Cylinder", ARC R&M, No. 1283, Oct. 1929.

50. Humphreys, J.S., "On a Circular Cylinder in a Steady Wind at Transition Reynolds Numbers", J. Fluid Mech., Vol. 9, Pt. 4, 1960, pp. 603-612.

51. Ericsson, L.E. and Reding, J.P., "Alleviation of Vortex-Induced Asymmetric Loads", J. Spacecraft and Rockets, Vol. 17, No. 6, 1980, pp. 548-553.

52. Ericsson, L.E., "Unsteady Flows", Progress in Astronautics and Aeronautics, Vol. 141, 1992, pp. 453-503.

53. O'Leary, C., Weir, B. and Walker, J.M., "Continuous Rotation Tests of a Generic Combat Aircraft Model in a Low Speed Wind Tunnel", DRA TechMemo Aero/Prop 42, 1993.

54. Ericsson, L.E., "Lateral Oscillations of Sting-Mounted Models at High Alpha", Journal of Spacecraft and Rockets, Vol. 27, No. 9, 1990, pp. 508-513.

55. Hall, R.M. "Forebody and Missile Side Forces and the Time Analogy", AIAA Paper 87-0327, Jan. 1987.

56. Beyers, M.E., Ch. 9.7 NAE, Rotary Balance Testing for Aircraft Dynamics, AGARD-AR-265, Dec. 1990, pp. 198-200, 214.

57. Beyers, M.E., "Correlations Based on Mathematical Model", Ch. 10.2, AGARD-AR-265, Dec. 1990, pp. 210-214.

58. Tobak, M. and Schiff, L.B., "On the Formulation of the Aerodynamic Characteristics in Aircraft Dynamics," NASA TR R-456, Jan. 1976.

59. Beyers, M.E., "A New Look at the Tobak-Schiff Model of Nonplanr Aircraft Dynamics", National Research Council, NAE-LTR-UA-101, Ottawa, Canada, Dec. 1989.

60. Beyers, M.E., "Subsonic Roll Oscillation Experiments on the Standard Dynamics Model", AIAA Paper 83-2134, Aug. 1983.

61. Ericsson, L. E., "Analysis of the Effect of Sideslip on Delta Wing Roll-Trim Characteristics," AIAA Paper 96-0788, Jan. 1996.

62. Wentz, W. H. and Kohlman, D. L., "Vortex Breakdown on Slender Sharp-Edged Wings,"Journal of Aircraft, Vol. 8, March 1971, pp. 156-161.

63. Ericsson, L. E. and King, H. H. C., "Rapid Prediction of High-Alpha Unsteady Aerodynamics of Slender-Wing Aircraft," Journal of Aircraft, Vol. 29, No. 1, Jan.-Feb. 1992, pp. 85-92.

64. Bergmann, B., Hummel, D., and Oelker, H-Chr., "Vortex Formation over a Close-Coupled Canard-Wing-Body Configuration in Unsymmetrical Flow," Paper 14, AGARD-CP-494, July 1991.

65. Ericsson, L. E., "Flow Physics of Critical States for Rolling Delta Wings," J. Aircraft, Vol. 32, No. 3, May-June 1995, pp. 603-610.

66. Alcorn, C. W., Croom, M. A., and Francis, M. S., "The X-31 Experiment: Aerodynamic Impediments to Post-Stall Agility," AIAA Paper 95-0362, Jan. 1995.

67. Smith, L. H., "Aerodynamic Characteristics of an Axisymmetric Body Undergoing a Uniform Pitching Motion," Ph. D. Thesis, Naval Postgraduate School, Monterey, California, Dec. 1974.

68. Smith, L. H. and Nunn, R. H., "Aerodynamic Characteristics of an Axisymmetric Body Undergoing a Uniform Pitching Motion," Journal of Spacecraft and Rockets, Vol. 13, No. 1, Jan. 1976, pp. 8-14.

69. Ericsson, L. E. and Reding, J. P., "Dynamics of Forebody Flow Separation and Associated Vortices," J. Aircraft, Vol. 22, No. 4, 1985, pp. 329-335.

70. Kamiya, N., Suzuki, S., Nakamura, M., and Yoshinaga, T., "Some Practical Aspects of the Burst of Laminar Separation Bubbles," ICAS-80-10.2, Sept. 1980.

71. Herbst, W. B., "Dynamics of Air Combat," Journal of Aircraft, Vol. 20, July 1983, pp. 594-598.

72. Ericsson, L. E. and Reding, J. P., Approximate Nonlinear Slender Wing Aerodynamics," Journal of Aircraft, Vol. 14, Dec. 1977, pp. 1197-1204.

73. Brown, S. F., "It Went Thataway," Popular Science, Oct. 1993, p. 26.

74. Ericsson, L. E, "Pitch Rate Effects on Delta Wing Vortex Breakdown," Journal of Aircraft, Vol. 33, No. 2, March-April 1996.

75. Richardson, D. "F-16 Fighting Falcon", Arco Publishing, Inc., New York, 1983.

76. Ericsson, L. E., "Challenges in High-Alpha Vehicle Dynamics", Prog. Aerospace Sci., Vol. 13, No. 4 1995, pp. 291-334.

77. Ericsson, L. E. and Beyers, M. E., "On the Flat Spin of Axisymmetric Bodies," Journal of Aircraft, Vol. 32, Nov.-Dec. 1995, pp. 1205-1212.

78. Yoshinaga, T. and Tate, A., "Flat Spin of Axisymmetric Bodies Near the Critical Reynolds Number Region," private communication of unpublished results, Dec. 20, 1985.

79. Keener, E. R., Chapman, G. T., Cohen, L., and Taleghani, J., "Side Forces on Forebodies at High Angles of Attack and Mach Numbers from 0.1 to 0.7," NASA TMX-3437, Feb. 1977.

80. Coe, Jr., P. L., Chambers, J. R., and Letko, W., "Asymmetric Lateral-Directional Characteristics of Pointed Bodies of Revolution at High Angles of Attack," NASA TN D-7095 (1972).

81. Jahnke, C. C. and Culick, F. E. C., "Aplication of Bifurcation Theory to the High-Angle-of- Attack Dynamics of the F-14," J. Aircraft, Vol. 31, Jan.-Feb. 1994, pp. 26-34.

82. Thompson, M., "Tendency to Spin Caused Crash of 31 F-14s Navy Says," San Jose Mercury News, April 6, 1993, p. 6A.

83. Ng, T. T., Ong, L. Y., Suarez, C. J., and Malcolm, G. N.,"Wing Rock Suppression Using Forebody Vortex Control", AIAA Paper 91-3227-CP, Aug. 1991.

84. Penna, P.J., "Qualitative Investigation of a Generic Fighter Model in Radio-Controlled Gliding Flight", NRC LM-AA-003, National Research Council, Ottawa, July 1992.

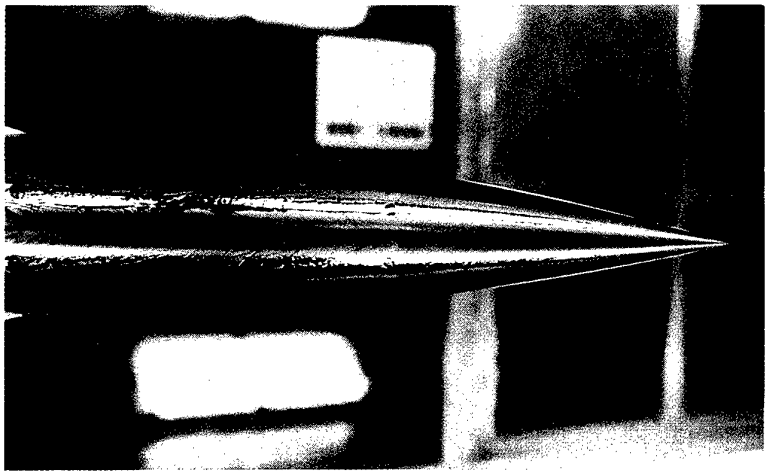

Fig A4.2.1 Near-symmetric forebody leeward flow pattern ($\alpha = 30°$)

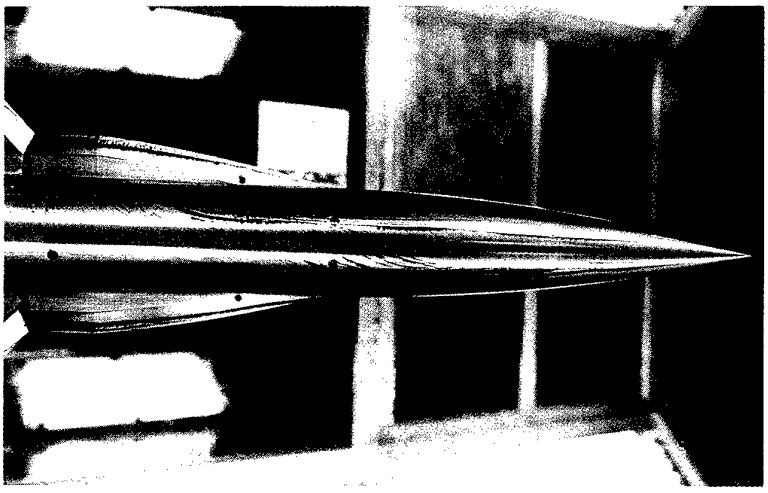

Fig A4.2.2 Asymmetric forebody leeward flow pattern ($\alpha = 39°$)

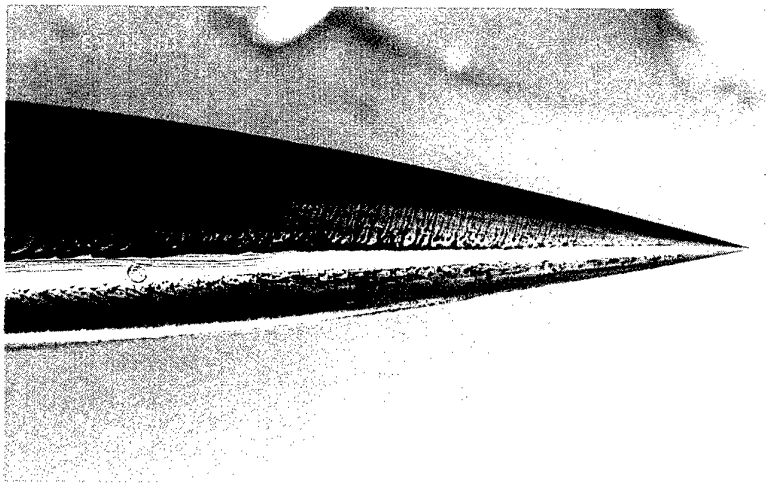

Fig A4.2.3 Forebody flow pattern at $\alpha = 41°$, $\phi_m = 90°$

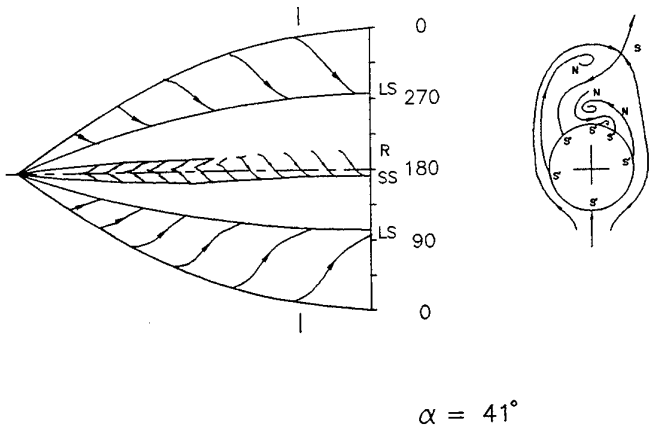

$\alpha = 41°$

Fig A4.2.4 Asymmetric vortex flow topology

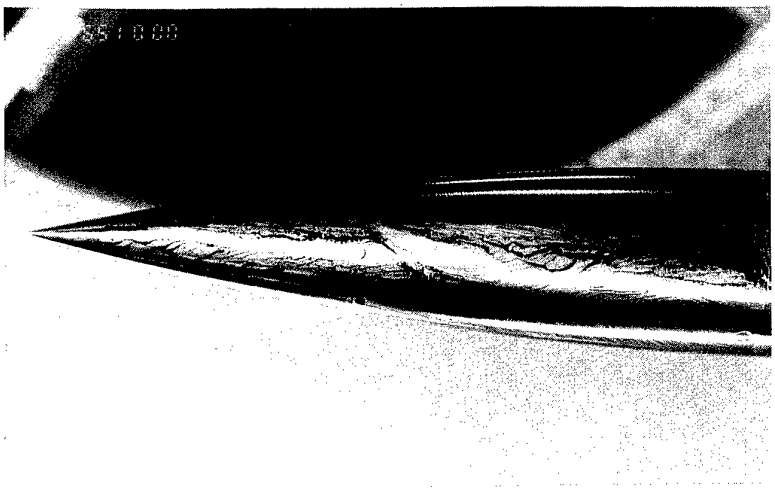

Fig A4.2.5 Forebody flow pattern at $\alpha = 46°$, $\phi_m = 292.5°$

Fig A4.2.6 Forebody flow pattern at $\alpha = 47°$, $\phi_m = 135°$

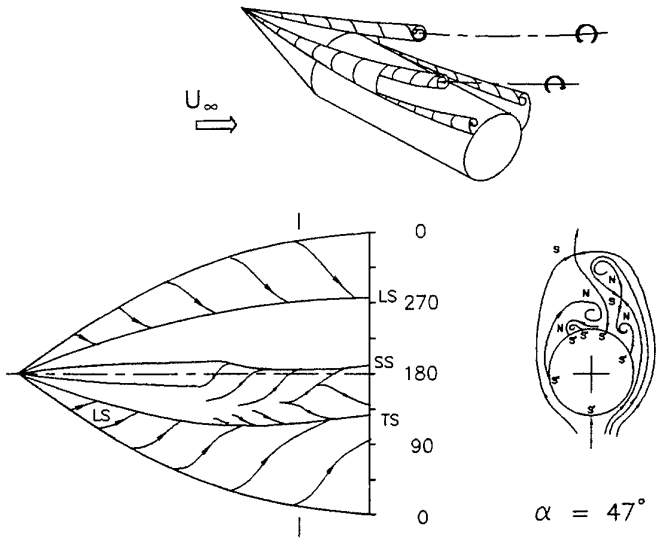

Fig A4.2.7 Asymmetric vortex flow with formation of second vortex pair

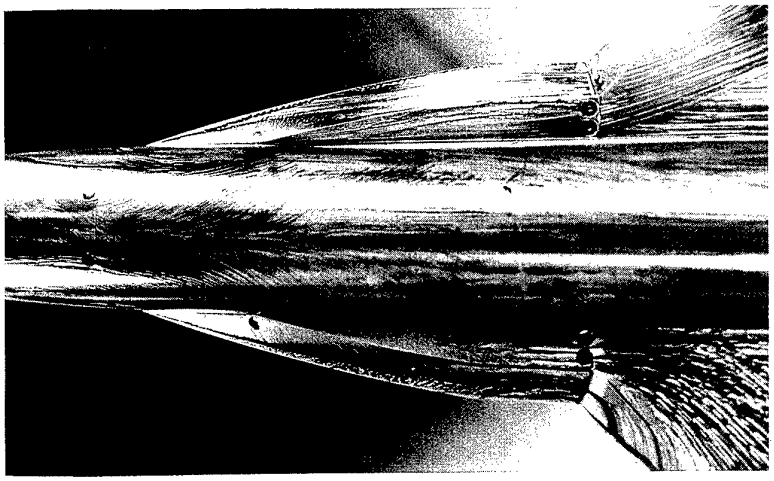

Fig A4.2.8 Forebody/LEX flow pattern at $\alpha = 49°$, $\phi_m = 180°$

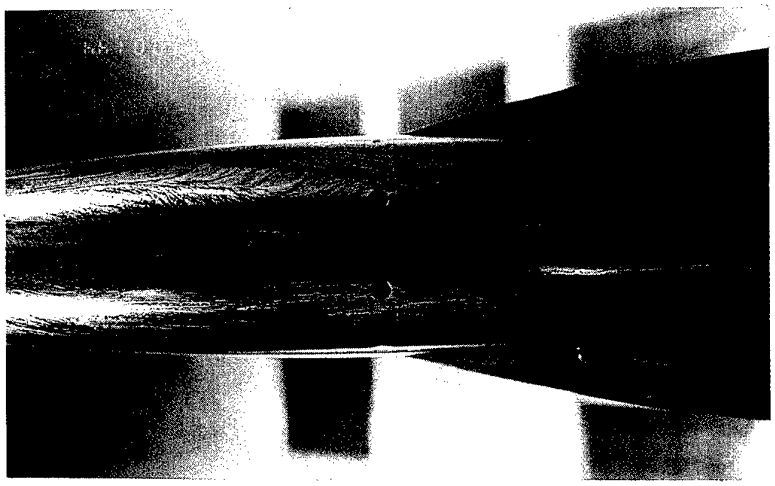

Fig A4.2.9 Forebody/LEX flow pattern at $\alpha = 51°$, $\phi_m = 180°$

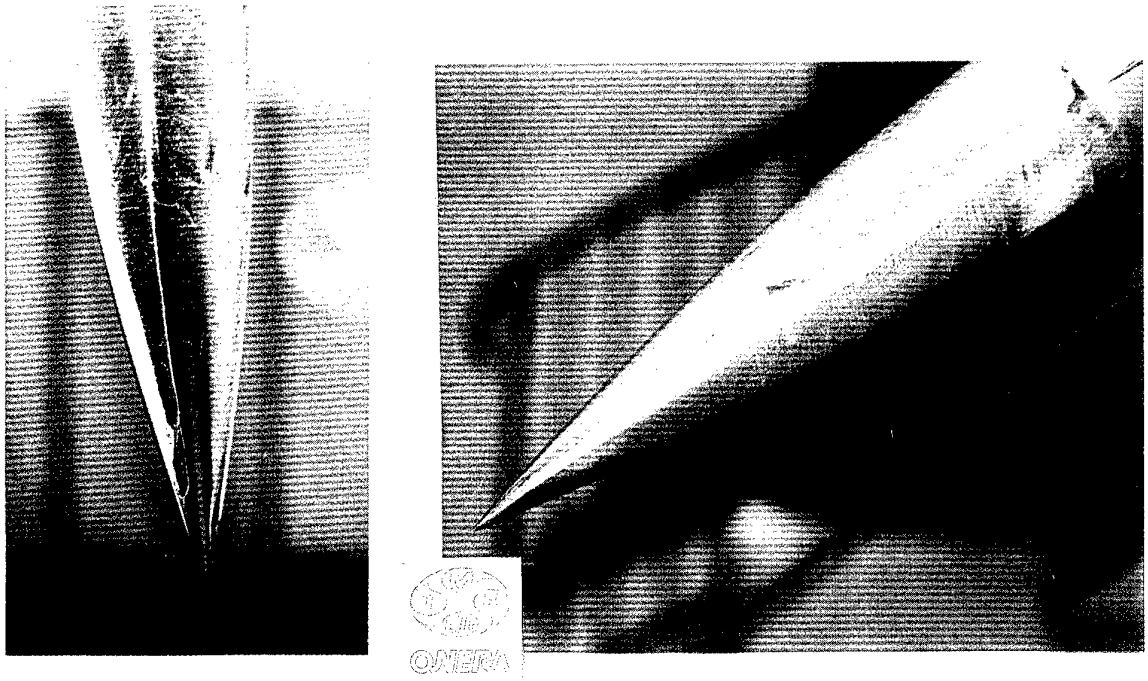

Fig A4.2.10 Oil flow visualization on BWLVH at $\alpha = 53°$

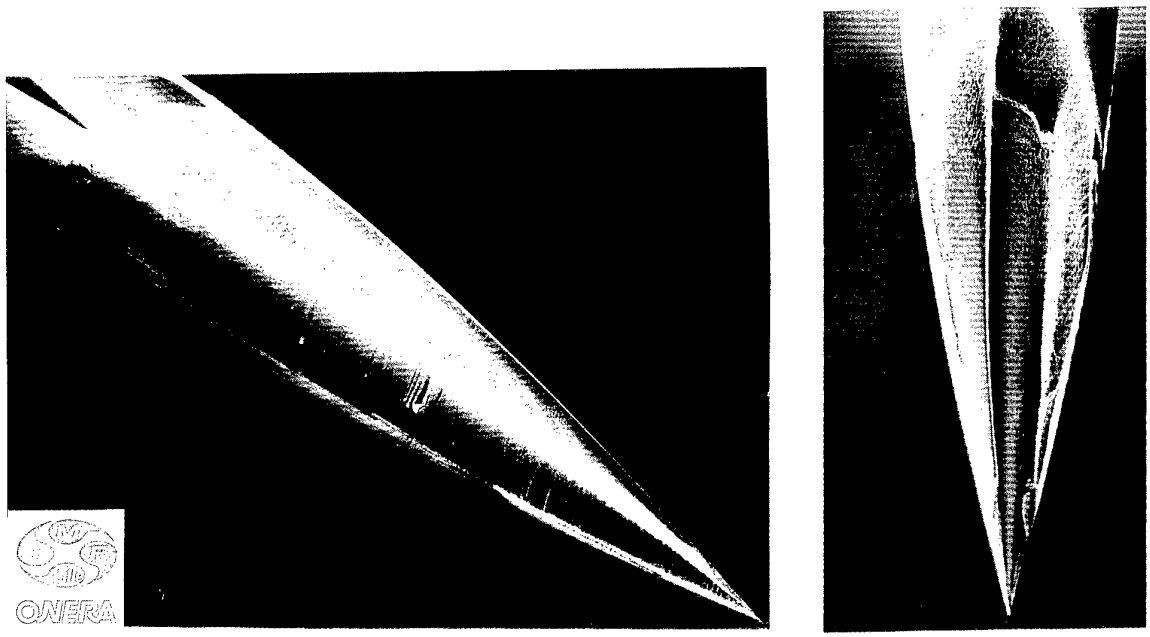

Fig A4.2.11 Oil flow visualization on BWLVHT at $\alpha = 53°$

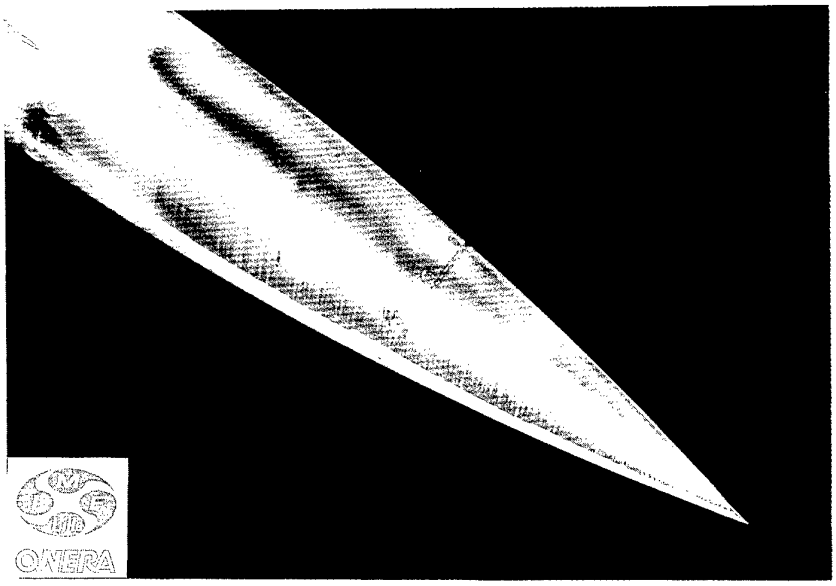

Fig A4.2.12 Acenaphtene visualization on BWLVHT at $\alpha = 53°$

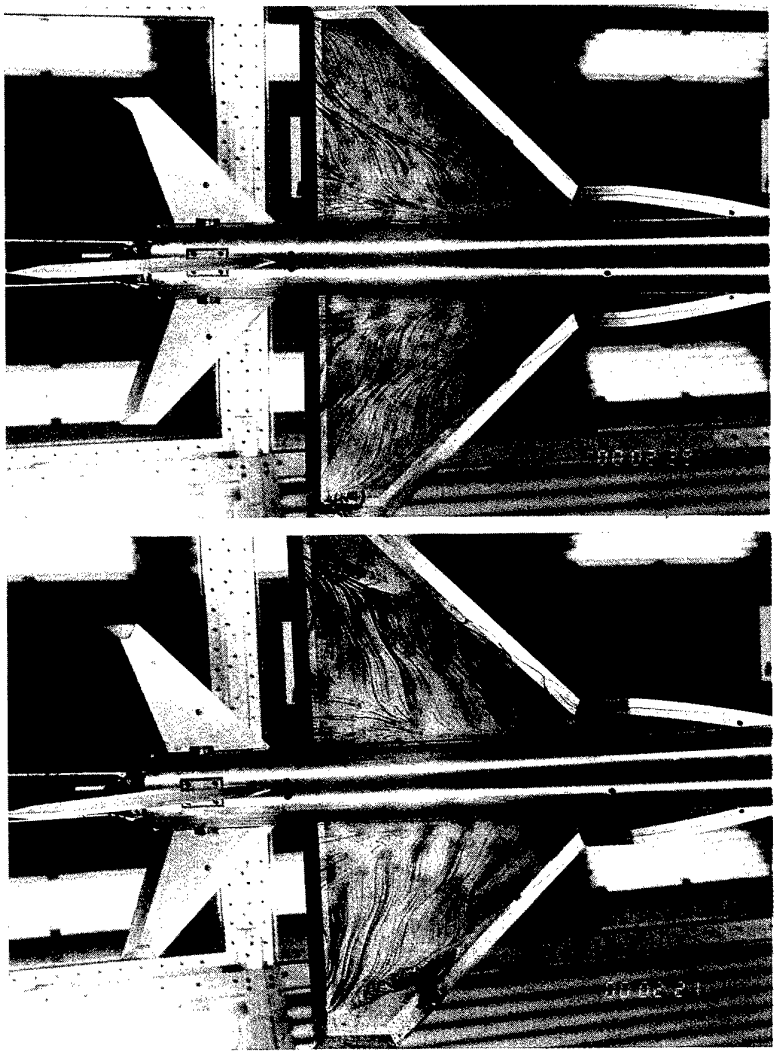

(a) $\alpha = 17°$

(b) $\alpha = 19°$

Fig A4.2.13 LEX/wing leeward flow pattern, U_∞=30 m/s

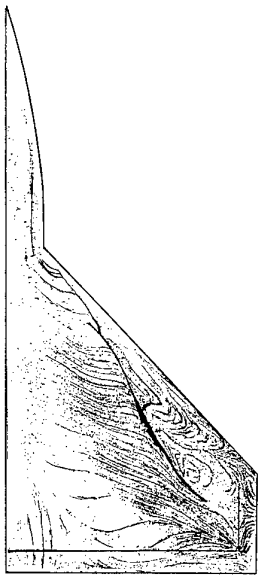

(a) Surface oil-flow pattern and laser sheet video image of LEX/wing

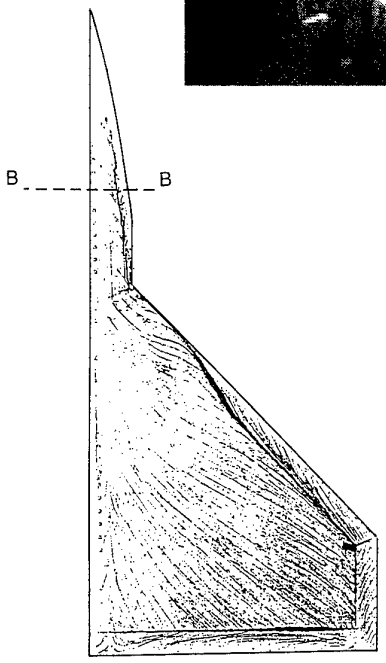

Fig A4.2.15 Surface oil-flow pattern and laser sheet video image of LEX/wing at $\alpha = 39°$, $U_\infty = 30$ m/s

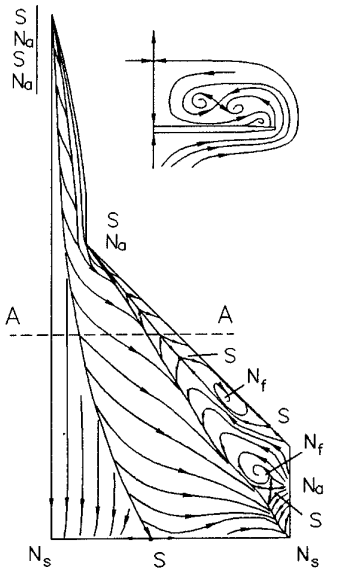

(b) Skin-friction line topology

Fig A4.2.14 BWLVH LEX/wing flow field at $\alpha = 20°$, $U_\infty = 30$ m/s

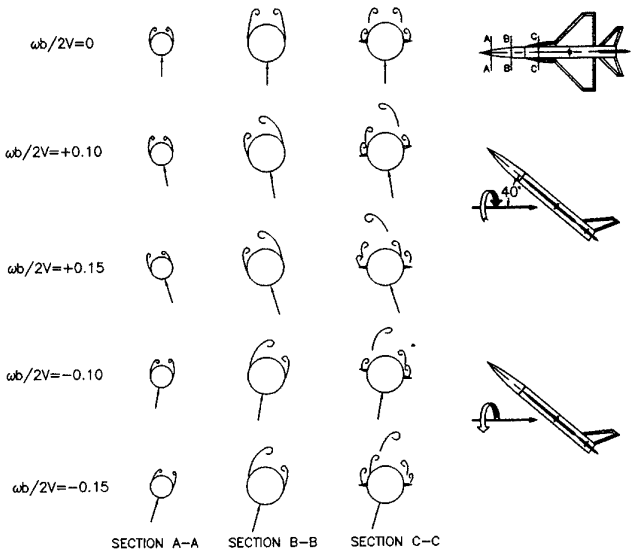

Fig A4.2.16 Analysis of flow visualization data in Fig 4.21

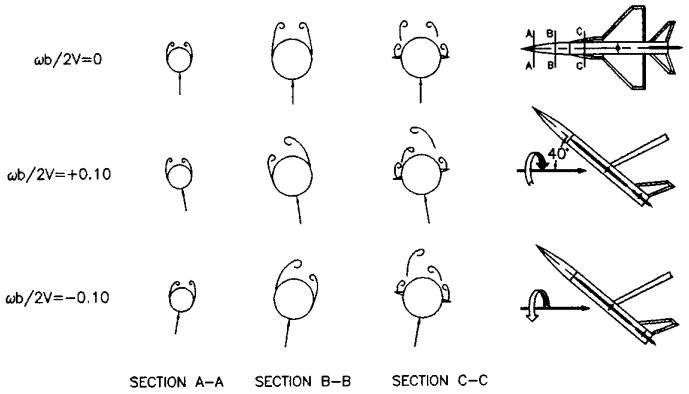

Fig A4.2.17 Analysis of flow visualization data in Fig 4.23

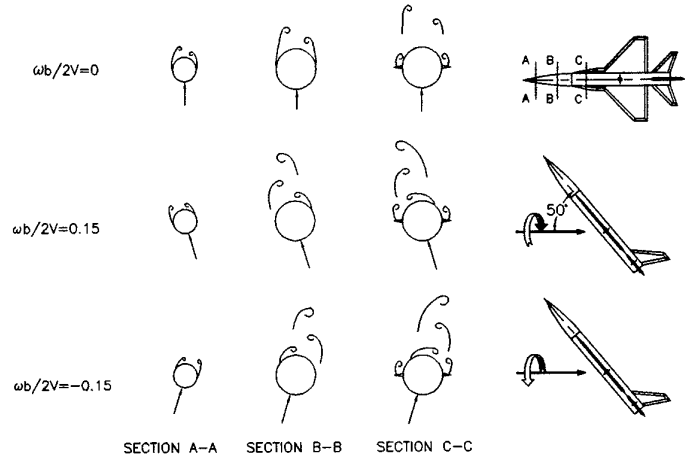

Fig A4.2.18 Analysis of flow visualization data in Fig 4.17a

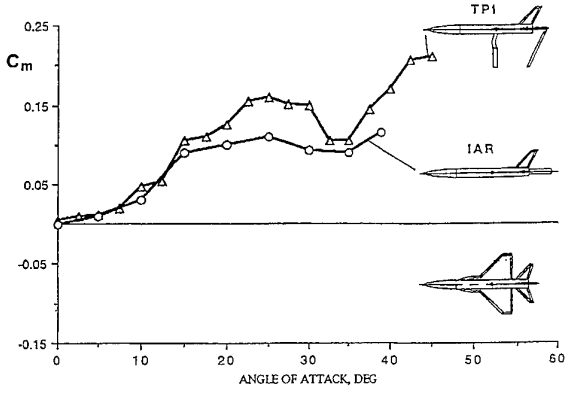

Fig A4.2.19 Strut-induced support interference

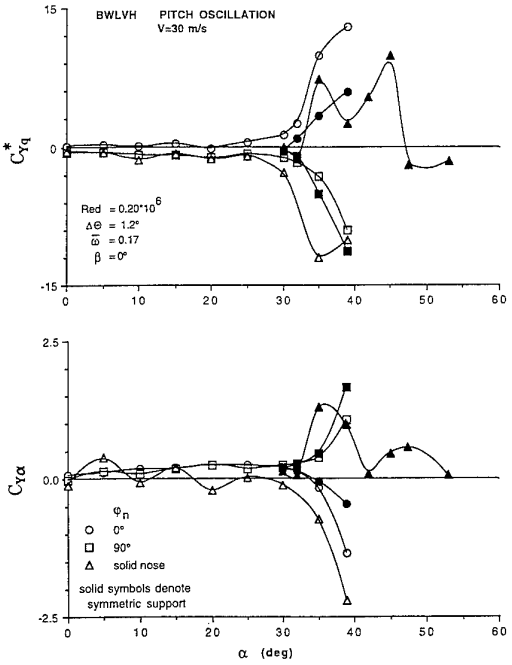

Fig A4.2.20 Effect of rotating nose tip on derivatives C_{Yq}^* and $C_{Y\alpha}$

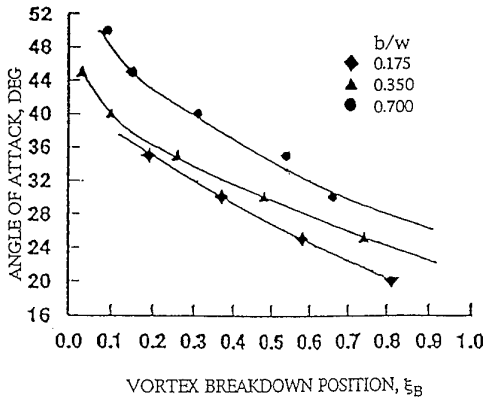

Fig A4.2.21 Wind tunnel wall interference effects on vortex breakdown of a 70 deg delta wing[23]

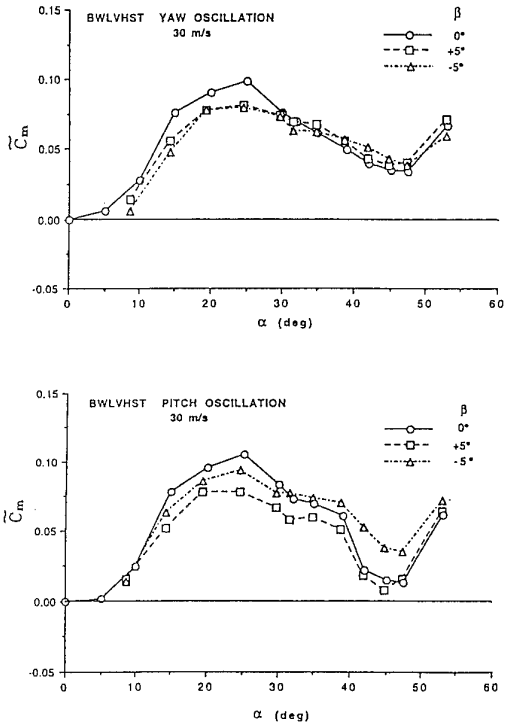

Fig A4.2.22 Effect of sideslip and motion on time-averaged pitching moment[2]

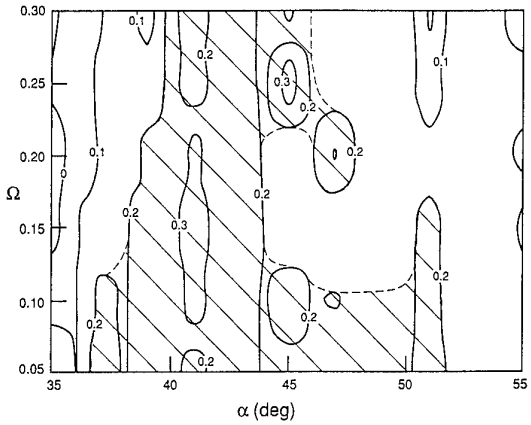

Fig A4.2.24 Incremental effect of support on vortex breakdown on coning cone-cylinder

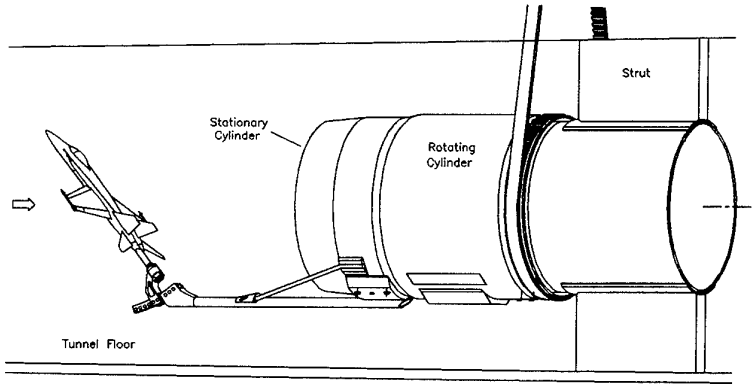

Fig A4.2.23 Orbital platform rotary apparatus

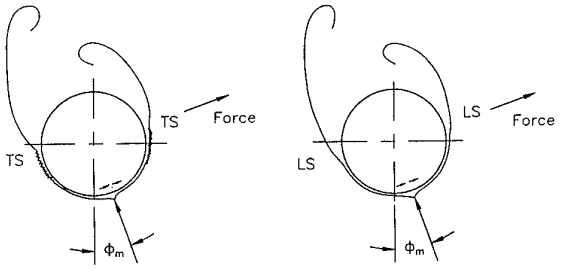

a. Turbulent crossflow b. Laminar crossflow

Fig A4.3.1 Crossflow characteristics of translating circular cross-section

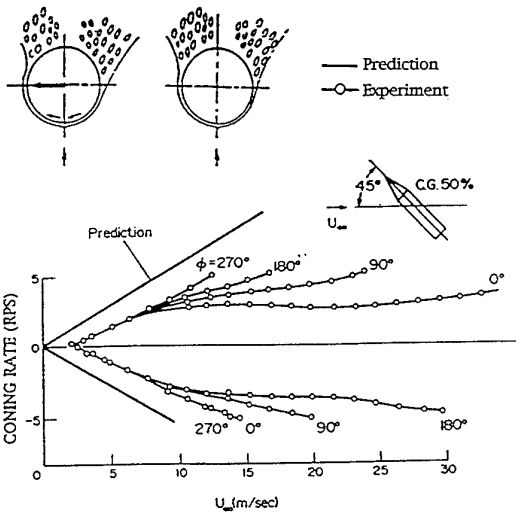

Fig A4.3.2 Coning characteristics of a pointed cone-cylinder body

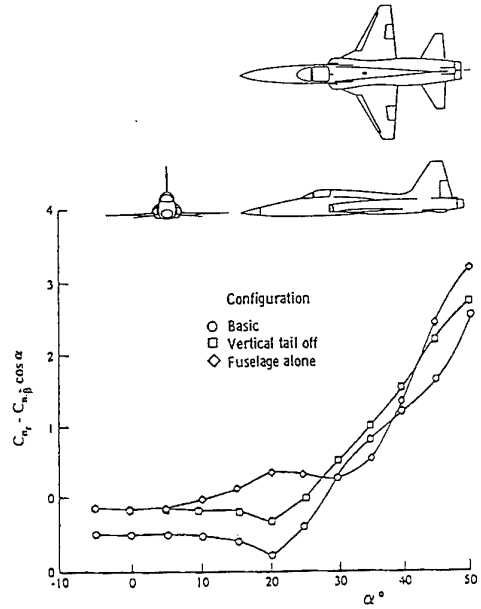

Fig A4.3.3 Yaw damping of advanced fighter aircraft model[35]

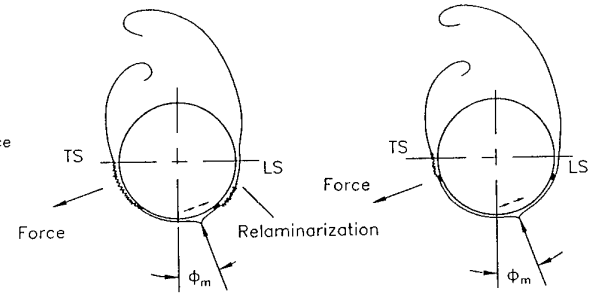

a. Trips at $\phi_t = \pm 40°$ b. Trips at $\phi_t = \pm 70°$

Fig A4.3.4 Crossflow characteristics of translating circular cross-section for laminar flow conditions

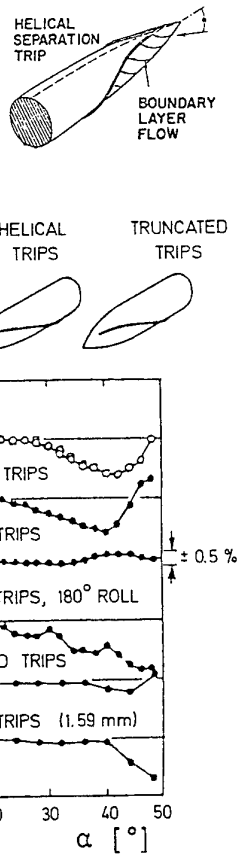

Fig A4.3.5 Effect of helical and straight body trips on side force of ogive-cylinder body[38]

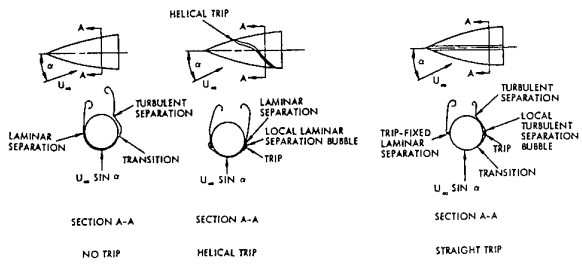

Fig A4.3.6 Conceptual effect of body trips on flow separation[13]

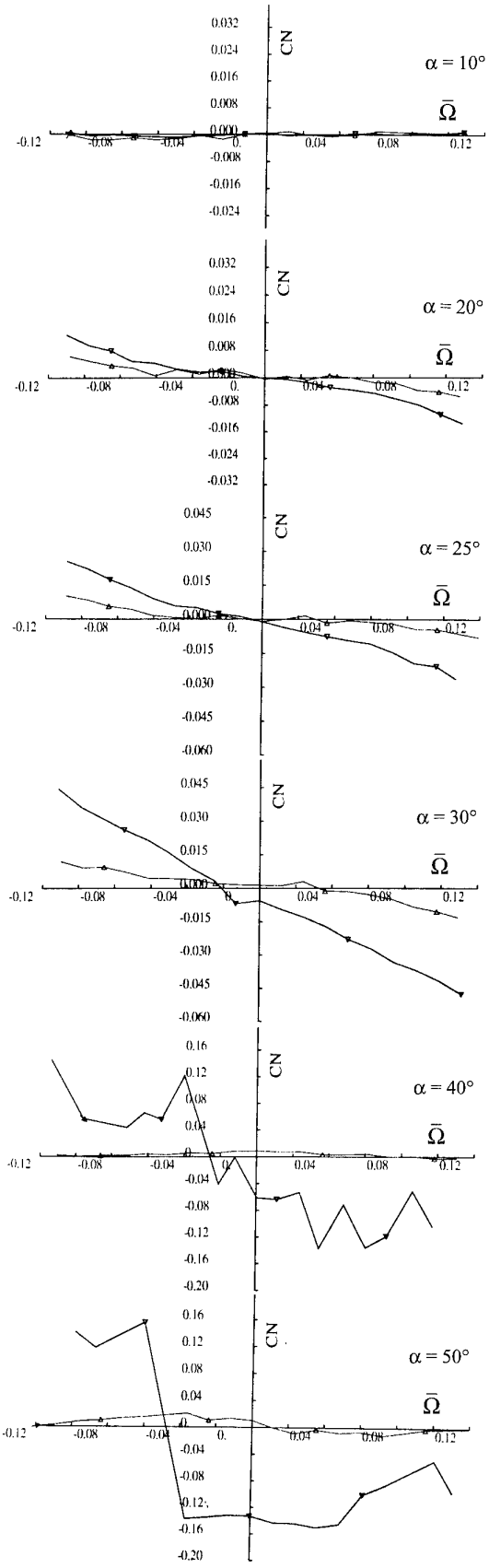

Fig A4.3.7 Effect of strakes and trips on $C_n(\Omega)$ characteristics for the AGARD WG16 model[40]

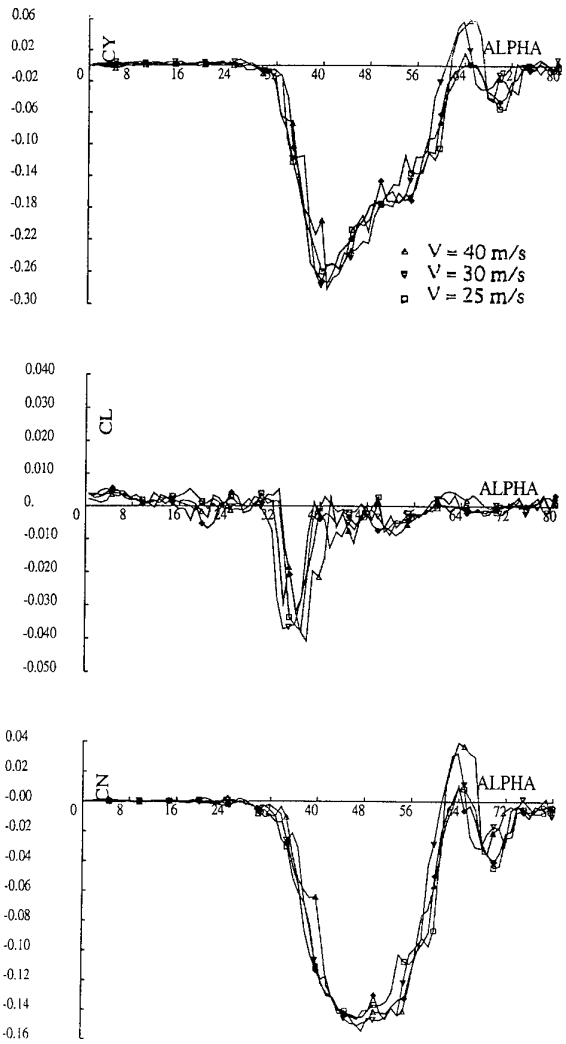

Fig. A4.3.8 Effect of Reynolds number on the lateral characteristics of the basic configuration (BC)[40]

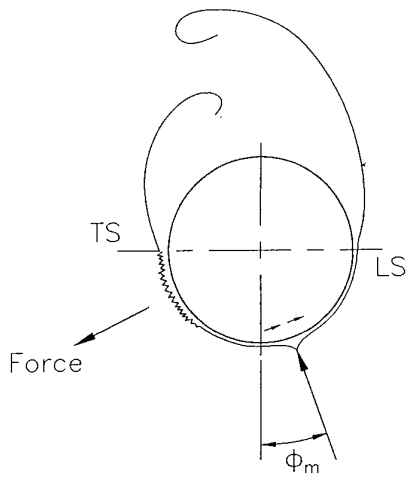

Fig A4.3.9 Crossflow geometry of translating circular cross-section at critical flow conditions

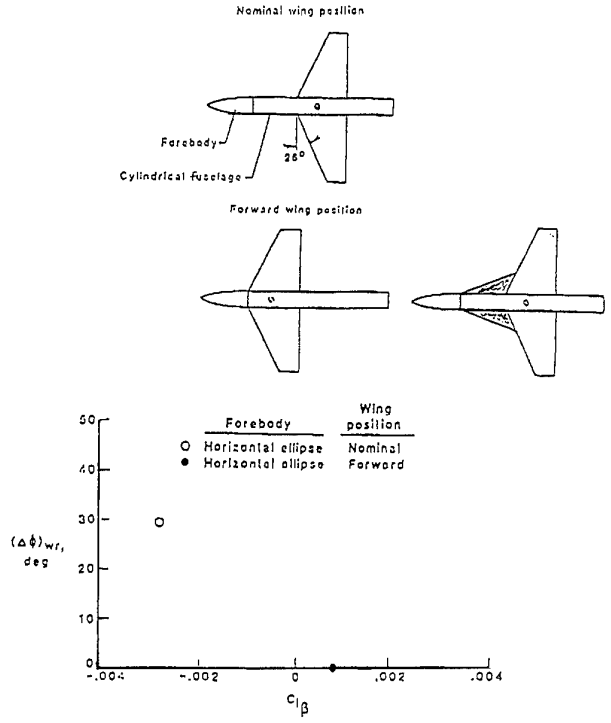

Fig A4.3.10 Effect of wing location on forebody-induced wing rock[42]

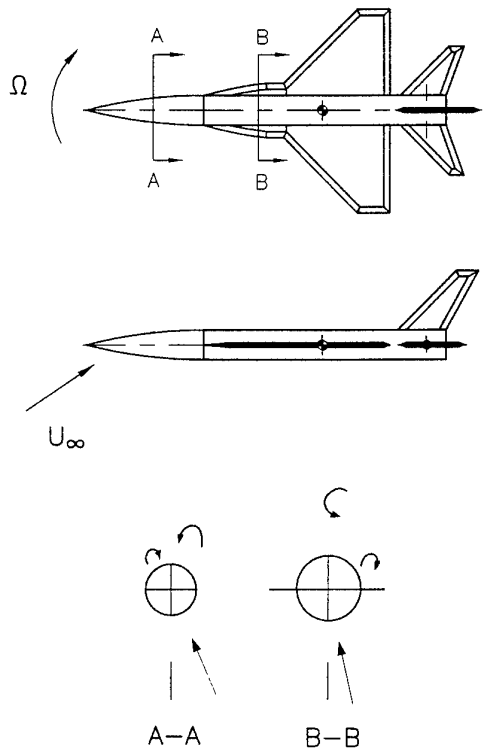

Fig A4.3.12 Forebody-LEX vortex interaction at $\Omega > 0$

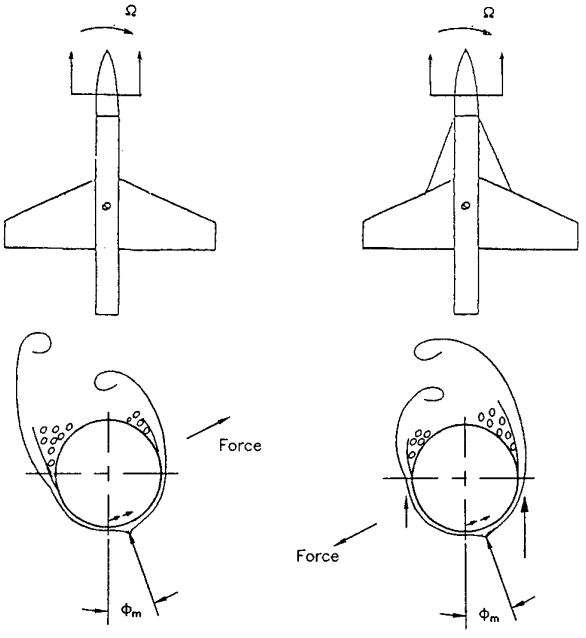

a. Without LEX

b. With LEX

Fig A4.3.11 Crossflow separation on a coning slender forebody

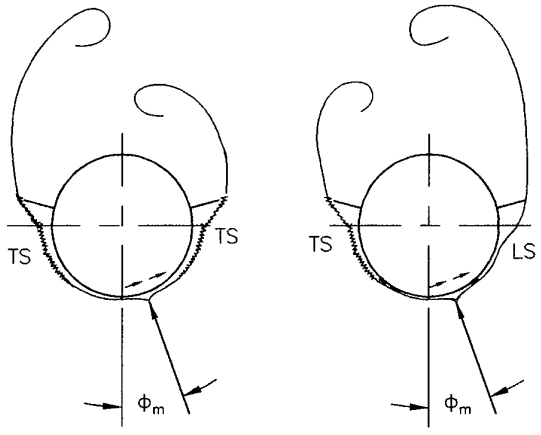

a. Turbulent incident crossflow without trips

b. Laminar incident crossflow with trips

Fig A4.3.13 Crossflow characteristics of translating circular cross-section with strakes

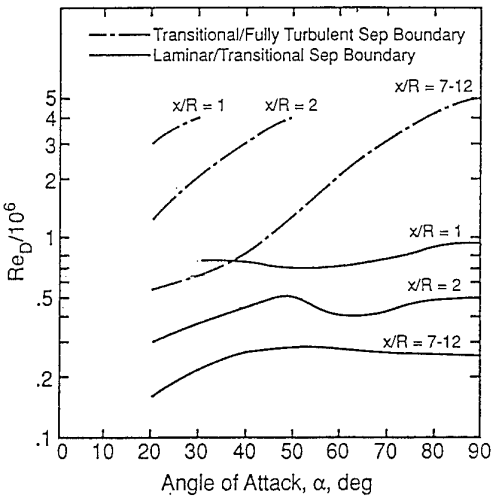

Fig A4.4.1 Critical Reynolds number boundaries on ogive nose (from Lamont, 1985)

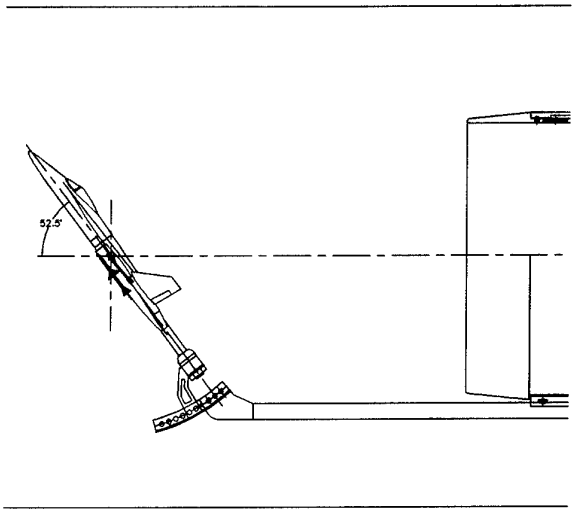

Fig A4.4.4 OPLEC support system at α = 52.5°

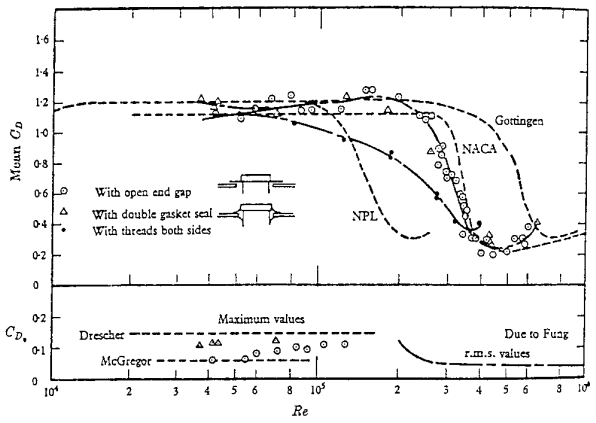

Fig A4.4.2 Mean and oscillating drag coefficient vs Reynolds number for circular cylinder[50]

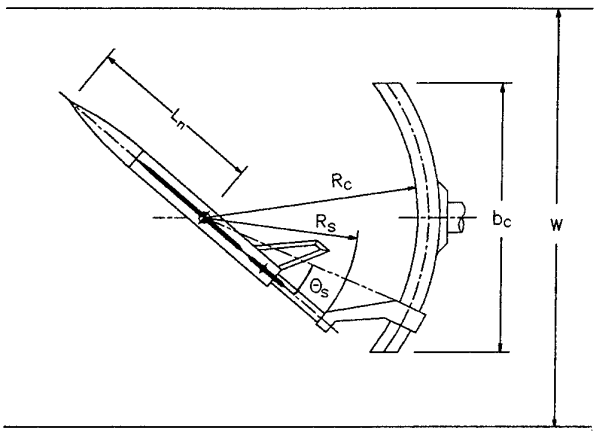

Fig A4.4.3 Schematic of test installation

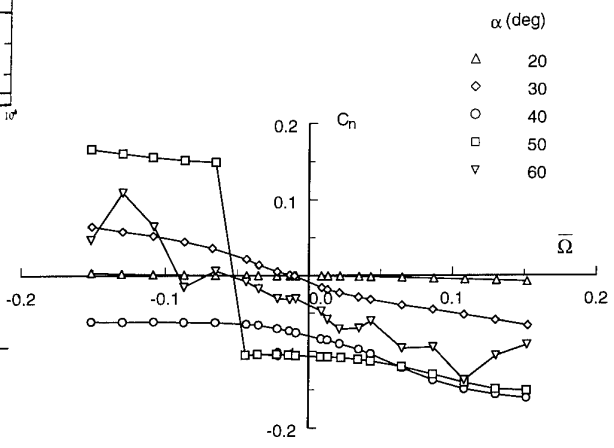

Fig A4.4.5 Body-alone characteristics at $Re_d = 0.3 \times 10^6$

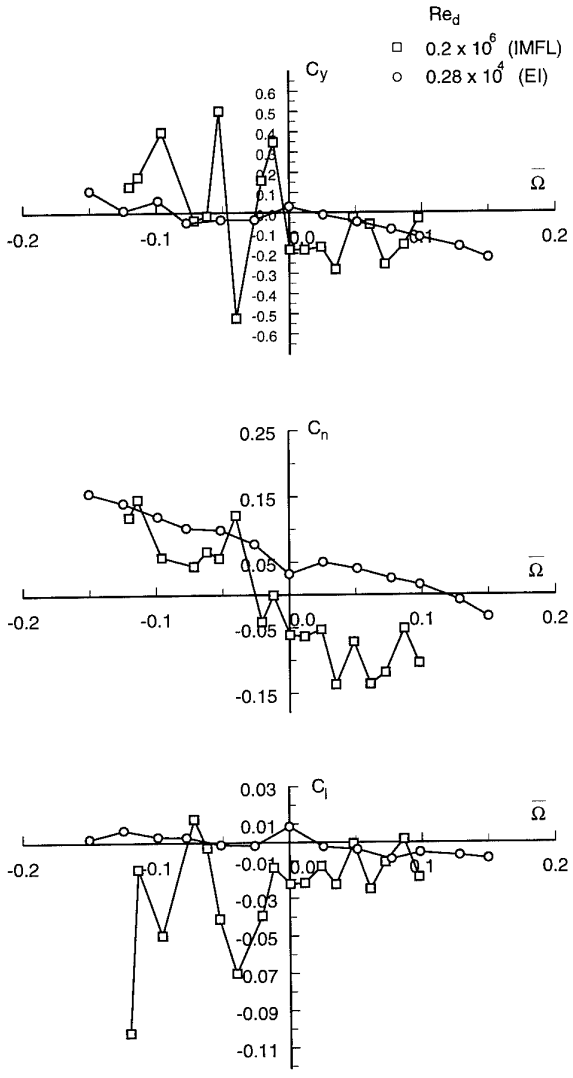

Fig A4.4.6 Rotary data on BWLVH at $\alpha = 40°$ and subcritical conditions

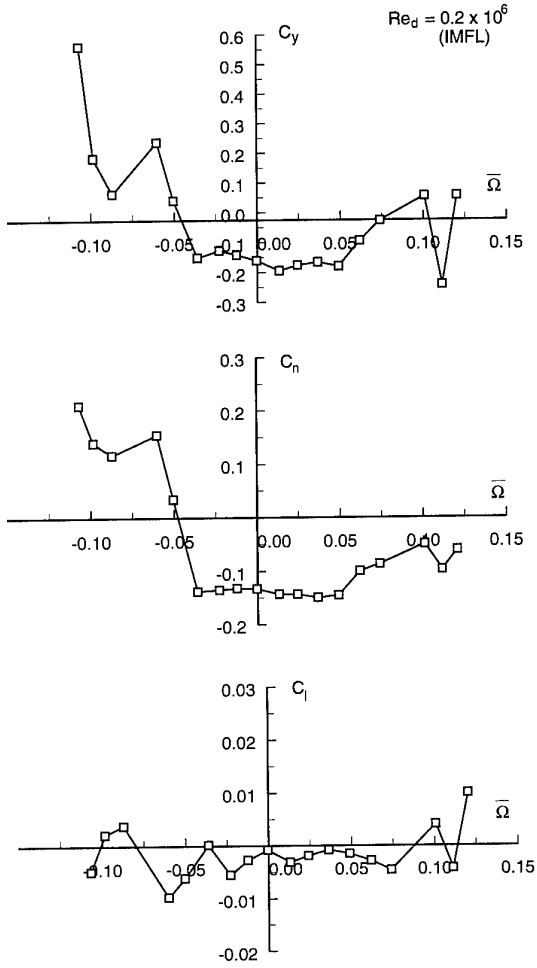

Fig A4.4.7 Rotary data on BWLVH at $\alpha = 50°$ and subcritical conditions

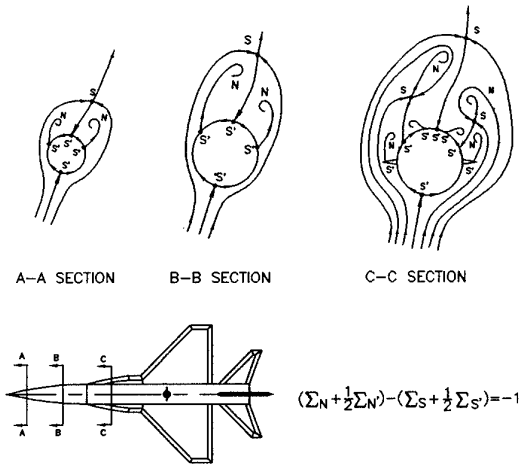

Fig A4.4.8 Crossflow topology on BWLVH at $\alpha = 40°$, $\Omega = -0.15$: flow state A

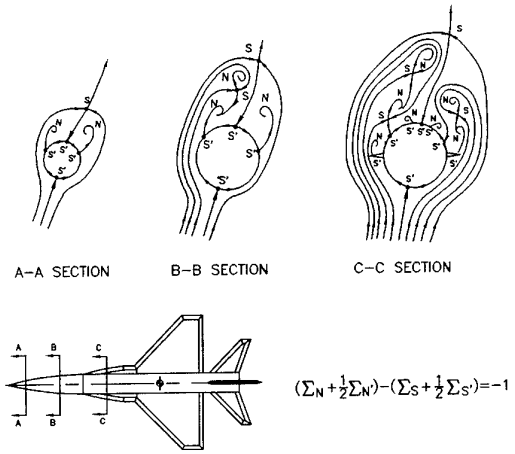

Fig A4.4.9 Crossflow topology on BWLVH at $\alpha = 40°$, $\Omega = -0.15$: flow state B

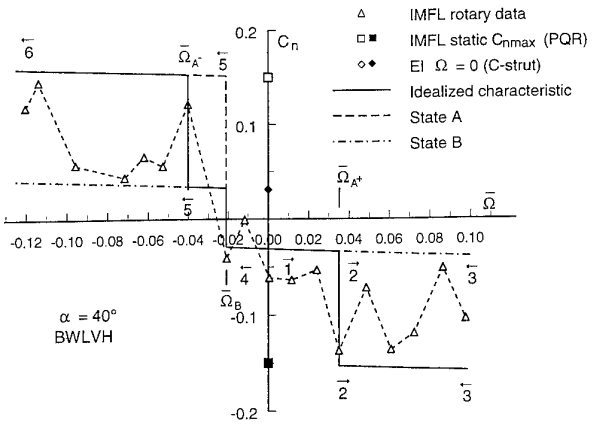

Fig A4.4.12 Interpretation of rotary characteristics of baseline configuration

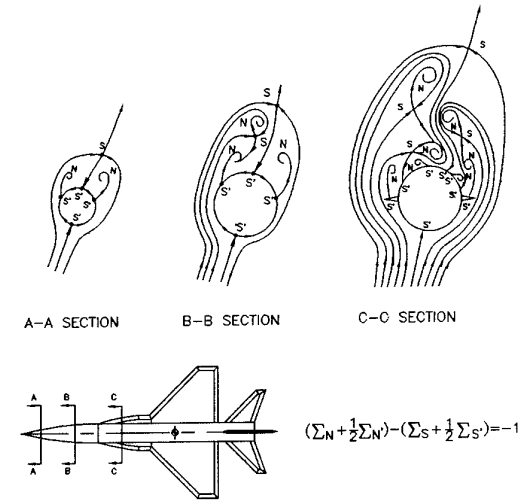

Fig A4.4.10 Crossflow topology on BWLVH at $\alpha = 50°$, $\Omega = -0.15$: flow state C

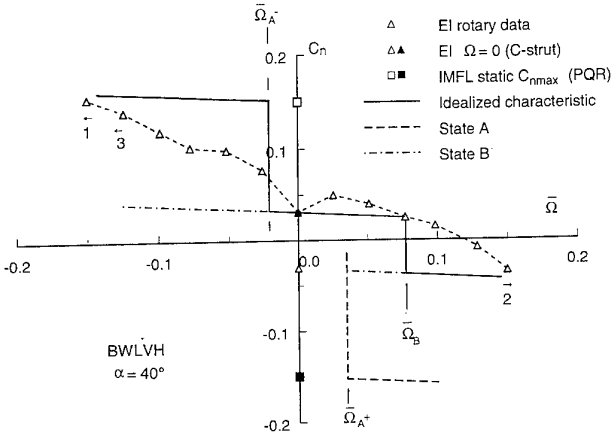

Fig A4.4.13 Interpretation of water tunnel rotary data at $\alpha = 40°$

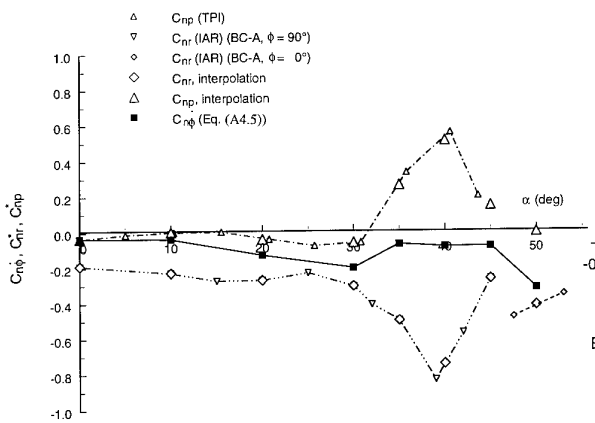

Fig A4.4.11 Evaluation of identity, Eq. (A4.5)

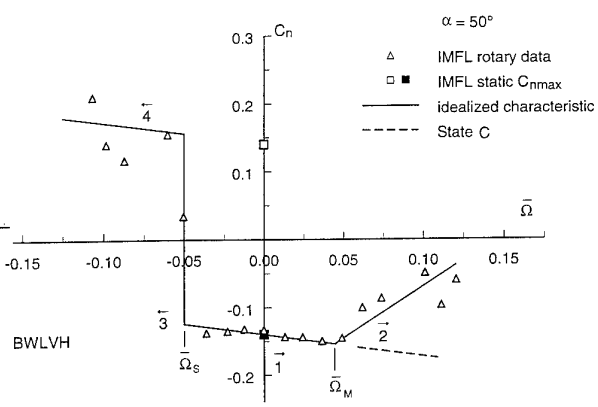

Fig A4.4.14 Interpretation of rotary data for baseline configuration ($\alpha = 50°$)

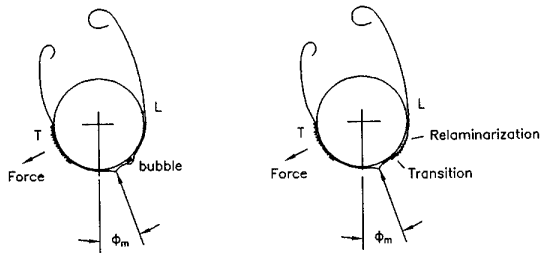

a. Flow state E b. Flow state F

Fig A4.4.15 Forebody crossflow conditions on BWLVHT in laminar incident flow

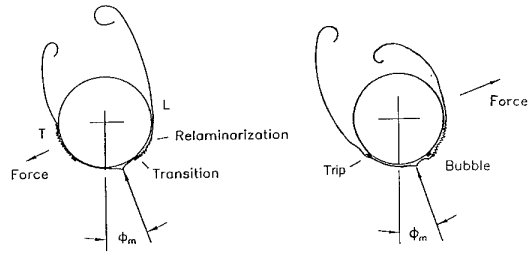

a. Flow state G b. Flow state H

Fig A4.4.16 Forebody crossflow conditions on BWLVHT with support interference in transitional incident flow

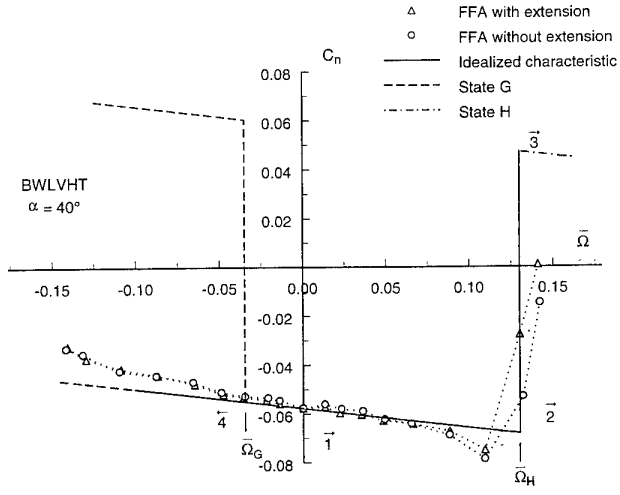

Fig A4.4.17 Interpretation of rotary data on BWLVHT (Fig 3.46)

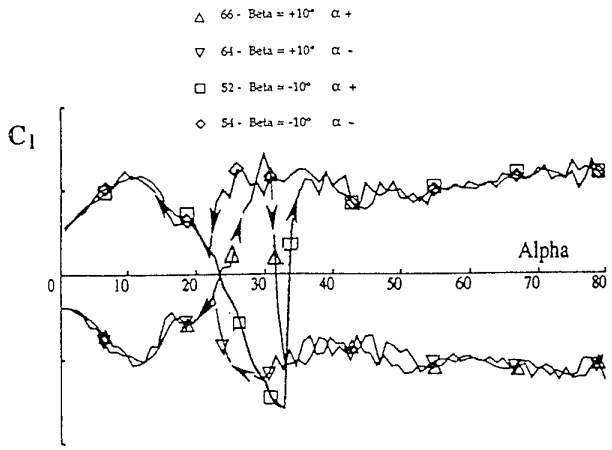

Fig A4.4.18 Effect of sideslip on $C_l(\alpha)$ for BWLVHST

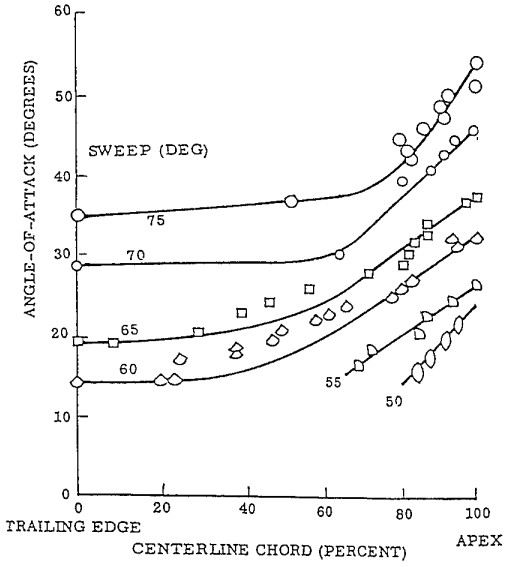

Fig A4.4.19 Effect of leading-edge sweep on delta wing vortex breakdown

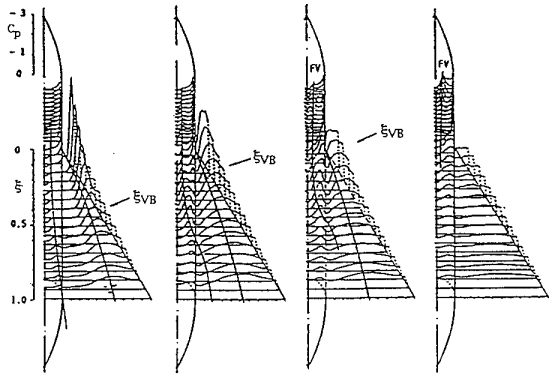

a. $\alpha = 19.3°$ b. $\alpha = 29.1°$ c. $\alpha = 34.1°$ d. $\alpha = 39.1°$

Fig A4.4.20 Three-dimensional stall of a delta-wing-body configuration[64]

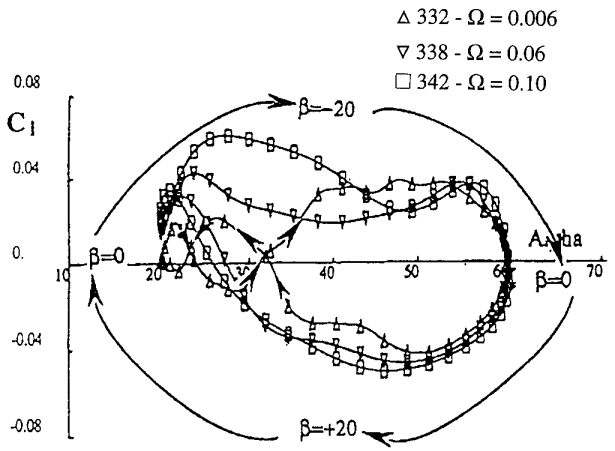

Fig A4.4.21 Effect of coning rate on $C_l(\alpha)$ for BWLVHST

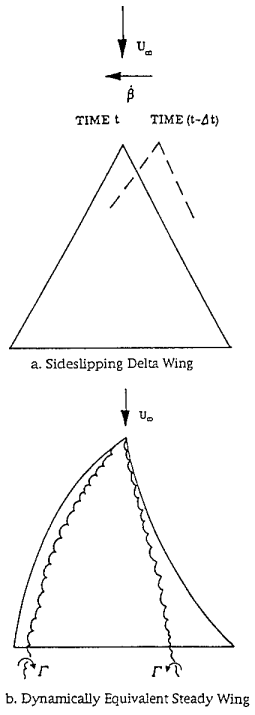

Fig A4.4.22 Effect of yaw rate on quasi-steady leading-edge geometry

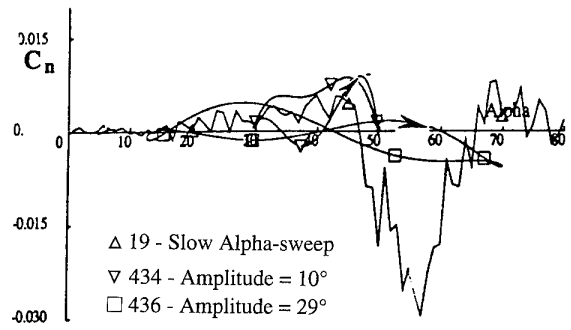

Fig A4.4.23 Effect of large-amplitude oscillations on $C_n(\alpha)$ for BWLVHST

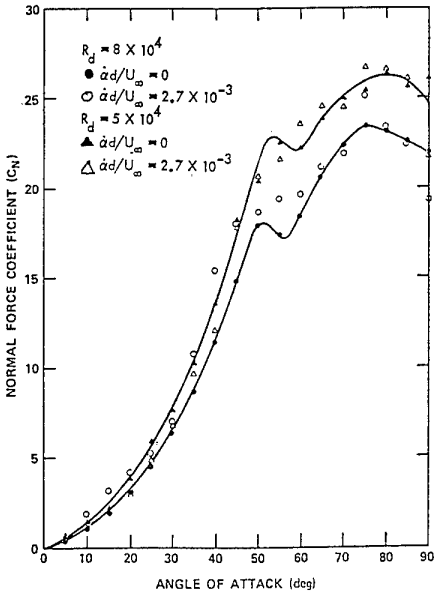

Fig A4.4.24 Pitch rate effect on ogive-cylinder normal force at critical flow conditions[67]

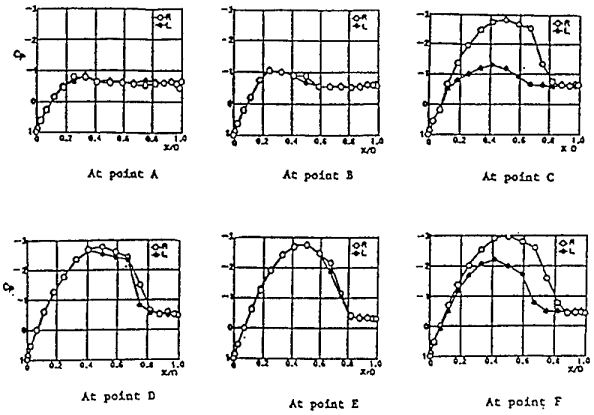

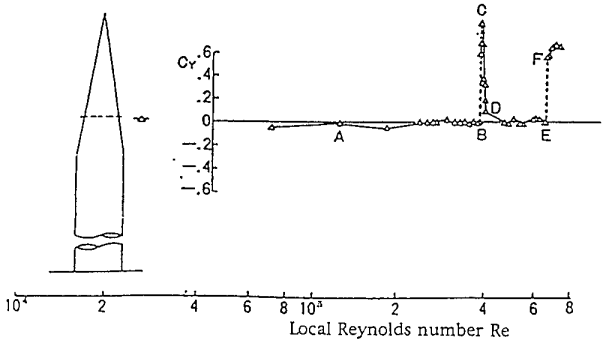

Fig A4.4.25 Cross-sectional pressure distribution on a 5.4 deg cone-cylinder at α = 90 deg[70]

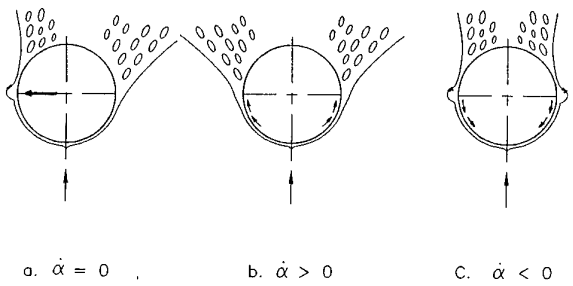

Fig A4.4.26 Conceptual effect of pitch rate on crossflow separation at $\alpha > 46°$

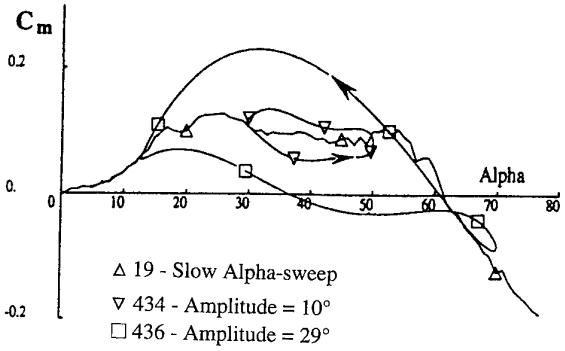

Fig A4.4.27 Effect of large-amplitude pitch oscillations on $C_{in}(\alpha)$ for BWLVHST

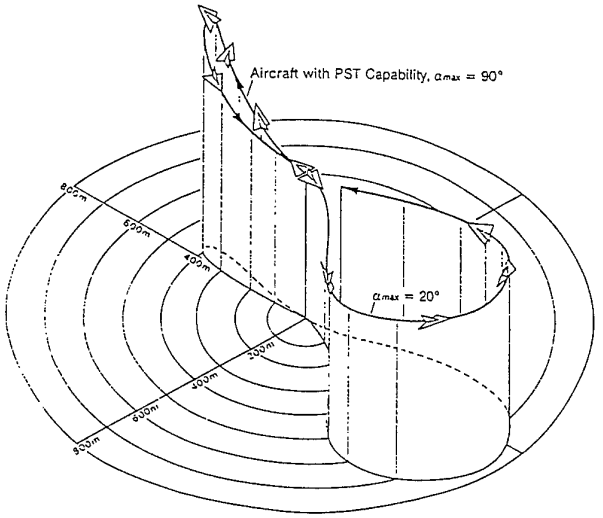

Fig A4.5.1 The Herbst manoeuvre[71]

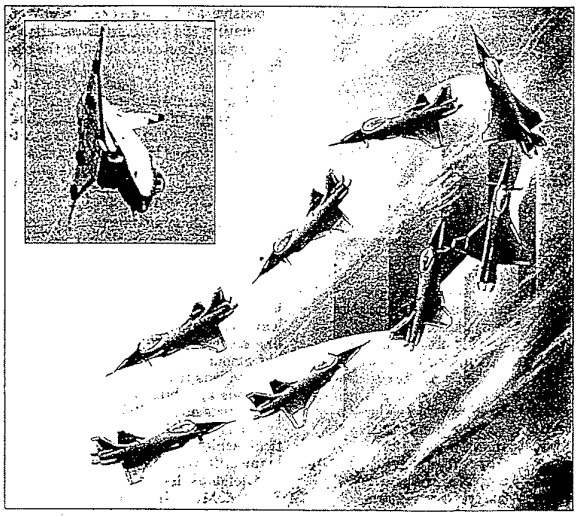

Fig A4.5.2 X-31 performing the Herbst manoeuvre[73]

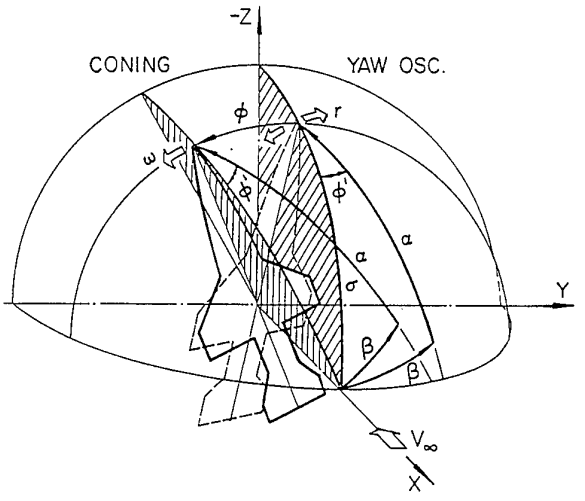

Fig A4.5.3 Relationships between characteristic motions

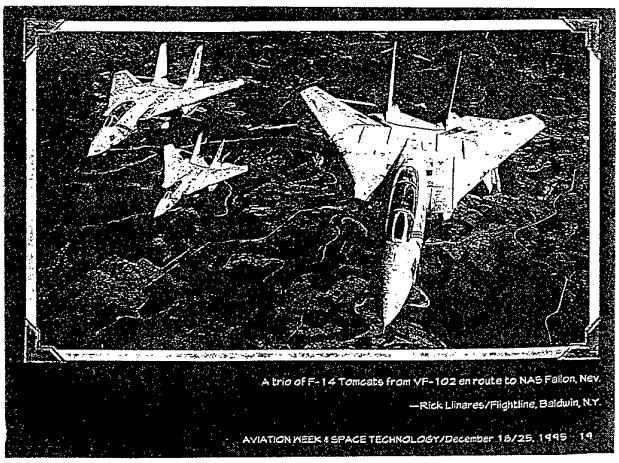

Fig A4.5.4 F-14 Tomcat

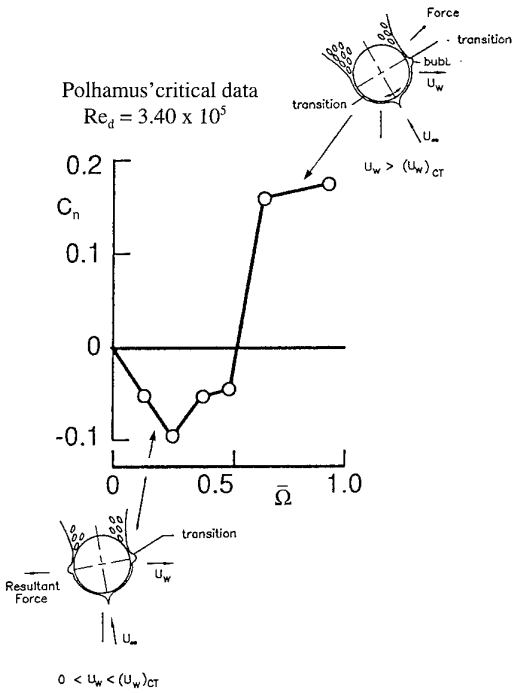

Fig A4.5.7 Flat-spin yawing moment at critical flow conditions[46]

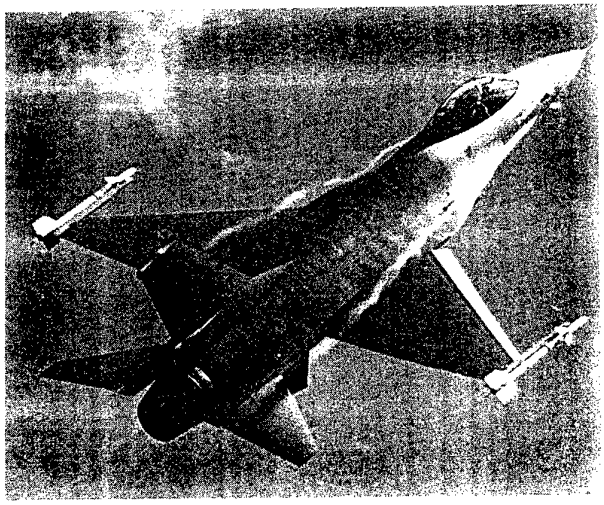

Fig A4.5.5 F-16 Fighting Falcon[75]

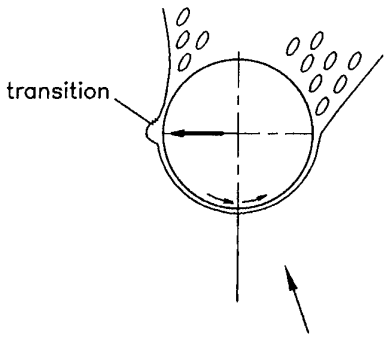

Fig A4.5.6 Subcritical/critical separation on a circular cross-section moving to the right

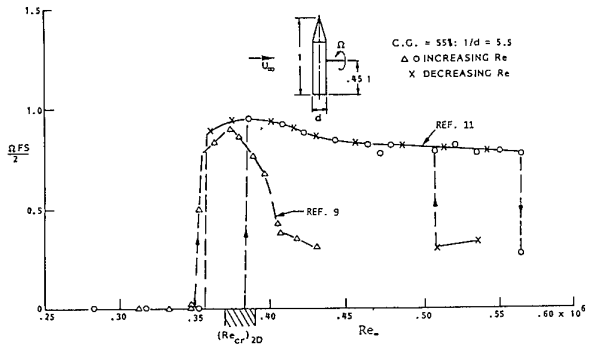

Fig A4.5.8 Flat spin characteristics of cone-cylinder[78]

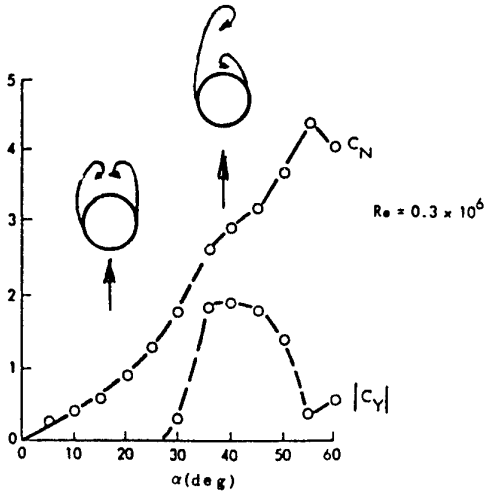

Fig A4.5.9 Effect of crossflow separation asymmetry on C_Y and C_N of a 5-caliber tangent-ogive[79]

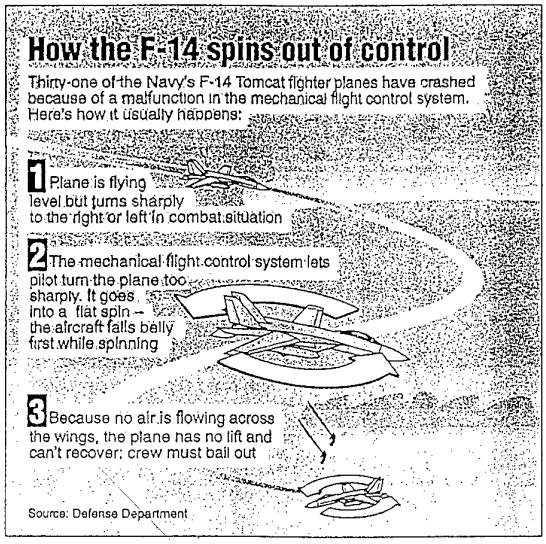

Fig A4.5.10 Flat spin of the F-14 aircraft[82]

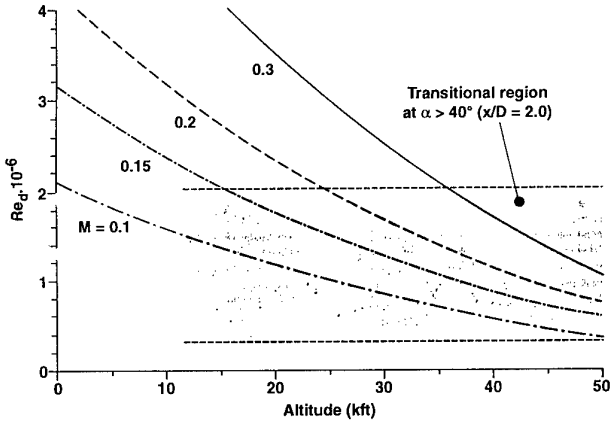

Fig A4.5.11 Typical forebody crossflow Reynolds number in full-scale flight

REPORT DOCUMENTATION PAGE

1. Recipient's Reference	2. Originator's Reference	3. Further Reference	4. Security Classification of Document
	AGARD-AR-305	ISBN 92-836-1043-1	UNCLASSIFIED/ UNLIMITED

5. Originator Advisory Group for Aerospace Research and Development
North Atlantic Treaty Organization
7 rue Ancelle, 92200 Neuilly-sur-Seine, France

6. Title
Cooperative Programme on Dynamic Wind Tunnel Experiments for Manoeuvring Aircraft

7. Presented at/sponsored by

8. Author(s)/Editor(s)	9. Date
Multiple	October 1996
10. Author's/Editor's Address	**11. Pages**
Multiple	248

12. Distribution Statement There are no restrictions on the distribution of this document. Information about the availability of this and other AGARD unclassified publications is given on the back cover.

13. Keywords/Descriptors

Wind tunnels
Fighter aircraft
Wind tunnel tests
Flow visualization
Dynamic tests
Pressure measurement
NATO
Aerodynamics
Flight maneuvers
Reliability
Models
Mathematical models
International cooperation

14. Abstract

This report presents the results of a multinational cooperative programme on Dynamic Wind Tunnel Experiments for Manoeuvring Aircraft. The program consisted of a series of dynamic experiments on models of a schematic combat aircraft configuration and of two generic aircraft forebodies. Ten wind tunnels in seven countries were involved. The dynamic tests included oscillatory, and in one case oscillatory-coning experiments. In several facilities, this was complemented by static and, in some cases, also dynamic flow visualization experiments in water tunnels. The forebody experiments included extensive surface pressure measurements under rotary conditions, carried out in a pressurized wind tunnel. The reliability of current test techniques was examined; and an expanded data base for dynamic data at high angles of attack is presented.

This report presents the results of work conducted by Working Group 16 of the AGARD Fluid Dynamics Panel.